

JULY 2020

**AJNR**

VOLUME 41 • PP 1135–1326

# AJNR

## AMERICAN JOURNAL OF NEURORADIOLOGY

JULY 2020  
VOLUME 41  
NUMBER 7  
WWW.AJNR.ORG

THE JOURNAL OF DIAGNOSTIC AND  
INTERVENTIONAL NEURORADIOLOGY

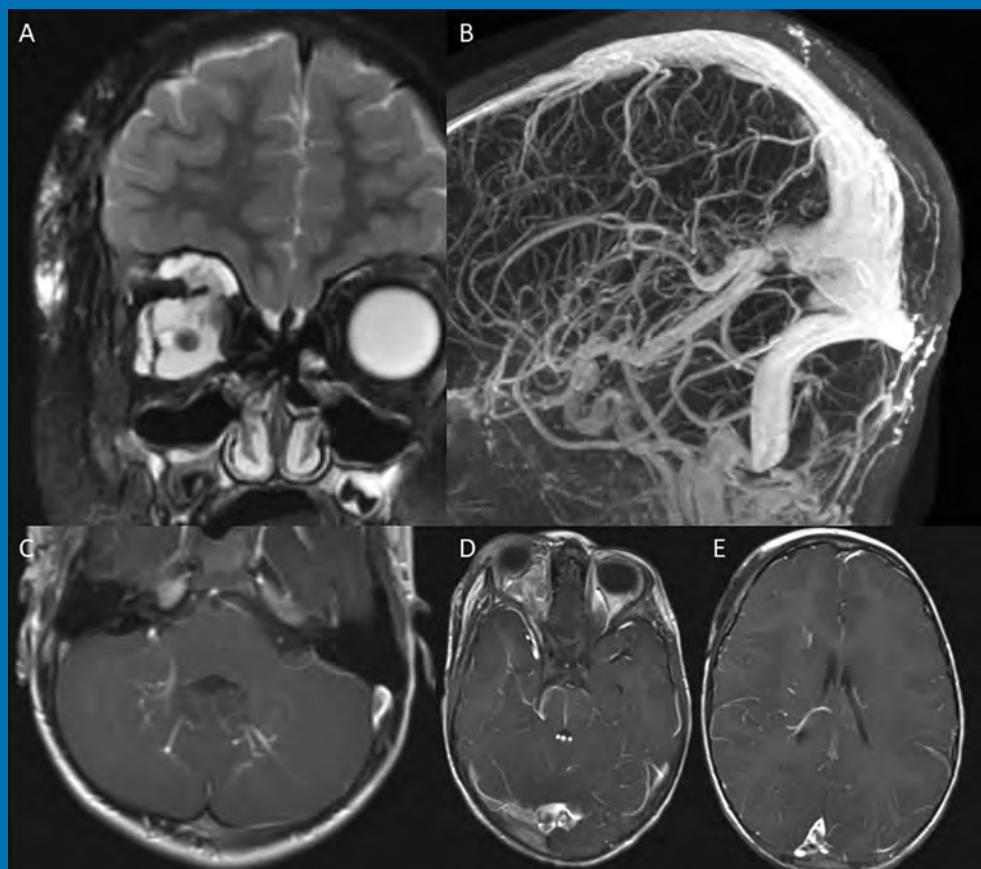
Cerebrovascular disease in COVID-19

Cervicofacial venous malformations associated with developmental  
venous anomalies

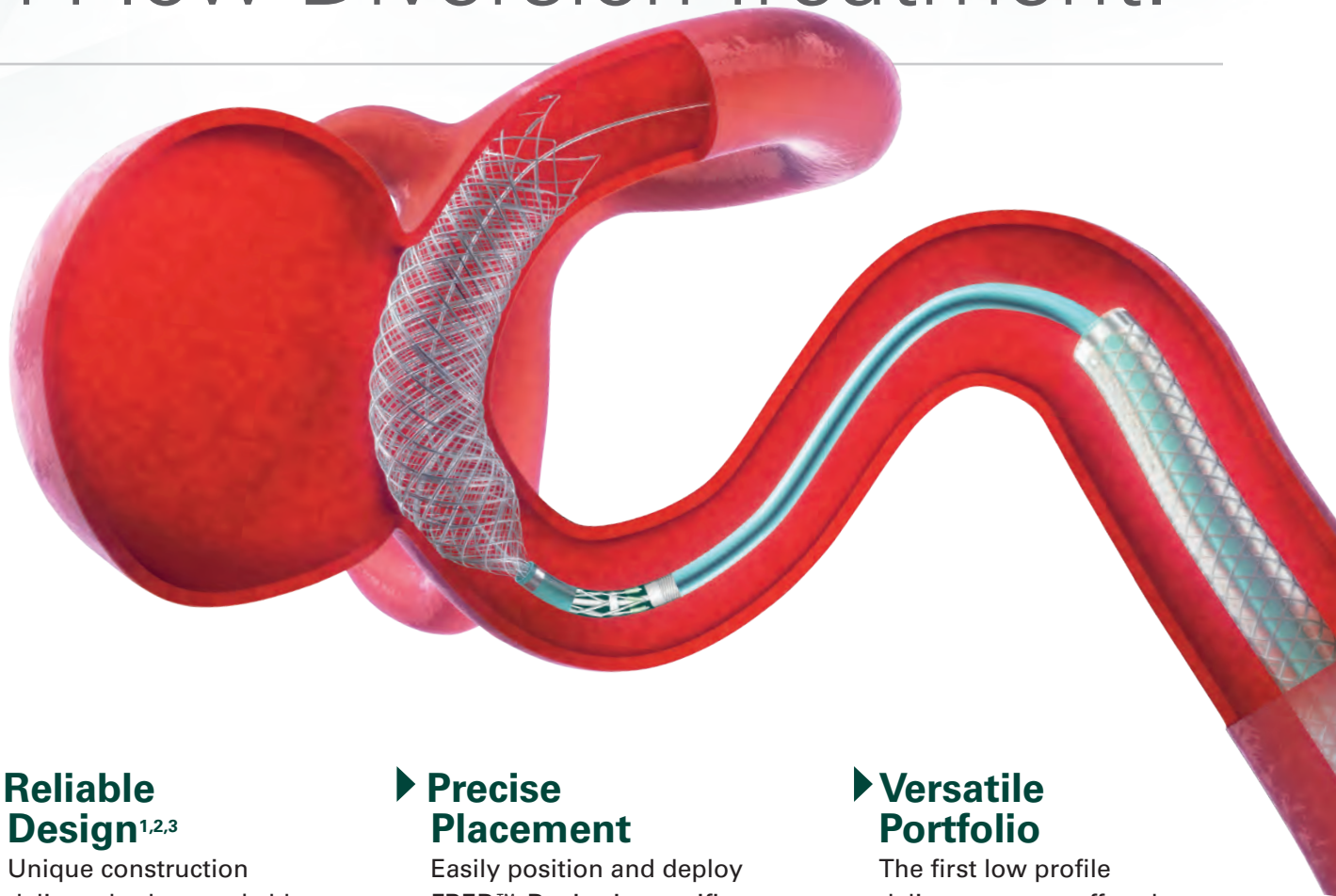
Posttreatment imaging in patients with head and neck cancer

Persistent blood flow inside the Woven EndoBridge device

Official Journal ASNR • ASFNR • ASHNR • ASPNR • ASSR



# The New Standard of **Ease and Simplicity** in Flow Diversion Treatment.



## ► **Reliable Design**<sup>1,2,3</sup>

Unique construction delivers both remarkable ease of use and excellent flow diversion<sup>1,2,3</sup>

## ► **Precise Placement**

Easily position and deploy FRED™ Device in specific, targeted locations<sup>4,5,6</sup>

## ► **Versatile Portfolio**

The first low profile delivery system offered in combination with large diameter and long length options

#### References:

1. TR11-211 2. TR13-171 3. TR15-055 4. TR13-192 5. TR15-072 6. TR19-145

The Flow Re-Direction Endoluminal Device (FRED™) System is indicated for use in the internal carotid artery from the petrous segment to the terminus for the endovascular treatment of adult patients (22 years of age or older) with wide-necked (neck width  $\geq 4$  mm or dome-to-neck ratio  $< 2$ ) saccular or fusiform intracranial aneurysms arising from a parent vessel with a diameter  $\geq 2.0$  mm and  $\leq 5.0$  mm.

Use of the FRED™ System is contraindicated under these circumstances: Patients in whom anticoagulant, anti-platelet therapy, or thrombolytic drugs are contraindicated. Patients with known hypersensitivity to metal such as nickel-titanium and metal jewelry. Patients with anatomy that does not permit passage or deployment of the FRED™ System. Patients with an active bacterial infection. Patients with a pre-existing stent in place at the target aneurysm. Patients in whom the parent vessel size does not fall within the indicated range. Patients who have not received dual anti-platelet agents prior to the procedure. For complete indications, contraindications, potential complications, warnings, precautions, and instructions, see instructions for use (IFU provided in the device).

**RX Only:** Federal (United States) law restricts this device to sale by or on the order of a physician.

MICROVENTION™ and FRED™ are registered trademarks of MicroVention, Inc. in the United States and other jurisdictions. © 2020 MicroVention, Inc. 04/2020.

# AJNR *go green*

***AJNR* urges American Society of Neuroradiology members to reduce their environmental footprint by voluntarily suspending their print subscription.**

The savings in paper, printing, transportation, and postage directly fund new electronic enhancements and expanded content.

The digital edition of *AJNR* presents the print version in its entirety, along with extra features including:

- Publication Preview
- Case Collection
- Podcasts
- The *AJNR* News Digest
- The *AJNR* Blog

It also reaches subscribers much faster than print. An electronic table of contents will be sent directly to your mailbox to notify you as soon as it publishes.

Readers can search, reference, and bookmark current and archived content 24 hours a day on [www.ajnr.org](http://www.ajnr.org).

ASNR members who wish to opt out of print can do so by using the *AJNR* Go Green link on the *AJNR* Website (<http://www.ajnr.org/content/subscriber-help-and-services>). Just type your name in the email form to stop print and spare our ecosystem.



# *We're Inside Every Great Neuroradiologist!*

## **ASNR MEMBERS RECEIVE**

### ***American Journal of Neuroradiology (AJNR)***

The leading neuroradiology research journal, published monthly

### ***Neurographics***

Bimonthly educational journal with CME for members

### **ASNR Annual Meeting**

Discounts for members on the field's premier conference

### **eCME**

Online collection of lectures and articles with SA-CME and Category 1 credit

### **Advocacy**

Coding/reimbursement, quality standards and practice guidelines; demonstrating neuroradiology's value!

### **Networking**

Access to 5,000 peers

... And More!

## **Join the leaders in neuroradiology today!**

## **Learn more at [www.asnr.org/join](http://www.asnr.org/join)**

# **ASNR**

## **American Society of Neuroradiology**

800 Enterprise Dr., Suite 205, Oak Brook, IL 60523 • (630)574-0220 • [membership@asnr.org](mailto:membership@asnr.org) • [www.asnr.org](http://www.asnr.org)

## LUCIEN LEVY BEST RESEARCH ARTICLE AWARD WINNER AND NOMINEES NAMED

This award is named for the late *AJNR* Senior Editor who championed its establishment and recognizes the best original research paper accepted in 2019. The winning paper was published electronically on March 12, 2020. It was selected by a vote of the *Journal's* Editor-in-Chief and Senior Editors.



The Editors of *AJNR* are pleased to announce the annual Lucien Levy Best Research Article Award has been presented to

### “Performance of Standardized Relative CBV for Quantifying Regional Histologic Tumor Burden in Recurrent High-Grade Glioma: Comparison against Normalized Relative CBV Using Image-Localized Stereotactic Biopsies”

by J.M. Hoxworth, J.M. Eschbacher, A.C. Gonzales, K.W. Singleton, G.D. Leon, K.A. Smith, A. Stokes, Y. Zhou, G.L. Mazza, A.B. Porter, M.M. Mrugala, R.S. Zimmerman, B.R. Bendok, D.P. Patra, C. Krishna, J.L. Boxerman, L.C. Baxter, K.R. Swanson, C.C. Quarles, K.M. Schmainda, and L.S. Hu

#### Other nominated papers were:

“A Method to Estimate Brain Volume from Head CT Images and Application to Detect Brain Atrophy in Alzheimer Disease” by V. Adduru, S.A. Baum, C. Zhang, M. Helguera, R. Zand, M. Lichtenstein, C.J. Griessenauer, and A.M. Michael

“Early Detection of Cancer: Evaluation of MRI Grading Systems in Patients with Suspected Nasopharyngeal Carcinoma” by A.D. King, J.K.S. Woo, Q.-Y. Ai, F.K.F. Mo, T.Y. So, W.K.J. Lam, I.O.L. Tse, A.C. Vlantis, K.W.N. Yip, E.P. Hui, B.B.Y. Ma, R.W.K. Chiu, A.T.C. Chan, Y.M.D. Lo, and K.C.A. Cha

“Defining Ischemic Core in Acute Ischemic Stroke Using CT Perfusion: A Multiparametric Bayesian-Based Model” by K. Nael, E. Tadayon, D. Wheelwright, A. Metry, J.T. Fifi, S. Tuhir, R.A. De Leacy, A.H. Doshi, H.L. Chang, and J. Mocco

“Functional Connectivity Associated with Health-Related Quality of Life in Children with Focal Epilepsy” by H. Nawani, M.L. Smith, A.L. Wheeler, and E. Widjaja

“Thrombectomy with Conscious Sedation Compared with General Anesthesia: A DEFUSE 3 Analysis” by C.J. Powers, D. Dornbos III, M. Mlynash, D. Gulati, M. Torbey, S.M. Nimjee, M.G. Lansberg, G.W. Albers, and M.P. Marks

“Large Neck and Strong Ostium Inflow as the Potential Causes for Delayed Occlusion of Unruptured Sidewall Intracranial Aneurysms Treated by Flow Diverter” by T. Su, P. Reymond, O. Brina, P. Bouillot, P. Machi, B.M.A. Delattre, L. Jin, K.O. Löfblad, and M.I. Vargas

“Ensemble of Convolutional Neural Networks Improves Automated Segmentation of Acute Ischemic Lesions Using Multiparametric Diffusion-Weighted MRI” by S. Winzeck, S.J.T. Mocking, R. Bezerra, M.J.R.J. Bouts, E.C. McIntosh, I. Diwan, P. Garg, A. Chutinet, W.T. Kimberly, W.A. Copen, P.W. Schaefer, H. Ay, A.B. Singhal, K. Kamnitsas, B. Glocker, A.G. Sorensen, and O. Wu



# FRED™

Flow Re-Direction  
Endoluminal Device

## FLOW DIVERSION.



## SIMPLIFIED.



**MicroVention Worldwide**  
**Innovation Center**  
35 Enterprise  
Aliso Viejo, CA 92656 USA  
**MicroVention UK Limited**  
**MicroVention Europe S.A.R.L.**  
**MicroVention Deutschland GmbH**  
**Web**

PH +1 714.247.8000

PH +1 44 (0) 191 258 6777  
PH +33 (1) 39 21 77 46  
PH +49 211 210 798-0  
[microvention.com](http://microvention.com)



## **Simplify** the MOC Process



## **Manage** your CME Credits Online

# **CMEgateway.org**

### **Available to Members of Participating Societies**

American Board of Radiology (ABR)  
American College of Radiology (ACR)  
American Roentgen Ray Society (ARRS)  
American Society of Neuroradiology (ASNR)  
Commission on Accreditation of Medical  
Physics Educational Programs, Inc. (CAMPEP)  
Radiological Society of North America (RSNA)  
Society of Interventional Radiology (SIR)  
SNM  
The Society for Pediatric Radiology (SPR)

### **It's Easy and Free!**

Log on to CME Gateway to:

- View or print reports of your CME credits from multiple societies from a single access point.
- Print an aggregated report or certificate from each participating organization.
- Link to SAMs and other tools to help with maintenance of certification.

### **American Board of Radiology (ABR) participation!**

By activating ABR in your organizational profile, your MOC-fulfilling CME and SAM credits can be transferred to your own personalized database on the ABR Web site.

### **Sign Up Today!**

go to [CMEgateway.org](http://CMEgateway.org)



Introducing  
**Eclipse 2L**  
DUAL LUMEN BALLOON CATHETER



**Balt's Access Portfolio Delivers Unique Solutions**



Visit [www.balt-usa.com](http://www.balt-usa.com) to learn more

**Balt USA**

29 Parker, Irvine, CA 92618 • tel 949.788.1443 fax 949.788.1444 • [balt-usa.com](http://balt-usa.com)

© 2019 BALT USA MKTG - 147 Rev. A



# AJNR




## AMERICAN JOURNAL OF NEURORADIOLOGY

JULY 2020  
VOLUME 41  
NUMBER 7  
WWW.AJNR.ORG

Publication Preview at [www.ajnr.org](http://www.ajnr.org) features articles released in advance of print.  
Visit [www.ajnrblog.org](http://www.ajnrblog.org) to comment on AJNR content and chat with colleagues  
and AJNR's News Digest at <http://ajnrndigest.org> to read the stories behind the  
latest research in neuroimaging.

1135 **PERSPECTIVES** *M. Hauben*

### REVIEW ARTICLES

-  1136 **Preserving Access: A Review of Stroke Thrombectomy during the COVID-19 Pandemic** *T.M. Leslie-Mazwi, et al.*
-  1142 **Tandem Carotid Lesions in Acute Ischemic Stroke: Mechanisms, Therapeutic Challenges, and Future Directions** *A.Y. Poppe, et al.*
-  1149 **Headache and Neuroimaging: Why We Continue to Do It** *J.E. Jordan, et al.*

**INTERVENTIONAL**

**INTERVENTIONAL**


**ADULT BRAIN**

### RADIOLOGY-PATHOLOGY CORRELATION







- 1156 **Squamous Cell Carcinoma Arising from Sinonasal Inverted Papilloma** *D.T. Ginat, et al.*

**HEAD & NECK**

### HEALTH CARE REFORM VIGNETTE

-   1160 **Implications of the Revisions and Revaluation of Office/Outpatient Evaluation and Management Codes for Neuroradiology Reimbursement** *K.Y. Wang, et al.*

### GENERAL CONTENTS

-  1165 **CT Scanning in Suspected Stroke or Head Trauma: Is it Worth Going the Extra Mile and Including the Chest to Screen for COVID-19 Infection?** *R.M. Kwee, et al, for the COVID-19 CT Investigators South-East Netherlands (CISEN) Study Group*
-  1170 **Cerebrovascular Disease in COVID-19** *M.F. Goldberg, et al.*
-  1173 **Hemorrhagic Posterior Reversible Encephalopathy Syndrome as a Manifestation of COVID-19 Infection** *A.M. Franceschi, et al.*
-  1177 **Surprise Diagnosis of COVID-19 following Neuroimaging Evaluation for Unrelated Reasons during the Pandemic in Hot Spots** *R. Jain, et al.*
-  1179 **Brain Imaging Use and Findings in COVID-19: A Single Academic Center Experience in the Epicenter of Disease in the United States** *A. Radmanesh, et al.*
-  1184 **COVID-19—Associated Miller Fisher Syndrome: MRI Findings** *J.E. Lantos, et al.*

**ADULT BRAIN**

**ADULT BRAIN**

**ADULT BRAIN**

**ADULT BRAIN**

**ADULT BRAIN**

**HEAD & NECK**

AJNR (Am J Neuroradiol ISSN 0195–6108) is a journal published monthly, owned and published by the American Society of Neuroradiology (ASNR), 800 Enterprise Drive, Suite 205, Oak Brook, IL 60523. Annual dues for the ASNR include approximately 21% for a journal subscription. The journal is printed by Cadmus Journal Services, 5457 Twin Knolls Road, Suite 200, Columbia, MD 21045; Periodicals postage paid at Oak Brook, IL and additional mailing offices. Printed in the U.S.A. POSTMASTER: Please send address changes to American Journal of Neuroradiology, P.O. Box 3000, Denville, NJ 07834, U.S.A. Subscription rates: nonmember \$410 (\$480 foreign) print and online, \$320 online only; institutions \$470 (\$540 foreign) print and basic online, \$935 (\$1000 foreign) print and extended online, \$380 online only (basic), \$825 online only (extended); single copies are \$35 each (\$40 foreign). Indexed by PubMed/MEDLINE, BIOSIS Previews, Current Contents (Clinical Medicine and Life Sciences), EMBASE, Google Scholar, HighWire Press, Q-Sensei, RefSeek, Science Citation Index, SCI Expanded, Meta/CZI, ReadCube, and Semantic Scholar. Copyright © American Society of Neuroradiology.

	1187	Ventricular Volume Is More Strongly Associated with Clinical Improvement Than the Evans Index after Shunting in Idiopathic Normal Pressure Hydrocephalus <i>J. Neikter, et al.</i>	ADULT BRAIN
🔑 📄 🎥	1193	Distinguishing Extravascular from Intravascular Ferumoxytol Pools within the Brain: Proof of Concept in Patients with Treated Glioblastoma <i>R.F. Barajas, Jr, et al.</i>	ADULT BRAIN
★ 🔑 📄 🎥	1201	High Spatiotemporal Resolution 4D Flow MRI of Intracranial Aneurysms at 7T in 10 Minutes <i>L.M. Gottwald, et al.</i>	ADULT BRAIN
📄 🎥	1209	Cervicofacial Venous Malformations Are Associated with Intracranial Developmental Venous Anomalies and Dural Venous Sinus Abnormalities <i>W. Brinjikji, et al.</i>	EXTRACRANIAL VASCULAR
	1215	<b>Commentary</b> Heterogeneous Continuum of Cerebral and Cervicofacial Venous Malformations <i>S. Manjila</i>	
🔑 🎥	1217	A Hemodynamic Mechanism Correlating with the Initiation of MCA Bifurcation Aneurysms <i>Z. Huang, et al.</i>	INTERVENTIONAL
	1225	Persistent Blood Flow inside the Woven EndoBridge Device More Than 6 Months after Intracranial Aneurysm Treatment: Frequency, Mechanisms, and Management—A Retrospective Single-Center Study <i>H.A. Nguyen, et al.</i>	INTERVENTIONAL
🎥	1232	Residual Flow inside the Woven Endo Bridge Device at Follow-Up: Potential Predictors of the Bicêtre Occlusion Scale Score 1 Phenomenon <i>M.T. Nawka, et al.</i>	INTERVENTIONAL
📄 📄	1238	Posttreatment Imaging in Patients with Head and Neck Cancer without Clinical Evidence of Recurrence: Should Surveillance Imaging Extend Beyond 6 Months? <i>A. Gore, et al.</i>	HEAD & NECK
	1245	Comparison of Intraoperative Sonography and Histopathologic Evaluation of Tumor Thickness and Depth of Invasion in Oral Tongue Cancer: A Pilot Study <i>B.C. Yoon, et al.</i>	HEAD & NECK
	1251	Prevalence of Sigmoid Sinus Dehiscence and Diverticulum among Adults with Skull Base Cephaloceles <i>H. Sotoudeh, et al.</i>	HEAD & NECK
🔑 📄 🎥	1256	Variable Refocusing Flip Angle Single-Shot Imaging for Sedation-Free Fast Brain MRI <i>R. Jabarkheel, et al.</i>	PEDIATRICS
🔑 📄	1263	Prevalence and Incidence of Microhemorrhages in Adolescent Football Players <i>B.R. Shah, et al.</i>	PEDIATRICS
	1269	<b>Commentary</b> Value of Advanced MR Imaging Techniques in Mild Traumatic Brain Injury <i>S. Hähnel, et al.</i>	
📄	1271	In Vivo Evaluation of White Matter Abnormalities in Children with Duchenne Muscular Dystrophy Using DTI <i>V. Preethish-Kumar, et al.</i>	PEDIATRICS FUNCTIONAL
★ 🔑 📄 🎥	1279	Automatic Machine Learning to Differentiate Pediatric Posterior Fossa Tumors on Routine MR Imaging <i>H. Zhou, et al.</i>	PEDIATRICS FUNCTIONAL
★ 📄	1286	Intra-Arterial Chemotherapy for Retinoblastoma in Infants ≤10 kg: 74 Treated Eyes with 222 IAC Sessions <i>A. Sweid, et al.</i>	PEDIATRICS
🔑	1293	Changes of Neurotransmitters in Youth with Internet and Smartphone Addiction: A Comparison with Healthy Controls and Changes after Cognitive Behavioral Therapy <i>H.S. Seo, et al.</i>	PEDIATRICS FUNCTIONAL
🔑 📄 🎥	1302	Brain Cortical Structure and Executive Function in Children May Be Influenced by Parental Choices of Infant Diets <i>T. Li, et al.</i>	PEDIATRICS FUNCTIONAL



- 1309 Spine MRI in Spontaneous Intracranial Hypotension for CSF Leak Detection: Nonsuperiority of Intrathecal Gadolinium to Heavily T2-Weighted Fat-Saturated Sequences** *T. Dobrocky, et al.*

**SPINE**



- 1316 Combination of Imaging Features and Clinical Biomarkers Predicts Positive Pathology and Microbiology Findings Suggestive of Spondylodiscitis in Patients Undergoing Image-Guided Percutaneous Biopsy** *S. Kihira, et al.*

**SPINE**

#### MEMORIALS

- 1323 Norman Leeds, MD** *R. D. Zimmerman*  
**1325 James T. Goodrich, MD, PhD** *J.A. Bello, et al.*  
**1326 35 YEARS AGO IN AJNR**

#### ONLINE FEATURES

##### LETTERS



- E49 Novel Coronavirus: What Neuroradiologists Should Do** *C. Jain, et al.*



- E50 Neuroradiologists and the Novel Coronavirus** *M.U. Antonucci, et al.*

- E51 Meta-Analysis as a Symptom: The Example of Flow Diverters** *E. Houdart*

#### BOOK REVIEWS *R.M. Quencer, Section Editor*

Please visit [www.ajnrblog.org](http://www.ajnrblog.org) to read and comment on Book Reviews.



A, Large venous malformation involving the right orbit and face. B, MRV shows ectatic torcula, which includes the entirety of the straight sinus. C–E, MRIs show multiple developmental venous anomalies.



Indicates Editor's Choices selection



Indicates Fellows' Journal Club selection



Indicates open access to non-subscribers at [www.ajnr.org](http://www.ajnr.org)



Indicates article with supplemental on-line table



Indicates article with supplemental on-line photo



Indicates article with supplemental on-line video



Evidence-Based Medicine Level 1



Evidence-Based Medicine Level 2



### EDITOR-IN-CHIEF

**Jeffrey S. Ross, MD**

*Professor of Radiology, Department of Radiology,  
Mayo Clinic College of Medicine, Phoenix, AZ*

### SENIOR EDITORS

**Harry J. Cloft, MD, PhD**

*Professor of Radiology and Neurosurgery,  
Department of Radiology, Mayo Clinic College of  
Medicine, Rochester, MN*

**Christopher G. Filippi, MD**

*Professor and Vice Chair of Biomedical and  
Translational Science,  
Donald and Barbara Zucker School of Medicine at  
Hofstra/Northwell,  
Lenox Hill Hospital and Greenwich Village  
Healthplex, New York, NY*

**Thierry A.G.M. Huisman, MD**

*Radiologist-in-Chief, Texas Children's Hospital,  
Houston, TX*

**Yvonne W. Lui, MD**

*Associate Professor of Radiology,  
Chief of Neuroradiology,  
New York University School of Medicine,  
New York, NY*

**C.D. Phillips, MD, FACR**

*Professor of Radiology, Weill Cornell Medical  
College, Director of Head and Neck Imaging,  
New York-Presbyterian Hospital, New York, NY*

**Lubdhra M. Shah, MD, MS**

*Professor of Radiology and Director of Spine  
Imaging, University of Utah Department of  
Radiology and Imaging Sciences, Salt Lake City, UT*

**Charles M. Strother, MD**

*Professor of Radiology, Emeritus, University of  
Wisconsin, Madison, WI*

### STATISTICAL SENIOR EDITOR

**Bryan A. Comstock, MS**

*Senior Biostatistician,  
Department of Biostatistics,  
University of Washington, Seattle, WA*

### ARTIFICIAL INTELLIGENCE DEPUTY EDITOR

**Peter D. Chang, MD**

*Assistant Professor-in-Residence,  
Departments of Radiological Sciences,  
Computer Sciences, and Pathology,  
Director, Center for Artificial Intelligence in  
Diagnostic Medicine (CAIDM),  
University of California, Irvine, Irvine, CA*

### EDITORIAL BOARD

Ashley H. Aiken, *Atlanta, GA*  
Lea M. Alhilali, *Phoenix, AZ*  
Kubilay Aydin, *Istanbul, Turkey*  
John D. Barr, *Dallas, TX*  
Ari Blitz, *Baltimore, MD*  
Barton F. Branstetter IV, *Pittsburgh, PA*  
Jonathan L. Brisman, *Lake Success, NY*  
Keith Cauley, *Danville, PA*  
James Y. Chen, *San Diego, CA*  
Asim F. Choudhri, *Memphis, TN*  
Daniel Chow, *Irvine, CA*  
J. Matthew Debnam, *Houston, TX*  
Seena Dehkharghani, *New York, NY*  
Yonghong Ding, *Rochester, MN*  
Clifford J. Eskey, *Hanover, NH*  
Saeed Fakhran, *Phoenix, AZ*  
Massimo Filippi, *Milan, Italy*  
Nils D. Forkert, *Calgary, Alberta, Canada*  
Wende N. Gibbs, *Hanover, AZ*  
Christine M. Glastonbury, *San Francisco, CA*  
John L. Go, *Los Angeles, CA*  
Philipp Göltz, *Erlangen, Germany*  
Allison Grayev, *Madison, WI*  
Brent Griffith, *Detroit, MI*  
Ajay Gupta, *New York, NY*  
Rakesh Kumar Gupta, *Haryana, India*  
Lothi Hacein-Bey, *Sacramento, CA*  
Christopher P. Hess, *San Francisco, CA*  
Andrei Holodny, *New York, NY*  
Benjamin Huang, *Chapel Hill, NC*  
Mahesh V. Jayaraman, *Providence, RI*  
Valerie Jewells, *Chapel Hill, NC*  
Christof Karmonik, *Houston, TX*  
Timothy J. Kaufmann, *Rochester, MN*  
Hillary R. Kelly, *Boston, MA*  
Toshibumi Kinoshita, *Akita, Japan*  
Kenneth F. Layton, *Dallas, TX*  
Alexander Lerner, *Los Angeles, CA*  
Michael Lev, *Boston, MA*  
Karl-Olof Lovblad, *Geneva, Switzerland*  
Franklin A. Marden, *Chicago, IL*  
Joseph C. McGowan, *Merion Station, PA*  
Stephan Meckel, *Freiburg, Germany*  
Christopher J. Moran, *St. Louis, MO*  
Takahisa Mori, *Kamakura City, Japan*  
Suresh Mukherji, *Ann Arbor, MI*  
Alexander J. Nemeth, *Chicago, IL*  
Renato Hoffmann Nunes, *Sao Paulo, Brazil*  
Sasan Partovi, *Cleveland, OH*  
Laurent Pierot, *Reims, France*  
Jay J. Pillai, *Baltimore, MD*  
Whitney B. Pope, *Los Angeles, CA*  
Joana Ramalho, *Lisbon, Portugal*

Otto Rapalino, *Boston, MA*  
Álex Rovira-Cañellas, *Barcelona, Spain*  
Paul M. Ruggieri, *Cleveland, OH*  
Amit M. Saindane, *Atlanta, GA*  
Maksim Shapiro, *New York, NY*  
Timothy Shepherd, *New York, NY*  
Mark S. Shiroishi, *Los Angeles, CA*  
Bruno P. Soares, *Baltimore, MD*  
Maria Vittoria Spampinato, *Charleston, SC*  
Khin Khin Tha, *Sapporo, Hokkaido, Japan*  
Krishnamoorthy Thamburaj, *Hershey, PA*  
Cheng Hong Toh, *Taipei, Taiwan*  
Aquila S. Turk, *Greenville, SC*  
Anja G. van der Kolk, *Utrecht, the Netherlands*  
Willem Jan van Rooij, *Tilburg, Netherlands*  
Arastoo Vossough, *Philadelphia, PA*  
Elysa Widjaja, *Toronto, Ontario, Canada*  
Max Wintermark, *Stanford, CA*  
Ronald L. Wolf, *Philadelphia, PA*  
Kei Yamada, *Kyoto, Japan*  
Carlos Zamora, *Chapel Hill, NC*  
Vahe M. Zohrabian, *New Haven, CT*

### EDITORIAL FELLOW

Matthew D. Alvin, *Baltimore, MD*

### SPECIAL CONSULTANTS TO THE EDITOR

#### AJNR Blog Editor

Neil Lall, *Denver, CO*

#### Case of the Month Editor

Nicholas Stence, *Aurora, CO*

#### Case of the Week Editors

Juan Pablo Cruz, *Santiago, Chile*

Sapna Rawal, *Toronto, Ontario, Canada*

#### Classic Case Editor

Sandy Cheng-Yu Chen, *Taipei, Taiwan*

#### Health Care and Socioeconomics Editor

Pina C. Sanelli, *New York, NY*

#### Physics Editor

Greg Zaharchuk, *Stanford, CA*

#### Podcast Editor

Wende N. Gibbs, *Phoenix, AZ*

#### Twitter Editor

Roger Jordan, *Houston, TX*

### Official Journal:

American Society of Neuroradiology  
American Society of Functional Neuroradiology  
American Society of Head and Neck Radiology  
American Society of Pediatric Neuroradiology  
American Society of Spine Radiology

*Founding Editor*  
Juan M. Taveras

*Editors Emeriti*  
Mauricio Castillo, Robert I. Grossman,  
Michael S. Huckabee, Robert M. Quencer

*Managing Editor*  
Karen Halm  
*Assistant Managing Editor*  
Laura Wilhelm  
*Editorial Assistant*  
Margaret B. Sabato  
*Executive Director, ASNR*  
Mary Beth Hepp



Title: Macy's 4th of July Fireworks Spectacular. Beautiful marvels of the interaction of matter and energy, shot from the Lower East Side of Manhattan.

*Manfred Hauben, MD, MPH, Pfizer Inc and NYU Langone Health, New York City*

# Preserving Access: A Review of Stroke Thrombectomy during the COVID-19 Pandemic

 T.M. Leslie-Mazwi,  K.M. Fargen,  M. Levitt,  C.P. Derdeyn,  S.K. Feske,  A.B. Patel, and  J.A. Hirsch



## ABSTRACT

**SUMMARY:** Thrombectomy for large-vessel-occlusion stroke is a highly impactful treatment. The spread of coronavirus 19 (COVID-19) across the United States and the globe impacts access to this crucial intervention through widespread societal and institutional changes. In this document, we review the implications of COVID-19 on the emergency care of large-vessel occlusion stroke, reviewing specific infection-control recommendations, available literature, existing resources, and expert consensus. As a population, patients with large-vessel occlusion stroke face unique challenges during pandemics. These are broad in scope. Responses to these challenges through adaptation of stroke systems of care and with imaging, thrombectomy, and postprocedural care are detailed. Preservation of access to thrombectomy must be prioritized for its public health impact. While the extent of required changes will vary by region, tiered planning for both escalation and de-escalation of measures must be a part of each practice. In addition, preparations described serve as templates in the event of future pandemics.

**ABBREVIATIONS:** ACE2 = angiotensin-converting enzyme 2; COVID-19 = coronavirus disease 19; ICU = intensive care unit; LVO = large-vessel occlusion; PPE = personal protective equipment; SARS-CoV-2 = Severe Acute Respiratory Syndrome coronavirus 2

The Severe Acute Respiratory Syndrome coronavirus 2 (SARS-CoV-2) is documented as entering the human population in Hubei province in China in late 2019.<sup>1,2</sup> The virus, when symptomatic, causes a predominantly respiratory illness with involvement of other organ systems, labeled coronavirus 2019 (COVID-19).<sup>3</sup> The infection has spread across the globe. Since the first case in Washington state in January 2020, the disease has been reported in all 50 states and at least 8 jurisdictions.<sup>4</sup> The infection reached pandemic proportions by March 11, 2020, with sustained risk of further global spread.<sup>5</sup> At the time of this writing, confirmed cases and mortality continue to rise.

In this document, we review the implications of this pandemic for the emergency care of large-vessel occlusion (LVO) stroke.<sup>6</sup> Thrombectomy for patients with LVO is one of the most powerful and impactful treatments in the history of medicine.<sup>7-9</sup> The COVID-19 pandemic threatens access to this crucial intervention. The American Heart Association/American Stroke Association has released temporary emergency guidelines for stroke centers in the United States.<sup>10</sup> It is anticipated that these will be revised and expanded as available evidence and experience increase. The focus of this article is specifically LVO stroke and its triage and management under these new conditions.

## SARS-COV-2 and LVO Stroke

Knowledge of the effect of SARS-CoV-2 on the cerebrovascular system is limited. The functional receptor for coronaviruses invasion into the human body is the angiotensin-converting enzyme 2 (ACE2), a membrane-bound aminopeptidase highly expressed in cardiac, vascular, and pulmonary tissue. ACE2 appears to play a crucial vascular and immunologic role.<sup>11</sup> Patients with underlying cardiovascular disease have more severe COVID-19 symptoms,<sup>12</sup> presumably associated with increased expression of ACE2. SARS-CoV-2 has been identified in postmortem brains,<sup>13</sup> but direct cerebrovascular effects remain unknown.

In a 1527-patient sample from China, a combined data point of cardiac or cerebrovascular disease was found in 16.4% of the

Received April 17, 2020; accepted after revision April 29.

From the Departments of Neurology (T.M.L.-M.), Neurosurgery (T.M.L.-M., A.B.P.), and Radiology (J.A.H.), Massachusetts General Hospital, Harvard Medical School, Boston, Massachusetts; Department of Neurosurgery (K.M.F.), Wake Forest School of Medicine, Winston-Salem, North Carolina; Departments of Neurological Surgery, Radiology, Mechanical Engineering and Stroke and Applied Neuroscience Center (M.L.), University of Washington, Seattle, Washington; Departments of Radiology and Neurology (C.P.D.), University of Iowa, Iowa City, Iowa; and Department of Neurology (S.K.F.), Brigham and Women's Hospital, Harvard Medical School, Boston, Massachusetts.

Please address correspondence to Thabele M. Leslie-Mazwi, MD, Departments of Neurosurgery and Neurology, Massachusetts General Hospital, Harvard Medical School, Wang 7-739R, 55 Fruit St, Boston, MA 02114; e-mail: tleslie-mazwi@mgh.harvard.edu

 Indicates open access to non-subscribers at [www.ajnr.org](http://www.ajnr.org)

<http://dx.doi.org/10.3174/ajnr.A6606>

total cohort but was 3 times more likely to occur in patients in intensive care settings.<sup>14</sup> In an article under peer review, 2.3% of 214 hospitalized patients with COVID-19 (and 4.6% of 88 severely affected patients) developed acute ischemic stroke during the course of the illness.<sup>15</sup>

COVID-19-induced inflammation, hypoxia, and diffuse intravascular coagulation increase the risk of arterial thromboembolic disease<sup>16,17</sup> and, therefore, presumably LVO stroke. Other potential mechanisms for arterial stroke in patients with COVID-19 include widespread proinflammatory cytokine responses, atherosclerotic plaque rupture due to local inflammation, hemodynamic changes predisposing to thrombosis or cerebral ischemia, and profound hypoxia.<sup>18,19</sup> Furthermore, LVO stroke in the COVID-19 population may be associated with worse outcomes because of reduced cardiovascular reserve.<sup>20</sup> The relative contributions of these factors remain to be explored, but early reports may indicate a meaningful rate of cerebrovascular events in patients with COVID-19.<sup>15,21,22</sup> Indeed, LVO stroke may be a presenting feature of the disease for a subset of patients with COVID-19.

### **Unique Challenges for the LVO Population during a Pandemic**

Beyond the direct biologic considerations, other unique challenges exist for patients with LVO in the context of the current pandemic. COVID-19 causes the most severe illness in the elderly with underlying cardiovascular and respiratory disease. These are phenotypes shared by many patients presenting with acute ischemic stroke, and comorbidities may represent an insurmountable challenge for the COVID-19-positive LVO population.

Requisite social distancing and self-isolation may cause patients with severe stroke to be less likely to be discovered by family or friends, increasing the time from symptom onset to mobilization of emergency services. Fear of contracting COVID-19 may limit willingness to present to health care.<sup>23</sup> Additionally, prolonged social distancing or quarantine may produce other consequences because social isolation is a recognized independent risk factor for mortality.<sup>24</sup>

There is a substantial strain on emergency systems during pandemics. Burdening of ambulance transports further contributes to delays. The need for separation also disrupts the team-based approach that underlies the stroke chain of care. Communication, central to treatment decisions, may be more difficult, including with family members who may not be with the patient physically. Patients with stroke are often transferred with fragmented or limited history available, making symptom detection for respiratory disease unreliable.

Transfers typically occur under conditions of intense time pressure, with disability at stake for patients and risk of infection for providers. Patients with LVO transferred from centers to which they initially present to centers that provide thrombectomy carry the risk of spreading infection. The steps necessary for appropriate precautions mean that time metrics for quality-of-care initiatives and certification purposes will likely be impaired.

Finally, the LVO stroke population has broad intensive care needs and often a prolonged need for institutionalization (hospitals or rehabilitation centers). Demand for personal protective equipment (PPE), ventilators, intensive care unit (ICU) beds, and

other hospital resources by patients with COVID-19 may disrupt the capacity to provide the high level of care required by the LVO population. These varied considerations are particularly important as treatment rates for LVO continue to increase, with thrombectomy occurring more than every other day at many centers.<sup>25</sup>

### **Guiding Principles for the Pandemic Response**

Given this background, certain principles must guide the collective response to all aspects of care of patients with LVO stroke during the COVID-19 pandemic:

1. We must find the appropriate balance between patient access and outcomes and the necessary compromises for provider and patient safety. Attempting to maintain historic metrics despite the multiple new considerations of COVID-19 places our health care providers at risk. However, protecting access to the remarkably potent therapeutic effect of thrombectomy is an imperative. Questions concerning which compromises are acceptable, effective, or appropriate remain open.
2. We must anticipate a rapid pace of change. In response to shifting data, recommended approaches change regularly. Therefore, stroke services must remain nimble and stay in communication with each other and hospital, regional, and national leadership. Frequent review of protocols is necessary, with clear lines of dissemination of changes.
3. We must strive for collaborative, noncompetitive, multidisciplinary interactions. The impact of this pandemic crosses specialty lines. It is essential that adequate exchange of information be available to identify emerging trends and therapeutic targets in the pandemic. Considerations of nationality, influence, reimbursement, and practice scope must be superseded by the need for collective action and information. Lessons learned in other practice environments already affected by the disease (China, Italy,<sup>26</sup> Singapore,<sup>27</sup> Spain, and elsewhere) can be applied to decisions made in emerging pandemic epicenters.

These principles apply to all areas of LVO care.

### **Considerations for Stroke Systems of Care**

COVID-19 will necessitate many changes in stroke care systems. Stroke networks must take charge of these changes to achieve the following goals: to provide unbroken access for patients to thrombectomy during the COVID-19 pandemic, distribute patients to open centers, minimize the time that referring hospitals spend searching for an accepting center, and simplify organization and communication. Meeting these goals will need to occur in the context of increasing resource use in the treatment of patients affected by the COVID-19 pandemic, which has already strained emergency department, ICU, anesthesia, and operating room resources.

Elective cases and clinics progressively have to be deferred to comply with social distancing and to conserve ICU capacity, ventilators, staff, and PPE for burgeoning COVID-19 caseloads. Decisions will be individualized on the basis of local conditions, but many US practices have already enacted these measures in regions where COVID-19 cases are escalating rapidly.



Messaging to patients should be clear, and a process instituted to ensure that once normalcy returns, patients can be rescheduled. In the early stages of the pandemic, case priority strata may be formed (for example, interventions over diagnostic angiograms), but as the pandemic gains increasing ground, all non-emergent procedures may need to be cancelled. As much as possible, thrombectomy for LVO should be protected from this withdrawal of services. Given the extraordinarily low number needed to treat and the risk of severe disability or death, coupled with the time sensitivity of the condition, thrombectomy should remain a protected and available treatment option. If system stress due to COVID-19 is extreme, criteria may need to be established for patient-treatment selection, with diminishing indications for thrombectomy procedures. For example, patients with medium vessel occlusions, large ischemic cores or very-late-window presentations may no longer be offered thrombectomy if the pandemic has a drastic local effect.

Health care workers are at risk of contracting the virus.<sup>28</sup> Institutional protocols must be reviewed to incorporate isolation procedures for the care of patients with LVO. Rarely will a patient be transferred for thrombectomy with a known COVID-19 disease status; more typically, a patient's COVID-19 status will be unknown with variable levels of suspicion. Furthermore, absence of patient symptoms cannot provide complete reassurance because this does not ensure lack of infection or inability to transmit the virus.<sup>29,30</sup> Screening of transfer patients or emergency department admissions for COVID-19 risk should be undertaken. Screens should include symptoms (including nonrespiratory),<sup>31</sup> history of exposure to possible infected individuals or high-risk professions, travel or geographic areas, and any recent COVID-19 testing with results.

Protective staff measures must include PPE for any exposure to a patient considered a potential COVID-19 case. Essential PPE includes, currently, at a minimum, gown, gloves, goggles (or face shields), and (depending on the degree of potential exposure) a surgical mask or either an N-95 mask or Powered Air-Purifying Respirators (PAPRs). The goal is prevention of viral particles contacting mucous membranes. As local infection rates intensify, COVID-19 staff may be required to take PPE precautions from emergency department arrival irrespective of symptom checklists for all presenting patients. This approach was applied in regions of Wuhan and Lombardy during the peak of the pandemic there.<sup>32</sup> Training staff on proper PPE donning and doffing techniques must be provided and documented. Symptom awareness and monitoring must extend across the entire care spectrum. Some centers are currently requiring all clinical staff to self-attest at the beginning of each shift to being COVID-19-symptom-free. A culture of nonstigmatized self-quarantine when infectious symptoms are present should be cultivated, and all providers should have access to testing.

In the face of COVID-19, staffing models will need to evolve. As infection becomes ubiquitous throughout health care systems, many staff will become secondarily infected and require treatment or will have to self-quarantine due to exposure history. This scenario poses challenges because at baseline, many hospitals run on limited staffing models. A 2019 survey of neurointerventional physicians revealed that 50% of physicians take mechanical

thrombectomy calls daily or every second day.<sup>33</sup> The situation is similar for neurointerventional nurses and radiology technologists; in a recent study from 20 stroke centers in the United States, less than half had call pools for stroke that exceeded 6 total nurses or technologists.<sup>34</sup> Hospitals, due to these limited teams, are, therefore, susceptible to severe disruption by viral infection or furloughs for staff exposure.

Effort to reduce simultaneous exposure must therefore be intensified. Any meetings among stroke providers (neurointerventional or otherwise) should be held virtually, including teaching sessions in academic settings, to prevent the risk of inadvertent exposure. In the most extreme versions of such social distancing regimens, no members of the neurointerventional team are routinely present at the hospital at all but remain available for emergencies only, including conducting all consults remotely. As the volume of infected personnel increases, many stroke service components will need to operate with minimal staffing of a few noninfected or previously infected but now recovered team members. If infection breaches a critical threshold, some emergency LVO services (including even ambulance transport) may not be possible at all. Call schedules need to be constructed with increased reserve to account for the possibility of losing members of a team during self-isolation periods.

Care systems must decide on emergency medical service protocols and sequential routing policies for patients with LVO to thrombectomy-capable centers if capacity is exceeded at 1 facility. In Lombardy, all catheter interventions were localized to a handful of sites, given the strain the rest of the region experienced from the needs of patients with COVID-19. For acute cardiac interventions, a total of 13 hubs were selected of 55 capable hospitals. These designated "hubs" accepted patients transferred from corresponding "spokes,"<sup>32</sup> allowing resources to be condensed and therefore consistently available for catheter-based interventions. Engagement of emergency medical service is a key piece of this routing effort to coordinate available thrombectomy for a region. Additionally, referring hospitals must be aware that thrombectomy services are continuing and of any routing policies if these are required. Hospital leadership at thrombectomy-capable centers should provide assurance that beds will remain available for such emergencies. Furthermore, insurance providers will need flexibility for out-of-network care, for example in the form of prearranged COVID-19 waivers.

Care systems will likely see a slowing of LVO care. Time metrics (door-to-CT, door-to-reperfusion, and so forth) may be dramatically affected due to slower stroke identification in the field, overburdened emergency departments, and difficulties in timely hospital transfers. Delays were observed in cardiac catheterization procedures in Hong Kong during the disease peak, primarily related to longer times from symptom onset to first medical contact and increased PPE requirements.<sup>35</sup> These delays must be acknowledged by certifying organizations as an unavoidable consequence of care under the current conditions.

Finally, sharing of best practices between centers allows combined flexibility of thought and planning to meet the rapid pace of adaptation in pandemics. This may be formalized into weekly virtual meetings among thrombectomy-capable centers or informally among looser networks of providers. In New

England, for example, the 8 thrombectomy-capable centers in Massachusetts and the centers in the neighboring states (Maine, New Hampshire, Vermont, Rhode Island, and Connecticut) have held a weekly virtual meeting during the pandemic to discuss and compare approaches and centralized information about the capacity to take patients for thrombectomy. This provides statewide coordination. Careful collection of data throughout, using Get With the Guidelines–Stroke (<https://www.heart.org/en/professional/quality-improvement/get-with-the-guidelines/get-with-the-guidelines-stroke>) or other platforms, will ensure the retrospective opportunity to assess the impact of emergency measures.

### **Considerations for Stroke Imaging**

Radiology technologists and other staff will encounter patients with LVO stroke early in the course of their evaluation, possibly before full vetting of the COVID-19 risk has occurred. The lowest number of staff necessary to transport patients to the scanner, move them onto the CT or MR imaging table, perform imaging, and then transport them to the next therapeutic destination should be the goal. Universal PPE use may be required in later stages of the pandemic, but symptom-triggered precautions are likely acceptable early on.

The role of adding CT chest imaging to scanning for patients presenting with stroke symptoms is yet to be validated, though CT findings are sensitive to COVID-19.<sup>36,37</sup> While this is currently not formally recommended in LVO evaluation, it has been applied in certain highly endemic areas. However, patients may become symptomatic later in their disease course, so if applied, this should not provide a false sense of reassurance in endemic areas.

Those who perform scanner cleaning after imaging patients at high risk of COVID-19 must account for the possibility of prolonged virus persistence on surfaces.<sup>38</sup> In centers with multiple scanners, there may be a logistic benefit to the designation of “clean” and “dirty” scanners for localizing PPE supplies, cleaning supplies, and other components of pandemic response. This may impact stroke workflow.

Finally, delays may be incurred in the interpretation of imaging depending on the location of the radiologist. For reads performed remotely in either a reading room or from a remote location outside the hospital, data transfers may delay radiologist response times. This delay may be less of a concern for centers with automated imaging interpretation,<sup>39</sup> but data under current pandemic conditions are not available for verification.

### **Considerations for Thrombectomy Procedures**

While procedural fundamentals are unchanged, there are various considerations for the actual procedural aspects of LVO care during the COVID-19 pandemic. The concept of a protected code stroke algorithm has been recently introduced to the literature,<sup>40</sup> reflecting the combined goal of emergent service provision and protection of service providers.

Consent for cases cannot occur in person because of remotely positioned teams and the need for social distancing. Dual attending consent (neurology and neurointerventional attending consensus) offers an option when family members

cannot be contacted, given that thrombectomy is the recommended standard of care. Witnessed telephone consent in conference call format for patients with indications outside the prescribed guidelines should be pursued. Family updates by telephone or video will keep relatives informed of treatment decisions and disease course. In areas dealing with a large volume of patients with COVID-19, hospital visitors may not be allowed at all, and telephone or video contact represents the link between family and the care system. Virtual connections can also be established at the procedural suite to allow non-neurointerventional members of the care team to participate in collaborative case decisions without their physical presence.

Procedural PPE use should be equivalent for all members of the care team (anesthesia, nursing, proceduralists, technologists, and so forth), and the number of staff members in a room should be strictly minimized. COVID-19 status and the PPE application process should be reviewed as part of the preprocedural case discussion with the care team (huddle). Caution should be taken with potential in-room exposures, including opening of cabinets for equipment. Equipment should be removed from storage cabinets if these are in the procedure room and placed in an accessible location that is not at risk of contamination.

Sedation choices for thrombectomy present challenges in the midst of a respiratory pandemic. Currently practice varies for the use of general anesthesia or conscious sedation during these cases. Limited published data are available at this time to guide decisions.<sup>41,42</sup> Intubation carries the appeal of a closed respiratory circuit, in theory exposing the staff caring for the patient to less viral load. However, bag-mask ventilation and intubation itself are highly aerosol-generating procedures. If required, all aerosol-generating procedures should ideally be accomplished in a negative pressure environment. The minimum number of staff required for intubation should be in attendance in full PPE. Beyond the use of video laryngoscopy to protect anesthesia staff, innovative modifications of the intubation technique are being explored.<sup>43</sup> With intubation and a closed respiratory circuit, the load of viral particles in the environment is reduced. However, any breach in the respiratory circuit (tube disconnections during transfer of the patient to the procedural table from the stretcher, suctioning, unrecognized cuff leak, or ventilator change) risks an exposure to individuals who may be falsely reassured by the patient’s intubated status. Use of conscious sedation when possible avoids this intense aerosolization. The utility of a mask worn by a patient with suspected or confirmed COVID-19<sup>40</sup> (as well as PPE for providers) depends on the status of the patient’s airway. If there is concern for airway patency or vomiting, then patient masks should be avoided. Irrespective of the individual approach to procedural sedation, all participants in mechanical thrombectomy must be well-versed in the use of PPE and appropriate precautions, including the proper techniques for donning and doffing.

Procedural sedation choices have implications beyond thrombectomy. Current recommendations for intubated patients are to avoid extubating in the angiography suite (unless the suite is a negative pressure environment).<sup>44</sup> Intubated patients require ventilators for both transport and care in the ICU. Conscious sedation potentially avoids occupying a ventilator (and therefore

an ICU bed) should a shortage exist. These airway considerations were reinforced in a recent release from the Society of Neurointerventional Surgery.<sup>44,45</sup> Local practice conditions will heavily influence decisions about sedation management for patients with LVO.

### Postprocedural Considerations

Postprocedure, the patient's destination can be determined by the nature of the case and the condition of the patient. Typically, ICU care is required, but patients who are doing well may be considered for observation in postoperative units before admission to a floor if ICU beds are limited or unavailable.<sup>44</sup> In addition to the typical stroke work-up, COVID-19 testing should be performed on all patients with stroke and prioritized because of implications for procedures such as swallowing evaluations and diagnostic work-up, as well as rehabilitation placement. This will assist with bed availability by ensuring more expeditious hospital throughput.

### Other Aspects of Thrombectomy during This Pandemic

Other components of this pandemic are important to acknowledge as they relate to thrombectomy. Family stress is high for all team members, with the unique situation of possible quarantine from family either at home or in an off-site location removed from the home, which increases isolation and anxiety.<sup>46,47</sup> Family and friends of team members will also experience stress related to the changes required during these times. Strategies should be shared for minimizing home exposures, including a defined in-home doffing area, laundry, showering after arrival home, and other measures that may be helpful in decreasing the risk of spread.

Empathy for colleagues is essential, including awareness of mental health stress. The possibility of extended time on-call increases the risk of mental health issues and poor clinical performance.<sup>48</sup> Team communication with clarity and immediacy will aid in maintaining morale. Cross-coverage between different role groups if furloughs for health become extensive should be expected. Finally, reimbursement and call coverage costs for care teams will be impaired in the larger context of the massive economic implications of the pandemic. Hospital leadership will be expected to address these concerns for the teams on the front lines of the pandemic battle.

### CONCLUSIONS

Thrombectomy for selected patients with acute ischemic stroke and LVO has a magnitude of benefit that exceeds almost any other time-critical intervention.<sup>49</sup> Access to thrombectomy must be maintained in the face of the current pandemic. This article outlines options to be considered. Tiered planning for both escalation and de-escalation of protective measures must be a part of each practice. As the pandemic gradually ebbs, the measures instituted can be peeled back in reverse order to allow a measured return to full capacity. The extent and magnitude of the changes required are not yet clear. In addition, preparations as described here should serve as templates to prepare us better for the next pandemic.<sup>50,51</sup> By considering these issues in our pandemic

response, we create a more resilient overall system of care for patients with LVO stroke everywhere.

Disclosures: Michael Levitt—UNRELATED: Consultancy: Minnetronix Inc; Grants/Grants Pending: Stryker, Covidien, Volcano Corp, Philips Healthcare, Comments: unrestricted educational and equipment grants\*; Stock/Stock Options: eLoupes, Synchrotron, Cerebrotech. Colin P. Derdeyn—UNRELATED: Consultancy: Penumbra, Genae, NoNo Inc, Comments: Data and Safety Monitoring Board member for these industry-sponsored clinical trials\*; Employment: University of Iowa Hospitals and Clinics.\* Steven K. Feske—UNRELATED: Grants/Grants Pending: Biogen, Comments: Biogen sponsors the CHARM trial.\* Aman B. Patel—UNRELATED: Consultancy: Penumbra, MicroVention, Medtronic, Comments: consultant, proctoring. Joshua A. Hirsch—UNRELATED: Consultancy: Medtronic, Relivant Medsystems, InNeuroCo; Grants/Grants Pending: Harvey L. Neiman Health Policy Institute. \*Money paid to the institution.

### REFERENCES

- Wang D, Hu B, Hu C, et al. **Clinical characteristics of 138 hospitalized patients with 2019 novel coronavirus-infected pneumonia in Wuhan, China.** *JAMA* 2020 Feb 7. [Epub ahead of print] CrossRef Medline
- Zhou P, Yang XL, Wang XG, et al. **A pneumonia outbreak associated with a new coronavirus of probable bat origin.** *Nature* 2020;579:270–73 CrossRef Medline
- Paules CI, Marston HD, Fauci AS. **Coronavirus infections: more than just the common cold.** *JAMA* 2020 Jan 23. [Epub ahead of print] CrossRef Medline
- Prevention CfDCA. Coronavirus 2019 2020.** <https://www.cdc.gov/coronavirus/2019-ncov/cases-updates/cases-in-us.html>. Accessed April 1, 2020
- World Health Organization. **Coronavirus Disease (COVID-19) Pandemic.** May 4, 2020. <https://www.who.int/emergencies/diseases/novel-coronavirus-2019>. Accessed March 31, 2020
- Leslie-Mazwi T, Chandra RV, Baxter BW, et al; Society of NeuroInterventional Surgery. **ELVO: an operational definition.** *J Neurointerv Surg* 2018;10:507–09 CrossRef Medline
- Goyal M, Menon BK, van Zwam WH, et al; HERMES collaborators. **Endovascular thrombectomy after large-vessel ischaemic stroke: a meta-analysis of individual patient data from five randomised trials.** *Lancet* 2016;387:1723–31 CrossRef Medline
- Albers GW, Marks MP, Kemp S, et al; DEFUSE 3 Investigators. **Thrombectomy for stroke at 6 to 16 hours with selection by perfusion imaging.** *N Engl J Med* 2018;378:708–18 CrossRef Medline
- Nogueira RG, Jadhav AP, Haussen DC, et al; DAWN Trial Investigators. **Thrombectomy 6 to 24 hours after stroke with a mismatch between deficit and infarct.** *N Engl J Med* 2018;378:11–21 CrossRef Medline
- Temporary emergency guidance to US stroke centers during the COVID-19 pandemic.** *Stroke* 2020 Apr 1. [Epub ahead of print] CrossRef Medline
- Turner AJ, Hiscox JA, Hooper NM. **ACE2: from vasopeptidase to SARS virus receptor.** *Trends Pharmacol Sci* 2004;25:291–94 CrossRef Medline
- Zheng YY, Ma YT, Zhang JY, et al. **COVID-19 and the cardiovascular system.** *Nat Rev Cardiol* 2020;17:259–60 CrossRef Medline
- Li YC, Bai WZ, Hashikawa T. **The neuroinvasive potential of SARS-CoV2 may play a role in the respiratory failure of COVID-19 patients.** *J Med Virol* 2020 Feb 27. [Epub ahead of print] CrossRef Medline
- Li B, Yang J, Zhao F, et al. **Prevalence and impact of cardiovascular metabolic diseases on COVID-19 in China.** *Clin Res Cardiol* 2020; 109:531–38 CrossRef Medline
- Mao L, Wang M, Chen S, et al. **Neurological Manifestations of Hospitalized Patients with COVID-19 in Wuhan, China: a retrospective case series study.** *MedRxiv* Feb 25, 2020. <https://www.medrxiv.org/content/10.1101/2020.02.22.20026500v1>. Accessed March 31, 2020



16. Klok FA, Kruip M, van der Meer NJM, et al. **Incidence of thrombotic complications in critically ill ICU patients with COVID-19.** *Thromb Res* 2020 Apr 10. [Epub ahead of print] CrossRef Medline
17. Lillicrap D. **Disseminated intravascular coagulation in patients with 2019-nCoV pneumonia.** *J Thromb Haemost* 2020;18:786–87 CrossRef Medline
18. Smeeth L, Thomas SL, Hall AJ, et al. **Risk of myocardial infarction and stroke after acute infection or vaccination.** *N Engl J Med* 2004; 351:2611–18 CrossRef Medline
19. Mehta P, McAuley DF, Brown M, et al; HLH Across Specialty Collaboration, UK. **COVID-19: consider cytokine storm syndromes and immunosuppression.** *Lancet* 2020;395:1033–34 CrossRef Medline
20. Driggin E, Madhavan MV, Bikdeli B, et al. **Cardiovascular considerations for patients, health care workers, and health systems during the coronavirus disease 2019 (COVID-19) pandemic.** *J Am Coll Cardiol* 2020 Mar 18. [Epub ahead of print] CrossRef Medline
21. Talen J. **COVID-19: Neurologists in Italy to Colleagues in US: Look for Poorly-Defined Neurologic Conditions in Patients with the Coronavirus.** *Neurology Today* March 27, 2020. <https://journals.lww.com/neurotodayonline/blog/breakingnews/pages/post.aspx?PostID=920>. Accessed March 31, 2020
22. Oxley TJ, Mocco J, Majidi S, et al. **Large-vessel stroke as a presenting feature of Covid-19 in the young.** *N Engl J Med* 2020 Apr 28. [Epub ahead of print] CrossRef Medline
23. Thornton J. **Stroke: “striking reductions” are seen in number of people with symptoms seeking help.** *BMJ* 2020;369:m1406 CrossRef Medline
24. Holt-Lunstad J, Smith TB, Layton JB. **Social relationships and mortality risk: a meta-analytic review.** *PLoS Med* 2010;7:e1000316 CrossRef Medline
25. Williams MM, Leslie-Mazwi T, Hirsch JA, et al. **Real-world effects of late window neurothrombectomy: procedure rates increase without night-time bias.** *J Neurointerv Surg* 2020;12:460–64 CrossRef Medline
26. Grasselli G, Pesenti A, Cecconi M. **Critical care utilization for the COVID-19 outbreak in Lombardy, Italy: early experience and forecast during an emergency response.** *JAMA* 2020 Mar 13. [Epub ahead of print] CrossRef Medline
27. Wong JEL, Leo YS, Tan CC. **COVID-19 in Singapore: current experience: critical global issues that require attention and action.** *JAMA* 2020 Feb 20. [Epub ahead of print] CrossRef Medline
28. Ran L, Chen X, Wang Y, et al. **Risk factors of healthcare workers with corona virus disease 2019: a retrospective cohort study in a designated hospital of Wuhan in China.** *Clin Infect Dis* 2020 Mar 17. [Epub ahead of print] CrossRef Medline
29. Chang D, Xu H, Rebaza A, et al. **Protecting health-care workers from subclinical coronavirus infection.** *Lancet Respir Med* 2020;8: e13 CrossRef Medline
30. Lauer SA, Grantz KH, Bi Q, et al. **The incubation period of coronavirus disease 2019 (COVID-19) From publicly reported confirmed cases: estimation and application.** *Ann Intern Med* 2020 Mar 10. [Epub ahead of print] CrossRef Medline
31. Pan L, Mu M, Yang P, et al. **Clinical characteristics of COVID-19 patients with digestive symptoms in Hubei, China: a descriptive, cross-sectional, multicenter study.** *Am J Gastroenterol* 2020;115: 766–73 CrossRef Medline
32. Stefanini GG, Azzolini E, Condorelli G. **Critical organizational issues for cardiologists in the COVID-19 outbreak: a frontline experience from Milan, Italy.** *Circulation* 2020 Mar 24. [Epub ahead of print] CrossRef Medline
33. Fargen KM, Arthur AS, Leslie-Mazwi T, et al. **A survey of burnout and professional satisfaction among United States neurointerventionalists.** *J Neurointerv Surg* 2019;11:1100–04 CrossRef Medline
34. Fargen KM, Ansari SA, Spiotta A, et al. **Influence of thrombectomy volume on non-physician staff burnout and attrition in neurointerventional teams.** *J Neurointerv Surg* 2020 Apr 3. [Epub ahead of print] CrossRef Medline
35. Tam CF, Cheung KS, Lam S, et al. **Impact of coronavirus disease 2019 (COVID-19) outbreak on ST-segment-elevation myocardial infarction care in Hong Kong, China.** *Circ Cardiovasc Qual Outcomes* 2020;13:e006631 CrossRef Medline
36. Fang Y, Zhang H, Xie J, et al. **Sensitivity of chest CT for COVID-19: comparison to RT-PCR.** *Radiology* 2020 Feb 19. [Epub ahead of print] CrossRef Medline
37. Ai T, Yang Z, Hou H, et al. **Correlation of chest CT and RT-PCR testing in coronavirus disease 2019 (COVID-19) in China: a report of 1014 cases.** *Radiology* 2020 Feb 26. [Epub ahead of print] CrossRef Medline
38. Kampf G, Todt D, Pfaender S, et al. **Persistence of coronaviruses on inanimate surfaces and their inactivation with biocidal agents.** *J Hosp Infect* 2020;104:246–51 CrossRef Medline
39. Vagal A, Wintermark M, Nael K, et al. **Automated CT perfusion imaging for acute ischemic stroke: pearls and pitfalls for real-world use.** *Neurology* 2019;93:888–98 CrossRef Medline
40. Khosravani H, Rajendram P, Notario L, et al. **Protected code stroke: hyperacute stroke management during the coronavirus disease 2019 (COVID-19) pandemic.** *Stroke* 2020 Apr 1. [Epub ahead of print] CrossRef Medline
41. Cheung JC, Ho LT, Cheng JV, et al. **Staff safety during emergency airway management for COVID-19 in Hong Kong.** *Lancet Respir Med* 2020;8:e19 CrossRef Medline
42. Sharma D, Rasmussen M, Han R, et al. **Anesthetic Management of Endovascular Treatment of Acute Ischemic Stroke During COVID-19 Pandemic: Consensus Statement from Society for Neuroscience in Anesthesiology & Critical Care (SNACC), endorsed by Society of Vascular & Interventional Neurology (SVIN), Society of Neuro-Interventional Surgery (SNIS), Neurocritical Care Society (NCS), and European Society of Minimally Invasive Neurological Therapy (ESMINT).** *J Neurosurg Anesthesiol* 2020 Apr 8. [Epub ahead of print] CrossRef Medline
43. Canelli R, Connor CW, Gonzalez M, et al. **Barrier enclosure during endotracheal intubation.** *N Engl J Med* 2020 Apr 3. [Epub ahead of print] CrossRef Medline
44. Fraser JF, Arthur AS, Chen M, et al. **Society of NeuroInterventional Surgery recommendations for the care of emergent neurointerventional patients in the setting of covid-19.** *J Neurointerv Surg* 2020 Apr 15. [Epub ahead of print] CrossRef Medline
45. Society of Neurointerventional Surgery. **Care Recommendations for Emergent Neurointerventional Patients in the Setting of COVID.** March 28, 2020. Accessed March 31, 2020
46. Chen Q, Liang M, Li Y, et al. **Mental health care for medical staff in China during the COVID-19 outbreak.** *Lancet Psychiatry* 2020;7: e15–16 CrossRef Medline
47. Greenberg N, Docherty M, Gnanapragasam S, et al. **Managing mental health challenges faced by healthcare workers during covid-19 pandemic.** *BMJ* 2020;368:m1211 CrossRef Medline
48. Pilcher JJ, Huffcutt AI. **Effects of sleep deprivation on performance: a meta-analysis.** *Sleep* 1996;19:318–26 CrossRef Medline
49. Martinez-Gutierrez JC, Leslie-Mazwi T, Chandra RV, et al. **Number needed to treat: a primer for neurointerventionalists.** *Interv Neuroradiol* 2019;25:613–18 CrossRef Medline
50. Bloom DE, Cadarette D. **Infectious disease threats in the twenty-first century: strengthening the global response.** *Front Immunol* 2019;10:549 CrossRef Medline
51. Gates B. **Innovation for pandemics.** *N Engl J Med* 2018;378:2057–60 CrossRef Medline



# Tandem Carotid Lesions in Acute Ischemic Stroke: Mechanisms, Therapeutic Challenges, and Future Directions

 A.Y. Poppe,  G. Jacquin,  D. Roy,  C. Stapf, and  L. Derex



## ABSTRACT

**SUMMARY:** Approximately 15% of patients undergoing endovascular thrombectomy for anterior circulation acute ischemic stroke have a tandem lesion, defined as a severe stenosis or occlusion of the cervical internal carotid artery ipsilateral to its intracranial occlusion. Patients with tandem lesions have worse outcomes than patients with isolated intracranial occlusions, but the optimal management of their carotid lesions during endovascular thrombectomy remains controversial. The main options commonly used in current practice include acute stent placement in the carotid lesion versus thrombectomy alone without definitive revascularization of the carotid artery. While treatment decisions for these patients are often complex and strategies vary according to clinical, anatomic, and technical considerations, only results from randomized trials comparing these approaches are likely to strengthen current recommendations and optimize patient care.

**ABBREVIATIONS:** AIS = acute ischemic stroke; c-ICA = cervical internal carotid artery; EVT = endovascular thrombectomy; IVT = intravenous thrombolysis; TL = tandem lesion

Approximately 15% of patients undergoing endovascular thrombectomy (EVT) for anterior circulation acute ischemic stroke (AIS) have a tandem lesion (TL), defined as a severe stenosis or occlusion of the cervical internal carotid artery (c-ICA) ipsilateral to its intracranial occlusion.<sup>1</sup> Studies of patients with TLs have generally included more men than women (approximately 60% versus 40%),<sup>2</sup> which likely reflects a true difference in the prevalence of carotid atherosclerosis according to sex.<sup>3</sup> Epidemiologic studies have also shown that extracranial artery disease is more prevalent among whites than blacks and Asians.<sup>3</sup>

Patients with TLs have worse outcomes than patients with isolated intracranial occlusions, with high rates of disability and death.<sup>4</sup> Intravenous thrombolysis (IVT) is less effective in patients with TLs, presumably owing to a larger clot burden and low

anterograde flow impeding thrombolytic drug access to the intracranial thrombus.<sup>4</sup>

Relatively few patients with TLs were included in the major randomized controlled trials of EVT, and management of the c-ICA was generally not specified by protocol or analyzed post hoc. In the absence of robust randomized trial data, no firm recommendations about optimal management can be forwarded, as reflected in the most recent American<sup>5</sup> and European<sup>6</sup> guidelines.


For this population of patients with AIS undergoing EVT, treatment decisions are often complex, and strategies vary according to clinical, anatomic, and technical considerations in addition to physician preference.

This article aims to review the pathophysiologic substrate of AIS related to TLs, the management options available for patients with such lesions, and directions for future research.

Received February 23, 2020; accepted after revision March 17.

From the Departments of Medicine (Neurology) (A.Y.P., G.J., C.S.), and Radiology (Neuroradiology) (D.R.), Centre Hospitalier de l'Université de Montréal, Montréal, Québec, Canada; Neurovascular Group (A.Y.P., G.J., C.S.), Axe Neurosciences, Centre de Recherche du Centre Hospitalier de l'Université de Montréal, Montréal, Québec, Canada; Stroke Center (L.D.), Department of Neurology, Neurological Hospital, Hospices Civils de Lyon, Lyon, France; and EA 7425 HESPER (L.D.), Health Services and Performance Research, Claude Bernard Lyon 1 University, Lyon, France.

Please address correspondence to Alexandre Y. Poppe, MD, Department of Medicine (Neurology), Centre Hospitalier de l'Université de Montréal, 900 rue St-Denis, R04-758, Montréal, Québec, Canada; e-mail: alexandre.poppe.chum@ssss.gouv.qc.ca

 Indicates open access to non-subscribers at [www.ajnr.org](http://dx.doi.org/10.3174/ajnr.A6582)  
<http://dx.doi.org/10.3174/ajnr.A6582>

## Mechanism of Stroke and Etiology of the Cervical Carotid Lesion

In patients with TLs, the mechanism of stroke usually involves artery-to-artery embolization of the clot from an atherosclerotic plaque or from a site of arterial dissection in the ICA to the intracranial circulation.

**Atherosclerotic Plaque versus Dissection.** Tandem lesions are most often atherosclerotic in nature, with an underlying plaque becoming unstable, rupturing, and triggering local thrombus

formation with distal embolization of thrombus fragments. Published series of acute TLs suggest that about 60%–70% are due to atherosclerotic plaque; 20%–30%, due to dissection; and the remainder, attributable to carotid webs and cardiac emboli.<sup>2,7</sup> In this last group, a large cardiac embolus presumably lodges in the c-ICA (possibly due to underlying atherosclerotic stenosis) and fragments to embolize in the intracranial circulation.

Radiologic differentiation of these various etiologies of carotid stenosis is possible and does not necessarily require conventional angiography. Noninvasive modalities like MRA and CTA have been found to identify carotid dissection with similar sensitivity and specificity.<sup>8</sup> In most settings, acute stroke imaging involves CTA. With this technique, dissection is suggested by the presence of a tapered or flame-shaped stenosis or occlusion occurring  $\geq 2$  cm from the ICA origin, often near the skull base.<sup>9</sup> Classic findings such as a double lumen or intimal flap may be found, but less commonly.<sup>10</sup> On plain CT, axial sections at the skull base can sometimes identify an ICA wall hematoma, appearing as a hyperdense or tissue-density crescent. In contrast, c-ICA occlusions of atherosclerotic etiology are generally at or near the ICA origin and may be associated with adjacent calcified plaque. Atherosclerosis in other cervical arteries may also favor this diagnosis over dissection.

Patients with TLs due to carotid dissection tend to have more favorable demographic profiles, being younger with fewer comorbidities than patients with atherosclerotic lesions.<sup>7</sup> Acute stent placement for an ICA dissection is less commonly performed than for atherosclerotic lesions,<sup>7,11,12</sup> most likely due to anatomic considerations (dissected segments may be long and tortuous) and the generally more favorable natural history of dissection, which involves spontaneous vessel wall healing with recanalization in up to 70% of patients.<sup>13</sup> If stent placement is performed for carotid dissection, the true lumen must be identified and multiple stents may be required to reconstruct the artery, though dissected flaps may be more easily opened by stent placement than hardened atherosclerotic plaques. Addressing the intracranial occlusion first and avoiding routine c-ICA stent placement in patients with dissection appears to be a safe approach.<sup>12</sup> Conversely, atherosclerotic lesions represent an important technical challenge, highlighted by longer procedural times, lower recanalization rates, and more procedural complications in some series.<sup>14</sup> If stent placement is performed for carotid lesions due to atherosclerotic plaque, angioplasty before and sometimes after stent placement may be required, particularly in calcified plaques.

Patients with dissection may thus be distinguished from those with atherosclerotic plaque as having different pathologies with potentially different treatment approaches and prognoses.<sup>15</sup>

**Severity of the Carotid Stenosis.** The severity of the cervical carotid lesion, that is, whether it is completely occlusive or merely stenotic, may also influence both the technical approach and outcomes. Traversing a complete occlusion may be more challenging and must often be done “blindly” because the distal lumen cannot be opacified. However, outcomes appear similar regardless of whether cervical ICA pathology is occlusive or stenotic.<sup>16</sup>

A distinct subgroup comprises patients with isolated acute c-ICA occlusion presenting with symptoms of ipsilateral hemispheric

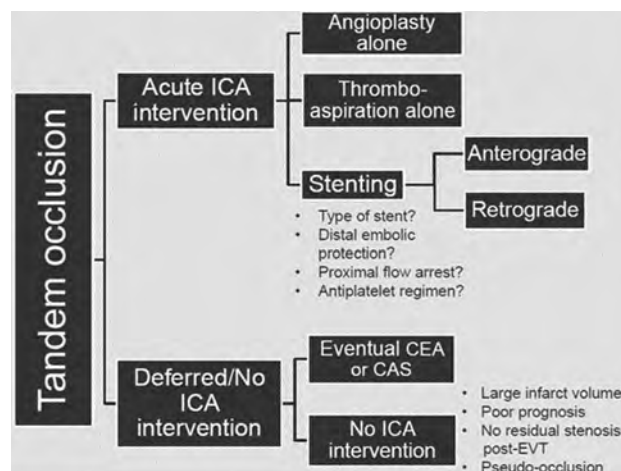


**FIG 1.** Schematic summarizing the main approaches to managing cervical carotid lesions in patients with tandem occlusions undergoing thrombectomy for acute stroke. CEA indicates carotid endarterectomy; CAS, carotid artery stent placement.

ischemia, usually due to impaired carotid artery territory perfusion (acute hemodynamic stroke) rather than intracranial clot embolization. These patients are infrequent in the setting of AIS, generally have a more favorable prognosis than patients with TLs, and are less often considered for EVT, given the absence of an intracranial occlusion.<sup>14</sup>

**Radiologic Differentiation of True Carotid Occlusion from Pseudo-Occlusion.** It is sometimes difficult to reliably identify patients with true TLs on CTA because about one-third of patients with presumed c-ICA tandem occlusions using this technique actually have intracranial carotid terminus occlusions (so-called ICA pseudo-occlusions) with delayed opacification of the c-ICA due to slow anterograde flow and a stagnant column of nonopacified blood.<sup>17,18</sup> In such cases, the pseudo-occlusion is usually only confirmed on angiography; however, delayed-phase CTA of the neck may be helpful in confirming true c-ICA occlusions.<sup>19</sup> Identifying a true tandem occlusion before EVT is helpful to properly plan the angiographic procedure, including determining how to traverse the c-ICA occlusion and permitting sufficient forethought regarding the need for c-ICA stent placement or angioplasty.

### Treatment Strategies and Challenges

The optimal management of patients with AIS and TLs undergoing EVT remains uncertain, being subject to multiple clinical, anatomic, and technical considerations.

**Should Acute Carotid Stent Placement Be Performed in Conjunction with Thrombectomy?** Two main approaches exist in patients with AIS with TLs undergoing EVT (Fig 1). The first is to traverse the c-ICA lesion, perform intracranial clot retrieval, and leave the c-ICA largely untreated for possible endarterectomy or stent placement in the ensuing days or weeks. This approach includes less definitive c-ICA recanalization strategies such as balloon angioplasty alone or thrombo-aspiration via a large-bore catheter and is sometimes used as an initial approach, with

**Postulated advantages of each treatment approach for patients with tandem lesions (acute stent placement versus no acute stent placement)**

Potential Advantages of Acute Stent Placement	Potential Advantages of No Acute Stent Placement
Treatment of the causative embolic lesion and lower risk of stroke recurrence	Lower risk of intracranial hemorrhage (avoidance of hyperperfusion, acute antiplatelet agents)
Improvement of cerebral perfusion with potential attenuation of infarct progression	Lower risk of iatrogenic artery-to-artery embolization during stent deployment
Contribution to spontaneous intracranial clot lysis	No risk of in-stent thrombosis
	Avoids delays in intracranial recanalization (if stent placement before thrombectomy)
	Lower risk of procedural bradycardia and hypotension from carotid baroreceptor activation with stent deployment

intraprocedural, stepwise progression to stent placement only if dynamic re-occlusion of the c-ICA occurs despite angioplasty. The second, more definitive approach is to recanalize the c-ICA using stent placement systematically during EVT, either before or following intracranial thrombectomy. These treatment strategies exemplify the competing risks that must be balanced in patients with TLs—that is, ischemic stroke progression or recurrence on the one hand versus intracranial hemorrhage on the other. Both are widely used in clinical practice, as seen in the STRATIS EVT registry (<https://www.medtronic.com/content/dam/medtronic-com/products/neurological/revascularization-stroke/stratis-systems-of-care.pdf>) in which 54% of patients with TLs were acutely stented and 46% were not.<sup>1</sup>

The putative advantages of acute stent placement in the c-ICA and foregoing acute stent placement are summarized in the Table. Acute c-ICA stent placement may more effectively treat the cause of stroke, favor intracranial clot lysis, and decrease the risk of recurrence while improving overall cerebral perfusion.<sup>20</sup> Acute stent placement is also associated with greater early c-ICA patency and perhaps better early neurologic improvement than angioplasty alone.<sup>21</sup> However, foregoing acute stent placement may avoid early administration of antiplatelet agents, which may increase the risk of intracranial hemorrhage in the immediate postrecanalization phase, particularly in patients having received IVT or having a large core of cerebral infarction.<sup>22,23</sup> Definitive c-ICA revascularization can also then be performed with an operation or stent placement in a delayed, more secure setting. Furthermore, acute stent placement carries an inherent risk of in-stent thrombosis, which may confer a worse prognosis.<sup>24</sup>

#### Should the Intracranial or Extracranial Lesions Be Treated First?

Stent placement may be performed either before intracranial thrombectomy (“anterograde”) or after thrombectomy (“retrograde”). Published series have shown that both approaches are commonly used<sup>25</sup> and suggest that both yield similar functional outcomes despite differences in recanalization times.<sup>26,27</sup>

There are theoretic advantages to the retrograde technique, including shorter intracranial recanalization time and avoidance of potential snagging of the retrievable stent in the struts of an already-deployed c-ICA stent.<sup>28</sup> Moreover, re-establishing antero-grade carotid flow may provoke distal migration of the intracranial thrombus, making it less amenable to thrombectomy. Stent placement of the c-ICA earlier in the procedure also subjects the patient to potential hemodynamic instability due to baroreceptor activation while cerebral perfusion is still impaired by the presence of an

intracranial occlusion. Furthermore, in some cases, merely traversing the ICA lesion with catheters to access the intracranial thrombus is sufficient to dilate the stenosis or occlusion and potentially obviate the need for stent placement. A potential disadvantage of the retrograde approach is that treating the extracranial carotid lesion after intracranial recanalization may be associated with recurrent embolization during stent deployment. Furthermore, in some cases, specific technical circumstances may mandate an antero-grade approach to gain access to the intracranial circulation. The debate regarding the order of stent placement relative to thrombectomy has recently been circumvented by some authors who have developed techniques using nearly simultaneous c-ICA revascularization and intracranial stent-retriever thrombectomy; however, adoption of this approach remains limited thus far.<sup>29,30</sup>

**What Type of Stent Should Be Used?** Dual-layer stents contain a second micromesh layer to theoretically better cover the atherosclerotic plaque and more effectively prevent dislodgement of debris.<sup>31</sup> However, some studies suggest that dual-layer stents may be associated with a higher rate of acute in-stent thrombosis when used for a TL during EVT,<sup>31,32</sup> while others do not.<sup>33</sup> Nevertheless, their use in the acute setting is not widespread. Otherwise, there are few data favoring one stent type over another in the acute setting (eg, open- or closed-cell). Balloon angioplasty before or following stent deployment may be performed to ensure an optimal intraluminal diameter, but the radial force of the stent may often be sufficient to achieve a satisfactory angiographic result.

**What Antithrombotic Regimen is Preferred?** If ICA stent placement is performed, antithrombotic medication must generally be given to prevent acute in-stent thrombosis and its associated potential risks of distal embolization or stent occlusion. However, the choice of optimal antithrombotic therapy in the setting of acute ICA stent placement during EVT remains unknown. The risk of in-stent thrombosis must be balanced against the risk of hemorrhagic transformation of infarcted cerebral tissue, with this latter risk of particular concern in patients having IVT<sup>34</sup> or having a large core of infarction. It is known that early administration of 300 mg of IV aspirin after IVT is associated with excess intracerebral hemorrhage and no clinical benefit, at least among patients not treated with EVT.<sup>34</sup> Therefore, whether IVT was given should influence the choice of acute antithrombotic medications.

The risk of intracranial hemorrhage in stented patients varies widely between series, with some<sup>22,35</sup> suggesting much higher

rates than those seen in the major EVT trials and other larger series suggesting no excess risk of bleeding,<sup>1,2</sup> even among patients treated with IVT.<sup>23,36</sup> Furthermore, the use of IVT appears safe and likely beneficial in patients with TLs who undergo stent placement.<sup>37</sup> In the Thrombectomy in Tandem Occlusion (TITAN) cohort, 24.7% of patients developed hemorrhagic infarction, and 14.2%, a parenchymal hematoma, similar to rates seen after thrombectomy for isolated intracranial occlusions.<sup>23</sup> In this cohort, acute carotid stent placement and antiplatelet therapy use were not predictors of parenchymal hematoma or hemorrhagic infarction.

Different antithrombotic regimens are described in the acute phase after acute ICA stent placement, including administration of aspirin alone<sup>38</sup> or in combination with clopidogrel at various dosages as well as the administration of glycoprotein IIb/IIIa inhibitors and heparin. Series in which glycoprotein IIb/IIIa inhibitors were given either intravenously or intra-arterially poststenting seem to demonstrate an excess risk of intracranial hemorrhage, suggesting that enteral antiplatelet agents may be safer in this setting.<sup>22</sup>

A small series evaluating delayed stent patency found greater rates of in-stent thrombosis among patients treated with aspirin only as opposed to aspirin and clopidogrel.<sup>24</sup> Stent thrombosis in this series was also attributed to the routine use of long, closed-cell stents.<sup>24</sup> In a retrospective series of 98 patients with stroke with an atherosclerotic TL who underwent acute stent placement and were given antiplatelet monotherapy with 250 mg of aspirin in the acute phase, the rate of stent occlusion within 7 days after stent placement was 10.3%.<sup>38</sup> In this series, early stent occlusion had no clinical consequences in terms of recurrence of stroke or worse outcome. This finding might be related to the long-standing nature of the atherosclerotic ICA stenosis, which may improve collateralization and hemodynamic tolerance.

Although practice varies widely, a reasonable strategy would be administration of a periprocedural aspirin bolus (about 300 mg), either orally, rectally, or intravenously (where available) with a clopidogrel bolus (300 mg) given orally. In patients at higher risk of bleeding, particularly those having received IV thrombolysis or having a large infarct core, the clopidogrel bolus may be delayed until after repeat brain imaging within the first 12–24 hours.

Even in cases of nonacute ICA stent placement, antiplatelet regimens are not uniform, though most experts suggest that the duration of dual-antiplatelet therapy beyond the acute phase should be at least 4–6 weeks, as extrapolated from the Carotid Revascularization Endarterectomy versus Stenting Trial (CREST) protocol, followed by a long-term single-antiplatelet agent (usually aspirin).<sup>39</sup> Unlike acute stent placement, in this more elective setting, patients can be administered antiplatelet agents before stent placement, which may theoretically decrease the risk of stent thrombosis.

Only limited data exist regarding the use of ticagrelor or prasugrel in carotid stent placement, and their use in this setting cannot be routinely recommended.<sup>40</sup> Cangrelor, an intravenous antiplatelet agent characterized by rapid onset and offset of action, has been used in some centers, but data are currently insufficient to recommend its routine use.<sup>41</sup>

Some interventionalists administer IV heparin when stent placement occurs during EVT,<sup>42</sup> theoretically decreasing the risk

of stent thrombosis while awaiting the onset of action of antiplatelet agents. Higher doses of heparin (70 U/kg) are associated with higher rates of intracerebral hemorrhage, particularly in combination with dual-antiplatelet regimens.<sup>43</sup> With lower doses of approximately 30 U/kg, hemorrhagic complications do not appear to be more common, though clinical outcomes are similarly not better. Strong recommendations can, therefore, be made regarding the use of lower-dose IV heparin in these patients.<sup>44</sup>

Further data to help guide the use of aspirin and heparin among patients undergoing EVT should be provided by the ongoing Multicenter Randomized CLinical trial of Endovascular treatment for Acute ischemic stroke in the Netherlands; the effect of periprocedural MEDication: antiplatelet agents, heparin, both or neither (MR CLEAN-MED) randomized trial (ISCRTN76741621).

**Is There a Role for Embolic Protection Devices?** For embolic protection devices using either distal filters or proximal flow reversal, data pertain almost exclusively to patients undergoing nonacute carotid stent placement for primary or secondary stroke prevention. The benefit of embolic protection devices during stent placement remains debated, and in the absence of high-quality comparative studies, their use is not universally endorsed.<sup>45</sup> Given the urgency of EVT for stroke and potential patient instability, embolic protection devices are rarely used in this setting.<sup>11</sup>

**Delayed Carotid Revascularization in Nonstented Patients.** Among patients not undergoing acute stent placement, it is reasonable to consider delayed revascularization, either with carotid endarterectomy or stent placement, in a secondary prevention paradigm. Although few data exist on the proportion of patients with TLs undergoing EVT who later benefit from deferred ICA revascularization, this number is likely relatively small (only 4 of 13 patients in the Endovascular Treatment for Small Core and Anterior Circulation Proximal Occlusion With Emphasis on Minimizing CT to Recanalization Times [ESCAPE] trial).<sup>46</sup> This small number may be due to poor poststroke recovery, large stroke volume, hemorrhagic transformation, or sufficient c-ICA revascularization by the bougie effect of cross-lesional catheter advancement. Clearly, patients with TLs undergoing EVT for stroke are a more severely affected population than most patients included in studies of nonacute carotid revascularization whose index events were generally minor strokes and retinal ischemic events.<sup>47</sup>

Consideration of delayed carotid intervention also raises the issue of how and when follow-up carotid imaging should be performed in these patients, both for those who are stented acutely (to assess delayed stent patency) and those who are not (to assess indications for delayed revascularization). Noninvasive imaging by carotid Doppler sonography or by CTA can reasonably be performed within a few days to weeks of the index stroke, with timing adapted to the patient's clinical status.

**Other Management Approaches.** Other treatment options are used only anecdotally, and little literature supports their use. One includes “sacrifice” of the c-ICA by coil embolization, so as to address the source of arterial emboli, and is more often used in situations in which c-ICA intraluminal thrombus suggests a high risk of embolization and adequate collateral flow is provided via the circle of Willis.<sup>34</sup> Similarly, in some patients who have



	Favours no stenting ←	→ Favours stenting
ICA lesion etiology	Dissection	Atherosclerosis
Infarct core volume	Large infarct/low ASPECTS	Small infarct/high ASPECTS
Quality of final intracranial recanalization	None or poor (mTICI 0-1)	Complete or near-complete (mTICI 2b-3)
Collateral circulation via circle of Willis	Good collaterals/complete circle of Willis	Poor collaterals/incomplete circle of Willis
Dynamic ICA re-occlusion on angiography	No active re-occlusion	Active re-occlusion
Use of IV thrombolysis	Yes	No
Systemic bleeding risk	Higher risk	Lower risk
Indication for long-term anticoagulation	Present	Absent

**FIG 2.** Clinical and radiologic factors influencing the decision to favor acute stent placement or no stent placement for patients with tandem lesions undergoing thrombectomy.

persistent c-ICA occlusion but favorable intracranial recanalization with adequate cross-filling, the c-ICA occlusion may simply be left untouched. Another approach that remains marginally used is emergent carotid endarterectomy in the hours following thrombectomy.<sup>48</sup> In cases of chronic c-ICA occlusions with recurrent embolic or hemodynamic ischemia, randomized trials have demonstrated that extracranial-to-intracranial arterial bypass procedures are not useful, so this delayed approach is not recommended.<sup>49,50</sup>

### Current Evidence for Management

**Data from the Major EVT Trials.** High-quality evidence for treatment of patients with TLs undergoing EVT remains limited. Three of the major randomized EVT trials excluded patients with a TL.<sup>51-53</sup> In the remaining trials, these patients represented 13%–32% of the study population.

The treatment effect of thrombectomy in patients with TLs was comparable with that of patients with isolated intracranial occlusions in the Highly Effective Reperfusion using Multiple Endovascular devices (HERMES) collaboration. However, this patient-level meta-analysis included only 122 patients with TLs,<sup>54</sup> and while a clear superiority of EVT over standard care was demonstrated, little has been published about how the c-ICA was addressed in the individual trials.<sup>46</sup>

Acute stent placement was used in a minority of patients with TLs in the ESCAPE (26.7%), the Multicenter Randomized Clinical Trial of Endovascular Treatment for Acute Ischemic Stroke in the Netherlands (MR CLEAN) (40%), and Endovascular Revascularization With Solitaire Device Versus Best Medical Therapy in Anterior Circulation Stroke Within 8 Hours (REVASCAT) (47.4%) trials.<sup>5</sup> Late-window EVT trials have similarly not provided meaningful guidance for patients with TLs. The DWI or CTP Assessment with Clinical Mismatch in the Triage of Wake-Up and Late Presenting Strokes Undergoing Neurointervention with Trevo (DAWN) trial included 27 patients with TLs in the EVT arm but mandated that no c-ICA stent

placement be performed<sup>55,56</sup> while the Endovascular Therapy Following Imaging Evaluation for Ischemic Stroke (DEFUSE-3) trial did not detail treatment approaches or outcomes in the TL subgroup.<sup>57,58</sup> Optimal acute management of the cervical ICA lesion in patients with TLs undergoing EVT, therefore, remains unclear.

### Evidence from Observational Studies.

Our international survey of stroke experts further highlighted this therapeutic uncertainty, with 75% of respondents admitting to having equipoise regarding therapy for these patients.<sup>11</sup> The existence of community equipoise is also echoed in several studies that were all observational and often only described stented patients.

Four main meta-analyses of these smaller case series have been published,<sup>20,25,26,59</sup> most with relatively few patients not having undergone acute stent placement and only 1<sup>59</sup> focusing primarily on whether acute stent placement was associated with different clinical outcomes than no stent placement. The large multicenter retrospective cases-series of 482 patients from the TITAN group was not included in these meta-analyses but suggests that stented patients receiving acute antiplatelet medications have more favorable outcomes than patients treated with angioplasty alone or those with no acute ICA intervention.<sup>37</sup> Another large multicenter EVT registry<sup>1</sup> also found better outcomes among stented patients, with both nonrandomized series suggesting 15%–20% higher rates of favorable outcome (mRS 0–2) at 90 days. Clearly, even adjusted analyses of observational data cannot entirely control for indication biases that may have favored stent placement in patients with an a priori better prognosis.

The Endovascular Acute Stroke Intervention (EASI) trial demonstrated that randomization of patients with TLs is possible.<sup>60</sup> In this single-center pragmatic care trial performed before the MR CLEAN results, patients with stroke were randomized to best medical management alone versus best medical management with EVT, and patients allocated to EVT who had a TL identified on CTA or conventional angiography underwent a second randomization, allocating them to acute ICA stent placement or not. The 24 patients included had similar functional outcomes whether stented or not but were too few to generate practice-changing conclusions. Nonetheless, the data have served as a proof-of-concept for the forthcoming Endovascular Acute Stroke Intervention–Tandem Occlusion (EASI-TOC) trial (NCT04261478).<sup>61</sup>

In the absence of high-level data to guide management decisions and if randomization in a clinical trial is not possible, observational data do suggest that some clinical and radiologic factors may favor acute stent placement, while others may argue against it (Fig 2).

### Conclusions and Future Directions

Strokes caused by a TL represent up to one-fifth of all strokes treated with EVT. Although randomized trials were not designed



to evaluate the efficacy of EVT in these patients, a subgroup analysis of individual TL patient data suggests that EVT results in better neurologic outcomes than standard treatment using IVT alone. Observational data suggest that combining acute c-ICA stent placement with intracranial thrombectomy may be the best strategy to treat patients with TLs, being associated with better functional outcomes and carotid patency. However, because robust scientific evidence is still lacking and antiplatelet agents and endovascular techniques and tools are in constant evolution, no consensus remains regarding the ideal therapeutic strategy for these patients. In this context, only the results of randomized-controlled trials like TITAN (NCT03978988) and EASI-TOC<sup>62</sup> will help determine the benefit of acute stent placement, or absence thereof, in patients with TLs.

Disclosures: Alexandre Y. Poppe—RELATED: Grant: Canadian Stroke Trials for Optimized Results, Comments: networking seed grant for Randomized Trial of Tandem Carotid Lesions (EASI-TOC)\*; UNRELATED: Other: Servier Laboratories, Bristol-Myers Squibb–Pfizer, Bayer AG, Comments: Servier Laboratories, institutional support for stroke fellowship; Bristol-Myers Squibb–Pfizer, Bayer AG, institutional support for electronic medical record service; OTHER RELATIONSHIPS: I am the Principal Investigator for a randomized trial studying patients with tandem carotid lesions undergoing endovascular thrombectomy (EASI-TOC, NCT04261478). Daniel Roy—UNRELATED: Payment for Development of Educational Presentations: Radiological Society of Quebec, Comments: payments for production of a workshop on CT angiography. \*Money paid to the institution.

## REFERENCES

- Jadhav AP, Zaidat OO, Liebeskind DS, et al. **Emergent management of tandem lesions in acute ischemic stroke.** *Stroke* 2019;50:428–33 CrossRef Medline
- Papanagiotou P, Haussen DC, Turjman F, et al; TITAN Investigators. **Carotid stenting with antithrombotic agents and intracranial thrombectomy leads to the highest recanalization rate in patients with acute stroke with tandem lesions.** *JACC Cardiovasc Interv* 2018;11:1290–99 CrossRef Medline
- Rockman CB, Hoang H, Guo Y, et al. **The prevalence of carotid artery stenosis varies significantly by race.** *J Vasc Surg* 2013;57:327–37 CrossRef Medline
- Kim YS, Garami Z, Mikulik R, et al. **Early recanalization rates and clinical outcomes in patients with tandem internal carotid artery/middle cerebral artery occlusion and isolated middle cerebral artery occlusion.** *Stroke* 2005;36:869–71 CrossRef Medline
- Powers WJ, Rabinstein AA, Ackerson T, et al. **Guidelines for the Early Management of Patients with Acute Ischemic Stroke: 2019 Update to the 2018 Guidelines for the Early Management of Acute Ischemic Stroke—A Guideline for Healthcare Professionals From the American Heart Association/American Stroke Association.** *Stroke* 2019;50:e344–418 CrossRef Medline
- Turc G, Bhogal P, Fischer U, et al. **European Stroke Organisation (ESO)–European Society for Minimally Invasive Neurological Therapy (ESMINT) Guidelines on Mechanical Thrombectomy in Acute Ischaemic Stroke Endorsed by Stroke Alliance for Europe (SAFE).** *Eur Stroke J* 2019;4:6–12 CrossRef Medline
- Gory B, Piotin M, Haussen DC, et al; TITAN Investigators. **Thrombectomy in acute stroke with tandem occlusions from dissection versus atherosclerotic cause.** *Stroke* 2017;48:3145–48 CrossRef Medline
- Provenzale JM, Sarikaya B. **Comparison of test performance characteristics of MRI, MR angiography, and CT angiography in the diagnosis of carotid and vertebral artery dissection: a review of the medical literature.** *AJR Am J Roentgenol* 2009;193:1167–74 CrossRef Medline
- Downer J, Nadarajah M, Briggs E, et al. **The location of origin of spontaneous extracranial internal carotid artery dissection is adjacent to the skull base.** *J Med Imaging Radiat Oncol* 2014;58:408–14 CrossRef Medline
- Lee VH, Brown RD Jr, Mandrekar JN, et al. **Incidence and outcome of cervical artery dissection: a population-based study.** *Neurology* 2006;67:1809–12 CrossRef Medline
- Jacquin G, Poppe AY, Labrie M, et al. **Lack of consensus among stroke experts on the optimal management of patients with acute tandem occlusion.** *Stroke* 2019;50:1254–56 CrossRef Medline
- Marnat G, Buhlmann M, Eker OF, et al. **Multicentric experience in distal-to-proximal revascularization of tandem occlusion stroke related to internal carotid artery dissection.** *AJNR Am J Neuroradiol* 2018;39:1093–99 CrossRef Medline
- Baracchini C, Tonello S, Meneghetti G, et al. **Neurosonographic monitoring of 105 spontaneous cervical artery dissections: a prospective study.** *Neurology* 2010;75:1864–70 CrossRef Medline
- Gliem M, Lee JI, Barckhan A, et al. **Outcome and treatment effects in stroke associated with acute cervical ICA occlusion.** *PLoS One* 2017;12:e0170247 CrossRef Medline
- Eker OF, Panni P, Dargazanli C, et al. **Anterior circulation acute ischemic stroke associated with atherosclerotic lesions of the cervical ICA: a nosologic entity apart.** *AJNR Am J Neuroradiol* 2017;38:2138–45 CrossRef Medline
- Anadani M, Spiotta A, Alawieh A, et al; TITAN (Thrombectomy In TANdem Lesions) Investigators. **Effect of extracranial lesion severity on outcome of endovascular thrombectomy in patients with anterior circulation tandem occlusion: analysis of the TITAN registry.** *J Neurointerv Surg* 2019;11:970–74 CrossRef Medline
- Grossberg JA, Haussen DC, Cardoso FB, et al. **Cervical carotid pseudo-occlusions and false dissections: intracranial occlusions masquerading as extracranial occlusions.** *Stroke* 2017;48:774–77 CrossRef Medline
- Kappelhof M, Marquering HA, Berkhemer OA, et al; MR CLEAN Investigators. **Accuracy of CT angiography for differentiating pseudo-occlusion from true occlusion or high-grade stenosis of the extracranial ICA in acute ischemic stroke: a retrospective MR CLEAN sub-study.** *AJNR Am J Neuroradiol* 2018;39:892–98 CrossRef Medline
- Volders D, Shewchuk JR, Marangoni M, et al. **Beyond the collaterals: additional value of multiphase CTA in acute ischemic stroke evaluation.** *Neuroradiol J* 2019;32:309–14 CrossRef Medline
- Sivan-Hoffmann R, Gory B, Armoiry X, et al. **Stent-retriever thrombectomy for acute anterior ischemic stroke with tandem occlusion: a systematic review and meta-analysis.** *Eur Radiol* 2017;27:247–54 CrossRef Medline
- Wallock M, Chapot R, Nordmeyer H, et al. **Treatment methods and early neurologic improvement after endovascular treatment of tandem occlusions in acute ischemic stroke.** *Front Neurol* 2019;10:127 CrossRef Medline
- Heck DV, Brown MD. **Carotid stenting and intracranial thrombectomy for treatment of acute stroke due to tandem occlusions with aggressive antiplatelet therapy may be associated with a high incidence of intracranial hemorrhage.** *J Neurointerv Surg* 2015;7:170–75 CrossRef Medline
- Zhu F, Labreuche J, Haussen DC, et al; TITAN (Thrombectomy in Tandem Lesions) Investigators. **Hemorrhagic transformation after thrombectomy for tandem occlusions.** *Stroke* 2019;50:516–19 CrossRef Medline
- Pop R, Zinchenko I, Quenardelle V, et al. **Predictors and clinical impact of delayed stent thrombosis after thrombectomy for acute stroke with tandem lesions.** *AJNR Am J Neuroradiol* 2019;40:533–39 CrossRef Medline
- Sadeh-Gonik U, Tau N, Friehmann T, et al. **Thrombectomy outcomes for acute stroke patients with anterior circulation tandem lesions: a clinical registry and an update of systematic review with meta-analysis.** *Eur J Neurol* 2018;25:693–700 CrossRef Medline
- Wilson MP, Murad MH, Krings T, et al. **Management of tandem occlusions in acute ischemic stroke: intracranial versus extracranial first and extracranial stenting versus angioplasty alone—a systematic**

- review and meta-analysis. *J Neurointerv Surg* 2018;10:721–28 CrossRef Medline
27. Haussen DC, Turjman F, Piotin M, et al; on behalf of the TITAN (Thrombectomy In TANdem Lesions) Investigators. **Head or neck first? Speed and rates of reperfusion in thrombectomy for tandem large vessel occlusion strokes.** *Intervent Neurol* 2019;8:92–100 CrossRef Medline
  28. Lockau H, Liebig T, Henning T, et al. **Mechanical thrombectomy in tandem occlusion: procedural considerations and clinical results.** *Neuroradiology* 2015;57:589–98 CrossRef Medline
  29. Maus V, Behme D, Maurer C, et al. **The ReWiSed CARE technique: simultaneous treatment of atherosclerotic tandem occlusions in acute ischemic stroke.** *Clin Neuroradiol* 2019 May 22. [Epub ahead of print] CrossRef Medline
  30. Paul AR, Entezami P, Nourollahzadeh E, et al. **Simultaneous revascularization of the occluded internal carotid artery using the Solitaire as a workhorse wire during acute ischemic stroke intervention.** *Interv Neuroradiol* 2020;26:205–10 CrossRef Medline
  31. Yilmaz U, Korner H, Muhl-Benninghaus R, et al. **Acute occlusions of dual-layer carotid stents after endovascular emergency treatment of tandem lesions.** *Stroke* 2017;48:2171–75 CrossRef Medline
  32. Bartolini B, Puccinelli F, Mosimann PJ, et al. **Evaluating the effectiveness and safety of the carotid Casper-RX stent for tandem lesions in acute ischemic stroke.** *J Neurointerv Surg* 2019;11:772–74 CrossRef Medline
  33. Pfaff JA, Maurer C, Broussalis E, et al. **Acute thromboses and occlusions of dual layer carotid stents in endovascular treatment of tandem occlusions.** *J Neurointerv Surg* 2020;12:33–37 CrossRef Medline
  34. Zinkstok SM, Roos YB; ARTIS investigators. **Early administration of aspirin in patients treated with alteplase for acute ischaemic stroke: a randomised controlled trial.** *Lancet* 2012;380:731–37 CrossRef Medline
  35. Stampfl S, Ringleb PA, Mohlenbruch M, et al. **Emergency cervical internal carotid artery stenting in combination with intracranial thrombectomy in acute stroke.** *AJNR Am J Neuroradiol* 2014;35:741–46 CrossRef Medline
  36. Anadani M, Spiotta AM, Alawieh A, et al; on behalf of the TITAN (Thrombectomy In TANdem Lesions) Investigators. **Emergent carotid stenting plus thrombectomy after thrombolysis in tandem strokes.** *Stroke* 2019;50:2250–52 CrossRef Medline
  37. Gory B, Haussen DC, Piotin M, et al; the Thrombectomy In TANdem lesions (TITAN) investigators. **Impact of intravenous thrombolysis and emergent carotid stenting on reperfusion and clinical outcomes in patients with acute stroke with tandem lesion treated with thrombectomy: a collaborative pooled analysis.** *Eur J Neurol* 2018;25:1115–20 CrossRef Medline
  38. Eker OF, Buhlmann M, Dargazanli C, et al. **Endovascular treatment of atherosclerotic tandem occlusions in anterior circulation stroke: technical aspects and complications compared to isolated intracranial occlusions.** *Front Neurol* 2018;9:1046 CrossRef Medline
  39. Brott TG, Hobson RW 2nd, Howard G, et al; CREST Investigators. **Stenting versus endarterectomy for treatment of carotid-artery stenosis.** *N Engl J Med* 2010;363:11–23 CrossRef Medline
  40. Olafson EM, DeGrote JR, Drofa A, et al. **A case series of 18 patients receiving ticagrelor after carotid stenting.** *J Pharm Pract* 2018;31:519–21 CrossRef Medline
  41. Aguilar-Salinas P, Agnoletto GJ, Brasiense LBC, et al. **Safety and efficacy of cangrelor in acute stenting for the treatment of cerebrovascular pathology: preliminary experience in a single-center pilot study.** *J NeuroInterv Surg* 2019;11:347–51 CrossRef Medline
  42. Nahab F, Kass-Hout T, Shaltoni HM. **Periprocedural antithrombotic strategies in acute ischemic stroke interventional therapy.** *Neurology* 2012;79:(Suppl 1):S174–81 CrossRef Medline
  43. Neuberger U, Moteva K, Vollherbst DF, et al. **Tandem occlusions in acute ischemic stroke - impact of antithrombotic medication and complementary heparin on clinical outcome and stent patency.** *J Neurointerv Surg* 2020 Jan 14. [Epub ahead of print] CrossRef Medline
  44. Zhu F, Piotin M, Steglich-Arnholm H, et al; TITAN (Thrombectomy In TANdem Lesions) Investigators. **Periprocedural heparin during endovascular treatment of tandem lesions in patients with acute ischemic stroke: a propensity score analysis from TITAN registry.** *Cardiovasc Intervent Radiol* 2019;42:1160–67 CrossRef Medline
  45. Ederle J, Featherstone RL, Brown MM. **Percutaneous transluminal angioplasty and stenting for carotid artery stenosis.** *Cochrane Database Syst Rev* 2007;CD000515 CrossRef Medline
  46. Assis Z, Menon BK, Goyal M, et al; ESCAPE Trialists. **Acute ischemic stroke with tandem lesions: technical endovascular management and clinical outcomes from the ESCAPE trial.** *J Neurointerv Surg* 2018;10:429–33 CrossRef Medline
  47. Rothwell PM, Eliasziw M, Gutnikov SA, et al; Carotid Endarterectomy Trialists' Collaboration. **Analysis of pooled data from the randomised controlled trials of endarterectomy for symptomatic carotid stenosis.** *Lancet* 2003;361:107–16 CrossRef Medline
  48. Labeyrie MA, Ducroux C, Civelli V, et al. **Endovascular management of extracranial occlusions at the hyperacute phase of stroke with tandem occlusions.** *J Neuroradiol* 2018;45:196–201 CrossRef Medline
  49. EC/IC Bypass Study Group. **Failure of extracranial-intracranial arterial bypass to reduce the risk of ischemic stroke: results of an international randomized trial.** *N Engl J Med* 1985;313:1191–1200 CrossRef Medline
  50. Powers WJ, Clarke WR, Grubb RL Jr, et al; COSS Investigators. **Extracranial-intracranial bypass surgery for stroke prevention in hemodynamic cerebral ischemia: the Carotid Occlusion Surgery Study randomized trial.** *JAMA* 2011;306:1983–92 CrossRef Medline
  51. Saver JL, Goyal M, Bonafe A, et al; SWIFT PRIME Investigators. **Stent-retriever thrombectomy after intravenous t-PA vs. t-PA alone in stroke.** *N Engl J Med* 2015;372:2285–95 CrossRef Medline
  52. Campbell BC, Mitchell PJ, Kleinig TJ, et al; EXTEND-IA Investigators. **Endovascular therapy for ischemic stroke with perfusion-imaging selection.** *N Engl J Med* 2015;372:1009–18 CrossRef Medline
  53. Bracard S, Ducrocq X, Mas JL, et al; THRACE investigators. **Mechanical thrombectomy after intravenous alteplase versus alteplase alone after stroke (THRACE): a randomised controlled trial.** *Lancet Neurol* 2016;15:1138–47 CrossRef Medline
  54. Goyal M, Menon BK, van Zwam WH, et al; HERMES collaborators. **Endovascular thrombectomy after large-vessel ischaemic stroke: a meta-analysis of individual patient data from five randomised trials.** *Lancet* 2016;387:1723–31 CrossRef Medline
  55. Nogueira RG, Jadhav AP, Haussen DC, et al; DAWN Trial Investigators. **Thrombectomy 6 to 24 hours after stroke with a mismatch between deficit and infarct.** *N Engl J Med* 2018;378:11–21 CrossRef Medline
  56. Tekle WG, Hassan AE, Jadhav AP, et al; on behalf of the DAWN Trial Investigators. **Impact of periprocedural and technical factors and patient characteristics on revascularization and outcome in the DAWN trial.** *Stroke* 2020;51:247–53 CrossRef Medline
  57. Albers GW, Marks MP, Kemp S, et al; DEFUSE 3 Investigators. **Thrombectomy for stroke at 6 to 16 hours with selection by perfusion imaging.** *N Engl J Med* 2018;378:708–18 CrossRef Medline
  58. Marks MP, Heit JJ, Lansberg MG, et al; DEFUSE 3 Investigators. **Endovascular treatment in the DEFUSE 3 study.** *Stroke* 2018;49:2000–03 CrossRef Medline
  59. Pires Coelho A, Lobo M, Gouveia R, et al. **Overview of evidence on emergency carotid stenting in patients with acute ischemic stroke due to tandem occlusions: a systematic review and meta-analysis.** *J Cardiovasc Surg (Torino)* 2019;60:693–702 CrossRef Medline
  60. Khoury NN, Darsaut TE, Ghostine J, et al; EASI Trial Collaborators. **Endovascular thrombectomy and medical therapy versus medical therapy alone in acute stroke: a randomized care trial.** *J Neuroradiol* 2017;44:198–202 CrossRef Medline
  61. Poppe AY, Jacquin G, Stapf C, et al. **A randomized pilot study of patients with tandem carotid lesions undergoing thrombectomy.** *J Neuroradiol* 2019 Sep 26. [Epub ahead of print] CrossRef Medline
  62. Poppe AY, Stapf C, Raymond J. **Letter by Poppe et al regarding article, "Emergent Carotid Stenting After Thrombectomy in Patients With Tandem Lesions."** *Stroke* 2017;48:E182 CrossRef Medline

# Headache and Neuroimaging: Why We Continue to Do It

 J.E. Jordan and  A.E. Flanders



## ABSTRACT

**SUMMARY:** The appropriate imaging of patients with headache presents a number of important and vexing challenges for clinicians. Despite a number of guidelines and studies demonstrating a lack of cost-effectiveness, clinicians continue to image patients with chronic nonfocal headaches, and the trend toward imaging is increasing. The reasons are complex and include the fear of missing a clinically significant lesion and litigation, habitual and standard of care practices, lack of tort reform, regulatory penalties and potential impact on one's professional reputation, patient pressures, and financial motivation. Regulatory and legislative reforms are needed to encourage best practices without fear of professional sanctions when following the guidelines. The value of negative findings on imaging tests requires better understanding because they appear to provide some measure of societal value. Clinical decision support tools and machine intelligence may offer additional guidance and improve quality and cost-efficient management of this challenging patient population.

**ABBREVIATIONS:** AI = artificial intelligence; CDS = clinical decision support; ED = emergency department

## EPIDEMIOLOGY

Appropriate imaging for patients presenting with headache continues to be a ubiquitous challenge for clinicians, and headache is an ancient problem—as old as humanity—with ancient references to headache in a number of archaic works.<sup>1,2</sup> The Ebers Papyrus (1200–1500 BC) referred to headache and other neurologic disorders. Visual symptoms associated with headache were described by Hippocrates in 400 BC. Aretaeus provided one of the earliest classifications of headache around 200 AD. Regarding treatment of headache, there is evidence of trepanation of 9000-year-old Neolithic skulls, suggesting some of the first therapeutic approaches. Hippocrates described cupping methods, using a cup to create a partial vacuum to induce blood-flow to the painful site for intense headache pain but cautioned against treatment of more benign headache causes. Aretaeus recommended

cupping if bloodletting from the arm or forehead did not relieve headache symptoms.<sup>2</sup>

Much criticism has been generated regarding overuse of advanced imaging modalities, given that most patients with chronic headache and a lack of focal neurologic signs or symptoms will have negative findings. This has been viewed as a costly and wasteful use of resources. Furthermore, headache syndromes account for an estimated 12 million visits per year in the United States, approximating over \$78 billion per year in direct and indirect costs.<sup>1,3,4</sup> Direct costs include outpatient services, medications, office or clinic visits, emergency department visits, laboratory and diagnostic services, and management of treatment of adverse effects. Indirect costs include the impact on education, career, earnings, social acceptance, patients' psychological and emotional control over their headaches/lives, lost days from productive work, housework, and social activities. The life-long prevalence of experiencing any type of headache is 96%. The global prevalence of tension headache is 40%, and migraine, 10%.<sup>2,4</sup> Of 301 acute and chronic diseases tracked by the Global Burden of Disease studies, 2 headache forms are ranked among those with the highest prevalence, tension and migraine headaches.<sup>5-7</sup>


Headache disorders now rank third among the worldwide causes of disability, measured in years of life lost to disability.<sup>6</sup> The age-adjusted prevalence of headache (16.1%) in US adults ranked third behind low back pain (28.1%) and knee pain (19.5%) in a review of chronic pain by the Institute of Medicine.<sup>8</sup> The prevalence rate for headache for the lowest socioeconomic

Received December 14, 2019; accepted after revision April 9, 2020.

From the Department of Radiology (J.E.J.), Providence Little Company of Mary Medical Center, Torrance, California; Department of Radiology (J.E.J.), Division of Neuroimaging and Neurointervention, Stanford University School of Medicine, Stanford, California; and Department of Radiology (A.E.F.), Division of Neuroradiology/ENT, Jefferson University Hospitals, Philadelphia, Pennsylvania.

Paper previously presented, in part, at: Annual Meeting of the American Society of Neuroradiology, May 18–23, 2019; Boston, Massachusetts.

Please address correspondence to John E. Jordan, MD, P.O. Box 6481, San Pedro, CA 90734; e-mail: john.jordan2@providence.org; @JohnJordanMD

 Indicates open access to non-subscribers at [www.ajnr.org](http://www.ajnr.org)

<http://dx.doi.org/10.3174/ajnr.A6591>



groups in the United States is about 75% higher than in the highest socioeconomic groups. The higher prevalence rates hold true for other causes of chronic pain as well, including low back pain, knee pain, and neck pain.<sup>8</sup> In short, a greater burden of chronic pain attributable to headache (and other chronic pain syndromes) appears to be borne by those who may have more limited resources for coping with chronic pain.

CLASSIFICATION SCHEMES

The first proposals in the modern era for the classification of headache disorders were made in the 1960s by the National Institutes of Health and the Research Group on Migraine and Headache of the World Federation of Neurology.<sup>9-11</sup> However, the work emanating from these groups was limited in that the work merely constituted a listing of a relatively few headache disorders without diagnostic criteria, and the clinical utility was limited.<sup>11</sup>

In 1988, the International Headache Society published the first clinically oriented classification system, the International Classification of Headache Disorders.<sup>12</sup> This gained international acceptance and is recognized by the World Health Organization as the definitive and reference standard for the classification and categorization of headache disorders. The third edition was published last year (Table 1).<sup>13</sup> Major US organizations providing clinical guidance include the US Headache Consortium, the American Academy of Neurology,

the American College of Emergency Physicians, and the American College of Radiology.

A number of authors have also sought to identify worrisome features that could warrant imaging of patients with headache to provide practical clinical guidance. The mnemonic SNOOP has been used to indicate features that could raise clinical concern and warrant imaging in both adult and pediatric populations such as the presence of the following: systemic symptoms (eg, fever, HIV), neurologic signs, onset pattern (eg, thunderclap, sudden), older age onset, or pattern change.<sup>14-17</sup> Other red flags include papilledema, systemic illness including rash or neck stiffness, headache triggered by cough or exertion, headache and pregnancy (or postpartum period), worst headache of one's life, and so forth.<sup>1</sup> The American College of Radiology has endeavored to provide guidance for imaging of patients with headache based on a number of clinical variants.<sup>18</sup> The American College of Radiology Appropriateness Criteria rank the use of imaging in patients with headache for a given clinical variant with a score of 1-9, with 7-9 meaning usually appropriate, 4-6 may be appropriate, and 1-3 usually not appropriate. If there is wide dispersion of scores among panel members, a ranking of "may be appropriate" can result, corresponding to a score of 5. All scoring is based on expert opinion and the Delphi method, in addition to a critical review of the existing literature. For example, in the case of chronic headache with no new features and normal neurologic examination findings, advanced imaging such as CT or MR imaging would not be considered appropriate. Conversely, a headache with new neurologic features would be considered appropriate for MR imaging or CT, with MR imaging having the highest ranking. A summary of the clinical variants is shown in Table 2.

Table 1: Headache Classification Committee of the International Headache Society—The International Classification of Headache Disorders

Part 1: The primary headaches
1) Migraine
2) Tension-type headache
3) Trigeminal autonomic cephalgia
4) Other primary headache disorders
Part 2: The secondary headaches—headache (or facial pain) attributed to:
5) Trauma or injury to the head and/or neck
6) Cranial or cervical vascular disease
7) Nonvascular intracranial disorder
8) A substance or its withdrawal
9) Infection
10) Disorder of homeostasis
11) Disorder of the cranium, neck, eyes, ears, nose, sinuses, teeth, mouth, or other facial or cervical structure
12) Psychiatric disorder
Part 3: Painful cranial neuropathies, other facial pains, and other headaches
13) Painful cranial neuropathies and other facial pain
14) Other headache disorders (not classifiable)

USE AND COST-EFFECTIVENESS OF IMAGING IN HEADACHE

Despite the availability of practice guidelines, appropriateness criteria, and practice parameters, the use of imaging in patients presenting with headache appears to be increasing. In a study reviewed in the *American Emergency Medical Journal*, it was found that imaging of patients presenting to the emergency department during a 10-year period (1998-2008) increased from just under 5% in 1998 to approximately 15% by 2008,<sup>19</sup> despite the rate of significant intracranial pathology declining in the same period from about 10% to <5%. The tripling of the imaging use rate for headache was accompanied by a tripling of the use of CT and MR imaging for all patients presenting to the emergency department. Other research published in *JAMA Internal Medicine* corroborated the trend with increasing use of neuroimaging for the entire headache population studied from 1995 through 2010, increasing from approximately 5% in 1995

Table 2: From the American College of Radiology Appropriateness Criteria—Headache Clinical Variants (revised, 2019)

Variant 1: Sudden, severe headache or "worst headache of life." Initial imaging.
Variant 2: New headache with optic disc edema. Initial imaging.
Variant 3: New or progressively worsening headache with one or more of the following "red flags": subacute head trauma, related activity or event (sexual activity, exertion, position), neurologic deficit, known or suspected cancer, immunosuppressed or immunocompromised state, currently pregnant, or 50 years of age or older. Initial imaging.
Variant 4: New headache. Classic migraine or tension-type primary headache. Normal neurologic examination findings. Initial imaging.
Variant 5: New primary headache of suspected trigeminal autonomic origin. Initial imaging.
Variant 6: Chronic headache. No new features. No neurologic deficit. Initial imaging.
Variant 7: Chronic headache. New features or increasing frequency. Initial imaging.

to 15% in 2010.<sup>20</sup> Equally concerning is that while advanced imaging use continued to increase, referrals to specialists for the headache population also increased in that time period, as well as the use of certain medications, especially the triptans and ergot alkaloids used to treat migraine headaches. Paradoxically, lifestyle modification that could be an effective tool to reduce use actually decreased from about 23.5% to 18.5% in the same period.<sup>4</sup>

The cost-effectiveness of imaging of patients with chronic headache and nonfocal neurologic signs or symptoms is lacking according to a number of published studies. From a historical perspective, even earlier published studies failed to show cost-effectiveness in the imaging of patients with headache and nonfocal neurologic examinations. This finding holds true even though imaging techniques and cost have evolved since the earlier studies. One of the earliest studies was performed by Larson et al,<sup>21</sup> who found that the cost of finding a case of brain tumor in 1980 was estimated to be at least \$1265 (\$3805 in 2018 dollars) for patients with abnormal findings on neurologic examinations and \$11,901 (\$35,799 in 2018 dollars) for patients with normal findings on neurologic examinations. Some years later Akpek et al<sup>22</sup> found similar results from a sample of 592 patients presenting with headache and no focal findings. Their calculations yielded a cost per clinically significant case using marginal cost estimates of \$23,400 (\$41,528 in 2018 dollars). Jordan et al<sup>23</sup> looked at a similarly presenting cohort of 328 patients undergoing MR imaging and hypothesized that MR imaging might be more sensitive in detecting significant pathology than CT. They found that only 1.5% of patients had clinically significant MR imaging results. The cost per clinically significant managed case detected was \$34,535 (2018 dollars). No statistically significant difference was found among referring specialties and clinically significant MR imaging results.<sup>2</sup>

Jordan et al<sup>23</sup> also studied patients in the emergency department (ED) presenting with headache and nonfocal neurologic examinations, hypothesizing that patients experiencing headache severe enough to prompt an ED visit might result in a higher yield of significant pathology. Their study focused on the use of CT, the most common technique used in EDs across the United States. They found that the cost for the CT and ED visit was approximately 3 times the cost of a routine outpatient visit. Moreover, they found that the incremental cost per clinically significant case detected in the ED was \$50,078 (2018 dollars).<sup>24</sup> Even in the pediatric patient population, cost-effectiveness of imaging of patients with headache and nonfocal neurologic examinations is lacking in lower-risk patients.<sup>25</sup>

## WHY WE CONTINUE TO IMAGE

Despite a lack of cost-effectiveness for significant pathology in patients without red flag signs, clinicians continue to fear the consequences of missing significant pathology because it is known that significant pathology can present with a sole symptom of headache. For example, Evans<sup>26</sup> performed a meta-analysis of the most common secondary causes of headache, reviewing the results of 3026 scans in his analysis. A small percentage of significant abnormalities that are known to manifest with headache was found. He found strokes in 1.2% of patients in his sample. Brain tumors were found in 0.8%. Other conditions resulting in headache as a sole symptom included hydrocephalus (0.3%), arteriovenous

malformations (0.2%), subdural hematomas (0.2%), and intracranial aneurysms (0.1%).<sup>26</sup> Evans also reviewed the yield of neuroimaging in patients with migraine headaches and no other worrisome features and found a similar low yield of significant pathology known for the potential to manifest with headache. That meta-analysis combined the results of multiple studies during an 18-year period totaled 1440 scans. The analysis only found an incidence of brain tumor in 0.3% of patients, arteriovenous malformation in 0.07%, and saccular aneurysm in 0.07%; but it found a higher prevalence of white matter abnormalities reported on MR imaging of 12%–46%.<sup>26</sup> Notwithstanding the experience in the United States, the National Clinical Guideline Center of the United Kingdom also found in a meta-analysis of 3700 patients with nonfocal headache that only 32 significant abnormalities were found or a yield of 0.86%. The analysis comprised 1800 MR images, 1862 CT scans, and 38 Doppler sonography studies published during approximately 14 years.<sup>27</sup>

A myriad of reasons may be proffered by practitioners, generalists, and specialists when justifying the imaging of patients with headache and a lack of red flags or focal neurologic abnormalities. In addition to the aforementioned, other chief concerns include defensive medicine, community standard of care, professional reputation concerns and fear of sanctions (National Practitioner Data Bank reports, state agency reporting, higher malpractice premiums, and so forth), a desire to avoid patient dissatisfaction, patient-driven demand and insistence on imaging (especially in pediatrics), and self-interest and financial motivation. In the digital age, social media reverberations, patient dissatisfaction, and patient satisfaction surveys heighten the sensitivity of clinicians to patient preferences. Forceful patient demands may be viewed by some practitioners as difficult to resist. These coupled with concerns about litigation and professional sanctions increase the likelihood of capitulation to patient demands, regardless of practice guidelines or imaging yields.

Defensive medicine costs have been considered major drivers of increasing health care expenditures. Furthermore, it appears that physicians are much more likely to blame defensive medicine for a major portion of escalating health care costs than policy makers. A 2005 survey revealed that 93% of “high-risk” specialists in Pennsylvania reported practicing defensively.<sup>28</sup> A 2008 study elicited a comparable response from 83% of Massachusetts physicians. The Massachusetts physicians indicated that between 20% and 30% of imaging studies and specialty referrals were ordered primarily for defensive purposes.<sup>29</sup> An important observation of the study also found that while physicians may initially order additional nonbeneficial tests due to defensive medicine, with time these tests tend to become incorporated into the standard of care of the community.<sup>29,30</sup>

Cost escalation attributable to defensive medicine is difficult to quantify. This issue stems, in part, from the fact that no national claims data exist, making it difficult to quantify these costs on a national scale. Rather, data are available to a varying degree state by state, and the risk profile of a given region may differ significantly from that in others. Nevertheless, policy makers do not fully agree with physicians on the national impact of medical liability costs on US health expenditures. For example, a study designed to estimate this impact found that the overall annual medical liability



system costs, including defensive medicine, were estimated to be \$55.6 billion (\$64.3 billion, in 2018 dollars) or 2.4% of total health care spending.<sup>31</sup> While significant in absolute terms, this is far below the 20%–30% of health expenditures often estimated by physicians and others.<sup>30</sup> The truth may lie somewhere between the two, but this is an important subject requiring further study.

### VALUE AND NEGATIVE IMAGING RESULTS

The increasing trend toward imaging lower-risk patients with chronic headache is commonly assumed to be of limited value when imaging study findings are negative; these studies are viewed as both costly and wasteful. Yet these assumptions may be too simplistic. “Value” is a term that is not coterminous with cost when it comes to health expenditures, and value from the patient’s perspective is not necessarily coterminous with that of payers or policy makers.<sup>32</sup> Negative test results are often highly valued by patients and providers, and this feature appears to underestimate the true societal value of imaging tests with negative findings when it comes to patients presenting with headache.

Imaging tests with negative findings may result in a reduction of patient or family anxiety, providing an anxiolytic effect for multiple parties (including providers). Other benefits of negative imaging results of patients with headache may include improvement in productivity, reduction in subsequent medical visits to both generalists and specialists, a reduction of subsequent costs of imaging, school performance improvement, decreases in psychological and behavioral problems, as well as opportunities for treatment of incidental findings such as sinus disease, which might actually be the cause of a headache.<sup>23,27,33</sup>

It has been shown that in patients presenting with chronic headache, those offered imaging earlier were less likely to be referred to a specialist such as a neurologist or psychiatrist.<sup>33</sup> This finding was even more striking when comparing patients with psychological or psychiatric disorders using proxy measures (Hospital Anxiety and Depression Scale), with a greater propensity toward referral among patients with positive results on the Hospital Anxiety and Depression Scale. A trend toward a decrease in subsequent imaging for those offered scanning sooner was also observed but not at the same level of statistical significance.<sup>33</sup> Referrals to specialists may generate further work-ups and interventions in addition to imaging, resulting in increases in direct costs for patients not offered imaging sooner rather than later. Indirect costs arising from patient anxiety such as reductions in productivity or time lost from work, school, and so forth also appear to take a toll and may be more costly from a societal perspective. Hence, imaging may be anxiolytic and reduce the anxiogenic effects and downstream costs resulting from not providing patients (and providers) with answers regarding their headaches early on.

The value of negative findings on imaging tests should not be overlooked, and this is an important area requiring further study. In the case of headache, further study of the anxiolytic effects of imaging also requires additional investigation. A growing body of literature has begun elucidating the clinical and economic benefits that can accrue from negative findings on imaging tests. Although beyond the scope of this manuscript to review in detail, such studies range from imaging using coronary CTA to lung cancer screening, etc., which is in contrast to the many studies

looking at various imaging modalities and organ systems with respect to negative or positive predictive value.<sup>34–36</sup>

### POTENTIAL REMEDIES AND FUTURE DIRECTIONS

Unquestionably, patients presenting with headache even in the chronic low-risk setting will continue to challenge practitioners and bring with them the inexorable pressures to image. Therefore, potential solutions and remedies must be multifaceted. With respect to defensive medicine, federal tort reform has been advocated by some to help shield practitioners from litigation if following practice guidelines. In the era of evidence-based medicine and best practices, such protections are becoming increasingly important, not only for improved patient management and outcomes but also for the most optimal allocation of limited resources.<sup>37</sup> Examples of tort reform include the capping of damages in medical malpractice cases or limiting professional sanctions if clinicians are following guidelines. Currently >30 states have laws limiting damages.<sup>38</sup> Such approaches may reduce malpractice insurance costs but probably will not eliminate defensive medicine practices without other measures being taken.<sup>39</sup>

State tort reform or federal tort reform or both are often advocated as a way to reduce damages and costs related to medical liability as well as reducing cost associated with the practice of defensive medicine. However, tort reform legislation can be challenged under the Fifth Amendment Equal Protection Clause and the Seventh Amendment clause on the right to a jury trial under the US constitution.<sup>40,41</sup> Notwithstanding, few federal courts have overturned malpractice tort reform, and it is unlikely that the Supreme Court would overturn federal malpractice tort reform because the lowest level of scrutiny is typically applied in reviewing the constitutionality of tort reform statutes.<sup>40,41</sup> In other words, if there is a rational public policy reason for the legislation, the courts are unlikely to overturn it.

The adoption of a no-fault system to compensate patients injured during medical practice has also been advocated as a potentially less costly and fairer way to deal with medical injuries.<sup>42</sup> This contrasts with the US tort liability system, which is considered a type of social insurance to compensate for injuries in a market-based economy. No-fault systems have become more popular in many developed Organization for Economic Cooperation and Development countries and are considered social insurance of goodwill, wherein the patients are compensated for medical injury without regard to a provider’s fault.<sup>42</sup> Moreover, no-fault systems are thought to be more efficient, fairer, and less costly. Judgment under such systems is more likely to rely on the opinions of experts rather than lay people as currently practiced under the jury system in the United States.

Other potential remedies and future directions include comparative effectiveness studies in the work-up and management of headache (eg, pharmaceuticals versus lifestyle interventions) and follow-up costs; alternative screening studies and/or alternate imaging approaches; patient cost-sharing of diagnostic testing; regulatory reform (eg, National Practitioner Data Bank, state reporting requirements); and clinical decision support and artificial intelligence (AI) tools. Relatively few studies have reviewed the comparative effectiveness of alternative approaches for the diagnosis and management of headache using nontraditional means, though

some studies have examined the comparative effectiveness of various pharmacologic therapies.<sup>43</sup> Yet, alternative approaches may be more cost-effective and improve outcomes for patients with chronic headache, particularly when there is a focus on preventative measures. For example, appropriate lifestyle interventions could be very effective in the management and prevention of headache while obviating more expensive interventions and imaging.<sup>44</sup> Alternative approaches may also avoid the complications of pharmacotherapies and medication overuse, which, in and of themselves, can have debilitating effects and result in the need for further costly interventions.<sup>5,45</sup>

Alternative imaging algorithms could be considered to ease patient and provider anxiety, given the anxiolytic effects that such information can provide.<sup>33</sup> For example, a significantly scaled-down version of a brain MR imaging examination might suffice with 1 or 2 sequences, while being less costly than conventional brain MR imaging protocols.<sup>15</sup> Moreover, patient cost-sharing could select patients who have a strong desire for imaging despite the absence of good clinical indications or red flags. In such cases, the patient's willingness to pay could inform policy prescriptions and decision-making, while reducing the burden on payers. In the current environment, patients are increasingly expressing a willingness to assume some costs for their health care. A recent survey conducted by Deloitte regarding consumer health preferences indicated that younger generations are more likely to be willing to pay some of their health care costs than older generations.<sup>46</sup> This survey has important implications for policy makers not only in the management of headache but for other disorders as well, given the recognition of limited resources for health expenditures. However, differential consumer payment schemes for health care can increase the risk of multitiered systems and disparities in health care.

In addition to tort reform, regulatory reform regarding physicians' credentials and reporting should also be an important consideration to counter defensive medicine practices. Calls for tort reform, even if successful, are unlikely to diminish defensive medicine practices as long as physicians fear professional sanctions and impugnement of their reputations. Malpractice judgments and regulatory requirements to report such verdicts (or even settlements) to state board agencies and the National Practitioner Data Bank can have chilling effects on physicians' practice patterns and cause them to be risk-averse. Even simple patient reports to licensing authorities can result in exhaustive and intimidating reviews of a physician's practices and credentials. Hence, even limiting damages to small dollar amounts would be unlikely to reassure physicians if their reputations could still be impugned in the process. Both best-practice guidelines that shield physicians following them and no-fault systems of awarding damages for injured patients would, in conjunction with tort reform, be more likely to shift the calculus affecting the behavior of physicians when it comes to defensive medicine.

Finally, clinical decision support (CDS) tools and AI algorithms also appear to be promising for helping clinicians navigate this complex clinical and public health problem. CDS systems are designed to provide clinicians, staff, patients, and others with knowledge and person-specific information, to enhance health and health care.<sup>47</sup> CDS comprises tools such as computerized alerts,

reminders to providers and patients, clinical guidelines, condition-specific order sets, and focused patient data reports.<sup>47</sup> Most CDS applications operate as components of electronic health records, though stand-alone CDS systems are also becoming increasingly available. Newer and fastest-growing CDS tools are powered by AI, neural networks, or deep/machine learning techniques. The recent guidance by the FDA on classifying and regulating CDS systems has been considered too ambiguous for developers to effectively follow. These systems have not been included in the FDA medical device category and therefore are not subject to FDA oversight, though effort is underway to change this.<sup>48</sup>

Emerging studies examining the role that AI could play in diagnosing and managing patients with headache have recently begun to appear in the literature. For example, a case-based reasoning AI-powered Clinical Decision Support System study diagnosed primary migraine and primary tension headache with a high degree of accuracy and performed better than the guideline-based Clinical Decision Support System (International Headache Society–International Classification of Headache Disorders).<sup>49</sup> It has also been shown that machine learning methods and feature selection can be used to support specialists in the classification of migraines automatically in patients undergoing MR imaging using DTI biomarkers.<sup>50</sup>

A recent study presented at the 70th Annual Meeting of the American Academy of Neurology in Los Angeles examined the safety of an artificial intelligence system for nonacute headache diagnosis and compared an AI system with the performance of neurologists in the diagnosis of nonacute headaches.<sup>51</sup> The study compared the performance of a support vector machine model in classifying the headache as primary versus secondary with that of 2 general neurologists. The support vector machine model trained to “read” clinical records had a better performance in the diagnosis of secondary headache (sensitivity = 90.2%; specificity = 93%) compared with the neurologists (sensitivity = 82%; specificity = 85%), and the correct headache diagnosis was achieved in 89%–94% of cases when the International Classification of Headache Disorders criteria were combined with machine learning models. Hence, early work in AI shows the potential to help generalist clinicians evaluate and manage difficult and often confusing cases of headache, on a par with or exceeding the skill of specialists.

## CONCLUSIONS

Despite a number of guidelines and studies demonstrating a lack of cost-effectiveness, clinicians continue to image patients with chronic nonfocal headaches, and the trend toward imaging is increasing. The reasons for this prevailing trend are complex and include the fear of missing a significant lesion and litigation, habitual and standard of care practices, lack of tort reform, regulatory penalties and the potential impact on one's professional reputation, patient pressure, and financial motivation. There is a need for further clarity on the cost of imaging versus not imaging (direct and indirect), especially with respect to the anxiolytic effects on patients. Scaled-down, less costly screening studies may offer alternative approaches. Comparative effectiveness studies, lifestyle interventions, and preventive measures must be further studied to identify the most effective and cost-effective measures that can be undertaken to assuage concerns and the tendency to

image patients with headache when clinical signs do not warrant it. Regulatory and legislative support to encourage best practices without fear of financial and professional sanctions when following guidelines is needed. Moreover, serious consideration needs to be given to the adoption of no-fault systems for compensation of injured patients currently practiced in many Organization for Economic Cooperation and Development countries.

Radiologists and other clinicians should be well-versed and conversant regarding the value of imaging tests with negative findings because they appear to provide some measure of value, from patient and societal perspectives, but further study is also needed in this area. Patient cost-sharing and willingness-to-pay schemes are worth exploring in the light of limited resources for health expenditures. Clinical decision support tools, AI, and machine learning may offer additional guidance and improve quality and cost-efficient management of this challenging patient population.




## REFERENCES

- Rizzoli P, Mullally WJ. **Headache.** *Am J Med* 2018;131:17–24 CrossRef Medline
- Koehler PJ, Boes CJ. **A history of non-drug treatment in headache, particularly migraine.** *Brain* 2010;133:2489–2500 CrossRef Medline
- Gooch CL, Pracht E, Borenstein AR. **The burden of neurological disease in the United States: a summary report and call to action.** *Ann Neurol* 2017;81:479–84 CrossRef Medline
- Mafi JN, Edwards ST, Pedersen NP, et al. **Trends in the ambulatory management of headache: analysis of NAMCS and NHAMCS Data 1999–2010.** *J Gen Intern Med* 2015;30:548–55 CrossRef Medline
- Global Burden of Disease Study 2013 Collaborators. **Global, regional, and national incidence, prevalence, and years lived with disability for 301 acute and chronic diseases and injuries in 188 countries, 1990–2013: a systematic analysis for the Global Burden of Disease Study 2013.** *Lancet* 2015;386:743–800 CrossRef Medline
- Steiner TJ, Birbeck GL, Jensen RH, et al. **Headache disorders are third cause of disability worldwide.** *J Headache Pain* 2015;16:58 CrossRef Medline
- Probyn K, Bowers H, Caldwell F, et al; CHES Team. **Prognostic factors for chronic headache.** *Neurology* 2017;89:291–301 CrossRef Medline
- Institute of Medicine (US) Committee on Advancing Paid Research, Care, Education, and Research. **Relieving pain in America: a blueprint for transforming prevention, care, education, and research.** National Academies Press; 2011 Medline
- Ad Hoc Committee on Classification of Headache of the National Institute of Health. **Classification of headache.** *JAMA* 1962;179:717–18
- World Federation of Neurology Research Group on Migraine and Headache. **J Neurol Sci** 1969;9:202
- Olesen J, Steiner TJ. **The International Classification of Headache Disorders, 2nd edn (ICDH-II).** *J Neurol Neurosurg Psychiatry* 2004;75:808–11 Medline
- Classification and diagnostic criteria for headache disorders, cranial neuralgias and facial pain: Headache Classification Committee of the International Headache Society.** *Cephalalgia* 1988;8(suppl 7):1–96 Medline
- Headache Classification Committee of the International Headache Society (HIS): the International Classification of Headache Disorders, 3rd edition.** *Cephalalgia* 2018;38:1–211 CrossRef Medline
- Dodick DW. **Diagnosing headache: clinical cues and clinical rules.** *Advanced Studies in Medicine* 2003;3:87–92
- Trofimova A, Vey BL, Mullins ME, et al. **Imaging of children with non-traumatic headaches.** *AJR Am J Roentgenol* 2018;210:8–17 CrossRef Medline
- Gofshteyn JS, Stephenson DJ. **Diagnosis and management of childhood headache.** *Curr Probl Pediatr Adolesc Health Care* 2016;46:36–51 CrossRef Medline
- Nye BL, Ward TN. **Clinic and emergency room evaluation and testing of headache.** *Headache* 2015;55:1301–08 CrossRef Medline
- Whitehead MT, Cardenas AM, Corey AS, et al; Expert Panel on Neurologic Imaging. American College of Radiology. **ACR Appropriateness Criteria: Headache.** 2019. <https://acsearch.acr.org/docs/69482/Narrative/>. Accessed July 30, 2019
- Gilbert JW, Johnson KM, Larkin GL, et al. **Atraumatic headache in US emergency departments: recent trends in CT/MRI utilization and factors associated with severe intracranial pathology.** *Emerg Med J* 2012;29:576–81 CrossRef Medline
- Callaghan BC, Kerber KA, Pace RJ, et al. **Trends in neuroimaging utilization for the entire headache population from 1995 through 2000 and 2005 through 2010.** *JAMA Intern Med* 2014;174:819–21 CrossRef Medline
- Larson EB, Omenn GS, Lewis H. **Diagnostic evaluation of headache: impact of computerized tomography and cost-effectiveness.** *JAMA* 1980;243:359–62 CrossRef Medline
- Akpek S, Arac M, Atilla S, et al. **Cost-effectiveness of computed tomography in the evaluation of patients with headache.** *Headache* 1995;35:228–30 CrossRef Medline
- Jordan JE, Ramirez GF, Bradley WG, et al. **Economic and outcomes assessment of magnetic resonance imaging in the evaluation of headache.** *J Natl Med Assoc* 2000;92:573–78 Medline
- Jordan YJ, Lightfoote JB, Jordan JE. **Computed tomography imaging in the management of headache in the emergency department: cost efficacy and policy implications.** *J Natl Med Assoc* 2009;101:331–35 CrossRef Medline
- Medina LS, Kuntz KM, Pomeroy S. **Children with headache suspected of having a brain tumor: a cost-effectiveness analysis of diagnostic strategies.** *Pediatrics* 2001;108:255–63 CrossRef Medline
- Evans RW. **Diagnostic testing for the evaluation of headaches.** *Neurol Clin* 1996;14:1–26 CrossRef Medline
- Kennis K, Kernick D, O'Flynn N; National Clinical Guideline Centre for Acute and Chronic Conditions, Royal College of Physicians, London. **Diagnosis and management of headaches in young people and adults; NICE Guideline.** *Br J Gen Pract* 2013;63:443–45 CrossRef Medline
- Studdert DM, Mello MM, Sage WM, et al. **Defensive medicine among high-risk specialist physicians in a volatile malpractice environment.** *JAMA* 2005;293:2609–17 CrossRef Medline
- Rothberg MB, Class J, Bishop TF, et al. **The cost of defensive medicine on 3 hospital medicine services.** *JAMA Intern Med* 2014;174:1867–68 CrossRef Medline
- Hermer LD, Brody H. **Defensive medicine, cost containment, and reform.** *J Gen Intern Med* 2010;25:470–73 CrossRef Medline
- Mello MM, Chandra A, Gawande AA, et al. **National costs of the medical liability system.** *Health Aff (Millwood)* 2010;29:1569–77 CrossRef Medline
- Porter ME. **What is value in health care?** *N Engl J Med* 2010;363:2477–81 CrossRef Medline
- Howard L, Wessely S, Leese M, et al. **Are investigations anxiolytic or anxiogenic? A randomised controlled trial of neuroimaging to provide reassurance in chronic daily headache.** *J Neurol Neurosurg Psychiatry* 2005;76:1558–64 CrossRef Medline
- Faxon DP, McCabe CH, Kreigel DE, et al. **Therapeutic and economic value of a normal coronary angiogram.** *Am J Med* 1982;73:500–5 CrossRef Medline
- Frishberg BM. **The utility of neuroimaging in the evaluation of headache in patients with normal neurologic examinations.** *Neurology* 1994;44:1191–97 CrossRef Medline
- Smulders MW, Jaarsma C, Nelemans PJ, et al. **Comparison of the prognostic value of negative non-invasive cardiac investigations in patients with suspected or known coronary artery disease—a meta-analysis.** *Eur Heart J Cardiovasc Imaging* 2017;18:980–87 CrossRef Medline

37. Hoelsing H; Joint Commission International. **Clinical Practice Guidelines: Closing the Gap Between Theory and Practice.** Elsevier 2016. <https://www.elsevier.com/clinical-solutions/insights/resources/insights-articles/clinical-practice/clinical-practice-guidelines-closing-the-gap-between-theory-and-practice>. Accessed August 24, 2019
38. Ryskamp D. **Medical Malpractice Damages Caps: A State by State Comparison.** Expert Institute. February 14, 2019. <https://www.theexpertinstitute.com/medical-malpractice-damages-caps-a-state-by-state-comparison/>. Accessed October 18, 2019
39. Waxman DA, Greenberg MD, Ridgely MS, et al. **The effect of malpractice reform on emergency department care.** *N Engl J Med* 2014;371:1518–25 CrossRef Medline
40. Office of Technology Assessment (OTA). **“Impact of legal reforms on medical malpractice costs.”** Library Office of Technology Assessment, US Congress, Washington DC. 20510. <https://www.princeton.edu/~ota/disk1/1993/9329/9329.PDF>. Accessed August 25, 2019
41. Turkington RC. **Constitutional limitations on tort reform: have the state courts placed insurmountable obstacles in the path of legislative responses to the perceived liability insurance crisis?** *Villanova Law Review* 1987;32:1299
42. **Medical Malpractice Systems around the Globe: Examples from the US- tort liability system and the Sweden- no fault system.** Document of the World Bank. <http://documents.worldbank.org/curated/en/421621468779085220/pdf/290110English0malpractice1systems.pdf>. Accessed August 25, 2019
43. Jackson JL, Cogbill E, Santana-Davila R, et al. **A comparative effectiveness meta-analysis of drugs for the prophylaxis of migraine headache.** *PLoS One* 2015;10:e0130733 CrossRef Medline
44. Sheeler RD, Garza I, Vargas BB, et al. **Chronic daily headache: ten steps for primary care providers to regain control.** *Headache* 2016;56:1675–84 CrossRef Medline
45. Westergaard ML, Munksgaard SB, Bendtsen L, et al. **Medication-overuse headache: a perspective review.** *Ther Adv Drug Saf* 2016;7:147–58 CrossRef Medline
46. **What matters most to the health care consumer? Insights for health care providers from the Deloitte 2016 Consumer Priorities in Health Care Survey.** <https://www2.deloitte.com/us/en/pages/life-sciences-and-health-care/articles/us-lshc-consumer-priorities-promo.html>. Accessed September 26, 2019
47. Clinical Decision Support. Office of the National Coordinator for Health Information Technology (ONC). <https://www.healthit.gov/topic/safety/clinical-decision-support>. Accessed August 25, 2019
48. Wicklund E. **FDA Urged to Clarify Clinical Decision Support Regulations.** mHEALTH INTELLIGENCE. <https://mhealthintelligence.com/news/fda-urged-to-clarify-decision-support-regulations>. Accessed August 19, 2019
49. Yin Z, Dong Z, Lu X, et al. **A clinical decision support system for the diagnosis of probable migraine and probable tension-type headache based on case-based reasoning.** *J Headache Pain* 2015;16:29 CrossRef Medline
50. Garcia-Chimeno Y, Garcia-Zapirain B, Gomez-Beldarrain M, et al. **Automatic migraine classification via feature selection committee and machine learning techniques over imaging and questionnaire data.** *BMC Med Inform Decis Mak* 2017;17:38 CrossRef Medline
51. Acosta J, Grimaldi F, Dorr F, et al. **Accuracy and safety of an artificial intelligent system for nonacute headache diagnosis.** *Neurology* 2018;90:(Suppl 15)



# Squamous Cell Carcinoma Arising from Sinonasal Inverted Papilloma

 D.T. Ginat,  A. Trzcinska, and  P. Horowitz

## ABSTRACT

**SUMMARY:** Sinonasal inverted papillomas occasionally undergo malignant transformation into squamous cell carcinoma, which can be associated with EGFR mutations. Since biopsy can potentially under-sample the tumor, CT and MRI can provide clues as to the presence of malignant transformation. In particular, this entity tends to appear different from benign inverted papilloma on imaging, including prominent bone erosions, necrosis, low diffusivity in the solid tumor components, and absence of the cerebriform pattern on MRI. The radiology findings, pathology features, and management of squamous cell carcinoma arising from inverted papilloma are described.

**ABBREVIATION:** EGFR = epidermal growth factor receptor

The patient is a 61-year-old male former 40 pack-year smoker who presented with headaches and discharge of material from his nose for the past 9 months. The patient also experienced diplopia with left lateral gaze and tongue deviation to the left. Examination revealed a sinonasal mass that appeared pinkish-red with a centrally necrotic, pearly-white core. The mass was biopsied at an outside hospital and interpreted as inverted papilloma. The patient was then referred to our institution for further management.

## IMAGING

CT showed diffuse opacification of the sphenoid sinuses, posterior ethmoid sinuses, and posterior nasal cavity with a relatively well-defined mass with peripheral enhancing components and central heterogeneous nonenhancing components, as well as associated extensive remodeling and erosion of the sphenoid sinus walls, floor of the sella, and clivus, including the left hypoglossal canal, which accounted for the tongue weakness (Fig 1). MR imaging demonstrated a large peripherally enhancing mass that appeared to potentially invade the bilateral cavernous sinuses and sella without a bone marrow replacement process beyond the mass (Fig 2). In particular, there was rather thin diffuse peripheral enhancement of the tumor with relatively low diffusivity and

central areas of heterogeneous T2 signal, indicative of necrosis with relatively high diffusivity. Based on the atypical imaging findings for benign inverted papilloma, the possibility of malignant transformation was suspected.

## Treatment

Endoscopic endonasal resection was performed, which showed viable tumor peripherally, with extensive central necrosis. The bulk of the tumor was removed with a combination of suction, debriding, and grasping instruments. The sella and right cavernous sinus were displaced peripherally, with good planes of separation and negative pathologic margins on the overlying mucosa. However, positive microscopic margins were noted along the left cavernous sinus wall, left sphenoid roof, and sphenoid floor, from which the mass appeared to be arising. The tumor also invaded the clivus, upper pharyngeal musculature, and left hypoglossal canal, which was decompressed but contained invasive gross tumor. These findings correlated well with the imaging findings (Fig 3), specifically with regard to areas of necrosis and viable tumor, though we were pleasantly surprised by the lack of invasion along the right side of the skull base. The resulting defect was repaired with a fascia lata graft and nasoseptal flaps, to provide healthy tissue covering the carotid arteries in preparation for planned adjuvant radiation therapy and weekly cisplatin. Postoperatively, the patient recovered well and experienced improved tongue mobility, resolution of the diplopia, and decreased headaches.

## Diagnosis

Intraoperative frozen sections revealed squamous cell carcinoma arising from sinonasal papilloma. Histologic sections showed a

Received March 4, 2020; accepted after revision March 26.

From the Departments of Radiology, Section of Neuroradiology (D.T.G.), Pathology (A.T.), and Surgery, Section of Neurosurgery (P.H.), University of Chicago, Chicago, Illinois.

Please address correspondence to Daniel Thomas Ginat, MD, MS, University of Chicago, 5841 S Maryland Ave, Chicago, IL 60637; e-mail: dtg1@uchicago.edu  
http://dx.doi.org/10.3174/ajnr.A6583

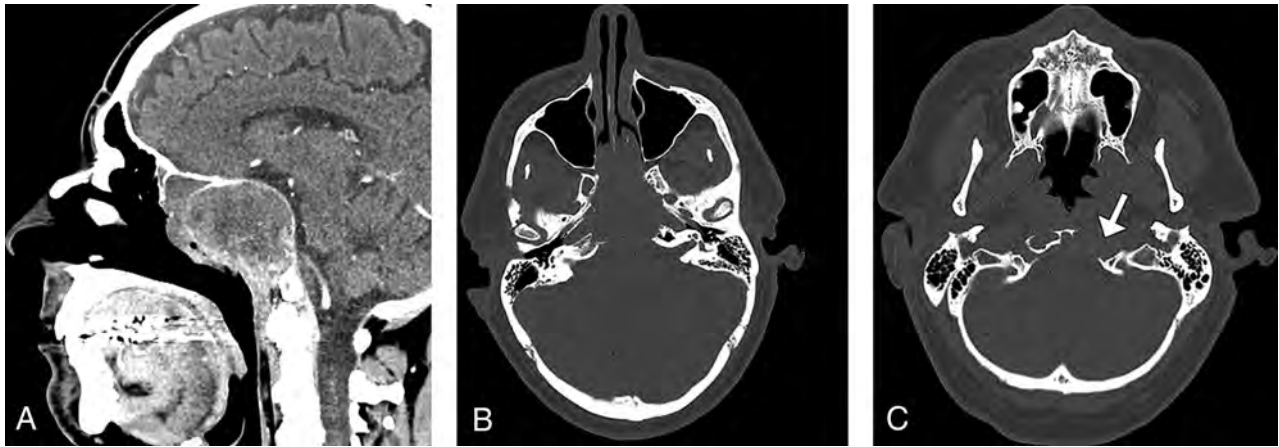


**FIG 1.** Sagittal postcontrast CT image (A) shows a fairly well-defined-but-heterogeneous mass in the posterior nasal cavity and ethmoid and sphenoid sinuses, with peripheral areas of enhancement and mixed areas of central hypoattenuation and hyperattenuation. Axial CT images in bone windows (B and C) show extensive erosion of the sinus walls and clivus, with involvement of the left hypoglossal canal (arrow).

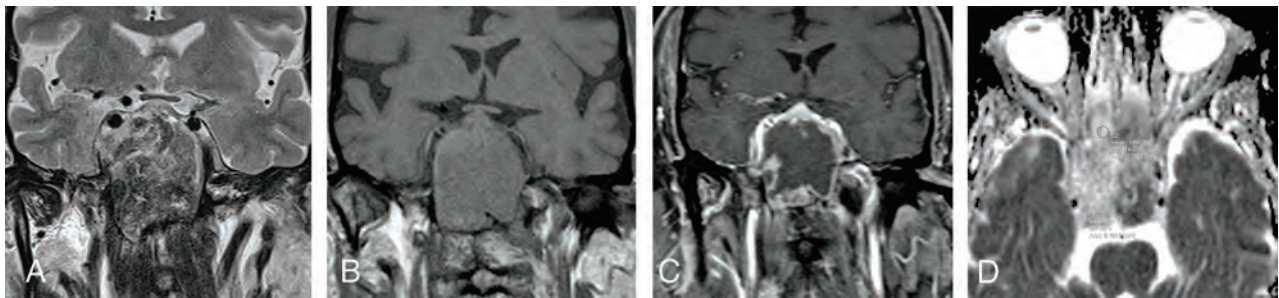


**FIG 2.** Coronal T2-weighted (A) MR imaging shows a heterogeneous mass occupying the sphenoid sinuses with extension into the cavernous sinuses and sella. The T1-weighted (B) and postcontrast T1-weighted (C) MR images show diffuse peripheral enhancement. The ADC map (D) shows relatively high diffusivity in the necrotic portions of the tumor and low diffusivity within the viable portions of the tumor.

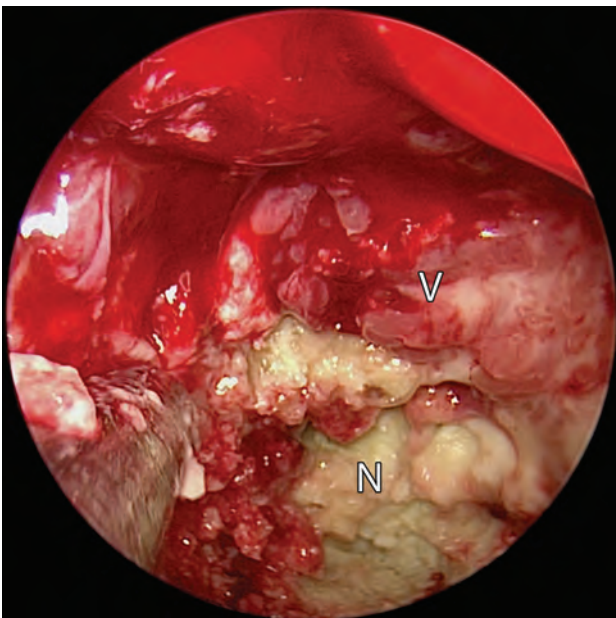


**FIG 3.** Endoscopic view during endonasal surgery shows viable (V) and necrotic (N) tumor components.

sinus lesion exhibiting an inverted growth pattern typical of a sinonasal papilloma, inverted type (Fig 4). The appearance of the lesional epithelium varied from conventional (acanthotic transitional-like epithelium with ciliated surface cells and intra-epithelial neutrophilic microabscesses) to dysplastic (squamous metaplasia with nuclear enlargement, nuclear membrane irregularity, hyperchromasia, loss of polarity, and increased mitotic activity). Rare foci of superficial invasion into the underlying stroma and extensive areas of necrosis were also present. Thus, the presence of a conventional inverted papilloma, together with extensive dysplasia, foci of invasive carcinoma, and, in particular, the extensive necrosis matched the clinicoradiologic suspicion. DNA was also isolated from the specimen, which revealed an *epidermal growth factor receptor* (EGFR) mutation involving a 9-base pair duplication in exon 20, along with several other alterations of uncertain significance.

## DISCUSSION

Inverted papilloma is a benign but locally aggressive sinonasal neoplasm. This lesion can be associated with squamous cell carcinoma in approximately 7%–16% of cases, either synchronously or metachronously.<sup>1–3</sup> Although inverted papillomas with malignant degeneration are most commonly located in the

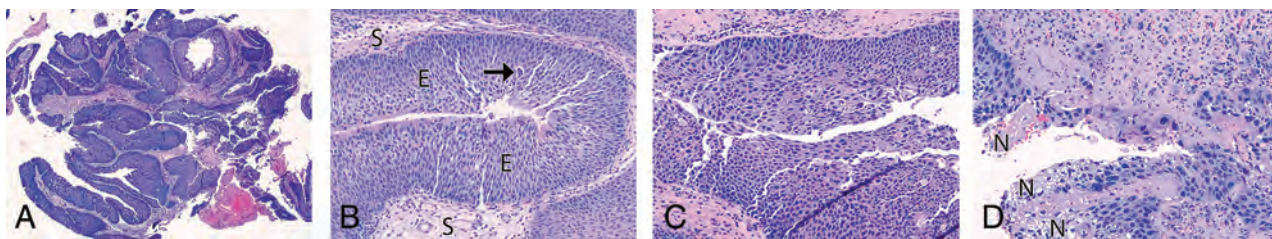


**FIG 4.** Hematoxylin-eosin-stained photomicrographs of the lesion show an inverted growth pattern from the sinonasal papilloma component (A,  $\times 4$  magnification), markedly thickened epithelium (E) with ciliated luminal cells and intraepithelial neutrophilic microcysts (arrow) growing downward into the underlying stroma (S) (B,  $\times 20$  magnification), areas of severe epithelial dysplasia (C,  $\times 20$  magnification), and foci of superficial invasion and tumor necrosis with apoptotic cells (N) (D,  $\times 20$  magnification).

lateral nasal cavity or maxillary sinus, tumors arising in the frontal sinus or the frontoethmoidal recess are proportionately most likely to be associated with carcinoma.<sup>2</sup> Sphenoid sinus involvement, such as in this case, is relatively uncommon for both benign inverted papillomas and those associated with squamous cell carcinoma.

Various risk factors are implicated in the malignant transformation of sinonasal papillomas, including human papillomavirus infection, smoking, occupational exposure, and DNA alterations, such as *EGFR* mutations.<sup>4,5</sup> Of note, *EGFR* is the gene that encodes the epidermal growth factor receptor, which is a cell membrane protein that is involved in tyrosine phosphorylation and cell proliferation. The specificity of *EGFR* mutations suggests that squamous cell carcinoma arising from the inverted papilloma disease spectrum is biologically distinct from other sinonasal squamous lesions.<sup>6</sup>

Distinguishing benign inverted papilloma and inverted papilloma associated with malignant transformation can be challenging clinically. Both entities can present with nasal obstruction and rhinorrhea, but epistaxis, vision changes, and pain are ominous signs suggestive of malignancy.<sup>3,7</sup> As in this case, the diagnosis is sometimes missed by biopsy because tissue containing malignant cells is not always obtained.<sup>3</sup> However, imaging with CT and MR imaging can help characterize these tumors in terms of identifying atypical features and delineating the extent of tumor for guiding further management.

Benign sinonasal inverted papillomas characteristically demonstrate osteitis at the attachment site on CT and a convoluted cerebriform pattern consisting of alternating bands of high and low signal on T2-weighted and postcontrast T1-weighted MR imaging sequences.<sup>8</sup> On the other hand, inverted papillomas with malignant transformation tend to have imaging characteristics distinct from those of benign inverted papillomas. In particular, the presence of bone erosions on CT is suggestive of malignancy,<sup>9</sup> though the margins of the tumor can be relatively sharp, with bone remodeling suggestive of a more indolent process as in this case. On MR imaging, the absence of the classic cerebriform or columnar pattern associated with inverted papilloma and the presence of necrotic components are indicative of squamous cell carcinoma.<sup>9,10</sup> In addition, the viable portions of tumors with malignant transformation tend to have significantly lower ADC values than benign inverted papillomas, with an average diffusion coefficient of  $1.1 \times 10^{-3} \text{ mm}^2/\text{s}$  versus of  $1.5 \times 10^{-3} \text{ mm}^2/\text{s}$ .<sup>9</sup> However, the presence of bulk necrosis in tumors is generally associated with elevated diffusivity.<sup>11</sup>

Aggressive surgical resection combined with postoperative adjuvant therapy, including chemotherapy and radiation, can be effective in managing even stage T4 squamous cell carcinomas arising from inverted papillomas.<sup>12</sup> The goal of surgery is obtaining negative microscopic margins, though with tumor invasion of critical skull base structures, this may not be possible in some cases. The anatomy of the tumor generally dictates the approach: Depending on the extent of disease, endoscopic sinus surgery alone, endoscopic sinus surgery plus endonasal or open anterior maxillotomy, and endoscopic sinus surgery plus an anterior craniotomy can be considered.<sup>12</sup> In this case, the tumor likely originated from the left sphenoid sinus, while growing displaced the cavernous sinuses, sella, and other structures outward, allowing a wide surgical corridor by an endoscopic endonasal approach simply by debriding the necrotic core. Because patients with sinonasal malignancies typically require adjuvant chemoradiation, repair of the skull base defect is an important consideration. Specifically, exposed neurovascular structures, such as the carotid arteries and cavernous sinuses, should be covered with healthy, preferably vascularized tissue or flaps, to the reduce risk of osteoradionecrosis or carotid blowout.

The prognosis of patients with inverted papillomas associated with squamous cell carcinoma depends largely on the tumor stage, with an overall 3-year disease-specific survival rate of 63%.<sup>3</sup> Most tumor recurrences are attributable to incomplete resection, and close life-long imaging follow-up is warranted, with biopsies performed depending on the imaging findings.<sup>1</sup> In certain cases with *EGFR* mutations, irreversible tyrosine kinase inhibitors can result in inactivation of *EGFR* signaling and growth inhibition.<sup>5</sup> However, there is evidence that most exon 20 insertion mutations confer resistance to *EGFR* tyrosine kinase inhibitor therapy, at least in lung cancer.<sup>13</sup>

### Case Summary

- It is not uncommon for sinonasal inverted papilloma to undergo malignant transformation into squamous cell carcinoma, which can be associated with *EGFR* mutations, as in this case.
- Because biopsy can undersample the lesion, the presence of aggressive features on imaging should raise the possibility of malignant transformation.
- The presence of necrosis and low diffusivity instead of a cerebriform appearance on MRI and extensive bone erosions demonstrated on CT are suggestive of associated squamous cell carcinoma.



- CT and MRI are useful for tumor localization and treatment-planning, which generally consists of surgical resection, chemotherapy, and radiation for inverted papillomas with malignant transformation.
- ADC can be useful for mapping heterogeneous tumors, with low diffusivity associated with viable portions of malignant neoplasm versus high diffusivity associated with bulk necrosis.

## REFERENCES

1. von Buchwald C, Bradley PJ. **Risks of malignancy in inverted papilloma of the nose and paranasal sinuses.** *Curr Opin Otolaryngol Head Neck Surg* 2007;15:95–98 CrossRef Medline
2. Kim K, Kim D, Koo Y, et al. **Sinonasal carcinoma associated with inverted papilloma: a report of 16 cases.** *J Craniomaxillofac Surg* 2012;40:e125–29 CrossRef Medline
3. Yasumatsu R, Nakashima T, Sato M, et al. **Clinical management of squamous cell carcinoma associated with sinonasal inverted papilloma.** *Auris Nasus Larynx* 2017;44:98–103 CrossRef Medline
4. Sahnane N, Ottini G, Turri-Zanoni M, et al. **Comprehensive analysis of HPV infection, EGFR exon 20 mutations and LINE1 hypomethylation as risk factors for malignant transformation of sinonasal-inverted papilloma to squamous cell carcinoma.** *Int J Cancer* 2019;144:1313–20 CrossRef Medline
5. Udager AM, McHugh JB, Goudsmit CM, et al. **Human papillomavirus (HPV) and somatic EGFR mutations are essential, mutually exclusive oncogenic mechanisms for inverted sinonasal papillomas and associated sinonasal squamous cell carcinomas.** *Ann Oncol* 2018;29:466–71 CrossRef Medline
6. Udager AM, Rolland DC, McHugh JB, et al. **High-frequency targetable EGFR mutations in sinonasal squamous cell carcinomas arising from inverted sinonasal papilloma.** *Cancer Res* 2015;75:2600–06 CrossRef Medline
7. Miyazaki T, Haku Y, Yoshizawa A, et al. **Clinical features of nasal and sinonasal inverted papilloma associated with malignancy.** *Auris Nasus Larynx* 2018;45:1014–19 CrossRef Medline
8. Fang G, Lou H, Yu W, et al. **Prediction of the originating site of sinonasal inverted papilloma by preoperative magnetic resonance imaging and computed tomography.** *Int Forum Allergy Rhinol* 2016;6:1221–28 CrossRef Medline
9. Yan CH, Tong CC, Penta M, et al. **Imaging predictors for malignant transformation of inverted papilloma.** *Laryngoscope* 2019;129:777–82 CrossRef Medline
10. Maroldi R, Farina D, Palvarini L, et al. **Magnetic resonance imaging findings of inverted papilloma: differential diagnosis with malignant sinonasal tumors.** *Am J Rhinol* 2004;18:305–10 CrossRef
11. Maeda M, Maier SE. **Usefulness of diffusion-weighted imaging and the apparent diffusion coefficient in the assessment of head and neck tumors.** *J Neuroradiol* 2008;35:71–78 CrossRef Medline
12. Li W, Lu H, Zhang H, et al. **Squamous cell carcinoma associated with inverted papilloma: recurrence and prognostic factors.** *Oncol Lett* 2020;19:1082–88 CrossRef Medline
13. Yasuda H, Kobayashi S, Costa DB. **EGFR exon 20 insertion mutations in non-small-cell lung cancer: preclinical data and clinical implications.** *Lancet Oncol* 2012;13:e23–31 CrossRef Medline



# Implications of the Revisions and Revaluation of Office/Outpatient Evaluation and Management Codes for Neuroradiology Reimbursement

 K.Y. Wang,  J.A. Hirsch,  G.N. Nicola,  L.P. Golding,  R.K. Lee, and  M.M. Chen



## ABSTRACT

**SUMMARY:** In the 2020 Final Rule, the Center for Medicare & Medicaid Services adopted a new coding structure and accepted the substantial increase in valuation for office/outpatient Evaluation and Management codes set to begin in 2021. Given budget neutrality requirements, the projected increase in reimbursement will require a reduction in the conversion factor to offset such increases. The aim is to inform neuroradiologists the impact of these proposed changes on reimbursement and the profession.

**ABBREVIATIONS:** AMA = American Medical Association; ACR = American College of Radiology; CF = conversion factor; CMS = Centers for Medicare & Medicaid Services; COVID-19 = coronavirus disease 2019; CPT = Current Procedural Terminology; E/M = evaluation and management; MDM = medical decision-making; MedPAC = Medicare Payment Advisory Commission; MPFS = Medicare Physician Fee Schedule; RUC = AMA/Specialty Society Relative Value Scale Update Committee; RVU = relative value unit

On November 1, 2019, the Centers for Medicare & Medicaid Services (CMS) finalized major revisions to the office/outpatient evaluation and management (E/M) Current Procedural Terminology (CPT) codes. These changes at first glance may not seem to impact diagnostic neuroradiology because radiologists typically do not bill office/outpatient E/M codes. However, on closer inspection, there are worrisome ramifications. The purpose of this article is to review these changes and discuss their impact on the profession. It is necessary to first understand Medicare reimbursement and how furnished services translate into fee schedule payments, to appreciate these implications.

To ensure an accurate determination in reimbursement, the American Medical Association (AMA) created the CPT system in 1965 to uniformly describe medical services and procedures.<sup>1</sup> Each service furnished is given a unique and billable CPT code, of which there are currently more than 10,000. Since 1992, the


compensation system for physician services by the CMS is based on a resource-based relative value scale as published in the Medicare Physician Fee Schedule (MPFS). Medicare payments reflect the actual resources used in furnishing specific services as well as preserving relativity among other services.<sup>1</sup> The relative compensation for furnishing a service is determined by assigning a relative value unit (RVU) and is dictated by 3 components: physician work (professional component), practice expense (technical component), and professional liability insurance. Physicians play an integral role in providing input toward the valuation of new and revised CPT codes. Through the AMA/Specialty Society Relative Value Scale Update Committee (RUC) and its robust survey of >50 specialty societies, valuations for CPT codes are determined. The RUC then recommends these valuations for the MPFS to the CMS, with acceptance rates that were historically >90%.<sup>2</sup>


Subsequently, the conversion factor (CF), which is determined by the CMS and can be viewed as a dollar amount multiplier, ultimately “converts” the work of the RVU to a dollar amount after a geographic cost adjustment. Most important, the calculation for the CF is revisited annually and is budget-neutral. In other words, any increase in relative expenditures in one area of physician services would need to be offset by decreases in other areas to maintain budget neutrality. With only minor annual adjustments, the CF has been relatively flat since its inception, ranging from \$35.7547 (2015) to \$36.0896 (2020). In contrast, the non-seasonally adjusted inflation rate for medical care during that same period was 11.6%.<sup>3</sup> However, with upcoming changes in 2021 to the new coding structure and valuation of the office/outpatient E/M CPT codes,<sup>2</sup> the CF for 2021 is almost certainly expected to be


Received March 17, 2020; accepted after revision April 21.

From the Department of Radiology (K.Y.W.), Baylor College of Medicine, Houston, Texas; Department of Radiology (J.A.H.), Massachusetts General Hospital, Boston, Massachusetts; Hackensack Radiology Group (G.N.N.), River Edge, New Jersey; Triad Radiology Associates (L.P.G.), Winston Salem, North Carolina; Department of Radiology (R.K.L.), Einstein Healthcare Network, Sydney Kimmel College at Thomas Jefferson University, Philadelphia, Pennsylvania; and Department of Neuroradiology (M.M.C.), Division of Diagnostic Imaging, University of Texas MD Anderson Cancer Center, Houston, Texas.

Please address correspondence to Kevin Yuqi Wang, MD, Baylor College of Medicine, Department of Radiology, BCM-310, One Baylor Plaza, Houston, TX 77030; e-mail: yuqiwbcm.edu; @MelissaChenMD

 Indicates open access to non-subscribers at [www.ajnr.org](http://www.ajnr.org)

 Indicates article with supplemental on-line tables.

 Indicates article with supplemental on-line photo.

<http://dx.doi.org/10.3174/ajnr.A6619>

revised downward to maintain budget neutrality with major implications for neuroradiologists.

## **HISTORICAL PERSPECTIVE OF OFFICE/OUTPATIENT E/M CODES**

The office/outpatient E/M codes are a category of CPT codes frequently billed by physicians who see patients in the office, ambulatory, or outpatient setting. E/M codes, in general, are the most frequently billed CPT codes, and specifically, office/outpatient E/M codes account for approximately 20% of all Medicare spending.<sup>1</sup> To bill one of these codes, the services furnished must meet certain documentation requirements based on the definition of the code. However, physicians have been increasingly vocal about E/M documentation requirements being administratively burdensome and redundant, resulting in unnecessary documentation irrelevant to the patient's care, not accurately capturing the most clinically meaningful level of care, and increasing the number and cost of audits.

The typical radiologist, particularly those focused on diagnostic imaging, may not be familiar with office/outpatient E/M codes. While E/M visits are provided by nearly all medical specialties, they represent a disproportionate component for those in primary care and certain office-based specialty settings.<sup>1</sup> For the reader to appreciate the extent of the granularity and burden in documentation and to better understand the rationale and implications for the upcoming changes, the current E/M visit documentation structure will be briefly discussed (On-line Figure). First, billing Medicare for an E/M visit requires the selection of the CPT code that accurately represents the level of E/M service furnished, of which there are 5 (eg, CPT codes 99201–99205 for new patients and CPT codes 99211–99215 for established patients). Unlike in imaging in which the complexity of patients is not captured by CPT codes, E/M codes capture different levels of complexity in patients based on the level of E/M services billed.<sup>4</sup> In general, the higher the complexity of the visit, the higher the level of E/M service and reimbursement for the CPT code. Three key components are mainly considered in determining the level of E/M service: history, physical examination, and medical decision-making (MDM). MDM documentation is the most challenging, and higher level codes in general require more extensive documentation. However, if a visit constitutes >50% of counseling or coordination of care, then only the time spent during the visit is used to determine the level of E/M service.

## **IMPETUS FOR CHANGE BY THE CMS**

In the backdrop of the “Patients Over Paperwork” initiative of the CMS launched in 2017 to reduce regulatory burdens, the increasingly outdated documentation requirements for E/M codes led the CMS to propose major changes to the coding, documentation, and payment structure of E/M visits when it released the 2019 MPFS proposed rule in July 2018. After considerable input from stakeholders, the finalized changes to E/M visits were released in the 2019 MPFS Final Rule in November 2018. They were slightly different from those in the 2019 MPFS proposed rule, and most were intended to take effect on January 1, 2021 (On-line Table 1). These changes specifically included

consolidating levels 2–4 E/M services to a single (also referred to as blended) rate of payment based on a weighted average of historical use obtained from the claims data. As a result, physicians who take care of patients with complex conditions who do not meet the requirements for a level 5 E/M visit would be compensated at the same rate as a level 2 E/M visit. Moreover, rather than using all 3 key components, the 2019 MPFS Final Rule allowed the option of satisfying documentation using either only MDM or time (regardless of whether >50% of the time was spent counseling or coordinating care). This option allowed physicians to document only factors that are most important in taking care of patients rather than the burdensome requirements under the current guidelines. Last, 3 new “extended visit” add-on G codes were adopted to report additional resource costs that were still not appropriately reflected in the revised outpatient E/M code set (GPRO1, GPC1X, and GCG0X).<sup>1</sup>

## **RESPONSE BY ORGANIZED MEDICINE**

Many specialty societies, including the American College of Radiology (ACR) and AMA, raised concern over the 2019 MPFS Final Rule, particularly the collapse of the payment of 2–4 levels of E/M services. In direct response to the changes by the CMS, the AMA established the Joint AMA CPT Workgroup on E/M represented by a wide array of specialties, stakeholders, and members of the CPT Editorial Panel and RUC to develop an alternative solution and derive their own set of consensus recommendations.<sup>1</sup> The Workgroup presented their recommendations to the Panel in February 2019 and the recommendations were aligned with the initiatives already established by the CMS. They were similarly intended to take effect on January 1, 2021, and also included the option of using either only MDM or time (On-line Table 1). Instead of consolidating them, the CPT Editorial Panel retained the 5 levels of E/M services for established patients (CPT codes 99211–99215) and modified new patient visits to 4 levels of E/M services by deleting CPT code 99201 (previously defined as a level 1 E/M visit for a new patient). The rationale was because level 1 and 2 E/M visits for new patients are currently differentiated by the 2 soon-to-be-defunct key components (history and physical examination). They also proposed the add-on CPT code (99XXX) for prolonged visits that would only be used when time (rather than MDM) is chosen to determine the level of E/M service. Additional changes included code descriptor revisions and modifications to the MDM and time-interpretive guidance. The AMA reports that its approach better reduces documentation burden, more accurately reflects the current practice of medicine, is more clinically intuitive, and is more likely to be adopted by third party payers than policies within the 2019 MPFS Final Rule.<sup>1</sup> The revised E/M codes were subsequently resurveyed and then revalued at the RUC meeting in April 2019, with the Committee's final recommendations ultimately being submitted to the CMS.

## **ADOPTION OF THE 2020 MPFS PROPOSED AND FINAL RULE**

The CMS largely adopted the alternative proposals set forth by the CPT Editorial Panel in the 2020 MPFS proposed rule of August 2019 (On-line Table 1).<sup>1</sup> Specifically, the CMS adopted the Panel's

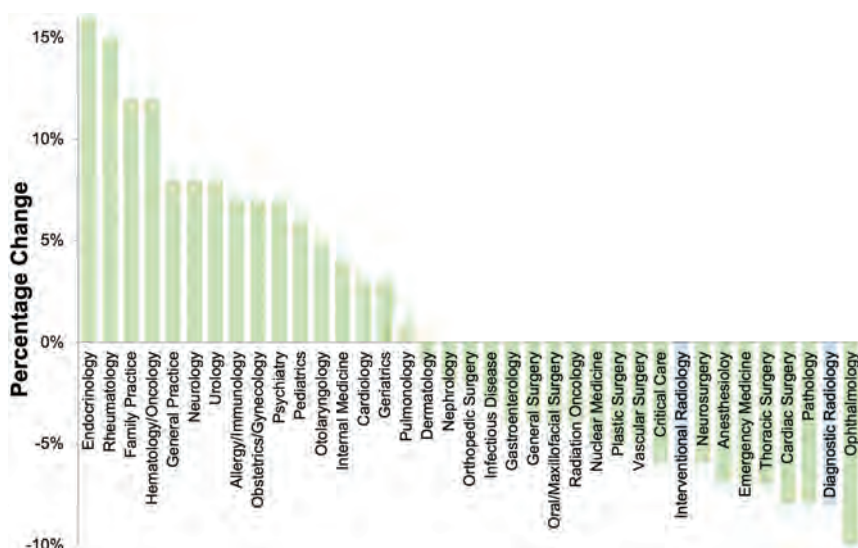


**FIGURE.** This histogram depicts the estimated percentage change in combined payment (encompassing work, practice expense, and malpractice RVUs) at the specialty level for the complete 2020 calendar year had the changes to the office/outpatient E/M visit coding and valuation hypothetically been in effect starting January 1, 2020 (rather than January 1, 2021). The blue bars highlight the 6% and 8% payment decreases projected for interventional and diagnostic radiology, respectively. This impact analysis was performed by the CMS, considered for illustrative purposes only, and adapted and modified from Table 120 of the 2020 MPFS Final Rule.<sup>2</sup>

interpretive guidance framework and coding language. CPT code 99201 was removed, and the remaining 4 established and 5 new patient levels of E/M services were preserved. The CMS accepted the RUC recommendations on the valuation of retained levels of E/M services rather than the previously proposed blended rate. In addition, the CMS adopted the new prolonged-visit CPT add-on code (99XXX). The 99XXX CPT add-on code may be used only with level 5 E/M visits and may be billed multiple times for the same encounter for every 15-minute increment of additional time required. In addition, because the CMS believed that the revalued E/M codes still do not accurately capture resource costs for certain types of E/M visits (eg, ongoing care during primary care and certain specialist visits related to a complex chronic condition), the add-on G code GPC1X initially proposed in the 2019 MPFS proposed rule will be retained. The update in valuation is scheduled to take effect on January 1, 2021. Work RVUs will increase by up to 46% depending on the E/M code, and the add-on GPC1X code was valued via a crosswalk to 100% of another CPT code valued at 0.33 work RVUs (On-line Table 2).<sup>1,2</sup>

### GLOBAL SURGERY CODES

In addition to the above recommendations, there were also RUC recommendations to adjust valuations for the E/M component of codes, with a global period to ensure relativity with the changes made to E/M visits.<sup>1</sup> Codes with a global period are often used by physicians billing for surgical procedures, and these global surgery codes previously existed with either a 10- or 90-day global period in which a certain number of postoperative E/M visits are assumed to be furnished and included in their valuation during that period. However, there are major challenges in accurately accounting for the number of expected postoperative visits typically furnished and the consequent accuracy of the valuation.<sup>5</sup>

Preliminary data from the RAND Corporation suggest that these global surgery codes may have been misvalued. For example, only 4% and 39% of the expected postoperative visits were reported for procedures with 10- and 90-day global periods, respectively.<sup>6</sup> Because of uncertainty regarding the number of appropriate postoperative E/M visits included as well as specifically how postoperative visits should be valued in global codes relative to stand-alone E/M visits, the CMS, at this time, did not adopt the RUC-recommended changes to these global surgery codes in the 2020 MPFS Final Rule. The rationale was that adopting the recommended revised values for E/M services to the global surgery codes would exacerbate any potential existing relativity issues and further contribute to potential misvaluation.<sup>2</sup>

### IMPLICATIONS FOR NEURORADIOLOGY

Why are these changes important to neuroradiology? At first glance, they may seem less relevant to specialties that do not routinely furnish office visits, though interventional radiologists do bill for E/M visits. More important however, the secondary effects and redistribution of payments as a result of the increased valuation of E/M visits are substantial. As mentioned above, the CMS is required by law to annually adjust the CF to maintain budget neutrality if changes in RVUs result in an increase or decrease in the overall fee schedule. Specifically, changes in RVUs may not result in annual Medicare expenditures differing by >\$20 million from what expenditures would have been without such changes. The office/outpatient E/M codes account for one of the largest portions of all Medicare spending, approximately 27% of allowed charges in 2017,<sup>7</sup> and even a small increase in valuation of E/M codes will result in a sizeable increase in overall Medicare spending if unadjusted. Given the statutory requirement for budget neutrality, the projected increases in E/M visit reimbursement will require a substantial reduction in the CF to offset such increases. Consequently, all services furnished will see decreases in payments due to the reduction in the CF. However, the increased valuation of E/M services will offset these decreases and may even increase overall payments for specialties that frequently bill for these services, whereas specialties that do not would see overall payment decreases.

In the 2020 MPFS proposed and Final Rule, the CMS published an estimated impact table at the specialty level regarding implementing changes to the E/M visits had they hypothetically been effective this year (Figure).<sup>1,2</sup> By specialty, diagnostic radiology would experience one of the largest reductions in payments, approximately 8%, and interventional radiology would also see a substantial decrease, albeit to a lesser degree.<sup>1,2</sup> The impact on neurointerventionalists is lessened because many have their own

clinics and bill E/M codes. The analysis does assume 100% use of the GPC1X add-on code by several specialties, though the CMS reports that the analysis is only for illustrative purposes. If the increased valuation of the E/M visits is further applied to global surgery codes, this step will likely trigger an additional reduction in the CF. To ensure relativity among other E/M services, a potential subsequent revaluation of other E/M codes including inpatient and nursing facility care services may further reduce the CF and result in further payment reductions for diagnostic and interventional radiology. Moreover, with the coronavirus disease 2019 (COVID-19) pandemic, expansion of telehealth services, including E/M codes, and payment parity by the CMS could impact the MPFS, particularly if relaxation of regulations continues after the pandemic.

Assuming a scenario under the 2020 MPFS Final Rule Impact Table,<sup>2</sup> a diagnostic neuroradiologist receiving \$400,000 annually from professional fees alone from managing a population comprising 30%–50% Medicare patients could see a payment decrease by \$6000–\$10,000 per year, with further impact depending on how private payers adjust reimbursements.

The changes proposed by the CMS will take effect on January 1, 2021, with the redistribution of payments from specialists to primary care physicians having been long advocated by the Medicare Payment Advisory Commission (MedPAC), a nonpartisan agency that provides analysis and advice on Medicare to Congress. The MedPAC has been concerned that the undervaluing of E/M services may lead to beneficiary access issues and influence the pipeline of physicians in primary care specialties. Similar concerns regarding access of Medicare beneficiaries to advanced imaging services as a result of the 2021 E/M policy change have been raised by the ACR.

## MITIGATION AND OPPORTUNITIES

Updating documentation and payment for primary care physicians to ensure adequate access for beneficiaries is important. However, to accomplish this with redistribution of reimbursement away from specialists could lead to access issues in other areas. Although reimbursement changes specifically apply to Medicare patients, there will likely be downstream effects to private payer contracts that are typically negotiated as a percentage of Medicare payments. The combination of payment decreases from both Medicare and private payers may result in a diminution of neuroradiology professional and technical fees.

Congress and the CMS could thoroughly study the impact of these revised E/M codes and assess unexpected shifts in claims to higher patient-complexity E/M codes. It is important that this analysis be performed before revising and revaluing any other E/M codes, such as those related to inpatient and nursing facility care. The CMS could evaluate the cost-sharing implications of these higher paying E/M services to the patient, who is required to pay a 20% copay of this higher valuation. This increased cost that is passed on to the patient may actually decrease access to primary care.<sup>8</sup> The ACR and ASNR have already urged Congress to consider temporarily suspending the budget-neutrality option by which the CMS is statutorily required to abide,<sup>7</sup> and this request was again reiterated by the ACR and the ASNR for the finalized implementation of the COVID-19 Phase 4 Relief

Package. Other options to mitigate the impact in the payment redistribution are to encourage a dampening policy so that reductions are phased in over multiple years or to implement a ceiling and floor in terms of maximum annual decreases and increases in payments at the specialty levels.

A potential mechanism to dampen the 2021 proposed changes includes the elimination of the add-on G code GPC1X. The add-on code alone will substantially exacerbate the payment redistribution already present in the E/M code changes. Multiple organizations, including MedPAC, have called into question the need for this particular code as well as the lack of guidance by the CMS in determining the necessity of billing for this code. The changes to the office/outpatient E/M code family, as well as other recent additions of CPT codes for chronic care management and complex chronic care management (CPT codes 99487, 99489–99490) and for care transition (CPT codes 99495–99496), signal that patient-facing and care coordination activities are most valued. As payment policy evolves, neuroradiologists should consider what opportunities are available within this new paradigm.

Neuroradiologists who perform spine procedures can consider taking a more active role in the longitudinal care of patients by expanding their practice to include a clinic that bills E/M services.<sup>9</sup> Advanced midlevel providers, such as nurse practitioners or physician assistants, could help coordinate the clinic, provide patient education, and follow-up with patients after the procedure.

Ultimately, these E/M changes are only relevant in a fee-for-service environment, and there are known efforts to move toward value-based payment models. With these come another impetus for radiologists to seek novel ways to offset decreases in fee-for-service payments with data-driven efforts to deliver and demonstrate value. Neuroradiologists will need to take a more active role in defining unique practice paradigms outside the traditional fee-for-service in which radiologists may have patient-facing activities. Currently, there may be limited opportunities for neuroradiologists to bill for these types of services, but the impetus to focus on face-to-face interactions and care coordination activities has never been stronger.

Disclosures: Joshua A. Hirsch—UNRELATED: Consultancy: Medtronic, Relievant Medsystems, InNeuroCo, Comments: Medtronic, consultant; Relievant Medsystems, Data Monitoring Committee member; InNeuroCo, consultant; Grants/Grants Pending: Harvey L. Neiman Health Policy Institute. Greg N. Nicola—UNRELATED: Board Membership: Hackensack Meridian Health Partners\*; Consultancy: Guidepoint; Stock/Stock Options: Neutigers. \*Money paid to the institution.

## REFERENCES

- Center for Medicare & Medicaid Services. **2020 Medicare Physician Fee Schedule Proposed Rule.** *Federal Register* 2019;84:40482–1289
- Center for Medicare & Medicaid Services. **2020 Medicare Physician Fee Schedule Final Rule.** *Federal Register* 2019;84:62568–3563
- Bureau of Labor Statistics. **Consumer Price Index. Latest Numbers.** 2020. <https://www.bls.gov/cpi/latest-numbers.htm>. Accessed January 19, 2020
- Chen MM, Hirsch JA, Lee RK, et al. **Determining the patient complexity of head CT examinations: implications for proper valuation of a critical imaging service.** *Curr Probl Diagn Radiol* 2020;49:177–81 CrossRef Medline
- Mulcahy AW, Merrell K, Mehrotra A. **Payment for services rendered: updating Medicare's valuation of procedures.** *N Engl J Med* 2020; 382:303–06 CrossRef Medline



6. Kranz AM, Ruder T, Mehrotra A, et al. **Claims-Based Reporting of Post-Operative Visits for Procedures with 10- or 90-Day Global Periods.** RAND Corporation. Research Reports. 2019. [https://www.rand.org/pubs/research\\_reports/RR2846.html](https://www.rand.org/pubs/research_reports/RR2846.html). Accessed February 17, 2020
7. American College of Radiology. **ACR Urges Congress to Suspend Budget Neutrality for E/M Changes in CY 2020 MPFS Proposed Rule.** October 1, 2019. News Releases Web site. <https://www.acr.org/Media-Center/ACR-News-Releases/2019/ACR-Urges-CMS-to-Suspend-Budget-Neutrality-for-E-and-M-Changes-in-CY-2020-MPFS-Proposed-Rule>. Accessed January 14, 2019
8. Ganguli I, Shi Z, Orav EJ, et al. **Declining use of primary care among commercially insured adults in the United States, 2008-2016.** *Ann Intern Med* 2020;172:240–47 CrossRef Medline
9. Soares GM. **The value of clinical interventional radiology.** *J Am Coll Radiology* 2011;8:318–24 CrossRef Medline

# CT Scanning in Suspected Stroke or Head Trauma: Is it Worth Going the Extra Mile and Including the Chest to Screen for COVID-19 Infection?

 R.M. Kwee,  J. Krdzalic,  B.A.C.M. Fasen, and  T.M.H. de Jaegere, for the COVID-19 CT Investigators South-East Netherlands (CISEN) Study Group



## ABSTRACT

**BACKGROUND AND PURPOSE:** Chest CT may be used as a tool for rapid coronavirus disease 2019 (COVID-19) detection. Our aim was to investigate the value of additional chest CT for detection of coronavirus 19 (COVID-19) in patients who undergo head CT for suspected stroke or head trauma in a COVID-19-endemic region.

**MATERIALS AND METHODS:** Our study included 27 patients (mean age, 74 years; range, 54–90 years; 20 men) who underwent head CT for suspected stroke ( $n = 21$ ) or head trauma ( $n = 6$ ), additional chest CT for COVID-19 detection, and real-time reverse transcriptase polymerase chain reaction testing in a COVID-19-endemic region. Sensitivity, specificity, and negative and positive predictive values of chest CT in detecting COVID-19 were calculated.

**RESULTS:** Final neurologic diagnoses were ischemic stroke ( $n = 11$ ), brain contusion ( $n = 5$ ), nontraumatic intracranial hemorrhage ( $n = 2$ ), brain metastasis ( $n = 1$ ), and no primary neurologic disorder ( $n = 8$ ). Symptoms of possible COVID-19 infection (ie, fever, cough, and/or shortness of breath) were present in 20 of 27 (74%) patients. Seven of 27 patients (26%) had real-time reverse transcriptase polymerase chain reaction confirmed COVID-19 infection. Chest CT results were 6 true-positives, 15 true-negatives, 5 false-positives, and 1 false-negative. Diagnostic performance values of chest CT were a sensitivity of 85.7%, specificity of 75.0%, negative predictive value of 93.8%, and positive predictive value of 54.6%.

**CONCLUSIONS:** The sensitivity of additional chest CT is fairly high. However, a negative result does not exclude COVID-19. The positive predictive value is poor. Correlation of chest CT results with epidemiologic history and clinical presentation, along with real-time reverse transcriptase polymerase chain reaction, is needed for confirmation.

**ABBREVIATIONS:** COVID-19 = coronavirus disease 2019; RT-PCR = real-time reverse transcriptase polymerase chain reaction


The coronavirus disease 2019 (COVID-19) pandemic has caused a global crisis. As of April 19, there were 2,356,475 confirmed cases and 162,070 deaths worldwide.<sup>1</sup> In regions where COVID-19 is highly endemic, some hospitals can barely handle the influx of patients.<sup>2–4</sup> Nevertheless, rapid triage and isolation of patients with suspected COVID-19 are essential to prevent hospital-related transmission of the virus to other patients and health care workers.<sup>5,6</sup> Stroke and traumatic brain injury are highly prevalent worldwide<sup>7</sup> and remain common reasons for emergency department visits.<sup>8</sup> These patients should be assessed for COVID-19 infection on emergency department arrival in

COVID-19-endemic areas. One possible strategy is to perform real-time reverse transcriptase polymerase chain reaction (RT-PCR) in patients who are being hospitalized. However, a major disadvantage of RT-PCR testing is that it takes several hours to obtain results. It has been suggested that chest CT may be used as a tool for rapid COVID-19 detection in endemic areas.<sup>9</sup> Head CT is the primary imaging technique of choice to evaluate patients with suspected stroke<sup>10,11</sup> or head trauma<sup>12</sup> in the emergency setting. Thus, it may be possible to perform additional chest CT for COVID-19 detection in 1 session with head CT. This approach could be particularly useful when rapid triaging is needed and RT-PCR testing capacity and the number of isolation rooms are limited. Furthermore, such a strategy poses a negligible extra burden on available CT equipment and radiology personnel. In addition, the additional radiation exposure of chest CT is not a major concern because patients with suspected stroke or head trauma are usually older and chest CT can be performed with a low-dose protocol.<sup>13</sup> Therefore, the purpose of our study was to investigate

Received April 20, 2020; accepted after revision April 29.

From the Department of Radiology (R.M.K., J.K., B.A.C.M.F., T.M.H.d.J.), Zuyderland Medical Center, Heerlen/Sittard/Geleen, the Netherlands.

Please address correspondence to Robert M. Kwee, MD, PhD, Department of Radiology, Zuyderland Medical Center, Henri Dunantstraat 5, 6419 PC Heerlen, the Netherlands; e-mail: rmkwee@gmail.com

 Indicates open access to non-subscribers at [www.ajnr.org](http://www.ajnr.org)

<http://dx.doi.org/10.3174/ajnr.A6607>

**Table 1: Radiological Society of North America chest CT classification system for reporting COVID-19 pneumonia (adapted from reference 15)**

COVID-19 Pneumonia Imaging Classification	Rationale	CT Findings
Typical appearance	Commonly reported imaging features of greater specificity for COVID-19 pneumonia	Peripheral, bilateral GGOs with or without consolidation or visible intralobular lines ("crazy-paving") Multifocal GGOs of rounded morphology with or without consolidation or visible intralobular lines (crazy-paving) Reverse halo sign or other findings of organizing pneumonia (seen later in the disease)
Indeterminate appearance	Nonspecific imaging features of COVID-19 pneumonia	Absence of typical features AND Presence of: Multifocal, diffuse, perihilar, or unilateral GGO with or without consolidation lacking a specific distribution and are non-rounded or non-peripheral Few very small GGO with a non-rounded and non-peripheral distribution
Atypical appearance	Uncommonly or not reported features of COVID-19 pneumonia	Absence of typical or indeterminate features AND Presence of: Isolated lobar or segmental consolidation without GGO Discrete small nodules (centrilobular, "tree-in-bud") Lung cavitation Smooth interlobular septal thickening with pleural effusion
Negative for pneumonia	No features of pneumonia	No CT features to suggest pneumonia

**Note:**—GGOs indicates ground-glass opacities

the value of additional chest CT for COVID-19 detection in patients who undergo head CT for suspected stroke or head trauma in a COVID-19-endemic region.

## MATERIALS AND METHODS

### Patients

This retrospective study was approved by the institutional review board of our hospital (Zuyderland Medical Center, Heerlen/Sittard/Geleen, the Netherlands) (No. Z2020061), and patient consent was waived. We included 27 consecutive patients (mean age, 74 years; range, 54–90 years; 20 men) who were evaluated for suspected stroke ( $n = 21$ ) or head trauma ( $n = 6$ ) in our hospital between March 12, 2020, and April 14, 2020. Our hospital, one of the largest general hospitals in the Netherlands, was located in a COVID-19-endemic region. Our study period encompassed the peak of the highest registered number of daily COVID-19 infections in the Netherlands.<sup>14</sup> During the study period, patients had to be transported to other hospitals because the intensive care unit of our hospital was becoming overloaded (as of April 1, 2020, eighty-three percent of all intensive care unit beds were occupied by patients with COVID-19). All 27 patients underwent head CT, additional chest CT for COVID-19 detection, and RT-PCR testing of nasopharyngeal and oropharyngeal swabs. In 3 patients with suspected stroke, CTA was also performed from the aortic arch to the vertex to evaluate for intracranial large-vessel occlusion.

### Chest CT Protocol

Chest CT was performed on either a 64-section CT scanner (Incisive; Philips Healthcare) or on a 64-section dual-source scanner (Somatom Definition Flash; Siemens). Scanning parameters were the following: collimation =  $64 \times 0.625$  or 0.6 mm, Tube voltage = 120 kV(peak), Tube current = 667 maximum mA or 404 maximum mA, pitch = 1.0 or 1.2, and matrix size 5 =

$12 \times 512$ . CT images were reconstructed with a lung kernel in the transverse plane with a 1.0-mm section thickness and a 1.0-mm increment. Images were also reconstructed in axial, coronal, and sagittal planes with a 3.0-mm section thickness.

### Chest CT Interpretation and Reference Standard

Chest CT findings were categorized according to the Radiological Society of North America chest CT classification system for reporting COVID-19 pneumonia—ie, typical, indeterminate, atypical, and negative (Table 1).<sup>15</sup> Typical and indeterminate chest CT findings were considered positive, whereas atypical and negative chest CT findings were considered negative for COVID-19. All chest CT scans were prospectively read by radiologists who were available when CT was performed. Results of RT-PCR testing, (ie, positive or negative for COVID-19 infection) served as the reference standard.

### Statistical Analysis

The number of true-positive, true-negative, false-positive, and true-negative chest CT results was determined. Subsequently, sensitivity, specificity, negative predictive value, and positive predictive value of chest CT in diagnosing COVID-19 were calculated. Statistical analyses were performed using SPSS Statistics for Windows (Version 20.0; IBM).

## RESULTS

### Patients

Final neurologic diagnoses were ischemic stroke ( $n = 11$ ), brain contusion ( $n = 5$ ), nontraumatic intracranial hemorrhage ( $n = 2$ ), brain metastasis ( $n = 1$ ), and no primary neurologic disorder ( $n = 8$ ). Correlation of symptoms of possible COVID-19 infection (ie, fever, cough, and/or shortness of breath<sup>16</sup>), chest CT findings, and RT-PCR results are shown in Table 2. Symptoms of possible COVID-19 infection were present in 20 of 27 (74%)

patients. The median time interval between CT and RT-PCR was 0 days (range, 0–7, days; interquartile range, 0–1 day). In 2 of 4 patients with a chest CT result positive for COVID-19 but negative findings on the initial RT-PCR, repeat RT-PCR was performed (with findings remaining negative). Seven of 27 patients (26%) had RT-PCR–confirmed COVID-19 infection. Six patients

**Table 2: Correlation between symptoms of possible COVID-19 infection (ie, fever, cough, and/or shortness of breath<sup>16</sup>), chest CT findings, and RT-PCR results**

	RT-PCR, Positive Results	RT-PCR, Negative Results
Chest CT, positive findings	5 <sup>a</sup> /1 <sup>b</sup>	3 <sup>a</sup> /2 <sup>b</sup>
Chest CT, negative findings	1 <sup>a</sup> /0 <sup>b</sup>	11 <sup>a</sup> /4 <sup>b</sup>

<sup>a</sup> Symptomatic patients.

<sup>b</sup> Asymptomatic patients.

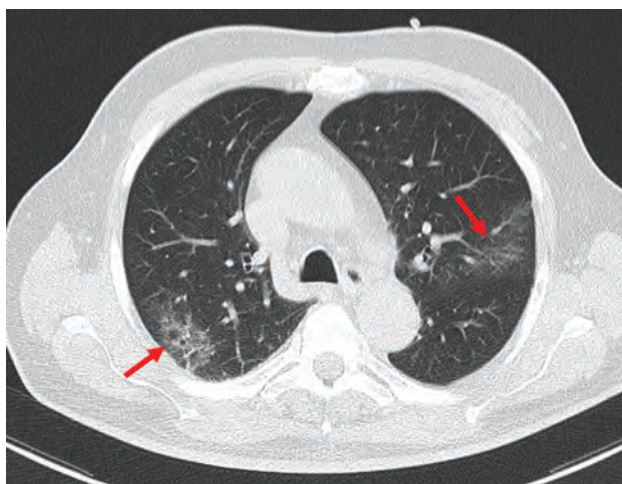


**FIG 1.** A 73-year-old male patient who underwent head CT and CTA to evaluate intracranial large-vessel occlusion. This patient did not have symptoms of COVID-19 infection (ie, no fever, cough, and/or shortness of breath). Axial chest CT image shows ground-glass opacities posteriorly located in both upper lobes (arrows). These CT features were interpreted as typical for COVID-19 pneumonia, which was confirmed by RT-PCR.

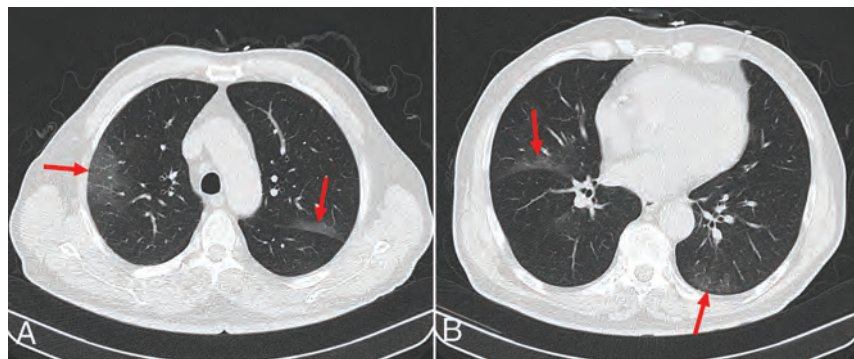


**FIG 2.** An 83-year-old male patient who underwent head CT for suspected stroke. This patient had symptoms of possible COVID-19 infection (cough and shortness of breath). Axial chest CT images at the level of the aortic arch (A) and heart (B) show ground-glass opacities posteriorly and peripherally, located in both upper lobes (arrows in A and B) and in the left lower lobe (arrow, B). These CT features were interpreted as typical for COVID-19 pneumonia, which was confirmed by RT-PCR.

with RT-PCR–confirmed COVID-19 were symptomatic, whereas 1 patient with RT-PCR–confirmed COVID-19 was asymptomatic. In the asymptomatic patient with RT-PCR–confirmed COVID-19, abnormalities suspicious for COVID-19 were already visible in the upper lung fields on CTA, which was confirmed on additional chest CT (Fig 1). In another patient with head trauma and fever, chest CT findings were negative, whereas RT-PCR 4 days after CT showed COVID-19. This patient was not isolated until the RT-PCR results were known.

### Diagnostic Yield of Chest CT

Typical, indeterminate, atypical, and negative chest CT features for COVID-19 were present in 3, 8, 2, and 14 patients, respectively. Figs 1 and 2 show examples of typical chest CT features of COVID-19, whereas Fig 3 shows an example of atypical chest CT features of COVID-19. Chest CT results were 6 true-positives, 15 true-negatives, 5 false-positives, and 1 false-negative. Diagnostic performance values of chest CT were a sensitivity of 85.7%, specificity of 75.0%, negative predictive value of 93.8%, and positive predictive value of 54.6%.

### DISCUSSION

Our initial experience in 27 patients with an emergency indication for head CT shows that the sensitivity of additional chest CT for COVID-19 is fairly high. An estimated 5%–80% of COVID-19-infected persons may be asymptomatic.<sup>17</sup> Although asymptomatic, they may transmit the disease to others.<sup>18–21</sup> In our study, 7 of 27 patients (26%) did not have symptoms of possible COVID-19 infection (ie, fever, cough, and/or shortness of breath<sup>16</sup>). One of these asymptomatic patients proved to be infected with COVID-19 by RT-PCR. This finding underlines the importance of vigilantly evaluating the lungs on CTA scans of patients with stroke in a COVID-19-endemic region, even when they are asymptomatic. However, a negative result does not exclude COVID-19. In 1 patient with head trauma and fever, chest CT had negative findings, whereas RT-PCR 4 days after CT showed COVID-19 infection. This patient was not isolated until the RT-PCR results were known and could have put other patients and health care workers at risk to become infected too. Furthermore, the positive predictive value of

chest CT was poor. If only chest CT results were used to make patient-management decisions, too many cases would unnecessarily occupy isolation rooms. Therefore, correlation with epidemiologic history and clinical presentation, along with the RT-PCR, is needed for confirmation.<sup>22</sup>

The diagnostic accuracy of chest CT has been investigated by a few previous studies,<sup>9,23,24</sup> in different populations. Our study is unique in that it investigated the value of additional chest CT in patients who already underwent head CT in a COVID-19-endemic region, compared with



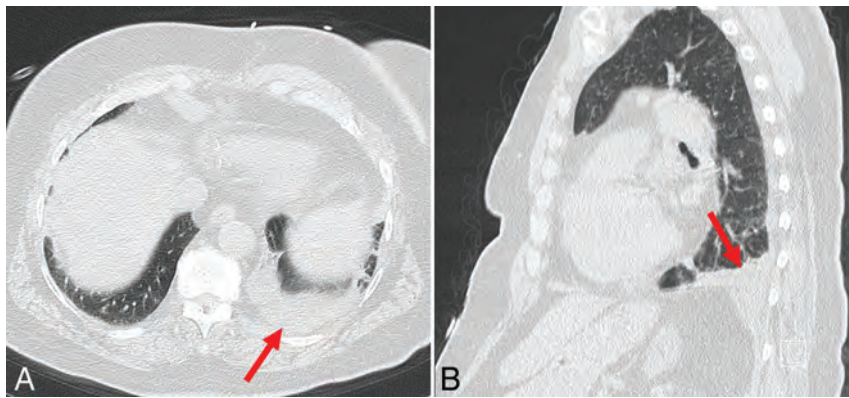


**FIG 3.** An 83-year-old female patient who underwent head CT for suspected stroke. This patient had symptoms of possible COVID-19 infection (shortness of breath). Axial (A) and sagittal (B) chest CT images show segmental consolidation in the left lower lobe (arrows, A and B) and no other long abnormalities. These CT features were interpreted as atypical for COVID-19 pneumonia. RT-PCR was negative for COVID-19.

previous studies that reported chest CT as a stand-alone method in patients who may otherwise not have undergone CT scanning.<sup>9,23,24</sup> Furthermore, our study also included asymptomatic patients (26% of our study population) with respect to possible COVID-19. Because of the inclusion of patients without any COVID-19 symptoms, the overall prevalence of COVID-19 infection in our study population was lower than that in previous studies<sup>9,23,24</sup> (26% in our study versus 39%–85% in previous studies<sup>9,23,24</sup>). Nevertheless, the fairly high sensitivity and poor specificity of additional chest CT is in line with the findings of previous studies that reported sensitivity and specificity values of 93.2%–97.0%, and 25.0%–53.3%, respectively.<sup>9,23,24</sup> Most important, our observation that a negative chest CT result does not exclude COVID-19 is supported by a study among passengers from the cruise ship *Diamond Princess*, which showed that 6 of 28 symptomatic patients with COVID-19 had normal chest CT findings.<sup>25</sup>

RT-PCR of nasopharyngeal and oropharyngeal specimens is considered the standard to diagnose COVID-19.<sup>26–29</sup> However, currently available RT-PCR tests are time-consuming (it takes several hours before the results are known), and there is still relatively limited RT-PCR testing capacity worldwide.<sup>30,31</sup> In a heavily constrained environment with a lack of sufficient RT-PCR testing capacity and a shortage of isolation beds, additional chest CT may be performed to detect COVID-19 in patients who have already undergone head CT. The data from this study may be used to weigh the potential advantages and disadvantages of performing additional chest CT in such settings. On a different note, additional chest CT in patients who require CT scanning of other body regions may also be helpful for taking appropriate actions in a timely manner to maintain the safety of the CT room. If chest CT findings are positive for possible COVID-19, the CT room should be decontaminated (room downtime for decontamination is typically between 30 minutes to 1 hour<sup>32</sup>) before scanning the next patient.

Our study has some limitations. First, the number of included patients was relatively low. Nevertheless, we were able to demonstrate the value of additional chest CT for COVID-19 detection in patients with suspected stroke or head trauma. Second, in

only 2 of 5 patients with positive findings on chest CT but negative findings on the initial RT-PCR was repeat RT-PCR performed (with findings remaining negative) due to the limited availability of RT-PCR kits in our hospital. Only patients in whom clinical suspicion of COVID-19 persisted were retested.

## CONCLUSIONS

The sensitivity of additional chest CT is fairly high. However, a negative result does not exclude COVID-19. The positive predictive value is poor. Correlation of chest CT results with epidemiologic history and clinical presentation, along with RT-PCR, is

needed for confirmation.

## REFERENCES

1. COVID-19 Dashboard by the Center for Systems Science and Engineering (CSSE) at Johns Hopkins University (JHU). <https://gisanddata.maps.arcgis.com/apps/opsdashboard/index.html#/bda7594740fd40299423467b48e9ecf6>. Accessed April 19, 2020
2. Italy's Health Care System Groans Under Coronavirus—a Warning to the World. *The New York Times*. March 27, 2020. <https://www.nytimes.com/2020/03/12/world/europe/12italy-coronavirus-health-care.html>. Accessed April 19, 2020
3. Marquez M, Moghe S. Inside a Brooklyn hospital that is overwhelmed with Covid-19 patients and deaths. CNN. March 31, 2020. <https://edition.cnn.com/2020/03/30/us/brooklyn-hospital-coronavirus-patients-deaths/index.html>. Accessed April 19, 2020
4. Rothfeld M. 13 Deaths in a Day: An 'Apocalyptic' Coronavirus Surge at an N.Y.C. Hospital. *The New York Times*. March 24, 2020. <https://www.nytimes.com/2020/03/25/nyregion/nyc-coronavirus-hospitals.html>. Accessed April 19, 2020
5. Centers for Disease Control and Prevention Interim Infection Prevention and Control Recommendations for Patients with Suspected or Confirmed Coronavirus Disease 2019 (COVID-19) in Healthcare Settings. <https://www.cdc.gov/coronavirus/2019-ncov/hcp/infection-control-recommendations.html>. Accessed April 19, 2020
6. Wang D, Hu B, Hu C, et al. Clinical characteristics of 138 hospitalized patients with 2019 novel coronavirus-infected pneumonia in Wuhan, China. *JAMA* 2020 Feb 7. [Epub ahead of print] CrossRef Medline
7. World Health Organization. Neurological Disorders. [https://www.who.int/mental\\_health/neur](https://www.who.int/mental_health/neur). Accessed April 19, 2020
8. Centers for Disease Control and Prevention. Emergency Department Visits. <https://www.cdc.gov/nchs/fastats/emergency-department.htm>. Accessed April 19, 2020
9. Ai T, Yang Z, Hou H, et al. Correlation of chest CT and RT-PCR testing in coronavirus disease 2019 (COVID-19) in China: a report of 1014 cases. *Radiology* 2020 Feb 26. [Epub ahead of print] CrossRef Medline
10. Kamalian S, Lev MH. Stroke imaging. *Radiol Clin North Am* 2019;57:717–32 CrossRef Medline
11. Salmela MB, Mortazavi S, Jagadeesan BD, et al; Expert Panel on Neurologic Imaging. ACR Appropriateness Criteria® Cerebrovascular Disease. *J Am Coll Radiology* 2017;14:S34–61 CrossRef Medline

12. Shetty VS, Reis MN, Aulino JM, et al. **ACR Appropriateness Criteria head trauma.** *J Am Coll Radiology* 2016;13:668–79 CrossRef Medline
13. Kang Z, Li X, Zhou S. **Recommendation of low-dose CT in the detection and management of COVID-2019.** *Eur Radiol* 2020 March 19. [Epub ahead of print] CrossRef Medline
14. National Institute for Public Health and the Environment. **Ontwikkeling COVID-19 in grafieken.** <https://www.rivm.nl/coronavirus-covid-19/grafieken>. Accessed April 19, 2020
15. Simpson S, Kay FU, Abbata S, et al. **Radiological Society of North America Expert Consensus Statement on Reporting Chest CT Findings Related to COVID-19: endorsed by the Society of Thoracic Radiology, the American College of Radiology, and RSNA.** *Radiology: Cardiothoracic Imaging* 2020;2:e200152 CrossRef
16. Centers for Disease Control and Prevention. **Coronavirus Disease 2019 (COVID-19): Symptoms of Coronavirus.** <https://www.cdc.gov/coronavirus/2019-ncov/symptoms-testing/symptoms.html>. Accessed April 19, 2020
17. Centre for Evidence-Based Medicine. **COVID-19: What proportion are asymptomatic?** <https://www.cebm.net/covid-19/covid-19-what-proportion-are-asymptomatic/>. Accessed April 19, 2020
18. Bai Y, Yao L, Wei T, et al. **Presumed asymptomatic carrier transmission of COVID-19.** *JAMA* 2020 Feb 21. [Epub ahead of print] CrossRef Medline
19. Hu Z, Song C, Xu C, et al. **Clinical characteristics of 24 asymptomatic infections with COVID-19 screened among close contacts in Nanjing, China.** *Sci China Life Sci* 2020;63:706–11 CrossRef Medline
20. Yu X, Yang R. **COVID-19 transmission through asymptomatic carriers is a challenge to containment.** <https://onlinelibrary.wiley.com/doi/pdf/10.1111/irv.12743>. Accessed April 19, 2020
21. Rothe C, Schunk M, Sothmann P, et al. **Transmission of 2019-nCoV infection from an asymptomatic contact in Germany.** *N Engl J Med* 2020;382:970–71 CrossRef Medline
22. **Novel Coronavirus Pneumonia Diagnosis and Treatment Plan (Provisional 7th Edition).** <http://www.gov.cn/zhengce/zhengceku/2020-03/04/5486705/files/ae61004f930d47598711a0d4cbf874a9.pdf>. Accessed April 19, 2020
23. Caruso D, Zerunian M, Polici M, et al. **Chest CT features of COVID-19 in Rome, Italy.** *Radiology* 2020 April 3. [Epub ahead of print] CrossRef Medline
24. Wen Z, Chi Y, Zhang L, et al. **Coronavirus disease 2019: initial detection on chest CT in a retrospective multicenter study of 103 Chinese subjects.** *Radiology: Cardiothoracic Imaging* 2020;2:e200092 CrossRef
25. Inui S, Fujikawa A, Jitsu M, et al. **Erratum: chest CT findings in cases from the cruise ship “Diamond Princess” with coronavirus disease 2019 (COVID-19).** *Radiology: Cardiothoracic Imaging* 2020;2:e204002 CrossRef
26. Huang C, Wang Y, Li X, et al. **Clinical features of patients infected with 2019 novel coronavirus in Wuhan, China.** *Lancet* 2020;395:497–506 CrossRef Medline
27. Guan WJ, Ni ZY, Hu Y, et al; China Medical Treatment Expert Group for Covid-19. **Clinical characteristics of coronavirus disease 2019 in China.** *N Engl J Med* 2020;382:1708–20 CrossRef Medline
28. World Health Organization. **WHO interim guidance for laboratory testing.** <https://www.who.int/emergencies/diseases/novel-coronavirus-2019/technical-guidance/laboratory-guidance>. Accessed April 19, 2020
29. Corman VM, Landt O, Kaiser M, et al. **Detection of 2019 novel coronavirus (2019-nCoV) by real-time RT-PCR.** *Euro Surveill* 2020;25 CrossRef Medline
30. Cheng MP, Papenburg J, Desjardins M, et al. **Diagnostic testing for severe acute respiratory syndrome-related coronavirus-2: a narrative review.** *Ann Intern Med* 2020 April 13. [Epub ahead of print] CrossRef Medline
31. National Institute for Public Health and the Environment. **Policy on testing for novel coronavirus disease (COVID-19).** <https://www.rivm.nl/en/novel-coronavirus-covid-19/what-are-we-doing-in-the-netherlands-in-response-to-the-coronavirus/testing-policy>. Accessed April 19, 2020
32. Mossa-Basha M, Meltzer CC, Kim DC, et al. **Radiology department preparedness for COVID-19: Radiology Scientific Expert Panel.** *Radiology* 2020 Mar 16. [Epub ahead of print] CrossRef Medline

# Cerebrovascular Disease in COVID-19

Michael F. Goldberg, Morton F. Goldberg, R. Cerejo, and A.H. Tayal



## ABSTRACT

**SUMMARY:** Coronavirus disease 19 (COVID-19) is a pandemic originating in Wuhan, China, in December 2019. Early reports suggest that there are neurologic manifestations of COVID-19, including acute cerebrovascular disease. We report a case of COVID-19 with acute ischemic stroke. To our knowledge, this is the first reported case of COVID-19-related cerebral infarcts that includes brain imaging at multiple time points and CT angiography. There is a growing body of published evidence that complications of COVID-19 are not limited to the pulmonary system. Neuroradiologists should be aware of a wide range of neurologic manifestations, including cerebrovascular disease.

**ABBREVIATIONS:** ACA = anterior cerebral artery; ACE2 = angiotensin converting enzyme 2; COVID-19 = coronavirus disease 19; SARS-CoV-2 = Severe Acute Respiratory Syndrome coronavirus-2

Coronavirus disease 2019 (COVID-19), the pandemic disease caused by the Severe Acute Respiratory Syndrome coronavirus-2 (SARS-CoV-2), began in December 2019, in Wuhan, China.<sup>1</sup> Common presenting symptoms and signs of COVID-19 include fever, cough, and shortness of breath.<sup>2</sup> In addition, there have been typical pulmonary findings that have been described on chest CT and chest radiographs.<sup>3</sup>

There is a growing body of published evidence that complications of COVID-19 are not limited to the pulmonary system.<sup>4</sup> They include a wide range of neurologic manifestations, such as acute cerebral infarcts.<sup>5,6</sup> We report a case of acute COVID-19 with acute cerebral infarcts, demonstrated by NCCT and extracranial/intracranial CTA. To our knowledge, this is the first reported case of COVID-19-related cerebral infarcts to include brain imaging at multiple time points and CT angiographic imaging.

## CASE REPORT

A 64-year-old man presented to the emergency department of Allegheny General Hospital with a wake-up stroke with symptoms of left-sided hemiparesis and shortness of breath. The patient's last

known well time was >4.5 hours from onset, and intravenous thrombolysis was not recommended. Sixteen days before admission, the patient had been evaluated for fever and myalgias and diagnosed with COVID-19 after testing positive for SARS-CoV-2. The diagnosis of COVID-19 was confirmed during the hospital admission via nasopharyngeal swab and reverse transcription polymerase chain reaction testing. The patient's relevant medical history included hypertension, aplastic anemia, and splenectomy.

In the emergency department, the patient was tachycardic and hypertensive; demonstrated rapid progressive acute hypoxemic respiratory failure; and required intubation with mechanical ventilation. A chest CT revealed extensive, bilateral ground-glass opacities, consistent with acute respiratory distress syndrome due to COVID-19. Due to respiratory and hemodynamic instability, immediate brain and CT angiographic imaging in the emergency department could not be performed safely.

Approximately 5 hours after hospital admission, NCCT revealed large areas of mild hypoattenuation and loss of gray-white differentiation in the territories of the right MCA and bilateral anterior cerebral arteries (ACAs) (Fig 1). Extracranial/intracranial CTA revealed a 20-mm segmental high-grade stenosis of the proximal ICA at the level of the ICA bifurcation (Fig 2). Given that the patient had evidence of mild, diffuse extracranial and intracranial atherosclerotic disease, the high-grade stenosis of the right ICA was favored to represent atherosclerotic disease; however, acute thrombus could have had a similar appearance. The intracranial CTA revealed no large-vessel occlusion, but there was markedly diminished flow in the distal branches of the right MCA and the bilateral ACAs (Fig 2). Approximately 24 hours later, a repeat NCCT

Received April 17, 2020; accepted after revision April 21.

From the Imaging Institute, Division of Neuroradiology (Michael F.G.), and Neuroscience Institute, Cerebrovascular Center (R.C., A.H.T.), Allegheny Health Network, Pittsburgh, Pennsylvania; and Department of Ophthalmology (Morton F.G.), Johns Hopkins Medical Institutions, Baltimore, Maryland.

Please address correspondence to Michael F. Goldberg, MD, MPH, Director, Division of Neuroradiology, Imaging Institute, Allegheny General Hospital, 320 E North Ave, Pittsburgh, PA 15212; e-mail: Michael.goldberg@ahn.org

Indicates open access to non-subscribers at [www.ajnr.org](http://www.ajnr.org)

<http://dx.doi.org/10.3174/ajnr.A6588>



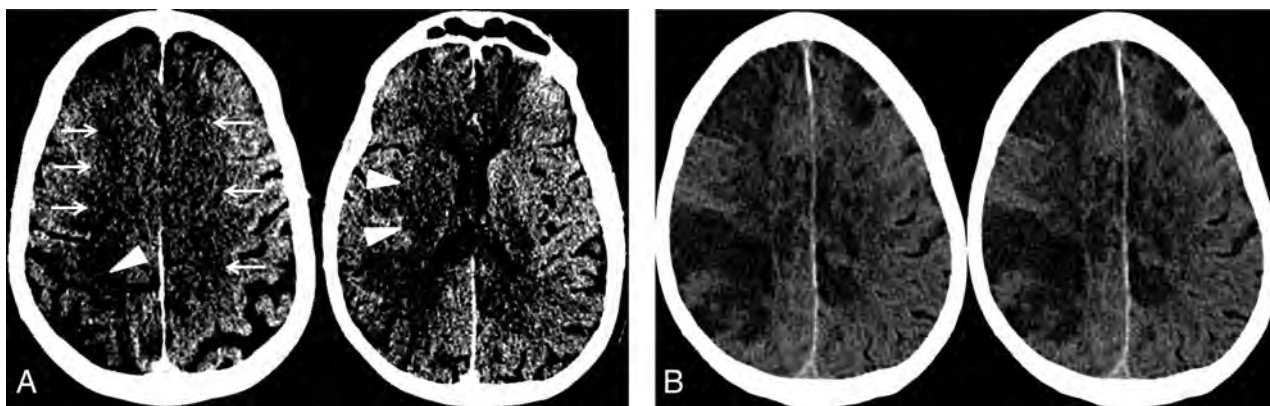


**FIG 1.** A, NCCT on the day of admission demonstrates subtle findings of acute ischemia in the right MCA (arrowheads) and bilateral ACA (arrows) territories, including hypoattenuation and loss of gray-white differentiation. B, Repeat NCCT on hospital day 2 demonstrates progression of acute infarcts in the right MCA and bilateral ACA territories, including worsening edema and mass effect.

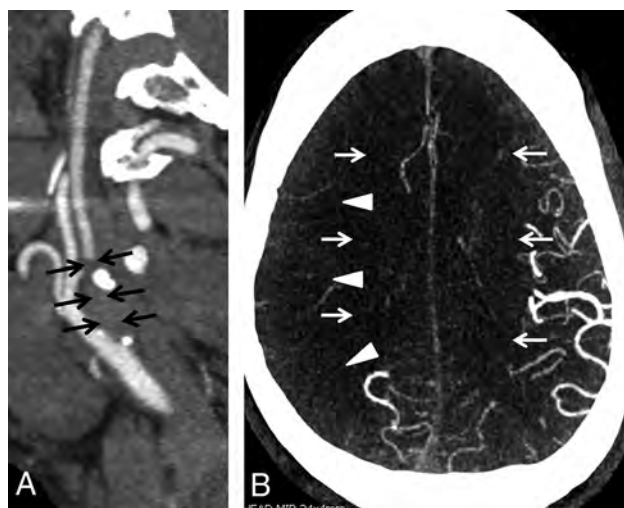


**FIG 2.** A, Sagittal MIP image from the extracranial CTA performed on the day of admission demonstrates a segmental high-grade stenosis of the proximal right internal carotid artery (arrows). There is normal flow in the right common carotid and external carotid arteries. B, Axial MIP of the intracranial CTA performed on the day of admission demonstrates markedly decreased vascular flow within the branches of the right MCA (arrowheads) and bilateral ACAs (arrows). Conversely, there is normal vascular flow in the left MCA and bilateral posterior cerebral artery territories.

revealed worsening cerebral edema and mass effect of the infarcts of the right MCA and bilateral ACA territories, consistent with the expected evolution of acute ischemia (Fig 1).

Laboratory testing showed an elevated white blood cell count and evidence of coagulopathy, including an elevated prothrombin time, increased D-dimer level, increased fibrinogen level, a markedly elevated serum ferritin level, and abnormal elevation of the antiphospholipid antibody, anticardiolipin immunoglobulin M.

## DISCUSSION

A recent case series of 214 patients with COVID-19 from Wuhan, China, reported that 36% of patients demonstrated neurologic manifestations, and acute cerebrovascular disease was reported in 6% of severely affected patients.<sup>5</sup> The precise mechanism for the

cerebral ischemia in the clinical setting of COVID-19 is not known, but there is strong evidence for the development of a transient hypercoagulable state, especially in severe disease.<sup>7</sup>

In a study of 191 patients with COVID-19 in Wuhan, China, researchers found that D-dimer levels of  $>1 \mu\text{g/L}$  were associated with an 18-fold increase in odds of death before discharge.<sup>2</sup> D-dimer is a product of fibrin clot degradation and is indicative of recent or current clot formation.

In Zhou et al,<sup>2</sup> patients with COVID-19 with an elevated serum ferritin level of  $>300 \mu\text{g/L}$  had a 9-fold increase in the odds of death before discharge. Hyperferritinemia, although nonspecific, can be a marker of an inflammatory response.<sup>8</sup> Hyperferritinemia can also be seen in the antiphospholipid syndrome and its variant, catastrophic antiphospholipid syndrome, both of which are associated with arterial and venous thromboses.<sup>9</sup> This patient with hyperferritinemia also had elevated anticardiolipin immunoglobulin M antibodies, and antiphospholipid syndrome has been recently implicated in the coagulopathy associated with cerebral ischemia in patients with COVID-19.<sup>10</sup>

Endothelial damage may also play a role in the pathogenesis of cerebral ischemia in severe COVID-19. Specifically, SARS-CoV-2 infects cells via binding of the spike protein of the virus to the angiotensin converting enzyme 2 (ACE2) receptors.<sup>11</sup> ACE2 receptors are found not only in the alveolar epithelial cells of the lungs but also in the vascular endothelium.<sup>12</sup> Therefore, patients with severe COVID-19 may be at risk of thrombogenesis and cerebral ischemia due to both biochemical hypercoagulable states and direct vascular endothelial injury. In our patient, this risk is a distinct possibility because there were large territorial infarcts despite the absence of an intracranial large-vessel occlusion.

In addition, myocardial injury has been reported in 22% of patients with COVID-19 requiring an intensive care unit, and cardiac embolization may also have a contributory role in COVID-19-related cerebral ischemia.<sup>13</sup>

Finally, this patient had evidence of atherosclerotic disease. Systemic infection, such as that demonstrated in this patient, is associated with activation of immune and inflammatory pathways leading to plaque disruption, serving as a source of thrombosis.<sup>14</sup>

This patient died on hospital day 3 due to COVID-19, and clinical and laboratory evaluations were incomplete; therefore, a



more precise pathogenic mechanism of the cerebral infarcts in this patient is indeterminate. It is also not known why only a small percentage of severely affected patients with COVID-19 have cerebral ischemia, whereas most do not.

In conclusion, we report a case of COVID-19 with acute cerebrovascular disease. We believe this is the first published case to include angiographic imaging. Manifestations of COVID-19 are not limited to the respiratory system, and neuroradiologists should be aware of the associated cerebrovascular disease and its potential underlying etiologies.

## ACKNOWLEDGMENT

Jeremy Virag. Administrative support in the preparation of this manuscript.

Disclosures: Morton F. Goldberg—UNRELATED: Board Membership: Board of Directors, EyeGate Pharmaceuticals, Comments: no relevance to submitted manuscript; Employment: Johns Hopkins Medical School; Stock/Stock Options: board membership, EyeGate Pharmaceuticals. Russell Cerejo—UNRELATED: Consultancy: Medical Advisory Board, iSchemaView.

## REFERENCES

- Phelan AL, Katz R, Gostin LO. The novel coronavirus originating in Wuhan, China: challenges for global health governance. *JAMA* 2020 Jan 30. [Epub ahead of print] CrossRef Medline
- Zhou F, Yu T, Du R, et al. Clinical course and risk factors for mortality of adult inpatients with Covid-19 in Wuhan, China: a retrospective cohort study. *Lancet* 2020;395:1054–62 CrossRef Medline
- Kanne JP, Little BP, Chung JH, et al. Essentials for radiologists on COVID-19: an update—radiology scientific expert panel. *Radiology* 2020 Feb 27. [Epub ahead of print] CrossRef Medline
- World Health Organization. Report of the WHO-China joint mission on coronavirus disease 2019 (COVID-19). February 16–24, 2020. <https://www.who.int/docs/default-source/coronaviruse/who-china-joint-mission-on-covid-19-final-report.pdf>. Accessed April 15, 2020
- Mao L, Jin H, Wang M, et al. Neurologic manifestations of hospitalized patients with coronavirus disease 2019 in Wuhan, China. *JAMA Neurol* 2020 Apr 10. [Epub ahead of print] CrossRef Medline
- Helms J, Kremer S, Merdji H, et al. Correspondence: neurologic features in severe SARS-CoV-2 infection. *N Engl J Med* 2020 Apr 15. [Epub ahead of print] CrossRef Medline
- Thachil J, Tang N, Gando S, et al. ISTH interim guidance on recognition and management of coagulopathy in COVID-19. *J Thromb Haemost* 2020;18:1023–26 CrossRef Medline
- Rosário C, Zandman-Goddard G, Meyron-Holtz EG, et al. The hyperferritinemic syndrome: macrophage activation syndrome, Still's disease, septic shock and catastrophic antiphospholipid syndrome. *BMC Med* 2013;11:185 CrossRef Medline
- Nayer A, Ortega L. Catastrophic antiphospholipid syndrome: a clinical review. *J Nephropathol* 2014;3:9–17 CrossRef Medline
- Zhang Y, Xiao M, Zhang S. Coagulopathy and antiphospholipid antibodies in patients with Covid-19. *N Engl J Med* 2020;382:e38 CrossRef Medline
- Hoffmann M, Kleine-Weber H, Schroeder S, et al. SARS-CoV-2 entry depends on ACE2 and TMPRSS2 and is blocked by a clinically proven protease inhibitor. *Cell* 2020;181:271–80.e8 CrossRef Medline
- Clerkin KJ, Fried JA, Raikhelkar J, et al. Coronavirus disease 2019 (Covid-19) and cardiovascular disease. *Circulation* 2020 Mar 21. [Epub ahead of print] CrossRef Medline
- Wang D, Hu B, Hu C, et al. Clinical characteristics of 138 hospitalized patients with 2019 novel coronavirus-infected pneumonia in Wuhan, China. *JAMA* 2020 Feb 7. [Epub ahead of print] CrossRef Medline
- Libby P, Loscalzo J, Ridker P, et al. Inflammation, immunity, and infection in atherothrombosis: JACC review topic of the week. *J Am Coll Cardiol* 2018;72:2071–81 CrossRef Medline

# Hemorrhagic Posterior Reversible Encephalopathy Syndrome as a Manifestation of COVID-19 Infection

A.M. Franceschi, O. Ahmed, L. Giliberto, and M. Castillo



## ABSTRACT

**SUMMARY:** We describe 2 hospitalized patients with confirmed coronavirus 19 (COVID-19) infection in whom brain imaging showed hemorrhagic posterior reversible encephalopathy syndrome, and we discuss the possible reasons for these findings and their relationship to the infection.

**ABBREVIATIONS:** ACE2 = angiotensin-converting enzyme 2; COVID-19 = coronavirus 19; PRES = posterior reversible encephalopathy syndrome; SARS-CoV-2 = Severe Acute Respiratory Syndrome coronavirus 2

The current pandemic of Severe Acute Respiratory Syndrome coronavirus 2 (SARS-CoV-2) coronavirus 19 (COVID-19) has, to date, infected nearly 2 million people worldwide, resulting in >120,000 deaths as of mid-April 2020, spreading across continents with cases reported in 213 countries and territories.<sup>1</sup> Thus far, the scientific literature in terms of diagnosis and therapeutics has primarily focused on the respiratory status of affected individuals.<sup>2</sup> Neurologic manifestations are becoming increasingly recognized<sup>3-5</sup> and have been described in 78 of 214 (36.4%) patients in a study of patients with severe and nonsevere conditions who are positive for COVID-19. The findings can be, in part, attributed to the affinity of SARS-CoV-2 coronavirus for the angiotensin-converting enzyme 2 (ACE2) receptor, which is a relatively common functional receptor in both the respiratory and nervous systems. In fact, in some patients, neurologic symptoms preceded respiratory illness by several days or were the only indicators of disease in otherwise asymptomatic COVID-19 carriers.<sup>5</sup> Postmortem data have demonstrated hyperemic and edematous brain parenchyma with associated neuronal degeneration in early postmortem studies of patients with SARS-CoV-2,<sup>6</sup> and similar neurologic manifestations have been reported in related coronavirus infections such as SARS and Middle East Respiratory Syndrome.<sup>7,8</sup>

## Case Reports

**Patient 1.** A 48-year-old male airline pilot was exposed to COVID-19 on March 12, 2020, and then self-quarantined. With the exception of obesity, the patient had no pertinent medical or surgical history and was not on any medications.

He subsequently developed fever and cough on March 17, had polymerase chain reaction testing positive for SARS-CoV-2, and was admitted into a local hospital for medical care. Two days later, the fever progressed to 105°F and he developed difficulty breathing and was transferred to a tertiary medical center for intensive care unit care and was placed on mechanical ventilation. On March 25, he developed shock with widely varying blood pressures from 70/30 to 180/90 mm Hg during his intensive care stay. On April 4, he was diagnosed with inflammatory cytokine release syndrome (high D-dimer, lactate dehydrogenase, C-reactive protein, and ferritin values) and developed an altered mental status. Noncontrast CT of the head was obtained and demonstrated focal vasogenic/cytotoxic edema in the posterior parieto-occipital regions bilaterally, which was subcortical in distribution, with a small right-sided hemorrhage (Fig 1); concurrently obtained CT venogram findings were normal. The patient was extubated and transferred to a medical floor on April 10, with gradual improvement in his mental status. MR imaging of the brain was performed on April 13 and confirmed vasogenic edema in the posterior parieto-occipital regions with subacute blood products suggestive of hemorrhagic posterior reversible encephalopathy syndrome (PRES). SWI revealed extensive petechial hemorrhages diffusely distributed throughout the corpus callosum (Fig 2).

**Patient 2.** A 67-year-old woman with multiple comorbidities and past medical history of hypertension, diabetes, coronary

Received April 18, 2020; accepted after revision April 24.

From the Neuroradiology Section, Department of Radiology (A.M.F.) and Department of Neurology (L.G.), Donald and Barbara Zucker School of Medicine at Hofstra/Northwell Health, Manhasset, New York; Department of Radiology (O.A.), Stony Brook University Hospital, Stony Brook, New York; and Neuroradiology Section, Department of Radiology (M.C.), University of North Carolina School of Medicine, Chapel Hill, North Carolina.

Please address correspondence to Ana M. Franceschi, MD, Department of Radiology, 300 Community Dr, Manhasset, NY, 11030-3816; e-mail: afranceschi@northwell.edu

Indicates open access to non-subscribers at www.ajnr.org

<http://dx.doi.org/10.3174/ajnr.A6595>

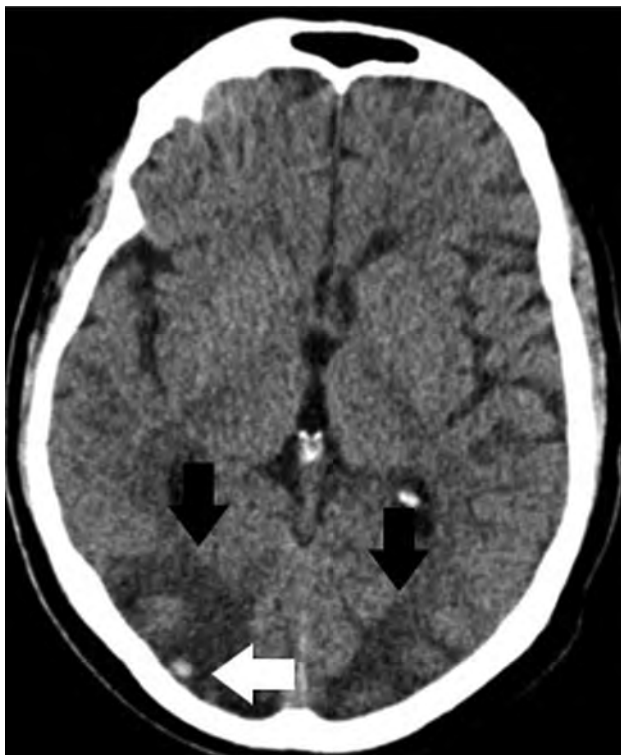


**FIG 1.** Axial noncontrast CT demonstrates edema in the posterior parieto-occipital regions (black arrows) with a superimposed small right-side hemorrhage (white arrow).

artery disease, gout, and asthma resided in a local rehabilitation and skilled nursing center affected by the COVID-19 outbreak.

On March 25, she developed altered mental status, including lethargy and confusion, and was transferred to our hospital. In the emergency department, the patient was afebrile, with laboratory values notable for Cr = 1.65, blood urea nitrogen = 23, lactate = 2.3, and mild hyponatremia. Arterial blood gases were normal, and she denied cough, chest pain, and shortness of breath. The patient had variations in blood pressure, ranging from 115/72 to 178/83 mm Hg at admission. Chest CT demonstrated bilateral multifocal ground-glass opacities concerning for COVID-19 pneumonia due to its high prevalence in the region. Findings of a polymerase chain reaction test were positive for SARS-CoV-2 on March 27. Noncontrast head CT demonstrated edema in the bilateral parieto-occipital regions with associated mass effect and cortical sulcal effacement (Fig 3). MR imaging of the brain performed on March 27 revealed multiple areas of restricted diffusion with associated edema, most extensive in the posterior parieto-occipital lobes but also in the right frontal lobe, basal ganglia, and cerebellar hemispheres. The SWI sequence demonstrated extensive superimposed hemorrhages in the parieto-occipital region along with abnormal enhancement (Fig 4). Findings of concurrently performed MR angiography of the head and neck were unremarkable: Specifically, evaluation of the posterior circulation demonstrated a patent verte-brobasilar system. The patient remained afebrile with normal respiratory status, including oxygen saturation; after gradual improvement in her mental status, she was discharged.

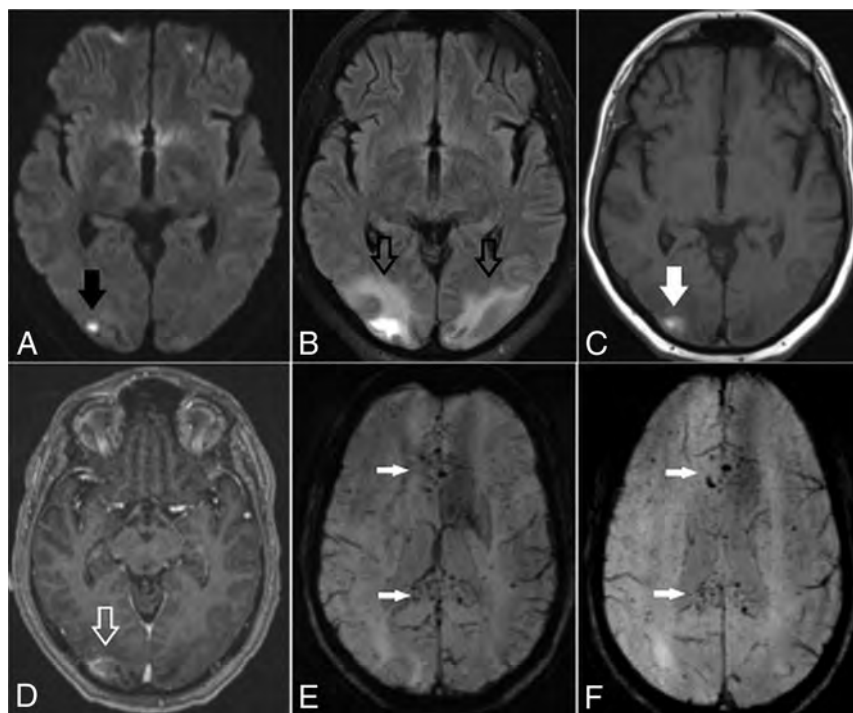


**FIG 2.** Brain axial DWI (A), FLAIR (B), precontrast T1-weighted (C), postcontrast T1-weighted (D), and susceptibility-weighted (E and F) images obtained 8 days after CT demonstrate a small infarct in the right occipital region (arrow, A), persistent edema in the posterior parieto-occipital regions (hollow black arrows, B), subacute blood products in the location of the infarction (solid white arrow, C), and some contrast enhancement (hollow white arrow, D). There are diffuse petechial hemorrhages on SWI throughout the corpus callosum (white arrows, E and F).

## DISCUSSION

PRES is a well-described phenomenon presenting clinically as an acute neurologic syndrome with headache, altered mental status, seizures, and/or visual disturbances and accompanied by fluctuations in blood pressure.<sup>9</sup> It is associated with conditions such as eclampsia and preeclampsia and various autoimmune and rheumatologic disorders, in the setting of cytotoxic and immunosuppressive treatments. The underlying pathophysiologic mechanism of PRES remains controversial but is commonly attributed to alterations in the integrity of the BBB, possibly due to loss of autoregulation and/or endothelial dysfunction. Dominant imaging features of PRES include vasogenic edema predominantly in the parieto-occipital lobes, though abnormalities may also be seen in the watershed distributions, frontal lobes, inferior temporal lobes, basal ganglia, brain stem, and cerebellum. Furthermore, reports have described hemorrhagic complications of PRES in 15%–20% of cases, including both petechial hemorrhages

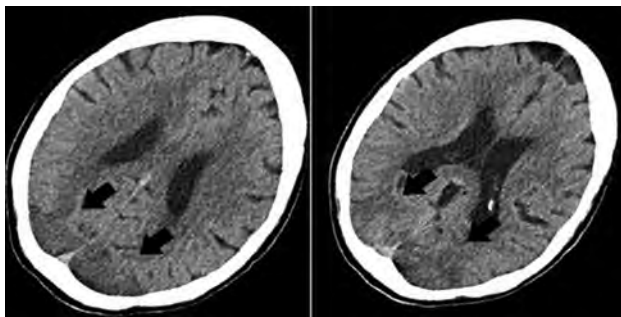


**FIG 3.** Axial noncontrast CT images demonstrate vasogenic/cytotoxic edema in the parieto-occipital regions suggestive of PRES (arrows).

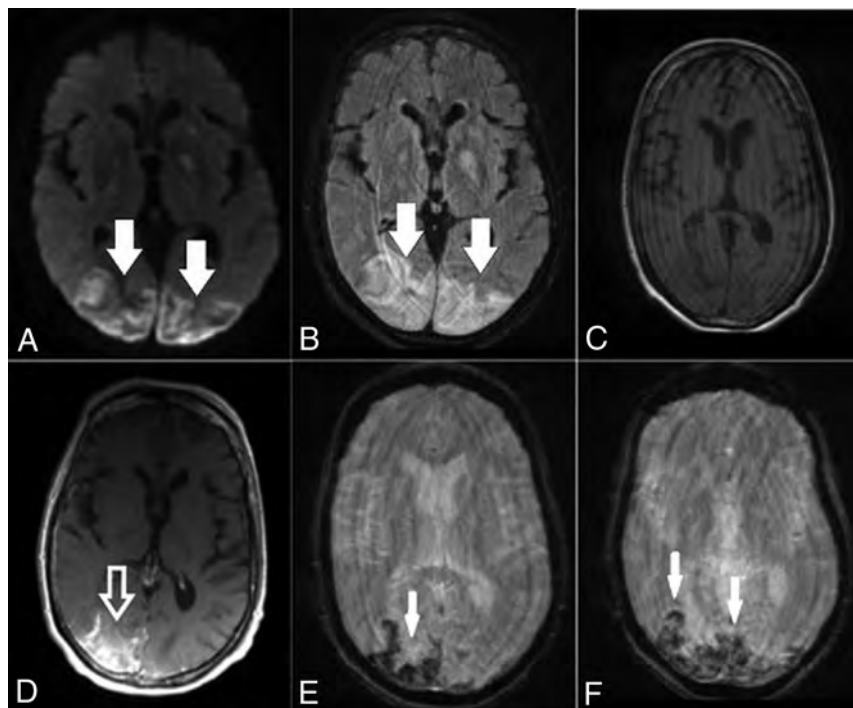


**FIG 4.** Brain axial DWI (A), FLAIR (B), precontrast T1-weighted (C), postcontrast T1-weighted (D) and SWI (E and F) obtained after CT demonstrate bilateral posterior infarctions (white arrows, A), edema in the posterior parieto-occipital regions (white arrows, B), and some contrast enhancement (hollow white arrow, D; compare with C). Selected SWI shows extensive blooming artifacts compatible with hemorrhages predominantly in the cortex (white arrows, E and F). Findings are more pronounced on the right side.

and intraparenchymal hematomas, as was the case with our patients. PRES-related intracranial hemorrhage has been associated with poor patient outcome.<sup>10-12</sup> In addition, abnormal contrast enhancement may also be seen in some patients with PRES as the parenchymal insult becomes subacute. Occasionally, patients may also develop cytotoxic edema, which is reflected by restricted diffusion on MR imaging, such as was seen in our patients.<sup>9,13</sup>

COVID-19-infected critically ill patients have a massive inflammatory reaction that is proposed to be due to rapid accumulation of T-cells and macrophages, resulting in release of a large number of cytokines into the bloodstream aiming to destroy

the offending pathogen and resulting in numerous clinical manifestations known commonly as cytokine release syndrome.<sup>14-16</sup> Classic laboratory findings of cytokine release syndrome include decreased T-cells and natural killer cells and, most important, an increase in interleukin 6, leading to clinical symptoms of fever and multiorgan dysfunction. This massive release of cytokines may damage and result in breakdown of the BBB and is a mechanism that may explain the development of PRES in our patients with COVID-19. Furthermore, hypoxia is a well-known trigger of inflammation, both at the local and systemic levels.<sup>17,18</sup> Both of our patients had labile blood pressures, with the first patient rapidly fluctuating from significant hypotension to severe hypertension in a short time. This also is a commonly described risk factor

for the development of PRES and may explain the neuroimaging findings. In addition, the COVID-19 virus, by means of the spike protein S1, has a high affinity for the human ACE2 receptors, which are expressed on numerous cells types, including the capillary endothelium.<sup>5,19-22</sup> Current data suggest that engagement of the endothelium by the virus can cause damage to its lining and result in increased permeability of the BBB. This scenario can result in loss of homeostatic regulation of blood flow to the brain, increased susceptibility to blood pressure changes, and, as in our patients, brain edema. The presence of superimposed hemorrhages may be related to coagulopathy, which is also a sequela of cytokine release syndrome due to liver dysfunction and consumption of clotting factors as part of the disseminated intravascular coagulation cascade.

It is suspected that endothelial damage to the BBB precedes the actual invasion of the virus into the brain. Once the virus accesses the brain, it may also attack neurons, by virtue of the S1-ACE2 interaction. This may be the prelude to severe parenchyma destruction seen in acute necrotizing encephalopathy.<sup>3,4,23-25</sup> In this context, can COVID-19-mediated PRES be considered a gateway to COVID-19-mediated acute necrotizing encephalopathy? Although the pathogenesis of postinfectious acute necrotizing encephalopathy may be related to the same cytokine storm that has been described in patients with COVID-19 and may also be responsible for some cases of PRES, a link between both is still not well established.<sup>3,19,25</sup> Acute necrotizing encephalopathy typically involves different brain regions, including the thalami, a finding not observed in our patients.<sup>4,23,24</sup> Both of our patients recovered with medical management and did not develop more ominous brain lesions, in line with described favorable clinical outcomes of most cases of non-COVID-19 PRES.



## CONCLUSIONS

We presented 2 patients with COVID-19 who demonstrated imaging findings compatible with hemorrhagic PRES. Although multifactorial, PRES in hospitalized patients with COVID-19 may be explained by a combination of cytokine release syndrome and direct SARS-CoV-2-mediated breakdown of the BBB, rendering patients susceptible to developing PRES, particularly in the setting of labile blood pressure. Despite significant brain abnormalities, both patients survived and showed normal mental status following the resolution of COVID-19-associated symptoms. PRES may be a neurologic manifestation of COVID-19 infection.

## REFERENCES

1. Coronavirus disease (COVID-19) Pandemic. Geneva: World Health Organization. 2020. <https://www.who.int/emergencies/diseases/novel-coronavirus-2019>. Accessed April 15, 2020
2. Jin Y, Cai L, Cheng Z, et al; for the Zhongnan Hospital of Wuhan University Novel Coronavirus Management and Research Team, Evidence-Based Medicine Chapter of China International Exchange and Promotive Association for Medical and Health Care (CPAM). **A rapid advice guideline for the diagnosis and treatment of 2019 novel coronavirus (2019-nCoV) infected pneumonia (standard version).** *Mil Med Res* 2020;7:4 CrossRef Medline
3. Filatov A, Sharma P, Hindi F, et al. **Neurological complications of coronavirus (COVID-19): encephalopathy.** *Cureus* 2020;12:e7352 CrossRef Medline
4. Poyiadji N, Shahin G, Noujaim D, et al. **COVID-19-associated acute hemorrhagic necrotizing encephalopathy: CT and MRI features.** *Radiology* 2020 Mar 31 [Epub ahead of print] CrossRef Medline
5. Mao L, Jin H, Wang M, et al. **Neurologic manifestations of hospitalized patients with coronavirus disease 2019 in Wuhan, China.** *JAMA Neurol* 2020 Apr 10 [Epub ahead of print] CrossRef Medline
6. National Health Commission of the People's Republic of China. **Diagnosis and treatment of the novel coronavirus pneumonia.** <http://www.nhc.gov.cn/>. Accessed April 15, 2020
7. Ding Y, He L, Zhang Q, et al. **Organ distribution of severe acute respiratory syndrome (SARS) associated coronavirus (SARS-CoV) in SARS patients: implications for pathogenesis and virus transmission pathways.** *J Pathol* 2004;203:622–30 CrossRef Medline
8. Arabi YM, Balkhy HH, Hayden FG, et al. **Middle East Respiratory Syndrome.** *N Engl J Med* 2017;376:584–94 CrossRef Medline
9. Bartyński WS, Boardman JF. **Distinct imaging patterns and lesion distribution in posterior reversible encephalopathy syndrome.** *AJNR Am J Neuroradiol* 2007;28:1320–27 CrossRef Medline
10. Hefzy HM, Bartyński WS, Boardman JF, et al. **Hemorrhage in posterior reversible encephalopathy syndrome: imaging and clinical features.** *AJNR Am J Neuroradiol* 2009;30:1371–79 CrossRef Medline
11. Sharma A, Whitesell RT, Moran KJ. **Imaging pattern of intracranial hemorrhage in the setting of posterior reversible encephalopathy syndrome.** *Neuroradiology* 2010;52:855–63 CrossRef Medline
12. Yamagami K, Maeda Y, Iihara K. **Variant type of posterior reversible encephalopathy syndrome associated with deep brain hemorrhage: case report and review of the literature.** *World Neurosurg* 2020;134:176–81 CrossRef Medline
13. Donmez FY, Basaran C, Kayahan Ulu EM, et al. **MRI features of posterior reversible encephalopathy syndrome in 33 patients.** *J Neuroimaging* 2010;20:22–28 CrossRef Medline
14. Mehta P, McAuley DF, Brown M, et al. **COVID-19: consider cytokine storm syndromes and immunosuppression.** *Lancet* 2020;395:1033–34 CrossRef Medline
15. Wang W, He J, Lie P, et al. **The definition and risks of cytokine release syndrome-like in 11 COVID-19-infected pneumonia critically ill patients: disease characteristics and retrospective analysis.** *MedRxiv* <https://www.medrxiv.org/content/10.1101/2020.02.26.20026989v1>. Accessed April 15, 2020
16. Xie J, Tong Z, Guan X, et al. **Clinical characteristics of patients who died of coronavirus disease 2019 in China.** *JAMA Netw Open* 2020;3:e205619 CrossRef Medline
17. Eltzschig HK, Carmeliet P. **Hypoxia and inflammation.** *N Engl J Med* 2011;364:656–65 CrossRef Medline
18. Bartels K, Grenz A, Eltzschig HK. **Hypoxia and inflammation are two sides of the same coin.** *Proc Natl Acad Sci USA* 2013;110:18351–52 CrossRef Medline
19. Baig AM, Khaleeq A, Ali U, et al. **Evidence of the COVID-19 virus targeting the CNS: tissue distribution, host-virus interaction, and proposed neurotropic mechanisms.** *ACS Chem Neurosci* 2020;11:995–98 CrossRef Medline
20. Netland J, Meyerholz DK, Moore S, et al. **Severe acute respiratory syndrome coronavirus infection causes neuronal death in the absence of encephalitis in mice transgenic for human ACE2.** *J Virol* 2008;82:7264–75 CrossRef Medline
21. Li YC, Bai WZ, Hashikawa T. **The neuroinvasive potential of SARS-CoV2 may play a role in the respiratory failure of COVID-19.** *J Med Virol* 2020 Feb 27 [Epub ahead of print] CrossRef Medline
22. Wrapp D, Wang N, Corbett KS, et al. **Cryo-EM structure of the 2019-nCoV spike in the prefusion conformation.** *Science* 2020;367:1260–63 CrossRef Medline
23. Wong AM, Simon EM, Zimmerman RA, et al. **Acute necrotizing encephalopathy of childhood: correlation of MR findings and clinical outcome.** *AJNR Am J Neuroradiol* 2006;27:1919–23 Medline
24. Abdelrahman HS, Safwat AM, Alsagheir MM. **Acute necrotizing encephalopathy in an adult as a complication of H1N1 infection.** *BJR Case Rep* 2019;5:20190028 CrossRef Medline
25. Wu X, Wu W, Pan W, et al. **Acute necrotizing encephalopathy: an underrecognized clinicoradiologic disorder.** *Mediators Inflamm* 2015;2015:792578 CrossRef Medline

# Surprise Diagnosis of COVID-19 following Neuroimaging Evaluation for Unrelated Reasons during the Pandemic in Hot Spots

R. Jain, M. Young, S. Dogra, H. Kennedy, V. Nguyen, and E. Raz



## ABSTRACT

**SUMMARY:** During the height of the recent outbreak of coronavirus 19 (COVID-19) in New York City, almost all the hospital emergency departments were inundated with patients with COVID-19, who presented with typical fever, cough, and dyspnea. A small number of patients also presented with either unrelated conditions (such as trauma) or other emergencies, and some of which are now known to be associated with COVID-19 (such as stroke). We report such a scenario in 17 patients who were admitted and investigated with CT spine imaging and CT angiography for nonpulmonary reasons (trauma = 13, stroke = 4). Their initial work-up did not suggest COVID-19 as a diagnosis but showed unsuspected/incidental lung findings, which led to further investigations and a diagnosis of COVID-19.

During the height of the recent outbreak of coronavirus 19 (COVID-19) in New York City, one of the worst affected regions in the United States, almost all hospital emergency departments were inundated with patients with COVID-19, who presented with typical fever, cough, and dyspnea, though a small number of patients also presented with either unrelated conditions (eg, trauma) or other atypical emergencies, some of which are now known to be associated with COVID-19 (eg, stroke).<sup>1</sup> We discuss 17 such patients who presented to the emergency department with nonpulmonary symptoms and did not raise the suspicion of COVID-19 at the time of admission. Initial nonpulmonary imaging in the emergency department led to the discovery of incidental lung findings that triggered further testing for Severe Acute Respiratory Syndrome coronavirus 2 (SARS-CoV-2) with an eventual diagnosis of COVID-19.

## MATERIALS AND METHODS

Four hundred seventy-three of a total of 3160 patients positive for COVID-19 who were admitted to NYU Langone Health, New York City, between March 1, 2020, and April 13, 2020, were investigated with various neuroimaging examinations (CT, MR imaging, and angiography), some of which included partial coverage of the bilateral lung fields. A confirmed case of COVID-19 was defined as a positive result on a real-time reverse

transcriptase polymerase chain reaction assay of nasopharyngeal or oropharyngeal swab specimens. While reviewing these 473 patients, we identified a subgroup of 17 patients (range, 44–93 years of age; mean age, 72 years; male/female ratio: 8:9) in whom COVID-19 as a diagnosis was not suspected at the time of admission and who underwent neuroimaging.

This study was approved by the NYU Grossman School of Medicine institutional review board, which granted both a waiver of informed consent and a waiver of the Health Insurance Portability and Accountability Act.

## RESULTS

The reason for the imaging study in these 17 patients was trauma ( $n = 13$ ) evaluated with spine CT (cervical spine = 11, thoracic spine = 2; with coverage of the posterior lungs) and acute stroke ( $n = 4$ ) evaluated with CT angiography of the brain and neck (with coverage of the lung apices). Twelve of 13 patients with trauma had a history of a mechanical fall related to syncope or dizziness. These CT studies did not show any findings related to spine trauma or acute stroke but revealed suspicious lung findings with multifocal, peripheral, ground-glass opacities in both lungs (Figure). Lung findings were mentioned prospectively in the imaging reports as suspicious for pneumonia and viral etiology. All these patients underwent further laboratory investigations based on the surprising lung findings, and the diagnosis of COVID-19 was confirmed with a reverse transcriptase polymerase chain reaction assay of nasopharyngeal or oropharyngeal swab specimens, according to the World Health Organization interim guidance.<sup>2</sup> Eight of 17 patients on further questioning after the COVID-19 diagnosis did confirm a history of cough in the days preceding presentation to the emergency department. Despite the initial admission not being related to pulmonary symptoms, 14 patients were eventually managed for varying

Received April 21, 2020; accepted after revision May 1.

From the Departments of Radiology (R.J., M.Y., S.D., H.K., V.N., E.R.) and Neurosurgery (R.J.), NYU Langone Health, New York, New York.

Please address correspondence to Rajan Jain, MD, Radiology and Neurosurgery, NYU Grossman School of Medicine, 660 First Ave, 2nd Floor, NY, NY 10016; e-mail: rajan.jain@nyulangone.org; @CoolAsANeuroRad

Indicates open access to non-subscribers at [www.ajnr.org](http://www.ajnr.org)

<http://dx.doi.org/10.3174/ajnr.A6608>

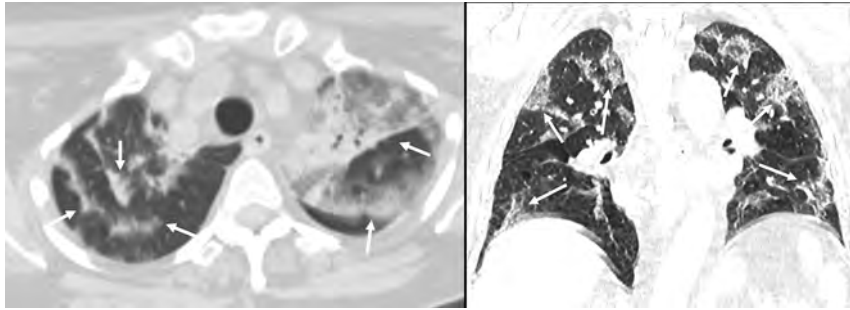


**FIGURE.** Axial and coronal CT images of 2 different patients, obtained from CTA of the neck (stroke evaluation) and CT of the thoracic spine (trauma evaluation), respectively, demonstrating typical multifocal, peripheral, ground-glass opacities in both lungs.

severity of respiratory symptoms and 6 patients had high oxygen requirements during their hospital stay. Three patients required a non-rebreather mask with an oxygen flow rate of  $>15$  L/min, and 3 patients needed endotracheal intubation and ventilator support. These patients required hospital admission for a mean of 7.29 days (range, 2–15 days), and 2 patients ultimately died due to COVID-19-related complications (1- and 6- day hospital stays).

## DISCUSSION

One of the major reasons for the very high community spread of SARS-CoV-2 (COVID-19) is that viral loads are being detected in asymptomatic individuals or mildly symptomatic patients.<sup>3,4</sup> Fifty-six percent of asymptomatic residents of a skilled nursing home facility tested positive for COVID-19 in a recent study and likely contributed to disease transmission.<sup>4</sup> High viral loads are almost always present soon after symptom onset, unlike SARS in 2002–2003, when viral shedding only happened after a patient was extremely symptomatic.<sup>3</sup> Our study builds on this evidence by demonstrating that during the height of the COVID-19 pandemic in hot spots, there are many unsuspected and asymptomatic patients who are admitted to the emergency department and urgent care centers for either non-COVID-19-related reasons or atypical COVID-19 symptoms. These patients may neither be initially screened for COVID-19 nor isolated with precautions needed to curb the spread of the virus because the admission appears unrelated to COVID-19. Therefore, they may come in contact with multiple health care workers in the emergency department, including first responders or even various imaging/laboratory technologists, who may not have taken all the required precautions while handling or treating them.

Our case series will have a major impact on medical practice policies. For example, imaging/laboratory technologists or even receptionists at these clinics, laboratories, and imaging centers who will be coming in first contact with many of these otherwise asymptomatic patients must enforce better physical distancing and strict contact precautions and improved screening practices. This practice will be especially important as hospitals/clinics start to open up their facilities for outpatient work in the near future. All patients presenting at inpatient and

outpatient imaging facilities at NYU Langone Health will now be screened for COVID-19-related symptoms and will need to wear masks regardless of their COVID-19 status, apart from similarly modified practice rules for radiology technologists and receptionists at the clinics and imaging centers.

## ACKNOWLEDGMENT

We would like to acknowledge the NYU Family Connect Program as well as thousands of front-line health care workers who were an inspiration for this project.

Disclosures: Rajan Jain—UNRELATED: Board Membership: Nuevozen Corp; Consultancy: Cancer Panels Inc; Royalties: Thieme. Eytan Raz—UNRELATED: Expert Testimony: various law firms; Royalties: Springer; Travel/Accommodations/Meeting Expenses Unrelated to Activities Listed: MicroVention.

## REFERENCES

1. Mao L, Jin H, Wang M, et al. **Neurologic manifestations of hospitalized patients with coronavirus disease 2019 in Wuhan, China.** *JAMA Neurol* 2020 Apr 10. [Epub ahead of print] CrossRef Medline
2. World Health Organization. **Clinical management of severe acute respiratory infection when novel coronavirus (nCoV) infection is suspected: interim guidance.** March 13, 2020. [https://www.who.int/publications-detail/clinical-management-of-severe-acute-respiratory-infection-when-novel-coronavirus-\(ncov\)-infection-is-suspected](https://www.who.int/publications-detail/clinical-management-of-severe-acute-respiratory-infection-when-novel-coronavirus-(ncov)-infection-is-suspected). Accessed February 5, 2020
3. Zou L, Ruan F, Huang M, et al. **SARS-CoV-2 viral load in upper respiratory specimens of infected patients.** *N Engl J Med* 2020;382:1177–79 CrossRef Medline
4. Arons MM, Hatfield KM, Reddy SC, et al. **Presymptomatic SARS-CoV-2 infections and transmission in a skilled nursing facility.** *N Engl J Med* 2020 Apr 24. [Epub ahead of print] CrossRef Medline

# Brain Imaging Use and Findings in COVID-19: A Single Academic Center Experience in the Epicenter of Disease in the United States

 A. Radmanesh,  E. Raz,  E. Zan,  A. Derman, and  M. Kaminetzky



## ABSTRACT

**SUMMARY:** Coronavirus disease 2019 (COVID-19) is a serious public health crisis and can have neurologic manifestations. This is a retrospective observational case series performed March 1–31, 2020, at New York University Langone Medical Center campuses. Clinical and imaging data were extracted, reviewed, and analyzed. Two hundred forty-two patients with COVID-19 underwent CT or MRI of the brain within 2 weeks after the positive result of viral testing (mean age,  $68.7 \pm 16.5$  years; 150 men/92 women [62.0%/38.0%]). The 3 most common indications for imaging were altered mental status (42.1%), syncope/fall (32.6%), and focal neurologic deficit (12.4%). The most common imaging findings were nonspecific white matter microangiopathy (134/55.4%), chronic infarct (47/19.4%), acute or subacute ischemic infarct (13/5.4%), and acute hemorrhage (11/4.5%). No patients imaged for altered mental status demonstrated acute ischemic infarct or acute hemorrhage. White matter microangiopathy was associated with higher 2-week mortality ( $P < .001$ ). Our data suggest that in the absence of a focal neurologic deficit, brain imaging in patients with early COVID-19 with altered mental status may not be revealing.

**ABBREVIATIONS:** CoV = coronavirus; COVID-19 = coronavirus disease 2019; SARS-COV-2 = Severe Acute Respiratory Syndrome coronavirus 2

The novel coronavirus (CoV), responsible for the December 2019 outbreak in Wuhan, China, has spread quickly around the world, leading to a global pandemic.<sup>1</sup> The virus shows similarities in cellular receptors and symptoms to Severe Acute Respiratory Syndrome CoV and has been named Severe Acute Respiratory Syndrome coronavirus 2 (SARS-COV-2), with the disease it causes called coronavirus disease 2019 (COVID-19).

As of April 25, 2020, there were 925,758 confirmed cases of COVID-19 and 52,217 total deaths in the United States.<sup>2</sup> The New York metropolitan area has become the epicenter of COVID-19 in the United States. As of April 24, 2020, the City of New York has had 146,139 confirmed cases of COVID-19 and 10,746 confirmed deaths due to the disease.<sup>3</sup>

A variety of neurologic manifestations have been reported in COVID-19, affecting as many as 36.4% of patients according to a report from Wuhan, China.<sup>4,5</sup> Clinically most important, acute ischemic infarcts and intracranial hemorrhage have been noted in these patients.<sup>6</sup>

Considering that altered mental status in patients with COVID-19 is common secondary to respiratory distress and hypoxemia, brain imaging is frequently considered. Anecdotally, it has been suggested that patients with COVID-19 are at specific risk for ischemic and hemorrhagic central nervous system complications.<sup>7</sup> Here, we report the use and findings of neurologic imaging in patients with COVID-19 during the initial month after the outbreak in the City of New York and analyze neuroimaging use as well as acute intracranial findings, including acute infarcts and intracranial hemorrhage.

## MATERIALS AND METHODS

This is a retrospective and Health Insurance Portability and Accountability Act–compliant study that was performed following the approval by the institutional review board. Informed consent was waived.

Patients seen at New York University Langone Medical Center (across the Manhattan and Brooklyn campuses) with a positive polymerase chain reaction from a nasal swab specimen for SARS-COV-2 diagnosed between March 1 and 31, 2020, with at least 1 brain imaging examination (CT or MRI) during the course of their recent hospital encounter and within 2 weeks following the positive result of viral testing were included. Electronic health records and neuroimaging studies were reviewed for age, sex, patient type (outpatient or inpatient status), clinical indication for brain imaging (from clinical notes),

Received April 25, 2020; accepted after revision May 3.

From the Department of Radiology, New York University School of Medicine, New York, New York.

Please address correspondence to Alireza Radmanesh, MD, New York University Langone Medical Center, 660 First Ave, 2nd Floor, New York, NY 10016; e-mail: Alireza.Radmanesh@nyulangone.org; @AliRadmanMD

 Indicates open access to non-subscribers at [www.ajnr.org](http://www.ajnr.org)

<http://dx.doi.org/10.3174/ajnr.A6610>



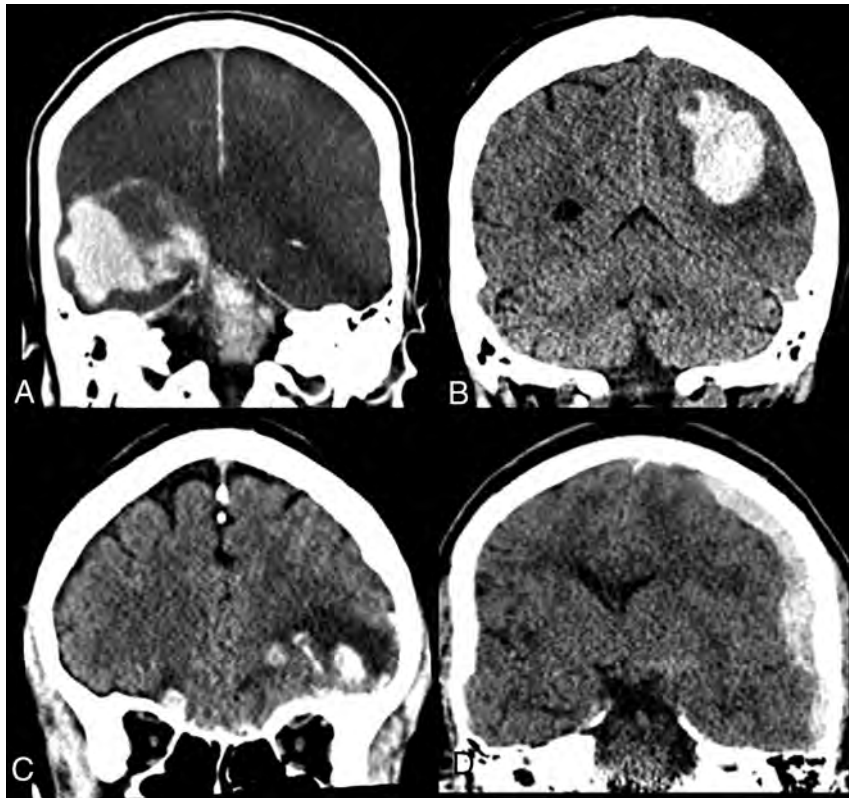


**FIG 1.** Acute intracranial hemorrhage in patients with COVID-19. *A*, A 74-year-old man with COVID-19, intubated for hypoxic respiratory failure and on heparin due to a history of stented carotid stenosis. On day 10 of intensive care unit admission, he suddenly became unresponsive, and neurologic examination revealed absent brain stem reflexes. Brain CT showed extensive supra- and infratentorial acute hemorrhage with subarachnoid and intraventricular extensions, along with cerebral swelling and hypodensity (likely hypoperfusion injury), as well as uncus, subfalcine, and transtentorial herniations. *B*, A 61-year-old woman with COVID-19 and compensated hepatic cirrhosis (due to primary sclerosing cholangitis). On day 7 of intensive care unit admission, the patient developed right-sided weakness and numbness. Brain CT showed left parietal intraparenchymal hemorrhage with surrounding vasogenic edema. *C*, A 68-year-old man with COVID-19 was found fallen. Head CT showed bilateral inferior frontal lobe hemorrhagic contusions and a small subarachnoid hemorrhage, suggesting traumatic brain injury, likely related to the fall. *D*, A 61-year-old man with COVID-19 who presented after a fall. Brain CT revealed acute left cerebral convexity subdural and left ambient cistern subarachnoid hemorrhage, possibly related to the fall.

imaging findings, and 2-week outcome (mortality, transition to hospice or comfort care, improved or stable clinical condition). For patients with imaging findings of acute or subacute infarcts, note was made of anterior-versus-posterior vascular territory involvement, small- or large-vessel occlusion infarct, the presence or absence of hemorrhagic transformation, and whether revascularization with mechanical thrombectomy was attempted, as well as the imaging outcome of revascularization. In cases of white matter microangiopathy, a neuroradiologist with 6 years of subspecialty experience graded microangiopathies as none, as much as expected for age or more than expected for age on CT and MRI.<sup>8</sup> Mean ages for different categorical variables were compared using a 2-tailed *t* test. The difference between ratios for categorical variables was examined using Fisher exact tests (QuickCalcs; [www.graphpad.com/quickcalcs/](http://www.graphpad.com/quickcalcs/)).

## RESULTS

### Imaging Use and Common Findings

Of 3661 patients with laboratory-confirmed diagnosis of SARS-CoV-2 between March 1 and 31, 2020, two hundred forty-two patients underwent at least 1 cross-sectional brain imaging examination. These 242 patients had a mean age of  $68.7 \pm 16.5$  years; there were 150 men (62.0%) and 92 women (38.0%), 231 inpatients and 11 outpatients. The patients from the emergency department were considered outpatients if they were discharged home from the emergency department and were considered inpatients if they were transferred from the emergency department to the intensive care unit or regular floors of the hospital. Two hundred 7 patients had only CT, 11 patients had only MRI, and 24 patients underwent both CT and MRI.

Overall, the most common abnormal findings seen on imaging were nonspecific white matter changes (hypodensity on CT or T2 hyperintensity on MRI, often attributed to microangiopathy) in 134 patients (55.4%), followed by chronic infarct in 47 patients (19.4%), acute or subacute infarcts in 13 patients (5.4%), and acute intracranial hemorrhage in 11 patients (4.5%). White matter microangiopathy was as much as expected for age in 108 and more than expected for age in 26 patients. One patient had imaging findings of widespread anoxic brain injury following a large acute supra- and infratentorial hemorrhage (Fig 1A).

The 3 most common clinical indications for brain imaging were the following: 1) altered mental status (102 patients, 42.1%, all were inpatients), 2) syncope/fall (79 patients, 32.6%, including 4 outpatients), and 3) focal neurologic deficit (30 patients, 12.4%, all were inpatients). Of note, 5 outpatients were imaged for nonacute headache, and 2 were imaged for generalized weakness. Of patients imaged for altered mental status, 42 (41.2%) had white matter microangiopathic changes, 29 (28.4%) had chronic infarcts, and 1 patient had an incidental meningioma. No patients with altered mental status as the indication for brain imaging demonstrated acute or subacute infarct or acute intracranial hemorrhage.

In a 2-week follow-up period, 63 patients died or were transitioned to hospice or comfort care and 179 showed improvement or stability. The mean age of patients with fatal outcome ( $76.4 \pm 13.1$  years) was significantly higher than that of the patients who remained stable or clinically improved during the subsequent 2 weeks ( $66.0 \pm 16.8$  years) ( $P$  value  $< .001$ ). White matter

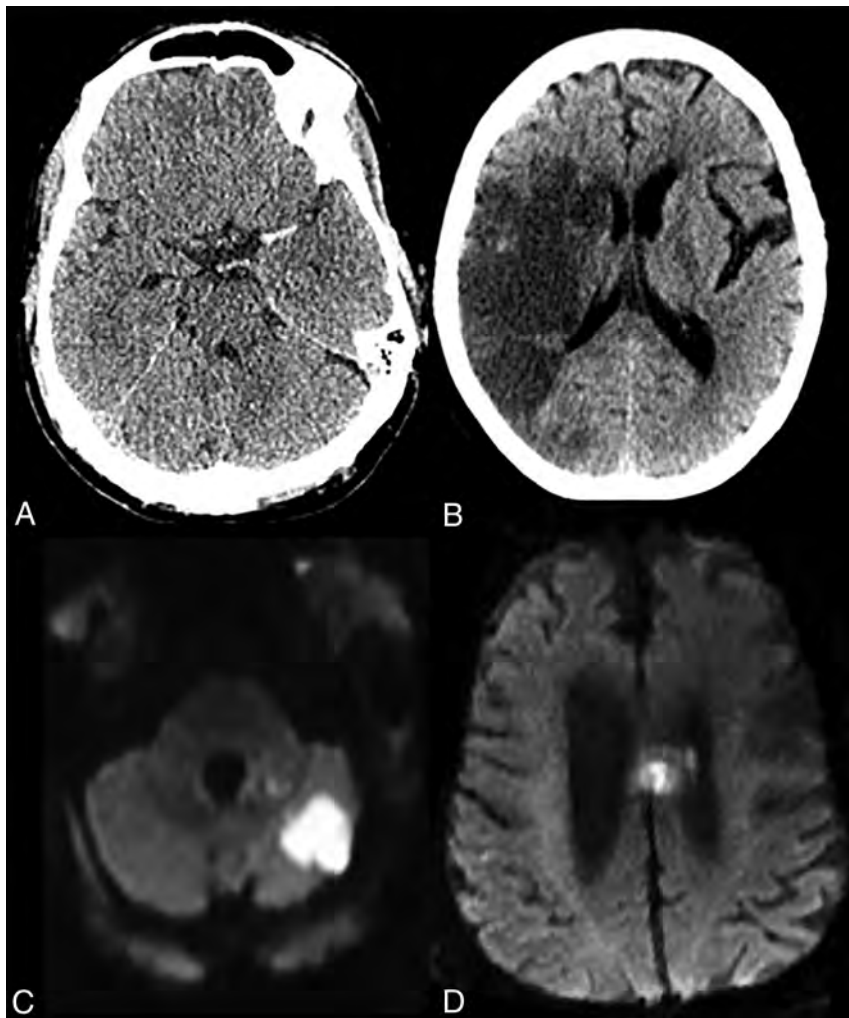


**FIG 2.** Acute or subacute infarct in patients with COVID-19. A, A 62-year-old man with COVID-19, intubated for acute hypoxic respiratory failure, who initially presented with left MCA syndrome. Noncontrast head CT showed a dense left MCA sign suggesting a left MCA occlusion, later confirmed on CT angiography and catheter angiography (not shown here). B, A 77-year-old woman with COVID-19 presented with left-sided weakness. Noncontrast CT showed an acute/subacute right MCA territory infarct. C, A 63-year-old COVID-19 patient with ataxia. Brain MRI revealed a patchy acute infarct in the left cerebellar hemisphere. D, A 78-year-old man with COVID-19 presented following an unwitnessed fall. Brain MRI showed left more than right cingulate gyrus and callosal body acute infarct.

microangiopathy on brain imaging showed an association with poor 2-week outcome ( $P < .001$ ). Two-week outcome was not significantly different between men and women ( $P = .88$ ).

#### Acute/Subacute Infarcts

Acute and subacute infarcts were categorized together because the distinction is often difficult on CT, which composed most of our examinations. In the 13 patients with acute/subacute infarct, 11 (84.6%) had a focal neurologic deficit as the primary indication for brain imaging and the remaining 2 patients were imaged for syncope/fall. Based on the Fisher exact test for comparing ratios, there was a highly statistically significant association between focal neurologic deficit and the presence of acute/subacute infarct ( $P < .001$ ). Of note, none of 102 patients scanned for altered mental

status alone were subsequently demonstrated to have acute or subacute infarct. In addition, 19 patients of a total of 29 with focal neurologic deficits (65.5%) showed no acute or subacute infarcts on CT or MRI.

In these 13 patients with acute or subacute infarct, 9 infarcts (69.2%) involved the anterior and 4 (30.8%) involved the posterior circulation territories. Four patients had large-vessel occlusions, including occlusion of the distal left ICA, proximal M1 segment of the left MCA (Fig 2A), right M2 segment (Fig 2B), and the right posterior cerebral artery. All 3 patients with anterior circulation large-vessel occlusions underwent mechanical thrombectomy with TICI 3, 2a, and 2b revascularizations, respectively.

In 6 of 13 patients with acute or subacute infarcts, the infarcts were noted at presentation, and in 7 patients, infarcts were detected during the hospitalization. Only 1 patient with acute or subacute infarct showed hemorrhagic transformation in the infarcted region after receiving intravenous tPA. Two other patients who received tPA did not show any complications. Three of 13 patients with acute or subacute infarcts also showed chronic infarcts on brain imaging. While 11 of 13 patients had some degree of white matter microangiopathy on brain imaging, none was perceived to be more than expected for age.

A statistically greater number of patients with acute/subacute infarcts on neuroimaging had white matter microangiopathic changes compared with patients without infarct (11 of 13 compared with 123 of 229,  $P = .04$ ).

On the other hand, no statistically significant difference was seen between patients with and without acute/subacute infarct in terms of age (mean,  $69.08 \pm 12.5$  years versus  $68.69 \pm 16.77$  years, respectively,  $P = .93$ ) or the presence of chronic infarct on brain imaging (10 of 13 versus 185 of 229,  $P = .72$ ).

#### Acute Hemorrhage

Eleven patients demonstrated areas of acute hemorrhage on brain CT or MRI. In 4 of these patients, review of history and prior imaging showed the hemorrhage to be present 4–8 weeks prior to the current hospital encounter and related to an automobile crash, tumor resection, shunt placement, and hypertensive hemorrhage. These cases were thus considered unrelated to COVID-19. Of the remaining 7 patients who were all hospitalized, 4 were

found fallen or brought to the hospital after a fall with a subsequent positive test for SARS-COV-2. All of these 4 patients also had respiratory distress and/or hypoxemia at presentation, presumably related to COVID-19. The causal relationship between the fall and COVID-19 is unclear. Two patients had dramatic intraparenchymal hemorrhage during the hospitalization (Fig 1A, -B), and both died. One remaining patient had a fall, and subsequent imaging revealed scattered convexity subarachnoid hemorrhage, believed to be posttraumatic, as well as a patchy area of acute infarct in the cingulate gyrus (Fig 2D). Among these 7 patients with acute intracranial hemorrhage, 4 hemorrhages were extra-axial, 1 was intra-axial, and 2 were mixed, with 6 being supratentorial and one being both supra- and infratentorial (Fig 1A).

Among these 7 patients with acute hemorrhage, the clinical indication for imaging was syncope/fall in 4 patients and focal neurologic deficit in 3 patients. None of 102 patients who were imaged for altered mental status had acute intracranial hemorrhage.

## DISCUSSION

Patients with COVID-19 may undergo brain imaging for a variety of clinical reasons. In a recently published series by Mao et al<sup>4</sup> from Wuhan, China, 36.4% of patients with COVID-19 were reported to have neurologic manifestations, including 28.2% with altered mental status or acute cerebrovascular disease.<sup>4</sup> We report on 242 of 3661 patients with COVID-19 (6.6%) who underwent brain imaging. The discrepancy between rates likely relates to multiple factors: Mao et al reported all perceived neurologic symptoms including nonspecific symptoms such as headaches or dizziness, whereas here we report neurologic symptoms specifically leading to imaging. In addition, there are likely to be individuals in our overall cohort who were too ill for imaging, though they may have had neurologic manifestations of disease.

While altered mental status was the most common clinical reason for brain imaging, no acute/subacute infarct or acute hemorrhage was identified in any patient imaged for altered mental status alone within the first 2 weeks after positive result of viral testing. On the other hand, the overwhelming majority of patients with imaging findings of acute/subacute infarct had focal neurologic deficits on clinical examination. Similarly, patients with acute hemorrhage had either focal neurologic deficits or a history of syncope or fall. Severe acute respiratory syndrome and hypoxemia that can be seen in COVID-19 can lead to altered mental status. While alteration in mental status warrants a complete clinical neurologic examination, if a trusted clinical examination fails to elicit a focal neurologic deficit and there is no history of syncope or fall, brain imaging may not be particularly revealing, an observation that is concordant with prior studies of brain imaging in acute altered mental status.<sup>9</sup>

Risks and benefits of imaging should certainly be considered in these patients who are highly contagious, with the potential risk of exposure to staff and other patients in the process of transport and imaging. On the other hand, the presence of a focal neurologic deficit, a recent episode of syncope or fall, or lack of a reliable neurologic examination appear to be good reasons to pursue neuroimaging in a neurologically symptomatic patient. We would like to caution the readers about interpreting this observation and applying it to their practice, particularly in view of the excessive use of the term “altered

mental status” as a clinical indication. In fact, the American College of Radiology Appropriateness Criteria support brain imaging for the evaluation of patients with altered mental status in most clinical scenarios. Therefore, we suggest that when the clinical indication for brain imaging of patients with COVID-19 is altered mental status, the radiologist should consider reviewing the electronic health record in more detail or discuss the risks and benefits with the requesting physician in order to ensure that the benefits of such examination outweigh the risks in the setting of a viral outbreak.<sup>10</sup>

The reported prevalence of stroke in the adult population in the United States is 3%.<sup>11</sup> Indeed, hospitalization for acute infection is associated with a transient increase in the risk of vascular events including stroke, with an odds ratio of 8.0 for 14 days preceding the stroke.<sup>12,13</sup> Previous studies have specifically reported acute cerebrovascular disease in COVID-19<sup>6</sup> and cited thromboembolic predisposition<sup>7</sup> and increased blood viscosity secondary to the virus attacking the  $\beta$  chain of hemoglobin and causing hypoxemia.<sup>14</sup> In our study, the overall rate of an acute/subacute infarction or acute hemorrhage is 8.3%. This may well be an under-representation of the true incidence of acute cerebrovascular events in these patients because some may have been too sick or declined too rapidly to warrant imaging.

Among those patients who were imaged, we found that 5.4% had acute/subacute infarcts. This is higher than the 4.2% incidence of stroke among the hospitalized patients with neuroimaging at our institution during March 2019 (personal communication, Dr Eytan Raz, New York University Langone Medical Center, April 19, 2020). The reason for the noted difference is likely multifactorial. In addition to possibly higher rates of infarct among patients with COVID-19 compared with hospitalized patients without COVID-19, this difference could be related to the less sick patients avoiding hospitals or emergency departments during the COVID-19 outbreak and resulting in an overall increased rate of presentation of more advanced stages of disease, or be related to primary teams requesting neuroimaging examinations more selectively during the outbreak in view of the limited resources.

Acute intracranial hemorrhage in patients with COVID-19 may result from fall/syncope<sup>15</sup> or could occur without a preceding mechanical trauma. Previously reported acute hemorrhagic necrotizing encephalopathy following COVID-19<sup>16</sup> was not seen in any of our patients, suggesting a low incidence of such findings.

Higher mortality was seen in patients with white matter microangiopathy compared with those without. This likely relates to a known association of these imaging changes with age and cardiovascular risk factors, which have both been associated with poor prognoses in patients with COVID-19. In the absence of a reliable medical history for these patients, microangiopathic changes can serve as a window to the patient’s long-standing underlying risk factors<sup>17</sup> and can provide potentially prognostic insights.

Limitations of the current study include variability in the imaging modality: CT and MRI findings were studied together and most (85.5%) patients had only CT. The high proportion of CT may result in under-reporting of acute imaging findings because the sensitivity of MRI is known to be higher. In many cases, causal and even temporal relationships between COVID-19 and the patient’s neurologic events are difficult to ascertain; therefore, any



conclusion with potential management implications must be confirmed with future investigations. Future prospective studies would help elucidate and pave the way toward more concrete guidelines. As the City of New York marches toward what we hope to be the downslope of the current outbreak, these data may help radiologists and neurologists across regions that are peaking at a later time and provide potential insight in case of future respiratory viral outbreaks.

Disclosures: Alireza Radmanesh—UNRELATED: Other: retirement accounts, with possible investments in biomedical companies; none would impact the content of this work. Eytan Raz—UNRELATED: Expert Testimony: various law firms; Royalties: Springer; Travel/Accommodations/Meeting Expenses Unrelated to Activities Listed: MicroVenture. Elcin Zan—OTHER RELATIONSHIPS: Consulting Fee or Honorarium, speaker honorarium but nothing relevant to the topic of this article: Advanced Accelerator Applications, a Novartis company.

## REFERENCES

1. Zhou P, Yang XL, Wang XG, et al. **A pneumonia outbreak associated with a new coronavirus of probable bat origin.** *Nature* 2020;579:270–73 CrossRef Medline
2. COVID-19 United States Cases by County. Johns Hopkins University of Medicine. May 10, 2020. <https://coronavirus.jhu.edu/us-map>. Accessed April 25, 2020
3. COVID-19: Data. NYC Health. City of New York. April 24, 2020. <https://www1.nyc.gov/site/doh/covid/covid-19-data.page>. Accessed April 25, 2020
4. Mao L, Jin H, Wang M, et al. **Neurologic manifestations of hospitalized patients with coronavirus disease 2019 in Wuhan, China.** *JAMA Neurol* 2020 Apr 10. [Epub ahead of print] CrossRef Medline
5. Wu Y, Xu X, Chen Z, et al. **Nervous system involvement after infection with COVID-19 and other coronaviruses.** *Brain Behav Immun* 2020 Mar 30. [Epub ahead of print] CrossRef Medline
6. Larson AS, Savastano L, Kadirvel R, et al. **COVID-19 and the Cerebro-Cardiovascular Systems: What do we Know so Far?** *J Am Heart Assoc* 2020:e016793. [Epub ahead of print] CrossRef Medline
7. Lodigiani C, Iapichino G, Carenzo L, et al. **Venous and arterial thromboembolic complications in COVID-19 patients admitted to an academic hospital in Milan, Italy.** *Thromb Res* 2020;191:9–14. [Epub ahead of print] CrossRef Medline
8. Ferguson KJ, Cvorovic V, MacLulich AMJ, et al. **Visual rating scales of white matter hyperintensities and atrophy: comparison of computed tomography and magnetic resonance imaging.** *J Stroke Cerebrovasc Dis* 2018;27:1815–21 CrossRef Medline
9. Shin S, Lee HJ, Shin J, et al. **Predictors of abnormal brain computed tomography findings in patients with acute altered mental status in the emergency department.** *Clin Exp Emerg Med*. 2018;5:1–6 CrossRef Medline
10. Luttrull MD, Boulter DJ, Kirsch CF, et al. **ACR Appropriateness Criteria®: Acute Mental Status Change, Delirium, and New Onset Psychosis.** *J Am Coll Radiol* 2019;16:S26–37 CrossRef Medline
11. Ovbiagele B, Nguyen-Huynh MN. **Stroke epidemiology: advancing our understanding of disease mechanism and therapy.** *Neurotherapeutics* 2011;8:319–29 CrossRef Medline
12. Ortel TL. **Acquired thrombotic risk factors in the critical care setting.** *Crit Care Med* 2010;38:S43–50 CrossRef Medline
13. Elkind MS, Carty CL, O'Meara ES, et al. **Hospitalization for infection and risk of acute ischemic stroke: the Cardiovascular Health Study.** *Stroke* 2011;42:1851–56 CrossRef Medline
14. Liu W, Li H. **COVID-19 attacks the 1-beta chain of hemoglobin and captures the porphyrin to inhibit human heme metabolism.** *ChemRxiv* 2020. [https://ravigollim.com/resources/COVID/COVID-19\\_\\_Attacks\\_the\\_1-Beta\\_Chain\\_of\\_Hemoglobin\\_and\\_Captures\\_the\\_Porphyrin\\_to\\_Inhibit\\_Human\\_Heme\\_Metabolism\\_v5.pdf](https://ravigollim.com/resources/COVID/COVID-19__Attacks_the_1-Beta_Chain_of_Hemoglobin_and_Captures_the_Porphyrin_to_Inhibit_Human_Heme_Metabolism_v5.pdf). Accessed April 21, 2020
15. Tapé C, Byrd KM, Aung S, et al. **COVID-19 in a patient presenting with syncope and a normal chest x-ray.** *R I Med J (2013)* 2020;103:50–51 Medline
16. Poyiadji N, Shahin G, Noujaim D, et al. **COVID-19-associated acute hemorrhagic necrotizing encephalopathy: CT and MRI features.** *Radiology* 2020 Mar 31. [Epub ahead of print] CrossRef Medline
17. van Dijk EJ, Breteler MM, Schmidt R, et al. **The association between blood pressure, hypertension, and cerebral white matter lesions: cardiovascular determinants of dementia study.** *Hypertension* 2004;44:625–30 CrossRef Medline



## COVID-19–Associated Miller Fisher Syndrome: MRI Findings

J.E. Lantos, S.B. Strauss, and E. Lin



## ABSTRACT

**SUMMARY:** Miller Fisher syndrome, also known as Miller Fisher variant of Guillain-Barré syndrome, is an acute peripheral neuropathy that can develop after exposure to various viral, bacterial, and fungal pathogens. It is characterized by a triad of ophthalmoplegia, ataxia, and areflexia. Miller Fisher syndrome has recently been described in the clinical setting of the novel coronavirus disease 2019 (COVID-19) without accompanying imaging. In this case, we report the first presumptive case of COVID-19–associated Miller Fisher syndrome with MR imaging findings.

**ABBREVIATIONS:** CN = cranial nerve; COVID-19 = coronavirus disease 2019; MFS = Miller Fisher syndrome; CNS = central nervous system; PNS = peripheral nervous system

Miller Fisher syndrome (MFS), also known as Miller Fisher variant of Guillain-Barré syndrome, is an acute peripheral neuropathy that can develop after exposure to various viral, bacterial, and fungal pathogens. It is often immune-mediated and associated with anti-GQ1b antibodies, characterized by a triad of ophthalmoplegia, gait ataxia, and areflexia. Ophthalmoplegia is due to involvement of cranial nerves III, IV, or VI. Ataxia is thought to be due to cerebellar involvement, and areflexia is due to lower motor neuron involvement. MFS has recently been described in the clinical setting of the novel coronavirus disease 2019 (COVID-19) without accompanying imaging findings.<sup>1</sup> While patients with COVID-19 typically present with fever, shortness of breath, and cough, neurologic manifestations, including headache, ataxia, cognitive impairment, anosmia, and stroke, have been reported.<sup>2–4</sup> One retrospective review of 214 patients found neurologic symptoms in 36.4% of patients, with involvement of the CNS (24.8%) greater than the peripheral nervous system (8.9%).<sup>4</sup> In this case, we report the first presumptive case of COVID-19–associated Miller Fisher syndrome with imaging.

A 36-year-old man with a remote history of left eye strabismus (asymptomatic for 30 years) was brought to the emergency department by ambulance, presenting with left eye drooping, blurry

vision, and reduced sensation and paresthesia in both legs for 2 days. He was in his usual state of health until 4 days before presentation, when he developed viral symptoms in a COVID-19-endemic region, reporting subjective fevers, chills, and myalgia. Physical examination was notable for a partial left third nerve palsy and decreased sensation below the knees to all modalities. MR imaging of the brain, including high-resolution imaging of the orbits and retro-orbital region, with and without gadolinium, was notable for striking enlargement, prominent enhancement with gadolinium, and T2 hyperintense signal of the left cranial nerve (CN) III (Figure). No other cranial nerves demonstrated abnormal signal or enhancement characteristics. MR imaging of the brain had normal findings. No cerebellar lesions were seen to explain the patient's ataxia. There were no findings of meningitis, encephalitis, demyelination, or infarction. MR imaging of the spine, which may have provided an imaging correlate for the patient's areflexia, was not performed.

The diagnosis of COVID-19 was confirmed by qualitative detection of Severe Acute Respiratory Syndrome coronavirus 2 RNA in a nasopharyngeal swab specimen by real-time reverse transcription polymerase chain reaction amplification and detection using TaqMan fluorescent oligonucleotide probes (Altona Diagnostics) on the Rotor-Gene Q instrument. Serologic ganglioside antibody testing was performed by semi-quantitative enzyme-linked immunosorbent assay (ARUP Laboratories) and showed Asialo GM1 antibody in the equivocal range, while testing for other antibodies, including anti-GQ1b, was negative. Nonetheless, the patient's hospital course was characterized by progressive ophthalmoparesis (including initial left CN III and eventual bilateral CN VI palsies), ataxia, and hyporeflexia, and the clinical picture

Received April 8, 2020; accepted after revision May 2.

From the Department of Radiology, Weill Cornell Medical Center/New York Presbyterian Hospital, New York, New York.

Please address correspondence to Joshua E. Lantos, MD, Department of Radiology, Weill Cornell Medical Center/New York Presbyterian Hospital, 1305 York Ave, 3rd Floor, New York, NY 10021; e-mail: jol9057@med.cornell.edu

Indicates open access to non-subscribers at www.ajnr.org

<http://dx.doi.org/10.3174/ajnr.A6609>

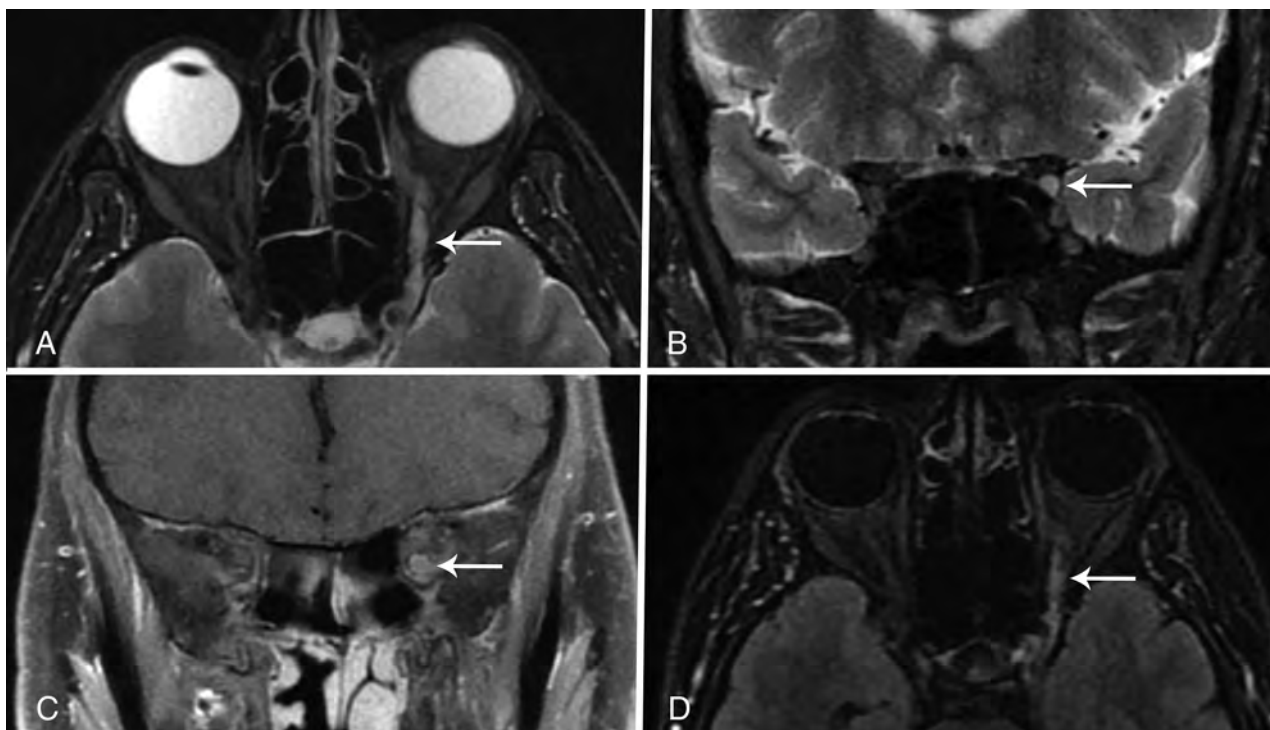


**FIGURE.** Axial and coronal T2-weighted fat-suppressed images through the orbits (A and B) demonstrate an enlarged CN III (arrow) with increased signal involving the nerve from the cavernous sinus through the orbit. Coronal T1-weighted fat-suppressed postcontrast image (C) also shows an enlarged CN III within the proximal orbit (arrow) and demonstrates marked enhancement of the nerve. The abnormal nerve is also visible on a whole-brain T2 FLAIR fat-suppressed postcontrast image (arrow, D).

was thought to be consistent with MFS from COVID-19 infection. The patient was treated with intravenous immunoglobulin, with subsequent improvement of neurologic symptoms. The patient also received hydroxychloroquine to treat the underlying COVID-19 infection. No repeat MR imaging was performed, and the patient was discharged after 4 days of hospitalization.

MFS accounts for 1%–5% of cases of Guillain-Barré syndrome in Western countries, affects men twice as often as women, and is preceded by an upper respiratory illness in most patients.<sup>5</sup> MFS presents commonly with diplopia (78%), ataxia (48%), or both (34%).<sup>6</sup> Our patient presented with symptoms of COVID-19 as well as diplopia, which was found to be due to a CN III palsy noted on the patient's clinical examination. MR imaging demonstrated corresponding enlargement, T2 hyperintensity, and enhancement of the affected CN III from the cavernous sinus through the orbit. This is the first presumptive case report of MFS associated with COVID-19 infection with imaging findings.

Although testing was negative for anti-GQ1b, the clinical picture was consistent with MFS, and the patient improved with treatment. Negative ganglioside antibody testing is a limitation of this report; however, a review of 123 patients with MFS found that 15% were negative for anti-GQ1b.<sup>7</sup> The GQ1b ganglioside is a cell surface component that is concentrated in the paranodal regions, cranial nerves III, IV, and VI. Anti-GQ1b antibodies have been shown to bind to fractions of *Campylobacter jejuni* and *Haemophilus influenzae* and are thought to cause the symptoms of MFS through molecular mimicry.<sup>8</sup>

When antibody testing is negative in patients with MFS, symptoms may be due to viral neurotropism rather than immune-mediated injury.<sup>9</sup> The functional receptor for COVID-19 is angiotensin-converting enzyme 2 and is present in neural tissue.<sup>4</sup> Access to the CNS may be either hematogenous or via retrograde neural propagation along bipolar cells. Retrograde propagation along the olfactory pathway may account for the occurrence of anosmia in some patients with COVID-19.<sup>4</sup> It has been proposed that retrograde propagation could lead to brain stem involvement and contribute to respiratory symptoms by affecting the nuclei that regulate respiratory rhythm such as chemoreceptors that detect changes in oxygen and CO<sub>2</sub>.<sup>10</sup> Understanding of COVID-19 pathophysiology in the CNS and peripheral nervous system and its contribution to morbidity and mortality is still in its infancy. Whether MFS is the result of immune-mediated injury or viral neurotropism, this potential complication should be recognized by clinicians and radiologists so that appropriate treatment can be offered to these symptomatic patients.

## REFERENCES

1. Gutierrez-Ortiz C, Mendez A, Rodrigo-Rey S, et al. **Miller Fisher syndrome and polyneuritis cranialis in COVID-19.** *Neurology* 2020 Apr 17. [Epub ahead of print] CrossRef Medline
2. Filatov A, Sharma P, Hindi F, et al. **Neurological complications of coronavirus (COVID19): encephalopathy.** *Cureus* 2020;12:e7352 CrossRef
3. Poyiadji N, Shahin G, Noujaim D, et al. **COVID-19-associated acute hemorrhagic necrotizing encephalopathy: CT and MRI features.** *Radiology* 2020 Mar 31. [Epub ahead of print] CrossRef Medline

4. Mao L, Jin H, Wang M, et al. **Neurologic manifestations of hospitalized patients with coronavirus disease 2019 in Wuhan, China.** *JAMA Neurol* 2020 Apr 10. [Epub ahead of print] CrossRef Medline
5. Bukhari S, Taboada J. **A case of Miller Fisher syndrome and literature review.** *Cureus* 2017;9:e1048 CrossRef
6. Mori M, Kuwabara S, Fukutake T, et al. **Clinical features and prognosis of Miller Fisher syndrome.** *Neurology* 2001;56:1104–06 CrossRef Medline
7. Nishimoto Y, Odaka M, Hirata K, et al. **Usefulness of anti-GQ1b IgG antibody testing in Fisher syndrome compared with cerebrospinal fluid examination.** *J Neuroimmunol* 2004;148:200–05 CrossRef Medline
8. Snyder LA, Rismondo V, Miller NR. **The Fisher variant of Guillain-Barre syndrome (Fisher syndrome).** *J Neuroophthalmol* 2009;29:312–24 CrossRef Medline
9. de Silva NL, Weeratunga P, Umapathi T, et al. **Miller Fisher syndrome developing as a parainfectious manifestation of dengue fever: a case report and review of the literature.** *J Med Case Rep* 2019;13:120 CrossRef Medline
10. Conde Cardona G, Quintana Pájaro LD, Quintero Marzola ID, et al. **Neurotropism of SARS-CoV 2: mechanisms and manifestations.** *J Neurol Sci* 2020;412:116824 CrossRef Medline

# Ventricular Volume Is More Strongly Associated with Clinical Improvement Than the Evans Index after Shunting in Idiopathic Normal Pressure Hydrocephalus

J. Neikter, S. Agerskov, P. Hellström, M. Tullberg, G. Starck, D. Ziegelitz, and D. Farahmand

## ABSTRACT

**BACKGROUND AND PURPOSE:** Ventricular enlargement in idiopathic normal pressure hydrocephalus is often estimated using the Evans index. However, the sensitivity of the Evans index to estimate changes in ventricular size postoperatively has been questioned. Here, we evaluated the postoperative change in ventricle size in relation to shunt response in patients with idiopathic normal pressure hydrocephalus, by comparing ventricular volume and the Evans index.

**MATERIALS AND METHODS:** Fifty-seven patients with idiopathic normal pressure hydrocephalus underwent high-resolution MR imaging preoperatively and 6 months after shunt insertion. Clinical symptoms of gait, balance, cognition, and continence were assessed according to the idiopathic normal pressure hydrocephalus scale. The ventricular volume of the lateral and third ventricles and the Evans index were measured using ITK-SNAP software. Semiautomatic volumetric analysis was performed, and postoperative changes in ventricular volume and the Evans index and their relationships to postoperative clinical improvement were compared.

**RESULTS:** The median postoperative ventricular volume decrease was 25 mL ( $P < .001$ ). The proportional decrease in ventricular volume was greater than that in the Evans index ( $P < .001$ ). The postoperative decrease in ventricular volume was associated with a postoperative increase in the idiopathic normal pressure hydrocephalus scale score ( $P = .004$ ). Shunt responders (75%) demonstrated a greater ventricular volume decrease than nonresponders ( $P = .002$ ).

**CONCLUSIONS:** Clinical improvement after shunt surgery in idiopathic normal pressure hydrocephalus is associated with a reduction of ventricular size. Ventricular volume is a more sensitive estimate than the Evans index and, therefore, constitutes a more precise method to evaluate change in ventricle size after shunt treatment in idiopathic normal pressure hydrocephalus.

**ABBREVIATIONS:** EI = Evans index; iNPH = idiopathic normal pressure hydrocephalus; VV = ventricular volume

Idiopathic normal pressure hydrocephalus (iNPH) is characterized by progressive gait and balance disturbance, cognitive impairment, and urinary incontinence.<sup>1–3</sup> Because iNPH is considered one of the few potentially treatable causes of dementia, its early diagnosis is imperative. Treatment primarily consists of shunt surgery, demonstrating high clinical improvement rates of 71%–84%.<sup>2–7</sup>

Ventriculomegaly on CT or MR imaging is mandatory to correctly diagnose iNPH.<sup>1,3,8</sup> In 1942, during the era of

pneumoencephalography, a method for the assessment of ventricular enlargement, in which the maximum transverse diameter of the frontal horns was divided by the greatest internal transverse diameter of the skull on coronal images, was introduced by W.A. Evans.<sup>9</sup> Since the subsequent development of CT and MR imaging, the Evans index (EI) is calculated on an axial section as the ratio between the maximum width of the frontal horns and the maximal internal diameter of the skull.<sup>10,11</sup>

A calculation of the EI is generally used in the diagnostic work-up of iNPH, and according to international guidelines, a ratio of  $>0.3$  constitutes a prerequisite for a diagnosis of probable iNPH.<sup>3</sup> However, because the width of the frontal horns provides little information about the shape of the ventricular system at large, the index provides just a crude estimate of the actual size of the ventricles. Accordingly, authors have argued that the EI is not an ideal method to estimate ventricular volume (VV) in iNPH.<sup>11</sup>

Received July 18, 2019; accepted after revision April 27, 2020.

From the Department of Clinical Neuroscience (J.N., S.A., P.H., M.T., D.F.), Institute of Neuroscience and Physiology, Hydrocephalus Research Unit, and Departments of Radiation Physics (G.S.), and Neuroradiology (D.Z.), Institute of Clinical Sciences, Sahlgrenska Academy, University of Gothenburg, Sahlgrenska University Hospital, Gothenburg, Sweden.

Please address correspondence to Dan Farahmand, MD, PhD, Department of Neurosurgery, Blå stråket 5, van 3, Sahlgrenska University Hospital, 413 45 Gothenburg, Sweden; e-mail: dan.farahmand@vgregion.se

<http://dx.doi.org/10.3174/ajnr.A6620>



Furthermore, decreases in EI have been shown to be poorly correlated with clinical improvement after shunt surgery,<sup>12,13</sup> whereas recent studies evaluating ventricular size by means of volumetric measurements have shown mean postoperative decreases of VV of 24%–28% in patients with improved iNPH, suggesting that such measurements may constitute more clinically relevant markers.<sup>14–17</sup>

Currently, there are no large-scale studies comparing postoperative changes in VV and the EI in patients with iNPH. Here, we evaluated postoperative changes in VV and the EI and investigated their relation to clinical outcome.

## MATERIALS AND METHODS

Sixty-six patients diagnosed with probable or possible iNPH<sup>3</sup> were consecutively included at the Hydrocephalus Research Unit, Sahlgrenska University Hospital, between 2013 and 2015. All patients received a ventriculoperitoneal ( $n = 63$ ) or ventriculoatrial ( $n = 3$ ) shunt (PS Medical Strata Adjustable Valve; Medtronic) with the opening pressure set at a medium level (setting 1.5). The ventricular catheters were placed frontally with the tip of the ventricular catheter inside the lateral ventricle.

Clinical assessments and MR imaging examinations were performed preoperatively and after 6 months in all patients. Two patients demonstrated shunt obstructions before the postoperative examinations. These 2 patients underwent shunt revision and were included in the study, with clinical assessment and MR imaging performed 6 months after the shunt revision. One patient was excluded due to a delay in follow-up after undergoing shunt revision. One patient presented with a subdural hematoma on postoperative MR imaging and was excluded. Seven patients demonstrated motion artifacts on preoperative ( $n = 4$ ) or postoperative ( $n = 3$ ) MR imaging and were excluded from the study. Characteristics of the remaining 57 patients are given in Table 1.

### Clinical Assessment

The patients were clinically evaluated before and 6 months after shunt insertion according to the iNPH scale,<sup>18</sup> comprising 4 symptom domains (gait, balance, neuropsychology, and continence) and yielding a total score (iNPH scale score) ranging between 0 and 100, with 100 representing normal performance among healthy individuals in an iNPH typical age range of 70–74 years. In cases without clear postoperative improvement, shunt dysfunction was ruled out using a head CT and radionuclide shuntography<sup>19</sup> or a lumbar infusion test.<sup>20</sup> Responders were defined as patients demonstrating a postoperative increase in the iNPH scale score of  $\geq 5$  points.<sup>18</sup>

### MR Imaging Volumetry and the Evans Index

Identical MR imaging scans with T1-weighted volume sequences with 1-mm scan resolution, from a 1.5T Intera (Philips Healthcare) or a 1.5T Achieva dStream (Philips Healthcare) scanner, were obtained at baseline and at the 6-month postoperative follow-up. Scan parameters were as follows: FOV =  $260 \times 260 \times 190$  mm<sup>3</sup>, TR = 25 ms, TE = 4.6 ms, and flip angle = 30°. The scan was reconstructed to a 0.5-mm image resolution. The MR imaging datasets of all images were transmitted in DICOM

**Table 1: Demographic data of the patients in the study ( $n = 57$ )**

Demographics	
Age (mean) (range) (yr)	74 $\pm$ 7 (49–91)
Sex (male/female)	42:15
Preoperative iNPH score (mean) (SD)	54 (20)
Postoperative iNPH score (mean) (SD)	66 (22)
Months from surgery to postoperative follow-up (mean) (range)	6 $\pm$ 1.6 (3–9)

format from the MR imaging storage unit to a personal computer. All image analyses were performed by J.N. and D.Z., who were blinded to clinical data.

The pre- and postoperative volumes of the third and the lateral ventricles were semiautomatically measured using the ITK-SNAP software (Version 3.6.0; www.itksnap.org).<sup>21</sup> Comparable images with clearly visualized ventricles and a histogram function of the image contrast were acquired using the Image Layer Inspector, Contrast Adjustment.<sup>21</sup> Mean image intensity was  $1368.9 \pm 239.4$  (arbitrary units). The volumetric measurement was performed automatically and was modified manually. The Thresholding Segmentation mode<sup>21</sup> was used for automatic segmentation, whereas the Paintbrush Mode and Polygon Mode<sup>21</sup> were used for manual modifications. The segmented volume was presented in voxels and in cubic millimeters. The voxel size was  $0.5 \times 0.5 \times 0.5$  mm in all examinations. The ventricular volume was the product of the number of voxels in each segmentation and the voxel volume (0.125 mm<sup>3</sup>).

The EI was measured using the Image Annotation Mode in ITK-SNAP<sup>21</sup> on axial MR imaging slices (aligned to the anterior and posterior commissures) and defined as the maximum width of the frontal horns anterior to the foramina of Monro divided by the maximum width of the inner skull, both measured on the same section.

### Statistics

Responders and nonresponders were compared with regard to postoperative decreases in ventricular volume and changes in the EI by means of the Mann-Whitney *U* test. Furthermore, the decreases in ventricular volume and the EI within the groups of responders and nonresponders, respectively, were tested using the Wilcoxon signed rank test. Correlations between preoperative and postoperative VVs and changes in the iNPH scale score were analyzed using the Spearman rank correlation test.

We evaluated the correlation between postoperative change in the iNPH scale score and postoperative decreases in ventricular volume and the EI, respectively, using regression models, assuming approximate normal distributions and adjusting for heteroscedasticity. We examined nonlinear effects for linear, piecewise linear, quadratic, and cubic functions of the explanatory variables. The best correlation was selected on the basis of the highest adjusted  $R^2$ . The effects per a 1-SD decrease were also calculated to compare the effects of the 2 explanatory variables. The 2 measurements were adjusted for each other in a multivariable model.

All tests were 2-tailed, and  $\alpha$  was set to  $<.05$ . All analyses were performed using SAS software, Version 9.4 (SAS Institute).

## Ethics Considerations

The study was approved by the local ethics committee in Gothenburg, D-number 328–14. All patient data were de-identified at the time of data analysis and presentation.

## RESULTS

The median postoperative VV decrease was 24 mL (p25 = 16 mL, p75 = 34 mL;  $P < .001$ ), equivalent to 18%, and the median postoperative decrease in the EI was 0.02 (interquartile range, 0.02;  $P < .001$ ) or 5%. The proportional decrease in VV was significantly larger ( $P < .001$ ) than the proportional decrease in the EI (Fig 1). Forty responders (93%) showed a >5% decrease in VV. Pre- and postoperative VVs correlated to a change in the iNPH scale score are presented in Table 2. Postoperative VV showed a weak-but-significant correlation with change in the iNPH scale score ( $r = -0.28$ ,  $P = .036$ ). Pre-

or postoperative decreases in VVs were not significantly correlated with either pre- or postoperative iNPH scale scores or a change in the iNPH scale scores.

Forty-three patients (75%) were shunt responders. A postoperative decrease in VV was significantly ( $P = .003$ ) larger in shunt responders (21%,  $n = 43$ ) than among nonresponders (13%,  $n = 14$ ). A postoperative decrease in VV was significantly correlated with the 4 symptom domains: gait and balance disturbance ( $P = .002$ ), neuropsychology ( $P = .010$ ), and continence ( $P = .012$ ). There was no correlation between postoperative change in the EI and each of these 3 symptom domains.

A postoperative decrease in VV and an increase in the iNPH scale score were significantly correlated; the iNPH scale increased by 16.4 (standard error, 4.6;  $P = .004$ ) per 1-SD decrease in VV within the interval of 20–40 mL, compared with the relation of VV decrease of <20 and >40 mL (mean,  $-0.64$ ; standard error, 5.4; and mean,  $-0.62$ ; standard error, 2.9), respectively (Fig 2). The adjusted  $R^2$  was 0.22 for the amount of explained variance in the model ( $P < .001$ ).

A postoperative EI decrease showed a significant linear relation to the increased iNPH scale score, with a mean increase of 7.6 (standard error, 1.7;  $P < .001$ ) per 1-SD decrease in the EI (Fig 3). The adjusted  $R^2$  was 0.08 for the amount of explained variance in the model ( $P = .040$ ).

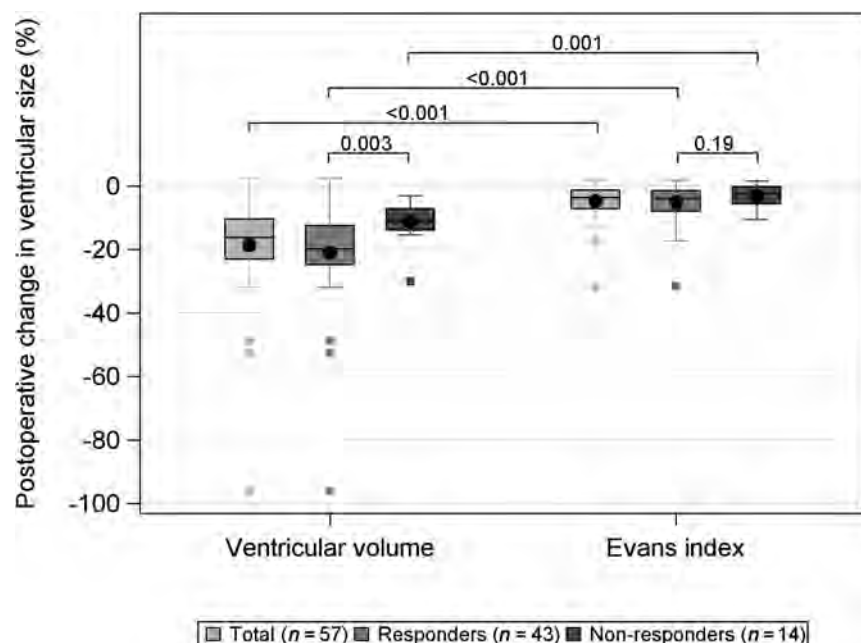


**FIG 1.** Box-and-whisker plot showing the change in ventricular size measured by VV and the EI after shunt treatment in 57 patients with iNPH. The *whiskers* denote values within the 1.5 interquartile range from the first and third quartiles, and the *boxes* represent outliers. The  $P$  values for the difference between responders (gray) and nonresponders (dark gray) are presented as well as the total (light gray). VV decreased significantly more than the EI for all groups. Responders had a significantly larger VV decrease than nonresponders. There was no difference in the EI between responders and nonresponders.

## DISCUSSION

The median postoperative decrease in VV (25 mL) in shunted patients with iNPH was similar to that found in previous studies.<sup>14–16</sup> The proportional postoperative decrease in ventricle size was >3 times greater when measuring VV (18%) compared with the EI (5%). Furthermore, the decrease in VV in the interval of 20–40 mL and the increase in the iNPH scale score were more strongly correlated than the decrease in the EI and the increase in the iNPH scale score; the mean increase in the iNPH scale score was 16.4 per 1-SD decrease in VV compared with 7.6 per 1-SD decrease in the EI.

**Table 2: Preoperative VV and postoperative absolute and relative decreases in VV among 57 patients operated on for iNPH**

	Median (Minimum, p25, p75, Maximum)	VV vs iNPH Scale Score <sup>a</sup>
Preoperative VV (mL)	141.4 (70.8, 133.4, 167.9, 317.8)	$r = -0.08$ $P = .59$
Postoperative VV (mL)	120.8 (4.1, 103.7, 137.9, 309.0)	$r = -0.28$ $P = .036$
Postoperative absolute decrease in VV (mL)	24.1 (–4.0, 15.9, 34.2, 100.1)	$r = 0.54$ $P < .001$
Postoperative relative decrease in VV (%)	16.3 (–2.1, 10.5, 23.1, 96.1)	$r = 0.56$ $P < .001$

<sup>a</sup> Spearman rank correlation test between VV and postoperative change in the iNPH scale score.

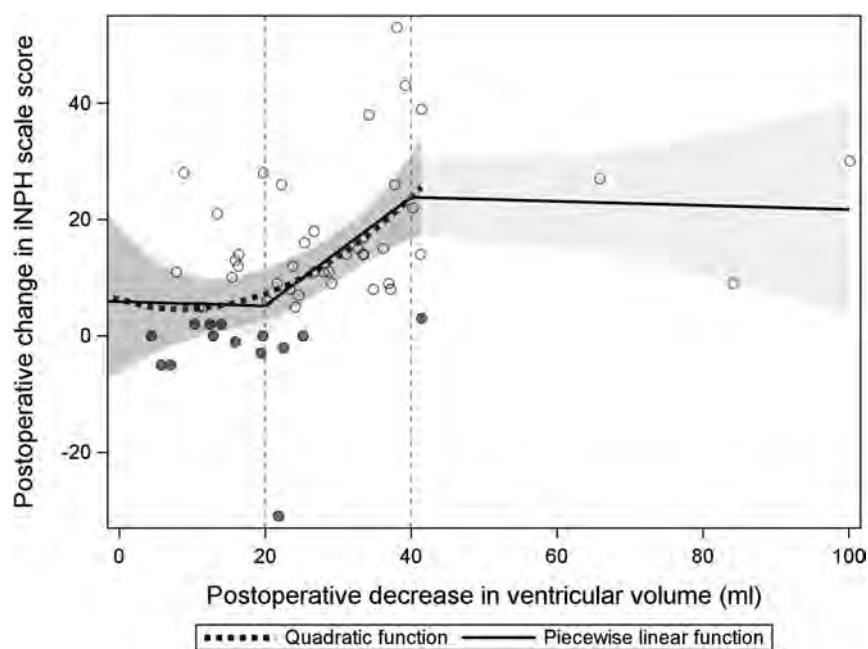


**FIG 2.** Scatterplot illustrating the relation between a postoperative decrease in ventricular volume and shunt response (INPH scale score) in the participants. Trend lines for a quadratic and piecewise linear function are shown. The shadowed gray areas represent the 95% confidence intervals for the quadratic function, and the bright gray area represents the same interval for the linear function.

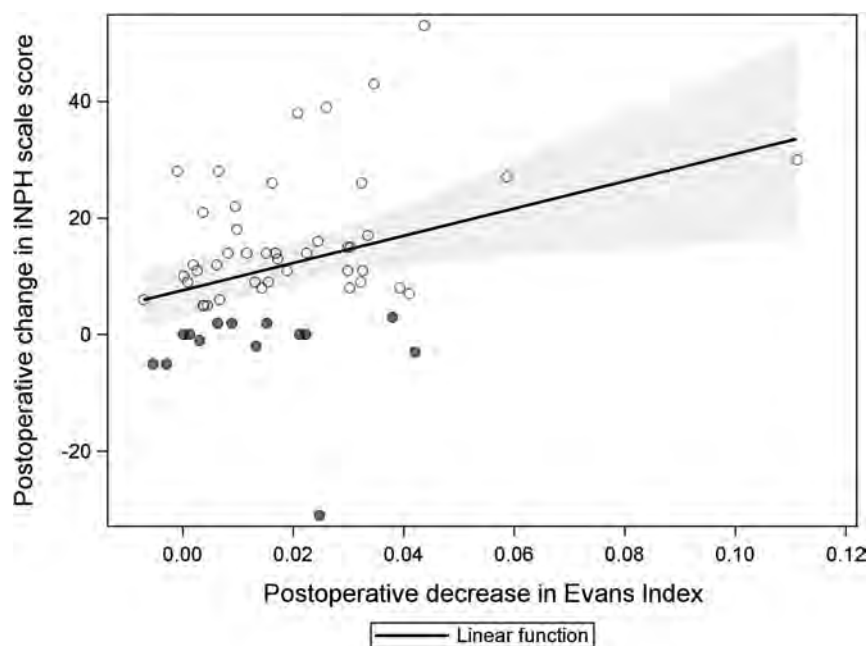


**FIG 3.** Scatterplot illustrating the linear relation between postoperative decrease in the EI and shunt response (INPH scale score). The shadowed area represents the 95% confidence intervals for the linear function.

The present study showed a stronger association between a decrease in VV and clinical improvement than the EI, which may indicate that increased VV may be better associated with symptoms of iNPH than the EI. Recently, Crook et al<sup>22</sup> found that volumetric measures of ventricle size were more strongly associated with gait and cognition than the EI. Future studies

on patients with iNPH correlating the different symptom domains to ventricular volume would be of great interest.

Most important, we observed that the postoperative changes in ventricle size using volumetric assessment were significantly greater in shunt responders compared with nonresponders. Using the EI for the same task did not result in a significant difference between the groups.

This finding shows that response to shunting is more closely related to changes in VV than in the EI and implies that assessment of VV could be a valuable supplementary tool in the clinical evaluation of shunt response.

We observed that a 20- to 40-mL decrease in VV was related to a significant clinical improvement, whereas neither smaller (<20 mL) nor larger VV decreases (>40 mL) were correlated with a response to shunting. That insufficient CSF drainage is associated with a lack of shunt response seems reasonable and corroborates previous studies showing that decreased shunt valve opening pressures (intended to increase the CSF drainage and potentially further decrease VV) were associated with an improved shunt response.<sup>7,23,24</sup> On the other hand, other studies have demonstrated that low shunt valve opening pressures were not more effective than higher opening pressures.<sup>7,23</sup> Differences in brain elasticity or CSF dynamic disturbance (eg, resistance to CSF outflow), factors not accounted for in this study, may explain differences in the postoperative reduction of VV among patients reported here.<sup>25</sup>

The improvement rate after shunt treatment of patients with iNPH in this study (75%) is consistent with that in previous studies.<sup>6,26,27</sup>

A limitation in this study is that only patients without a clear postoperative improvement underwent

invasive evaluation for shunt patency, while in the remainder, significant improvement was regarded as proof of a working shunt. Because both shuntography and a lumbar infusion test are invasive procedures, we only performed these tests in cases in which shunt patency was doubted. Future studies in which shunt patency is systematically



**FIG 4.** Ventricule volume segmentation in the ITK-SNAP software showing how susceptibility artifacts from the shunt valve appeared on the postoperative MR imaging.

determined would be valuable in evaluating shunt patency using VV measurements.

### Methodologic Aspects

Previously, studies demonstrated good interrater agreement using ITK-SNAP for volumetric measurements.<sup>21,28–30</sup> Here, using a Thresholding Segmentation Algorithm in ITK-SNAP<sup>21</sup> for all measurements, we standardized the data to facilitate comparison. The Thresholding Segmentation Algorithm in ITK-SNAP was able to automatically expand from a selected region to wide parts of the ventricles, but for the narrow parts of the ventricles, the CSF voxels had to be corrected manually. Similarly, manual corrections were required in areas where the borders were only thin membranes or were partly blurred due to minor head motion, because the segmentation function did not always respect the ventricular borders. These corrections have involved a degree of partial volume effect.<sup>31</sup> We believe that partial volume effect, at ventricular borders, does not seriously affect the volumetric measurements in patients with iNPH because the ventricles occupy a relatively large proportion of the measured region. We therefore consider the volumetric measurements using ITK-SNAP accurate and reliable, albeit time-consuming because of the need for manual corrections.

Susceptibility artifacts from metal components of the shunt valve can potentially reach into the lateral ventricle ipsilateral to the site of shunt placement and disturb the VV measurement on the postoperative MR imaging scans. We observed these susceptibility artifacts present in 3 patients, but in all of these patients, the contour of the wall of the lateral ventricle was clearly visible. Figure 4 shows postoperative MR imaging in 1 patient, in which susceptibility artifacts from the shunt valve extended into the right lateral ventricle without affecting the contour of the wall of the lateral ventricle. Therefore, we believe that the susceptibility artifacts did not affect the volumetric measurements in the present study. However, we found the presence of the susceptibility artifacts on postoperative MR imaging scans to be a limiting factor for measurement of total

intracranial volumes; therefore, this measure was not assessed in this study.

There are various methods to determine volumes of brain structures. Voxel-based volume measurement uses voxel intensity to identify the desired brain structure on MR imaging. Atlas-based volumetric analysis uses a reference atlas.<sup>32</sup> Currently, there are no volumetric reference atlases for iNPH; therefore, the use of an intensity-based method seems appropriate to evaluate VV in patients with iNPH. Previously, Ambarki et al<sup>33</sup> used the SyntheticMR software (<https://syntheticmr.com/company/>) to measure intracranial volume and found it fast (<3 minutes) and reproducible. Qiu et al<sup>34</sup> have tested ventricular volu-

metric measurement using different segmentation algorithms, including algorithms used in ITK-SNAP. The development of accurate, fast, and easy-to-use volumetric segmentation software is important for further studies in evaluating the standardized use of volumetry in patients with iNPH.

### CONCLUSIONS

Clinical improvement after shunt surgery in iNPH is associated with a reduction in VV; shunt responders showed a greater decrease in VV than nonresponders. Furthermore, the proportional decrease in VV was significantly greater than that in the EI, showing that volumetric measurement is a more sensitive method to evaluate change in ventricular size after shunting in iNPH.

### ACKNOWLEDGMENTS

We thank Aldina Pivodic at Statistiska Konsultgruppen for statistical support.

Disclosures: Johanna Neikter—**RELATED:** Grant: Göteborgs Läkaresällskap. Mats Tullberg—**UNRELATED:** Employment: Neuroscience and Physiology, Sahlgrenska Academy, University of Gothenburg.

### REFERENCES

1. Marmarou A, Black P, Bergsneider M, et al; International NPH Consultant Group. **Guidelines for management of idiopathic normal pressure hydrocephalus: progress to date.** *Acta Neurochir Suppl* 2005;95: 237–40 CrossRef Medline
2. Ishikawa M, Hashimoto M, Kuwana N, et al. **Guidelines for management of idiopathic normal pressure hydrocephalus.** *Neurol Med Chir (Tokyo)* 2008;48(Suppl):S1–23 CrossRef Medline
3. Relkin N, Marmarou A, Klinge P, et al. **Diagnosing idiopathic normal-pressure hydrocephalus.** *Neurosurgery* 2005;57(Suppl):S4–16; discussion ii–v CrossRef Medline
4. Marmarou A, Bergsneider M, Klinge P, et al. **The value of supplemental prognostic tests for the preoperative assessment of idiopathic normal-pressure hydrocephalus.** *Neurosurgery* 2005;57 (Suppl 3):S2–17 CrossRef



5. Bergsneider M, Black PM, Klinge P, et al. **Surgical management of idiopathic normal-pressure hydrocephalus.** *Neurosurgery* 2005; 57(Suppl):S29–39; discussion ii–v CrossRef Medline
6. Toma AK, Papadopoulos MC, Stapleton S, et al. **Systematic review of the outcome of shunt surgery in idiopathic normal-pressure hydrocephalus.** *Acta Neurochir (Wien)* 2013;155:1977–80 CrossRef Medline
7. Farahmand D, Sæhle T, Eide PK, et al. **A double-blind randomized trial on the clinical effect of different shunt valve settings in idiopathic normal pressure hydrocephalus.** *J Neurosurg* 2016;124:359–67 CrossRef Medline
8. Farahmand D, Qvarlander S, Malm J, et al. **Intracranial pressure in hydrocephalus: impact of shunt adjustments and body positions.** *J Neurol Neurosurg Psychiatry* 2015;86:222–28 CrossRef Medline
9. Evans WA. **An encephalographic ratio for estimating ventricular enlargement and cerebral atrophy.** *Archives of Neurology and Psychiatry* 1942;47:931 CrossRef
10. Synek V, Reuben JR, Du Boulay GH. **Comparing Evans' index and computerized axial tomography in assessing relationship of ventricular size to brain size.** *Neurology* 1976;26:231–33 CrossRef Medline
11. Toma AK, Holl E, Kitchen ND, et al. **Evans' index revisited: the need for an alternative in normal pressure hydrocephalus.** *Neurosurgery* 2011;68:939–44 CrossRef Medline
12. Meier U, Paris S, Gräwe A, et al. **Is there a correlation between operative results and change in ventricular volume after shunt placement? A study of 60 cases of idiopathic normal-pressure hydrocephalus.** *Neuroradiology* 2003;45:377–80 CrossRef Medline
13. Meier U, Mutze S. **Correlation between decreased ventricular size and positive clinical outcome following shunt placement in patients with normal-pressure hydrocephalus.** *J Neurosurg* 2004;100:1036–40 CrossRef Medline
14. Hiraoka K, Yamasaki H, Takagi M, et al. **Changes in the volumes of the brain and cerebrospinal fluid spaces after shunt surgery in idiopathic normal-pressure hydrocephalus.** *J Neurol Sci* 2010;296:7–12 CrossRef Medline
15. Tsunoda A, Mitsuoka H, Bandai H, et al. **Intracranial cerebrospinal fluid distribution and its postoperative changes in normal pressure hydrocephalus.** *Acta Neurochir (Wien)* 2001;143:493–99 CrossRef Medline
16. Anderson RC, Grant JJ, de la Paz R, et al. **Volumetric measurements in the detection of reduced ventricular volume in patients with normal-pressure hydrocephalus whose clinical condition improved after ventriculoperitoneal shunt placement.** *J Neurosurg* 2002;97:73–79 CrossRef Medline
17. Virhammar J, Laurell K, Cesarini KG, et al. **Increase in callosal angle and decrease in ventricular volume after shunt surgery in patients with idiopathic normal pressure hydrocephalus.** *J Neurosurg* 2018;130:130–35 CrossRef Medline
18. Hellstrom P, Klinge P, Tans J, et al. **A new scale for assessment of severity and outcome in iNPH.** *Acta Neurol Scand* 2012;126:229–37 CrossRef Medline
19. Wikkelsö C, Andersson H, Lindberg S, et al. **'Shuntography': a radio-nuclide scanning method for evaluation of cerebrospinal fluid shunt patency.** *Nucl Med Commun* 1983;4:88–93
20. Malm J, Lundkvist B, Eklund A, et al. **CSF outflow resistance as predictor of shunt function. a long-term study.** *Acta Neurol Scand* 2004;110:154–60 CrossRef Medline
21. Yushkevich PA, Piven J, Hazlett HC, et al. **User-guided 3D active contour segmentation of anatomical structures: significantly improved efficiency and reliability.** *Neuroimage* 2006;31:1116–28 CrossRef Medline
22. Crook JE, Gunter JL, Ball CT, et al. **Linear vs volume measures of ventricle size: relation to present and future gait and cognition.** *Neurology* 2020;94:e549–56 CrossRef Medline
23. Delwel EJ, de Jong DA, Dammers R, et al. **A randomised trial of high and low pressure level settings on an adjustable ventriculoperitoneal shunt valve for idiopathic normal pressure hydrocephalus: results of the Dutch Evaluation Programme Strata Shunt (DEPSS) trial.** *J Neurol Neurosurg Psychiatry* 2013;84:813–17 CrossRef Medline
24. Boon AJ, Tans JT, Delwel EJ, et al. **Dutch normal pressure hydrocephalus study: baseline characteristics with emphasis on clinical findings.** *Eur J Neurol* 1997;4:39–47 CrossRef Medline
25. Tans JT, Poortvliet DC. **Reduction of ventricular size after shunting for normal pressure hydrocephalus related to CSF dynamics before shunting.** *J Neurol Neurosurg Psychiatry* 1988;51:521–25 CrossRef Medline
26. Klinge P, Hellström P, Tans J, et al; On behalf of the European iNPH Multicentre Study Group. **One-year outcome in the European multicentre study on iNPH.** *Acta Neurol Scand* 2012;126:145–53 CrossRef Medline
27. Kahlon B, Sjunnesson J, Rehnöron S. **Long-term outcome in patients with suspected normal pressure hydrocephalus.** *Neurosurgery* 2007;60:327–32 CrossRef
28. Lindberg K, Kouti A, Ziegelitz D, et al. **Three-dimensional volumetric segmentation of pituitary tumors: assessment of inter-rater agreement and comparison with conventional geometric equations.** *J Neurol Surg B Skull B* 2018;79:475–81 CrossRef Medline
29. John JP, Wang L, Moffitt AJ, et al. **Inter-rater reliability of manual segmentation of the superior, inferior and middle frontal gyri.** *Psychiatry Res* 2006;148:151–63 CrossRef Medline
30. Akudjedu TN, Nabulsi L, Makelyte M, et al. **A comparative study of segmentation techniques for the quantification of brain subcortical volume.** *Brain Imaging Behav* 2018;12:1678–95 CrossRef Medline
31. Tohka J. **Partial volume effect modeling for segmentation and tissue classification of brain magnetic resonance images: a review.** *World J Radiol* 2014;6:855–64 CrossRef Medline
32. Despotovic I, Goossens B, Philips W. **MRI segmentation of the human brain: challenges, methods, and applications.** *Comput Math Methods Med* 2015;2015:450341 CrossRef Medline
33. Ambarki K, Lindqvist T, Wåhlin A, et al. **Evaluation of automatic measurement of the intracranial volume based on quantitative MR imaging.** *AJNR Am J Neuroradiol* 2012;33:1951–56 CrossRef Medline
34. Qiu W, Yuan J, Rajchl M, et al. **3D MR ventricle segmentation in pre-term infants with post-hemorrhagic ventricle dilatation (PHVD) using multi-phase geodesic level-sets.** *Neuroimage* 2015;118:13–25 CrossRef Medline

# Distinguishing Extravascular from Intravascular Ferumoxytol Pools within the Brain: Proof of Concept in Patients with Treated Glioblastoma

R.F. Barajas, Jr, D. Schwartz, H.L. McConnell, C.N. Kersch, X. Li, B.E. Hamilton, J. Starkey, D.R. Pettersson, J.P. Nickerson, J.M. Pollock, R.F. Fu, A. Horvath, L. Szidonya, C.G. Varallyay, J.J. Jaboin, A.M. Raslan, A. Dogan, J.S. Cetas, J. Ciporen, S.J. Han, P. Ambady, L.L. Muldoon, R. Woltjer, W.D. Rooney, and E.A. Neuwelt



## ABSTRACT

**BACKGROUND AND PURPOSE:** Glioblastoma-associated macrophages are a major constituent of the immune response to therapy and are known to engulf the iron-based MR imaging contrast agent, ferumoxytol. Current ferumoxytol MR imaging techniques for localizing macrophages are confounded by contaminating intravascular signal. The aim of this study was to assess the utility of a newly developed MR imaging technique, segregation and extravascular localization of ferumoxytol imaging, for differentiating extravascular-from-intravascular ferumoxytol contrast signal at a delayed 24-hour imaging time point.

**MATERIALS AND METHODS:** Twenty-three patients with suspected post-chemoradiotherapy glioblastoma progression underwent ferumoxytol-enhanced SWI. Segregation and extravascular localization of ferumoxytol imaging maps were generated as the voxel-wise difference of the delayed (24 hours) from the early (immediately after administration) time point SWI maps. Continuous segregation and extravascular localization of ferumoxytol imaging map values were separated into positive and negative components. Image-guided biologic correlation was performed.

**RESULTS:** Negative segregation and extravascular localization of ferumoxytol imaging values correlated with early and delayed time point SWI values, demonstrating that intravascular signal detected in the early time point persists into the delayed time point. Positive segregation and extravascular localization of ferumoxytol imaging values correlated only with delayed time point SWI values, suggesting successful detection of the newly developed extravascular signal.

**CONCLUSIONS:** Segregation and extravascular localization of ferumoxytol MR imaging improves on current techniques by eliminating intrinsic tissue and intravascular ferumoxytol signal and may inform glioblastoma outcomes by serving as a more specific metric of macrophage content compared with uncorrected T1 and SWI techniques.

**ABBREVIATIONS:** CRT = chemoradiotherapy; GBCA = gadolinium-based contrast agent; IDH = isocitrate dehydrogenase; SELFI = segregation and extravascular localization of ferumoxytol imaging; TAMs = tumor-associated macrophages and microglia

Standard of care surgical resection and Stupp protocol chemoradiotherapy (CRT; temozolomide with conformal irradiation) results in a 14.2-month median overall survival for patients with *isocitrate dehydrogenase* (IDH) wild-type glioblastoma.<sup>1-3</sup> Following CRT, some patients undergo an inflammatory response that manifests as transiently progressive gadolinium-based contrast agent (GBCA) enhancement on MR imaging,

commonly termed “pseudoprogression.”<sup>4-7</sup> The development of pseudoprogression may improve overall survival, but this relationship is not completely understood.<sup>8-10</sup> This gap in clinical knowledge is exacerbated by the inability of GBCA MR imaging to distinguish pseudoprogression from true glioblastoma

Ramon F. Barajas, Jr and Daniel Schwartz contributed equally to this document.

This work was supported, in part, by National Institutes of Health grants CA19911 (to E.A.N.), CA137488-15S1 (to E.A.N. and R.F.B. Jr), 1 L30 CA220897-01 (to R.F.B. Jr), KL2TR002370 (to R.F.B. Jr), the Walter S. and Lucienne Driskill Foundation (to E.A.N.), and a Veterans Administration Merit Review grant (to E.A.N.).

Please address correspondence to Edward A. Neuwelt, MD, Blood-Brain Barrier Program, Oregon Health & Science University, Portland, OR 97239; e-mail: neuwelte@ohsu.edu; @LabBarajas

Indicates open access to non-subscribers at www.ajnr.org

Indicates article with supplemental on-line table.

Indicates article with supplemental on-line video.

<http://dx.doi.org/10.3174/ajnr.A6600>

Received August 16, 2019; accepted after revision April 2, 2020.

From the Departments of Radiology (R.F.B. Jr, D.S., B.E.H., J.S., D.R.P., J.P.N., J.M.P., L.S., C.G.V.), Advanced Imaging Research Center (R.F.B. Jr, D.S., X.L., A.H., W.D.R.), Knight Cancer Institute Translational Oncology Research Program (R.F.B. Jr), Departments of Neurology (H.L.M., C.N.K., L.S., C.G.V., P.A., L.L.M., E.A.N.), Medical Informatics and Clinical Epidemiology (R.F.F.), Radiation Medicine (J.J.), Neurological Surgery (A.M.R., A.D., J.S.C., J.C., S.J.H., E.A.N.), Pathology (R.W.), and Blood-Brain Barrier Program (H.L.M., C.N.K., L.S., C.G.V., P.A., L.L.M., E.A.N.), Oregon Health & Science University, Portland, Oregon; Department of Diagnostic Radiology (L.S.), Heart and Vascular Center, Semmelweis University, Budapest, Hungary; and Portland Veterans Affairs Medical Center (E.A.N.), Portland, Oregon.

regrowth.<sup>11</sup> Establishing a definitive diagnosis by surgical biopsy or follow-up MR imaging delays therapy for true disease recurrence and may adversely affect overall survival.<sup>8-13</sup> Therefore, the development of a biologically specific imaging metric of inflammation may improve clinical outcomes.

Tumor-associated macrophages and microglia (TAMs) are a major constituent of the immune response of the brain to glioblastoma therapy and account for up to 40% of the cellular tumor mass.<sup>4</sup> Because TAMs are professional iron recyclers with properties that are directly linked to phagocytosis, ultra-small superparamagnetic iron oxide-enhanced MR imaging is well-suited for the detection of inflammation.<sup>14,15</sup> TAMs-mediated neuroinflammation has been visualized in vivo using delayed time point MR imaging, 24 hours after intravenous administration of ultrasmall superparamagnetic iron oxide ferumoxytol (Feraheme; AMAG Pharmaceuticals) in preclinical glioblastoma models.<sup>15</sup> Ferumoxytol is FDA-approved for intravenous iron supplementation but can be used off-label as an MR imaging contrast agent.<sup>16</sup> Early time point MR imaging (immediately following intravenous ferumoxytol administration) allows the quantification and localization of the intravascular agent;<sup>17</sup> however, its prolonged circulating half-life limits facile interpretation of extravascular signal changes in the glioblastoma microenvironment at delayed time point imaging up to 48 hours later.<sup>18</sup>

We hypothesized that the localization of glioblastoma TAMs could be improved by a combined imaging and analytic approach of early and delayed time point MR imaging with ferumoxytol. We assessed the use of SWI at multiple imaging time points to produce high-resolution segregation and extravascular localization of ferumoxytol imaging (SEIFI) maps for the putative isolation of extravascular ferumoxytol as a surrogate marker of TAMs. Using a well-characterized cohort of patients with clinically suspected glioblastoma progression, we show the following: 1) Signal on delayed time point SWI is partially a reflection of persistent intravascular ferumoxytol, 2) the generation of SEIFI maps allows the localization of TAMs-accumulated extravascular ferumoxytol signal that is only observed in the delayed time point of imaging, and 3) positive SEIFI values, in part, tend to stratify overall survival in patients with glioblastoma.

## MATERIALS AND METHODS

### Patient Population

This retrospective Oregon Health & Science University institutional review board-approved study included subjects meeting the following inclusion criteria: 1) histologically confirmed diagnosis of glioblastoma (World Health Organization classification, grade IV glioma); 2) documentation of *IDH-1* mutational and *O-6-methylguanine-DNA methyltransferase promoter methylation* status (R132H; Clinical Laboratory Improvement Amendments, No. 38D2018256); 3) a Karnofsky Performance Score (KPS) of more than 50; 4) prior maximal safe resection followed by CRT using the Stupp protocol;<sup>2</sup> 5) GBCA MR imaging demonstrating evidence of preliminary progressive disease according to Response Assessment in Neuro-Oncology criteria;<sup>6</sup> 6) subsequent GBCA MR imaging within 72 hours before ferumoxytol MR imaging; and 7) SWI performed before and following intravenous ferumoxytol administration. The early time point of imaging was defined by SWI within 10 minutes of intravenous ferumoxytol administration.

Delayed time point imaging was defined by SWI performed approximately 24 hours following intravenous ferumoxytol administration. Exclusion criteria included the absence of delayed time point ferumoxytol-enhanced T1-weighted MR imaging or SWI. None of the patients who met the inclusion criteria were excluded from analysis.

Twenty-three patients were studied between January 2012 and January 2018 (On-line Table). Medical records established either glioblastoma recurrence or pseudoprogression as the etiology for preliminary progressive disease. Sixteen patients (70% of the cohort) were diagnosed with recurrent tumor. Four of these patients underwent standard-of-care re-resection to establish disease status via histologic analysis. The remaining 19 patients were diagnosed with either pseudoprogression (5 with *IDH* wild-type, 2 with *IDH*-mutant) or recurrent tumor via integration of patient clinical course and serial GBCA MR imaging. Thirteen patients received dexamethasone (mean,  $3.74 \pm 4.56$  mg) concurrent with ferumoxytol administration. Four patients with tumor recurrence received bevacizumab (10 mg/kg) before or the same day as ferumoxytol administration. Dexamethasone and bevacizumab were administered to reduce the clinical adverse effects of vasogenic edema.

### Image Acquisition

All patients underwent 3T MR imaging (Ingenia; Philips Healthcare) examinations using 1 of 2 imaging protocols. Protocol 1 (12 patients) entailed MR imaging for 3 consecutive days, whereas protocol 2 (11 patients) entailed MR imaging for 2 consecutive days. 3D-SWI (TR/TE/flip angle = 26 ms/20 ms/15°, FOV = 210 mm<sup>2</sup>, imaging matrix = 512<sup>2</sup>, in-plane resolution = 0.41<sup>2</sup>, 116 contiguous axial slices with 2.2-mm section thickness, 1.1-mm overlap producing 232 evaluable slices) was performed before, immediately following (early time point), and 24 hours (delayed time point) after intravenous ferumoxytol administration (~15-minute infusion at a dose of up to 510 mg). Gradient echo 3D T1-weighted images (TR/TE/flip angle = 8.14 ms/3.72 ms/8°, 160 contiguous 1-mm-thick axial slices) were acquired pre- and post-gadoteridol gadolinium chelate (GBCA, ProHance; Bracco Diagnostics; 0.1 mmol/kg) and ferumoxytol administration. GBCA-enhanced sequences were performed before ferumoxytol administration. All MR imaging measurements were completed on the same instrument for each participant.

**Contrast-Enhancement Segmentation.** A neurologic radiologist with 10 years of experience (R.F.B. Jr) reviewed contrast-enhanced T1-weighted volumes (GBCA and delayed ferumoxytol) and manually marked a large ROI that covered all possible enhancement in both T1-weighted datasets. These preliminary ROIs were then automatically segmented into contrast-enhancing and nonenhancing voxels, as previously described,<sup>19</sup> allowing the generation of a lesion-wide enhancement mask from which SEIFI values were assessed; the results of the segmentation were visually inspected, and none required manual intervention.

### Generation of SEIFI Maps

Figure 1 illustrates the SEIFI calculation. Briefly, SWI magnitude images (precontrast, early time point, and delayed time point) were rigidly registered to the non-contrast-enhanced T1-weighted volume (3dAllineate, Analysis of Functional Neuro Images



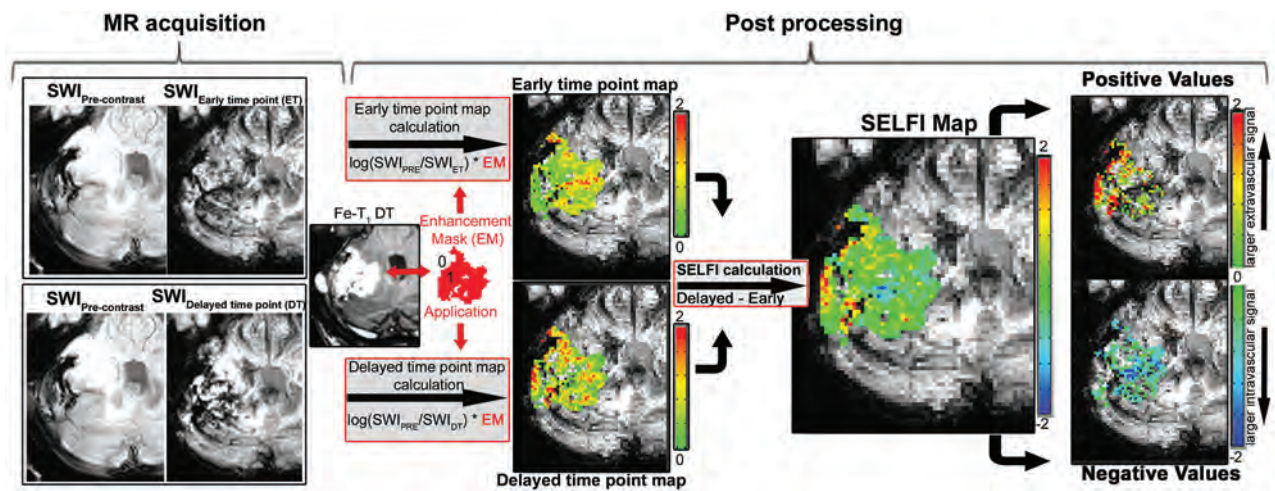


**FIG 1.** Segregation and Extravascular Localization of Ferumoxytol Imaging (SELF) processing pipeline. *Left*, The MR acquisition of susceptibility weighted imaging (SWI) is performed prior to (pre-contrast), immediately after (early time point; ET), and 24 h following ferumoxytol administration (delayed time point; DT). *Middle*, Post processing of early and delayed time point maps are calculated on a voxel wise basis as the log of the quotient of the pre to post-contrast images. *Right*, SELF is calculated as the difference of the delayed time point map from the early time point maps. The SELF map can be further segmented into positive (“extravascular”, delayed time point signal > early time point signal, “SELF +”) and negative (“intravascular”, early time point signal > delayed time point signal, “SELF −”) values (*right*). Fe-T indicates Ferumoxytol T1-weighted Delayed Time point.

[AFNI]; <http://afni.nimh.nih.gov/afni>). Early and delayed time point maps were created by taking the natural log of the ratio of a pre-contrast voxel to the same postcontrast voxel so that the magnitude of a value of a voxel was proportional to the concentration of contrast. Any resulting negative values (voxels in which SWI signal increased after the administration of contrast agent, <5% of the voxels in all cases) were considered noise and removed from both maps. For the early time point, this step produced a CBV map. SELF maps were created by taking the voxelwise difference of the delayed time point map from the early time point map (3dcalc, AFNI; [https://afni.nimh.nih.gov/pub/dist/doc/program\\_help/3dcalc.html](https://afni.nimh.nih.gov/pub/dist/doc/program_help/3dcalc.html); Fig 1, middle):

$$SELF_i = \log\left(\frac{SWI_{pre}}{SWI_{DT}}\right) - \log\left(\frac{SWI_{pre}}{SWI_{ET}}\right),$$

where  $i$  is a voxel,  $SWI_{pre}$  is the value of the voxel on the noncontrast SWI,  $SWI_{ET}$  is the value of the voxel on the SWI immediately after contrast, and  $SWI_{DT}$  is the value of the voxel on the delayed SWI (~24 hours after contrast administration). Mean values from the generated maps were calculated within both the GBCA and ferumoxytol contrast-enhancing ROI (3dmaskave, AFNI; [https://afni.nimh.nih.gov/pub/dist/doc/program\\_help/3dmaskave.html](https://afni.nimh.nih.gov/pub/dist/doc/program_help/3dmaskave.html)). Mean negative (SELF−) and positive (SELF+) portions of the SELF maps were calculated separately so that the absolute value of each positive and negative voxel was proportional to the relative contribution of that voxel (Fig 1, right):

$$SELF+ = \frac{1}{n} \sum_{SELF_i > 0}^n i,$$

$$SELF- = \frac{1}{n} \sum_{SELF_i < 0}^n i,$$

where  $n$  is the number of voxels within the enhancement mask,  $i$  is a voxel within the enhancement mask,  $SWI_{pre}$  is the

noncontrast SWI,  $SWI_{ET}$  is the SWI immediately after contrast, and  $SWI_{DT}$  is the delayed SWI (~24 hours after contrast administration). The log function was used so that nonlinearities in ratio variables could be linearized, so that the ratios were equidistant and the dependent variable was not weighted in favor of the denominator. For example, the ratios of 5/2 and 2/5 are not equidistant from 1 until the log is performed [ $\log_{10}(5/2) = 0.40$  and  $\log_{10}(2/5) = -0.40$ ]. This feature allows centering of the displacement of the relationship evenly around zero irrespective of which variable is in the numerator or denominator. Likewise, the introduction of a log-transform equilibrates the magnitude of an effect (both positive and negative) within 2 hypothetical voxels. Finally, in an effort to provide a single aggregate per tumor score of both the magnitude and spatial extent of inflammatory infiltrate, primarily for the purpose of testing against overall survival (see Statistical Analysis), mean SELF+ values were scaled by the proportion of voxels that were positive relative to the number of voxels that were enhanced in the postferumoxytol T1-weighted volume.

### Image-Guided Tissue Sampling and Specimen Processing

To investigate the biologic processes associated with SELF metrics, we performed stereotactic tissue sampling in a patient with newly diagnosed glioblastoma at the time of the initial surgical resection. Six sampling sites were prospectively marked on an intraoperative neuronavigational device on the basis of the presence or absence of 24-hour delayed ferumoxytol signal. The precise location of the sampling sites was recorded (screen shots and MR imaging coordinates) at the time of intraoperative biopsy and allowed coregistration with T1-weighted gadolinium-enhanced and SELF MR imaging sequences.

Immunohistochemical staining with CD34 (microvascular density), CD68 (TAMs), Dx1 (dextran ferumoxytol coating), and Perls Prussian blue (iron) allowed a subjective assessment using a 4-tier ordinal scale (0, no immunoreactivity; 3, intense immunoreactivity),



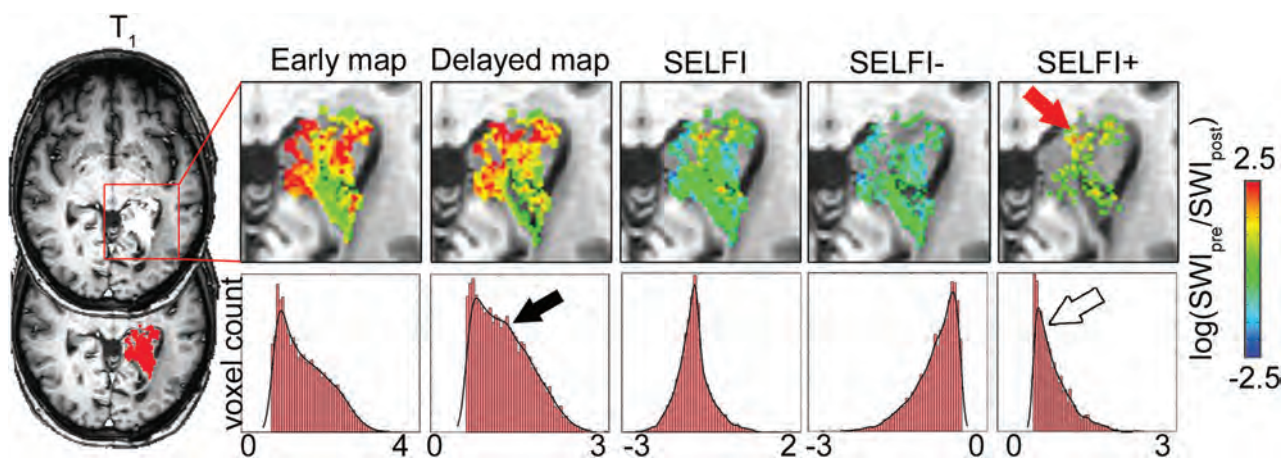


**FIG 2.** Specific extravascular ferumoxytol accumulation is localized by SELF1+ values. T1-weighted ferumoxytol-enhanced image and automated enhancement segmentation masks are shown on the left. Similarities are observed between early time point (*leftmost map*) and delayed time point maps (*second from left*). The hump shown in the histogram of the delayed time point map (*black closed arrow*) represents the remaining intravascular ferumoxytol; this signal is removed in the SELF1+ map (*rightmost histogram, open arrow*). The specific extravascular signal that arises from ferumoxytol contrast accumulation in the delayed time point is only clearly visualized by the SELF1 technique (*red closed arrow, rightmost map*).

with 4 high-power fields at a magnification of 20 $\times$  or greater. Additionally, to better understand the location of ferumoxytol at the 24-hour delayed imaging time point, we performed immunofluorescent histochemistry (Dx1 and Iba1 [for TAMs localization] antibodies) on tissue obtained from a rat model of syngeneic glioblastoma after 13 days of intracerebral growth using an Institutional Animal Care and Use Committee–approved protocol. Antibody labeling was visualized using an LSM 780 confocal microscope (Zeiss). A total of 136 images were obtained with 0.3- $\mu$ m optical sectioning. An attending neuropathologist (R.W., with >20 years of experience) who was blinded to the imaging results performed all qualitative immunohistochemical assessments.

### Statistical Analysis

The Pearson  $r$  tested for correlation between imaging metrics. Student  $t$  tests assessed differences between signal intensity and SELF1 metrics. Overall survival was classified in *IDH* wild-type glioblastoma from the date of surgical diagnosis until death or last follow-up date for patients without an event. Survival analysis was performed using multivariate Cox regression analysis, covarying for age and KPS, on mean delayed time point and aggregate SELF1+ scores as calculated above (SPSS, Version 25.0; IBM).  $P$  values < .05 were considered statistically significant.

## RESULTS

### Comparison of Enhancing GBCA and Ferumoxytol Volume and Signal Intensity

The cohort-wide root volumes of GBCA enhancement significantly exceeded those of delayed ferumoxytol enhancement (paired  $t_{(22)} = 2.25$ ,  $P = .03$ ), as did the mean normalized T1 image intensity within enhancing ROIs (paired  $t_{(22)} = 2.77$ ,  $P = .01$ ). Despite significant differences in enhancement volumes and intensities, GBCA and ferumoxytol T1-enhancement volumes were significantly correlated ( $r_{(21)} = 0.87$ ,  $P < .01$ ) as were normalized T1 signal intensities ( $r_{(21)} = 0.87$ ,  $P = .01$ ). Finally, the

enhancing volumes in GBCA and ferumoxytol were correlated with their respective normalized intensities ( $r_{(21)} = 0.51$  and  $0.53$ ,  $P < .01$ , respectively). All findings presented here were of the same statistical significance in both GBCA- and ferumoxytol-enhancing ROIs; therefore, only values derived from ferumoxytol-enhancing ROIs are reported, unless GBCA and ferumoxytol are directly compared.

### Comparison of Ferumoxytol-Enhanced Early Time Point, Delayed Time Point, and SELF1 Map Measurements

Early and delayed time point SWI measurements were significantly correlated, suggesting that intravascular ferumoxytol signal contaminates delayed measurements when using the standard uncorrected approach ( $r_{(21)} = 0.56$ ,  $P < .01$ ). An example of early time point, delayed time point, SELF1 maps, and corresponding voxelwise histograms from a single patient with disease recurrence can be found in Fig 2. Both SELF1+ (extravascular) and SELF1– (remaining intravascular signal at the delayed imaging time point) were correlated with delayed time point SWI measurements ( $r_{(21)} = 0.87$  and  $-0.48$ , respectively,  $P < .03$ ; Fig 3A, top right), confirming the contamination of intravascular ferumoxytol in delayed time point SWI measurements. However, only SELF1– values were significantly correlated with early time point SWI measurements, confirming localization of intravascular signal ( $r_{(21)} = 0.87$ ,  $P < .001$ ; Fig 3A, top left).

### Comparison of SELF1 Measurements and Intensity of T1 Enhancement

Normalized signal intensity of delayed time point ferumoxytol T1 enhancement was correlated with SELF1+ (extravascular) measurements and delayed time point SWI maps ( $r_{(21)} = 0.68$  and  $0.75$ ,  $P < .001$ , respectively), but not with SELF1– (intravascular) measurements ( $r_{(21)} = -0.19$ ,  $P > .3$ ; Fig 3B, bottom right). Most interesting, the normalized signal intensity of GBCA T1 enhancement was not correlated with delayed time point SWI maps or SELF1 measures ( $r_{(21)} = 0.33$ ,  $0.33$ , and  $-0.13$ ,  $P > .1$ ; Fig 3B, bottom left), suggesting that the functional significance of the magnitude

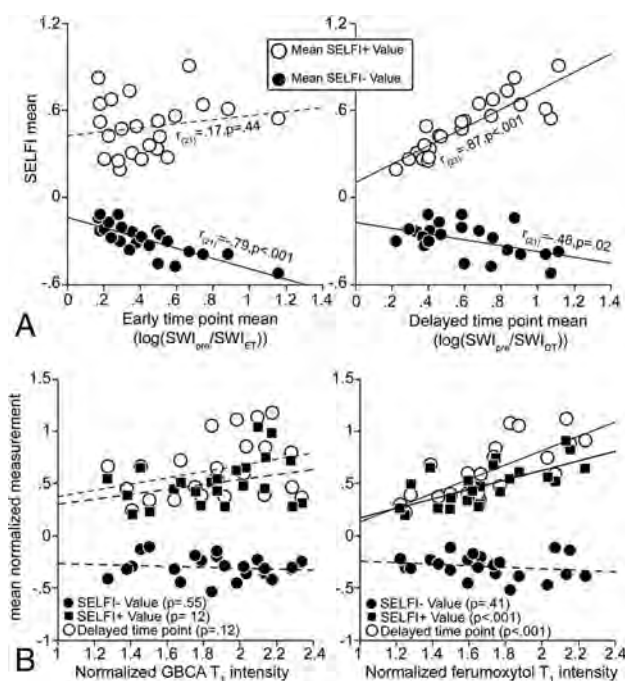


**FIG 3.** SELFI technique discriminates intravascular from extravascular ferumoxytol contrast pools. **A**, Intravascular ferumoxytol signal (SELFI-, solid circle) is observed in both the early time point (left panel) and the delayed time point maps (right panel), contaminating the signal on the latter. Conversely, SELFI+ values (empty circles) are correlated with only delayed time point map values (right panel), suggesting that the metric is not present in the early imaging time point. **B**, The relationship of GBCA (left panel) and delayed ferumoxytol (right panel) T1 intensity to SELFI metrics. SELFI+ values (solid squares) and delayed time point map mean values (empty circles) demonstrate a significant correlation with only delayed ferumoxytol (right panel) and not GBCA T1 enhancing signal (left panel) intensity. SELFI- values (solid circles) are not correlated with enhancement signal intensity. Note that statistically significant ( $P < .05$ ) regressions are shown as solid lines and non-significant regressions are represented by dashed lines. Each point on the graph represents a patient's mean imaging value. ET indicates early time point; DT, delayed time point.

of delayed ferumoxytol T1 enhancement differs from that of GBCA T1 enhancement.

### SELFI Association with Tumor Biology

Stereotactic image-guided tissue sampling in a patient with newly diagnosed *IDH* wild-type glioblastoma allowed for the collection of 6 specimens (4 enhancing, 2 nonenhancing) (Fig 4). Increasing SELFI+ values demonstrated increasing TAMs infiltration (Fig 5A). Conversely, decreasing SELFI- values demonstrated increasing microvascular density. We observed TAMs-specific intracellular uptake of ferumoxytol 24 hours after administration in a syngeneic glioblastoma rat model (Fig 5B and On-line Video). Ferumoxytol contrast was not visualized within the extravascular extracellular space.

### Ferumoxytol MR Imaging Measurements and Overall Survival

The overall cohort survival ranged from 5.83 to 91.0 months (median, 16.6 months). Cox regression survival analysis of the 19

patients with *IDH* wild-type disease progression (5 pseudoprogressions, 14 disease recurrences) was nonsignificant for the delayed time point metric ( $B = -0.13$ , Wald = 0.017,  $P > .8$ ), though it approached significance for the tumor-wide SELFI+ metric ( $B = 2.98$ , Wald = 2.57,  $P = .1$ ). Higher KPS and age were significantly associated with longer and shorter survival, respectively, in the SELFI+ metric multivariate model ( $P = .02$  and  $.05$ , respectively) but not in the delayed time point model ( $P = .06$  and  $.06$ ), further demonstrating the clinical value of isolating inflammation-specific signal with the SELFI+ metric.

### DISCUSSION

We investigated whether SELFI maps could be used to distinguish extravascular from intravascular ferumoxytol pools in 23 patients with CRT-treated glioblastoma at the time of presumed disease progression. Our results suggest that SELFI+ values represent accumulated extravascular ferumoxytol after 24 hours and that SELFI- values delineate the persistence of contaminating intravascular ferumoxytol at the delayed imaging time point. Preliminary biologic assessment using stereotactic image-guided tissue sampling techniques suggests that increasing SELFI+ values localize regions of increasing TAMs infiltration, while decreasing SELFI- values localize regions of increasing microvascular density. Higher aggregate SELFI+ values were found to trend toward lower overall survival within this small cohort. These observations suggest that both T1 and T2\* MR imaging signal changes in the delayed time point are partially a reflection of persistent contamination by intravascular ferumoxytol, which precludes an accurate assessment of the accumulation of extravascular contrast. This retrospective study supports our hypothesis that SELFI maps provide an approach to localize extravascular ferumoxytol contrast accumulation in the delayed time point by eliminating intrinsic tissue and intravascular signal. Our results suggest that the SELFI technique may serve as a more specific imaging metric for localizing TAMs within the glioblastoma microenvironment compared with the currently used uncorrected T1 and SWI sequences. Taken together, the SELFI technique presented here advances neuro-oncologic research and practice by possibly providing a clinically feasible biomarker of accumulating phagocytic immune cells in the central nervous system, including TAMs, and may inform survival outcomes in patients with Stupp protocol-treated *IDH* wild-type glioblastoma.

Prior investigations have explored the localization of TAMs using T2\*-weighted imaging based on the inverse linear relationship with  $R_2^*$  signal relaxation rates, demonstrating that macrophage infiltration and microglia activation within injured central nervous system tissue are responsible for the accumulation of iron oxide nanoparticles.<sup>20</sup> However, previous reports have not accounted for intrinsic tissue (iron as a by-product of prior tissue bleeding) or persistent intravascular ferumoxytol signal.<sup>18</sup> Indeed, Iv et al<sup>18</sup> have painstakingly revealed that glioblastoma regions devoid of macrophage accumulation demonstrate T2\*-weighted signal changes in the delayed time point of ferumoxytol imaging. Our results suggest that the observed SWI signal changes include a combination of 2 spatially separate and functionally distinct ferumoxytol pools: 1) residual intravascular ferumoxytol, and 2) extravascular intercellular accumulation within



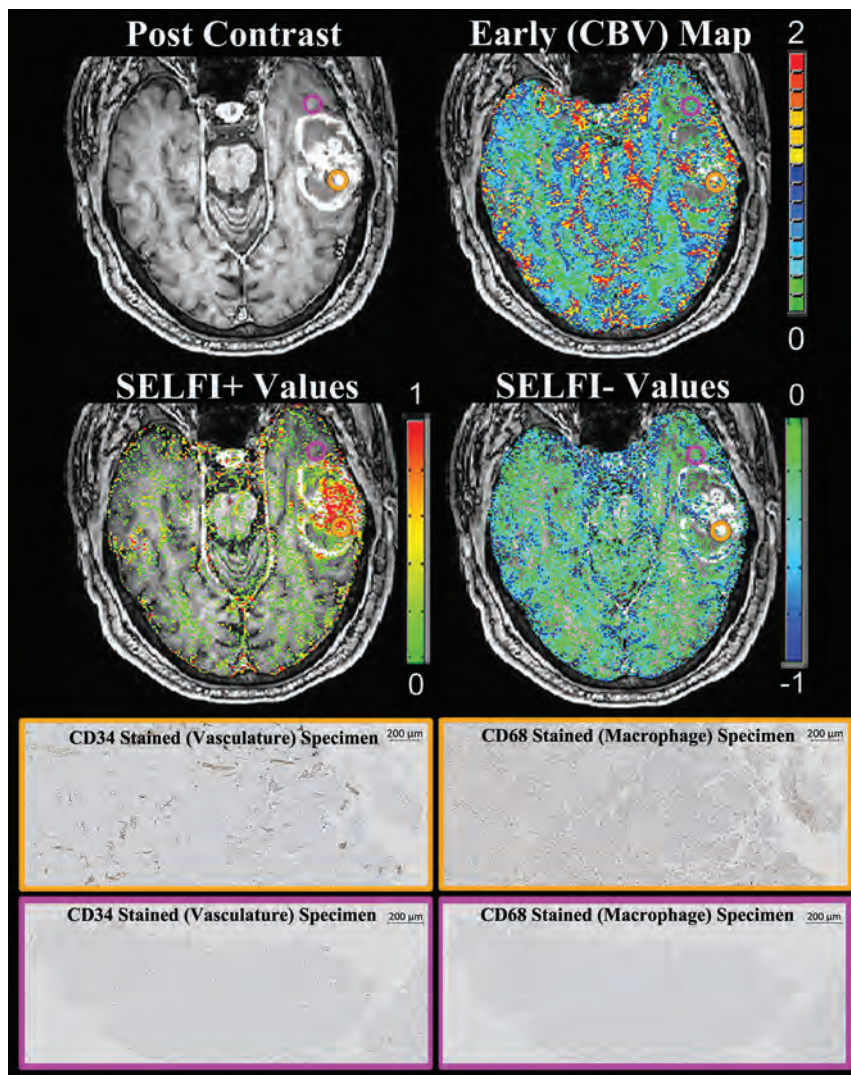


**FIG 4.** SELFI technique characterizes the glioblastoma immune microenvironment. We performed image-guided tissue sampling in a 64-year-old man with newly diagnosed *IDH* wild-type glioblastoma to determine whether SELFI MR imaging could differentiate intravascular-from-extravascular ferumoxytol signal. Preoperative T1-weighted gadolinium-enhanced images (Row 1) were integrated into the intraoperative neuronavigational device, allowing sampling of enhancing (orange ROI,  $n = 4$ ) and nonenhancing (purple ROI,  $n = 2$ ) regions. Regions with decreased SELFI- values (Row 2 right) and elevated cerebral blood volume (Row 1 right) demonstrate elevated microvascular density (CD34) counts (Row 3 left). Conversely, regions with elevated SELFI+ values (Row 2 left) demonstrate marked TAMs infiltration (CD68; Row 3 right). SELFI regions with values near zero demonstrate neither marked microvascular density nor TAMs infiltration (Row 4). No ferumoxytol staining was observed within the extravascular extracellular interstitial tumor space (not shown). We note that CBV maps would not have been capable of specifically localizing TAMs infiltration because regions of elevated CBV and decreased SELFI- values are not spatially similar to regions of elevated SELFI+ values. This biologic paradigm is well-demonstrated about the medial enhancing wall. This case example provides preliminary data showing that the SELFI imaging approach is a feasible method to discriminate intravascular-from-extravascular ferumoxytol contrast pools.

TAMs. Therefore, the use of uncorrected delayed time point ferumoxytol-enhanced MR imaging may lead to falsely positive inflammatory “hotspots” due to persistent intravascular contrast. If ferumoxytol-associated MR imaging signal changes are dependent on transport across the blood-brain barrier in the context of activated innate immunity, accurate quantification of brain parenchymal TAMs requires an account of residual

intravascular signal. SELFI is a method for the deconvolution of intra- and extravascular signal contributions observed within delayed time point ferumoxytol-enhanced MR imaging.

SELFI MR imaging would be extremely valuable in future in vivo investigations of the immune microenvironment within glioblastoma. Glioblastoma cells have complex inhibitory mechanisms to suppress and escape local immune surveillance.<sup>4,21</sup> The consequence is the establishment of a protumoral immunosuppressive microenvironment that promotes unchecked glioblastoma growth.<sup>22</sup> Functionally, the immunosuppressive microenvironment serves as a biologic feature that contributes to the development of glioblastoma therapeutic resistance.<sup>23</sup> Rigorous pioneering work by Macdonald et al<sup>5</sup> and Stupp et al<sup>2,3</sup> has made GBCA-enhanced MR imaging the standard of care for monitoring glioblastoma response to therapy. After therapy, neuroinflammation (pseudoprogression) is characterized by enlarging enhancement that spontaneously resolves.<sup>6</sup> Unfortunately, GBCA-enhanced MR imaging lacks specificity in characterizing therapeutic failure because local regional tumor regrowth cannot be prospectively distinguished from therapy-mediated neuroinflammation.<sup>24</sup> Pseudoprogression has been consistently observed in 30% of patients undergoing therapy,<sup>4-7</sup> with some investigators reporting increased survival.<sup>8-13</sup> While not designed to directly assess the added value of the SELFI metric to gadolinium enhancement for the diagnosis and prognosis of glioblastoma, our study does further address the need for the development of a biologically specific imaging metric capable of localizing neuroinflammation.<sup>25,26</sup> The noninvasive quantification of the tumor immune response may provide additional diagnostic and prognostic information beneficial to the planning and monitoring of therapy, and SELFI is a molecular imaging approach by which the glioblastoma innate immune microenvironment can be characterized.

SELFI+ values could be a prognostic biomarker of overall survival in patients with CRT-treated *IDH* wild-type glioblastoma. The

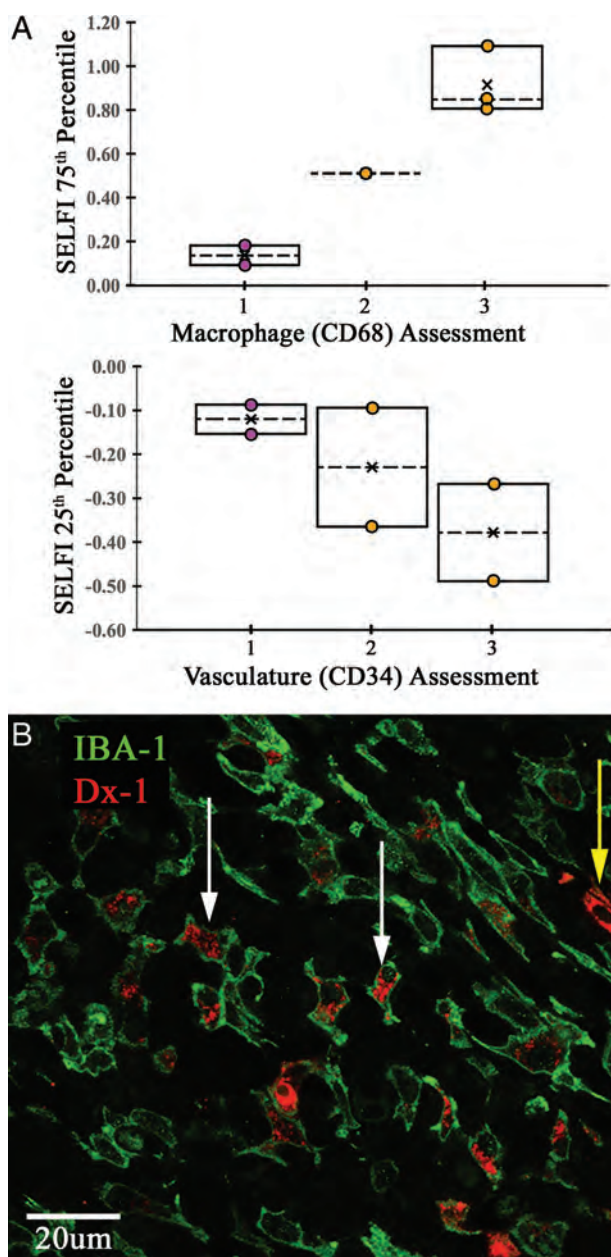


**FIG 5.** Relationship between SELF values and glioblastoma tumor biology. **A**, Boxplots of macrophage (top) and microvascular density (middle) qualitative assessment using a 0 (no immunoreactivity) to 3 (intense immunoreactivity) ordinal scale are plotted against continuous SELF values for 6 tissue specimens (4 enhancing [orange circles], 2 nonenhancing [purple circles]). A positive association was observed between increasing SELF and macrophage values. Conversely, a negative association was observed between decreasing SELF values and increasing microvascular density within the tissue specimen. Central *x* indicates mean; dashed line, median. **B**, Immunofluorescence (bottom) from a syngeneic glioblastoma rat model demonstrates intracellular localization of ferumoxytol (red, Dx1) within macrophages/microglia (green, Iba-1; white arrows) and tumor vasculature (yellow arrow) 24 hours following administration. No Dx1 immunofluorescence is observed within the extravascular extracellular space.

lack of a clinically prognostic biomarker of the tumor immune microenvironment is a critical gap in knowledge in the era of immunotherapy. Novel therapeutic techniques aimed at immune augmentation require an appropriate molecular imaging metric to

demonstrate changes in the targeted biologic mechanism. Immune checkpoint blockade leads to an increased antitumor immune response, which results in therapy-mediated inflammation.<sup>27</sup> The interaction between tumor and cytotoxic T-cells is considered a key target for checkpoint inhibition, but emerging evidence suggests that checkpoint blockade also influences therapeutic efficacy through innate immunity.<sup>28</sup> Preliminary reports suggest that checkpoint efficacy is characterized by marked proinflammatory lymphohistiocytic infiltration.<sup>28</sup> Given the potential importance of TAMs activation in glioblastoma therapy, the development of a biologically specific imaging metric of protumoral and proinflammatory macrophage accumulation would be clinically indispensable. We are prospectively evaluating the utility of delayed ferumoxytol MR imaging in subjects receiving standard-of-care CRT with or without concurrent checkpoint inhibitors in primary and metastatic brain tumors (clinicaltrials.gov; NCT00103038, NCT03347617, and NCT03325166). The SELF approach may provide additional prognostic value within this clinical context.

Small sample size and the retrospective nature of this study are limitations that caution against overinterpretation of these findings; future prospective investigations should verify these imaging characteristics within a separate larger cohort of patients. While ferumoxytol phagocytosis by TAMs is a proposed mechanism for the observed signal characteristics, validation must include a larger cohort of image-guided tissue sampling to verify the biologic correlate. Unfortunately, histopathologic confirmation of differential TAMs accumulation based on SELF+ values is not available in all our patients. Finally, the cohort sample size and characteristics provided insufficient statistical power to assess the diagnostic value of SELF or the prognostic implications of SELF in *IDH* wild-type glioblastoma. Notably, ferumoxytol-enhanced MR imaging is a clinically feasible tool for the study of brain tumors with a positive safety profile.<sup>29</sup>

## CONCLUSIONS

This study describes the newly developed SELF technique for the differentiation of extravascular ferumoxytol contrast signal from residual intravascular signal at a 24-hour delayed imaging time point within CRT-treated glioblastoma. SELF improves on current techniques by eliminating contributions from intrinsic tissue and intravascular signal through voxelwise subtraction of early and delayed time point ferumoxytol maps. Once prospectively validated, this methodology may prove to be a spatially specific biomarker for the accumulation of phagocytic cells such as TAMs within the glioblastoma-immune microenvironment and may help inform treatment and clinical management of glioblastoma.

## ACKNOWLEDGMENTS

The first author thanks Bethany Barajas, MSN, for her helpful comments regarding this article; the many clinical collaborators, including Joseph Anderson-Bussiere and Shannon Spruell, for their helpfulness; and the many wonderful patients included in this study who selflessly contributed their time to undergo research medical imaging while confronting a deadly disease. The



first author dedicates this research to the memory of Rachel Dawn Gabani.

Disclosures: Ramon F. Barajas, Jr.—*RELATED: Grant*: National Institutes of Health.\* Daniel Schwartz—*RELATED: Grant*: National Institutes of Health, Walter S. and Lucienne Driskill Foundation, Veterans Administration Merit Review.\* Bronwyn E. Hamilton—*UNRELATED: Royalties*: Elsevier, *Comments*: book editor/author royalties. David R. Pettersson—*UNRELATED: Employment*: Oregon Health & Science University. Edward A. Neuwelt—*RELATED: Grant*: National Institutes of Health grants CA199111, CA137488-1S1, 1 L30 CA220897-01, the Walter S. and Lucienne Driskill Foundation, and by a Veterans Administration Merit Review grant, *Comments*: This work was supported, in part, by National Institutes of Health grants CA199111, CA137488-1S1, 1 L30 CA220897-0; the Walter S. and Lucienne Driskill Foundation; and a Veterans Administration Merit Review grant, all to E.A. N. Jeremy Ciporen—*UNRELATED: Patents (Planned, Pending or Issued)*: consultant SPIWAY. \*Money paid to the institution.

## REFERENCES

- Ostrom QT, Gittleman H, Xu J, et al. **CBTRUS Statistical Report: Primary Brain and Other Central Nervous System Tumors Diagnosed in the United States in 2009–2013.** *Neuro Oncol* 2016;18:v1–75 CrossRef Medline
- Stupp R, Mason WP, van den Bent MJ, et al; European Organisation for Research and Treatment of Cancer Brain Tumor and Radiotherapy Groups; National Cancer Institute of Canada Clinical Trials Group. **Radiotherapy plus concomitant and adjuvant temozolomide for glioblastoma.** *N Engl J Med* 2005;352:987–96 CrossRef Medline
- Stupp R, Hegi ME, Mason WP, et al; European Organisation for Research and Treatment of Cancer Brain Tumour and Radiation Oncology Groups; National Cancer Institute of Canada Clinical Trials Group. **Effects of radiotherapy with concomitant and adjuvant temozolomide versus radiotherapy alone on survival in glioblastoma in a randomised phase III study: 5-year analysis of the EORTC-NCIC trial.** *Lancet Oncol* 2009;10:459–66 CrossRef Medline
- Domingues P, Gonzalez-Tablas M, Otero A, et al. **Tumor infiltrating immune cells in gliomas and meningiomas.** *Brain Behav Immun* 2016;53:1–15 CrossRef Medline
- Macdonald DR, Cascino TL, Schold SC Jr, et al. **Response criteria for phase II studies of supratentorial malignant glioma.** *J Clin Oncol* 1990;8:1277–80 CrossRef Medline
- Wen PY, Macdonald DR, Reardon DA, et al. **Updated response assessment criteria for high-grade gliomas: Response Assessment in Neuro-Oncology working group.** *J Clin Oncol* 2010;28:1963–72 CrossRef Medline
- Okada H, Weller M, Huang R, et al. **Immunotherapy response assessment in neuro-oncology: a report of the RANO working group.** *Lancet Oncol* 2015;16:e534–42 CrossRef Medline
- Li H, Li J, Cheng G, et al. **IDH mutation and MGMT promoter methylation are associated with the pseudoprogression and improved prognosis of glioblastoma multiforme patients who have undergone concurrent and adjuvant temozolomide-based chemoradiotherapy.** *Clin Neurol Neurosurg* 2016;151:31–36 CrossRef Medline
- Gunjur A, Lau E, Taouk Y, et al. **Early post-treatment pseudo-progression amongst glioblastoma multiforme patients treated with radiotherapy and temozolomide: a retrospective analysis.** *J Med Imaging Radiat Oncol* 2011;55:603–10 CrossRef Medline
- Nasser M, Gahramanov S, Netto JP, et al. **Evaluation of pseudoprogression in patients with glioblastoma multiforme using dynamic magnetic resonance imaging with ferumoxytol calls RANO criteria into question.** *Neuro Oncol* 2014;16:1146–54 CrossRef Medline
- van Dijken BR, van Laar PJ, Holtman GA, et al. **Diagnostic accuracy of magnetic resonance imaging techniques for treatment response evaluation in patients with high-grade glioma; a systematic review and meta-analysis.** *Eur Radiol* 2017;27:4129–44 CrossRef Medline
- Grossman R, Shimony N, Hadelberg U, et al. **Impact of resecting radiation necrosis and pseudoprogression on survival of patients with glioblastoma.** *World Neurosurg* 2016;89:37–41 CrossRef Medline
- Melguizo-Gavilanes I, Bruner JM, Guha-Thakurta N, et al. **Characterization of pseudoprogression in patients with glioblastoma: is histology the gold standard?** *J Neurooncol* 2015;123:141–50 CrossRef Medline
- Nairz M, Theurl I, Swirski FK, et al. **“Pumping iron”—how macrophages handle iron at the systemic, microenvironmental, and cellular levels.** *Pflugers Arch* 2017;469:397–418 CrossRef Medline
- McConnell HL, Schwartz DL, Richardson BE, et al. **Ferumoxytol nanoparticle uptake in brain during acute neuroinflammation is cell-specific.** *Nanomedicine* 2016;12:1535–42 CrossRef Medline
- Toth GB, Varallyay CG, Horvath A, et al. **Current and potential imaging applications of ferumoxytol for magnetic resonance imaging.** *Kidney Int* 2017;92:47–66 CrossRef Medline
- Varallyay CG, Nesbit E, Fu R, et al. **High-resolution steady-state cerebral blood volume maps in patients with central nervous system neoplasms using ferumoxytol, a superparamagnetic iron oxide nanoparticle.** *J Cereb Blood Flow Metab* 2013;33:780–86 CrossRef Medline
- Iv M, Samghabadi P, Holdsworth S, et al. **Quantification of macrophages in high-grade gliomas by using ferumoxytol-enhanced MRI: a pilot study.** *Radiology* 2019;290:198–206 CrossRef Medline
- Horvath A, Varallyay CG, Schwartz D, et al. **Quantitative comparison of delayed ferumoxytol T1 enhancement with immediate gadoteridol enhancement in high grade gliomas.** *Magn Reson Med* 2018;80:224–30 CrossRef Medline
- Bendszus M, Stoll G. **Caught in the act: in vivo mapping of macrophage infiltration in nerve injury by magnetic resonance imaging.** *J Neurosci* 2003;23:10892–96 Medline
- Jackson C, Ruzevick J, Phallen J, et al. **Challenges in immunotherapy presented by the glioblastoma multiforme microenvironment.** *Clin Dev Immunol* 2011;2011:732413 CrossRef Medline
- Wei B, Wang L, Zhao X, et al. **The upregulation of programmed death 1 on peripheral blood T cells of glioma is correlated with disease progression.** *Tumor Biol* 2014;35:2923–29 CrossRef Medline
- Heddleston JM, Li Z, McLendon RE, et al. **The hypoxic microenvironment maintains glioblastoma stem cells and promotes reprogramming towards a cancer stem cell phenotype.** *Cell Cycle* 2009;8:3274–84 CrossRef Medline
- Barajas RF Jr, Chang JS, Segal MR, et al. **Differentiation of recurrent glioblastoma multiforme from radiation necrosis after external beam radiation therapy with dynamic susceptibility-weighted contrast-enhanced perfusion MRI.** *Radiology* 2009;253:486–96 CrossRef Medline
- Barajas RF Jr, Hamilton BE, Schwartz D, et al. **Combined iron oxide nanoparticle ferumoxytol and gadolinium contrast enhanced MRI defines glioblastoma pseudo-progression.** *Neuro Oncol* 2019;21:517–26 CrossRef Medline
- Barajas RF Jr, Hodgson JG, Chang JS, et al. **Glioblastoma multiforme regional genetic and cellular expression patterns: influence on anatomic and physiologic MR imaging.** *Radiology* 2010;254:564–76 CrossRef Medline
- Ranjan S, Quezado M, Garren N, et al. **Clinical decision making in the era of immunotherapy for high grade-glioma: report of four cases.** *BMC Cancer* 2018;18:239 CrossRef Medline
- Gordon SR, Maute RL, Dulken BW, et al. **PD-1 expression by tumour-associated macrophages inhibits phagocytosis and tumour immunity.** *Nature* 2017;545:495–99 CrossRef Medline
- Nguyen KL, Yoshida T, Kathuria-Prakash N, et al. **Multicenter safety and practice for off-label diagnostic use of ferumoxytol in MRI.** *Radiology* 2019;293:554–64 CrossRef Medline

# High Spatiotemporal Resolution 4D Flow MRI of Intracranial Aneurysms at 7T in 10 Minutes

L.M. Gottwald, J. Töger, K. Markenroth Bloch, E.S. Peper, B.F. Coolen, G.J. Strijkers, P. van Ooij, and A.J. Nederveen



## ABSTRACT

**BACKGROUND AND PURPOSE:** Patients with intracranial aneurysms may benefit from 4D flow MR imaging because the derived wall shear stress is considered a useful marker for risk assessment and growth of aneurysms. However, long scan times limit the clinical implementation of 4D flow MR imaging. Therefore, this study aimed to investigate whether highly accelerated, high resolution, 4D flow MR imaging at 7T provides reliable quantitative blood flow values in intracranial arteries and aneurysms.

**MATERIALS AND METHODS:** We used pseudospiral Cartesian undersampling with compressed sensing reconstruction to achieve high spatiotemporal resolution (0.5 mm isotropic, ~30 ms) in a scan time of 10 minutes. We analyzed the repeatability of accelerated 4D flow scans and compared flow rates, stroke volume, and the pulsatility index with 2D flow and conventional 4D flow MR imaging in a flow phantom and 15 healthy subjects. Additionally, accelerated 4D flow MR imaging with high spatiotemporal resolution was acquired in 5 patients with aneurysms to derive wall shear stress.

**RESULTS:** Flow-rate bias compared with 2D flow was lower for accelerated than for conventional 4D flow MR imaging ( $0.31 \pm 0.13$ ,  $P = .22$ , versus  $0.79 \pm 0.17$  mL/s,  $P < .01$ ). Pulsatility index bias gave similar results. Stroke volume bias showed no difference for accelerated as well as for conventional 4D flow compared to 2D flow MR imaging. Repeatability for accelerated 4D flow was similar to that of 2D flow MR imaging. Increased temporal resolution for wall shear stress measurements in 5 intracranial aneurysms did not show a consistent effect for the wall shear stress but did show an effect for the oscillatory shear index.

**CONCLUSIONS:** Highly accelerated high spatiotemporal resolution 4D flow MR imaging at 7T in intracranial arteries and aneurysms provides repeatable and accurate quantitative flow values. Flow rate accuracy is significantly increased compared with conventional 4D flow scans.

**ABBREVIATIONS:** CS = compressed sensing;  $N_{card}$  = number of reconstructed cardiac timeframes; OSI = oscillatory shear index; PROUD = PROspective Undersampling in multiple Dimensions; R = acceleration factor; SENSE = sensitivity encoding; UIA = unruptured intracranial aneurysm; WSS = wall shear stress;  $WSS_{PS}$  = peak systolic WSS;  $WSS_{TA}$  = time-averaged WSS

Intracranial aneurysms can threaten a patient's life because of the risk of rupture followed by hemorrhagic stroke, which is associated with high morbidity and mortality.<sup>1,2</sup> Therefore, intracranial aneurysms need to be monitored regularly to assess whether they remain stable and asymptomatic or grow, with an increased risk of rupture. Treatment choices range from medical follow-up for stable aneurysms to coiling or clipping for growing aneurysms when the risk of rupture is considered too high.<sup>1,2</sup> For patients with unruptured intracranial aneurysms (UIAs) that

need long-term follow-up and who have no contraindications for MR imaging, it is advised to consider MR imaging rather than CTA.<sup>2</sup> Typical MR imaging examinations use TOF or gadolinium contrast to visualize the aneurysms; however, advanced 4D flow MR imaging sequences can additionally visualize and quantify complex blood flow patterns in the aneurysm.<sup>3</sup>

Received February 12, 2020; accepted after revision April 21.

From the Departments of Radiology and Nuclear Medicine (L.M.G., E.S.P., P.v.O., A.J.N.), and Biomedical Engineering and Physics (B.F.C., G.J.S.), Amsterdam University Medical Centers, University of Amsterdam, Amsterdam, the Netherlands; Department of Diagnostic Radiology (J.T.), Skane University Hospital, Lund, Sweden; and Lund University Bioimaging Center (K.M.B.), Lund University, Lund, Sweden.

Funding was obtained by the Netherlands Organization for Scientific Research grant No. 13928 (HTSM2014).

Please address correspondence to Lukas M. Gottwald, MSc, Department of Radiology and Nuclear Medicine, Amsterdam University Medical Centers, location AMC, University of Amsterdam, Meibergdreef 9, 1105 AZ Amsterdam, the Netherlands; e-mail: lukas.gottwald@outlook.com

Indicates open access to non-subscribers at www.ajnr.org

Indicates article with supplemental on-line table.

Indicates article with supplemental on-line photos.

Indicates article with supplemental on-line video.

<http://dx.doi.org/10.3174/ajnr.A6603>

In addition to measurements of basic blood flow volumes and velocities, 4D flow MR imaging allows the estimation of hemodynamic biomarkers, including wall shear stress (WSS).<sup>4,5</sup> Those have generated interest because abnormal WSS might be an indicator for aneurysm growth.<sup>6,7</sup> Moreover, it has been shown that the aneurysm wall is thin in regions of high WSS and vice versa.<sup>8,9</sup> This finding suggests that 4D flow MR imaging can provide added value in the clinical assessment of aneurysms. However, the implementation of 4D flow MR imaging in routine clinical practice has been hampered by long scan times required to achieve sufficient spatiotemporal resolution to image the complex blood flow patterns in the aneurysm.

A way to improve 4D flow MR imaging of intracranial aneurysms is the use of 7T MR imaging. The increased SNR compared with 3T can be exploited to obtain increased spatiotemporal resolution and/or reduced scan times.<sup>10</sup> High spatiotemporal resolution is desirable because it has been shown that hemodynamic parameters such as mean flow, peak flow, flow waveform, WSS, and oscillatory shear index<sup>11</sup> (OSI) are influenced by spatial and temporal resolution of 4D flow MR imaging measurements.<sup>12</sup> A rule of thumb is that, to be clinically acceptable, the scan time should not exceed 10 minutes<sup>13</sup> to fit into the clinical workflow and for patient comfort. Advanced accelerated 4D flow MR imaging techniques using pseudospiral Cartesian sampling with compressed sensing<sup>14</sup> (CS) can be used to achieve such short scan times. These techniques have already proved effective to accelerate 4D flow MR imaging of the aorta and carotid arteries.<sup>15,16</sup> While we believe such a method could also be beneficial for intracranial 4D flow acquisitions at 7T, this benefit has not been thoroughly validated so far.

Therefore, the aim of this study was to investigate whether highly accelerated, high resolution 7T 4D flow MR imaging can provide reliable quantitative blood flow values in intracranial arteries. Specifically, we investigated flow accuracy in a flow phantom as well as healthy subjects. Furthermore, we aimed to explore the use of this accelerated sequence for deriving WSS in patients with unruptured intracranial aneurysms.

## MATERIALS AND METHODS

### **Undersampled 4D flow MR Imaging Acquisition and CS Reconstruction**

Accelerated 4D flow MR imaging was acquired on two similar 7T systems (Achieva 7T; Philips Healthcare), one located at the National 7T Facility, Lund, Sweden, and one at the Spinoza Center for Neuroimaging, Royal Netherlands Academy of Arts and Sciences, Amsterdam, the Netherlands. The scanners were equipped with a 32-channel receive head coil (2TX/32RX; NovaMedical) and an in-house-developed software modification called (PROspective Undersampling in multiple Dimensions [PROUD]), which enables a pseudospiral  $k_y/k_z$ -plane acquisition scheme designed for incoherent undersampling with a variable sampling density.<sup>15,16</sup> The acquisition was performed continuously without cardiac triggering. The signal of a peripheral pulse transducer was stored with the  $k$ -space data and used for retrospective binning in different cardiac time-frames. Due to physiologic heart rate variability, the resulting  $k$ - $t$  space was randomly filled, which is favorable for CS reconstruction and enabled retrospective changes of the temporal resolution.<sup>16</sup>

Reconstructions were performed off-line in Matlab R2016a (MathWorks) using MRecon (GyroTools) in combination with the

Berkeley Advanced Reconstruction Toolbox (<https://mrirecon.github.io/bart/>).<sup>17</sup> A nonlinear parallel imaging and CS reconstruction were performed using a total variation sparsifying operator in time as previously described.<sup>16</sup>

### **Flow Phantom**

A flow phantom was constructed, consisting of two merging plastic tubes surrounded by water (On-line Fig 1). Table salt (~20 g/L) was added to the water to improve  $B_1$  field homogeneity. The inlets were connected to a custom-made MR imaging-compatible mechanical pulsatile pump placed on the scanner table. A linear actuator, in the form of a servo motor (CM2-X-56B20A; MUSCLE CORPORATION) coupled to a ball screw actuator (VLACT55-12-0150; THK CO., LTD.), was used to produce a pulsatile flow (peak flow rate, 2 mL/s; pump output, 0.175 L/min; heart rate, 57 beats per minute). The pump software provided a trigger signal to the MR imaging system for retrospective binning. The flow phantom was scanned at the National 7T Facility, Lund, Sweden.

At both inlets as well as the outlet, 2D flow MR imaging was acquired and considered as a reference (spatial resolution,  $0.3 \times 0.3 \times 3.0 \text{ mm}^3$ ; temporal resolution, 26.0 ms). The 2D flow scans were performed at the beginning and end of the experiment to verify flow stability. Two 4D flow scans were obtained with sensitivity encoding (SENSE) with an acceleration factor  $R = 3$  (spatial resolution, 0.5 mm isotropic; temporal resolution, 65.8–87.7 ms). Moreover, six PROUD 4D flow scans were obtained with nominal acceleration factors of  $R = 4, 8, 12, 16, 32$  (spatial resolution, 0.5 mm isotropic). These scans were reconstructed in 15 different combinations of effective acceleration factors and number of cardiac frames ( $N_{\text{card}}$ ) (temporal resolution, 26.3–87.7 ms). Detailed scan parameters are listed in the On-line Table. All measurements were performed in the same session without interrupting the flow in the phantom.

### **Healthy Subjects**

Fifteen healthy subjects (9 men/6 women; mean age,  $25.4 \pm 1.2$  years) were included in the study. Ethical approval was obtained at the Regional Ethical Review Board in Lund, Sweden, or waived by the local ethics committee of the Amsterdam University Medical Centers, University of Amsterdam, Amsterdam, the Netherlands. Written informed consent was provided by all subjects.

After scout scans to locate the intracranial arteries in the circle of Willis, five blocks of flow MR imaging scans were performed in a randomized order per subject: 1) SENSE 4D flow, 2) PROUD 4D flow, 3) PROUD 4D flow rescan, 4) 2D flow, and 5) 2D flow rescan. The 4D flow scans (spatial resolution, 0.5 mm isotropic) were placed in a transversal plane to include the greatest possible part of the vasculature. The 2D flow scans were placed in a sagittal plane orthogonal to both left and right middle cerebral arteries and were considered as the reference for flow measurements (spatial resolution,  $0.5 \times 0.5 \times 3.0 \text{ mm}^3$ ; mean temporal resolution,  $31.3 \pm 0.6 \text{ ms}$ ;  $N_{\text{card}} = 30$ ). The PROUD 4D flow scans were reconstructed with three different numbers of cardiac frames ( $N_{\text{card}} = 7, 15, 30$ ), resulting in different mean temporal resolutions ( $134.0 \pm 2.7 \text{ ms}$ ,  $62.6 \pm 1.2 \text{ ms}$ ,  $31.3 \pm 0.6 \text{ ms}$ ) and mean acceleration factors  $R = 5.7 \pm 0.1$ ,  $10.6 \pm 0.2$ ,  $19.9 \pm 0.3$ , respectively. The SENSE 4D flow



scans were reconstructed into 7 cardiac frames. Detailed scan parameters are shown in the On-line Table.

### Patients with Unruptured Intracranial Aneurysms

Five patients with UIAs (2 men/3 women; mean age, 63.1  $\pm$  3.6 years) were scanned. Subjects provided written informed consent before the start of the study, which was approved by the local ethics committee of the Amsterdam University Medical Centers, University of Amsterdam, Amsterdam, the Netherlands.

A PROUD 4D flow scan was added to the examination protocol with a scan time of around 10 minutes. These scans were reconstructed with  $N_{\text{card}} = 10, 30$  and  $R = 9.9 \pm 0.2, 26.1 \pm 0.6$ , respectively (spatial resolution, 0.5 mm isotropic; mean temporal resolution,  $94.7 \pm 3.6$  and  $31.6 \pm 1.2$  ms). Detailed scan parameters are shown in the On-line Table.

### Flow Analysis

Quantitative flow analysis was performed using Segment,<sup>18</sup> Version 2.2 (Medviso; <http://medviso.com/>).

**Flow Phantom.** All 4D flow MR imaging scans were resliced to the positions of the three 2D flow MR imaging scans (outlet, inlet right, and inlet left). A ROI was drawn on the cross-section of each tube, and these ROIs were copied to all datasets. Background phase correction was performed by defining a donut-shaped region as static tissue around the actual ROI. 4D flow scans were compared with the 2D flow scans, and mean differences over the three ROIs were measured of the peak flow rate, systolic stroke volume, and diastolic flow rate standard error. The systolic part (half of a cardiac cycle) was used for flow quantification, and the diastolic part for diastolic flow rate standard error calculation.

The 2D flow MR imaging scans were analyzed for repeatability by comparing the scan and rescan values.

**Healthy Subjects.** All 4D flow MR imaging scans were resliced to the positions of the two 2D flow MR imaging scans. ROIs were drawn on the cross-section of both MCAs in every dataset. Background phase correction was performed as in the flow phantom experiment. The first 4D flow MR imaging scans were compared with the first 2D flow MR imaging scan in peak flow rate, stroke volume, and the pulsatility index. The pulsatility index was calculated as the difference between the cross-sectional mean velocities at systole/maximum and diastole/minimum velocity divided by the mean velocity over the cardiac cycle.<sup>19</sup> Repeatability of the 2D flow MR imaging scan and the PROUD 4D flow MR imaging scan was analyzed by comparing the scan/rescan variability.

**Patients with UIAs.** The PROUD 4D flow MR imaging scans were postprocessed into a phase-contrast MRA,<sup>20</sup> which was used with the magnitude images to segment the intracranial vasculature and the aneurysms. WSS was calculated using in-house-developed software<sup>21</sup> in Matlab R2016a by multiplying the wall shear rate by the dynamic viscosity of blood ( $3.2 \times 10^{-3}$  Pa·s). We performed two types of WSS calculations: WSS calculated at peak systole ( $WSS_{\text{PS}}$ ) and time-averaged WSS ( $WSS_{\text{TA}}$ ), in which the WSS is expressed as the average over the cardiac cycle. The  $WSS_{\text{TA}}$ ,  $WSS_{\text{PS}}$ , and OSI were calculated for five patients with UIAs and expressed as the

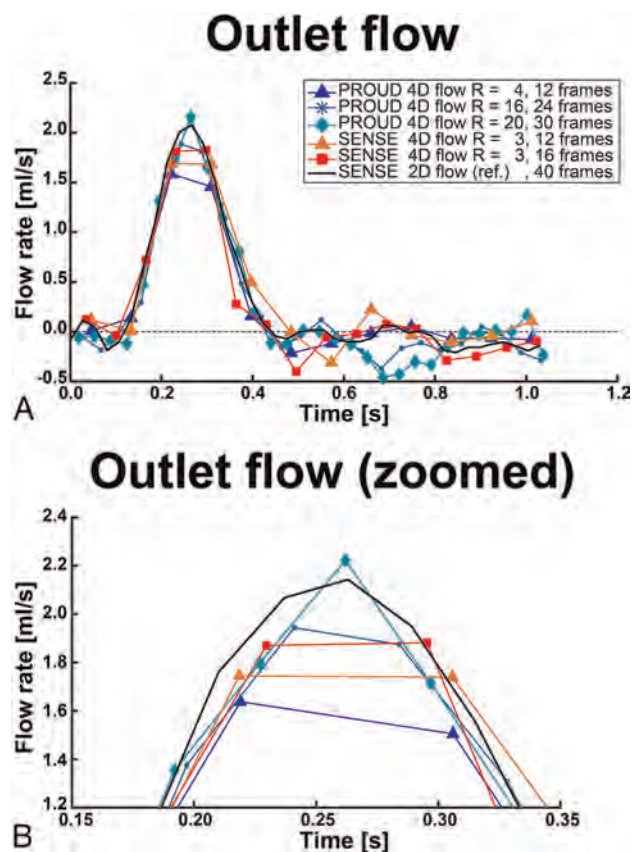


**FIG 1.** A, Flow rates of the outlet ROI of exemplary low (12 frames), moderate (16–24 frames), and high temporal resolution (30–40 frames). B, Zoomed view into the peak flow rate of the outlet ROI.

spatial mean value over the two ROIs: UIA only or surrounding vessel. Streamline flow visualizations of the aneurysms were made in GTFlow, Version 3.2.4 (GyroTools).

**Statistical Analysis.** Differences between two flow scans (A and B) were tested by orthogonal regression analysis and Spearman rank  $\rho$  as well as Bland-Altman plots ( $X = A, Y = A - B$ ). Bland-Altman results were presented as the bias or mean difference  $\pm$  standard error of the mean and limits of agreement. A Wilcoxon signed rank test was used for statistical evaluations with a  $P < .05$  level of significance.

## RESULTS

### Flow Phantom

Flow phantom measurements showed good accuracy even at high acceleration factors (peak flow rate difference,  $<10\%$ ). The best trade-off between acceleration and flow rate error was obtained for  $R = 20\text{--}30$  and  $N_{\text{card}} \geq 30$ . For a small peak flow rate error, at least 30 cardiac frames were needed.

Flow rates measured at the outlet ROI for low, moderate, and high temporal resolution are depicted in Fig 1. The differences between 2D flow and 4D flow MR imaging (2D flow – 4D flow) over all ROIs and scan sequences are listed in Table 1, and more flow rates are shown in On-line Fig 2.

Compared with 2D flow MR imaging, PROUD 4D flow MR imaging with  $N_{\text{card}} \geq 30$  showed the smallest peak flow rate



**Table 1: Results of the flow phantom analysis in terms of peak flow rate difference, stroke volume difference, and the SD of the diastolic flow**

Sequence	Acceleration Factor	Cardiac Frames	Mean Peak Flow Rate Difference (mL/s) (%)	Mean Stroke Volume Difference (mL) (%)	Mean Diastolic Flow Rate SE (mL/s)
4D PROUD-1	32	12	-0.65 (-46.7%)	-0.036 (-15.3%)	0.028
4D PROUD-2	24	12	-0.52 (-35.0%)	-0.024 (-5.3%)	0.018
4D PROUD-3	16	12	-0.47 (-32.9%)	-0.040 (-14.3%)	0.033
4D PROUD-5	8	12	-0.45 (-31.6%)	-0.031 (-9.4%)	0.035
4D PROUD-4	12	12	-0.36 (-25.5%)	-0.024 (-7.4%)	0.021
4D PROUD-6	4	12	-0.34 (-23.9%)	-0.027 (-10.4%)	0.027
4D SENSE-1	3	12	-0.31 (-22.5%)	-0.007 (-5.2%)	0.047
4D SENSE-2	3	16	-0.27 (-21.5%)	-0.027 (-11.5%)	0.031
4D PROUD-5	16	24	-0.19 (-15.0%)	-0.002 (-3.2%)	0.029
4D PROUD-3	32	24	-0.18 (-13.5%)	-0.013 (-3.7%)	0.029
4D PROUD-6	8	24	-0.17 (-10.4%)	-0.028 (-10.6%)	0.024
4D PROUD-6	24	24	-0.13 (-8.0%)	-0.008 (-0.8%)	0.028
4D PROUD-5	26	40	-0.08 (-8.8%)	-0.011 (-2.0%)	0.027
4D PROUD-4	30	30	-0.06 (-7.8%)	0.005 (-3.3%)	0.022
4D PROUD-6	10	30	0.05 (1.9%)	-0.029 (-12.4%)	0.027
4D PROUD-6	13	40	-0.04 (-2.4%)	-0.031 (-11.4%)	0.024
4D PROUD-5	20	30	-0.03 (-4.3%)	0.003 (-4.9%)	0.034
2D reference-2	2	40	-0.05 (-3.7%)	-0.006 (-3.0%)	0.010
2D reference-1 <sup>a</sup>	2	40	0.00 (0.0%)	0.000 (-0.0%)	0.011

**Note:**—SE indicates standard error.

<sup>a</sup> Used as a comparison baseline.

**Table 2: Results of the healthy subject analysis in terms of peak flow rate difference, peak flow rate repeatability, stroke volume difference, stroke volume repeatability, and pulsatility index difference**

	Comparison Pairs		Bland-Altman			Orthogonal Regression	
	A (Frames)	B (Frames)	Bias	LoA	P	Equation	$\rho$
Peak flow rate difference (mL/s)	2D reference-1 (30)	4D PROUD-1 (30)	0.31 ± 0.13	1.41	.22	y = 1.14x - 0.80	0.67
	2D reference-1 (30)	4D PROUD-1 (15)	0.51 ± 0.13	1.44	.03	y = 1.15x - 1.04	0.66
	2D reference-1 (30)	4D PROUD-1 (7)	0.76 ± 0.13	1.44	<.01	y = 0.90x - 0.42	0.60
	2D reference-1 (30)	4D SENSE (7)	0.79 ± 0.17	1.81	.01	y = 0.83x - 0.19	0.36
Peak flow rate repeatability (mL/s)	4D PROUD-1 (30)	4D PROUD-2 (30)	0.14 ± 0.08	0.90	.61	y = 0.87x + 0.28	0.87
	4D PROUD-1 (15)	4D PROUD-2 (15)	0.12 ± 0.08	0.87	.90	y = 0.84x + 0.37	0.88
	4D PROUD-1 (7)	4D PROUD-2 (7)	0.09 ± 0.07	0.71	.77	y = 0.90x + 0.17	0.89
	2D reference-1 (30)	2D reference-2 (30)	0.19 ± 0.08	0.86	.38	y = 1.01x - 0.23	0.86
Stroke volume difference (mL)	2D reference-1 (30)	4D PROUD-1 (30)	0.11 ± 0.09	0.94	.53	y = 0.99x - 0.08	0.64
	2D reference-1 (30)	4D PROUD-1 (15)	0.11 ± 0.09	0.94	.45	y = 0.97x - 0.04	0.64
	2D reference-1 (30)	4D PROUD-1 (7)	0.14 ± 0.09	0.93	.36	y = 0.95x - 0.03	0.64
	2D reference-1 (30)	4D SENSE (7)	0.15 ± 0.11	1.18	.36	y = 1.06x - 0.29	0.46
Stroke volume repeatability (mL)	4D PROUD-1 (30)	4D PROUD-2 (30)	0.08 ± 0.04	0.43	.57	y = 0.98x - 0.05	0.93
	4D PROUD-1 (15)	4D PROUD-2 (15)	0.08 ± 0.04	0.42	.60	y = 0.98x - 0.04	0.92
	4D PROUD-1 (7)	4D PROUD-2 (7)	0.07 ± 0.04	0.44	.64	y = 1.00x - 0.08	0.92
	2D reference-1 (30)	2D reference-2 (30)	0.06 ± 0.04	0.47	.80	y = 1.10x - 0.28	0.92
Pulsatility index difference (a.u.)	2D reference-1 (30)	4D PROUD-1 (30)	0.01 ± 0.04	0.39	.41	y = 1.97x - 0.82	0.15
	2D reference-1 (30)	4D PROUD-1 (15)	0.18 ± 0.04	0.39	<.01	y = 1.51x - 0.60	0.10
	2D reference-1 (30)	4D PROUD-1 (7)	0.31 ± 0.03	0.33	<.01	y = 0.01x + 0.51	0.01
	2D reference-1 (30)	4D SENSE (7)	0.31 ± 0.03	0.35	<.01	y = 0.03x + 0.50	0.02

**Note:**—LoA indicates limits of agreement; a.u., arbitrary units.

underestimation. Furthermore, PROUD 4D flow MR imaging with  $N_{\text{card}} = 24$  underestimated peak flow rate, comparable with conventional SENSE-accelerated 4D flow MR imaging. All PROUD 4D flow scans with  $N_{\text{card}} = 12$  underestimated peak flow rate to a greater extent than 4D flow scans with  $N_{\text{card}} = 24$ . Stroke volume differences had no clear trend over the temporal resolutions, and the error was never higher than 15%. Diastolic flow rate standard error showed higher signal variation for the 4D flow than the 2D flow scans, but no clear trend with acceleration could be observed.

The 2D flow MR imaging repeatability analysis showed steady pump conditions (Bland-Altman: bias,  $0.002 \pm 0.007$  mL/s; limits of agreement, 0.14 mL/s; regression,  $y = 0.98x + 0.00$ ,  $\rho = 0.99$ ).

### Healthy Subjects

Flow measurements in healthy subjects showed good agreement between highly accelerated ( $R = 20$ ) high temporal resolution 4D flow and 2D flow scans.

Examples of magnitude and phase images of the three 4D flow scans are shown in On-line Fig 3. Image quality was

comparable, but more blurring was visible for high acceleration, particularly in the magnitude images. Peak flow rate differences between 2D flow and 4D flow MR imaging are shown in Table 2 and On-line Fig 4. It can be seen that the flow rate difference decreased for higher temporal resolutions. For  $N_{\text{card}} = 7, 15$ , flow rate difference values were significantly different, but not for  $N_{\text{card}} = 30$ . Orthogonal regression analysis revealed an improved correlation between

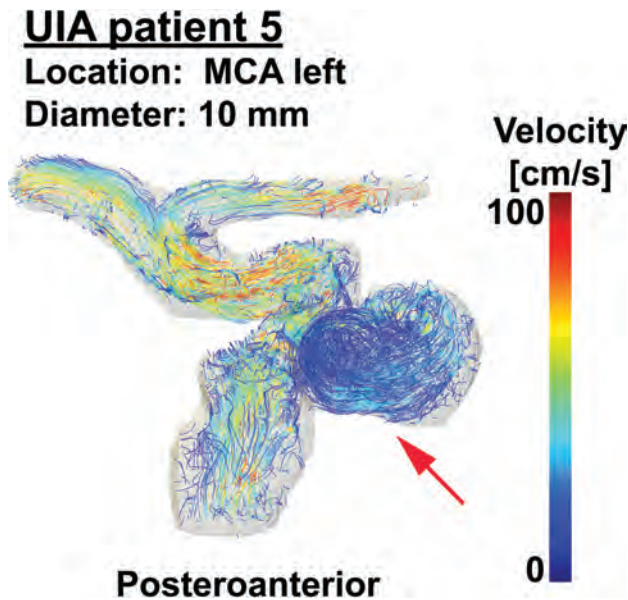


**FIG 2.** Streamlines of patient 5 with an UIA to visualize blood flow patterns in the aneurysm (red arrow) of 10-mm diameter located at the left MCA. A video of streamlines of all five patients with UIAs over the cardiac cycle can be seen in the On-line Video. MCA indicates middle cerebral artery.

2D and 4D flow MR imaging when using a higher number of cardiac frames. Similar peak flow rate repeatability (bias and limits of agreement) was observed for PROUD 4D flow compared with the 2D flow scans (Table 2 and On-line Fig 5). No significant differences in stroke volumes were observed for the four 4D flow scans compared with the 2D flow scans (Table 2 and On-line Fig 6). The stroke volume in PROUD 4D flow and 2D flow scans also had similar repeatability (Table 2 and On-line Fig 7). Pulsatility index differences were significant for 4D flow MR imaging with  $N_{\text{card}} = 7, 15$ , compared with the 2D flow MR imaging, but not for 4D flow MR imaging with  $N_{\text{card}} = 30$  (Table 2 and On-line Fig 8). However, the Spearman  $\rho$  did not indicate a high correlation for the pulsatility index between 2D flow and 4D flow MR imaging.

#### Patients with UIAs

The 4D flow MR imaging scans in the patients with UIAs showed a trend toward higher OSI for increased temporal resolution, but a similar trend could not be found in the WSS of all aneurysms.

Vortices were seen in the streamline visualizations for patients 1, 4, and 5 (Fig 2), but not for patients 2 and 3. Streamlines over the cardiac cycle of all patients are visualized in the On-line Video. Visualizations of  $WSS_{TA}$ ,  $WSS_{PS}$ , and OSI of patient 5 for  $N_{\text{card}} = 10, 30$  are shown in Fig 3. With increased temporal resolution, the  $WSS_{PS}$  and the OSI increased as well in some areas of the aneurysm wall. In Fig 4, the mean values of  $WSS_{TA}$ ,  $WSS_{PS}$ , and OSI per UIA are presented as well as the mean values of  $WSS_{TA}$  and  $WSS_{PS}$  of their in- and outflow vessels. In the UIAs of patients 2 and 5 as well as in the vessel in all patients,  $WSS_{PS}$  was higher than  $WSS_{TA}$ , regardless of the temporal resolution. In the UIAs of patients 3 and 5,  $WSS_{TA}$  and  $WSS_{PS}$  were higher for  $N_{\text{card}} = 30$  than for  $N_{\text{card}} = 10$  frames. In the UIAs of

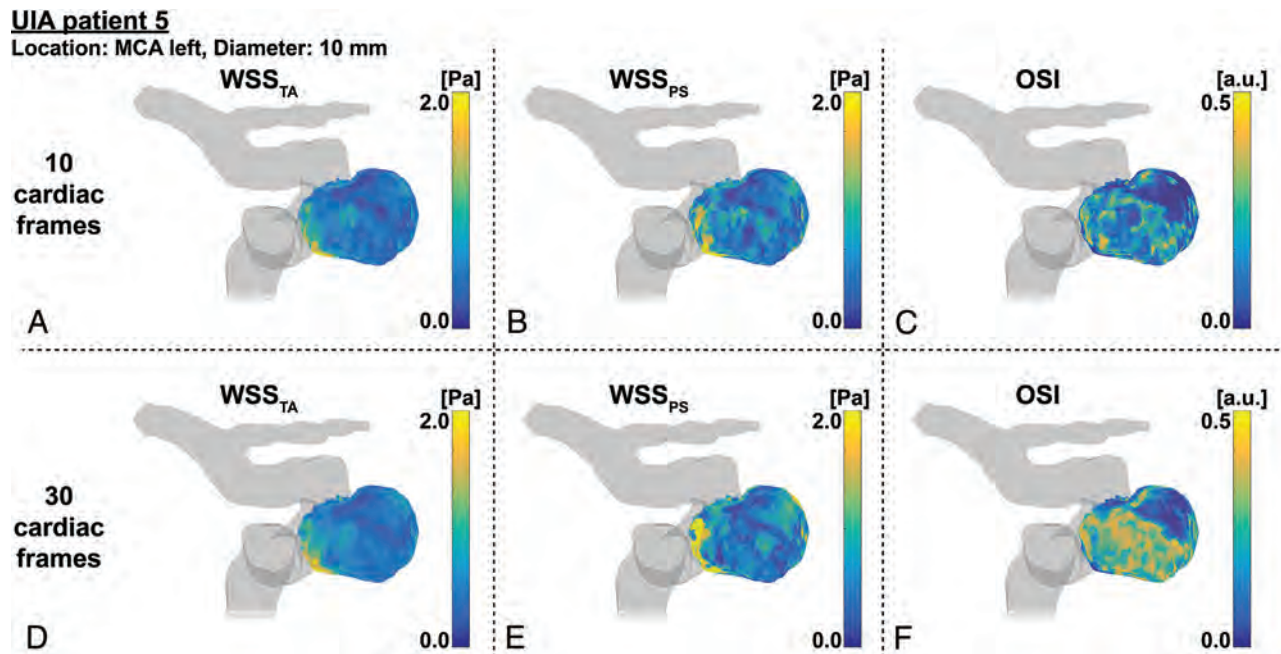


**FIG 3.** Example WSS and OSI analysis of patient 5. Time-averaged WSS on the left, peak-systolic WSS in the middle, and OSI on the right for datasets with either 10 (upper row) or 30 (lower row) cardiac frames. MCA indicates middle cerebral artery; a.u., arbitrary units.

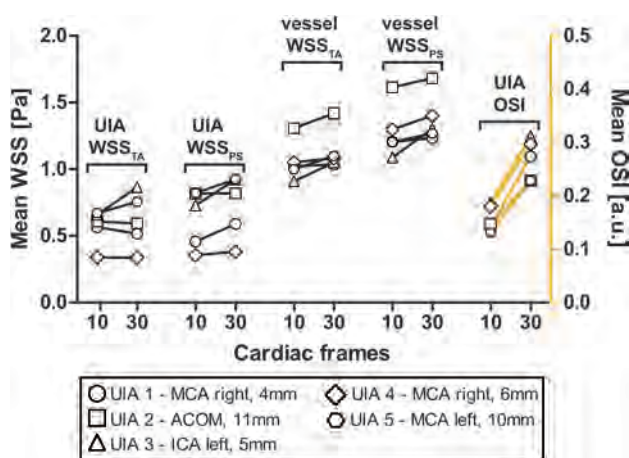


**FIG 4.** The changes in time-averaged WSS, peak systolic WSS, and OSI in the aneurysm and in the surrounding vessel when increasing the temporal resolution from 10 to 30 cardiac frames, or from 95 to 32 ms, respectively. ACOM indicates anterior communicating artery; ICA, internal carotid artery; MCA, middle cerebral artery; a.u., arbitrary units.

patients 1, 2, and 4, no clear difference or trend between the two temporal resolutions was observed. In all UIAs, the OSI was higher for  $N_{\text{card}} = 30$  than for  $N_{\text{card}} = 10$  frames.

## DISCUSSION

This study investigated whether highly accelerated high resolution 4D flow MR imaging in intracranial arteries and aneurysms at 7T can provide reliable quantitative flow values in a clinically acceptable scan time of about 10 minutes using a pseudospiral Cartesian sampling scheme with CS reconstruction. Results showed that stroke volumes and peak flow rate values from 4D flow MR imaging, with  $R = 20$ – $30$  acceleration and a high temporal resolution of 30 cardiac frames, were similar to those obtained with 2D flow MR imaging.

Pulsatile flow phantom experiments were used to investigate the trade-off between scan acceleration and accuracy of flow measurements. The error in the peak flow rate decreased with an increasing number of cardiac frames, and stroke volume was underestimated in an acceptable level even for high temporal resolution ( $<3\times$  difference of 2D rescan). The diastolic flow rate standard error in 4D flow scans showed 2–4 times larger variation than the 2D reference scans, and there was no clear trend observable for changes in acceleration or temporal resolution. Thus, we interpret this finding as acceptable random reconstruction- or undersampling-based artifacts. Taken together, we used  $R = 30$  as maximum acceleration factor for the in vivo scans when reconstructing the data into 30 cardiac frames. In vivo measurements then confirmed that highly accelerated 4D flow MR imaging with a high temporal resolution resulted in small errors compared with 2D flow MR imaging. Furthermore, PROUD 4D flow MR imaging was superior to conventional 4D flow MR imaging, especially for those reconstructed in 30 cardiac frames, which resulted in the lowest peak flow rate difference. When we compared PROUD with conventional 4D flow MR imaging, the flow rate accuracy (peak flow rate difference to 2D

flow MR imaging) was increased by 60%, while both had the same scan duration.

Reduced scan time is important for patients, which is why high acceleration is needed. However, there are only a few reports on acceleration factors above 10, especially at 7T field strength. Comparable high acceleration is only reported for acquisition and reconstruction similar to methods used in this study, which all deal with large multidimensional datasets. Cheng et al<sup>22</sup> reported  $R \approx 19$  for accelerated 4D flow MR imaging in the heart at 3T and also used temporal total variation in the reconstruction. Walheim et al<sup>23</sup> reported  $R = 19$  for accelerated 5D flow MR imaging in the aorta at 3T. Rich et al<sup>24</sup> demonstrated 4D flow imaging of the aortic valve at 1.5T with acceleration up to a factor 27. Gu et al<sup>25</sup> also acquired 4D flow data in the intracranial arteries, but at 1.5T, and reported a usable acceleration up to a factor of 30.

Considering the aneurysm and surrounding intracranial vasculature, two main observations could be made from the derived WSS. First,  $WSS_{PS}$  and  $WSS_{TA}$  as well as OSI in the vessels were higher with increased temporal resolution. Second,  $WSS_{PS}$  was higher than  $WSS_{TA}$  regardless of the temporal resolution. These two observations can be explained by the increased peak flow rate accuracy observed in the phantom experiment and healthy subjects. Measured WSS in the aneurysms was lower than in the surrounding intracranial vasculature, which is in line with previous results.<sup>26</sup> Increased temporal resolution resulted in increased OSI in all aneurysms, which has also been reported previously.<sup>12</sup> Most interesting, increased temporal resolution resulted in increased WSS in only two aneurysms but rather constant WSS in three aneurysms. Moreover,  $WSS_{PS}$  was higher than  $WSS_{TA}$  in only two aneurysms. Thus, we did not observe a clear trend for the WSS in the aneurysms. A likely explanation can be found in the differences in size and geometry of the aneurysms; for a UIA with low and constant flow, the improved temporal resolution will not change WSS estimations.<sup>26</sup> For cases of complex flow patterns, this finding suggests that flow and WSS estimations in aneurysms will benefit from the improved temporal resolution provided by our accelerated protocols. We will pursue studies in larger cohorts of patients to further investigate the added value of high temporal resolution WSS in aneurysm rupture risk predictions.

Previous studies on WSS do not agree on which WSS calculation method should be used,<sup>4,13,26–28</sup> but temporal fluctuations in WSS were associated with aneurysm risk of growth or formation.<sup>11,27</sup> Thus, indicators like the OSI<sup>11</sup> or the aneurysm formation indicator<sup>27</sup> were developed to express these temporal fluctuations in WSS. Most of these models use a reference vector, commonly the time-averaged WSS vector, based on the assumption that the endothelial cells are preferentially aligned in the direction of this vector.<sup>27</sup> When one uses these metrics, it is likely that a higher temporal resolution will give a more accurate outcome of temporal fluctuations in WSS.

A possible key application for high temporal resolution 4D flow MR imaging data is the combination of 4D flow MR imaging with computational fluid dynamics simulations, which have been shown to be a useful clinical tool for the prediction of the



initiation, growth, and rupture of aneurysms.<sup>13,26</sup> Prior research combining fluid dynamics and 4D flow showed better agreement than calculations alone.<sup>4,29</sup> MR imaging-guided computational fluid dynamics can be used to correct the MR imaging-measured flow field, forcing it to satisfy the fluid mechanics equations. It can also be used as a means of reducing imperfections in the 4D flow MR imaging measurements and may improve the ability to accurately derive clinically relevant secondary parameters such as WSS and pressure gradients at a much higher level of detail and confidence than was previously possible.<sup>29,30</sup>

Because highly accelerated 4D flow MR imaging with high temporal resolution provided reliable quantitative flow values, we encourage using 4D flow MR imaging more often for UIA monitoring and growth prediction in future clinically focused studies.<sup>6,26</sup> The techniques must be investigated in a larger study of patients with UIAs to determine whether the derived WSS is affected by either the calculation method or the temporal resolution or both. If it turns out that high temporal resolution does not add any value for clinical outcome, then the acceleration of the 4D flow MR imaging scan can be used to improve coverage and resolution or to further shorten the scan duration. Eventually, a consensus on 4D flow MR imaging followed by WSS calculation and analysis for intracranial aneurysm is desirable.

### Limitations

A more complex phantom could mimic the intracranial arteries and their flow distribution better. Moreover, a pump with combined systolic pulsatile and diastolic steady flow could reduce the signal variation during the diastolic period. Furthermore, temporal fluctuations in WSS or OSI are sensitive to deviations induced by high acceleration. This limitation might be reduced when combining 4D flow MR imaging with computational fluid dynamics, which performs well in de-noising and preserving details in the velocity profiles. Finally, the study population to investigate the effect of increased temporal resolution for WSS calculations in patients with UIAs was too small to draw a significant conclusion.

### CONCLUSIONS

Highly accelerated high spatiotemporal resolution 4D flow MR imaging in intracranial arteries and aneurysms at 7T provides repeatable quantitative flow values in a clinically acceptable scan time of ~10 minutes, using pseudospiral Cartesian sampling with compressed sensing reconstruction. In vivo measurements showed that the accuracy of the flow rate was significantly increased compared with conventional low temporal resolution 4D flow scans. Data from patients with unruptured intracranial aneurysms show that the improved temporal resolution influences the oscillatory shear index.

### ACKNOWLEDGMENT

We would like to thank Eva L. Leemans and Bart M.W. Cornelissen for the collection of the patient data, which was funded by the Stichting Toegepast Wetenschappelijk Instituut voor Neuromodulatie.

grant 13928. The Foundation for the Technical Sciences (Stichting voor de Technische Wetenschappen) is a Dutch foundation that was founded in 1981 and aims to realize the transfer of knowledge between technical sciences and users. To this end, Stichting voor de Technische Wetenschappen brings researchers and potential users together and finances technical-scientific research.\* \*Money paid to the institution.

### REFERENCES

- Steiner T, Juvela S, Unterberg A, et al. **European stroke organization guidelines for the management of intracranial aneurysms and subarachnoid haemorrhage.** *Cerebrovasc Dis* 2013;35:93–112 CrossRef Medline
- Thompson BG, Brown RD, Amin-Hanjani S, et al; American Heart Association Stroke Council, Council on Cardiovascular and Stroke Nursing, and Council on Epidemiology and Prevention; American Heart Association; American Stroke Association. **Guidelines for the management of patients with unruptured intracranial aneurysms.** *Stroke* 2015;46:2368–2400 CrossRef Medline
- Markl M, Frydrychowicz A, Kozerke S, et al. **4D flow MRI.** *J Magn Reson Imaging* 2012;36:1015–36 CrossRef Medline
- van Ooij P, Potters WV, Guédon A, et al. **Wall shear stress estimated with phase contrast MRI in an in vitro and in vivo intracranial aneurysm.** *J Magn Reson Imaging* 2013;38:876–84 CrossRef Medline
- Coolen BF, Calcagno C, van Ooij P, et al. **Vessel wall characterization using quantitative MRI: what's in a number?** *MAGMA* 2018;31:201–22 CrossRef Medline
- Boussel L, Rayz V, McCulloch C, et al. **Aneurysm growth occurs at region of low wall shear stress: patient-specific correlation of hemodynamics and growth in a longitudinal study.** *Stroke* 2008;39:2997–3002 CrossRef Medline
- Chung BJ, Mut F, Putman CM, et al. **Identification of hostile hemodynamics and geometries of cerebral aneurysms: a case-control study.** *AJNR Am J Neuroradiol* 2018;39:1860–66 CrossRef Medline
- Blankena R, Kleinloog R, Verweij BH, et al. **Thinner regions of intracranial aneurysm wall correlate with regions of higher wall shear stress: a 7T MRI study.** *AJNR Am J Neuroradiol* 2016;37:1310–17 CrossRef Medline
- Cebral JR, Detmer F, Chung BJ, et al. **Local hemodynamic conditions associated with focal changes in the intracranial aneurysm wall.** *AJNR Am J Neuroradiol* 2019;40:510–16 CrossRef Medline
- van Ooij P, Zwanenburg JJM, Visser F, et al. **Quantification and visualization of flow in the circle of Willis: time-resolved three-dimensional phase contrast MRI at 7 T compared with 3 T.** *Magn Reson Med* 2013;69:868–76 CrossRef Medline
- Ku DN, Giddens DP, Phillips DJ, et al. **Hemodynamics of the normal human carotid bifurcation: in vitro and in vivo studies.** *Ultrasound Med Biol* 1985;11:13–26 Medline
- Cibis S, Potters WV, Gijzen FJ, et al. **The effect of spatial and temporal resolution of cine phase contrast MRI on wall shear stress and oscillatory shear index assessment.** *PLoS One* 2016;11:e0163316–15 CrossRef Medline
- Boussel L, Rayz V, Martin A, et al. **Phase-contrast magnetic resonance imaging measurements in intracranial aneurysms in vivo of flow patterns, velocity fields, and wall shear stress: comparison with computational fluid dynamics.** *Magn Reson Med* 2009;6:409–17 CrossRef Medline
- Lustig M, Donoho D, Pauly JM. **Sparse MRI: The application of compressed sensing for rapid MR imaging.** *Magn Reson Med* 2007;58:1182–95 CrossRef Medline
- Peper ES, Gottwald LM, Zhang Q, et al. **Highly accelerated 4D flow cardiovascular magnetic resonance using a pseudo-spiral Cartesian acquisition and compressed sensing reconstruction for carotid flow and wall shear stress.** *J Cardiovasc Magn Reson* 2020;22:7 CrossRef Medline
- Gottwald LM, Peper ES, Zhang Q, et al. **Pseudo-spiral sampling and compressed sensing reconstruction provides flexibility of temporal resolution in accelerated aortic 4D flow MRI: a comparison with**

Disclosures: Lukas M. Gottwald—RELATED: Grant: Stichting voor de Technische Wetenschappen, Comments: Stichting voor de Technische Wetenschappen,



- K-T principal component analysis. *NMR Biomed* 2020;33:e4255 CrossRef Medline
17. Uecker M, Ong F, Tamir JJ, et al. **Berkeley advanced reconstruction toolbox.** In: *Proceedings of the International Society for Magnetic Resonance in Medicine*, May 30 to June 5, 2015; Toronto, Ontario, Canada; 2486
  18. Heiberg E, Sjögren J, Ugander M, et al. **Design and validation of Segment: freely available software for cardiovascular image analysis.** *BMC Med Imaging* 2010;10:1 CrossRef Medline
  19. Bouvy WH, Geurts LJ, Kuijff HJ, et al. **Assessment of blood flow velocity and pulsatility in cerebral perforating arteries with 7-T quantitative flow MRI.** *NMR Biomed* 2016;29:1295–1304 CrossRef Medline
  20. Bock J, Frydrychowicz A, Stalder AF, et al. **4D phase contrast MRI at 3 T: effect of standard and blood-pool contrast agents on SNR, PC-MRA, and blood flow visualization.** *Magn Reson Med* 2010;63:330–38 CrossRef Medline
  21. Potters WV, van Ooij P, Marquering H, et al. **Volumetric arterial wall shear stress calculation based on cine phase contrast MRI.** *J Magn Reson Imaging* 2015;41:505–16 CrossRef Medline
  22. Cheng JY, Hanneman K, Zhang T, et al. **Comprehensive motion-compensated highly accelerated 4D flow MRI with ferumoxytol enhancement for pediatric congenital heart disease.** *J Magn Reson Imaging* 2016;43:1355–68 CrossRef Medline
  23. Walheim J, Dillinger H, Kozerke S. **Multipoint 5D flow cardiovascular magnetic resonance - accelerated cardiac- and respiratory-motion resolved mapping of mean and turbulent velocities.** *J Cardiovasc Magn Reson* 2019;21:42 CrossRef Medline
  24. Rich A, Potter LC, Jin N, et al. **A Bayesian model for highly accelerated phase-contrast MRI.** *Magn Reson Med* 2016;76:689–701 CrossRef Medline
  25. Gu T, Korosec FR, Block WF, et al. **PC VIPR: a high-speed 3D phase-contrast method for flow quantification and high-resolution angiography.** *AJNR Am J Neuroradiol* 2005;26:743–49 Medline
  26. Shojima M, Oshima M, Takagi K, et al. **Magnitude and role of wall shear stress on cerebral aneurysm: computational fluid dynamic study of 20 middle cerebral artery aneurysms.** *Stroke* 2004;35:2500–05 CrossRef Medline
  27. Mantha A, Karmonik C, Benndorf G, et al. **Hemodynamics in a cerebral artery before and after the formation of an aneurysm.** *AJNR Am J Neuroradiol* 2006;27:1113–18 Medline
  28. Schnell S, Wu C, Ansari SA. **Four-dimensional MRI flow examinations in cerebral and extracerebral vessels: ready for clinical routine?** *Curr Opin Neurol* 2016;29:19–28 CrossRef Medline
  29. Töger J, Zahr MJ, Aristokleous N, et al. **Blood flow imaging by optimal matching of computational fluid dynamics to 4D-flow data.** *Magn Reson Med* 2020 Apr 8. [Epub ahead of print] CrossRef Medline
  30. Bakhshinejad A, Baghaie A, Vali A, et al. **Merging computational fluid dynamics and 4D-Flow MRI using proper orthogonal decomposition and ridge regression.** *J Biomech* 2017;58:162–73 CrossRef Medline

# Cervicofacial Venous Malformations Are Associated with Intracranial Developmental Venous Anomalies and Dural Venous Sinus Abnormalities

W. Brinjikji, I.T. Mark, V.M. Silvera, and J.B. Guerin



## ABSTRACT

**BACKGROUND AND PURPOSE:** Prior studies have suggested an association between the presence of cervicofacial venous malformations and intracranial developmental venous anomalies. We reviewed our institutional cohort of patients with cervicofacial venous malformations and examined the spectrum of intracranial venous anomalies, including developmental venous anomalies, cavernous malformations, and dural venous sinus abnormalities.

**MATERIALS AND METHODS:** Consecutive patients who presented to our institution with cervicofacial venous malformations and underwent postcontrast MR imaging were studied. Three neuroradiologists reviewed brain MRIs for the presence of developmental venous anomalies, dural venous sinus ectasia, and cavernous malformations. The prevalence of developmental venous anomalies in this patient population was compared with an age- and sex-matched control group without venous malformations at a ratio of 1:2. Categorical variables were compared with  $\chi^2$  tests.

**RESULTS:** Sixty-three patients with venous malformations met the inclusion criteria with a mean age of  $38.3 \pm 24.0$  years. The overall presence of developmental venous anomalies in patients with venous malformations was 36.5% (23/63) compared with 7.9% (10/126) in controls ( $P < .001$ ). The prevalence of dural venous sinus ectasia was 9.5% (6/63) compared with 0% for controls ( $P = .002$ ). One patient with a venous malformation had a cavernous malformation compared with 1 patient in the control group ( $P = .62$ ). In 73.9% of patients (17/23), developmental venous anomalies were along the same metamere; and in 82.6% of patients, developmental venous anomalies were ipsilateral to the venous malformations.

**CONCLUSIONS:** Our case-control study demonstrated a significant association between cervicofacial venous malformations and cerebral developmental venous anomalies as well as between cervicofacial venous malformations and dural venous sinus abnormalities. Our findings suggest that venous malformations may be the result of a segmental in utero insult to cells involved in cerebrofacial venous development.

**ABBREVIATIONS:** CVMS = cerebrofacial venous metamerism syndrome; DVA = developmental venous anomaly; VM = venous malformation

Venous malformations (VMs) are slow-flow vascular malformations characterized by soft-tissue swelling and bluish skin discoloration. Pathologic studies have found that these lesions consist of dilated venous channels in the soft tissues which, in the face and neck, generally drain into the external jugular system.<sup>1</sup> While the pathogenesis of these lesions is unclear, genetic studies suggest that most of these lesions are due to somatic mutations in either the *TEK receptor tyrosine kinase (TEK)* or

*phosphatidylinositol-4,5-bisphosphate 3-kinase catalytic subunit alpha (PIK3CA)* gene pathways.<sup>2,3</sup>

Several recent studies have demonstrated an association between VMs and intracranial venous anomalies, specifically developmental venous anomalies (DVAs). The Toronto Western Hospital group found that patients with VMs were 3 times more likely to have DVAs compared with age-matched controls.<sup>1</sup> This association makes sense from a pathophysiologic point of view because somatic mutations affecting venous endothelial progenitor cells could presumably affect the cerebral venous system if they occur before cell migration (Fig 1).<sup>4</sup> This mechanism is proposed for metamerism disorders such as cerebrofacial arteriovenous metamerism syndrome, cerebrofacial venous metamerism syndrome (CVMS), and spinal arteriovenous metamerism syndrome.<sup>5</sup> Recently, our group observed that a subset of patients with VMs also have abnormalities affecting the dural venous

Received January 11, 2020; accepted after revision April 23.

From the Departments of Radiology (W.B., I.T.M., V.M.S., J.B.G.), and Neurosurgery (W.B.), Mayo Clinic, Rochester, Minnesota.

Please address correspondence to Waleed Brinjikji, MD, Department of Radiology, Mayo Clinic, 200 1st St SW, Rochester, MN 55905; e-mail: brinjikji.waleed@mayo.edu

<http://dx.doi.org/10.3174/ajnr.A6617>

# Cerebrofacial Venous Metameric Syndrome Classification (CVMS)

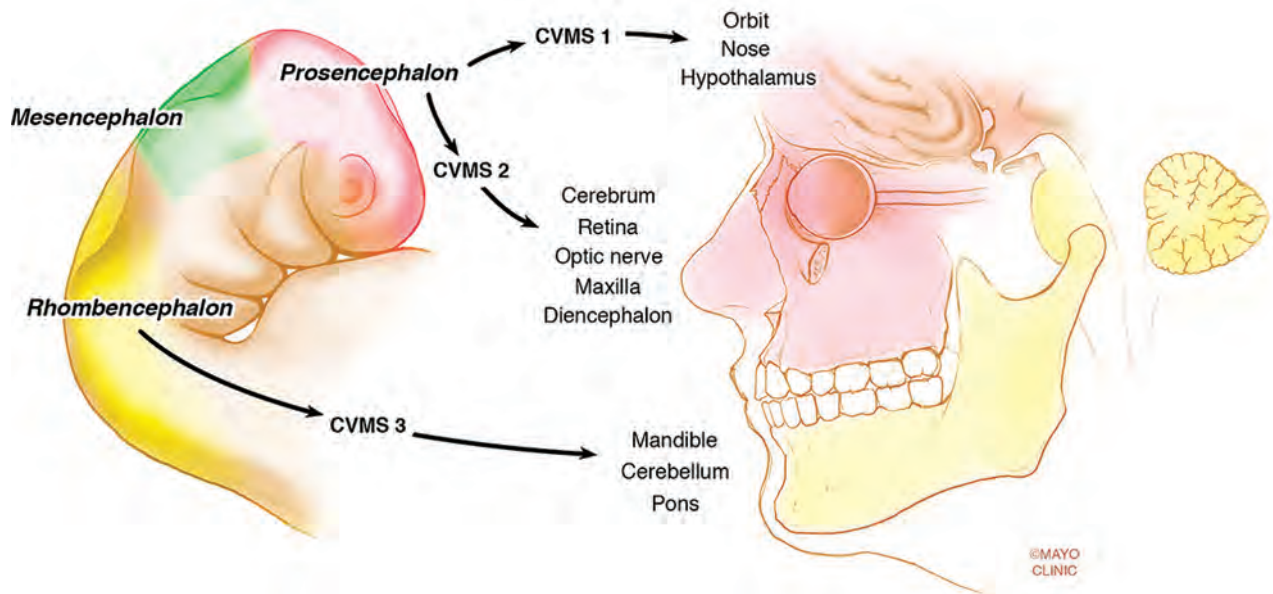


**FIG 1.** Demonstration of the metameric distribution of somatic mutations affecting venous endothelial progenitor cells that could presumably affect the cerebral venous system if they occur before cell migration. Reprinted with permission of the Mayo Foundation for Medical Education and Research. All rights reserved.

sinuses, including the presence of a persistent falcine sinus and persistent ballooning of the torcula.

To study the association between VMs and intracranial venous anomalies, including DVAs and dural venous sinus abnormalities, we performed a case-control study examining the prevalence of these findings in a consecutive cohort of patients with VMs and compared this cohort with a group of age- and sex-matched controls.

## MATERIALS AND METHODS

### Patient Population

Following institutional review board approval, we queried our data base of patients with VMs who had presented to our institution during the past 5 years and included patients who had brain or face MRIs with postcontrast T1-weighted imaging. At our institution, patients with VMs routinely undergo MRIs of the brain and face with and without intravenous contrast. VMs were confirmed by a combination of physical examination and imaging-based findings through our multidisciplinary Vascular Anomalies Clinic.<sup>6,7</sup> Imaging findings strongly suggestive of a VM on MR imaging were the following: 1) a septate lobulated mass that was hyperintense on T2-weighted and hypointense on T1-weighted images without mass effect; 2) phleboliths, which are characteristically hypointense on T1- and T2-weighted sequences; 3) the presence of fluid-fluid levels; 4) the absence of vascular flow voids on spin-echo sequences; 5) infiltration of the lesion through tissue planes; 6) the absence of arterial or early venous enhancement; and 7) the presence of diffuse enhancement on delayed images. On clinical examination, VMs generally

appeared as faint blue, soft, and easily compressible, nonpulsatile masses that enlarged with the Valsalva maneuver in dependent positions and were compressible with application of local pressure.

Both pediatric and adult patients with VMs were included in this study. We also selected a group of age- and sex-matched controls (case/control ratio of 1:2) from an institutional data base that was used to estimate the prevalence of brain DVAs in the general population. The data base consisted of consecutive patients who underwent a contrast-enhanced brain MR imaging during a 2-year period (2016–2017) with the terms “developmental venous anomaly,” “DVA,” “venous angioma,” “venous anomaly,” and “vascular anomaly” in their report, which amounted to examinations of 18,073 individuals. The findings were then confirmed by a single radiologist.

### Imaging Analysis

All imaging was reviewed by 3 radiologists. Images were analyzed for the following findings: 1) the presence of a DVA, 2) deep or superficial drainage of the DVA, 3) location and side of the DVA, 4) the presence of dural venous sinus anomalies including dural ectasia and persistent falcine sinus, and 5) the presence of cavernous malformations. While vascular malformations of the CNS can consist of DVAs, cavernous malformations, or capillary telangiectasias, the latter was not included in this study.<sup>8–10</sup> In addition to intracranial imaging, face and neck MRIs were evaluated for the location and size of the VM. For patients who had both DVAs and VMs, we also reviewed the imaging to determine whether the vascular anomalies occurred along the same



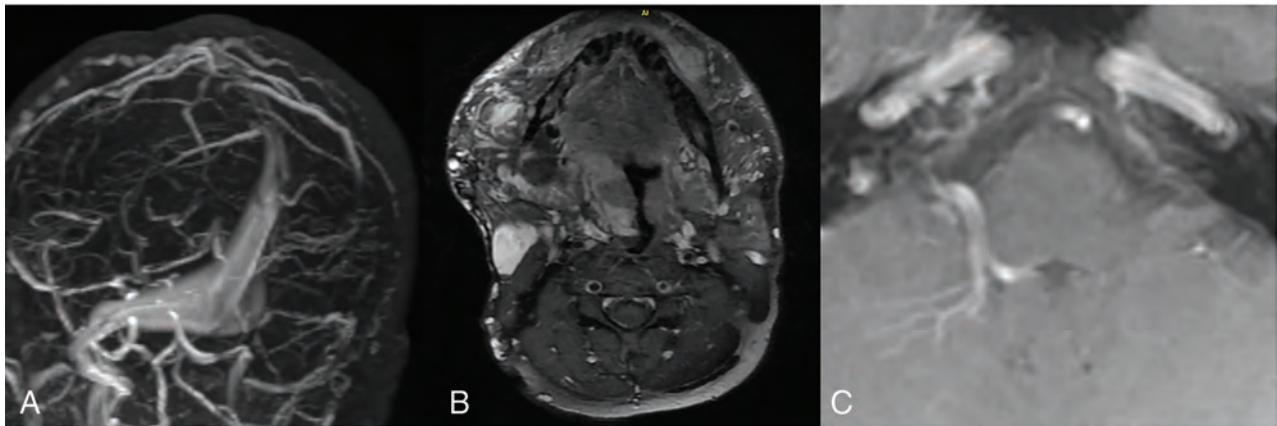


**FIG 2.** A 38-year-old man with a history of large trans-spacial cervicofacial venous malformation causing periodic airway obstruction. A, MRV shows a large and ectatic torcula and medial right transverse sinus. B, Postcontrast T1 MR imaging of the face shows an extensive venous malformation predominantly involving the right face, tongue, and hypopharynx. C, Postcontrast MR imaging shows a DVA in the right cerebellum.

metamere. The 3 metameres of the craniofacial system include the medial prosencephalic group (olfactory) with involvement of the forehead, nose, hypothalamus, corpus callosum, and hypophysis (CVMS 1); the lateral prosencephalic group (optic) with involvement of the temporo-parietal-occipital lobes, optic nerve, retina, thalamus, eye, cheek, and maxilla (CVMS 2); and the rhombencephalic/mesencephalon (otic) group with involvement of the cerebellum, brain stem, lower face, mandible, petrous bone, and maxilla (CVMS 3).<sup>11</sup> Further analysis examined the association between age and the occurrence of malformations.

### Statistical Analysis

The primary outcome of this study was the prevalence of a DVA in the VM population and in controls. Prevalence rates were compared using a  $\chi^2$  test. A separate  $\chi^2$  analysis of DVAs in patients with and without CVMS was performed. A Student *t* test was used to compare continuous variables. All statistical analyses were performed using JMP 13.0 (SAS Institute).

## RESULTS

### Patient and Control Population

We included 63 patients with VMs and 126 controls. The mean age of the VM population was  $38.3 \pm 24.0$  years compared with  $38.3 \pm 23.8$  years for controls; 58.7% of patients in both the VM group (37/63) and non-VM group (74/126) were female. Of the patients in the control group, none had any documentation of a VM in their chart and there was no evidence of VMs or other cutaneous vascular malformations on review of their available brain and face MR imaging examinations. Most of the patients did not have any other CNS diagnosis (88.9%), while a small portion had a diagnosis of migraines (9.5%) and epilepsy (1.6%).

### Venous Malformation Characteristics and Location

In the VM cohort, 22 patients (34.9%) had VMs isolated to the left side of the face, 27 patients (42.9%) had VMs only on the right side of the face, and 14 patients (22.2%) had bilateral VMs. When we categorized VM locations in descending frequency, the most common locations were the masticator space (44%, 28 patients), buccal space (21 patients, 33.3%), lingual space (13

patients (20.6%), orbit (8 patients, 12.7%), posterior oropharynx or hypopharynx (7 patients, 11.1%), posterior neck (7 patients, 11.1%), lip (3 patients, 4.8%), and other (3 patients, 4.8%). There was no association between age and the occurrence of malformations ( $P = .46$ ).

### Prevalence of DVA and DVA Characteristics

Of the 63 patients with VMs, DVAs were present in 36.5% of patients (23/63) compared with 7.9% of controls (10/126,  $P < .001$ ). In 73.9% of cases (17/23), DVAs were along the same metamere, and in 82.6% of cases, DVAs were ipsilateral to the VM. In the cases in which the DVAs and VMs were along the same metamere, 8 had CVMS 3, 4 had CVMS 2, and 5 had CVMS 2 + 3. There was no significant difference in the prevalence of DVAs in patients with or without CVMS ( $P = .22$ ).

In the VM + DVA cohort, 11 patients had 1 DVA and 12 patients had multiple DVAs. In 10 patients, DVAs drained to the superficial venous system; in 7 patients, DVAs drained into the deep venous system; and in 6 patients, DVAs drained into both the superficial and venous systems. DVAs were located on the right side in 10 patients and left side in 7 patients and were bilateral in 6 patients. Fourteen patients had supratentorial DVAs, 5 patients had infratentorial DVAs, and 4 patients had both supratentorial and infratentorial DVAs. One patient had a cavernous malformation associated with a DVA. There was no association between VM location and the presence of DVAs. There was no association between age ( $P = .63$ ) or sex ( $P = .79$ ) and DVAs. Examples of VMs associated with DVAs are provided in Figs 2–5.

### Dural Venous Sinus Abnormalities

On review of brain MRIs, 6 patients with VMs (9.5%) had dural venous sinus abnormalities compared with 0% of controls ( $P = .002$ ). All 6 patients had ectasia of the torcula. In addition, 4 patients had a persistent falcine sinus. There was no association between age and dural venous sinus abnormality ( $P = .46$ ). All patients with dural venous sinus abnormalities also had intracranial DVAs, 4 of which were along the same metamere as the VM. Of the patients with CVMS, 2 had CVMS 2 and 2 had CVMS 2 + 3. Examples are provided in Figs 2, 3, and 5.

## DISCUSSION

Our large series examining the prevalence of cerebral and dural venous abnormalities in patients with VMs demonstrated a number of interesting findings. First, we found that the prevalence of DVAs among patients with VMs was >4 times higher than that in our age- and sex-matched controls. As seen in 1 prior study,

we found that DVAs were along the same metamere in nearly 75% of cases and were ipsilateral to the VM in nearly 80% of cases. One novel finding from our study was that nearly 10% of patients with VMs also have abnormalities associated with the dural venous sinuses, in particular ectasia of the torcula and the presence of a persistent falcine sinus. The findings from our study

are important because they suggest a high likelihood of a common pathway involved in the formation of cervicofacial VMs, intracranial DVAs, and dural venous sinuses.

To date, there has been 1 case-control study examining the association between VMs and DVAs.<sup>1</sup> The Toronto Western Hospital group recently published an article demonstrating a prevalence of DVAs in 28.6% of patients compared with just 9.5% of age- and sex-matched controls. The authors found that in 83.3% of cases, the DVAs were ipsilateral to the VM, and in 75% of cases, the DVAs were along the same metamere. In our series, we found a slightly higher rate of DVAs associated with VMs in a larger patient population, but we found a nearly identical rate of DVAs being ipsilateral or along the same metamere as the VM. The higher rate of DVA detection is likely because only patients with postcontrast MRIs were included in this study. Other series demonstrated or suggested an association between VMs and DVAs. Boukobza et al<sup>12</sup> found that 20% of patients with facial VMs had DVAs on cerebral angiography, with most of these patients having

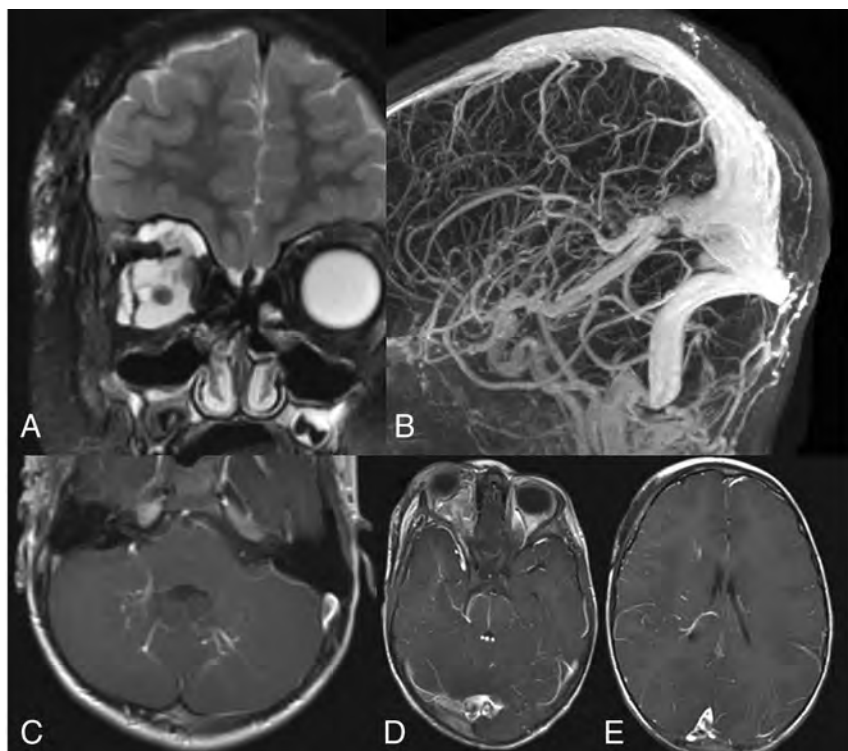


**FIG 3.** A 5-year-old child with history of right orbital venous malformation. A, T2 with fat saturation MR imaging shows a large venous malformation involving the right orbit and face. B, MRV shows a markedly ectatic torcula, which includes the entirety of the straight sinus. C–E, T1 post-contrast MRIs show multiple developmental venous anomalies, including the bilateral cerebellar hemispheres, brain stem, right temporal lobe, and right frontal lobe.

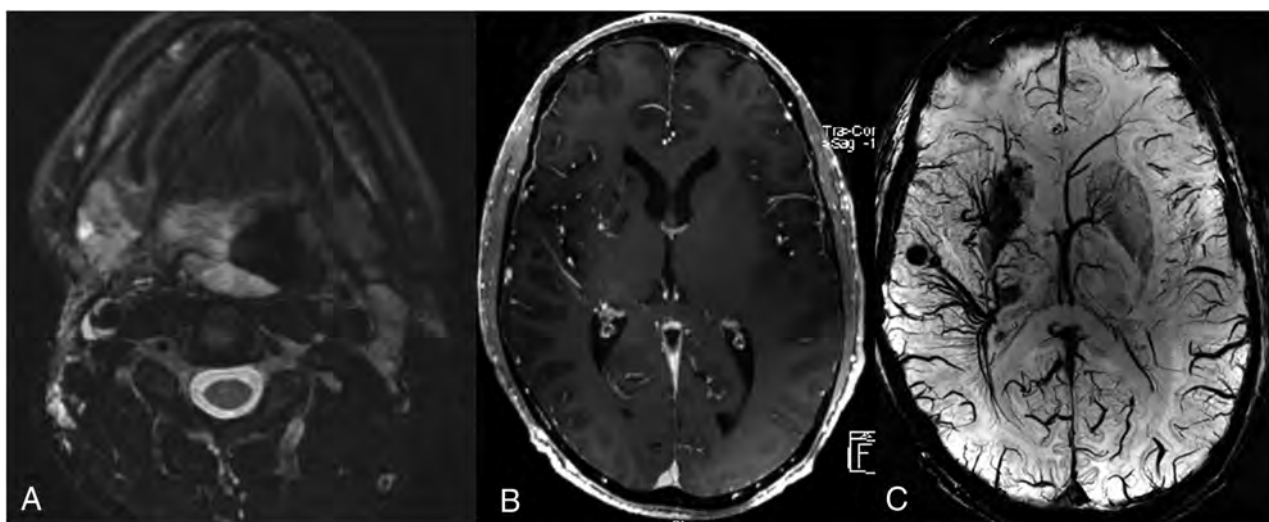


**FIG 4.** A 38-year-old man with extensive airway malformation. A, T2 FS MR imaging shows an extensive venous malformation involving the airway and tongue base. B, Axial postcontrast MR imaging shows extensive DVAs of the right frontal lobe, basal ganglia, and temporal lobe. C, T2 SWI shows the extensive DVAs and multiple cavernomas in the radicles of the DVAs.

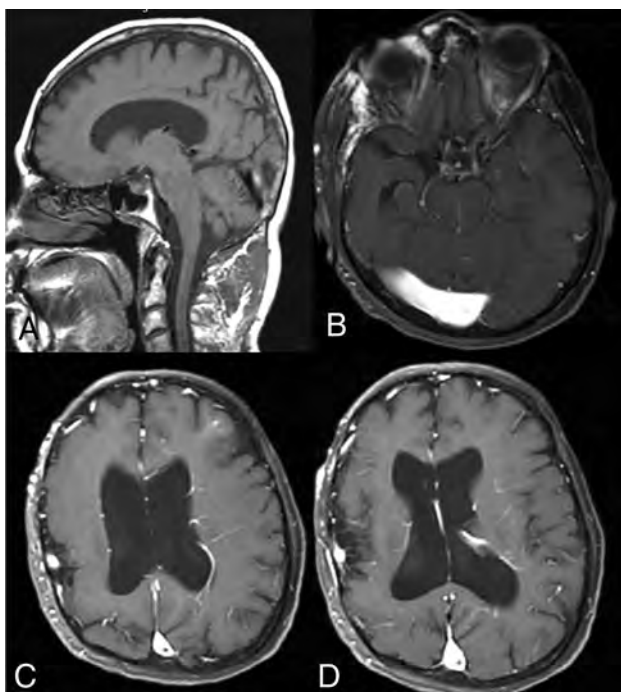


**FIG 5.** A 45-year-old man with developmental delay and bilateral facial VMs (not shown). A, Sagittal T1 MR imaging shows an ectatic torcula, which is also confirmed on axial T1 postcontrast MR imaging (B). C and D, Axial postcontrast MR imaging shows multiple extensive DVAs involving the left cerebral hemisphere. The patient also had polymicrogyria of the right hemisphere.

multiple DVAs. Most of these DVAs were extensive and drained into a tortuous deep venous system, and in most cases, DVAs were ipsilateral to the VM.<sup>12</sup> Several case reports have described patients with extensive facial venous malformations and ipsilateral DVAs.<sup>4,5,11,13-15</sup>

The pathogenesis of DVA is not clear. A number of mechanisms have been proposed for the formation of DVAs. Some authors have postulated that DVAs can form later in cerebral venous development due to functional adaptations to local venous thrombosis or due to failed development of superficial or deep veins.<sup>16</sup> However, given the association between DVAs and VMs in our study, we believe that in at least some cases, they must be the result of errors in vasculogenesis of the venous system early in embryonic life. It would otherwise be difficult to explain how and why they are so closely linked to VMs. Unlike VMs, which have at least a few well-defined somatic mutations associated with their development, to date, there have been no genetic mutations associated with DVAs. The unilateral nature of DVAs and facial VMs can be hypothesized to be related to a prothrombotic state due to venous thrombosis and occlusion in the setting of a metameric disorder.<sup>1</sup>

Another interesting finding from our study was the high prevalence of dural venous sinus abnormalities in patients with VMs. Nearly 10% of patients had abnormal ectasia of the torcula, and approximately 6% had a persistent falcine sinus. Torcular ballooning is a well-described phenomenon during the development of the fetal dural venous sinus system. During the fourth-to-fifth fetal months, superficial veins of the expanding cerebral hemispheres increase in size and drain into the transverse sinus,

resulting in a period of ballooning of both the transverse sinuses and the torcula.<sup>17,18</sup> This in utero imaging finding was frequently misdiagnosed as a dural sinus malformation until it was recognized as a phase in the normal dural venous sinus development.

There have been a few case reports describing the presence of dural venous sinus abnormalities in patients with CVMS (ie, DVAs and facial VMs along the same metamere). The first reported case by Mohamed et al<sup>19</sup> was in an infant who had multiple posterior fossa DVAs, cavernous malformations, a facial VM, and torcular ectasia from a dural sinus malformation. In this case, the dural sinus malformation had multiple points of shunting and required treatment. In a subsequent series of 30 patients with dural sinus malformations, Barbosa et al<sup>20</sup> found that 6 patients also had vascular anomalies of the face, which were likely venous malformations. Unlike the cases referenced in the articles by Mohamed et al<sup>19</sup> and Barbosa et al,<sup>20</sup> in our series, no patients had any evidence of arteriovenous shunting associated with the dural venous sinus ectasia. Nevertheless, we hypothesize that the presence of VMs, DVAs, and dural venous sinus ectasia represents associations along a pathophysiologic spectrum similar to that of VM, DVA, and dural sinus malformations.

Our study may provide some insight into an interesting and not uncommon phenotype of patients with cervicofacial VMs. The pathophysiologic and genetic mechanisms of VMs associated with DVAs (with or without dural venous sinus abnormalities) almost certainly points to the presence of a somatic mutation. There have been a few somatic mutations associated with the development of venous vascular malformations, including in the *PIK3CA* and *TEK* genes.<sup>21</sup> These genetic associations have led to promising research in the treatment of VMs. Perhaps there is a different/specific gene that results in metameric venous malformations. Further research into identifying genetic mutations in this patient population may provide insight into disease pathophysiology and targeted treatment of venous vascular malformations in this population.

### Limitations

Our study has limitations. First, it was retrospective and is subject to the biases of retrospective studies, including selection bias. Only a few patients in our series underwent SWI, which would likely be significantly more sensitive for detecting tiny cavernous malformations than conventional gradient recalled-echo imaging. There was a wide spectrum of scanners and imaging protocols used in the evaluation of VMs in our study, and imaging was variably performed on 1.5T, 3T, and 7T MR imaging machines. While we did find that a substantial proportion of patients with facial venous malformations also had dural venous sinus malformations, the converse (ie, the proportion of patients with dural venous sinus malformations without facial venous malformations) is more difficult to pin down. This issue is because these malformations are often not reported and a unifying terminology for these malformations has never really been established; thus, it is difficult to identify such patients from text searches of radiology reports.

### CONCLUSIONS

In the largest study to date on this topic, we found that patients with cervicofacial VMs were significantly more likely to have



intracranial DVAs and dural venous sinus abnormalities compared with normal age- and sex-matched controls. In most cases, DVAs and VMs occurred along the same metamere, suggesting that the prevalence of CVMS in this patient population is underestimated. Our findings suggest that there is a developmental link in the formation of venous abnormalities affecting the brain, dura, and face in a subset of patients.

## REFERENCES

1. Brinjikji W, Hilditch CA, Tsang AC, et al. **Facial venous malformations are associated with cerebral developmental venous anomalies.** *AJNR Am J Neuroradiol* 2018;39:2103–07 CrossRef Medline
2. Castel P, Carmona FJ, Grego-Bessa J, et al. **Somatic PIK3CA mutations as a driver of sporadic venous malformations.** *Sci Transl Med* 2016;8:332ra42 CrossRef Medline
3. Ten Broek RW, Eijkelenboom A, van der Vleuten CJ, et al. **Comprehensive molecular and clinicopathological analysis of vascular malformations: a study of 319 cases.** *Genes Chromosomes Cancer* 2019;58:541–50 CrossRef Medline
4. Agid R, Terbrugge KG. **Cerebrofacial venous metamerism syndrome 2 plus 3: facial and cerebral manifestations.** *Interv Neuroradiol* 2007;13:55–58 CrossRef Medline
5. Krings T, Geibprasert S, Luo CB, et al. **Segmental neurovascular syndromes in children.** *Neuroimaging Clin N Am* 2007;17:245–58 CrossRef Medline
6. Flors L, Leiva-Salinas C, Maged IM, et al. **MR imaging of soft-tissue Vascular malformations: diagnosis, classification, and therapy follow-up.** *Radiographics* 2011;31:1321–40; discussion 1340–41 CrossRef Medline
7. Wassef M, Blei F, Adams D, et al; Board and Scientific Committee. **Vascular anomalies classification: recommendations from the International Society for the Study of Vascular Anomalies.** *Pediatrics* 2015;136:e203–14 CrossRef Medline
8. Abula A, Wait SD, Uschold T, et al. **Developmental venous anomaly, cavernous malformation, and capillary telangiectasia: spectrum of a single disease.** *Acta Neurochir (Wien)* 2008;150:487–89; discussion 489 CrossRef Medline
9. McCormick PW, Spetzler RF, Johnson PC, et al. **Cerebellar hemorrhage associated with capillary telangiectasia and venous angioma: a case report.** *Surg Neurol* 1993;39:451–57 CrossRef Medline
10. Rigamonti D, Johnson PC, Spetzler RF, et al. **Cavernous malformations and capillary telangiectasia: a spectrum within a single pathological entity.** *Neurosurgery* 1991;28:60–64 Medline
11. Bhattacharya JJ, Luo CB, Suh DC, et al. **Wyburn-Mason or Bonnet-Dechaume-Blanc as cerebrofacial arteriovenous metamerism syndromes (CAMS): a new concept and a new classification.** *Interv Neuroradiol* 2001;7:5–17 CrossRef Medline
12. Boukobza M, Enjolras O, Guichard JP, et al. **Cerebral developmental venous anomalies associated with head and neck venous malformations.** *AJNR Am J Neuroradiol* 1996;17:987–94 Medline
13. Goulao A, Alvarez H, Garcia Monaco R, et al. **Venous anomalies and abnormalities of the posterior fossa.** *Neuroradiology* 1990;31:476–82 CrossRef Medline
14. Portilla P, Husson B, Lasjaunias P, et al. **Sturge-Weber disease with repercussion on the prenatal development of the cerebral hemisphere.** *AJNR Am J Neuroradiol* 2002;23:490–92 Medline
15. Ramli N, Sachet M, Bao C, et al. **Cerebrofacial venous metamerism syndrome (CVMS) 3: Sturge-Weber syndrome with bilateral lymphatic/venous malformations of the mandible.** *Neuroradiology* 2003;45:687–90 CrossRef Medline
16. Pereira VM, Geibprasert S, Krings T, et al. **Pathomechanisms of symptomatic developmental venous anomalies.** *Stroke* 2008;39:3201–15 CrossRef Medline
17. Robertson F. **Torcular dural sinus malformation.** *J Neurointerv Surg* 2018;10:423 CrossRef Medline
18. Manjila S, Bazil T, Thomas M, et al. **A review of extraaxial developmental venous anomalies of the brain involving dural venous flow or sinuses: persistent embryonic sinuses, sinus pericranii, venous varices or aneurysmal malformations, and enlarged emissary veins.** *Neurosurg Focus* 2018;45:E9 CrossRef Medline
19. Mohamed Z, Batista LL, Sachet M, et al. **Growing dural sinus malformation with associated developmental venous anomaly, multiple cavernomas and facial venous malformation in an infant: an associated disease or a disease spectrum?** *Interv Neuroradiol* 2002;8:421–30 CrossRef Medline
20. Barbosa M, Mahadevan J, Weon YC, et al. **Dural sinus malformations (DSM) with giant lakes, in neonates and infants: review of 30 consecutive cases.** *Interv Neuroradiol* 2003;9:407–24 CrossRef Medline
21. Limaye N, Kangas J, Mendola A, et al. **Somatic activating PIK3CA mutations cause venous malformation.** *Am J Hum Genet* 2015; 97:914–21 CrossRef Medline



# Heterogeneous Continuum of Cerebral and Cervicofacial Venous Malformations

In this issue, Brinjiki et al<sup>1</sup> demonstrate a remarkable association between cervicofacial venous malformations (VMs) and cerebral developmental venous anomalies (DVAs), as well as between cervicofacial VMs and dural venous sinus anomalies in a retrospective study involving healthy age- and sex-matched controls. In this study, the venous malformations involving the face and neck drain into the external jugular system and fit into the following criteria: septate lobulated mass hyperintense on T2 and hypointense on T1 MR images without mass effect, the presence of phleboliths and fluid-fluid levels, the absence of vascular flow voids on spin-echo sequences, infiltration of the lesion into tissue planes, the absence of arterial or early venous enhancement, and the presence of diffuse enhancement on delayed MR images. Intracranial venous drainage was evaluated by the presence of a DVA, superficial-versus-deep drainage of a DVA, side and location of a DVA, and the presence of cavernous malformations and dural venous sinus anomalies such as dural ectasia and persistent falcine sinuses (PFS). The authors have also examined the combined VM-DVA cases for their occurrence in the same metamere, either medial prosencephalic, lateral prosencephalic and/or otic (rhombencephalic/mesencephalic) as the case may be. Their findings suggest that VMs result from a segmental in utero insult to cells involved in cerebral/cervicofacial venous development.

They found a significant association with facial venous malformations and ipsilateral DVAs, concordant with the existing literature, and a novel observation of dural venous sinus anomalies associated with the PFS and torcular ectasia in 6% and 10% of VMs, respectively. Of note, the authors should be commended for examining over 550 venograms of patients 0–20 years of age who did not have facial VMs and who did not have any dural sinus anomalies. I would like to present these anomalies as a part of the heterogeneous continuum, which comprises intracranial venous and dural sinus malformations, associated with cavernous angiomas, telangiectasias, and venous ectasias or varices. These are well-elucidated by the seminal article by Lasjaunias (with multiple posterior fossa DVAs, cavernous malformations, and torcular ectasia from dural sinus malformation), as well as many articles published by the prominent cerebrovascular group led by Robert Spetzler, already referenced in the article.

Several interesting observations are presented by the authors:

1. The cervicofacial VMs and intracranial DVAs appear to have occurred along the same side in same metameres. Metameric lesions as in cerebrofacial arteriovenous metamerism syndrome, cerebrofacial venous metamerism syndrome, and spinal arteriovenous metamerism syndrome are already described in literature; however, the underlying genetics and metamerism association of intracranial DVAs need to be studied in a larger prospective study. I would like to compare the authors' work with that of Oza et al,<sup>2</sup> who demonstrated focal cerebellar atrophy, lip/nasal cleft, and gray matter heterotopias occurring on the same side as a facial hemangioma in posterior fossa malformations, hemangiomas, arterial anomalies, cardiac defects, eye abnormalities, and sternal or ventral defects (PHACES) syndrome.
2. The in utero insult does not explain how the presence of cervicofacial VMs favors development of other listed intracranial malformations in the continuum in infants and adults; moreover, there has been evidence of de novo development of pediatric and adult cavernous malformations and intracranial DVAs in patients on close radiologic surveillance. Cranial irradiation, coexistent vascular malformations, genetic/hormonal factors, previous intracranial surgery, or even apparently unrelated intracranial lesions have been considered risk factors for de novo cavernomas in the brain.<sup>3–9</sup> There is evidence of multiple bilateral cavernomas with and without a family history, the interval growth being generally attributed to recurrent bleeds (rather than tumor tissue proliferation); however, there are cases of lesion growth reported without hemosiderin in or around these lesions. The cavernomas seen in association with DVAs are most likely of acquired etiology rather than true congenital vascular malformations; this is also supported by the fact that the coexistence of cavernous malformations and DVAs is more common in the adults than children.
3. The authors have demonstrated a subset of venous malformations with dural venous sinuses including PFS and persistent ballooning of the torcula, the latter without obvious laterality, in a limited subset of patients. The associated dystrophy of adjacent brain around venous and dural sinus anomalies is

not adequately studied, given the limited sample size. The juxtaposed developmental brain anomalies as well as the hypometabolic activities of the brain in the vicinity of these venous malformations should be evaluated vividly in symptomatic cases. For example, Manjila et al<sup>10</sup> classified the PFS, with and without the association of supratentorial brain ectasia associated with these venous/dural sinus anomalies. Similarly, Larvie et al<sup>11</sup> published metabolic abnormalities in the adjacent brain parenchyma, as assessed by FDG-PET, in more than three-fourths of DVAs in a series of 25 cases.

Future studies on brain ectasia/atrophy and focal metabolic brain activities around DVAs as well as the genetic role in metabolic venous malformations (as in *PIK3CA* and *TEK* genes) can provide more useful clinical and radiologic insights into the developmental genetics of these uncommon phenotypes in the heterogeneous continuum of cervicofacial and cerebral venous malformations.

## REFERENCES

1. Brinjikji W, Mark IT, Silvera VM, et al. **Cervicofacial venous malformations are associated with intracranial developmental venous anomalies and dural venous sinus abnormalities.** *AJNR Am J Neuroradiol* 2020;41:??-??
2. Oza VS, Wang E, Berenstein A, et al. **PHACES association: a neuro-radiologic review of 17 patients.** *AJNR Am J Neuroradiol* 2008;29:807-13 CrossRef Medline
3. Maeder P, Gudinchet F, Meuli R, et al. **Development of a cavernous malformation of the brain.** *AJNR Am J Neuroradiol* 1998;19:1141-45 Medline
4. Cakirer S. **De novo formation of a cavernous malformation of the brain in the presence of a developmental venous anomaly.** *Clin Radiology* 2003;58:251-56 CrossRef Medline
5. Dillon WP, Wilson CB, Hieshima GB, et al. **Hemorrhagic venous malformations: the role of venous restriction.** In: *Proceedings of the American Society of Neuroradiology Annual Meeting*, St. Louis, Missouri, May 31-June 5, 2002
6. Dillon WP. **Cryptic vascular malformations: controversies in terminology, diagnosis, pathophysiology, and treatment.** *AJNR Am J Neuroradiol* 1997;18:1839-46 Medline
7. Campeau NG, Lane JI. **De novo development of a lesion with the appearance of a cavernous malformation adjacent to an existing developmental venous anomaly.** *AJNR Am J Neuroradiol* 2005;26:156-59 Medline
8. Detwiler PW, Porter RW, Zabramski JM, et al. **De novo formation of a central nervous system cavernous malformation: implications for predicting risk of hemorrhage: case report and review of the literature.** *J Neurosurg* 1997;87:629-32 CrossRef Medline
9. Chakravarthy H, Lin TK, Chen YL, et al. **De novo formation of cerebral cavernous malformation adjacent to existing developmental venous anomaly: an effect of change in venous pressure associated with management of a complex dural arterio-venous fistula.** *Neuroradiol J* 2016;29:458-64 CrossRef Medline
10. Manjila S, Bazil T, Matthew Mani S, et al. **A review of extraaxial developmental venous anomalies of the brain involving dural venous flow or sinuses: persistent embryonic sinuses, sinus pericranii, venous varices or aneurysmal malformations, and enlarged emissary veins.** *Neurosurg Focus* 2018;45:E9 CrossRef Medline
11. Larvie M, Timerman D, Thum JA. **Brain metabolic abnormalities associated with developmental venous anomalies.** *AJNR Am J Neuroradiol* 2015;36:475-80 CrossRef Medline

 S. Manjila

Skull Base and Cerebrovascular Surgery  
Department of Neurosurgery

Hartford Hospital, Hartford, Connecticut

MidState Medical Center, Meriden, Connecticut

The Hospital of Central Connecticut, New Britain, Connecticut

<http://dx.doi.org/10.3174/ajnr.A6694>

# A Hemodynamic Mechanism Correlating with the Initiation of MCA Bifurcation Aneurysms

 Z. Huang,  M. Zeng,  W.G. Tao,  F.Y. Zeng,  C.Q. Chen,  L.B. Zhang, and  F.H. Chen



## ABSTRACT

**BACKGROUND AND PURPOSE:** Previous studies have reported that MCA bifurcation aneurysms usually emerge on inclined bifurcations; however, the reason is unclear. We designed this study to explore hemodynamic mechanisms that correlate with the initiation of MCA bifurcation aneurysms.

**MATERIALS AND METHODS:** Fifty-four patients with unilateral MCA bifurcation aneurysms and 54 control patients were enrolled in this study after propensity score matching, and their clinical and CTA data were collected. We extracted the morphologic features of aneurysmal MCA bifurcations to build a simplified MCA bifurcation model and performed a computational fluid dynamics analysis.

**RESULTS:** The presence of MCA aneurysms correlated with smaller parent-daughter angles of MCA bifurcations ( $P < .001$ ). Aneurysmal MCA bifurcations usually presented with inclined shapes. The computational fluid dynamics analysis demonstrated that when arterial bifurcations became inclined, the high-pressure regions and low wall shear stress regions shifted from the apexes of the arterial bifurcations to the inclined daughter arteries, while the initial sites of MCA bifurcation aneurysms often overlapped with the shifted high-pressure regions and low wall shear stress regions.

**CONCLUSIONS:** Our results suggest that the initiation of MCA bifurcation aneurysms may correlate with shifts of high-pressure regions and low wall shear stress regions that occur on inclined MCA bifurcations.

**ABBREVIATIONS:** CFD = computational fluid dynamics; HPR = high-pressure region; LWSS = low wall shear stress; LWSSR = low wall shear stress region; PSM = propensity score matching; RD = ratio of diameter; ROC = receiver operating characteristic

The occurrence of intracranial aneurysms is generally thought to be due to arterial wall weakening and/or the influence of hemodynamics.<sup>1–4</sup> Most studies on aneurysm etiology have focused on hemodynamics. Because the geometric shapes of intracranial arteries are diverse, their hemodynamics are also complex. Arterial bifurcations are common sites for intracranial aneurysms. The bifurcations are generally exposed to extreme hemodynamic stress; those with special morphologic features that significantly

divert blood flow from the direction of flow of the parent vessels are a risk factor for aneurysm formation.<sup>1,5,6</sup> Previous studies have reported that the inclined MCA bifurcations with a widening angle are likely to harbor aneurysms,<sup>7,8</sup> but mechanisms by which the aneurysms develop on MCA bifurcations are controversial and need to be elucidated.<sup>8–11</sup> The present study was designed to extract the morphologic features of aneurysmal MCA bifurcations from clinical data, build a simplified MCA bifurcation model based on these extracted features, perform computational fluid dynamics (CFD) analysis on the aneurysmal MCA bifurcations and simplified models, and finally, to explore the hemodynamic mechanisms that could trigger aneurysm initiation.

## MATERIALS AND METHODS

### Case Selection and Matching


Patients with unilateral MCA bifurcation aneurysms confirmed by CTA from July 2016 to March 2019 were enrolled in our study. Exclusion criteria were as follows: 1) fusiform or dissecting aneurysms, 2) trifurcation types of MCAs, and 3) aneurysms of >10 mm. In addition, we reviewed healthy subjects without


Received November 29, 2019; accepted after revision February 22, 2020.

From the Departments of Neurosurgery (Z.H., M.Z., F.H.C., W.G.T.), and Radiology (F.Y.Z., C.Q.C.), Xiangya Hospital, Central South University, Changsha, China; and Department of Neurosurgery (L.B.Z.), School of Medicine, Yale University, New Haven, Connecticut.

This work was supported by National Natural Science Foundation of China (grant No. 81873756).

Please address correspondence to Fenghua H. Chen, PhD, MD, Department of Neurosurgery, Xiangya Hospital, Central South University, No. 87 Xiangya Rd, Kaifu District, Changsha, 410008, China; e-mail: xyswcfh@csu.edu.cn

 Indicates open access to non-subscribers at [www.ajnr.org](http://www.ajnr.org)

 Indicates article with supplemental on-line photo.

<http://dx.doi.org/10.3174/ajnr.A6615>

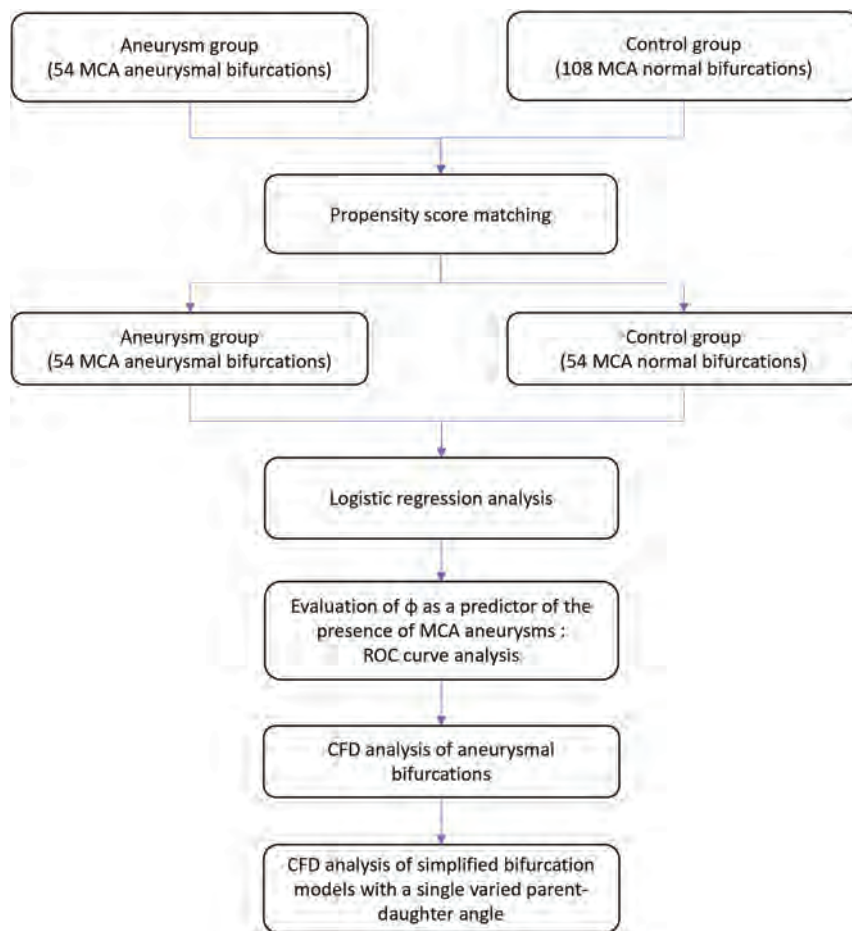


**FIG 1.** Flow diagram of the study population and procedure.

intracranial aneurysms from the general population during the same time period. Of the 162 patients enrolled in our study, 54 with unilateral MCA aneurysms were assigned to the aneurysm group and 108 without intracranial aneurysms, to the control group. General data including age, sex, smoking, drinking, hypertension, hyperlipidemia, and diabetes were collected. Propensity score matching (PSM) was used for selecting the cases in the 2 groups, and the variables listed above were used as matching parameters. The matched cases included 54 with unilateral MCA aneurysms and 54 without intracranial aneurysms. A flow diagram of our study is shown in Fig 1. All procedures in this retrospective study that involved human participants were approved by the ethics committee of our hospital and were performed in accordance with the institutional ethics standards, the 1964 Declaration of Helsinki and its later amendments, or comparable ethical standards. Informed consent was obtained from all individual participants included in the study.

### Morphologic Features

3D CTA data were reconstructed using Materialise Mimics software (Version 21.0; <https://www.materialise.com/en/medical/mimics-innovation-suite/mimics>), and morphologic data were measured using the Materialise 3-matic research software (Version 13.0; <https://www.materialise.com/en/software/3-matic>). Two certified neuroradiologists

(F.Y.Z. and C.Q.C.), who were blinded to the clinical data, independently evaluated the morphologic data and resolved disagreements by consensus. The parent artery was defined as the M1 trunk of the MCA, and the daughter artery, as the M2 branch of the MCA.

The measuring methods of 6 angles in the control group are shown in Fig 2A. The measuring methods of diameters are depicted in Fig 2D. Four ratios of diameters (RDs) were used for analysis. They were separately defined as  $RD_{L1}$ , the ratio of the left upper daughter-parent artery diameters;  $RD_{L2}$ , the ratio of left lower daughter-parent artery diameters;  $RD_{R1}$ , the ratio of right upper daughter-parent artery diameters; and  $RD_{R2}$ , the ratio of right lower daughter-parent artery diameters.

The measuring methods of 6 angles in the aneurysm group are described in Fig 2B, and the diameter measuring methods are shown in Fig 2D. The ratio of parent-daughter artery diameters was separately termed as  $RD_A$  on the aneurysm side and  $RD_{NA}$  on the nonaneurysmal side. For the contralateral side, the ratio of upper daughter-parent artery diameters was defined as  $RD_{C1}$ , and the ratio of lower daughter-parent artery diameters was

$RD_{C2}$ . The method for deciding the location of an MCA bifurcation aneurysm is described in Fig 2C.<sup>12</sup> The long axis of an aneurysm was measured as aneurysm size. Aneurysm neck width was also measured.

### CFD Analysis

We reconstructed 3D MCA bifurcation models in Mimics research software (Materialise NV) for all 54 cases with MCA aneurysms and 20 cases in the control group. Then, the aneurysmal MCA bifurcation models were virtually removed using the 3-matic research software, and their initial status was simulated. All 3D models were exported to Fluent solver (Version 19.1; ANSYS) for CFD analysis.

After extracting some hemodynamic features from the above CFD analyses, we constructed a group of simplified 3D MCA bifurcations models with variable single parent-daughter angles. For these models, parent-daughter angle of the MCA bifurcations was set to  $120^\circ$  (based on the mean value of  $\phi_{NA}$ ,  $118.81^\circ \pm 21.35^\circ$ ), and another was varied from  $120^\circ$  to  $30^\circ$  with intervals of  $10^\circ$  (based on the range of  $\phi_A$ ,  $31.95^\circ$ – $124.89^\circ$ ). The diameters of the parent and daughter arteries were set to 4 and 3 mm, respectively. For all 3D models, blood flow was modeled as a laminar Newtonian fluid, with a density of  $1050 \text{ kg/m}^3$  and dynamic viscosity of  $0.0032 \text{ Pa} \times \text{s}$ . The inlet boundary of the parent artery was defined as the mass-



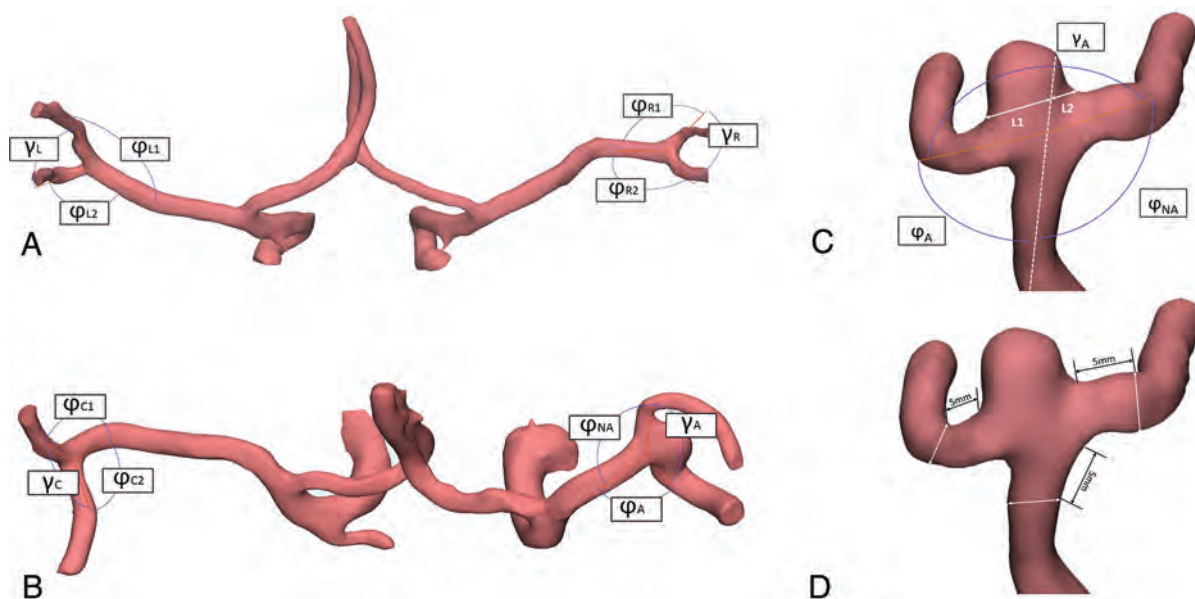


**FIG 2.** Schematic drawing of the angles measured in our study. A and B, The parent-daughter angle was defined as the angle between the M1 trunk and different M2 branches, and the daughter-daughter angle was the angle between 2 M2 branches. C, In the MCA aneurysm bifurcation, lines L1 and L2 were crossed in the aneurysm neck and then measured to decide on which side of the M2 branch the aneurysm was located. D, The measurements of diameters were performed 5 mm beyond the bifurcation apex.

**Table 1: Summary of clinical data**

	Before PSM			After PSM <sup>a</sup>		
	Control Group (n = 108)	Aneurysm Group (n = 54)	P Value	Control Group (n = 54)	Aneurysm Group (n = 54)	P Value
Male sex (%)	61 (56.5)	18 (33.3)	.009	26 (48.1)	18 (33.3)	.17
Age (mean) (yr)	43.65 ± 19.34	60.35 ± 9.87	<.001	57.39 ± 8.79	60.35 ± 9.87	.102
Hypertension (%)	30 (27.8)	29 (53.7)	.002	25 (46.3)	29 (53.7)	.564
Diabetes (%)	15 (13.9)	8 (14.8)	1	12 (22.2)	8 (14.8)	.457
Hyperlipidemia (%)	24 (22.2)	28 (51.9)	<.001	19 (35.2)	28 (51.9)	.12
Smoking (%)	30 (27.8)	12 (22.2)	.568	20 (37.0)	12 (22.2)	.14
Alcohol use (%)	27 (25.0)	9 (16.7)	.316	16 (29.6)	9 (16.7)	.171
$\Phi$ (mean)	124.88° ± 10.92°	107.98° ± 12.3°	<.001	120.27° ± 10.50°	107.98° ± 12.31°	<.001
$\gamma$ (mean)	98.25° ± 20.54°	128.51° ± 16.69°	<.001	106.68° ± 18.51°	128.51° ± 16.69°	<.001
RD (mean) (mm)	0.76 ± 0.08	0.79 ± 0.11	.022	0.76 ± 0.08	0.79 ± 0.11	.093

<sup>a</sup> Variables as parameters for PSM included sex, age, hypertension, diabetes, hyperlipidemia, smoking, and Alcohol use (rows 1–7 in Table 1).

flow inlet at 0.0034 kg/s, and the outlet boundaries of 2 daughter arteries were defined as zero-static pressure.<sup>8,13,14</sup>

### Statistical Analysis

Data were analyzed using R Studio (Version 1.1.383; <http://rstudio.org/download/desktop>). Student *t* tests and ANOVA analyses were used to compare continuous variables, and the Pearson  $\chi^2$  test was used for comparing categorical variables. Pearson correlation tests were used to analyze correlations between 2 continuous variables. Multiple variables were analyzed using logistic regression. To predict which daughter artery was prone to developing an MCA aneurysm, receiver operating characteristic (ROC) curve analysis was performed. *P* values < .05 were considered statistically significant.

## RESULTS

### Demographics

The clinical data of both groups before and after PSM are summarized in Table 1. Of 54 subjects in the control group, 28

were women and 26 men, with a mean age of 57.39 ± 8.79 years. Of 54 patients with aneurysms, 36 were women and 18 men, with a mean age of 60.35 ± 9.87 years. Twenty-two (40.74%) patients were confirmed to have ruptured aneurysms, and 17 (31.48%), to have multiple aneurysms. Logistic regression analysis based on morphologic parameters of MCA bifurcations showed that the presence of MCA aneurysms correlated with the parent-daughter angle (Table 2).

### Morphologic Features of Nonaneurysmal and Aneurysmal MCA Bifurcations

There was no statistically significant difference between groups among the 7 parent-daughter angles ( $\phi_{L1}$ ,  $\phi_{L2}$ ,  $\phi_{R1}$ ,  $\phi_{R2}$ ,  $\phi_{NA}$ ,  $\phi_{C1}$ ,  $\phi_{C2}$ ; Table 3 and Fig 3A). The daughter-daughter angles ( $\gamma_A$  and  $\gamma_C$ ) in patients with aneurysms were significantly larger than those ( $\gamma_L$  and  $\gamma_R$ ) in the control group (Table 3 and vFig 3B).

For the aneurysm group, parent-daughter angles on the inclining side of the aneurysm ( $\phi_A$ ) were significantly smaller than the other 3 parent-daughter angles ( $\phi_{NA}$ ,  $\phi_{C1}$ ,  $\phi_{C2}$ ) (Fig 3A), whereas the daughter-daughter angles on the aneurysm side ( $\gamma_A$ ) were significantly larger than the angle of the contralateral side ( $\gamma_C$ ) (Fig 3B). The mean aneurysm size was  $5.05 \pm 1.98$  mm, and the mean aneurysm neck diameter was  $4.68 \pm 1.54$  mm. The optimal parent-daughter angle threshold to predict the daughter artery that was likely to harbor an MCA aneurysm was determined by ROC analysis. The ROC curve showed that the optimal threshold was 100.06 (area under the curve, 0.903), with 84.1% sensitivity and 81.5% specificity (Fig 3C).

### Influence of Aneurysm Rupture on MCA Bifurcation Morphology

There was no significant difference between the parent-daughter and daughter-daughter angles or the RDs on aneurysmal and nonaneurysmal sides of the ruptured and unruptured aneurysmal MCA bifurcations (Table 4).

### Influence of Aneurysm Size and Neck Width on Parent-Daughter Angles of MCA Bifurcations

Correlation analysis showed that the sizes and neck widths of MCA aneurysms were not significantly correlated with parent-daughter angles (On-line Figure).

### Hemodynamic Features of Aneurysmal MCA Bifurcations and Simplified MCA Bifurcation Models

The CFD analysis performed on all MCA aneurysms showed that after the aneurysms were virtually removed, compared with control MCA bifurcations (On-line Digital Content 1; [https://yaleedu-my.sharepoint.com/:b/g/personal/fenghua\\_chen\\_yale\\_edu/EV5HuHzoJrRBsp1nO86pKgQBxPempPz4zSsXWBH2Ap-eR3w?e=u79Us0](https://yaleedu-my.sharepoint.com/:b/g/personal/fenghua_chen_yale_edu/EV5HuHzoJrRBsp1nO86pKgQBxPempPz4zSsXWBH2Ap-eR3w?e=u79Us0)), their initial sites presented high-pressure

regions (HPRs) and low-wall shear stress regions (LWSSRs) (Fig 4A and On-line Digital Content 2; [https://yaleedu-my.sharepoint.com/:b/g/personal/fenghua\\_chen\\_yale\\_edu/EV5HuHzoJrRBsp1nO86pKgQBxPempPz4zSsXWBH2Ap-eR3w?e=u79Us0](https://yaleedu-my.sharepoint.com/:b/g/personal/fenghua_chen_yale_edu/EV5HuHzoJrRBsp1nO86pKgQBxPempPz4zSsXWBH2Ap-eR3w?e=u79Us0)). The CFD analysis of simplified 3D MCA bifurcation models revealed that when a single parent-daughter angle decreased from  $120^\circ$  to  $30^\circ$ , the HPR and LWSSR shifted from the apex of the bifurcation to the daughter artery wall on the same side, and the maximum shifted distance was 2.03 mm (Fig 4B–D and On-line Digital Content 3; [https://yaleedu-my.sharepoint.com/:b/g/personal/fenghua\\_chen\\_yale\\_edu/EV5HuHzoJrRBsp1nO86pKgQBxPempPz4zSsXWBH2Ap-eR3w?e=u79Us0](https://yaleedu-my.sharepoint.com/:b/g/personal/fenghua_chen_yale_edu/EV5HuHzoJrRBsp1nO86pKgQBxPempPz4zSsXWBH2Ap-eR3w?e=u79Us0)).

## DISCUSSION

The mechanism of intracranial aneurysm initiation remains unclear. Intracranial arterial bifurcations frequently harbor aneurysms. When blood flow enters an arterial bifurcation, it exhibits complex hemodynamic features, some of which may correlate with aneurysm formation.<sup>2,5,15,16</sup> In this study, we analyzed a series of MCA bifurcations with and without aneurysms and explored the hemodynamic factors involved in aneurysm development. We found that MCA aneurysms were commonly located on the inclined MCA bifurcations, consistent with previous studies.<sup>8,10</sup> Our results revealed that inclined MCA aneurysmal bifurcations are usually caused by smaller single parent-daughter angles, but other parent-daughter angles maintain sizes similar to the 2 parent-daughter angles on the contralateral “normal” MCA bifurcations. CFD analysis based on the above morphologic features showed that when MCA bifurcations become inclined, the HPRs and LWSSRs shift from the apexes of the arterial bifurcations to the ipsilateral daughter arteries, and this hemodynamic feature may correlate with the initiation of MCA bifurcation aneurysms.

Considering that the parent-daughter angle may be affected by the aneurysm size, we enrolled only patients with small MCA aneurysms. We analyzed the correlation between the parent-daughter angle of the MCA bifurcation and aneurysm size and neck width. The results suggested that the size of the parent-daughter angle on the aneurysm side might not be affected by aneurysm growth. Our data also showed that aneurysm rupturing had little influence on MCA bifurcation morphology.<sup>8</sup> Unlike some previous groups that based their measurements on 2D projecting images of MCA bifurcations,<sup>8,17</sup> we used 3D measuring tools available in Mimics research software, so we did not adopt all the parameters used in those studies. We considered that by using the 3D coordinate, our data would be more representative of the real conditions in MCA bifurcations.

Some studies have reported that the daughter-daughter angle is correlated with the presence of an intracranial aneurysm,<sup>8,10</sup> which is consistent with our results. We found that of all the parent-daughter angles in the aneurysm

**Table 2: Logistic regression analysis of morphologic factors associated with MCA aneurysms after PSM**

	OR	95% CI	P Value
(Intercept)	0.000	0.000–0.061	.006
Mean parent-daughter angle	1.095	1.053–1.145	<.001
Mean RD	0.130	0.001–15.004	.406

**Table 3: Angles in the control and aneurysmal groups**

Variable/Group	Angle	Value		P Value	
		Mean	Range		
Parent-daughter angles					
Control group (n = 54)	$\phi_{R1}$ (°)	117.98 ± 23.5	62.59–160.36	<.001	
	$\phi_{R2}$ (°)	118.87 ± 17.32	76.56–164.27		
	$\phi_{L1}$ (°)	119.13 ± 19.65	72.06–156.86		
	$\phi_{L2}$ (°)	125.09 ± 18.77	82.03–167.11		
Aneurysmal group (n = 54)	$\phi_A$ (°)	81.38 ± 20.1	31.95–124.89		
	$\phi_{NA}$ (°)	118.81 ± 21.35	82.42–163.84		
	$\phi_{C1}$ (°)	116.41 ± 22.89	50.44–160.78		
	$\phi_{C2}$ (°)	115.31 ± 17.26	81.74–148.75		
Daughter-daughter angles					
Control group (n = 54)	$\gamma_R$ (°)	110.61 ± 28.33	46.64–168.98	<.001	
	$\gamma_L$ (°)	102.75 ± 20.69	65.3–152.16		
Aneurysmal group (n = 54)	$\gamma_A$ (°)	141.13 ± 21.04	85.87–175.72		
	$\gamma_C$ (°)	115.89 ± 23.84	62.84–170.17		

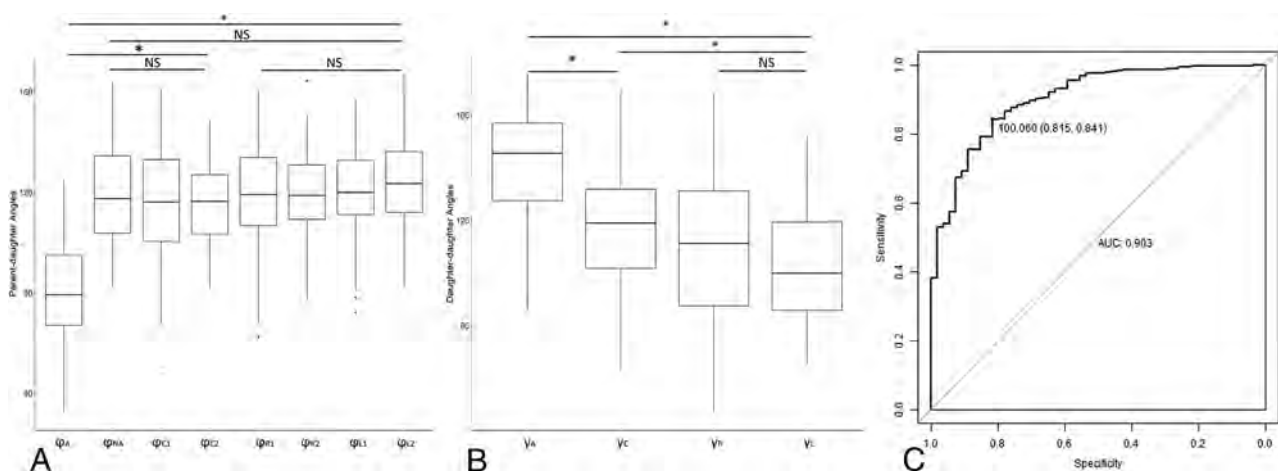


**FIG 3.** A, The size of  $\phi_A$  was significantly different from that of the other 3 parent-daughter angles in the aneurysmal group and the 4 parent-daughter angles in the control group. There were no statistically significant differences among the 3 parent-daughter angles in the aneurysmal group and all 4 parent-daughter angles in the control group. B, The size of  $\gamma_A$  was significantly different from that of another daughter-daughter angle in the aneurysmal group and 2 daughter-daughter angles in the control group. There were no statistically significant differences between the 2 daughter-daughter angles in the control group. C, An optimal threshold of 100.06° for  $\phi_A$  (area under the curve, 0.903) with 84.1% sensitivity and 81.5% specificity revealed that the daughter artery that is apt to harbor an MCA aneurysm is the artery with a smaller parent-daughter angle. NS indicates no statistical significance ( $P > .05$ ); asterisk, statistical significance ( $P < .05$ ).

**Table 4: Comparison of angles and diameters between ruptured and unruptured MCA aneurysms**

Variables		Ruptured Aneurysm <sup>a</sup> n = 22	Unruptured Aneurysm <sup>a</sup> n = 23	P Value
Parent-daughter angles	$\phi_A$ (°)	84.08 ± 20.77	79.53 ± 19.74	.423
	$\phi_{NA}$ (°)	120.22 ± 21.17	117.85 ± 21.76	.691
	$\phi_{C1}$ (°)	115.35 ± 22.45	117.15 ± 23.52	.777
	$\phi_{C2}$ (°)	117.53 ± 18.56	113.78 ± 16.43	.449
Daughter-daughter angles	$\gamma_A$ (°)	137.01 ± 24.69	143.97 ± 17.99	.265
	$\gamma_C$ (°)	117.67 ± 19.04	114.67 ± 26.87	.634
Aneurysmal side RDs	RD <sub>A</sub> (mm)	0.80 ± 0.17	0.73 ± 0.22	.244
	RD <sub>NA</sub> (mm)	0.90 ± 0.22	0.84 ± 0.14	.234
Nonaneurysmal side RDs	RD <sub>C1</sub> (mm)	0.75 ± 0.14	0.72 ± 0.20	.549
	RD <sub>C2</sub> (mm)	0.78 ± 0.14	0.82 ± 0.20	.469

<sup>a</sup> Values are presented as means.

group, the only difference was observed in the parent-daughter angle ( $\phi_A$ ) on the aneurysm inclining side. This suggests that the difference between the daughter-daughter angle ( $\gamma_A$ ) on the aneurysmal side and the contralateral daughter-daughter angle ( $\gamma_C$ ) is largely attributable to the parent-daughter angle ( $\phi_A$ ). Moreover, ROC curve analysis showed that the parent-daughter angle ( $\phi_A$ ) was useful for predicting which daughter artery is likely to harbor an MCA aneurysm. These results suggest that a single smaller parent-daughter angle may play an important role in MCA aneurysm occurrence. Prospective studies should be performed to test the predictive value in subjects with smaller parent-daughter angles of MCA bifurcations.

To explore the possible hemodynamic mechanism behind this unique shape, we further performed CFD analysis on 3D aneurysmal MCA bifurcations reconstructed from CTA data. By comparing the differences before and after virtual MCA aneurysm removal, we observed that the initiation sites of aneurysms overlapped with HPRs and LWSSRs, and these areas inclined to the daughter artery that had a smaller parent-daughter angle. Because hemodynamic data of CFD analysis on aneurysmal bifurcations are difficult to compare, we

constructed a group of simplified bifurcation models to analyze hemodynamic changes on varying a single parent-daughter angle. The CFD analysis of these simplified models reconfirmed the previous finding in the 3D models of actual aneurysmal MCA bifurcations—that is, when one of the parent-daughter angles becomes smaller, the HPR and LWSSR shift from the apex of the arterial bifurcation to the daughter artery. We also observed that the HPR range widened and the distal high-pressure gradient became steeper, but the pressure and wall shear stress were not dramatically altered. Combining these results with the fact that the inclined HPR and LWSSR overlap with an MCA aneurysm site, we inferred that the inclined HPRs and LWSSRs may correlate with the initiation of the aneurysm.

According to previous studies, high or low wall shear stress (LWSS) may cause aneurysm formation.<sup>1,3,4,18</sup> The wall shear stress curve data supported the hypothesis that LWSS was a possible reason. Similar LWSS values also exist on the apexes of normal MCA bifurcations, however, the normal distribution of LWSS seldom causes aneurysms. Rather, the abnormal shift of LWSS may be the real reason. Why can the HPR and LWSSR on



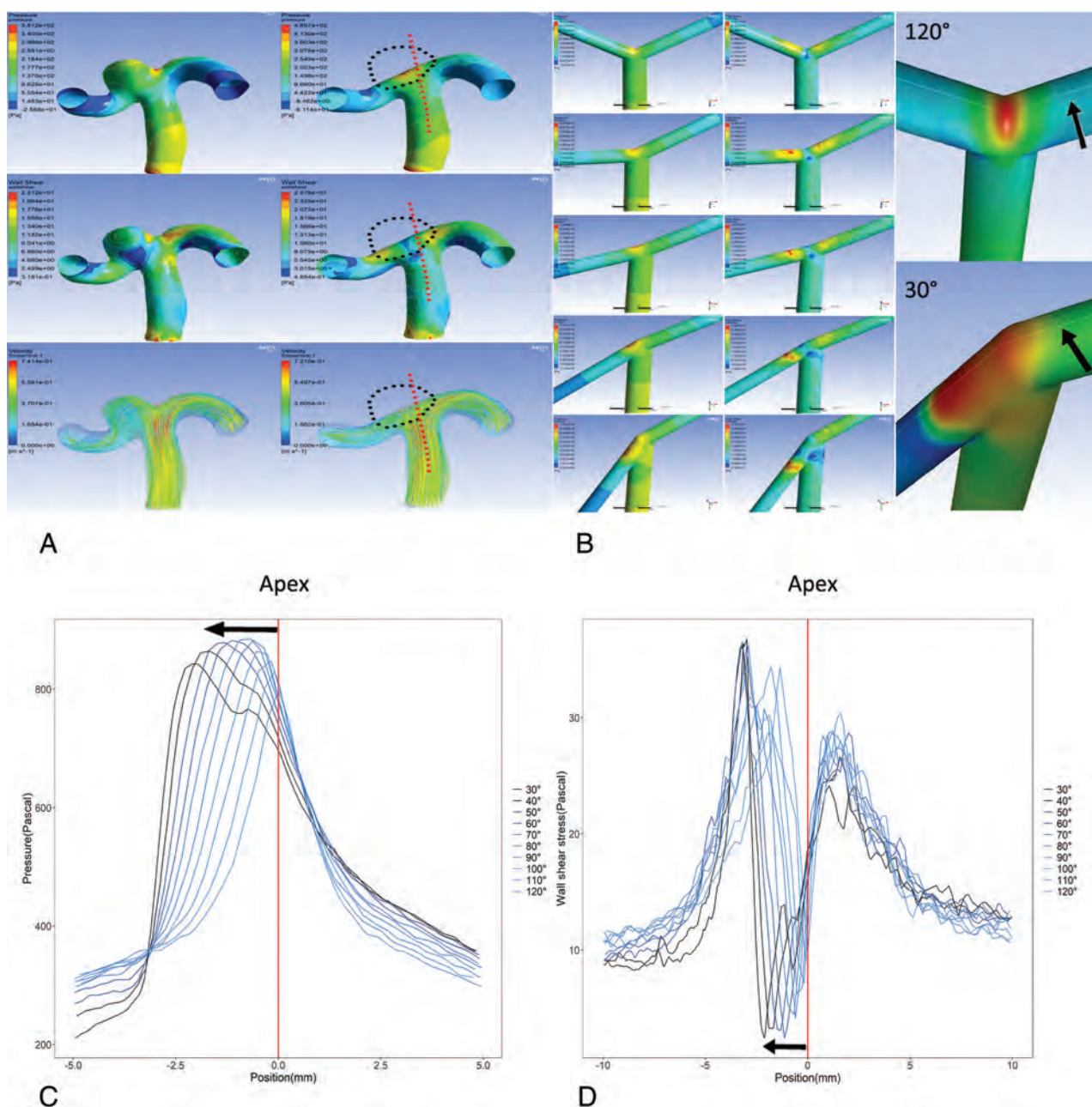


**FIG 4.** CFD analysis. A, CFD analysis on an aneurysmal MCA bifurcation shows the initial sites of aneurysms overlap with HPRs and LWSSRs, and these sites incline to the daughter artery with a smaller parent-daughter angle (*first row*, pressure contour; *second row*, wall shear stress contour; *third row*, blood flow direction. See also On-line Digital Content 2). B, CFD analysis of simplified 3D MCA bifurcation models. When a single parent-daughter angle varied from 120° to 30°, HPRs and LWSSRs were displaced from the apex of the bifurcation to the same daughter artery wall (detailed demonstrations are also shown in On-line Digital Content 3); the values of hemodynamic parameters were obtained along the virtual path (*black arrows*) in the simplified 3D MCA bifurcation models. C and D, The distribution of pressure and wall shear stress shifts along the virtual path when a single parent-daughter angle varies from 120° to 30°. The HPR and LWSSR (*black arrows*) shift from the apex to the left daughter artery, which has a smaller parent-daughter angle. The *red line* represents the bifurcation apex, the *left part* represents the daughter artery with a variable angle, and the *right part* represents the daughter artery with a fixed angle.

the daughter arterial wall form an aneurysm but cannot when they are located on the apex? Previous studies offer some clues.<sup>3,18-22</sup> Specifically, unlike the arterial wall, the apex of a cerebral arterial bifurcation lacks a tunica media and forms a “gap” that is filled with fibers from the tunica adventitia, namely the “apical ridge.” This structure is composed of collagen fibers and can, therefore, bear stronger impingement of blood flow than the arterial wall.

On the basis of the above inferences, we propose the following mechanism of MCA aneurysm initiation. Compared with symmetric MCA bifurcations in which high-pressure and LWSS fall on the “strong” apical ridge, the high-pressure and LWSS of asymmetric MCA bifurcations fall on the relatively “weak” arterial wall. Because the arterial wall cannot bear this stress, arterial structures—especially the elastic laminae—will be damaged under the long-term impact of blood flow and an aneurysm will emerge



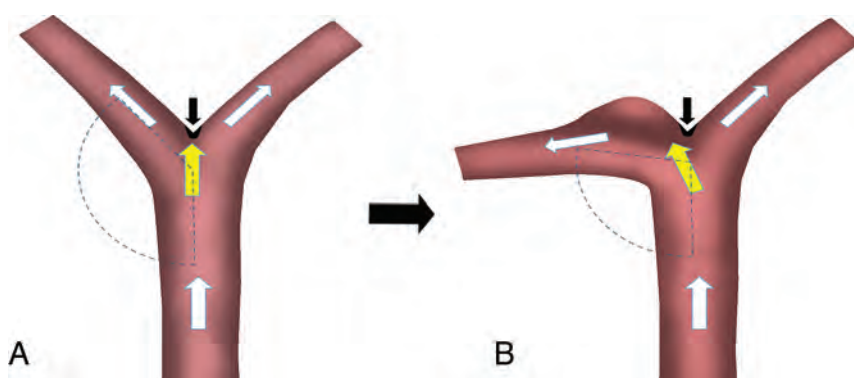


**FIG 5.** Schematic drawing of the hypothetical correlation between the inclined MCA bifurcation and aneurysm initiation. If the HPR and LWSSR locate on the strong apical ridge (black arrow), an MCA bifurcation with normal parent-daughter angles is not likely to develop an aneurysm (A). If the HPR and LWSSR shift to the weak ipsilateral arterial wall (yellow arrow), an inclined MCA bifurcation with asymmetric parent-daughter angles is more likely to develop an aneurysm (B). White arrows indicate blood flow direction.

(Fig 5). Although this hypothesis considers the influence of the MCA bifurcation structure on the formation of an intracranial aneurysm to some extent, it also emphasizes the core role of hemodynamics. Whether these events are universal is unknown, and our theory still needs to be examined and confirmed by further investigations based on biologic models.

Our study has some limitations that need to be considered. First, we examined cross-sectional data. Although our analysis showed no significant correlation between parent-daughter angles on the aneurysmal bifurcations and aneurysm size or neck width, the local geometry of the arteries may still be affected, which would reduce the accuracy of hemodynamic analysis. To minimize the effect of aneurysm size and represent the initial status of aneurysm formation, only small MCA aneurysms of <10 mm were included in our study; therefore, our results may not be generalizable to all MCA aneurysms. Second, our findings revealed a stronger correlation between the parent-daughter angle of the MCA bifurcation and the presence of aneurysms; however, it is unclear whether this is a cause-and-effect relationship. Future studies should be performed to help identify high-risk individuals who are likely to develop aneurysms.

## CONCLUSIONS

An inclined MCA bifurcation caused by a single smaller parent-daughter angle is prone to develop an aneurysm. When a single parent-daughter angle of an MCA bifurcation decreases, the HPR and LWSSR shift from the apex of the arterial bifurcation to the daughter artery wall. This hemodynamic change may be associated with the initiation of an MCA bifurcation aneurysm.

## ACKNOWLEDGMENTS

The authors thank Jun Zhou, PhD (College of Chemistry and Chemical Engineering, Hunan University), for assistance with CFD analysis.

Disclosures: Zheng Huang—RELATED: Grant: National Natural Science Foundation of China (grant No. 81873756). Comments: The grant was used to buy some software for this study.\* Feiyue Y. Zeng—RELATED: Grant: National Science Foundation of China (grant No.81873756).\* Longbo B. Zhang—RELATED: Grant: National Natural Science Foundation of China (grant No.81873756).\* Fenghua H. Chen—RELATED: Grant: National Natural Science Foundation of China (grant No. 81873756). \*Money paid to the institution.

## REFERENCES

1. Kulcsár Z, Ugron Á, Marosfoi M, et al. Hemodynamics of cerebral aneurysm initiation: the role of wall shear stress and spatial wall shear stress gradient. *AJNR Am J Neuroradiol* 2011;32:587–94 CrossRef Medline
2. Wang J, Tan HQ, Zhu YQ, et al. Complex hemodynamic insult in combination with wall degeneration at the apex of an arterial bifurcation contributes to generation of nascent aneurysms in a canine model. *AJNR Am J Neuroradiol* 2014;35:1805–12 CrossRef Medline
3. Xiao W, Qi T, He S, et al. Low wall shear stress is associated with local aneurysm wall enhancement on high-resolution MR vessel wall imaging. *AJNR Am J Neuroradiol* 2018;39:2082–87 CrossRef
4. Diabougba MR, Morel S, Bijlenga P, et al. Role of hemodynamics in initiation/growth of intracranial aneurysms. *Eur J Clin Invest* 2018;48:e12992 CrossRef
5. Meng H, Wang Z, Hoi Y, et al. Complex hemodynamics at the apex of an arterial bifurcation induces vascular remodeling resembling cerebral aneurysm initiation. *Stroke* 2007;38:1924–31 CrossRef Medline
6. Chien A, Sayre J. Morphologic and hemodynamic risk factors in ruptured aneurysms imaged before and after rupture. *AJNR Am J Neuroradiol* 2014;35:2130–35 CrossRef Medline
7. Sadatomo T, Yuki K, Migita K, et al. Differences between middle cerebral artery bifurcations with normal anatomy and those with aneurysms. *Neurosurg Rev* 2013;36:437–45 CrossRef Medline
8. Song J, Zhu F, Qian Y, et al. Morphological and hemodynamic differences between aneurysmal middle cerebral artery bifurcation and contralateral nonaneurysmal anatomy. *Neurosurgery* 2017;81:779–86 CrossRef Medline
9. Can A, Ho AL, Dammers R, et al. Morphological parameters associated with middle cerebral artery aneurysms. *Neurosurgery* 2015;76:721–26 CrossRef Medline
10. Baharoglu MI, Lauric A, Safain MG, et al. Widening and high inclination of the middle cerebral artery bifurcation are associated with presence of aneurysms. *Stroke* 2014;45:2649–55 CrossRef Medline
11. Farnoush A, Avolio A, Qian Y. Effect of bifurcation angle configuration and ratio of daughter diameters on hemodynamics of bifurcation aneurysms. *AJNR Am J Neuroradiol* 2013;34:391–96 CrossRef Medline
12. Zhang XJ, Gao BL, Li TX, et al. Association of basilar bifurcation aneurysms with age, sex, and bifurcation geometry. *Stroke* 2018;49:1371–76 CrossRef
13. Jansen IG, Schneiders JJ, Potters WV, et al. Generalized versus patient-specific inflow boundary conditions in computational fluid dynamics simulations of cerebral aneurysmal hemodynamics. *AJNR Am J Neuroradiol* 2014;35:1543–48 CrossRef Medline
14. Karmonik C. Toward improving fidelity of computational fluid dynamics simulations: Boundary conditions matter. *AJNR Am J Neuroradiol* 2014;35:1549–50 CrossRef Medline
15. Alfano JM, Kolega J, Natarajan SK, et al. Intracranial aneurysms occur more frequently at bifurcation sites that typically experience

- higher hemodynamic stresses.** *Neurosurgery* 2013;73:497–505 CrossRef Medline
16. Chung BJ, Mut F, Putman CM, et al. **Identification of hostile hemodynamics and geometries of cerebral aneurysms: a case-control study.** *AJNR Am J Neuroradiol* 2018;39:1860–66 CrossRef Medline
  17. Tütüncü F, Schimansky S, Baharoglu MI, et al. **Widening of the basilar bifurcation angle: association with presence of intracranial aneurysm, age, and female sex.** *J Neurosurg* 2014;121:1401–10 CrossRef Medline
  18. Meng H, Tutino VM, Xiang J, et al. **High WSS or Low WSS? Complex interactions of hemodynamics with intracranial aneurysm initiation, growth, and rupture: toward a unifying hypothesis.** *AJNR Am J Neuroradiol* 2014;35:1254–62 CrossRef Medline
  19. Rowe AJ, Finlay HM, Canham PB. **Collagen biomechanics in cerebral arteries and bifurcations assessed by polarizing microscopy.** *J Vasc Res* 2003;40:406–15 CrossRef Medline
  20. Yamazoe N, Hashimoto N, Kikuchi H, et al. **Elastic skeleton of intracranial cerebral aneurysms in rats.** *Stroke* 1990;21:1722–26 CrossRef Medline
  21. Kim C, Kikuchi H, Hashimoto N, et al. **Involvement of internal elastic lamina in development of induced cerebral aneurysms in rats.** *Stroke* 1988;19:507–11 CrossRef Medline
  22. Cebal JR, Duan X, Chung BJ, et al. **Wall mechanical properties and hemodynamics of unruptured intracranial aneurysms.** *AJNR Am J Neuroradiol* 2015;36:1695–703 CrossRef Medline

# Persistent Blood Flow inside the Woven EndoBridge Device More Than 6 Months after Intracranial Aneurysm Treatment: Frequency, Mechanisms, and Management—A Retrospective Single-Center Study

H.A. Nguyen, S. Soize, P.-F. Manceau, L. Vudang, and L. Pierot

## ABSTRACT

**BACKGROUND AND PURPOSE:** Due to its high safety and great efficacy, flow disruption with the Woven EndoBridge (WEB) device is increasingly used to treat intracranial aneurysms. We recently identified patients with intracranial aneurysm treated with the WEB who presented with residual blood flow inside the device (“contrast-in-WEB” phenomenon) more than 6 months posttreatment. This series reports the frequency and underlying mechanisms and discusses management of this phenomenon.

**MATERIALS AND METHODS:** All patients presenting with the contrast-in-WEB phenomenon in the prospectively collected data base of patients with aneurysm treated with the WEB were retrospectively collected and analyzed.

**RESULTS:** From June 2011 to February 2019, one hundred twenty-seven patients with 133 aneurysms were treated with the WEB and had DSA follow-up at 6 months or later. Eight patients (6.3%) presented with the phenomenon. All aneurysms were wide-neck bifurcation aneurysms, including 7 unruptured and 1 ruptured aneurysm located at the MCA (5 aneurysms), anterior communicating artery (2 aneurysms), and basilar artery (1 aneurysm). All except 1 patient received dual-antiplatelet therapy preprocedure. All except 1 patient received dual-antiplatelet therapy postoperatively for at least 1 month. The most likely mechanism of the phenomenon is the absence of intradevice thrombosis related to perioperative dual-antiplatelet medication. The phenomenon is also likely associated with a low risk of bleeding except when there is residual blood flow against the aneurysm wall or in the dome.

**CONCLUSIONS:** Contrast-in-WEB is a relatively rare phenomenon possibly induced by dual-antiplatelet therapy continued post-WEB procedure. In most cases, no additional treatment is required.

**ABBREVIATIONS:** DAPT = dual-antiplatelet therapy; DL = dual-layer; SL = single-layer

Flow disruption with the Woven EndoBridge (WEB; Sequent Medical, Aliso Viejo, California) system is a new approach for treatment of wide-neck bifurcation aneurysms.<sup>1</sup> The system disrupts blood flow entering the aneurysm by inducing intra-aneurysmal (and intradevice) thrombosis that usually occurs hours following the procedure. Because the WEB is an intrasaccular device, dual-antiplatelet treatment is not necessary before or after the procedure, and its use can be extended to ruptured aneurysms.<sup>2-6</sup> Since its first use in humans in 2011, the safety and efficacy of the WEB has been evaluated in several prospective, multicenter, Good Clinical Practice

studies.<sup>2-5,7-14</sup> The level of procedural safety has been extremely high with no mortality and a morbidity rate of between 0.7% and 3.0% at 1 month.<sup>2,3</sup> Adequate occlusion (complete occlusion and residual neck) according to the WEB occlusion scale was observed between 79.1% and 84.6% after 1-year follow-up.<sup>2-4</sup> Long-term efficacy is still being evaluated after the so-called “compression” phenomenon, more a “retraction” process related to thrombosis into the device as part of the healing process, was reported.<sup>15,16</sup> A recent publication about the global population of 3 European WEB studies confirms robust stability of the treatment at 2-year follow-up.<sup>17</sup>

During the follow-up of our large series of patients treated with the WEB since 2011, we observed the presence of residual flow inside the device >6 months after treatment (“contrast-in-WEB phenomenon”). Because this phenomenon was not previously analyzed, we conducted a retrospective study to investigate its incidence and underlying mechanisms and to propose optimal patient management.

Received February 6, 2020; accepted after revision April 14.

From the Department of Radiology (H.A.N., L.V.), Bach Mai Hospital, Hanoi, Vietnam; and Department of Neuroradiology (H.A.N., S.S., P.-F.M., L.P.), Hôpital Maison-Blanche, Reims, France.

Please address correspondence to Laurent Pierot, MD, PhD, Department of Neuroradiology, Hôpital Maison-Blanche, 45 rue Cognacq-Jay, 51092 Reims cedex, France; e-mail: lpierot@gmail.com  
<http://dx.doi.org/10.3174/ajnr.A6593>

## MATERIALS AND METHODS

This retrospective, single-center study was conducted between June 2011 and February 2019. According to the retrospective design of the study, institutional review board or ethics committee approval was not required. Patients gave oral informed consent for their data use.

### Study Design

Patients were included if

- They had an intracranial aneurysm treated with the WEB device with or without adjunctive materials.
- They were followed-up with DSA at 6 months or later.
- There was residual flow inside the device at least 6 months posttreatment.

Patients were excluded if they did not have at least a 6-month DSA follow-up or if they refused to participate in the study.

### WEB Embolization Technique

All patients had coagulation evaluation before the WEB procedure, which included prothrombin time–international normalized ratio, activated clotting time, fibrinogen, and platelet count.

The procedure was performed on a biplane angiographic system (AlluraClarity; Philips Healthcare) with patients under general anesthesia. Patients with unruptured aneurysms received dual-antiplatelet therapy a few days before the procedure, using 2 different protocols, which were implemented successively using aspirin, 75 mg/day, plus clopidogrel, 75 mg/day for 5 days, or aspirin, 75 mg/day, plus ticagrelor, 90 mg, twice daily for 2 days. We did not perform antiplatelet testing. All patients (with ruptured and unruptured aneurysms) received a loading dose of IV heparin (Panpharma; Luitré, France), 50 U/kg, after femoral puncture followed by IV infusion of 1000 U/h during the procedure. Postoperatively, all patients received aspirin, 75 mg/day, for at least 5 weeks; with stent placement or WEB protrusion, clopidogrel or ticagrelor (same doses) was also given with variable durations.

Triaxial access (long introducer sheath, distal access catheter, and microcatheter) was used routinely for the placement of the WEB device. The microcatheter was a VIA (Sequent Medical).

Using measurements obtained on 3D-DSA images, we performed WEB device sizing. The size of aneurysm including width, height, and neck was measured in 2 orthogonal planes. Then, following oversizing recommendations (1 mm added to the average width and a decrease of 1 mm in height), we chose the WEB.

### Imaging Follow-Up

Anatomic follow-up was performed by 3T MR imaging and DSA according to a previously published protocol.<sup>18</sup> In the most recent follow-up (since September 2018), VasoCT (Philips Healthcare) was performed using a diluted iodine contrast agent with 15% iodixanol (Visipaque 270; GE Healthcare) and an 85% saline solution. The total volume used was 90 mL at an injection rate of 3 mL/s.

### Data Collection

A prospective data base of all patients with aneurysms treated with the WEB is maintained. The files and follow-up images of

all patients were reviewed by a physician not involved in the WEB procedures to identify all patients with persistent contrast inside the WEB at 6 months' follow-up or later. Aneurysm characteristics and treatment modalities were collected in the electronic medical records system and retrospectively reviewed.

To determine the role of dual-antiplatelet therapy (DAPT) in the occurrence of the contrast-in-WEB phenomenon, we analyzed the files of the 119 patients treated during the recruitment period who did not present with the phenomenon. The reasons for placing the patients under DAPT after the procedure were collected.

### Data Analysis

An interventional neuroradiologist with 4 years' experience independently analyzed the images. The following elements were analyzed on 2D-DSA and VasoCT: Opacification of the WEB was classified as complete when the full device was opacified with contrast and partial when it was partially opacified with contrast (Fig 1). Additionally, the presence of contrast in the aneurysm neck or in the aneurysm sac (at the level of the dome) was evaluated.

In addition to evaluating residual flow in the WEB device and the aneurysm, we evaluated potential modification of the WEB shape by observation and direct measurement of the distance between both proximal and distal markers in the same DSA projection using 2D-DSA nonsubtracted images.

## RESULTS

From June 2011 to February 2019, one hundred twenty-seven patients with 133 aneurysms (124 unruptured and 9 ruptured) were treated with the WEB device (20 patients/21 aneurysms with the WEB-dual-layer [DL], 107 patients/112 aneurysms with the WEB-single layer [SL] or WEB-single-layer spherical [SLS]) and had DSA follow-up at 6 months or later. Eight patients (6.3%) met the inclusion/exclusion criteria of the study for the contrast-in-WEB phenomenon.

### Aneurysm Characteristics

The study group comprised 8 aneurysms presenting with residual blood flow in the device at 6 months' follow-up or later. Seven aneurysms were unruptured, and one was ruptured. All aneurysms were wide-neck bifurcation aneurysms located at the MCA (5 aneurysms), anterior communicating artery (2 aneurysms), and basilar artery (1 aneurysm). Regular shape was dominant (6 aneurysms). Aneurysm characteristics are shown in Table 1.

### Antiplatelet Treatment

Preoperative coagulation evaluation findings were normal in all patients.

Three of 8 patients with the contrast-in-WEB phenomenon received long-term antiplatelet therapy before treatment of cerebral aneurysms due to their comorbidities, including mono antiplatelet therapy in 1 (patient 5) and DAPT in 2 (patients 4 and 6). Before the procedure, 1 patient received DAPT with oral aspirin, 75 mg, and clopidogrel, 75 mg, daily for 5 days (patient 1) and 6 patients received DAPT with aspirin, 75 mg, and



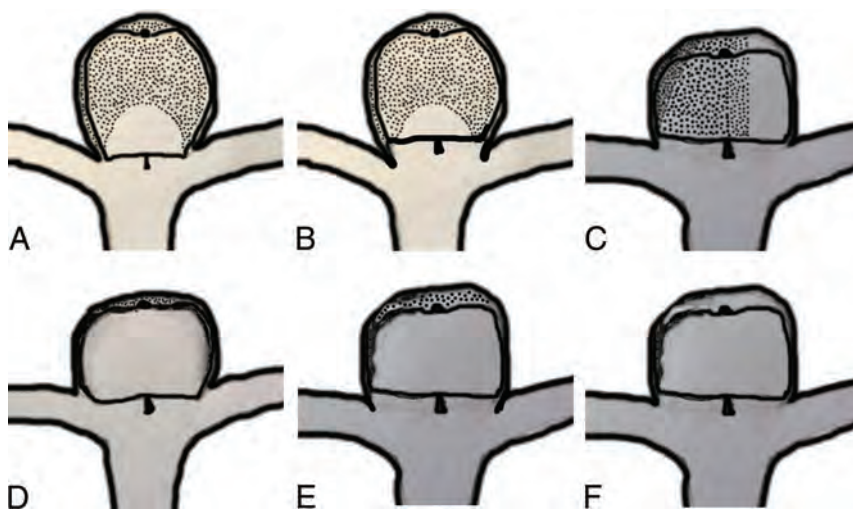


**FIG 1.** Different types of contrast-in-WEB phenomenon. Areas with black spots are thrombosed. A, Partial opacification of the WEB without opacification of the neck or aneurysm. B, Partial opacification of the WEB and opacification of the neck (neck remnant). C, Partial opacification of the WEB and aneurysm dome (aneurysm remnant). D, Complete opacification of the WEB without opacification of the neck or aneurysm. E, Complete opacification of the WEB and opacification of the neck (neck remnant). F, Complete opacification of the WEB and opacification of the aneurysm (aneurysm remnant).

**Table 1: Aneurysm characteristics and WEB deployed**

No.	Location	Sac Width (mm)	Sac Height (mm)	Neck Width (mm)	Dome-to-Neck Ratio	Ruptured Status <sup>a</sup>	WEB Deployed
1	AcomA	6.0	4.7	4.5	1.3	0	SL 7-3
2	BA	3.4	5.0	3.2	1.1	0	SL 5-3
3	MCA	7.2	5.9	5.5	1.3	0	SL 8-3
4	MCA	6.7	4.0	6.0	1.1	0	SL 7-3
5	MCA	5.3	3.9	4.4	1.2	0	SL 6-3
6	MCA	3.2	4.5	3.3	1.0	0	SL 4.5-3
7	MCA	5.2	5.0	4.4	1.2	0	SL 7-3
8	AcomA	3.7	4.1	3.0	1.2	1	SL 4.5-2

**Note:**—AcomA indicates anterior communicating artery; BA, basilar artery.

<sup>a</sup> 0, Unruptured; 1, ruptured.

ticagrelor, 90 mg, twice daily for 2 days (patients 2 to 7). After the intervention, 6 of the 7 patients with unruptured aneurysm were treated with DAPT for at least 2 months: One because the patient (patient 3) was treated with the WEB and stent (DAPT for 3 months), 1 because the patient (patient 7) had a WEB protrusion (DAPT for 2 months), and the remaining 4 patients (patients 1, 4, 5, and 6) due to comorbidities, with permanent DAPT in 2 (patients 4 and 6), DAPT for 3 months in 1 (patient 5), and DAPT for 2 years in 1 (patient 1). The patient with a ruptured aneurysm (patient 8) was treated with DAPT for 1 month followed by mono antiplatelet therapy due to the WEB protrusion.

Among the 119 patients who did not present with the contrast-in-WEB phenomenon, 36 (30.3%) received DAPT after the procedure. In 20 patients, this treatment was given due to placement of a stent (15 patients) or a flow diverter (5 patients) during the procedure. Three patients were treated permanently with DAPT related to cardiac disease or previous stroke, and 13 patients, due to WEB protrusion.

## Procedure

The WEB alone was successfully deployed and detached in 7 aneurysms. One MCA aneurysm was treated with the WEB and a rescue stent because of important WEB protrusion (patient 3). All WEBs used were WEB-SL, including 27 devices in 2 aneurysms, 21 devices in 1, and 17 devices in 5. In all except 1 patient (patient 4), the WEB was oversized in width according to current recommendations. The size of the WEB is reported in Table 1.

## Complications and Initial Results

No intraoperative complications occurred in any patient.

Immediate postoperative DSA, including 2D-DSA in all patients and VasoCT in 3 patients, showed residual flow inside the WEB in 3 patients and inside as well as around the WEB in 5 patients.

## Clinical and Imaging Follow-Up

The mean follow-up time was  $18.75 \pm 13.4$  months (range, 6–48 months). All patients remained clinically normal during the follow-up period (mRS 0). No bleeding or rebleeding was observed during this period.

DSA follow-up was performed at 6 months in all except 1 patient, at 1 year in all except 1 patient who was pregnant, at 2 years in 2 patients, and at 4 years in 1 patient.

All aneurysms and patients underwent at least 1 VasoCT during the follow-up, showing partial WEB opacification without neck or aneurysm opacification (Fig 2) in 3 patients (patients 2, 5, and 6), complete WEB opacification without neck or aneurysm opacification (Fig 3) in 3 patients (patients 1, 7, and 8), partial WEB opacification and neck opacification (Fig 4) in 1 patient (patient 3), and complete WEB opacification and dome opacification (Fig 5) in 1 patient (patient 4). This last patient was treated with an inappropriately oversized (mean aneurysm width, 6.7 mm, and the implanted device was a WEB 17 SL 7 × 3 mm) WEB device.

Measurement of the WEB postoperatively and during follow-up did not reveal height modification. Among 7 patients followed up after 6 months, the residual opacified part was completely thrombosed at 1 year in 1 patient (patient 5, in this patient DAPT was discontinued after 3 months), had slightly decreased after 4 years in 1 patient (patient 1), and was unchanged after 1 year in 3 patients (patients 4, 6, and 8) and after 2 years in 2 patients (patients 2 and 3). The height modification of the WEB is shown in Table 2.

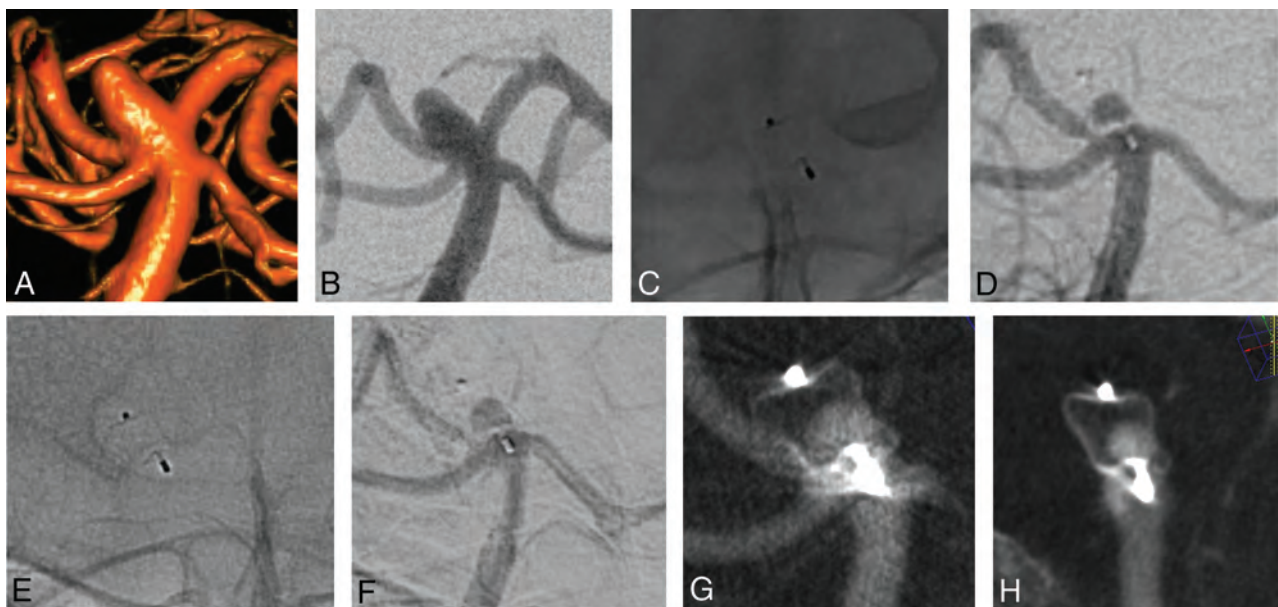


**FIG 2.** 3D (A) and 2D (B) DSA show a basilar artery aneurysm. Nonsubtraction (C) and subtraction (D) images of the first DSA follow-up after 1 year show partial filling of the WEB with contrast. A similar finding is observed at 2 years (E and F). VasoCT in 2 different views (G and H) confirms a partial opacification of the WEB and no opacification of the aneurysm.

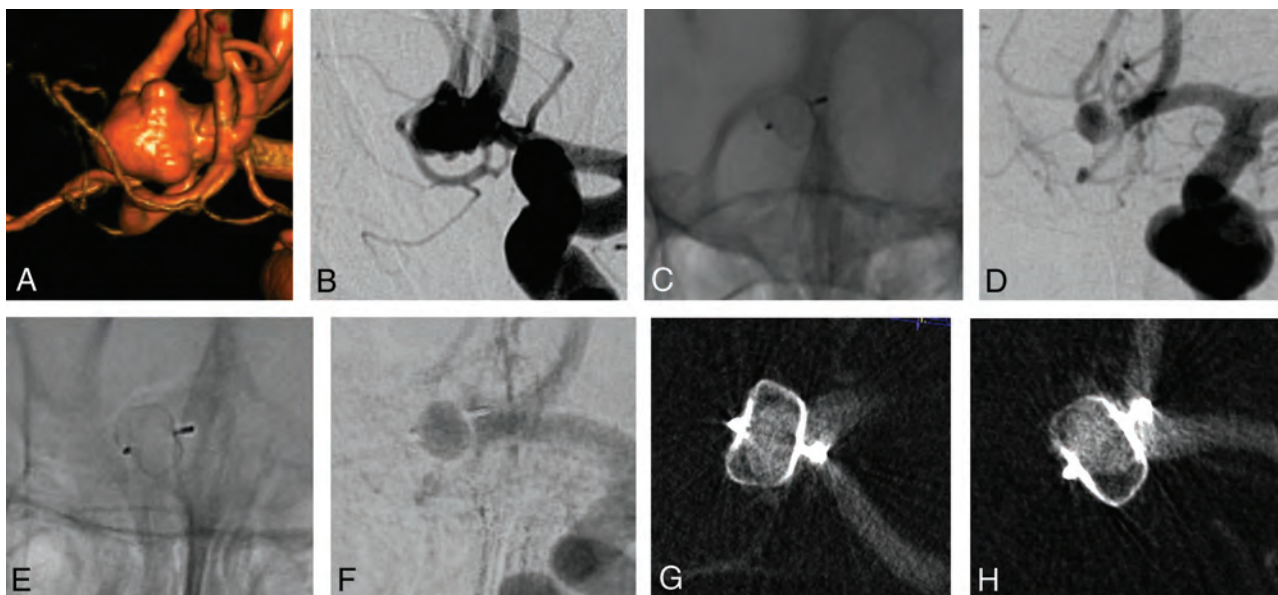


**FIG 3.** 3D (A) and 2D (B) DSA show an anterior communicating artery aneurysm. Nonsubtraction (C) and subtraction (D) images of the first DSA follow-up after 6 months and of the latest DSA follow-up after 4 years (E and F) show complete filling of the WEB with contrast. VasoCT in 2 different views (G and H) shows opacification of the WEB and no opacification of the aneurysm.

### Retreatment

The patient who had residual flow in the aneurysm dome (patient 4) was retreated by clipping 15 months after the initial WEB procedure.

### DISCUSSION

This series describes a phenomenon, contrast-in-WEB, observed after WEB aneurysm treatment, which is persistent blood flow inside the WEB device  $\geq 6$  months post-WEB treatment. The

phenomenon is illustrated by a persistent opacification inside the WEB device on DSA and is well-visualized on VasoCT. This persistent WEB opacification can be partial or complete and is sometimes associated with residual opacification of the neck or dome. This phenomenon has been very rarely reported in the literature (2 cases, one of them being included in the present series) and was relatively rare (6.3%) in our single-center series.<sup>19,20</sup> It likely also exists after aneurysm coiling as shown by some experimental studies but is difficult to depict due to coil artifacts.<sup>21</sup> The phenomenon was observed in both ruptured and unruptured aneurysms exclusively with the WEB-

**Table 2: WEB shape modification**

No.	Height Postoperat-ion (mm)	Height after 6 Months (mm)	Height after 1 Year (mm)	Height after 2 Years (mm)	Height after 3 Years (mm)	Height after 4 Years (mm)
1	6.2	5.8	5.8	5.9	5.6	5.8
2	3.6	—	3.4	3.6	—	—
3	7.8	7.9	7.6	7.7	—	—
4	5.5	5.9	5.1	—	—	—
5	5.4	6.0	5.8	—	—	—
6	4.1	4.2	4.1	—	—	—
7	6.0	6.0	—	—	—	—
8	3.7	3.7	3.8	—	—	—

**Note:**— indicates no imaging was performed at this date.

SL and was persistent in all but 1 patient (the longest follow-up being 4 years). Thus, further thrombosis inside the WEB is rarely observed during follow-up, when the phenomenon is detected at 6 months.

### Mechanisms

The first important point is that the persistence of blood flow inside the device shows that thrombosis inside the device did not occur; instead, blood flow is related to coagulation factors related to the patient or the treatment the patient received or mechanical factors related to the device.

Findings of the coagulation evaluation (prothrombin time—international normalized ratio, activated clotting time, fibrinogen levels, and platelet count) systematically performed before all endovascular treatment procedures of aneurysms were normal in all patients. All patients received heparin treatment during the procedure, which was stopped within 24 hours postprocedure; therefore, it seems unlikely that heparin plays a role in the phenomenon. In all except 1 case, patients received DAPT preprocedure. Finally, all except 1 patient received DAPT postoperatively for at least 1 month. DAPT is used preoperatively because the WEB treatment is dedicated to wide-neck bifurcation aneurysm treatment associated with a higher risk of thromboembolic complications than narrow-neck aneurysms during endovascular treatment.<sup>22</sup> Moreover, in case of WEB treatment failure, an alternative endovascular treatment option is stent-assisted coiling using DAPT. DAPT is used postoperatively if a stent is placed in combination with the WEB or in cases in which there is WEB protrusion with reduction of the caliber of 1 bifurcation branch. DAPT likely prevents initiation of the intradevice thrombosis process, which will not occur even after a change to mono antiplatelet therapy or even after stopping all antiplatelet medications.

Thirty-six patients treated with the WEB and receiving DAPT after the procedure did not present with the contrast-in-WEB phenomenon. Among them, an additional device (stent or flow diverter) was placed in front of the aneurysm neck in 20 patients and probably explained why these patients did not present with the phenomenon. However, it seems that the placement of a stent did not completely prevent the phenomenon because 1 patient with it was treated with the WEB and a stent. Finally, 13 patients received DAPT because of WEB protrusion, and the fact that they did not present with the phenomenon shows that other individual factors play a role.

All patients were treated with the WEB-SL; this phenomenon was not observed with dual-layer devices (WEB-DL). Because a

limited number of patients (20/127 or 15.7%) were treated with the WEB-DL in our global series, it is not possible to confirm whether this phenomenon also occurs with this device. According to their design, the dual-layer devices have a double layer at the proximal surface level, while single-layer devices have 1 layer. The new braiding used for single-layer devices is different from that used for dual-layer devices and includes a high wire density; both devices offer equivalent anatomic results in long-term follow-up.<sup>17</sup>

Another potential factor is mechanical and related to oversizing in the width of the WEB device. Oversizing the WEB width is associated with lateral compression and device deformation, which can potentially modify the porosity of the device, especially at its periphery. However, the expectation is that the more oversized the device is, the lower its porosity will be, which has been confirmed by some laboratory tests (unpublished data). Even so, the only case in which the device was not oversized (patient 4) was associated with a less favorable anatomic situation (contrast in the WEB and in the aneurysm dome), which required retreatment.

Finally, in 1 patient (patient 3), a rescue stent was placed in front of the aneurysm neck after the WEB deployment. In this patient, the stent potentially played a role in the contrast-in-WEB phenomenon occurrence and the neck opacification that was observed in this patient by displacing the WEB too much.

At the moment, on the basis of our series, we hypothesize that the contrast-in-WEB phenomenon likely occurs due to perioperative antiplatelet medication (namely postoperative DAPT). Additionally, our series reveals that the worst cases (association of neck or aneurysm opacification) seem to be associated with WEB undersizing or additional stent placement.

### Management of Contrast-in-WEB Phenomenon

According to the hypothesized mechanism of the phenomenon, its prevention should focus on fine-tuning the perioperative antiplatelet medication, which suggests avoiding postoperative DAPT; this has 2 consequences: 1) DAPT can be given preoperatively but has to be stopped postoperatively, and 2) patients under chronic DAPT for other health problems should probably not be treated with the WEB. As discussed, the WEB device still needs to be adequately oversized in width, given that it does not seem to play a role in the contrast-in-WEB phenomenon.<sup>16</sup>

The next question is what to do in cases of existing contrast-in-WEB phenomenon? Briefly, 3 situations can be encountered. First, the contrast is only visible inside the WEB device and not around it (Figs 2 and 3). In this case, because there is no blood flow in contact with the aneurysm wall, the risk of rebleeding is probably very low or nonexistent and no additional treatment is required other than regular follow-up. Second, when contrast is seen inside the WEB and at the neck (Fig 4), the risk of bleeding is probably low, as in the case of any neck remnant.<sup>23</sup> In this case, regular follow-up is required to identify any increase in the size of the contrast



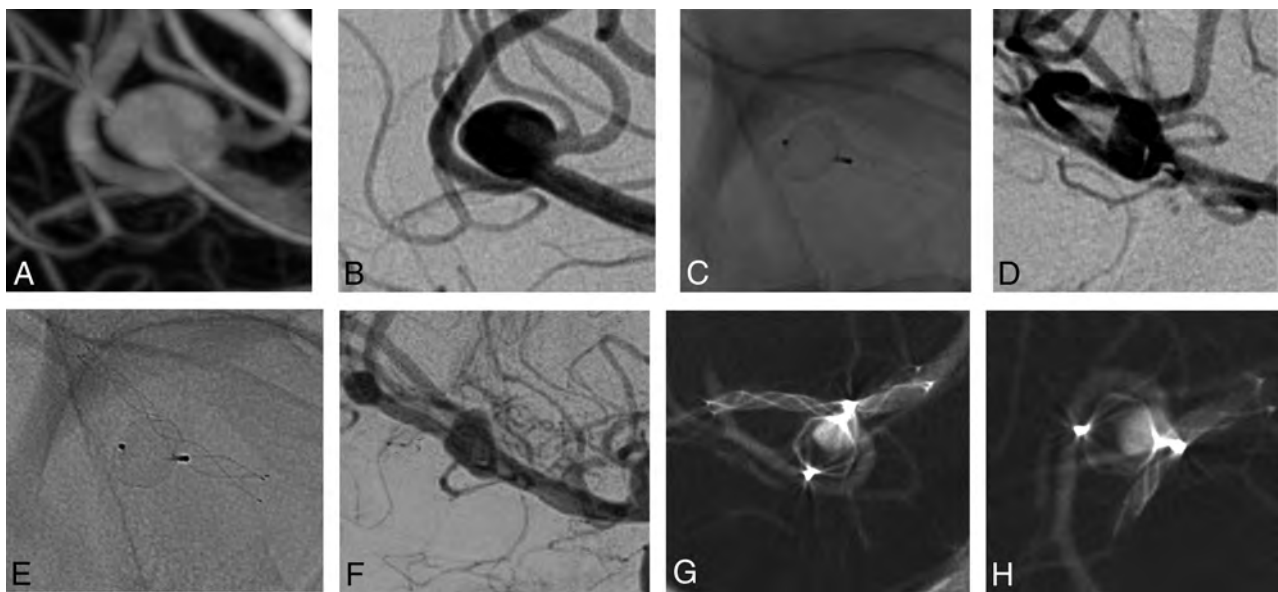


**FIG 4.** 3D (A) and 2D (B) DSA show an MCA aneurysm. Nonsubtraction (C) and subtraction (D) images of the first DSA follow-up after 6 months and of the latest DSA follow-up after 2 years (E and F) show partial opacification of the WEB and the aneurysm sac, confirmed by VasoCT in 2 different views (G and H).

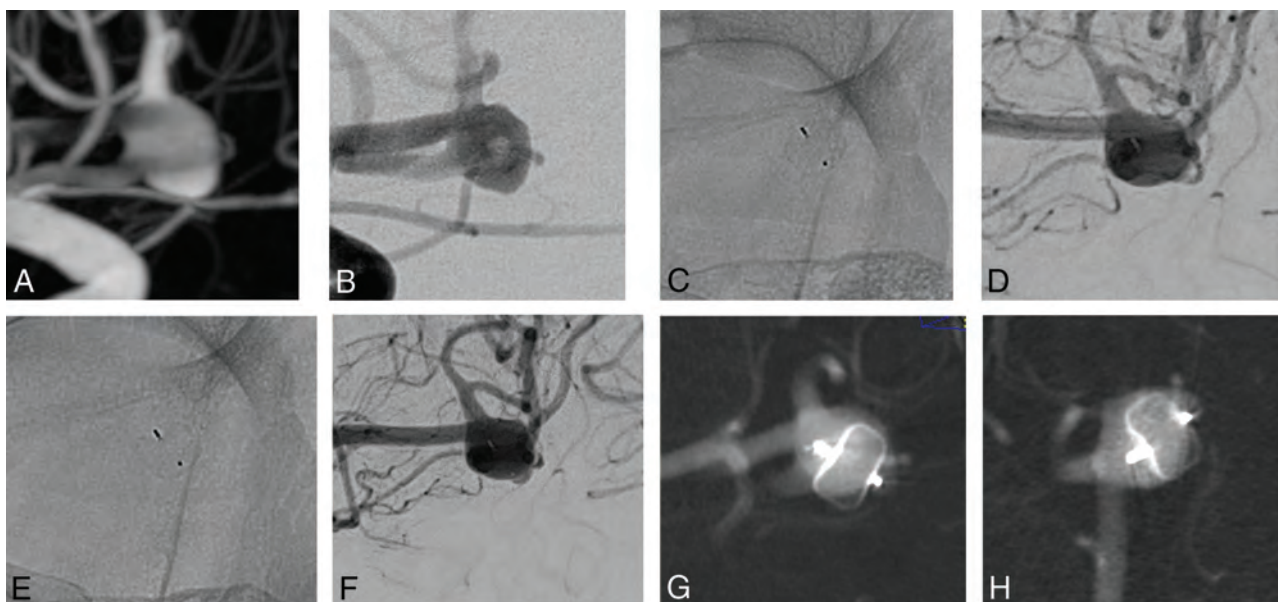


**FIG 5.** 3D (A) and 2D (B) DSA show an MCA aneurysm. Nonsubtraction (C) and subtraction (D) images of the first DSA follow-up after 6 months and of the latest DSA follow-up after 1 year (E and F) show complete opacification of the WEB and the aneurysm dome, confirmed by VasoCT in 2 different views (G and H).

opacification outside the WEB. Finally, in case of opacification in the WEB and at the level of the dome (Fig 5), an additional treatment should be proposed (patient 4). Potential additional treatments have been discussed previously in the literature.<sup>24,25</sup>

#### **Contrast-in-WEB Phenomenon and WEB Shape Modification**

An ancillary finding in this series is that in cases of the contrast-in-WEB phenomenon, there is no WEB shape modification. This phenomenon was initially reported by Cognard and Januel<sup>15</sup> and erroneously named “compression.” Pierot<sup>26</sup> subsequently suggested

that this phenomenon was not compression but is part of the healing process, with thrombus formation and retraction leading to retraction of the device itself.

The contrast-in-WEB phenomenon confirms the hypothesis of Pierot<sup>26</sup> that in case of absence of intra-WEB thrombosis, there is no WEB shape modification.

#### **Limitations**

This series has several limitations. First it is a retrospective, single-center series. Because this study reports a phenomenon that



was previously unknown, there is no other option than to report it in this way. Second, we have proposed several hypotheses regarding the mechanisms of this phenomenon, yet there is clearly a need for further investigation and studies to understand this phenomenon fully. Finally, we have made several suggestions regarding the management of this phenomenon, but a clearer understanding of the underlying mechanisms will potentially change treatment recommendations.

## CONCLUSIONS

This series reports a rare phenomenon (6.3%) observed after aneurysm treatment with the WEB that consists of delayed opacification of the WEB  $\geq 6$  months after the procedure. Further studies are needed to understand this phenomenon that is potentially related to the use of DAPT postoperatively as well as insufficient coverage of the neck. According to this preliminary series, the phenomenon seems to be associated with a low risk of bleeding, but larger studies with longer follow-up are needed to confirm this point.

Disclosures: Laurent Pierot—RELATED: Consulting Fee or Honorarium: MicroVention; UNRELATED: Consultancy: Balt, phenox, Vesalio.

## REFERENCES

- Gawlitza M, Soize S, Manceau PF, et al. **An update on intrasaccular flow disruption for the treatment of intracranial aneurysms.** *Expert Rev Med Devices* 2019;16:229–36 CrossRef Medline
- Pierot L, Moret J, Barreau X, et al. **Safety and efficacy of aneurysm treatment with WEB in the cumulative population of three prospective, multicenter series.** *J Neurointerv Surg* 2018;10:553–59 CrossRef Medline
- Arthur AS, Molyneux A, Coon AL, et al; WEB-IT Study Investigators. **The safety and effectiveness of the Woven EndoBridge (WEB) system for the treatment of wide-necked bifurcation aneurysms: final 12-month results of the pivotal WEB Intrasaccular Therapy (WEB-IT) Study.** *J Neurointerv Surg* 2019;11:924–30 CrossRef Medline
- Lubicz B, Klisch J, Gauvrit JY, et al. **WEB-DL endovascular treatment of wide-neck bifurcation aneurysms: short- and midterm results in a European Study.** *AJNR Am J Neuroradiol* 2014;35:432–38 CrossRef Medline
- Liebig T, Kabbasch C, Strasilla C, et al. **Intrasaccular flow disruption in acutely ruptured aneurysms: a multicenter retrospective review of the use of the WEB.** *AJNR Am J Neuroradiol* 2015;36:1721–27 CrossRef Medline
- van Rooij SB, van Rooij WJ, Peluso JP, et al. **WEB treatment of ruptured intracranial aneurysms: a single-center cohort of 100 patients.** *AJNR Am J Neuroradiol* 2017;38:2282–87 CrossRef Medline
- Klisch J, Sychra V, Strasilla C, et al. **The Woven EndoBridge Cerebral Aneurysm Embolization Device (WEB II): initial clinical experience.** *Neuroradiology* 2011;53:599–607 CrossRef Medline
- Pierot L, Klisch J, Liebig T, et al. **WEB-DL endovascular treatment of wide-neck bifurcation aneurysms: long-term results in a European series.** *AJNR Am J Neuroradiol* 2015;36:2314–19 CrossRef Medline
- Pierot L, Spelle L, Molyneux A, et al; WEBCAST and French Observatory Investigators. **Clinical and anatomical follow-up in patients with aneurysms treated with the WEB device: 1-year follow-up report in the cumulated population of 2 prospective, multicenter series (WEBCAST and French Observatory).** *Neurosurgery* 2016;78:133–41 CrossRef Medline
- Pierot L, Moret J, Turjman F, et al. **WEB treatment of intracranial aneurysms: feasibility, complications, and 1-month safety results with the WEB DL and WEB SL/SLS in the French Observatory.** *AJNR Am J Neuroradiol* 2015;36:922–27 CrossRef Medline
- Pierot L, Moret J, Turjman F, et al. **WEB treatment of intracranial aneurysms: clinical and anatomic results in the French Observatory.** *AJNR Am J Neuroradiol* 2016;37:655–59 CrossRef Medline
- Pierot L, Molyneux A, Byrne J. **O-020 WEB® aneurysm treatment: preliminary results of WEBCAST 2 study.** *J Neurointerv Surg* 2016;8 (Suppl 1):A13–14
- Pierot L, Costalat V, Moret J, et al. **Safety and efficacy of aneurysm treatment with WEB: results of the WEBCAST study.** *J Neurosurg* 2016;124:1250–56 CrossRef Medline
- Pierot L, Gubucz I, Buhk J, et al. **Safety and efficacy of aneurysm treatment with the WEB: results of the WEBCAST 2 study.** *AJNR Am J Neuroradiol* 2017;38:1151–55 CrossRef Medline
- Cognard C, Januel AC. **Remnants and recurrences after the use of the WEB intrasaccular device in large-neck bifurcation aneurysms.** *Neurosurgery* 2015;76:522–30 CrossRef Medline
- Herbretreau D, Bibi R, Narata AP, et al. **Are anatomic results influenced by WEB shape modification? Analysis in a prospective, single-center series of 39 patients with aneurysms treated with the WEB.** *AJNR Am J Neuroradiol* 2016;37:2280–86 CrossRef Medline
- Pierot L, Moret J, Barreau X et al. **Aneurysm treatment with Woven EndoBridge in the cumulative population of three prospective, multicenter series: 2-year follow-up.** *Neurosurgery* 2020 Jan 20. [Epub ahead of print] CrossRef Medline
- Soize S, Gawlitza M, Raoult H, et al. **Imaging follow-up of intracranial aneurysms treated by endovascular means.** *Stroke* 2016;47:1407–12 CrossRef Medline
- Timsit C, Soize S, Benaissa A, et al. **Contrast-enhanced and time-of-flight MRA at 3T compared with DSA for the follow-up of intracranial aneurysms treated with the WEB device.** *AJNR Am J Neuroradiol* 2016;37:1684–89 CrossRef Medline
- Nawka MT, Sedlacik J, Frölich A, et al. **Multiparametric MRI of intracranial aneurysms treated with the Woven EndoBridge (WEB): a case of Faraday's cage?** *J Neurointerv Surg* 2018;10:988–94 CrossRef Medline
- Chueh JY, Vedantham S, Wakhloo AK, et al. **Aneurysm permeability following coil embolization: packing density and coil distribution.** *J Neurointerv Surg* 2015;7:676–81 CrossRef Medline
- Pierot L, Cognard C, Anxionnat R, et al; for the CLARITY Investigators. **Ruptured intracranial aneurysms: factors affecting the rate and outcome of endovascular treatment complications in a series of 782 patients (CLARITY study).** *Radiology* 2010;256:916–23 CrossRef Medline
- Johnston SC, Dowd CF, Higashida RT, et al; CARAT Investigators. **Predictors of rehemorrhage after treatment of ruptured intracranial aneurysms.** *Stroke* 2008;39:120–25 CrossRef Medline
- Pierot L, Bannery C, Batchinsky-Parrou V, et al. **Clipping of recanalized intracerebral aneurysms initially treated by the Woven EndoBridge device.** *J Neurointerv Surg* 2019;11:807–11 CrossRef Medline
- Durner G, Özpeynirci Y, Schmitz B, et al. **Clipping as re-treatment strategy after treatment of a cerebral aneurysm with the Woven EndoBridge embolization device: case report.** *J Neurosurg* 2018 Mar 1. [Epub ahead of print] CrossRef Medline
- Pierot L. **Letter: WEB aneurysm treatment: occlusion stability and “compression.”** *Neurosurgery* 2015;77:E666–67 CrossRef Medline

# Residual Flow Inside the Woven EndoBridge Device at Follow-Up: Potential Predictors of the Bicêtre Occlusion Scale Score 1 Phenomenon

M.T. Nawka, A. Lohse, M. Bester, J. Fiehler, and J.-H. Buhk



## ABSTRACT

**BACKGROUND AND PURPOSE:** The Woven EndoBridge (WEB) device is an established technique for the treatment of intracranial aneurysms. Occasionally, persistent opacification inside the WEB lumen can be observed at follow-up (previously described as Bicêtre Occlusion Scale Score 1). We evaluated potential risk factors of this phenomenon, hypothesizing that initial deviation of the WEB device from the aneurysm axis, size of the aneurysmal neck surface, or inappropriate WEB sizing correlates with Bicêtre Occlusion Scale Score 1 findings.

**MATERIALS AND METHODS:** We systematically reviewed all patients treated with the WEB device between February 2014 and December 2018 in our neurointerventional center. Patients with midterm follow-up DSA available were considered for aneurysm evaluation applying the Bicêtre Occlusion Scale Score. WEB angle deviation from the aneurysm axis, neck widths, and WEB sizes were collected.

**RESULTS:** We included 65 patients with 67 intracranial aneurysms. Eleven of 67 (16.4%) intracranial aneurysms showed the Bicêtre Occlusion Scale Score 1 phenomenon at follow-up. Anterior-posterior projections of WEB axis deviation (angles measured in degrees) were significantly different between the Bicêtre Occlusion Scale Score 1 cohort (median  $\pm$  interquartile range,  $17 \pm 17$ ) and all other Bicêtre Occlusion Scale Scores (median  $\pm$  interquartile range,  $7 \pm 11$ ;  $P = .023$ ), whereas in lateral projections, no significant difference was observed (median  $\pm$  interquartile range,  $10 \pm 10$  versus  $8 \pm 9$ ;  $P = .169$ ). Neck or aneurysm recurrence, but not the Bicêtre Occlusion Scale Score 1 phenomenon, occurred significantly more often in patients with inappropriate WEB sizing compared with appropriate WEB sizing (median  $\pm$  interquartile range,  $1 \pm 1.3$  versus  $0 \pm 0$ ;  $P < .001/P = .664$ ).

**CONCLUSIONS:** The Bicêtre Occlusion Scale Score 1 phenomenon is associated with an initial deviation of the WEB device from the aneurysm axis but does not correlate with aneurysmal neck surface measurements or WEB sizing.

**ABBREVIATIONS:** AcomA = anterior communicating artery; BOSS = Bicêtre Occlusion Scale Score; IA = intracranial aneurysms; IQR = interquartile range; WOS = WEB Occlusion Scale; WEB = Woven EndoBridge

Endovascular treatment of wide-neck intracranial aneurysms (IA) with the Woven EndoBridge system (WEB; Micro-Vention) has been shown to be a reliable approach to provide flow disruption, demonstrating satisfactory aneurysm occlusion rates in previous studies.<sup>1-3</sup> Due to the risk of recurrence of IA, the performance of follow-up examinations is obligatory, and CTA, MRA, DSA, or flat panel CT are commonly used modalities to verify long-term stability.<sup>4-7</sup> Contrast opacification inside the

WEB lumen typically occurs during the procedure directly after WEB deployment, but occasionally isolated residual inflow of contrast media into the WEB-carrying dome can be observed at follow-up DSA.<sup>6</sup> The former WEB Occlusion Scale (WOS) has been revised, and the newer Bicêtre Occlusion Scale Score (BOSS) includes situations with residual intradevice WEB filling, to categorize this finding.<sup>6</sup> The clinical impact of this phenomenon concerning aneurysm rupture risk and antiaggregation is not yet known, but consideration for retreatment has been emphasized because the risk of rebleeding from ruptured aneurysms after WEB treatment seems to be an issue in this context.<sup>6,8</sup> Nevertheless, it is important to differentiate isolated residual WEB filling (BOSS 1) and aneurysm remnants or recurrence (BOSS 3), which more frequently require retreatment.<sup>6</sup>

The purpose of our study was to evaluate potential factors determining and influencing the development of BOSS 1 findings

Received February 1, 2020; accepted after revision April 23.

From the Department of Diagnostic and Interventional Neuroradiology, University Medical Center Hamburg-Eppendorf, Hamburg, Germany.

Please address correspondence to Marie T. Nawka, MD, University Medical Center Hamburg-Eppendorf, Martinistr 52, 20246 Hamburg-Eppendorf, Germany; e-mail: m.nawka@uke.de



Indicates article with supplemental on-line photo.

<http://dx.doi.org/10.3174/ajnr.A6605>

at midterm follow-up DSA, using a retrospective single-center case series. We primarily hypothesized that axis deviation of the WEB inside the aneurysm might result in residual intradevice filling. This seems logical with regard to the structure of the device: The flow-disrupting effect of the WEB can be considered optimal when the device is located exactly in the direction of the main geometric axis of the aneurysm, leading to blood flow against the proximal recess of the device, where wire density is highest. If the device is tilted, the flow might hit its "shoulder," where wire density decreases substantially compared with the center. This result might lead to incomplete thrombus formation within the WEB. However, it might not necessarily lead to recurrence as long as the neck of the aneurysm is fully covered. Further hypotheses were that a larger aneurysmal neck surface, the width of the WEB device, and suboptimal sizing of the WEB (undersizing) possibly correlate with the occurrence of the BOSS 1 phenomenon at midterm follow-up.

## MATERIALS AND METHODS

### Population

This retrospective study was conducted in accordance with the 1964 Declaration of Helsinki, and the local ethics review committee waived individual informed consent. We systematically retrospectively reviewed all patients with ruptured and unruptured intracranial aneurysms treated with the WEB device in our neurovascular center between February 2014 and December 2018. Patients with at least 1 midterm follow-up DSA (on average 6 months postprocedure) available were considered in this study.

### Endovascular Procedure and Antiaggregation

Initial DSA examinations and procedures were performed on a biplane angiographic system (Allura Clarity FD 20/20; Philips Healthcare), with the patient under general anesthesia in all procedures. Using transfemoral catheterization, selective series of the respective artery in anterior-posterior and lateral projections were obtained, and a 3D rotational angiography as well as an additional working view projection were acquired. On the basis of the 3D rotational angiography, aneurysm measurements were performed and the appropriate WEB size was chosen. WEB sizing was conducted following the respective recommendations of the company (Sequent Medical; WEB Device Selection Guide; MicroVention). After WEB positioning, a control angiogram was obtained to evaluate appropriate placement and contrast media stasis inside the device. If the WEB position was unsatisfactory, the device was resheathed and repositioned. A final DSA run was conducted after WEB detachment.

Follow-up DSA was performed using transfemoral catheterization and obtaining a selective series of the respective artery in anterior-posterior and lateral projections. Additionally, a dedicated contrast-enhanced flat panel CT scan was acquired, using the neuroangiographic x-ray C-arm (Allura Clarity FD 20/20), equipped with a flat panel detector.

We administered 100 mg of aspirin and 75 mg of clopidogrel 1 week prior to elective treatment of unruptured IA. Periprocedural anticoagulation with 2500 IU of heparin was performed in all cases. In ruptured IA, 250 mg of aspirin was administered during the intervention. In all cases, single antiaggregation with

100 mg/day of aspirin was continued for 6 weeks postprocedure, unless protrusion of the WEB device into the carrying vessel was observed; in those cases, an additional 75 mg of clopidogrel daily was deemed necessary, and in individual cases, antiaggregation was prescribed for up to 6 months.

### Image Analysis

Our standard follow-up regimen for patients treated with the WEB device includes MRA and DSA at 6 months, and additional long-term follow-up MRA is regularly performed after 18 months. DSA images were evaluated by 2 independent, experienced neuro-radiologists with >4 years' experience in WEB treatment (J.-H.B. and M.B.). Aneurysm occlusion rates were assessed applying the BOSS: 0 = no aneurysm filling, 0' = opacification of the proximal recess, 1 = opacification inside the WEB, 2 = neck remnant, 3 = aneurysm remnant with contrast agent inside the sac between the wall and the WEB device.<sup>6</sup> Residual filling of the WEB device was analyzed using primarily flat panel CT and anterior-posterior and lateral DSA series, respectively. Additional grading of aneurysm occlusion at midterm follow-up DSA and long-term follow-up MRA was assessed according to the WOS: WOS A = complete aneurysm occlusion, WOS B = neck remnant, and WOS C = aneurysm remnant.<sup>9</sup>

All IA were assessed regarding implantation of the WEB device, and potential deviation from the aneurysm axis was measured in lateral and anterior-posterior planes. We subsequently performed arbitrary categorization of each intracranial aneurysm into 1 of the following 3 groups, depending on the extent of deviation: A (0°–15°), B (16°–30°), and C (31°–45°). To objectively determine the respective aneurysm axis in each case, we defined it as an orthogonal line toward the aneurysm neck plane.<sup>10</sup> We further collected the width of each WEB device and all aneurysm neck widths, measuring the largest and smallest diameters, respectively. Aneurysm neck surfaces were calculated by multiplying the minor and major aneurysm neck radii by  $\pi$ . Additionally, we analyzed WEB sizing for each aneurysm, determining the average aneurysm width from anterior-posterior and lateral projections, measuring the smallest aneurysm height and subsequently matching the chosen WEB device to the Device Selection Table according to the company's latest recommendations (WEB Device Selection Guide), resulting in a dichotomous classification: appropriate or inappropriate WEB sizing.

### Statistics

Quantitative variables were described as mean  $\pm$  SD, while qualitative variables were reported as number and percentage. Categorical variables were compared using the  $\chi^2$  or the Fisher exact test, as appropriate. The Mann-Whitney *U* test was applied when data did not follow a normal distribution. A *P* value of .05 was considered statistically significant. Statistical analysis was performed using SPSS Statistics 24.0 (IBM) and Excel 2016 (Microsoft).

## RESULTS

### Patient and Aneurysm Characteristics

The follow-up range for the DSA examinations postprocedure was 5.5–7.8 months (median, 6.1 months) and 14–24 months

(median, 18 months) for long-term MRA. Regarding the overall collective, 52/65 patients were women (80%) and 13/65 (20%) were men, with a mean age of  $55.0 \pm 9.6$  years; range, 30–81 years. Fifty-three of 67 IA (79.1%) were unruptured, and 14/67 (20.9%) IA were treated in the setting of subarachnoid hemorrhage, including 3 cases of retreatment due to aneurysm recurrence after prior coiling or clipping. Forty-six of 67 (68.7%) IA were located in the anterior circulation (anterior communicating artery [AcomA], 22; MCA, 6; internal carotid artery, 15; anterior choroidal artery, 1; posterior communicating artery, 2), whereas 21/67 (31.3%) IA were located in the posterior circulation (basilar artery, 17; PICA, 4). Intraoperative thromboembolic events occurred in 2 patients (3.1%), both treated by intravenous administration of tirofiban and dual-antiplatelet treatment for 3 months, showing no permanent clinical deficits. No contrast agent allergies or periprocedural hemorrhages occurred. In 2 cases, an additional stent was placed. Fifty-two patients were treated with the WEB 21 system, and in 15 patients, the WEB 17 device was implanted. mRS scores at midterm follow-up were available for 53/65 patients (81.5%), with 48 patients presenting with an mRS of 0 (90.6%). The mRS score was 1 in 1 patient (1.9%), 2 in 3 patients (5.7%, of whom 2 patients presented with incidental IA, and 1 patient, with a ruptured intracranial aneurysm with a pre-existing mRS of 2), and 4 in 1 patient (1.9%, who had a ruptured intracranial aneurysm). Twelve mRS values were missing at midterm follow-up.

Isolated residual WEB filling (BOSS 1) at midterm follow-up DSA occurred in 11/67 IA (16.4%). Of all BOSS 1 cases, 10 (91%) IA were located in the anterior circulation (AcomA 6; internal carotid artery 3; posterior communicating artery 1), whereas 1 (9%) intracranial aneurysm was located in the PICA. All BOSS 1 cases were unruptured aneurysms; no postoperative bleeding occurred in the BOSS 1 collective at midterm follow-up. Three patients (27%) of the BOSS 1 collective and 8 patients (14%) of the control group, including the remaining BOSS scores, received antiplatelet therapy (aspirin) at midterm follow-up because antiaggregation was mandatory for at least 6 months in those cases.

Following the WOS grading at midterm follow-up DSA, 9 patients (82%) showed complete aneurysm occlusion in the BOSS 1 cohort, 1 patient (9%) had a neck remnant, and 1 patient (9%) presented with an aneurysm remnant. In the control collective, 45 patients (81%) showed complete aneurysm occlusion, 8 patients (14%) demonstrated a neck remnant, and in 3 cases (5%), an aneurysm remnant was detected. We observed no significant difference between the BOSS 1 group and the control cohort at midterm follow-up DSA (median  $\pm$  interquartile range [IQR]:  $1 \pm 0$ ;  $1 \pm 0$ ;  $P = .961$ ).

Long-term MRA could be performed in 8 patients of the BOSS 1 cohort (73%), all showing complete aneurysm occlusion (100%). In the control collective, 32 of 56 patients (57%) underwent long-term follow-up MRA; 22 patients showed complete aneurysm occlusion (69%), 8 patients presented with a neck remnant (25%), and 2 patients were graded as having aneurysm remnants (6%).

### BOSS Classification

BOSS grading at midterm follow-up of all IA is shown in Table 1. Three of 11 patients with BOSS 1 had additional long-term

**Table 1: BOSS classification of the overall patient cohort according to Caroff et al<sup>6</sup>**

BOSS Classification	Description	Distribution No. (%)
0	No residual flow inside the aneurysm or the WEB	19 (28.4%)
0'	Opacification of the proximal recess of the WEB	22 (32.8%)
1	Residual flow inside the WEB	11 (16.4%)
2	Neck remnant	12 (17.9%)
3	Aneurysm remnant	3 (4.5%)
1 + 3	Contrast media depicted inside and around the device	0 (0%)

follow-up DSA 1 year after initial treatment (27.3%), whereas 8 patients did not appear for their appointments (72.7%). In 2 patients, BOSS 1 findings were still verifiable at long-term DSA; in 1 patient, BOSS 1 phenomenon disappeared 1 year after initial therapy (Figure 1).

### Deviation of the WEB Device from the Aneurysm Axis

To determine an exact analysis, we assessed the deviation of the WEB device from the aneurysm axis in both direct (working projection) and perpendicular views on the affected bifurcation using a selective series of the respective artery and 3D rotational angiography, similar to the projections used for obtaining measures to choose a WEB. See the On-line Figure for an exemplary illustration of axis measurements in an incidental AcomA aneurysm. Following the respective axis measurements, aneurysms of the BOSS 1 cohort and all other BOSS grades were grouped according to their axis deviation angle as described above: A ( $0^\circ$ – $15^\circ$ ), B ( $16^\circ$ – $30^\circ$ ), and C ( $31^\circ$ – $45^\circ$ ). Table 2 provides a detailed presentation of the axis deviation grading for patients in the subgroups BOSS 1 and all other BOSS grades. Axis deviation of the WEB device in an anterior-posterior orientation was significantly different between the BOSS 1 cohort and all other BOSS grades (median  $\pm$  IQR:  $17 \pm 17$  versus  $7 \pm 11$ ;  $P = .023$ ). No significant difference was detected between the 2 groups when assessing lateral projections (median  $\pm$  IQR:  $10 \pm 10$  versus  $8 \pm 9$ ;  $P = .169$ ).

### Aneurysm Characteristics and WEB Widths

No significant difference was detected between patients with BOSS 1 and all other BOSS grades regarding the width of each WEB device according to the measurements of each average aneurysm width and the corresponding WEB-selection table for correct sizing of the device (WEB Device Selection Guide; median  $\pm$  IQR:  $6 \pm 1$  versus  $6 \pm 2$ ;  $P = .296$ ).

Aneurysm diameters were measured in millimeters with 2 lengths for each aneurysm and sorted in 2 groups according to the longest and shortest diameters, respectively. No significant differences could be observed between either the BOSS 1 cohort and all other patients concerning the longest neck diameter (median  $\pm$  IQR:  $4.0 \pm 1.4$  versus  $4.0 \pm 1.9$  mm;  $P = .446$ ) or the shortest neck diameter (median  $\pm$  IQR:  $3.1 \pm 1.5$  versus  $3.2 \pm 1.4$  mm;  $P = .697$ ). Following the calculations described above, aneurysm neck surfaces are indicated in square millimeters. No significant difference was found comparing patients with BOSS 1 and all other BOSS classifications regarding aneurysmal neck



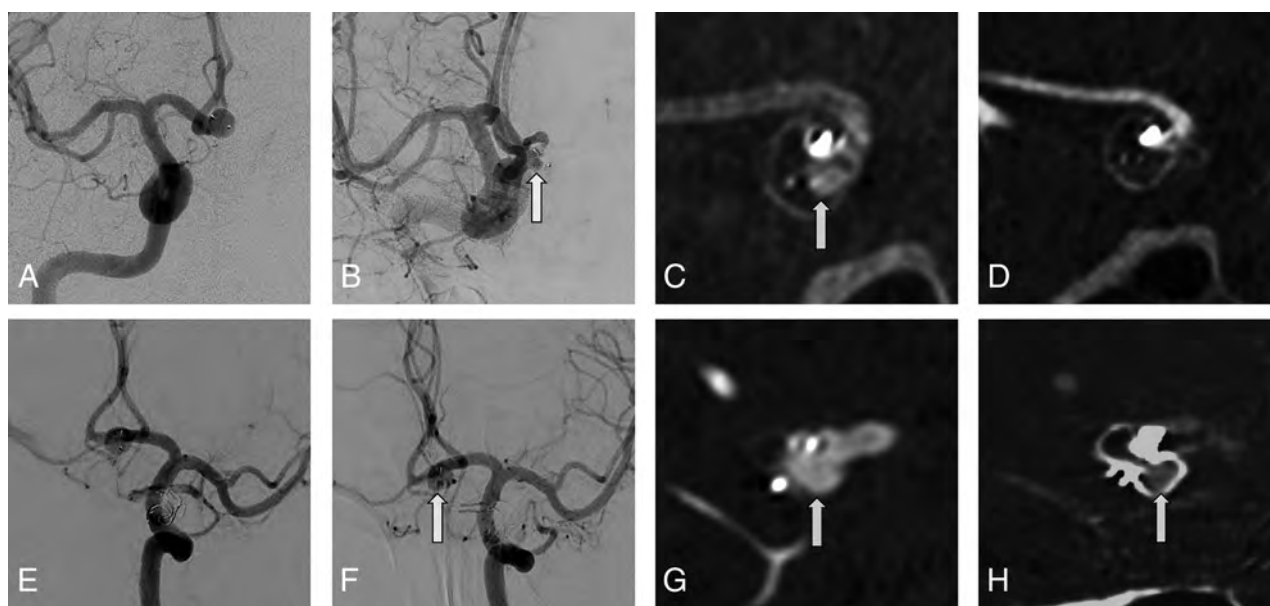


**FIG 1.** Two different patients (patient 1: A–D; patient 2: E–H) initially presenting with incidental AcomA aneurysms. Arrows indicate residual WEB filling at follow-up examinations (BOSS 1). A, Initial DSA of a patient treated with a WEB 27 device (single-layer, 6 × 4). B, Corresponding follow-up DSA after 6 months. C, Corresponding follow-up flat panel CT after 6 months. D, Corresponding follow-up flat panel CT after 1 year. Note the clearance of the residual intradevice filling. E, Initial DSA of a patient treated with a WEB 21 device (single-layer, 7 × 3). F, Corresponding follow-up DSA after 7 months. G, Corresponding follow-up flat panel CT after 7 months. H, Corresponding follow-up flat panel CT after 1 year. Note the remaining BOSS 1 phenomenon.

**Table 2: Grading of axis deviation (WEB device axis from the aneurysm axis)**

	Collective Distribution (No.)			Mean ± IQR (BOSS 1 vs all Other BOSS Grades), P Value
	All (67)	BOSS 1 (11)	BOSS 0, 0', 2, 3 (56)	
Working projection of bifurcation				
A (0°–15°)	48 (71.6%)	4 (36.4%)	44 (78.6%)	17 ± 17 vs 7 ± 11, <i>P</i> = .023
B (16°–30°)	15 (22.4%)	5 (45.4%)	10 (17.8%)	
C (31°–45°)	3 (4.5%)	2 (18.2%)	1 (1.8%)	
Not ratable	1 (1.5%)	0 (0.0%)	1 (1.8%)	
Perpendicular to bifurcation				
A (0°–15°)	58 (86.6%)	8 (72.8%)	50 (89.3%)	10 ± 10 vs 8 ± 9, <i>P</i> = .169
B (16°–30°)	8 (11.9%)	2 (18.2%)	6 (10.7%)	
C (31°–45°)	1 (1.5%)	1 (9.0%)	0 (0.0%)	

areas (median ± IQR: 9.6 ± 7.6 versus 10.0 ± 8.0 mm<sup>2</sup>; *P* = .588).

### WEB Sizing

In 57/67 patients, WEB sizing was considered appropriate (85.1%), whereas in 10/67 patients (14.9%), the WEB device was regarded as undersized (*n* = 8) or oversized (*n* = 2). WEB sizing was not associated with BOSS 1 findings at midterm follow-up (*P* = .664). Neck or aneurysm recurrence was significantly higher in patients with inappropriate WEB sizing compared with patients with appropriate WEB sizing (median ± IQR: 1 ± 1.3 versus 0 ± 0; *P* < .001). When we compared different WEB generations, no significant difference could be observed between patients treated with the WEB 17 and WEB 21 systems (median ± IQR: 1 ± 1 versus 1 ± 0; *P* = .227).

### DISCUSSION

Residual intradevice opacification on DSA follow-up examinations is a common finding after WEB treatment; because its etiology and clinical impact are not entirely clarified, this phenomenon requires further analysis.<sup>6</sup>

Because endovascular rating scales for coiling are not satisfactory for assessing aneurysm occlusion rates after WEB deployment, a uniform WEB rating scale has been previously introduced into clinical routine.<sup>6</sup> The 4-grade WOS was initially proposed by Lubicz et al,<sup>9</sup> in 2014, and was modified by Caroff et al,<sup>6</sup> in 2016, to meet the

need of identifying aneurysm subgroups, becoming the Bicêtre Occlusion Scale Score.<sup>11,12</sup> The BOSS includes grading of residual WEB filling (BOSS 1), though BOSS 1 findings can sometimes be difficult to depict and need to be strictly distinguished from BOSS 1 + 3 and BOSS 3 categories. To assess WEB deployment and positioning, flat panel CT has proved highly beneficial.<sup>13</sup> Aneurysm remnants or recurrent IA (BOSS 3) must be considered for retreatment because they have the risk of rebleeding, whereas in BOSS 1, patients can be observed using subsequent DSA follow-up examinations because the rupture risk is probably low.<sup>6</sup> Dealing with patients who underwent WEB treatment in the setting of SAH might differ; to date, no reports of rebleeding in BOSS 1 are available, which is consistent with our collective. Furthermore, no reliable data concerning long-term behavior of BOSS 1 findings exist.

During WEB treatment, adequate positioning of the device inside the aneurysmal sac is a crucial step because incorrect placement requires resheathing and replacement. An ideal alignment of the WEB device to the aneurysm axis is preferable, but sometimes the final position of the device is a compromise due to difficult aneurysm access or aneurysm configuration. If one hypothesized that an initial axis deviation of the device from the aneurysm axis correlates with BOSS 1 findings, this assumption could be partially verified by our results: Axis deviation in the anterior-posterior orientation on midterm follow-up DSA showed correlation to permanent blood flow into the device (BOSS 1).

In addition, most IA in the overall collective were located in the AcomA, where aneurysm access is achieved through the anterior cerebral artery and might sometimes be impeded by sharp curves between these vessels and is thus less straightforward compared with IA located in different areas. Especially in small AcomA aneurysms, catheterization might be challenging and requires consideration of the aneurysm neck orientation.<sup>14</sup> Complex anatomies in the AcomA region can eventually be overcome using smaller microcatheters with different tip shapes, and variation in the degree of the stiffness of the microcatheter could additionally be valuable, thus potentially improving microcatheter stability inside the aneurysm dome.<sup>14-16</sup>

If the microcatheter cannot be located in the anatomic center of the aneurysm dome, WEB deployment must be conducted from an oblique starting position. Because this course of axis deviation is difficult to ascertain from lateral projections, this difficulty might explain the missing correlation between BOSS 1 findings and determination of the lateral axis deviation. Because hemodynamic conditions and flow dynamics are crucial factors in the development of aneurysm recurrence, the AcomA location might be of high importance for the development of residual WEB filling because flow conditions are particularly complex in the AcomA region.<sup>17-19</sup> Hemodynamic studies confirmed that blood flow was faster in wide-neck IA;<sup>20</sup> however, the presence of a wide aneurysm neck as a risk factor for the development of aneurysm recurrence after WEB treatment could not be confirmed in our study. This issue might be explained by a relatively small range of neck widths in our collective (1.4–6.9 mm). Following aneurysm morphometrics, we furthermore aimed to assess the potential impact of aneurysm neck diameters and aneurysmal neck surfaces on the BOSS 1 phenomenon. Most interesting, this assumption could not be confirmed by our statistics; however, our results are in line with a recently published study by Goertz et al,<sup>21</sup> detecting no correlation between maximum aneurysm diameter/neck width and procedure-related complications after WEB treatment.

Not only correct deployment of the device but also WEB sizing is a crucial issue during the treatment process, and the official WEB-sizing scale recommends an appropriate choice of the device (WEB Device Selection Guide). Inappropriate sizing of the WEB device was found to be uncommon in patients with BOSS 1, whereas oversizing or undersizing of the WEB device resulted in substantially higher neck or aneurysm recurrence rates at follow-up. According to these findings, Cagnazzo et al<sup>22</sup> confirmed that undersizing of the WEB device is more common in incompletely occluded unruptured and ruptured IA. Especially in the

setting of treating ruptured IA, the primary objective is fast aneurysm occlusion, and imperfect WEB sizing can more likely be accepted than in the treatment of incidental IA where substantial case preparation is obligatory. However, assessment of BOSS 1 findings in ruptured aneurysms needs to be further evaluated in larger future studies. Following aneurysm treatment with the WEB device, adequate follow-up examinations are deemed necessary because aneurysm occlusion rates differ between unruptured and ruptured IA.<sup>3</sup> However, visualization of the WEB cavity and thus detection of BOSS 1 phenomenon in MRA is impeded due to radiofrequency shielding effects.<sup>23</sup> Therefore, BOSS 1 verification should generally be performed by DSA or flat panel CT.<sup>13,23</sup>

### Limitations

This study had several limitations. First, it was a retrospective analysis based on a relatively small single-center population. Additionally, we evaluated only the first (midterm) follow-up DSA. Because BOSS 1 cases might decrease and available DSA examinations after 12 months were sparse in our patient cohort, the rate of BOSS 1 findings after 1 year needs to be evaluated in further studies aiming to assess its clinical relevance. Because the impact of BOSS 1 findings might be higher in ruptured aneurysms due to the additional risk of aneurysm re-rupture, a potential correlation should be evaluated in future studies because our collective could not provide enough ruptured WEB cases.

### CONCLUSIONS

Occurrence of the BOSS 1 phenomenon at midterm follow-up is a common finding in patients treated with the last 2 generations of the WEB device, showing an association with the initial deviation of the WEB device from the aneurysm axis. Inappropriate WEB sizing does not typically lead to BOSS 1 phenomenon, but it is a risk factor for neck or aneurysm recurrence. To further assess the clinical impact of the BOSS 1 phenomenon, long-term follow-up DSA examinations will be useful to evaluate potential correlations among BOSS 1 findings, aneurysm recurrence, and rebleeding.

Disclosures: Jens Fiehler—UNRELATED: Consultancy: Acandis, Cerenovus, Medtronic, MicroVention, Stryker; Grants/Grants Pending: Acandis, Cerenovus, Medtronic, MicroVention, Stryker; Payment for Lectures Including Service on Speakers Bureaus: Penumbra; Stock/Stock Options: Tegus Corporation; OTHER RELATIONSHIPS: Managing Director of Eppdata. Jan-Hendrik Buhk—UNRELATED: Consultancy: Acandis, Cerenovus, MicroVention, Stryker; Employment: University Hospital Hamburg-Eppendorf. \*Money paid to individual.

### REFERENCES

1. van Rooij S, Sprengers ME, Peluso JP, et al. A systematic review and meta-analysis of Woven EndoBridge single layer for treatment of intracranial aneurysms. *Interv Neuroradiol* 2020 Feb 6. [Epub ahead of print] CrossRef Medline
2. Kaya HE, Bakdik S, Keskin F, et al. Endovascular treatment of intracranial aneurysms using the Woven EndoBridge (WEB) device: retrospective analysis of a single center experience. *Clin Imaging* 2020;59:25-29 CrossRef Medline
3. Zhang SM, Liu LX, Ren PW, et al. Effectiveness, safety and risk factors of Woven EndoBridge device in the treatment of wide-neck intracranial aneurysms: systematic review and meta-analysis. *World Neurosurg* 2020;136:e1-23 CrossRef Medline

4. Ozpeynirci Y, Braun M, Schmitz B. **CT angiography in occlusion assessment of intracranial aneurysms treated with the WEB device.** *J Neuroimaging* 2019;29:481-86 CrossRef Medline
5. Mine B, Tancredi I, Aljishi A, et al. **Follow-up of intracranial aneurysms treated by a WEB flow disrupter: a comparative study of DSA and contrast-enhanced MR angiography.** *J Neurointerv Surg* 2016;8:615-20 CrossRef Medline
6. Caroff J, Mihalea C, Tuilier T, et al. **Occlusion assessment of intracranial aneurysms treated with the WEB device.** *Neuroradiology* 2016;58:887-85 CrossRef Medline
7. van Rooij S, Peluso JP, Sluzewski M, et al. **Mid-term 3T MRA follow-up of intracranial aneurysms treated with the Woven EndoBridge.** *Interv Neuroradiol* 2018;24:601-07 CrossRef Medline
8. Cognard C, Januel AC. **Remnants and recurrences after the use of the WEB intrasaccular device in large-neck bifurcation aneurysms.** *Neurosurgery* 2015;76:522-30 CrossRef Medline
9. Lubicz B, Klisch J, Gauvrit JY, et al. **WEB-DL endovascular treatment of wide-neck bifurcation aneurysms: short- and midterm results in a European study.** *AJNR Am J Neuroradiol* 2014;35:432-38 CrossRef
10. Duan Z, Li Y, Guan S, et al. **Morphological parameters and anatomical locations associated with rupture status of small intracranial aneurysms.** *Sci Rep* 2018;8:6440 CrossRef Medline
11. Caroff J, Mihalea C, Ikka L, et al. **Interobserver variability in the assessment of aneurysm occlusion with the WEB aneurysm embolization system.** *J Neurointerv Surg* 2017;9:e11-12 CrossRef Medline
12. Fiorella D, Arthur A, Byrne J, et al. **Interobserver variability in the assessment of aneurysm occlusion with the WEB aneurysm embolization system.** *J Neurointerv Surg* 2015;7:591-95 CrossRef Medline
13. Caroff J, Mihalea C, Neki H, et al. **Role of C-arm VasoCT in the use of endovascular WEB flow disruption in intracranial aneurysm treatment.** *AJNR Am J Neuroradiol* 2014;35:1353-57 CrossRef Medline
14. Asif KS, Sattar A, Lazzaro MA, et al. **Consecutive endovascular treatment of 20 ruptured very small (<3 mm) anterior communicating artery aneurysms.** *Interv Neurol* 2016;5:57-64 CrossRef Medline
15. Sluzewski M, Bosch JA, van Rooij WJ, et al. **Rupture of intracranial aneurysms during treatment with Guglielmi detachable coils: incidence, outcome, and risk factors.** *J Neurosurg* 2001;94:238-40 CrossRef Medline
16. Wang CC, Lv N, Feng ZZ, et al. **Intra-aneurysmal microcatheter looping technique for stent-assisted embolization of complex intracranial aneurysms.** *Interv Neuroradiol* 2015;21:580-84 CrossRef Medline
17. Luo B, Yang X, Wang S, et al. **High shear stress and flow velocity in partially occluded aneurysms prone to recanalization.** *Stroke* 2011;42:745-53 CrossRef Medline
18. Huang DZ, Jiang B, He W, et al. **Risk factors for the recurrence of an intracranial saccular aneurysm following endovascular treatment.** *Oncotarget* 2017;8:33676-82 CrossRef Medline
19. Castro MA, Putman CM, Sheridan MJ, et al. **Hemodynamic patterns of anterior communicating artery aneurysms: a possible association with rupture.** *AJNR Am J Neuroradiol* 2009;30:297-302 CrossRef Medline
20. Tateshima S, Chien A, Sayre J, et al. **The effect of aneurysm geometry on the intra-aneurysmal flow condition.** *Neuroradiology* 2010; 52:1135-41 CrossRef Medline
21. Goertz L, Liebig T, Siebert E, et al. **Risk factors of procedural complications related to Woven EndoBridge (WEB) embolization of intracranial aneurysms.** *Clin Neuroradiol* 2019 Feb 7. [Epub ahead of print] CrossRef Medline
22. Cagnazzo F, Ahmed R, Zannoni R, et al. **Predicting factors of angiographic aneurysm occlusion after treatment with the Woven EndoBridge device: a single-center experience with midterm follow-up.** *AJNR Am J Neuroradiol* 2019;40:1773-78 CrossRef Medline
23. Nawka MT, Sedlacik J, Frölich A, et al. **Multiparametric MRI of intracranial aneurysms treated with the Woven EndoBridge (WEB): a case of Faraday's cage?** *J Neurointerv Surg* 2018;10:988-94 CrossRef Medline

# Posttreatment Imaging in Patients with Head and Neck Cancer without Clinical Evidence of Recurrence: Should Surveillance Imaging Extend Beyond 6 Months?

A. Gore, K. Baugnon, J. Beitler, N.F. Saba, M.R. Patel, X. Wu, B.J. Boyce, and A.H. Aiken



## ABSTRACT

**BACKGROUND AND PURPOSE:** Early detection of residual or recurrent disease is important for effective salvage treatment in patients with head and neck cancer. Current National Comprehensive Cancer Network guidelines do not recommend standard surveillance imaging beyond 6 months unless there are worrisome signs or symptoms on clinical examination and offer vague guidelines for imaging of high-risk patients beyond that timeframe. Our goal was to evaluate the frequency of clinically occult recurrence in patients with head and neck squamous cell carcinoma with positive imaging findings (Neck Imaging Reporting and Data Systems scores of 2–4), especially after 6 months.

**MATERIALS AND METHODS:** This institutional review board–approved, retrospective data base search queried neck CT reports with Neck Imaging Reporting and Data Systems scores of 2–4 from June 2014 to March 2018. The electronic medical records were reviewed to determine outcomes of clinical and radiologic follow-up, including symptoms, physical examination findings, pathologic correlation, and clinical notes within 3 months of imaging.

**RESULTS:** A total of 255 cases, all with Neck Imaging Reporting and Data Systems scores of 2 or 3, met the inclusion criteria. Fifty-nine patients (23%) demonstrated recurrence (45 biopsy-proven, 14 based on clinical and imaging progression), and 21 patients (36%) had clinically occult recurrence (ie, no clinical evidence of disease at the time of the imaging examination). The median overall time to radiologically detected, clinically occult recurrence was 11.4 months from treatment completion.

**CONCLUSIONS:** Imaging surveillance beyond the first posttreatment baseline study was critical for detecting clinically occult recurrent disease in patients with head and neck squamous cell carcinoma. More than one-third of all recurrences were seen in patients without clinical evidence of disease; and 81% of clinically occult recurrences occurred beyond 6 months.

**ABBREVIATIONS:** CECT = contrast-enhanced CT; HNSCCA = head and neck squamous cell carcinoma; HPV = human papillomavirus; NCCN = National Comprehensive Cancer Network; NI-RADS = Neck Imaging Reporting and Data Systems

Posttreatment surveillance imaging for head and neck cancer is complex and challenging. Altered anatomy from surgical resections, complex reconstructive surgery, and adjuvant radiation frequently define a new radiologic baseline. Despite these challenges, imaging surveillance plays a critical role in detecting early submucosal recurrences and is vital to optimizing salvage therapy.<sup>1–3</sup>

The Neck Imaging Reporting and Data System (NI-RADS) was developed to risk-stratify and standardize management recommendations on the basis of posttreatment imaging findings in patients with head and neck cancer.<sup>4,5</sup> The NI-RADS template standardizes nomenclature and facilitates unambiguous and uniform reporting. Radiologists commit to a discrete level of suspicion that maps to a clear management recommendation to optimize patient care. The NI-RADS template includes numeric categories of 0–4 based on index of suspicion for tumor recurrence at both the primary and nodal sites. A category of 0 reflects an incomplete examination, usually indicating a baseline examination or one without a suitable comparison. NI-RADS category 1 indicates no evidence of recurrence, and these patients continue routine surveillance. Categories 2 and 3 indicate a positive imaging finding, reflecting low and high suspicion for tumor recurrence, respectively. For patients with NI-RADS 2, it is recommended that clinicians consider direct visual

Received November 4, 2019; accepted after revision April 18, 2020.

From the Departments of Radiology and Imaging Sciences (A.G., K.B., X.W., A.H.A.), Radiation Oncology (J.B.), Hematology/Oncology (N.F.S.), and Otolaryngology (N.F.S., M.R.P., B.J.B., A.H.A.), Emory University School of Medicine, Atlanta, Georgia.

Paper previously presented at: Annual Meeting of the American Society of Neuroradiology, May 18–23, 2019; Boston, Massachusetts.

Please address correspondence to Ashley H. Aiken, MD, Department of Radiology and Imaging Sciences, Emory University Hospital, 1364 Clifton Rd NE, Atlanta, GA 30322; e-mail: ashley.aiken@emoryhealthcare.org



Indicates article with supplemental on-line table.

<http://dx.doi.org/10.3174/ajnr.A6614>



inspection for mucosal abnormalities or PET imaging for deep abnormalities and subsequent follow-up with earlier imaging (typically 2–3 months instead of 6 months). Biopsy consideration is recommended for NI-RADS 3. Category 4 indicates definite recurrence, established pathologically or by definite radiologic or clinical progression. A detailed description of NI-RADS has been published.<sup>5</sup>

Previous publications have established the frequency of NI-RADS scores and their positive predictive value for recurrence by category. Krieger et al<sup>3</sup> evaluated 618 targets and found 85.4% scored as NI-RADS one, 9.4% scored as NI-RADS 2, and 5.2% scored as NI-RADS 3, with failure rates of 3.79%, 17.2%, and 59.4% respectively. A recent article by Hsu et al<sup>6</sup> looked only at the first posttreatment examination in 199 patients and found that the rates of treatment failure increased with each incremental NI-RADS category from 1 to 3 (4.3%, 9.1%, and 42%), with a strong association between the NI-RADS score and treatment failure (hazard ratio = 2.6 at the primary site, hazard ratio = 5.2 in the neck).

Although many studies have demonstrated increased sensitivity for detecting disease recurrence with combined FDG-PET/CT, current evidence-based recommendations are limited in guiding imaging surveillance in these patients.<sup>3,7,8</sup> Wangyattawanich et al<sup>8</sup> suggested that patients with an incomplete response (NI-RADS 2) to treatment for head and neck squamous cell carcinoma (HNSCCA) should undergo more frequent clinical and imaging surveillance compared with those with a complete response (NI-RADS 1). Imaging with PET/CT at least 12 weeks after the completion of treatment is generally agreed to be the optimal time for initial posttreatment baseline imaging, though a recent publication raises the possibility that this baseline imaging could occur as early as 8 weeks after treatment.<sup>7,9–12</sup> However, beyond the first posttreatment examination, there remains wide variation in clinical practice, imaging surveillance technique (contrast-enhanced CT [CECT] alone, PET/CT, PET/CECT, MR imaging, and so forth), frequency, and duration.

The National Comprehensive Cancer Network (NCCN; [https://www.nccn.org/professionals/physician\\_gls/default.aspx](https://www.nccn.org/professionals/physician_gls/default.aspx)) is a comprehensive set of clinical practice guidelines in oncology that detail sequential management decisions and interventions and provide recommendations for clinical follow-up. These recommendations are based on knowledge of current evidence-based research and consensus-based management. Although the NCCN recommends posttreatment imaging within 6 months after treatment, concrete recommendations for a surveillance algorithm beyond this point remain ambiguous in patients with head and neck cancer due to the lack of consensus data. Currently, the guidelines state that any further re-imaging beyond 6 months can be considered on the basis of “worrisome or equivocal signs/symptoms, smoking history, and areas inaccessible to clinical examination.” A large percentage of patients with head and neck malignancies have a smoking history and are susceptible to submucosal recurrences, nearly all of which are inaccessible or difficult to discern on clinical examination. Thus, most institutions and referring providers elect to image asymptomatic patients for surveillance. Given the limited data and ambiguous guidance, it is understandable that there is wide variation in clinical practice for these patients. More concerning is that some providers may

strictly adhere to the concrete recommendations from the NCCN and only image up to 6 months after treatment regardless of patient risk factors. Even after intent of curative therapy, up to 50% of patients with HNSCCA experience recurrences, most of which occur well beyond 6 months, particularly within the first 2–3 years of treatment.<sup>13</sup> To our knowledge, there are no previous studies to document the frequency of imaging-detected recurrence in patients with asymptomatic head and neck cancer.

The purpose of our retrospective study was to evaluate the incidence of clinically occult recurrences detected by imaging alone (positive imaging findings, NI-RADS 2–4) in patients undergoing surveillance imaging at our institution. We also hypothesized that a considerable portion of clinically occult recurrences (in patients with NI-RADS 2–4) are detected beyond the NCCN recommended 6 months.

## MATERIALS AND METHODS

### *Patient Selection and Data Collection*

A Health Insurance Portability and Accountability Act–compliant, institutional review board–approved retrospective data base search of radiology reports containing the NI-RADS lexicon was performed from June 2014 to March 2018. Head and neck cancer NI-RADS reports were identified using an institutional data base search software containing a repertoire of dictated NI-RADS template reports. A search of posttreatment PET/CT and CECT neck soft-tissue reports was conducted with queries of NI-RADS scores 2, 3, or 4 at either the primary site or the neck. The output included the total number of reports that used the NI-RADS-structured reporting system and had a suspicious finding scored with NI-RADS 2–4 in the impression section of the radiology report.

Inclusion criteria were the following: 1) patients with HNSCCA who had undergone definitive treatment; 2) patients who underwent a clinical examination by either otolaryngology, radiation oncology, or medical oncology within 3 months of imaging; and 3) continued imaging and clinical follow-up of NI-RADS 2–4 lesions or biopsy of the imaging abnormality. Exclusion criteria included patients who already had a biopsy-proven recurrence (local, regional, or distant) before the imaging examination.

By definition, NI-RADS 1 category denotes negative findings on an imaging examination, with “no radiologic evidence of recurrence.” Therefore, any recurrence in this category would be radiographically occult. Thus, patients with NI-RADS 1 were not queried in the current study. NI-RADS 4 category represents “definitive recurrence,” strictly applied at our institution to biopsy-proven recurrence or clear clinical and radiographic progression, so patients are, by definition, symptomatic in the vast majority of people.

Clinical evidence of disease recurrence was defined by any clinical examination finding or symptom within the clinical note that raised concern for recurrence. Examples of suspicious clinical examination findings included new palpable abnormalities on physical examination or a finding deemed suspicious by Ear, Nose, and Throat physicians on office-based flexible fiber optic endoscopy. Common clinical symptoms related to treatment or expected sequelae of postradiation changes, including thickening

of the skin and platysma, radiation mucositis, and thickening of the laryngeal structures/laryngeal edema, were not classified as “clinical suspicion of recurrence.” Patients without worrisome symptoms or physical examination findings to indicate recurrence were deemed to have clinically occult recurrence.

### Image Interpretation

All posttreatment PET/CECT and CECT scans were interpreted using the NI-RADS template by 1 of 4 head and neck–trained neuroradiologists (31, 16, 11, and 10 years of experience), whose interobserver agreement was previously shown to be 0.821.<sup>3</sup> For each patient, both the primary site and neck were assigned a separate NI-RADS category of either 1, 2, 3, or 4, and all NI-RADS 2 subcategories (2a and 2b) were recorded as a category 2, because the level of suspicion is the same. Interpreting radiologists reviewed prior clinical history, physical examination, and endoscopic notes and compared baseline imaging, including pretreatment FDG avidity, when available.

### Surveillance Protocol

The imaging surveillance algorithm for patients with head and neck malignancy used at our institution mirrors the algorithm published in the American College of Radiology White Paper.<sup>5</sup> Three months following completion of definitive therapy (surgery and radiation and/or chemotherapy; chemoradiation therapy), patients undergo a whole-body PET/CT and a neck CECT. If the patient continues to demonstrate no clinical evidence of disease recurrence, he or she continues to be imaged every 6 months for 1 year with a CECT of the neck followed by another CECT of the neck 1 year thereafter. At any point during this algorithm, if there is suspicion of recurrence, the patient may undergo PET/CT imaging as well. At our institution, PET/CT imaging follows a standard protocol, and images are acquired on Discovery 600 and 690 PET/CT scanners (GE Healthcare). Patients fast for 6 hours before injection of 10–14 mCi of FDG. For patients with a blood glucose level of  $\geq 200$  mg/dL, imaging is deferred due to the altered biodistribution of FDG. PET/CT images are acquired from the skull vertex to the midthighs 1 hour after injection of FDG. In addition, a CECT of the neck with the arms down is performed after the PET/CT using a split-bolus technique with 55 mL injected at 2.5 mL/s, followed by a 40-second delay and another 55 mL at the same rate, with a total scan delay of 90 seconds. Axial images are acquired from the frontal sinuses to the mediastinum at 1.25-mm section thickness (pitch, 0.984:1; gantry rotation, 0.7 seconds; FOV, 25 cm; 120 kV[peak]; and smart milliampere with a noise index of 13.78). Reformatted images are reconstructed at 2.5-mm thickness in the axial planes and 3 mm in the sagittal and coronal planes.

### Statistics

Descriptive statistics were performed to assess the frequency of clinically occult HNSCCa recurrences in patients with NI-RADS scores of 2 or 3.

## RESULTS

Our data base search yielded a total of 404 unique cases. One hundred forty-nine of these cases were excluded because they

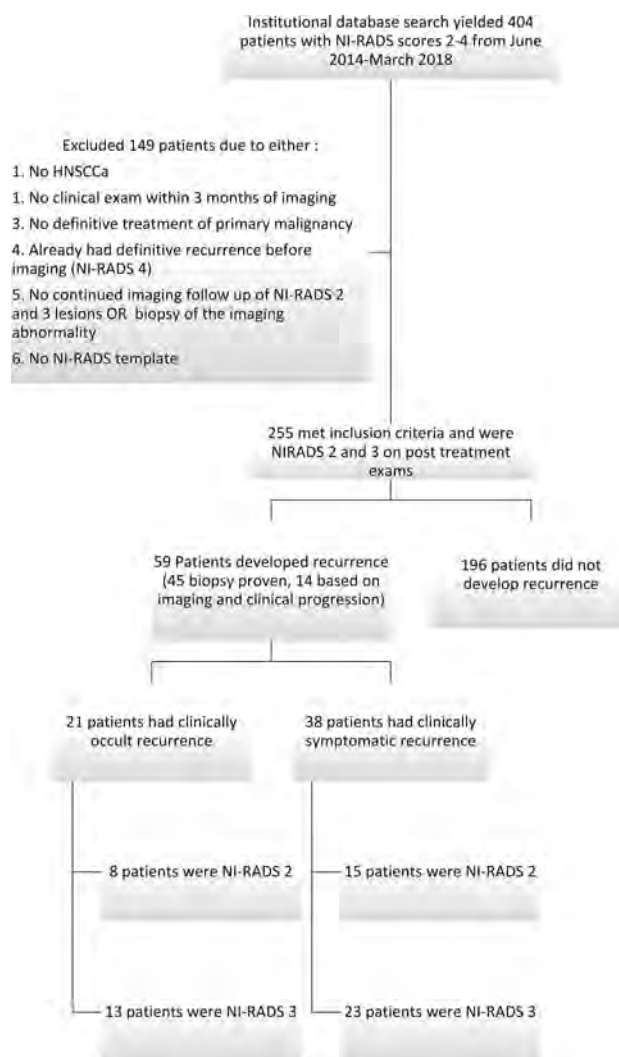


**FIG 1.** Flowchart demonstrating patient selection criteria and recurrences.

either did not have HNSCCa, did not strictly adhere to the NI-RADS template, had no clinical follow-up within 3 months of imaging, had biopsy-proven recurrence before imaging (all 38 of NI-RADS 4 cases), or did not have follow-up of NI-RADS 2 or 3 lesions or biopsy of the imaging abnormality. A total of 255 cases with NI-RADS scores of 2 ( $n = 197$ ) or 3 ( $n = 58$ ) met the inclusion criteria (Fig 1). The 38 patients with NI-RADS 4 had either biopsy-proven locoregional ( $n = 33$ ) recurrence or distant recurrence ( $n = 5$ ) before obtaining a NI-RADS 4 on imaging. Therefore, these patients were excluded. Most of these patients were undergoing imaging to assess a response to chemotherapy in the setting of unsalvageable recurrence or distant metastasis or were on a clinical trial.

A total of 59 patients ( $n = 23$ , NI-RADS 2;  $n = 36$ , NI-RADS 3) (23%) had disease recurrence (45 biopsy-proven, 14 based on imaging progression on follow-up examination and clinical progression), with 17 recurrences diagnosed at  $< 6$  months, 16 recurrences between 6 and 12 months, 6 recurrences between 12 and 18 months, and 20 after 18 months. The biopsy-proven recurrences ( $n = 45$ ) included 28 NI-RADS 3 and 17 NI-RADS

## Patient demographics

NI-RADS Score	No. of Cases	Sex	Mean Age (yr)	Smoking History	Subsite of Primary Tumor	T-Stage	HPV Status	Recurrences
NI-RADS 2	197	62 F 135 M	64	75.6% (149)	Oral cavity (73) Oropharynx (48) Hypopharynx (18) Larynx (49) Nasopharynx (7) Unknown (2)	T1 (35) T2 (35) T3 (32) T4 (10) T4a (56) T4b (9) Unknown (20)	32 (+) 9 (−) 2 Unknown	Total: 23 (8 clinically occult recurrences)  17 Biopsy-proved 6 Imaging and clinical progression
NI-RADS 3	58	17 F 41 M	63	75.9% (44)	Oral cavity (28) Oropharynx (17) Hypopharynx (4) Larynx (8) Nasopharynx (1)	T1 (4) T2 (14) T3 (5) T4 (8) T4a (17) T4b (6) Unknown (4)	0 (+) 1 (−) 1 Unknown	Total: 36 (13 clinically occult recurrences)  28 Biopsy-proved 8 Imaging and clinical progression
NI-RADS 4	38	10 F 28 M	63.4	71.1% (27)	Oral cavity (8) Oropharynx (16) Hypopharynx (2) Larynx (11) Nasopharynx (1)	T1 (4) T2 (7) T3 (6) T4 (1) T4a (15) T4b (1) Unknown (4)	8 (+) 4 (−) 1 Unknown	All patients excluded  33 Biopsy-proved recurrence 5 Imaging and clinical progression
Total (276 CECT, 17 PET/CECT)	293	89 F 204 M	63.5	75.1% (220)	Oral cavity (109) Oropharynx (81) Hypopharynx (24) Larynx (68) Nasopharynx (9) Unknown (2)	T1 (43) T2 (56) T3 (43) T4 (19) T4a (88) T4b (16) Unknown (28)	40 (+) 14 (−) 4 Unknown	59 NI-RADS 2 and 3 38 NI-RADS 4 (excluded)

2 recurrences. The recurrences based on imaging and clinical progression ( $n=14$ ) included 8 NI-RADS 3 and 6 NI-RADS 2. Twenty-one (36%; eight NI-RADS 2 and 13 NI-RADS 3) patients with recurrence did not demonstrate clinical signs or symptoms at the time of recurrence diagnosis. Although our inclusion criteria required a clinical examination within 3 months of the index imaging examination, many were examined on the same day, with a mean time between clinical examination and the time of index imaging of only 11.3 days (range, 0–88 days). The Table and On-line Table summarize the demographics, T-staging, human papillomavirus (HPV) status, smoking history, and treatment of our study sample.

Of all clinically occult recurrences, 38% had a NI-RADS score of 2 and 62% had a score of 3. Seventeen of these recurrences occurred at the primary site (14 submucosal and 3 mucosal), and 7 occurred within the lymph nodes. Time to recurrence was defined as the number of months from treatment to biopsy-proven recurrence ( $n=45$ ) or definitive clinical and imaging progression ( $n=14$ ). The median time to clinically occult recurrence was  $16.5 \pm 5.9$  months for NI-RADS 2 (range, 6.3–58.2 months, with outliers excluded) and  $9.7 \pm 10.9$  months for patients with NI-RADS 3 (range, 3–107.9 months, with outliers excluded) (Fig 2). The combined median time to clinically occult recurrence was 11.4 months. Of all patients with clinically occult recurrence, 6 (29%) patients underwent surgical salvage, 10 (47%) were treated with re-irradiation and chemotherapy, 2 (10%) patients opted for hospice care and were not candidates for salvage surgery, and 3 (14%) patients sought salvage treatment at outside institutions. Examples of patients with clinically occult recurrences are shown in Figs 3 and 4.

## DISCUSSION

HNSCCa is an aggressive malignancy with only about 50% of patients receiving an initial cure. Depending on the subsite of tumor and treatment, studies have demonstrated a wide range of recurrence from 22% to 86%.<sup>14–16</sup> We report a 23% recurrence rate (59 patients of 255) in our heterogeneous cohort.

Early identification of recurrence is critical for optimizing salvage therapy in attempts to improve survival and functional outcomes. The data regarding the exact relationship between early identification of recurrence and outcome are limited, especially the role of imaging to detect recurrences earlier than the clinical examination. To our knowledge, there are no data regarding the frequency of imaging-detected recurrences in asymptomatic patients, how much earlier imaging can detect recurrences, or the effect on outcome. This study is directed at answering the first question regarding the frequency of imaging-detected recurrence in asymptomatic patients. Although imaging surveillance in patients with HNSCCa is a common clinical practice, the technique, exact timing, and duration remains variable and inconsistent due to lack of data and guidelines. The NCCN only recommends surveillance imaging within the first 6 months, with no concrete recommendation beyond this period, despite many patients with head and neck carcinoma having a smoking history and recurrences often being submucosal. Previous studies have shown that the highest risk of recurrence occurs in the first 2 years after treatment.<sup>1,17,18</sup> At our institution, asymptomatic patients follow the imaging surveillance recommendations outlined in the American College of Radiology NI-RADS White Paper, namely PET/CECT at 3 months followed by CECT at 6-month intervals  $\times 2$  and then CECT of the neck at 1-year

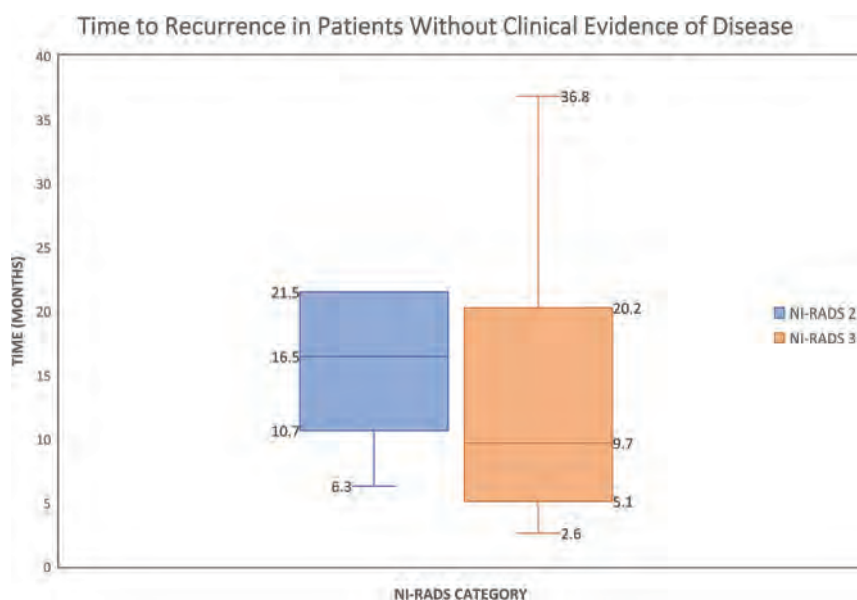


**FIG 2.** The median time to recurrence was  $16.5 \pm 5.9$  months for NI-RADS 2 (range, 6.3–58.2 months, with outliers excluded) and  $9.7 \pm 10.9$  months for NI-RADS 3 (range, 3–107.9 months, with outliers excluded). There are 2 outliers (not shown in figure) with values of 58.2 months for NI-RADS-2 and 107.9 months for NI-RADS 3.

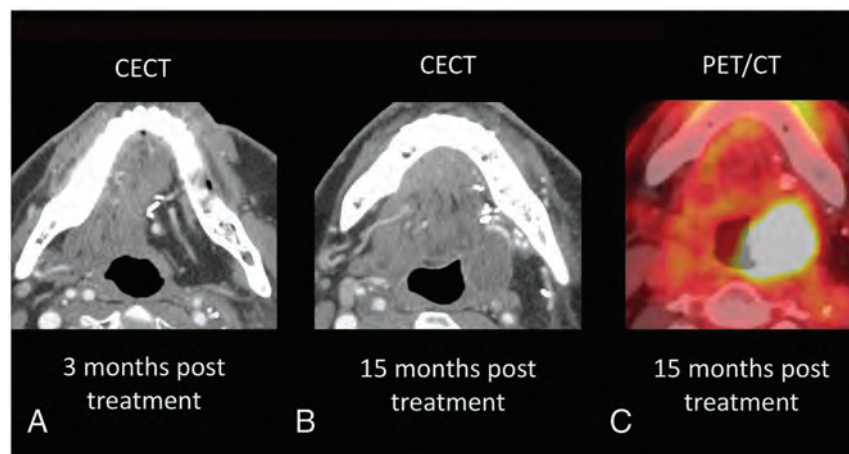


**FIG 3.** A, A 53-year-old man with a history of T2N0M0 left-tongue squamous cell carcinoma status post left hemiglossectomy and flap reconstruction. Surveillance imaging demonstrates a new hypoattenuating mass within the left floor of the mouth along the flap margin (B), with corresponding hypermetabolism on PET/CT (C). On clinical examination, no oropharyngeal narrowing, bulge, or ulcerations were detected. The patient did not have worrisome clinical symptoms suspicious for clinical recurrence. This new mass was clinically occult and biopsy-proved recurrent disease. Recurrence was detected 15 months posttreatment.

intervals for 2 years in most patients. MR imaging surveillance is used for most sinonasal tumors, skull base tumors, salivary neoplasms, and any tumors with intracranial or intraorbital extension. Because our institution has a robust standard imaging algorithm for almost all advanced-stage HNSCCs using CECT and PET/CECT, we elected to study this cohort.

Imaging detected more than one-third of cases before clinical examination: Approximately 36% of patients (21 of 59 recurrences) with proven recurrence had no clinical evidence of recurrent disease, and the recurrence was detected by

imaging alone (8 scored NI-RADS 2 and 13 scored NI-RADS 3). Our study demonstrates that imaging detected recurrence earlier than clinical examination in more than one-third of patients. There has been a growing number of studies assessing the value of  $^{18}\text{F}$  FDG-PET/CT in posttreatment surveillance imaging, with many authors arguing that routine follow-up is critical,<sup>7,9,10,12,19</sup> and some have even gone further to suggest site-specific recommendations.<sup>20,21</sup> One can hypothesize that imaging surveillance may be especially important in patients with asymptomatic locoregional recurrences that may be salvageable, improving disease-free survival.<sup>22</sup>

Imaging detected subclinical recurrences beyond 6 months in most patients: Our standardized surveillance algorithm enabled detection of recurrences beyond 6 months and earlier than clinical examination/symptoms in 81% of asymptomatic patients (17 of 21), though we do not have data regarding the effect on outcome. This data, revealing a noteworthy number of clinically occult recurrences with a large percentage occurring beyond 6 months, would argue in favor of a more robust surveillance algorithm beyond the post-treatment baseline examination recommended by the NCCN guidelines. The exact frequency and duration can likely be tailored on the basis of the initial stage, HPV status, smoking history, and so forth and is an important area for future study. A study by Abidi et al<sup>23</sup> demonstrated a lower frequency of subclinical recurrences with FDG-PET/CT in 8% of surveyed patients between 8 and 36 months. Some studies have also demonstrated improved survival outcomes

with earlier detection of recurrences beyond the first 6 months.<sup>5,24,25</sup> For example, Wong et al<sup>24</sup> demonstrated that the overall 5-year tumor-free survival following surgical salvage was 26%, whereas those patients with late detection or those whose disease was not considered salvageable either via surgery, radiation therapy, or chemotherapy only achieved a mean survival of 7 months. Imaging is critical for identifying early disease recurrence, which often occurs beyond 6 months and can be seen in patients without worrisome clinical and physical examination findings.



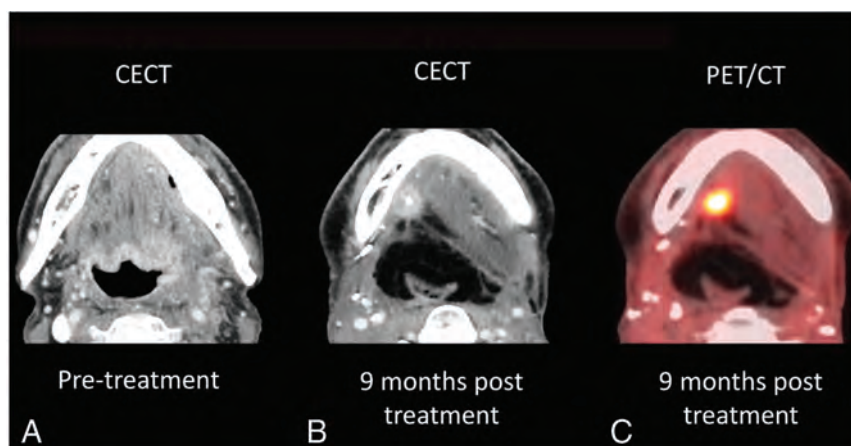


**FIG 4.** A 62-year-old man with pT4aN2b HPV-negative squamous cell carcinoma of the left base of the tongue with extension into the floor of mouth and inferiorly to the hypopharynx (partially visualized in A). Surgically, the patient underwent total glossectomy and laryngectomy with a left anterolateral thigh flap reconstruction of the pharynx and base of the tongue. B, An enhancing 1.4-cm nodule with central cystic change in the right floor of the mouth along the margin of the flap. On clinical examination, no mucosal masses, bulges, or suspicious ulcerations were detected. The patient did not have worrisome clinical symptoms to suspect clinical recurrence. This new mass along the flap margin demonstrated marked FDG avidity on PET/CT (C) and was biopsy-proved recurrence. Recurrence was detected 9 months posttreatment.

### Treatment Options for Recurrences

The concept that earlier detection of recurrence in asymptomatic patients yields a survival benefit is controversial and needs further study; some authors have shown a survival benefit,<sup>20,26</sup> whereas others have not.<sup>27-31</sup> Although this study was not designed or powered to assess outcome or survival, we retrospectively investigated treatment options used for our recurrences. In our study, 6 patients (29%) with clinically occult recurrence underwent salvage surgery ( $n = 4$ , NI-RADS 2; and  $n = 2$ , NI-RADS 3) with curative intent. One (5%) patient with NI-RADS 3 underwent chemoradiation with curative intent, while the remaining patients with clinically occult recurrence received palliative care (with 1 patient forgoing surgical salvage with curative intent). In patients who had symptomatic recurrence, 24% ( $n = 9$ ) underwent salvage surgery with curative intent.

When we compared the 2 scenarios, 29% ( $n = 6$ ) of our patients with clinically occult recurrence were able to undergo successful surgical salvage compared with 24% ( $n = 9$ ) of patients with symptomatic recurrence. For patients with locoregional recurrence in addition to distant metastases, treatment was primarily palliative. A total of 3 patients with symptomatic recurrence declined further treatment: Two decided on hospice care, and one was unable to undergo treatment due to a life-threatening infection. Ten patients were treated with re-irradiation and chemotherapy in both groups. Although this study was not designed to determine survival benefit or the effect on treatment options of early imaging detection, the authors believe that they are very important questions and would be the next step for optimizing surveillance.

### Mucosal Recurrence

In addition to identifying asymptomatic submucosal recurrences, our study also identified 2 asymptomatic mucosal recurrences

(albeit, one with nodal involvement as well). One patient was examined at an outside facility 30 days prior to imaging without an endoscopy report, and the other demonstrated recurrence in the oropharynx in addition to node involvement. In these 2 patients, the clinical examination was an average of 14 days before the imaging examination. Just as posttreatment imaging is complicated in the patient with post-treatment head and neck cancer, the mucosal examination can be difficult, especially in the radiated larynx. Although typically the clinical exam is the workhorse for detecting mucosal recurrences and imaging for submucosal recurrences, perhaps unexpectedly, imaging can also play a role in detecting asymptomatic mucosal recurrences. The complex post radiated mucosa can make the clinical exam difficult, and imaging can help to direct the clinical exam for added

sensitivity in some cases.

### Limitations

The primary limitations of our study were the retrospective design, a heterogeneous population with a mixture of stages and subsites, and sample size. The primary aim of our article was to show that a standardized imaging surveillance algorithm resulted in earlier detection, with the logical next question being whether earlier detection would result in different treatment options for the patient and/or survival benefits. Our study was not designed to answer these questions, predominately due to its retrospective nature without a control group and a heterogeneous cohort with mixed subsites, stages, HPV status, and risk factors such as smoking history. At our institution, all patients undergo standard surveillance imaging; thus, we do not have access to a cohort of asymptomatic patients followed by clinical examination alone for comparison. Intuitively, those patients for whom early imaging detection of disease recurrence offers more options for surgical salvage should have better prognoses than those whose recurrences are detected after involving vital structures like the carotid artery, skull base, or prevertebral musculature. We believe this is a critical question but very difficult to design a prospective study for because most HNSCCs do undergo some form of surveillance imaging in asymptomatic patients, albeit nonstandardized. This study also followed patients only to determine the presence of disease either by biopsy or progression or the absence of disease by resolution of abnormal findings on imaging on subsequent follow-up. A long-term follow-up of this cohort would be needed to assess whether earlier radiographic detection translates into better outcomes and improved survival. Our study was also underpowered for subset analysis to extrapolate whether certain patient groups (eg, higher tumor stage, smoking history, HPV status, subsite, and so forth) should warrant more frequent

surveillance. We believe that this is an important next question for future larger, multi-institutional studies.

## CONCLUSIONS

Imaging surveillance beyond the first posttreatment baseline study was critical for earlier detection of recurrent disease. More than one-third of all imaging-detected recurrences were seen in patients with no clinical evidence of disease. Most of these recurrences occurred beyond 6 months from the end of treatment. These findings underscore the importance of extending the current NCCN guidelines of imaging surveillance beyond the first 6 months of treatment. Further study is warranted to determine which patients would benefit most from asymptomatic imaging surveillance.

Disclosures: Mihir R. Patel—UNRELATED: Travel/Accommodations/Meeting Expenses Unrelated to Activities Listed: Intuitive Surgical.

## REFERENCES

- Beswick DM, Gooding WE, Johnson JT, et al. Temporal patterns of head and neck squamous cell carcinoma recurrence with positron-emission tomography/computed tomography monitoring. *Laryngoscope* 2012;122:1512–17 CrossRef Medline
- Isles MG, McConkey C, Mehanna HM. A systematic review and meta-analysis of the role of positron emission tomography in the follow up of head and neck squamous cell carcinoma following radiotherapy or chemoradiotherapy. *Clin Otolaryngol* 2008;33:210–22 CrossRef Medline
- Krieger DA, Hudgins PA, Nayak GK, et al. Initial performance of NI-RADS to predict residual or recurrent head and neck squamous cell carcinoma. *AJNR Am J Neuroradiol* 2017;38:1193–99 CrossRef Medline
- Aiken AH, Farley A, Baugnon KL, et al. Implementation of a novel surveillance template for head and neck cancer: Neck Imaging Reporting and Data System (NI-RADS). *J Am Coll Radiol* 2016;13:743–46.e1 CrossRef Medline
- Aiken AH, Rath TJ, Anzai Y, et al. ACR Neck Imaging Reporting and Data Systems (NI-RADS): A White Paper of the ACR NI-RADS Committee. *J Am Coll Radiol* 2018;15:1097–1108 CrossRef Medline
- Hsu D, Chokshi FH, Hudgins PA, et al. Predictive value of first post-treatment imaging using standardized reporting in head and neck cancer. *Otolaryngol Head Neck Surg* 2019;161:978–85 CrossRef Medline
- McDermott M, Hughes M, Rath T, et al. Negative predictive value of surveillance PET/CT in head and neck squamous cell cancer. *AJNR Am J Neuroradiol* 2013;34:1632–36 CrossRef Medline
- Wangaryattawanich P, Branstetter BF, Hughes M, et al. Negative predictive value of NI-RADS category 2 in the first posttreatment FDG-PET/CT in head and neck squamous cell carcinoma. *AJNR Am J Neuroradiol* 2018;39:1884–88 CrossRef Medline
- Koshkareva Y, Branstetter BF, Gaughan JP, et al. Predictive accuracy of first post-treatment PET/CT in HPV-related oropharyngeal squamous cell carcinoma. *Laryngoscope* 2014;124:1843–47 CrossRef Medline
- Leung AS, Rath TJ, Hughes MA, et al. Optimal timing of first post-treatment FDG PET/CT in head and neck squamous cell carcinoma. *Head Neck* 2016;38(Suppl 1):E853–58 CrossRef Medline
- Ong SC, Schöder H, Lee NY, et al. Clinical utility of 18F-FDG PET/CT in assessing the neck after concurrent chemoradiotherapy for locoregional advanced head and neck cancer. *J Nucl Med* 2008;49:532–40 CrossRef Medline
- Gilbert MR, Branstetter BF, Kim S. Utility of positron-emission tomography/computed tomography imaging in the management of the neck in recurrent laryngeal cancer. *Laryngoscope* 2012;122:821–25 CrossRef Medline
- Ang KK, Trotti A, Brown BW, et al. Randomized trial addressing risk features and time factors of surgery plus radiotherapy in advanced head-and-neck cancer. *Int J Radiat Oncol Biol Phys* 2001;51:571–78 CrossRef
- Vikram B, Strong EW, Shah JP, et al. Failure at the primary site following multimodality treatment in advanced head and neck cancer. *Head Neck Surg* 1984;6:720–23 CrossRef Medline
- Mizrachi A, Migliacci JC, Montero PH, et al. Neck recurrence in clinically node-negative oral cancer: 27-year experience at a single institution. *Oral Oncol* 2018;78: 94–101 CrossRef Medline
- Manikantan K, Khode S, Dwivedi RC, et al. Making sense of post-treatment surveillance in head and neck cancer: when and what of follow-up. *Cancer Treat Rev* 2009;35:744–53 CrossRef Medline
- Schwartz DL, Barker J, Chansky K, et al. Postradiotherapy surveillance practice for head and neck squamous cell carcinoma: too much for too little? *Head Neck* 2003;25:990–99 CrossRef Medline
- Wensing BM, Merks MAW, Krabbe PFM, et al. Oral squamous cell carcinoma and a clinically negative neck: the value of follow-up. *Head Neck* 2011;33:1400–05 CrossRef Medline
- Ghosh-Laskar S, Mummudi N, Rangarajan V, et al. Prognostic value of response assessment fluorodeoxyglucose positron emission tomography-computed tomography scan in radically treated squamous cell carcinoma of head and neck: long-term results of a prospective study. *J Cancer Res Ther* 2019;15:596–603 CrossRef Medline
- de Visscher AV, Manni JJ. Routine long-term follow-up in patients treated with curative intent for squamous cell carcinoma of the larynx, pharynx, and oral cavity: does it make sense? *Arch Otolaryngol Head Neck Surg* 1994;120:934–39 CrossRef Medline
- Boysen M. Value of follow-up in patients treated for squamous cell carcinomas of the oral cavity and oropharynx. *Recent Results Cancer Res* 1994;134:205–14 CrossRef Medline
- Janot F, de Raucourt D, Benhamou E, et al. Randomized trial of postoperative reirradiation combined with chemotherapy after salvage surgery compared with salvage surgery alone in head and neck carcinoma. *J Clin Oncol* 2008;26:5518–23 CrossRef Medline
- Abidi S, Vasanawala M, Segall G. Is F18-FDG PET useful in surveillance of head and neck cancer. *Journal of Nuclear Medicine* 2019;60(Suppl 1):1258
- Wong LY, Wei WI, Lam LK, et al. Salvage of recurrent head and neck squamous cell carcinoma after primary curative surgery. *Head Neck* 2003;25:953–59 CrossRef Medline
- Lowe VJ, Boyd JH, Dunphy FR, et al. Surveillance for recurrent head and neck cancer using positron emission tomography. *J Clin Oncol* 2000;18:651–58 CrossRef Medline
- Ritoe SC, de Vegt F, Scheike IM, et al. Effect of routine follow-up after treatment for laryngeal cancer on life expectancy and mortality: results of a Markov model analysis. *Cancer* 2007;109:239–47 CrossRef Medline
- Lester SE, Wight RG. ‘When will I see you again?’ Using local recurrence data to develop a regimen for routine surveillance in post-treatment head and neck cancer patients. *Clin Otolaryngol* 2009;34:546–51 CrossRef Medline
- Boysen M, Lövdal O, Tausjö J, et al. The value of follow-up in patients treated for squamous cell carcinoma of the head and neck. *Eur J Cancer* 1992;28:426–30 CrossRef Medline
- Francis DO, Yueh B, Weymuller EA, et al. Impact of surveillance on survival after laryngeal cancer in the Medicare population. *Laryngoscope* 2009;119:2337–44 CrossRef Medline
- Saussez S, Dekeyser C, Thill MP, et al. Importance of clinical and radiological follow-up in head and neck cancers. *B-ENT* 2007;3:179–84 Medline
- De Felice F, Musio D, Tombolini V. Follow-up in head and neck cancer: a management dilemma. *Advances in Otolaryngology* 2015; 2015:1–4 CrossRef

# Comparison of Intraoperative Sonography and Histopathologic Evaluation of Tumor Thickness and Depth of Invasion in Oral Tongue Cancer: A Pilot Study

 B.C. Yoon,  M.D. Bulbul,  P.M. Sadow,  W.C. Faquin,  H.D. Curtin,  M.A. Varvares, and  A.F. Juliano

## ABSTRACT

**BACKGROUND AND PURPOSE:** For primary squamous cell carcinoma of the oral tongue, accurate assessment of tumor thickness and depth of invasion is critical for staging and operative management. Currently, typical imaging modalities used for preoperative staging are CT and MR imaging. Intraoperatively, CT or MR imaging cannot provide real-time guidance, and assessment by manual palpation is limited in precision. We investigated whether intraoperative sonography is a feasible technique for assessment of tumor thickness and depth of invasion and validated its accuracy by comparing it with histopathologic evaluation of the resected specimen.

**MATERIALS AND METHODS:** Twenty-six patients with squamous cell carcinoma of the oral tongue who underwent tumor resection by a single surgeon between March 31, 2016, and April 26, 2019, were prospectively identified. Intraoperative sonography was obtained in planes longitudinal and transverse to the long axis of the tumor. Twenty-two patients had archived images that allowed measurements of tumor thickness and depth of invasion sonographically. Two patients had dysplasia and were excluded. The remaining 20 patients had histologic tumor thickness and histologic depth of invasion measured by a single pathologist.

**RESULTS:** The mean sonographic tumor thickness was  $7.5 \pm 3.5$  mm, and the mean histologic tumor thickness was  $7.0 \pm 4.2$  mm. Mean sonographic depth of invasion and histologic depth of invasion were  $6.6 \pm 3.4$  and  $6.4 \pm 4.4$  mm, respectively. There was excellent correlation between sonographic and histologic measurements for both tumor thickness and depth of invasion with Pearson correlation coefficients of 0.95 (95% CI, 0.87–0.98) and 0.95 (95% CI, 0.87–0.98), respectively.

**CONCLUSIONS:** Intraoperative sonography can provide reliable, real-time assessment of the extent of tongue tumors.

**ABBREVIATIONS:** DOI = depth of invasion; OTSCC = oral tongue squamous cell carcinoma; TT = tumor thickness; uDOI = ultrasound-derived depth of invasion; US = sonography; uTT = ultrasound-derived tumor thickness

The recently updated, eighth edition of the *Cancer Staging Manual* of the American Joint Committee on Cancer incorporates the depth of invasion (DOI) of oral cavity cancers as an independent prognostic factor, in addition to tumor thickness (TT).<sup>1</sup> Preoperative CT and MR imaging have been shown to delineate TT and DOI with good correlation to pathologically determined TT and DOI for lesions of  $>5$  mm.<sup>2,3</sup> However, the ability to perform intraoperative real-time assessment of tumor thickness and DOI as well as deep margin extent remains limited. Currently, manual palpation is the mainstay technique for tumor

evaluation during an operation in attempting to achieve the goal of a gross 1-cm clearance at all margins with a goal of 0.5-cm microscopic clearance on permanently fixed tissue.<sup>4</sup> Although manual palpation may be adequate for determination of the more superficial, mucosal extent of a tumor, it is limited for precise assessment of the deep margin and the border between involved tissue and normal/healthy tissue. Furthermore, the current criterion standard for TT and DOI is histologic evaluation, which can only be performed after the tumor has been resected.

Sonography (US) is being increasingly recognized as a valuable tool in the assessment of intraoral tumor extent.<sup>3,5</sup> For instance, a recent study demonstrated that intraoperative sonography can be used for adequate demarcation of the deep-resection margins for tongue cancers.<sup>6</sup> In this study, we extend the previous findings to determine the accuracy of intraoperative sonography in assessing TT (uTT) and DOI (uDOI) of oral tongue squamous cell carcinomas (OTSCC), comparing them with the criterion standard postexcision, histopathologically assessed TT and DOI.

Received March 19, 2020; accepted after revision April 24.

From the Departments of Radiology (B.C.Y.), and Pathology (P.M.S., W.C.F.), Massachusetts General Hospital, Boston, Massachusetts, and Departments of Otolaryngology Head and Neck Surgery (M.D.B., M.A.V.), Radiology (H.D.C., A.F.J.), and Pathology (P.M.S., W.C.F.), Massachusetts Eye and Ear, Boston, Massachusetts.

Please address correspondence to A.F. Juliano, MD, Massachusetts Eye and Ear, 243 Charles St, Boston, MA 02114; e-mail: Amy\_Juliano@meei.harvard.edu; @amyjuliano

<http://dx.doi.org/10.3174/ajnr.A6625>



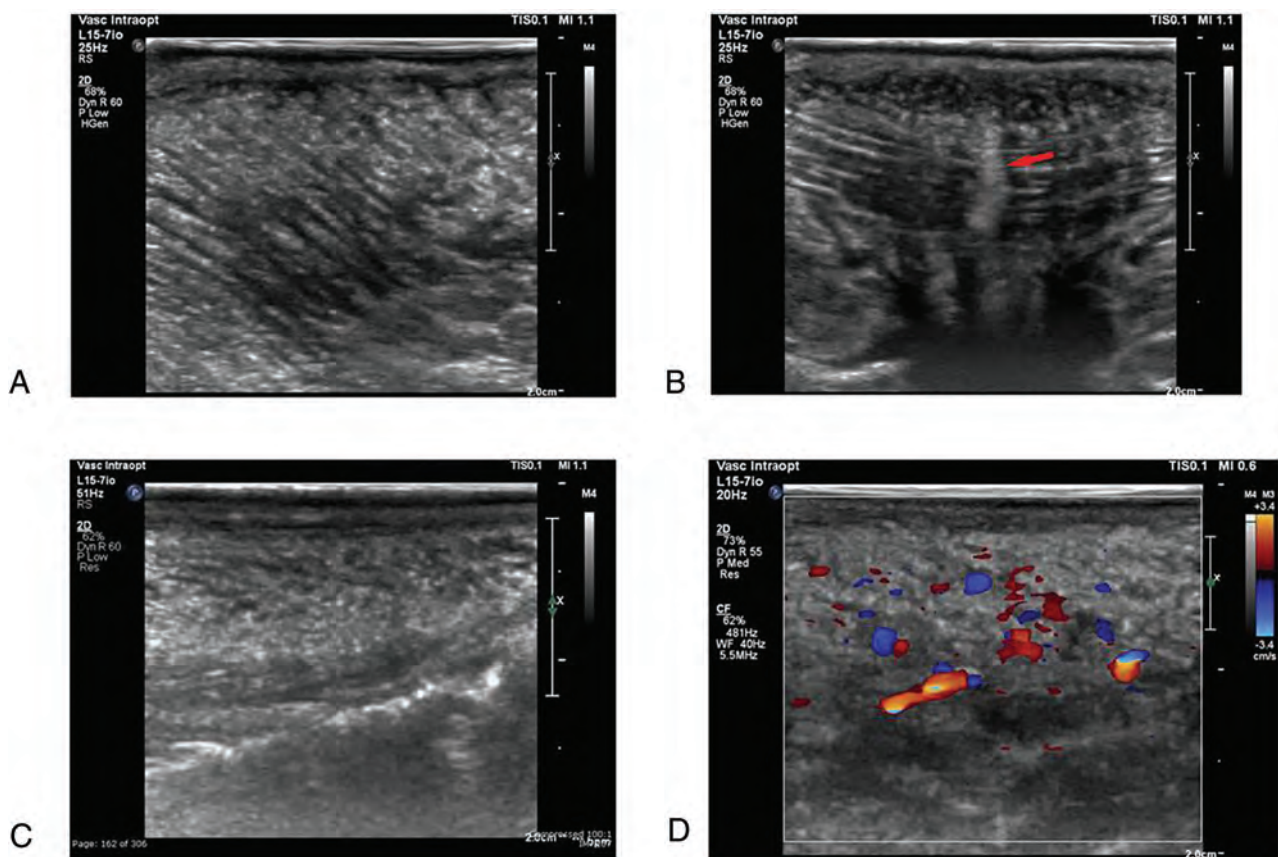


**FIG 1.** Gray-scale sonographic images of the normal oral tongue (A–C). Normal muscle striations can be seen in the parameian oral tongue (A, sagittal) and in the midline dorsum of the tongue (B, transverse). Note that in the midline, the median fibrous septum is discernable as an echogenic line (arrow in B). At the lateral edge of the oral tongue, the parenchyma is mildly heterogeneous and hyperechoic (C, sagittal). D, Doppler sonography image of the lateral oral tongue shows fairly even distribution of blood flow throughout the parenchyma.

## MATERIALS AND METHODS

### Study Design

Patients with previously untreated OTSCC were prospectively identified. They underwent tumor resection under US guidance by a single surgeon between March 31, 2016, and April 26, 2019. All US was performed by a single head and neck radiologist along with the surgeon and an US technologist. Patient data were obtained from medical records, including age, sex, and histologic tumor stage. This study was approved by the institutional review board of Massachusetts Eye and Ear.

### Surgical Resection with Intraoperative Sonographic Guidance

Each patient was placed under general anesthesia. Good exposure was gained of the oral cavity by gentle retraction of the lips and oral commissures. Visual inspection and manual palpation of the tongue tumor was performed to identify tumor location and estimate tumor extent.

Intraoperative US was performed before, during, and following tumor resection using a broadband compact linear array transducer (L15-7io; Philips Healthcare). The US transducer was sheathed with a sterile probe cover, with US gel placed inside the probe cover against the transducer end. Copious sonography gel was applied to the oral tongue on top of the tumor. The probe was then placed on the gel/tumor by the radiologist, and the tumor was

imaged. Compared with the normal tongue (Fig 1), the tumor is abnormally hypoechoic and distorts the normal tongue architecture (Fig 2). Extra care was taken to rest the probe gently on the gel without applying undue pressure on the tumor, to prevent external forces from the probe compressing and thereby potentially distorting and artificially altering the measured uTT and uDOI (Fig 3). Real-time scanning of the tumor was performed in all directions, to gain an understanding of tumor size, extent, morphology, and contour both at the superficial and deep margins. Using B-mode and Doppler sonography, we obtained still images and cine video clips in planes longitudinal and transverse to the long axis of the tumor, with the transducer oriented perpendicular to the deepest portion of the tumor. Still images of representative landmark locations demonstrating uTT and uDOI were obtained.

Partial glossectomy then commenced, with the surgeon bearing in mind the attendant trajectory needed to produce approximately 1.0 cm of gross deep margin clearance.<sup>6</sup> One-third to one-half of the way through tumor extirpation, the surgeon paused and gray-scale and Doppler US was again performed to evaluate the deep margin of resection along with inspection and palpation (Fig 3E). The tumor and resection trajectory were noted, and the margin of clearance between the tumor and cut edge was noted and measured at various points along the trajectory.

Resection then resumed, with the surgeon modifying the resection trajectory as needed on the basis of the clearance margin



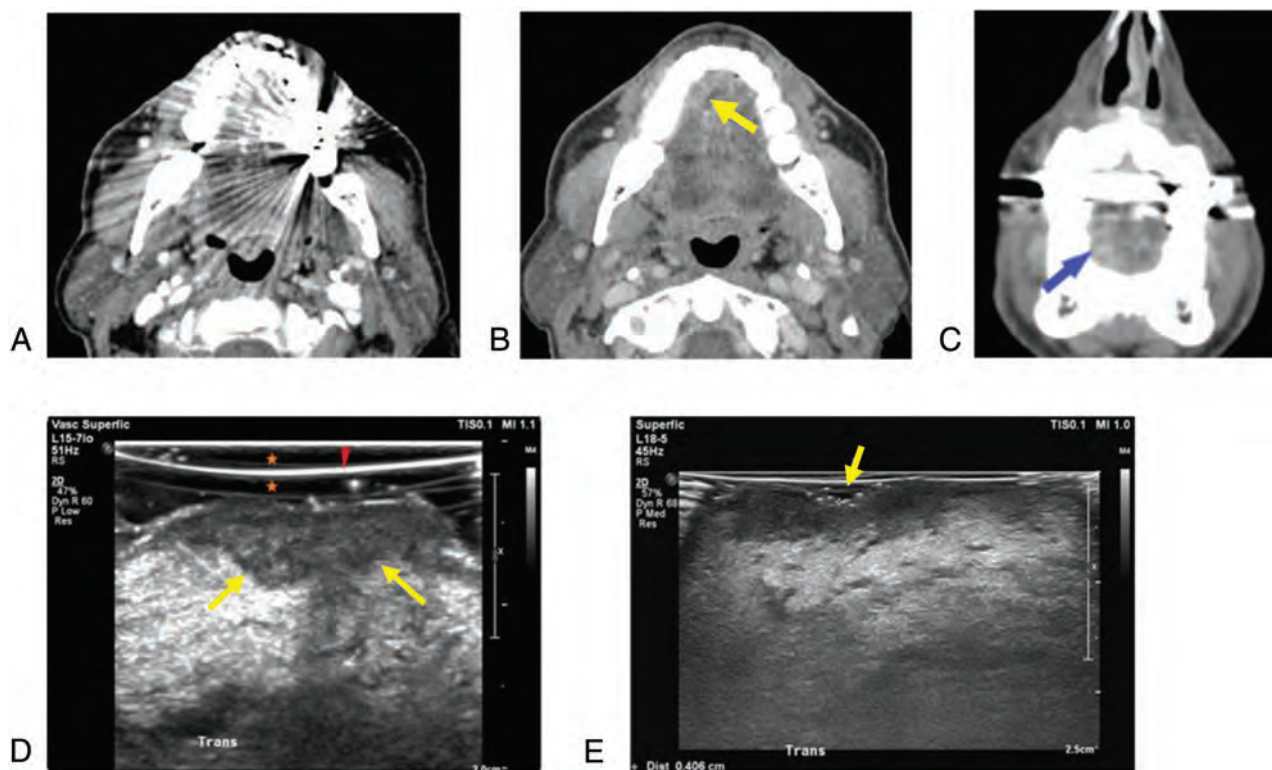


**FIG 2.** A, Axial contrast-enhanced CT image through the oral tongue is degraded by streak artifacts from metallic dental amalgam; the known right lateral oral tongue cancer cannot be appreciated. B, Re-angled contrast-enhanced CT image scanned at a tilted angle to avoid streak artifacts shows an area of subtle heterogeneous enhancement (arrow), likely representing the tumor. C, Coronal reformatted CT image shows the area (arrow) appearing relatively subtle and ill-defined. D, Intraoperative gray-scale sonography image shows an area of lobulated hypoechogenicity representing the tumor (arrows). The sonography probe was sheathed in a sterile probe cover (arrowhead), with sonography gel on either side of it (asterisks). Note how the probe was suspended lightly on the gel against the tongue to avoid distorting the natural contour of the tumor. E, Intraoperative gray-scale sonography image shows an endophytic ulcerated area of the tumor (marked by calipers). Sonography gel (arrow) coats the tongue in a thick layer, enabling visualization of the natural contour of the tumor.

noted. Following complete tumor extirpation, sonography was performed for a third time, this time on the resected surgical specimen (Fig 3F). Scanning in all directions was performed, cine video images were obtained in longitudinal and transverse planes, and still images were acquired at representative locations, with special attention paid to the interface between tumor tissue and healthy tissue and the margin of clearance between that interface and the resected surface. The surgical specimen was then taken to the frozen section laboratory and examined by both the surgeon and the attending pathologist (see below).

### Imaging Analysis

Measurements of uTT and uDOI from intraoperative sonography images were made by 2 neuroradiologists, one with 15 years of neuro-/head and neck radiology experience (A.F.J.) and the other with 6 years of neuro-/head and neck radiology experience (B.C.Y.). Images were displayed on the PACS. The uTT was measured from the superficial surface of the tumor to the deepest point of tumor invasion (Fig 4), following a path that is perpendicular to the tongue surface. The uDOI was measured from the level of projected normal mucosal surface<sup>7</sup>/basement membrane adjacent to the tumor to the deepest point of tumor invasion (Fig 4), along a path perpendicular to the tongue surface. Consensus measurements were used for analysis.

### Statistical Analysis

Statistical analysis was performed using GraphPad Prism software (Version 8; GraphPad Software). The Pearson correlation was used to determine the correlation between the sonographic and histopathologic assessments.

### Intraoperative and Postoperative Tissue Analysis

Histopathologic analysis on the resected specimen was performed in 2 stages: measurements made by gross and microscopic evaluation intraoperatively, including selected frozen sections of the specimen, as is routine for surgery, and routine gross and histopathologic analyses postoperatively.

In the frozen section laboratory, the specimen was oriented by the surgeon along with the head and neck pathologist (P.M.S.). Gross measurements of the resection specimen were made along with gross measurements of the tumor to the closest surgical margins, leaving the oriented specimen largely intact for further prosection following fixation in formalin. After gross measurements of the tumor distance to the surgical margins (in centimeters or millimeters) were recorded, the closest margins to the tumor (on the main specimen), up to 6, were taken directly from the specimen, with a perpendicular (radial) section made to approximate the closest distance of tumor to the true surgical resection edge. This tissue was frozen in optimal cutting temperature compound

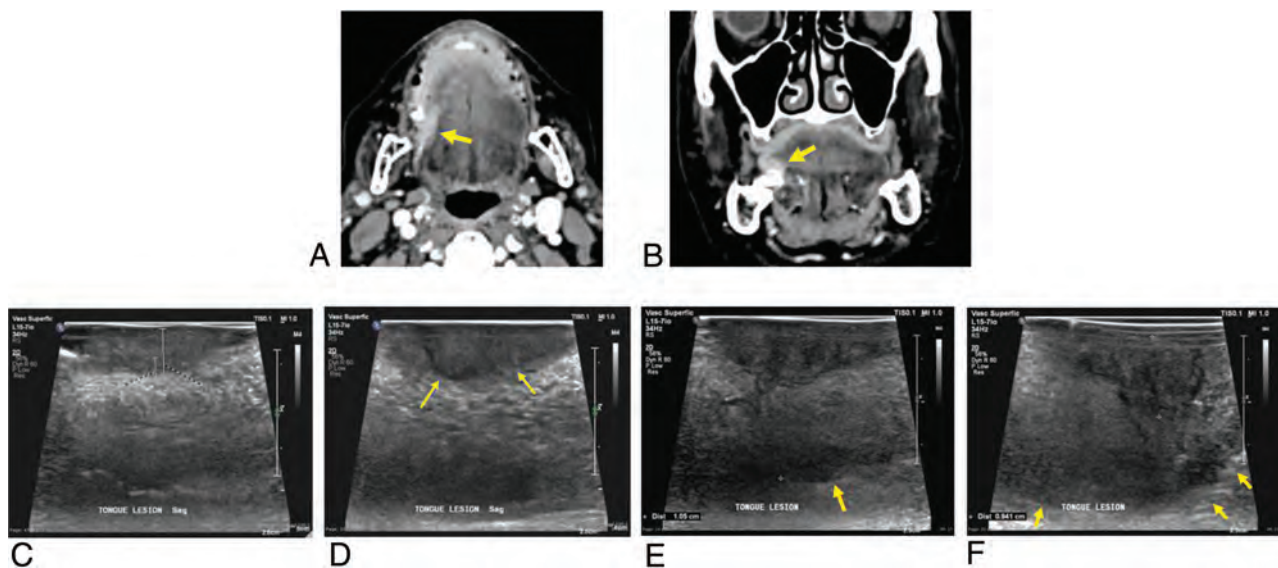


**FIG 3.** Axial (A) and coronal (B) contrast-enhanced CT images show the enhancing right lateral tongue tumor (arrows in A and B). However, it is difficult to appreciate on these images whether there may be exophytic or endophytic components that may render DOI different from TT. C, Intraoperative gray-scale sonography image obtained at the edge of the tumor demonstrates the exophytic nature of the tumor at that site. Rulers show measurements taken for uDOI (on the left) and uTT (on the right). D, The arrows denote the deep margin of the tumor. E, Intraoperative sonography image obtained during resection but before complete extirpation. Air can be seen at the resected interface as an echogenic line (arrow). Calipers show the margin of clearance between tumor and resection plane. F, Intraoperative sonography image obtained following complete extirpation of tumor. Air is seen throughout the resected edge (arrows). Calipers demarcate the tumor. Special attention was paid to ensure that the resection margins were free of tumor.

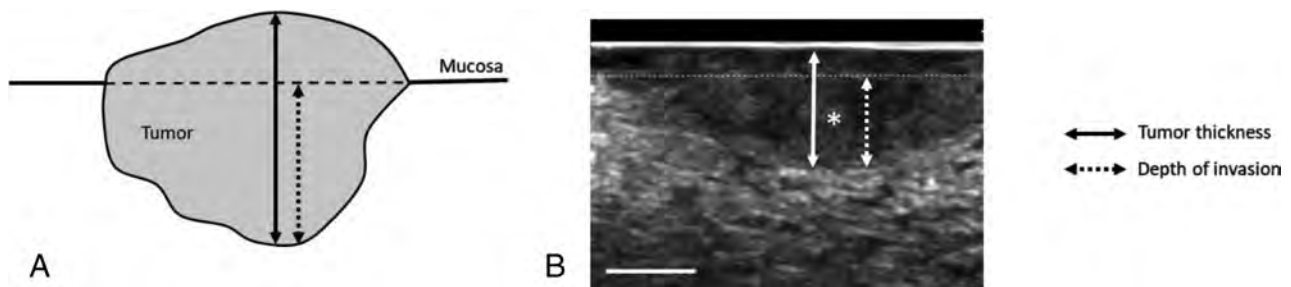


**FIG 4.** A, Schematic representation of tumor thickness and depth of invasion. B, Representative, intraoperative sonography image of a tongue squamous cell carcinoma. The lesion is seen as a circumscribed, hypoechoic mass (asterisk). Scale bar = 1cm.

with a 4- $\mu$ m section cut using a cryostat. The tissue section, placed on positively charged glass slides, was fixed in ethanol and stained with hematoxylin-eosin for intraoperative histologic review. Distance to the surgical margins was measured microscopically using a professional light microscope (Olympus BX51 microscope with Olympus DP27 camera). Following intraoperative evaluation of surgical margins, the tissue (main specimen) was placed in formalin preservative and fixed for permanent processing and histologic review. The frozen “margin” remnant tissue was transferred to cassettes for formalin fixation (the optimal cutting temperature compound is water/formalin soluble) and re-analyzed on permanent section following proper fixation and paraffin embedding.

## RESULTS

A total of 26 patients with OTSCC were included in this series. Among this cohort, 22 patients had archived images in the PACS that allowed measurements to be made sonographically (uTT,

uDOI). Two patients had dysplasia and were excluded. Of the remaining 20 patients, all had both histopathologic TT and DOI measured by a single pathologist (Table).

The mean uTT was  $7.5 \pm 3.5$  mm, and the mean histopathologic TT was  $7.0 \pm 4.2$  mm. The mean uDOI and histopathologic DOI were  $6.6 \pm 3.4$  mm and  $6.4 \pm 4.4$  mm, respectively. There was a strong correlation between sonographic and histologic measurements for both TT and DOI with Pearson correlation coefficients of 0.95 (95% CI, 0.87–0.98) and 0.95 (95% CI, 0.87–0.98), respectively (Fig 5).

## DISCUSSION

Sonographic imaging of the tongue tumor, surrounding tissues, and interface between tumor and normal tissue was successfully performed intraoperatively in all cases without adverse events. A strong correlation was observed between sonographic and histopathologic measurements of both TT and DOI.

# Patient characteristics

Patient No.	Age (yr)	Sex	uTT (mm)	hTT (mm)	uDOI (mm)	hDOI (mm)	Lymphovascular Invasion	Perineural Invasion	Nodal Metastasis
1	75	F	5	5	5	5	No	No	No
2	70	F	9	9	9	9	No	Yes	No
3	44	M	4	5	4	3	No	No	No
4	81	M	7	5	7	5	No	No	No
5	66	M	4	2.5	3	2.5	No	No	NA
6	29	F	6.5	4	6.5	4	No	No	NA
7	53	F	7	6	3	2	No	Yes	No
8	27	M	8	9	8	9	Indeterminate	Yes	No
9	75	F	3	2	3	1	No	No	NA
10	61	M	5	4	3	4	No	No	No
11	61	M	10	10	9	7	No	No	No
12	46	M	15	13	10	13	No	Yes	No
13	46	M	8.5	10	8.5	9	No	Yes	Yes
14	65	M	8	7	8	7	No	Yes	No
15	57	M	14	15	14	15	No	No	Yes
16	65	M	3	2	3	1.5	No	No	No
17	76	F	8	8	6	8	No	No	No
18	78	M	13	16	13	16	Yes	Yes	No
19	82	M	7	5	6	5	No	Yes	No
20	50	F	4	3	3	2.5	No	No	NA

**Note:**—hTT indicates histologic tumor thickness; hDOI, histologic depth of invasion; NA, not applicable.

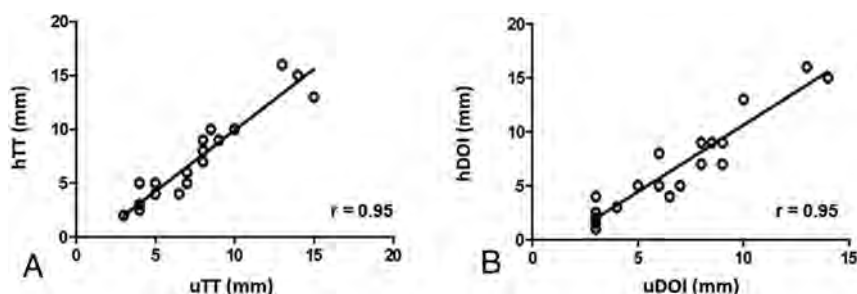


**FIG 5.** A, Correlation between sonography and histologic tumor thickness measurements ( $r =$  Pearson coefficient;  $n = 20$ ). B, Correlation between sonography and histologic depth of invasion measurements ( $r =$  Pearson coefficient;  $n = 20$ ).

Intraoperative US has been shown to be critically helpful in the guidance of tumor resection in various parts of the body.<sup>8</sup> Real-time sonography performed immediately before and during surgical resection can help to inform the resection trajectory by demonstrating the tumor and illustrating exophytic or endophytic components, as well as the surrounding uninvolved tissue, clearance margin between tumor and resection surface, vessels, and so forth. With real-time sonography, the surgeon can be reassured that the resection trajectory (for the purpose of tumor clearance) is adequate and optimal, or can be alerted to the need to modify the resection trajectory (for the purpose of organ preservation) to balance the need for adequate tumor margins and preservation of the maximal amount of uninvolved tissue. This assurance is particularly critical for a small-but-functionally-critical organ such as the oral tongue, vital for speech, swallowing, food intake, and airway preservation. In this study, we have shown that sonography has good accuracy in determining the TT and DOI of oral tongue masses, ensuring that it is a reliable method for surgical guidance.

One of the limitations of sonography is the variability in image acquisition between different lesions and different

operators. In this series, for instance, the initial several cases were performed with the transducer placed directly over and applying pressure to the tumor, which effectively compresses the lesion and possibly underestimates the TT. With increasing experience and awareness of this issue and with the need to ensure that we distinguish exophytic from endophytic portions of the tumor, we began to apply a thick layer of sonography gel on the tumor and suspend the transducer within the gel without pressure on the tumor, thus avoiding distortion

of tumor configuration. Of note, histopathologic assessment can also be affected by distortion during resection and histologic preparation, including, among other mechanical distortions, tissue-retraction artifacts.

No substantial increase in operative time was observed in this series, though there remains a potential for prolonging the operative time depending on the availability of equipment and/or expertise of the sonographer at each facility/institution. Although the tumor margins were relatively well-defined in the current series, they may be more obscured depending on the tumor histology and/or transducer types. In addition, if the tumor shape is irregular, then measurements may be subject to variability depending on which point and path is selected for measuring purposes; however, this is the case for both sonography and frozen section evaluation.

## CONCLUSIONS

This pilot study demonstrates that intraoperative sonography can provide objective, real-time assessment of TT and DOI with excellent correlation with histologic evaluation. This information is extremely helpful intraoperatively, allowing (1) resection with clear

margins upfront, important since positive margins cannot be revised in second surgeries to a level of disease control of that of an initially negative resection margin,<sup>9-11</sup> (2) choice of elective neck dissection to be performed in a clinically N0 neck (advisable at a threshold of 4 mm DOI) in the same surgical episode. It also provides accurate staging information for multidisciplinary management of the patient going forward. Additional work is needed to confirm the high level of correlation between sonographic and histologic measurements of TT and DOI and to deploy the use of ultrasound more widely in the care of patients with oral cancer.








Disclosures: William C. Faquin—UNRELATED: Board Membership: American Cancer Society, Comments: Editor-in-Chief for *Cancer Cytopathology*; Expert Testimony: medicolegal firms, Comments: rare expert testimony for medicolegal cases unrelated to this article.

## REFERENCES

1. Lydiatt WM, Patel SG, O'Sullivan B, et al. **Head and neck cancers: major changes in the American Joint Committee on Cancer eighth edition Cancer Staging Manual.** *CA Cancer J Clin* 2017;67:122–37 CrossRef Medline
2. Weimar EA, Huang SH, Lu L, et al. **Radiologic-pathologic correlation of tumor thickness and its prognostic importance in squamous cell carcinoma of the oral cavity: implications for the eighth edition Tumor, Node, Metastasis Classification.** *AJNR Am J Neuroradiol* 2018;39:1896–902 CrossRef Medline
3. Shintani S, Yoshihama Y, Ueyama Y, et al. **The usefulness of intra-oral ultrasonography in the evaluation of oral cancer.** *Int J Oral Maxillofac Surg* 2001;30:139–43 CrossRef Medline
4. Wong LS, McMahon J, Devine J, et al. **Influence of close resection margins on local recurrence and disease-specific survival in oral and oropharyngeal carcinoma.** *Br J Oral Maxillofac Surg* 2012;50:102–08 CrossRef
5. Narayana HM, Panda NK, Mann SB, et al. **Ultrasound versus physical examination in staging carcinoma of the mobile tongue.** *J Laryngol Otol* 1996;110:43–47 CrossRef Medline
6. Tarabichi O, Kanumuri V, Juliano AF, et al. **Intraoperative ultrasound in oral tongue cancer resection: feasibility study and early outcomes.** *Otolaryngol Head Neck Surg* 2018;158:645–48 CrossRef Medline
7. Hegde P, Roy S, Shetty T, et al. **Tumor infiltration depth as a prognostic parameter for nodal metastasis in oral squamous cell carcinoma.** *Int J Appl Basic Med Res* 2017;7:252–57 CrossRef Medline
8. Grondona P, Meola C, Floris F, et al. **Ultrasound-guided liver resection: early experience in a district general hospital.** *J Ultrasound* 2008;11:162–67 CrossRef Medline
9. Patel RS, Goldstein DP, Guillemaud J, et al. **Impact of positive frozen section microscopic tumor cut-through revised to negative on oral carcinoma control and survival rates.** *Head Neck* 2010;32:1444–51 CrossRef Medline
10. Bulbul MG, Tarabichi O, Sethi RK, et al. **Does clearance of positive margins improve local control in oral cavity cancer? A meta-analysis.** *Otolaryngol Head Neck Surg* 2019;161:235–44 CrossRef Medline
11. Varvares MA, Poti S, Kenyon B, et al. **Surgical margins and primary site resection in achieving local control in oral cancer resections.** *Laryngoscope* 2015;125:2298–307 CrossRef Medline



# Prevalence of Sigmoid Sinus Dehiscence and Diverticulum among Adults with Skull Base Cephaloceles

 H. Sotoudeh,  G. Elsayed,  S. Ghandili,  O. Shafaat,  J.D. Bernstock,  G. Chagoya,  T. Atchley,  P. Talati,  D. Segar,  S. Gupta, and  A. Singhal

## ABSTRACT

**BACKGROUND AND PURPOSE:** Cephaloceles are relatively rare conditions caused by a congenital and/or acquired skull defect. The incidence of associated venous brain anomalies with regard to cephaloceles remains to be fully elucidated. Accordingly, we sought to assess the prevalence of sigmoid sinus dehiscence and diverticula in patients with spontaneous skull base cephaloceles.

**MATERIALS AND METHODS:** Our institutional data base was retrospectively queried from 2005 to 2018. Patients in whom spontaneous skull base cephaloceles were identified were ultimately included in the study cohort. These patients subsequently had their sigmoid sinuses re-evaluated with focused attention on the possible presence of dehiscence and/or diverticula.

**RESULTS:** We identified 56 patients: 12 men and 44 women. After re-evaluation of the sigmoid sinuses, evidence of dehiscence and/or diverticula was noted in 21 patients. The right sigmoid sinus was involved in 11 patients, and the left sigmoid sinus was involved in 7 patients, including 3 cases of diverticulum. In 3 patients, evidence of bilateral sigmoid sinus dehiscence and diverticula was noted. Female sex was associated with sigmoid sinus dehiscence and diverticula by univariate analysis ( $P = .019$ ). By linear regression, cephalocele volume was negatively associated with sigmoid sinus dehiscence and diverticula (coefficient,  $-2266$ ,  $P$  value  $< .007$ , adjusted  $R^2 = 0.1077$ ). By univariate logistic regression using average cephalocele volume as a cutoff, we demonstrate a statistically significant finding of lower volumes being associated with sigmoid sinus dehiscence and diverticula with an odds ratio of 3.58 ( $P = .05$ ).

**CONCLUSIONS:** The prevalence of sigmoid sinus dehiscence and diverticula in patients with cephalocele is high. Female sex is associated with sigmoid sinus dehiscence and diverticula. The cephalocele volume appears to be inversely proportional to sigmoid sinus dehiscence and diverticula.

**ABBREVIATIONS:** ICP = intracranial pressure; IIH = idiopathic intracranial hypertension; SSDD = sigmoid sinus dehiscence and diverticula; CSF = cerebrospinal fluid

A cephalocele consists of herniation of the brain (encephalocele), meninges (meningocele), and/or both (meningoencephalocele) through a skull defect. Skull base cephaloceles can be congenital, spontaneous, or secondary to a litany of causes.<sup>1-3</sup> Congenital skull base cephaloceles are rare and constitute  $<10\%$

of all cephaloceles and are typically due to defects in primary ossification within the anterior neuropore but can also be due to increased intracranial pressure (ICP) in utero.<sup>1,4</sup> Spontaneous skull base cephaloceles form most cephaloceles diagnosed in adulthood and unlike congenital cephaloceles are not associated with other gross anomalies. The osseous defects are presumed to be secondary to the pulsation of arachnoid granulations, which can be associated with increased ICP.<sup>1,2,5</sup> The most common locations for spontaneous skull base cephaloceles are the cribriform plate, sphenoid sinus, and tegmen tympani;<sup>1,6,7</sup> these spontaneous cephaloceles are typically asymptomatic unless a CSF leak develops. As mentioned above, secondary cephaloceles result from myriad underlying etiologies (eg, trauma, surgery, skull base neoplasms, infection, inflammation, and radionecrosis).<sup>1,8,9</sup>

Sigmoid sinus dehiscence and diverticula (SSDD) are a clinical entity that has been reported to be associated with pulsatile tinnitus.<sup>10,11</sup> In a retrospective study by Schoeff et al,<sup>12</sup> in 2014,

Received January 4, 2020; accepted after revision April 24.

From the Division of Neuroradiology, Departments of Radiology (H.S., A.S.) and Neurosurgery (G.E., G.C., T.A.), University of Alabama at Birmingham, Birmingham, Alabama; Department of Radiology (S. Ghandili), Aventura Hospital, Miami, Florida; Department of Radiology and Interventional Neuroradiology (O.S.), Isfahan University of Medical Sciences, Isfahan, Iran; Russell H. Morgan Department of Radiology and Radiological Science (O.S.), Johns Hopkins University School of Medicine, Baltimore, Maryland; Department of Neurological Surgery (J.D.B., D.S., S. Gupta), Brigham and Women's Hospital, Harvard Medical School, Boston, Massachusetts; and Department of Neurological Surgery (P.T.), Massachusetts General Hospital, Harvard Medical School, Boston, Massachusetts.

H. Sotoudeh and G. Elsayed contributed equally to this work.

Please address correspondence to Houman Sotoudeh, MD, Division of Neuroradiology, Department of Radiology, University of Alabama at Birmingham, 619 19th St S, Birmingham, AL 35294; e-mail: hsotoudeh@uabmc.edu; @Houmansotoudeh  
<http://dx.doi.org/10.3174/ajnr.A6602>

the prevalence of SSDD in patients with pulsatile tinnitus was found to be 23% and was female-predominate. Most interesting, the prevalence of SSDD in asymptomatic patients in whom imaging was performed has been reported to be 1.2%. Of note, several interventions have been described that treat the pulsatile tinnitus caused by SSDD.<sup>13,14</sup>

SSDD has been associated with other radiographic findings, including empty sella, dehiscence of the superior semicircular canal, and increased ICPs.<sup>12</sup> Several mechanisms have been proposed for SSDD, which include pulsation of blood flow from the sigmoid sinus, osteoporosis, and the pulsation of CSF secondary to idiopathic intracranial hypertension (IIH).<sup>11-13,15,16</sup> Of note, recent studies have failed to show an association between SSDD and pulsatile tinnitus in patients with IIH.<sup>16</sup> It is possible that the SSDD is not the actual cause of pulsatile tinnitus and the SSDD and pulsatile tinnitus both are different manifestations of IIH.

There remain no well-established diagnostic criteria for SSDD, and diagnosis is based on visual assessment of CT scans using the bone window. Sigmoid sinus dehiscence is defined as the absence of normal cortical bone overlying the sigmoid sinus, thereby leading to direct contact of the sinus with mastoid air cells (air-on-sinus sign); this must be visible on 2 consecutive slices in 2 orthogonal planes.<sup>16</sup> Sigmoid sinus diverticula have been defined as focal outpouchings of the sigmoid sinus into the adjacent mastoid air cells or the mastoid cortex.

The potential association of SSDD and skull base cephaloceles (another manifestation of IIH) is currently unknown. Understanding such a relationship may ultimately be helpful in further elucidating the governing physiopathology of SSDD; strong associations between SSDD and cephaloceles would appear to favor CSF pulsation as the cause of SSDD as opposed to venous pulsations. Accordingly, we performed a retrospective study to quantify the prevalence of SSDD in patients with known skull base cephaloceles. In addition, we also sought to describe the association between SSDD and the size, location, contents, and symptoms of the patients with cephaloceles.

## MATERIALS AND METHODS

### Patients

All experiments and methods were performed in accordance with relevant guidelines and regulations set forth by the institutional review board of the University of Alabama at Birmingham, which approved the study (IRB-300000880). The study was performed in compliance with guidelines and regulations set forth by the National Institutes of Health. All patients were included as part of the institutional review board criteria for human research. All Health Insurance Portability and Accountability Act identifiers have been deleted from the presented images. Our institutional PACS data base was queried for the word “cephalocele” in all radiology reports from 2005 to 2018. Adult patients with spontaneous skull base cephaloceles were included in this study. Available imaging for each patient included a head CT with or without contrast, brain MR imaging with or without contrast, and/or a maxillofacial/temporal bone CT. These films were reviewed by a neuroradiologist with more than a decade of clinical experience.

### Outcomes

Anomalies involving the sigmoid sinuses were documented in these patients with focused attention on dehiscence and diverticula. As mentioned above, sigmoid sinus dehiscence was defined as loss of normal bone coverage of the sigmoid sinus and direct contact of the sigmoid sinus with mastoid air cells (air-on-sinus sign) in at least 2 consecutive slices in 2 orthogonal planes. Sigmoid sinus diverticulum was defined as a focal outpouching of the sigmoid sinus into the adjacent mastoid air cells or the mastoid cortex. Note that the presence of a sigmoid sinus diverticulum does not necessarily suggest the presence of dehiscence but rather indicates an abnormal focal outpouching of the sigmoid sinus. The radiologist also documented the location, size, and content of cephaloceles (ie, meninges versus meninges and brain tissue). The patient's symptoms were obtained from the study indication and/or a review of the medical records. Cephalocele content was defined using MR imaging (ie, CSF versus CSF with brain tissue). If MR imaging was not available, the surgical note, the density of cephalocele, or the tethering of atrophic brain tissue toward the cephalocele or both were used as a proxy for the cephalocele. If no brain tissue was seen during an operation, the density of the cephalocele was equal to that of CSF, and there was no tethering of atrophic brain tissue toward the cephalocele, the cephalocele was assumed to contain only CSF. The cephalocele content was determined via MR imaging in all except 4 patients. In these 4 patients, the cephaloceles were isodense with CSF on CT and no evidence of tethering of brain tissue was noted. Three of these patients underwent surgical repair, and no brain tissue was noted during the operation. Accordingly, all 4 patients were considered to have only CSF-containing cephaloceles.

### Statistical Analyses

SSDD and cephalocele categorical characteristics were analyzed using  $\chi^2$  tests, and SSDD and cephalocele continuous characteristics were analyzed using a nonparametric approach with Kruskal-Wallis tests. Cephalocele volume was calculated by the following equation: Volume = Product of Triplanar Dimensions  $\times$  0.5. A single-variable linear regression was performed between volume and SSDD to help determine the correlation. A supportive single-variable logistic regression was performed using the average volume as a cutoff for a binomial dependent variable relative to SSDD. A multivariate logistic regression, controlling for sex, laterality, location, and cephalocele volume was performed with SSDD as the dependent binomial variable. Statistical analysis based on individual locations of the cephaloceles was not possible because of the small number within each group. We, therefore, pooled the participants into 3 main categories for further analyses: 1) anterior cephaloceles (ethmoidal, sphenoidal, cribriform plate, and sellar cephaloceles), 2) foraminal cephaloceles (cephaloceles through foramen of ovale and the Meckel cave), and 3) temporal cephaloceles (temporal apex and tegmen tympani cephaloceles).

## RESULTS

Fifty-six patients with cephaloceles were included in our retrospective study. Forty-four patients were women (79%). The average age of the group was 50.9 years. An anterior cephalocele (through the ethmoid and sphenoid sinuses, cribriform plate, and

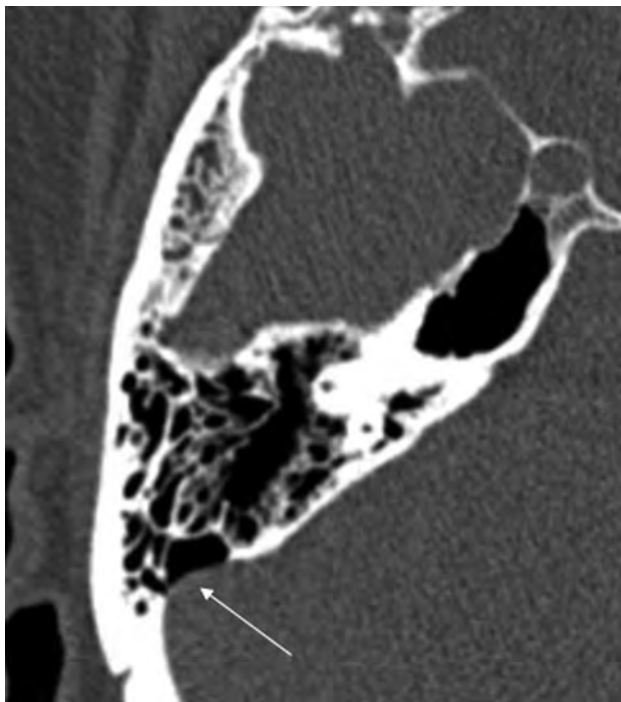


**FIG 1.** Dehiscence of the right sigmoid sinus (arrow). Lack of osseous coverage of the sigmoid sinus with the air-on-sinus sign.

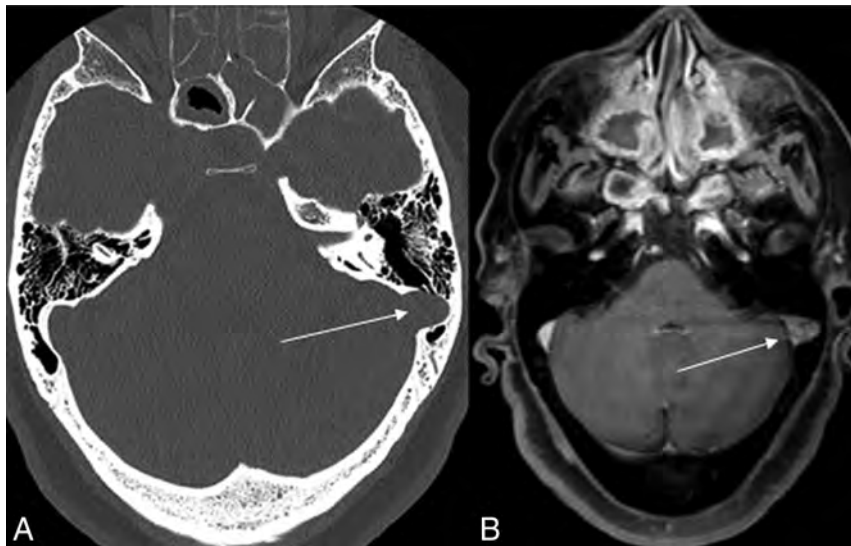


**FIG 2.** Diverticulum of the left sigmoid sinus (arrow) with focal protrusion of the sigmoid sinus toward the mastoid air cells. The left sigmoid sinus was normal in shape above and below this section (A, Bone window CT; B, Postcontrast T1 MR imaging).

sella) was found in 33 patients (58.9%), while only 4 patients had one through the skull base foramina (ie, the foramen of ovale and the Meckel cave). The remaining patients ( $n = 19$ ) had temporal bone cephaloceles (through the temporal apex and tegmen tympani). In 22 patients (39.3%), the cephalocele contained brain tissue and meninges (encephalomeningoceles); the remaining 34 patients had cephaloceles that contained only meninges (meningoceles). The average cephalocele volume was  $2979 \text{ mm}^3$ .

The most common presenting symptom was rhinorrhea (24 patients, 42.9%). In 22 patients (39.3%), the cephalocele was diagnosed incidentally during work-up for headaches (without other symptoms related to IIH). Other presenting symptoms were headaches secondary to IIH in 2 patients (3.6%), otorrhea in 1 patient (1.8%), bilateral hearing loss in 1 patient (1.8%), meningitis in 4 patients (7%), and meningitis with CSF leak in 2 patients (3.6%). Twenty-three patients (41.1%) were managed conservatively, and 33 patients (58.9%) underwent surgical repair.

Of 56 patients with cephaloceles, 21 patients were also shown to have SSDD, a prevalence of 37.5%. Most of these patients were women, with only 1 man having been identified. In 11 patients, the right sigmoid sinus (Fig 1) was involved, and in 7 patients, the left sigmoid sinus was involved, including 3 cases of diverticulum (Fig 2). In 3 patients, evidence of bilateral SSDD was noted. The presence of an SSDD did not contribute to any group differences in the location of a cephalocele, content, or symptoms (Table 1).

Most interesting, there was a significant inverse association between the volume of the cephalocele and the presence of an SSDD. Patients with an SSDD had a lower mean cephalocele volume ( $1562.4 \pm 1511.8 \text{ mm}^3$ ) compared with those without one (mean =  $3828.6 \pm 3559.4 \text{ mm}^3$ ,  $P = .015$ ). By multivariate logistic regression, controlling for sex, laterality, and location, cephalocele volume remained significantly associated with SSDD ( $P = .036$ ). In addition, as cephalocele volume decreased, there was an association

with SSDD (coefficient,  $-2266$ ;  $P$  value  $< .007$ , adjusted  $R^2 = 0.1077$ ). The 95% confidence intervals vary widely due to overfitting of the univariate linear regression ( $-3873.20$  to  $-659.14$ ) supporting a potentially inconclusive finding due to collinearity. To further investigate this inverse association, we performed a univariate logistic regression analysis using the nearest to average volume ( $3086 \text{ mm}^3$ ) as the cutoff versus the association of SSDD with cephaloceles. An odds ratio of 3.58 of cephaloceles below average volume is associated with SSDD with a 95% CI, 2.3–4.86 and a  $P$  value = .05 (Table 2).

## DISCUSSION

To our knowledge, this is the first study to evaluate the prevalence of SSDD in patients with cephaloceles. Within our cohort, the prevalence of SSDD in patients with cephalocele was shown to be 37.5%. We found a strong

association between the presence of SSDD and female sex. Similar sex associations have been reported in patients with SSDD in the context of elevated ICPs.<sup>11,12</sup> In 2017, in the systematic review by Wang et al,<sup>17</sup> 90.4% of patients with pulsatile tinnitus and SSDD were women.<sup>17</sup> Despite the literature, only 2 of our patients with SSDD had documented evidence of increased ICP and none of our patients presented with pulsatile tinnitus. Our findings match those of a recent study by

**Table 1: Univariable analysis of cephaloceles and SSDD**

	Cephalocele Only (n = 35)	Cephalocele and SSDD (n = 21)	Total (n = 56)	P Value
Age (yr)				.71
Mean (SD)	51.5 (13.6)	49.7 (11.9)	50.8 (12.9)	
Range	27–79	27–67	27–79	
Sex				.019
Female	24 (68.6%)	20 (95.2%)	44 (78.6%)	
Male	11 (31.4%)	1 (4.8%)	12 (21.4%)	
Symptoms				.235
Bilateral hearing loss	0 (0.0%)	1 (4.8%)	1 (1.8%)	
CSF leak	15 (42.9%)	9 (42.9%)	24 (42.9%)	
Incidental	17 (48.6%)	5 (23.8%)	22 (39.3%)	
Headache secondary to IIH	1 (2.9%)	1 (4.8%)	2 (3.6%)	
Meningitis	1 (2.9%)	3 (14.3%)	4 (7.1%)	
Meningitis with CSF leak	1 (2.9%)	1 (4.8%)	2 (3.6%)	
Otorrhea	0 (0.0%)	1 (4.8%)	1 (1.8%)	
Content of cephalocele				.672
Brain and meninges	13 (37.1%)	9 (42.9%)	22 (39.3%)	
Meninges	22 (62.9%)	12 (57.1%)	34 (60.7%)	
Location				.866
Anterior skull base	21 (60.0%)	12 (57.1%)	33 (58.9%)	
Skull base foramina	2 (5.7%)	2 (9.5%)	4 (7.1%)	
Temporal bone	12 (34.3%)	7 (33.3%)	19 (33.9%)	
Volume of cephalocele (mm <sup>3</sup> )				.015
Mean (SD)	3828 (3559)	1562 (1511)	2979 (3144)	
Median (minimum-maximum)	40–12,617	30–4872	30–12,617	
Cephalocele repaired?				.141
No	17 (48.6%)	6 (28.6%)	23 (41.1%)	
Yes	18 (51.4%)	15 (71.4%)	33 (58.9%)	

**Table 2: Logistic regression for volume less than average (3086 mm<sup>3</sup>) versus SSDD association with cephalocele**

	Presence of SSDD
Volume below average 3086 mm <sup>3</sup>	OR = 3.58 95% CI, 2.30–4.86 P = .05
Constant	0.25 (−0.85–1.35)
Observations	56
Log likelihood	−34.91
Akaike information criterion	73.81

Lansley et al<sup>16</sup> and raise questions with regard to SSDD as the proximal cause of pulsatile tinnitus. In patients with IIH, the pulsatile tinnitus can be secondary to IIH itself rather than SSDD.

The inverse relationship noted between the volume of cephalocele and SSDD will require further investigation. One potential explanation is that increased ICP may manifest in several different ways (eg, empty sella, prominent subarachnoid spaces around optic nerves, cephalocele formation, and SSDD). Accordingly, one may postulate that once SSDD develops in patients with cephaloceles, this anomaly provides a “pressure outlet” so that elevated ICP is more likely to contribute to further dehiscence in lieu of continued cephalocele growth. Also, an association between SSDD and cephaloceles may favor CSF pulsation as the cause of the SSDD as opposed to venous pulsations.

A little less than half of our patients were found to have CSF rhinorrhea that required treatment, and in our cohort, the second most common reason for discovery of the cephalocele was purely incidental. Current treatment options for

symptomatic SSDD include the classic transmastoid and retro-sigmoid open surgical approaches; more recent endovascular approaches involving coil embolization and stent placement have also begun to emerge.<sup>12–14,18</sup> Given our findings and recent literature, we recommend evaluation of IIH before invasive treatment of SSDD in patients with pulsatile tinnitus.

### Limitations

Our study has a few limitations. First, it is a retrospective analysis that includes a relatively heterogeneous group of patients and imaging from our institutional data base; thus, it does not include patients who may have received treatment at outside institutions. Second, only the sigmoid sinus was evaluated, and the presence of additional intracranial venous anomalies and stenosis could not be evaluated, given that dedicated CT MR venography of both were not performed. Third, this is a relatively small cohort that may not be adequately powered to find subtle differences between groups with and without SSDD. Statistically, the study is underpowered and does not offer conclusive evidence for its findings but offers the first literature reports of possible associations among sex, the presence of SSDD, and its volume with cephaloceles. While our study found a significant inverse relationship between cephalocele volume and the presence of SSDD ( $P = .036$ ), the lack of a strong linear association (per  $R^2 = 0.1077$ ) may ultimately reflect an underpowered study. Our logistic regression demonstrated an odds ratio of 3.58 for smaller volumes and increased association with SSDD with a  $P$  value at exactly .05 while using the cutoff of average volume, though the range of volumes for the cephaloceles analyzed is wide. A more extensive investigation is warranted and may ultimately be accomplished via the provision of an appropriately powered multi-institutional study.



## CONCLUSIONS

Within our cohort, the prevalence of SSDD in patients with a cephalocele was shown to be 37.5%. Herein we report a potential association between female sex and an inverse relationship between cephalocele volume and SSDD. We did not find any differences between the presence and absence of SSDD in patients with cephaloceles when comparing age, location of cephalocele, content, or clinical symptoms. SSDD and skull base cephaloceles may share an underlying common pathophysiology such as IIH. Further studies are needed to evaluate the exact mechanisms between these skull base and venous pathologies.

Disclosures: Joshua D. Bernstock—RELATED: positions and equity in CITC Ltd and Avidea Technologies and a member of the POKIT Diagnostic Board of Scientific Advisors.

## REFERENCES

1. Connor SE. **Imaging of skull-base cephaloceles and cerebrospinal fluid leaks.** *Clin Radiol* 2010;65:832–41 CrossRef Medline
2. Lloyd KM, DelGaudio JM, Hudgins PA. **Imaging of skull base cerebrospinal fluid leaks in adults.** *Radiology* 2008;248:725–36 CrossRef Medline
3. Naidich TP, Altman NR, Braffman BH, et al. **Cephaloceles and related malformations.** *AJNR Am J Neuroradiol* 1992;13:655–90 Medline
4. Mann SS, Naidich TP, Towbin RB, et al. **Imaging of postnatal maturation of the skull base.** *Neuroimaging Clin N Am* 2000;10:1–21 Medline
5. Wilkins RH, Radtke RA, Burger PC. **Spontaneous temporal encephalocele: case report.** *J Neurosurg* 1993;78:492–98 CrossRef Medline
6. Gacek RR, Gacek MR, Tart R. **Adult spontaneous cerebrospinal fluid otorrhea: diagnosis and management.** *Am J Otol* 1999;20:770–76 Medline
7. Shetty PG, Shroff MM, Fatterpekar GM, et al. **A retrospective analysis of spontaneous sphenoid sinus fistula: MR and CT findings.** *AJNR Am J Neuroradiol* 2000;21:337–42 Medline
8. Chang DW, Langstein HN, Gupta A, et al. **Reconstructive management of cranial base defects after tumor ablation.** *Plast Reconstr Surg* 2001;107:1346–55; discussion 56–57 CrossRef Medline
9. Yilmazlar S, Arslan E, Kocaeli H, et al. **Cerebrospinal fluid leakage complicating skull base fractures: analysis of 81 cases.** *Neurosurg Rev* 2006;29:64–71 CrossRef Medline
10. Harvey RS, Hertzano R, Kelman SE, et al. **Pulse-synchronous tinnitus and sigmoid sinus wall anomalies: descriptive epidemiology and the idiopathic intracranial hypertension patient population.** *Otol Neurotol* 2014;35:7–15 CrossRef Medline
11. Liu Z, Chen C, Wang Z, et al. **Sigmoid sinus diverticulum and pulsatile tinnitus: analysis of CT scans from 15 cases.** *Acta Radiol* 2013;54:812–86 CrossRef Medline
12. Schoeff S, Nicholas B, Mukherjee S, et al. **Imaging prevalence of sigmoid sinus dehiscence among patients with and without pulsatile tinnitus.** *Otolaryngol Head Neck Surg* 2014;150:841–46 CrossRef Medline
13. Eisenman DJ. **Sinus wall reconstruction for sigmoid sinus diverticulum and dehiscence: a standardized surgical procedure for a range of radiographic findings.** *Otol Neurotol* 2011;32:1116–19 CrossRef Medline
14. Otto KJ, Hudgins PA, Abdelkafy W, et al. **Sigmoid sinus diverticulum: a new surgical approach to the correction of pulsatile tinnitus.** *Otol Neurotol* 2007;28:48–53 CrossRef Medline
15. Hou ZQ, Han DY. **Pulsatile tinnitus in perimenopausal period.** *Acta Otolaryngol* 2011;131:896–904 CrossRef Medline
16. Lansley JA, Tucker W, Eriksen MR, et al. **Sigmoid sinus diverticulum, dehiscence, and venous sinus stenosis: potential causes of pulsatile tinnitus in patients with idiopathic intracranial hypertension?** *AJNR Am J Neuroradiol* 2017;38:1783–88 CrossRef Medline
17. Wang AC, Nelson AN, Pino C, et al. **Management of sigmoid sinus associated pulsatile tinnitus: a systematic review of the literature.** *Otol Neurotol* 2017;38:1390–96 CrossRef Medline
18. Shastri RK, Chaudhary N, Pandey AS, et al. **Venous diverticula causing pulsatile tinnitus treated with coil embolization and stent placement with resolution of symptoms: report of two cases and review of the literature.** *Otol Neurotol* 2017;38:e302–07 CrossRef Medline

# Variable Refocusing Flip Angle Single-Shot Imaging for Sedation-Free Fast Brain MRI

 R. Jabarkheel,  E. Tong,  E.H. Lee,  T.M. Cullen,  U. Yousaf,  A.M. Loening,  V. Taviani,  M. Iv,  G.A. Grant,  S.J. Holdsworth,  S.S. Vasanawala, and  K.W. Yeom



## ABSTRACT

**BACKGROUND AND PURPOSE:** Conventional single-shot FSE commonly used for fast MRI may be suboptimal for brain evaluation due to poor image contrast, SNR, or image blurring. We investigated the clinical performance of variable refocusing flip angle single-shot FSE, a variation of single-shot FSE with lower radiofrequency energy deposition and potentially faster acquisition time, as an alternative approach to fast brain MR imaging.

**MATERIALS AND METHODS:** We retrospectively compared half-Fourier single-shot FSE with half- and full-Fourier variable refocusing flip angle single-shot FSE in 30 children. Three readers reviewed images for motion artifacts, image sharpness at the brain-fluid interface, and image sharpness/tissue contrast at gray-white differentiation on a modified 5-point Likert scale. Two readers also evaluated full-Fourier variable refocusing flip angle single-shot FSE against T2-FSE for brain lesion detectability in 38 children.

**RESULTS:** Variable refocusing flip angle single-shot FSE sequences showed more motion artifacts ( $P < .001$ ). Variable refocusing flip angle single-shot FSE sequences scored higher regarding image sharpness at brain-fluid interfaces ( $P < .001$ ) and gray-white differentiation ( $P < .001$ ). Acquisition times for half- and full-Fourier variable refocusing flip angle single-shot FSE were faster than for single-shot FSE ( $P < .001$ ) with a 53% and 47% reduction, respectively. Intermodality agreement between full-Fourier variable refocusing flip angle single-shot FSE and T2-FSE findings was near-perfect ( $\kappa = 0.90$ ,  $\kappa = 0.95$ ), with an 8% discordance rate for ground truth lesion detection.

**CONCLUSIONS:** Variable refocusing flip angle single-shot FSE achieved 2× faster scan times than single-shot FSE with improved image sharpness at brain-fluid interfaces and gray-white differentiation. Such improvements are likely attributed to a combination of improved contrast, spatial resolution, SNR, and reduced T2-decay associated with blurring. While variable refocusing flip angle single-shot FSE may be a useful alternative to single-shot FSE and, potentially, T2-FSE when faster scan times are desired, motion artifacts were more common in variable refocusing flip angle single-shot FSE, and, thus, they remain an important consideration before clinical implementation.

**ABBREVIATIONS:** SSFSE = single-shot FSE; vrfSSFSE = variable refocusing single-shot FSE

Fast MR imaging sequences commonly used to image infants and young children are often a derivative of T2-weighted MR imaging with shorter acquisition times.<sup>1</sup> While fast MR imaging sequences have, to date, shown lower image quality compared with standard T2-weighted FSE MR imaging, they do provide a faster method for evaluating the global brain and are particularly useful for assessing fluid-filled spaces or structures.<sup>2</sup> Historically,

fast MR imaging was clinically implemented to reduce the radiation exposure of serial CT imaging in shunted children and avoid sedation often required for lengthier conventional MR imaging scans on children.<sup>3-5</sup>

There are various types of fast MR imaging, including single-shot FSE (SSFSE), balanced steady-state free precession, and hybrid methods using a combination of gradient- and spin-echoes.<sup>2,6-11</sup>


Received December 24, 2019; accepted after revision April 18, 2020.


From the Stanford University School of Medicine (R.J.); and Departments of Radiology (E.T., A.M.L., V.T., M.I.), Electrical Engineering (E.H.L.), and Neurosurgery (G.A.G.), Stanford University, Stanford, California; Department of Radiology (T.M.C., U.Y., S.S.V., K.W.Y.), Lucile Packard Children's Hospital, Stanford University, Palo Alto, California; and Department of Anatomy and Medical Imaging and Centre for Brain Research (S.J.H.), Faculty of Medical and Health Sciences, University of Auckland, Auckland, New Zealand.


This work was supported by National Institutes of Health grants R01 EB009690, P41 EB015891, IR21HD0838030IA1; the Tashia and John Morgridge Faculty Scholars fund; GE Healthcare; and the ASNR Comparative Effective Research Award.

Paper previously presented, in part, at: International Pediatric Radiology Conjoint Meeting and Exhibition, May 15–20, 2016; Chicago, Illinois.

Please address correspondence to Kristen W. Yeom, MD, Department of Radiology, Stanford University, 725 Welch Rd MC 5654, Stanford, CA, 94304; e-mail: kyeom@stanford.edu; @RJabarkheel; @KristenYeom

 Indicates open access to non-subscribers at [www.ajnr.org](http://www.ajnr.org)

 Indicates article with supplemental on-line tables.

 Indicates article with supplemental on-line photos.

<http://dx.doi.org/10.3174/ajnr.A6616>

All of these techniques are fast and therefore easy to implement without sedation. However, either limited resolution and blurring (SSFSE), poor tissue contrast (balanced steady-state free precession), or sensitivity to off-resonance and system imperfections (gradient- and spin-echoes) limits these fast MR imaging sequences from being used for broader clinical applications beyond evaluation of fluid structures. The PROPELLER method may combat motion and provide higher resolution.<sup>12</sup> PROPELLER is an FSE-based method, whereby several parallel data lines that form “blades” are acquired in a radial (or propeller-like) *k*-space acquisition. Because the blades rotate around the center of the *k*-space, this central oversampling provides redundancy of information, which can be used for motion correction. Nonetheless, PROPELLER poses challenges of lengthy acquisition times, requiring a greater degree of patient cooperation.

Among the various fast MR imaging approaches, SSFSE has emerged as one of the most frequently used pulse sequences, largely because of its T2-weighted contrast, speed, and robustness to motion, off-resonance, and system imperfections.<sup>13</sup> However, SSFSE has limitations due to its high rate of radiofrequency energy deposition—particularly at 3T—which translates into high specific absorption rate values.<sup>14</sup> Delays between the acquisition of consecutive slices need be introduced, resulting in section TRs longer than the time necessary to simply play the pulse sequence waveforms, to remain within the FDA specific absorption rate guidelines. While this issue is more pronounced when using the body coil for excitation, a delay is still required when using a transmit/receive head coil.<sup>15</sup>

Recently, a variation of SSFSE with variable refocusing flip angles (variable refocusing single-shot FSE [vrfSSFSE]) has been described.<sup>16</sup> This flip angle modulation was originally introduced to reduce T2-decay-associated blurring, mostly in the context of volumetric imaging.<sup>17–19</sup> Coincidentally, the flip angle modulation also reduces radiofrequency energy deposition and thus the specific absorption rate; hence, the aforementioned delays between acquisitions of successive slices can be shortened, resulting in faster imaging. Despite the potential benefits of faster imaging, the image quality of the brain using low refocusing flip angle SSFSE remains unknown. Furthermore, with vrfSSFSE, signal levels tend to oscillate over the echo train and are, thus, more vulnerable to motion-related signal loss, which might impede clinical interpretability. In this study, we sought to investigate a faster MR imaging approach that incorporates vrfSSFSE and examine its potential clinical applicability.<sup>20</sup>

## MATERIALS AND METHODS

### **Subjects Undergoing SSFSE and vrfSSFSE**

Our institution, the Lucile Packard Children's Hospital (Palo Alto, California) has integrated vrfSSFSE as part of our fast MR imaging brain protocol since April 2014. After institutional review board approval with waived consent, we retrospectively identified 30 consecutive children referred for noncontrast, sedation-free fast brain MR imaging between December 2015 and April 2016. Children who had undergone back-to-back conventional half-Fourier SSFSE, half-Fourier vrfSSFSE, and full-Fourier vrfSSFSE sequences at 3T MR imaging were included. The median age of patients was 6 years (age range, 8 months to 20 years).

Clinical characteristics of patients who had SSFSE and vrfSSFSE images are listed in On-line Table 1.

### **Subjects Undergoing T2-FSE and Full-Fourier vrfSSFSE**

We also retrospectively identified 38 consecutive children who had undergone back-to-back T2-FSE and full-Fourier vrfSSFSE scans at 3T MR imaging in October 2016 as part of a quality-assurance project. The median age of patients who had both T2-FSE and full-Fourier vrfSSFSE scans was 6 years (age range, 1 week to 17 years). Clinical characteristics of patients who had T2-FSE and full-Fourier vrfSSFSE images are listed in On-line Table 2.

### **Imaging Methods**

All subjects were scanned on a 3T Discovery MR750 scanner (GE Healthcare) with an 8-channel head coil.

**SSFSE and vrfSSFSE Image Acquisition.** The MR imaging protocol comprised 3 orthogonal planes of SSFSE (constant refocusing flip angle of 130°) and coronal vrfSSFSE. SSFSE parameters were the following: FOV = 18–22 cm (adjusted to each patient's anatomy), array coil spatial sensitivity encoding parallel imaging factor = 2, half-Fourier with homodyne reconstruction, effective TE = 86 ms, matrix = 256 × 256, and bandwidth = 83 kHz. Contiguous, 4-mm-thick slices with interleaved section ordering were used. The vrfSSFSE sequences had the same parameters, but auto-calibrating parallel imaging was used instead of array coil spatial sensitivity encoding. Full-Fourier vrfSSFSE was performed in addition to half-Fourier vrfSSFSE with homodyne reconstruction.<sup>21</sup> The TR for each sequence was recorded.

**T2-FSE and Full-Fourier vrfSSFSE Image Acquisition.** Axial full-Fourier vrfSSFSE parameters were the following: section thickness = 4 mm, 0.5 skip, FOV = 18–22 cm, matrix = 256 × 256, average TR/TE = 960/160 ms. Axial T2-FSE autocalibrating reconstruction for Cartesian imaging parameters were the following: section thickness = 4 mm, 0.5 skip, FOV = 18–22 cm, matrix = 512 × 256, with average TR/TE times = 3000/100 ms.

### **SSFSE versus vrfSSFSE Image-Quality Evaluation**

Two blinded, board-certified neuroradiologists with Certificates of Added Qualification (K.W.Y., >10 years; M.I., >5 years' experience) and 1 pediatric radiology fellow (T.M.C.) independently evaluated coronal half-Fourier SSFSE, half-Fourier vrfSSFSE, and full-Fourier vrfSSFSE sequences in random order with regard to individual patients and the sequence type. The reviewers assessed the following image features: motion artifacts, image sharpness at the brain-fluid interfaces (eg, cortical surface, cerebral sulci, or cerebellar fissures), and image sharpness within the brain substance, specifically targeting tissue contrast at the gray-white differentiation. Motion artifacts were scored on the basis of motion-related signal drop-out. Sharpness took into account factors that contributed to better visualization of boundaries of solid-fluid and solid-solid structures. Note that higher sharpness scores could be attributed to a combination of factors, including improved image contrast (such as contrast at the cortical surface or within the brain parenchyma at the gray-white differentiation), improved spatial resolution and SNR, and reduced T2-decay-associated blurring. For

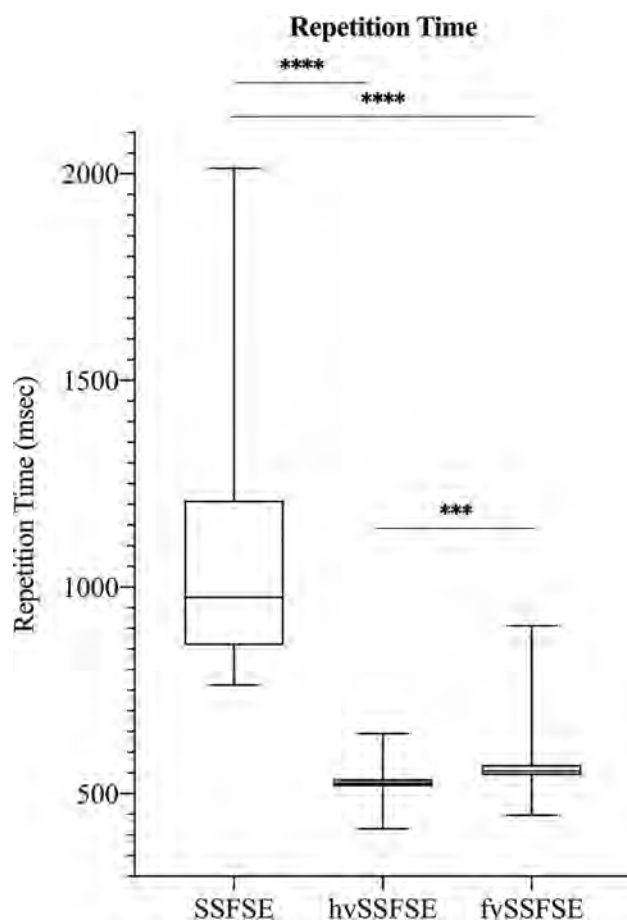


**FIG 1.** TRs of SSFSE and vrfSSFSE. Box-and-whisker plots for each sequence are shown with the *middle bar* representing the median, the *box* representing the 25th and 75th percentiles, and the *upper and lower bars* representing the range. Half-Fourier vrfSSFSE (hvSSFSE) and full-Fourier vrfSSFSE (fvSSFSE) have significantly faster TRs compared with SSFSE ( $P < .001$ ). hvSSFSE has a significantly faster TR compared with fvSSFSE ( $P < .001$ ). All comparisons of TRs were assessed using the Mann-Whitney test.

scoring, we used the following modified 5-point Likert scale: 1, nondiagnostic; 2, limited study; 3, suboptimal quality; 4, not affecting diagnostic quality, minimal artifacts or image-quality problems; 5, diagnostic, no artifacts or excellent image quality.

#### Evaluation of T2-FSE and Full-Fourier vrfSSFSE Image Findings

Two blinded board-certified neuroradiologists with Certificates of Added Qualification (K.W.Y. and E.T., >2 years' experience) independently reviewed axial T2-FSE and full Fourier vrfSSFSE images in a random order and with at least a 2-week interval to avoid recall bias between the 2 sequences. The reviewers recorded all detectable pathologic brain lesions. T2-FSE served as the ground truth. The full-Fourier vrfSSFSE findings were considered in agreement with T2-FSE only if all abnormal findings found on T2-FSE were also detected on full-Fourier vrfSSFSE in an all-or-none grading manner. We did not evaluate agreement for minor T2\*-related features, such as focal hemosiderin or mineralization.

#### Statistical Analysis

Wilcoxon matched-pairs signed ranked tests were used to compare radiologists' ratings between SSFSE and vrfSSFSE sequences.

Mann-Whitney tests were used to compare TRs between SSFSE and vrfSSFSE sequences. Interrater agreement for SSFSE and vrfSSFSE image-quality evaluation was assessed with the Fleiss  $\kappa$  statistic because we had 3 readers. Following interrater agreement analyses between SSFSE and vrfSSFSE raw scores, Fisher exact tests were used to compare the fraction of scans rated highly, 4 or 5, for each image-quality parameter for SSFSE and vrfSSFSE sequences. Intermodality agreement between full-Fourier vrfSSFSE and T2-FSE findings for a given reader was assessed using the Cohen  $\kappa$ . Wilcoxon matched-pairs signed rank tests, Mann-Whitney tests, Fisher exact tests, and Cohen  $\kappa$  were all calculated using GraphPad Prism software (Version 8.2.1; GraphPad Software). The Fleiss  $\kappa$  statistic was calculated using Excel (Version 16.29; Microsoft).

## RESULTS

Overall, vrfSSFSE sequences showed significantly faster acquisition times compared with SSFSE (Fig 1). Specifically, half-Fourier vrfSSFSE (mean, 528 ms) and full-Fourier vrfSSFSE (mean, 597 ms) had a 53% and 47% decrease in TR, respectively, compared with SSFSE (mean, 1120 ms;  $P < .001$ ). There was no instance in which either vrfSSFSE or SSFSE was considered nondiagnostic within the narrow clinical scope for which fast MR imaging was obtained (evaluation of ventricular size, cyst, or large fluid collection).

#### Motion Artifacts

SSFSE scored significantly higher (ie, had less motion-related signal loss) than both half-Fourier vrfSSFSE and full-Fourier vrfSSFSE (mean, 4.6 versus 3.8 versus 3.7, respectively;  $P < .001$ ; Fig 2A and Table 1). Figure 3 shows an example of motion-related signal loss that might be seen with vrfSSFSE. While these artifacts were less common for SSFSE, 77% and 80% of half-Fourier vrfSSFSE and full-Fourier vrfSSFSE, respectively, showed minimal-to-no artifacts (Table 2).

#### Image Sharpness at the Brain-Fluid Interfaces

Both half-Fourier vrfSSFSE and full-Fourier vrfSSFSE scored higher than SSFSE (mean, 4.2 versus 4.1 versus 3.4, respectively;  $P < .001$ ; Fig 2B). Figure 4 shows an example of improved sharpness with vrfSSFSE, particularly at the cortical-sulcal interface.

#### Image Sharpness/Tissue Contrast at the Gray-White Differentiation

Both half-Fourier vrfSSFSE and full-Fourier vrfSSFSE scored higher than SSFSE (mean, 4.4 versus 4.4 versus 3.5, respectively;  $P < .001$ ; Fig 2C). Figure 5 shows an example of improved image sharpness stemming from higher tissue contrast and spatial resolution and SNR with more distinct gray-white differentiation on vrfSSFSE, including improved anatomic detail of smaller structures such as the cerebellar folia.

#### Comparison of the vrfSSFSE Sequences

There were no statistically significant differences for motion artifacts or overall image sharpness.

#### SSFSE and vrfSSFSE Image-Quality Interrater Agreement

Raters varied on the basis of the image-quality parameter assessed. There was substantial interrater agreement for motion artifacts



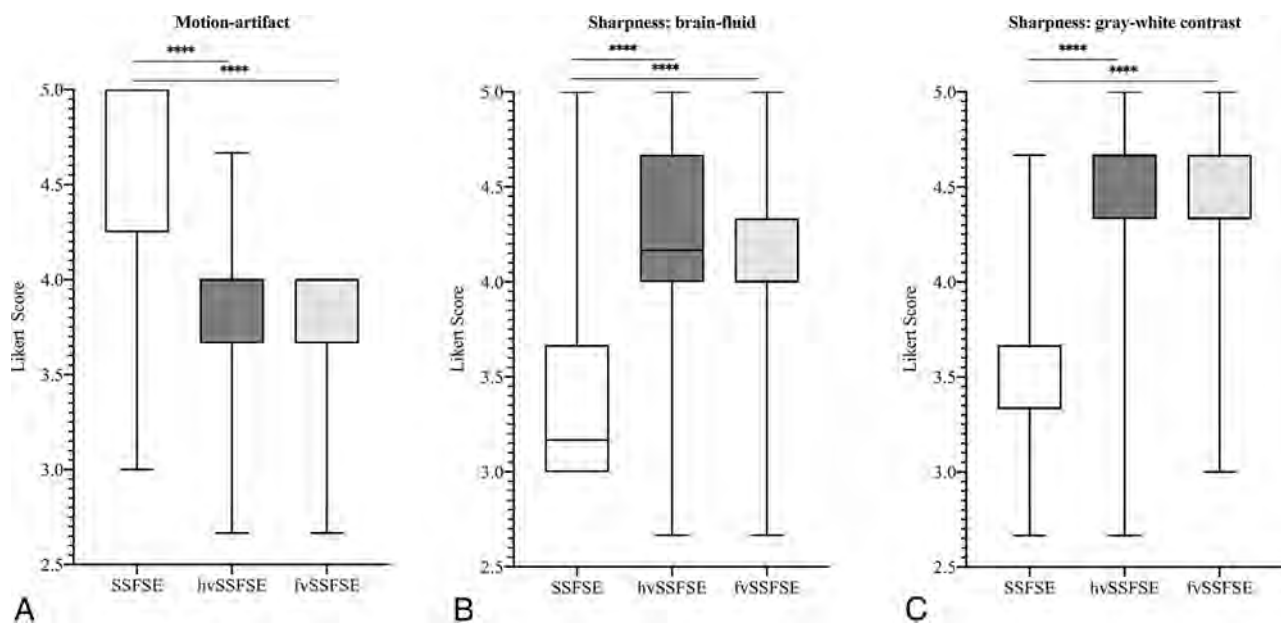


**FIG 2.** Image-quality ratings of SSFSE and vrfSSFSE. Box-and-whisker plots for each image-quality parameter (Motion artifact, Sharpness: brain-fluid, and Sharpness: gray-white contrast rated on a 5-point Likert scale) for a given sequence with the *middle bar* representing the median, the *box* representing the 25th and 75th percentile, and the *upper and lower bars* representing the range. **A**, SSFSE scans scored significantly higher than both hvSSFSE and fvSSFSE scans on motion artifacts ( $P < .001$ ). hvSSFSE and fvSSFSE scans did not differ significantly for Motion artifact ( $P > .5$ ). **B**, hvSSFSE and fvSSFSE scans were rated significantly better than SSFSE scans for Sharpness: brain-fluid ( $P < .001$ ). hvSSFSE and fvSSFSE scans did not differ significantly for Sharpness: brain-fluid ( $P > .2$ ). **C**, hvSSFSE and fvSSFSE scans were rated significantly better than SSFSE scans for Sharpness: gray-white contrast ( $P < .001$ ). hvSSFSE and fvSSFSE scans did not differ significantly for Sharpness: gray-white contrast ( $P > .9$ ). All comparisons of image-quality ratings were made using the Wilcoxon matched-pairs signed-rank test.

**Table 1: Mean image-quality ratings of SSFSE and vrfSSFSE scans and interrater agreement<sup>a</sup>**

	Motion Artifact <sup>b</sup>	Sharpness: Brain-Fluid <sup>c</sup>	Sharpness: gray-white contrast <sup>d</sup>
SSFSE	4.6 ± 0.6 (0.63, substantial)	3.4 ± 0.7 (0.43, moderate)	3.5 ± 0.6 (−0.03, poor)
Half-Fourier vrfSSFSE	3.8 ± 0.5 (0.39, fair)	4.2 ± 0.6 (0.32, fair)	4.4 ± 0.7 (0.07, slight)
Full-Fourier vrfSSFSE	3.7 ± 0.5 (0.37, fair)	4.1 ± 0.5 (0.23, fair)	4.4 ± 0.6 (0.03, slight)
Pooled	(0.62, substantial)	(0.47, moderate)	(0.15, slight)

<sup>a</sup>Wilcoxon matched-pairs signed-rank test was used to compare reader image-quality ratings of sequences.

<sup>b</sup>SSFSE was scored significantly higher than both half- and full-Fourier vrfSSFSE for Motion Artifact ( $P < .001$ ).

<sup>c</sup>Both vrfSSFSE sequences were rated significantly higher than SSFSE for Sharpness: Brain-Fluid ( $P < .001$ ).

<sup>d</sup>Both vrfSSFSE sequences were rated significantly higher than SSFSE for Sharpness: gray-white contrast ( $P < .001$ ).

( $\kappa = 0.62$ ). There was moderate agreement for image sharpness at the brain-fluid interfaces ( $\kappa = 0.47$ ) and slight agreement for image sharpness/tissue contrast at gray-white differentiation ( $\kappa = 0.15$ ). Table 1 provides interrater agreement on a pooled-sequence basis for image-quality parameters and on an individual-sequence basis by image-quality parameters. While there is slight-to-moderate interrater agreement for image sharpness at brain-fluid interfaces and gray-white differentiation, both half-Fourier vrfSSFSE and full-Fourier vrfSSFSE had significantly more images rated either a 4 (very good) or 5 (excellent) compared with SSFSE for these image-quality parameters ( $P < .001$ ; Table 2).

#### Comparison of T2-FSE and Full-Fourier vrfSSFSE

Intermodality agreement between T2-FSE and full-Fourier vrfSSFSE findings for a given reader was almost perfect, with  $\kappa = 0.90$  and  $\kappa = 0.95$ , respectively. Side-by-side examples that compare T2-FSE and full-Fourier vrfSSFSE are shown in Fig 6 and

On-line Fig 1. With T2-FSE as ground truth, full-Fourier vrfSSFSE demonstrated an 8% discordance rate. One reviewer missed a small cyst or cavity on full-Fourier vrfSSFSE that was detectable on T2-FSE (On-line Fig 2). Both reviewers missed a focal intraparenchymal hemorrhage on full-Fourier vrfSSFSE that was detected on T2-FSE.

#### DISCUSSION

Fast MR imaging of the brain has transformed the management of children with shunted hydrocephalus or ventriculomegaly by reducing the radiation exposure of serial CT head examinations and sedation that might be required for a lengthier conventional MR imaging of the brain. Since its initial use for ventricular assessment, however, many pediatric hospitals have increasingly adopted various fast MR imaging methods for other clinical conditions such as cyst evaluation, venous thrombosis, congenital anomalies, Chiari

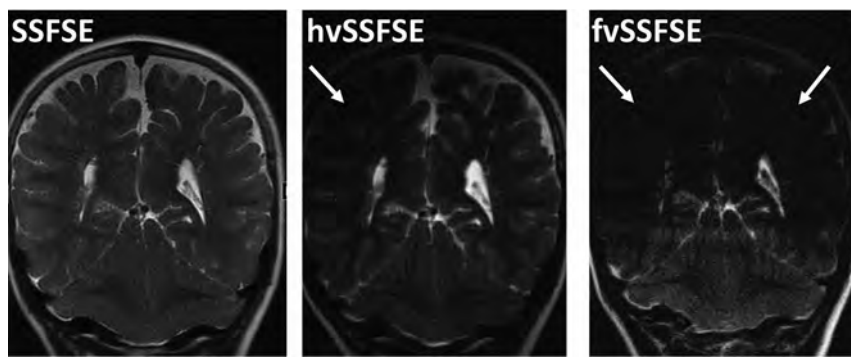


**FIG 3.** Example of motion-related signal loss. An 8-year-old girl presented for ventricular assessment. Half-Fourier vrfSSFSE (hvSSFSE) and full-Fourier vrfSSFSE (fvSSFSE) images show motion-related signal loss (arrows) on some of the slices that compromised image detail.

**Table 2: Fraction of SSFSE and vrfSSFSE scans rated highly, 4 or 5, for readers' assessments<sup>a</sup>**

	Motion Artifact <sup>b</sup>	Sharpness: Brain-Fluid <sup>c</sup>	Sharpness: gray-white contrast <sup>d</sup>
SSFSE	94%	37%	50%
Half-Fourier vrfSSFSE	80%	91%	90%
Full-Fourier vrfSSFSE	77%	96%	94%

<sup>a</sup> Fisher exact tests were used to compare the fraction of scans rated highly, 4 or 5, for each image-quality parameter for SSFSE and vrfSSFSE sequences.

<sup>b</sup> There was no statistically significant difference in the fraction of SSFSE scans rated either a 4 (very good) or 5 (excellent) for Motion-Artifact as compared to vrfSSFSE sequences ( $P > .1$ ).

<sup>c</sup> Both vrfSSFSE sequences had a higher fraction of images rated either 4 or 5 as compared to SSFSE for Sharpness: Brain-Fluid ( $P < .001$ ).

<sup>d</sup> Both vrfSSFSE sequences had a higher fraction of images rated either 4 or 5 as compared to SSFSE for Sharpness: Gray-White Contrast ( $P < .0001$ ).



**FIG 4.** Example of image sharpness or blurring. A 3-year-old girl presented for ventricular assessment. Half-Fourier vrfSSFSE (hvSSFSE) and full-Fourier vrfSSFSE (fvSSFSE) images (arrows) show improved sharpness or reduced blurring, compared with the corresponding conventional SSFSE, particularly along the cortical margins where the cortical surface is better distinguished against the overlying subarachnoid spaces.

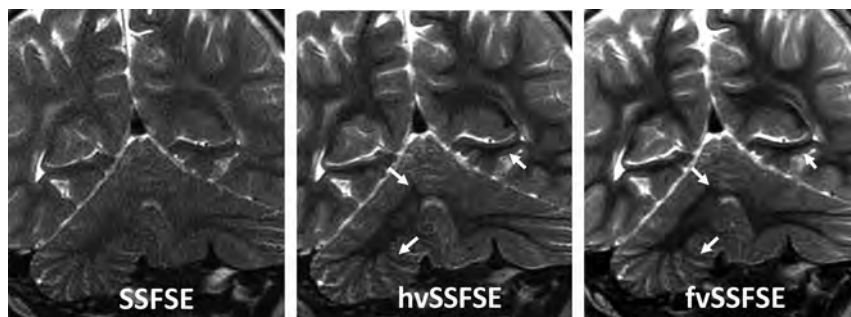


**FIG 5.** Example of magnified views demonstrating differences in tissue contrast. A 2-year-old boy presented for ventricular assessment. Half-Fourier vrfSSFSE (hvSSFSE) and full-Fourier vrfSSFSE (fvSSFSE) images show improved tissue contrast (arrows) that allows improved visualization of the gray-white junction, cerebellar folia detail, as well as posterior hippocampal regions.

malformations, and postoperative hemorrhage.<sup>5,11,22</sup> Greater recognition of radiation-related cancer risks of repeat head CT examinations, in part, has driven such expanded clinical indications because lifetime cancer mortality risk due to radiation exposure from head CT in a 1-year-old child is estimated to be 0.07%, an order of magnitude higher than that of adults.<sup>13,23-25</sup> Potential risks and adverse effects of sedation in children are other contributing factors.<sup>26</sup>

Among the various fast MR imaging approaches, SSFSE is frequently used for its speed and excellent T2-weighted contrast. A central limitation of SSFSE, however, is its high rate of radiofrequency energy deposition due to refocusing pulse trains with a constant flip angle, which results in high specific absorption rates. The high specific absorption rate of SSFSE mandates a longer TR, in which motion between acquisitions of sections could lead to misregistration. In this study, we tested whether a variation of SSFSE with variable refocusing flip angles (thus decreasing radiofrequency energy deposition) could reduce TRs and thereby facilitate faster imaging compared with conventional SSFSE. We also sought to compare image quality between vrfSSFSE and conventional SSFSE and then compare the diagnostic performance of vrfSSFSE against T2-FSE used in standard-of-care brain MR imaging protocols.

In this study, we applied variable refocusing flip angles for potential fast MR imaging optimization of the pediatric brain. We found that vrfSSFSE sequences significantly reduced TRs and therefore overall scan times by around 50%. Although vrfSSFSE was more vulnerable to motion-related signal loss, it gave rise to images with improved tissue contrast, spatial resolution, and SNR, compared with SSFSE and suggested a potential clinical role for vrfSSFSE in evaluating the brain beyond cysts or ventricles.

To address the potential for vrfSSFSE to have an expanded clinical role, we evaluated the clinical performance of vrfSSFSE for evaluating the pediatric brain, including normal

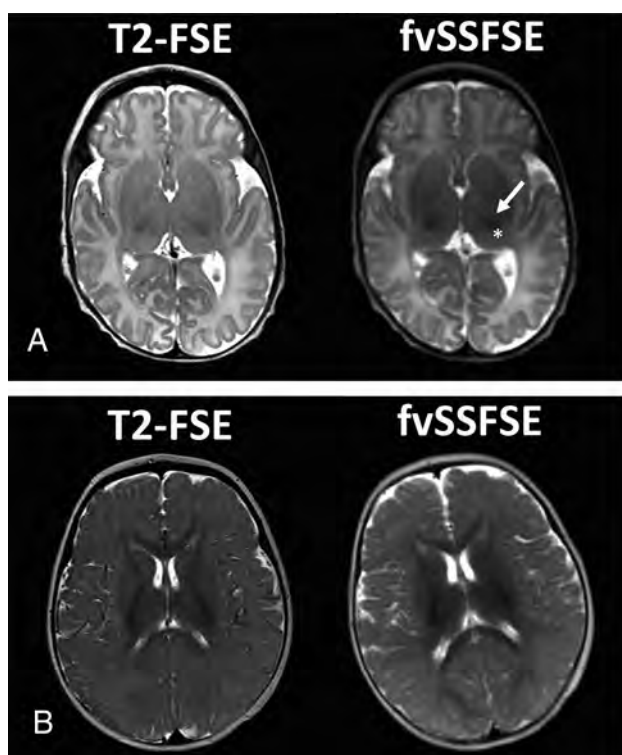


**FIG 6.** Normal pediatric infant brain. High tissue contrast that is feasible with full-Fourier vrfSSFSE (fvSSFSE) compared with conventional SSFSE robustly delineates both gray-white differentiation as well as the myelination pattern that nearly resembles that of conventional T2-FSE. Because SSFSE is acquired with long echo trains (during which the signal intensity decays), image blurring occurs. This effect arises from the different signal intensities of each echo, depending on their individual TEs. **A**, An infant with premature birth history, now near-term in age, presents for screening MR imaging. Note age-appropriate myelination with dark signal in the thalamus (*asterisk*) and posterior limb of internal capsule (*arrow*). **B**, A 6-month-old male infant with spasms nutans, who presented for screening MR imaging to exclude optic chiasm glioma. In this older infant, myelination has further progressed and is age-appropriate.

and abnormal findings such as brain malformations and injury, etc., across all ages, using T2-FSE as the ground truth. On the basis of our results, vrfSSFSE performed comparable with standard-of-care T2-FSE and with near-perfect intermodality agreement, suggesting a potential role for integrating vrfSSFSE as an alternative to T2-FSE if anesthesia-free MR imaging or reduced scan times are desired. We also propose that vrfSSFSE could be a faster alternative to PROPELLER, as shown in On-line Fig 3.

A prior study has shown that improved image quality and soft-tissue contrast are feasible by applying a refocusing flip angle optimization framework to the HASTE sequence, generating image contrast on a par with T2-FSE for adult brain tumors.<sup>27</sup> An important contributor to vrfSSFSE performance in lesion detection might be its image sharpness related to improved tissue contrast and spatial resolution, facilitating lesion detection both at the cortical surface and within the brain substance. Because a variable refocusing flip angle train modifies the signal decay of tissues with different T2 relaxation constants, an image contrast is produced that is different from the traditional constant flip angle refocusing train. This may potentially make vrfSSFSE better

suited to highlighting differences in brain tissue structures, including gray-white differentiation. While vrfSSFSE did miss a few cases of focal hemorrhage, small T2\*-susceptibility lesions may be difficult to detect, even on T2-FSE.

One important limitation was the relative lack of motion in our patient cohort. With low-refocusing flip angle SSFSE, signal tends to oscillate over the echo train and is potentially more vulnerable to motion-related signal loss.<sup>20</sup> We, therefore, likely underestimated the potential detrimental effects of motion-related signal loss that could impede clinical interpretation. However, there is also a trade-off in which faster vrfSSFSE might be more successful at quickly imaging motion-prone patients during a quiescent period in the scanner, eg, imaging an infant with a swaddle-and-feed before waking up. Other limitations include suboptimal interrater agreement, particularly for image sharpness/tissue contrast at the gray-white junction—which likely stemmed from subjective differences for what constitutes scores of 4 or 5. When we examined a subset of scans rated either 4 or 5 for each sequence for a given image quality, we continued to find that vrfSSFSE sequences provided a significant improvement in image sharpness and contrast. It is also possible that there was unconscious bias. While all readers were blinded to sequence types, which were reviewed in random order, it is conceivable that differences between SSFSE and vrfSSFSE sequences outside of image quality affected reported ratings. Another important limitation is our small sample size; a larger cohort study would be needed to more fully assess the clinical utility of low-refocusing flip angle SSFSE for specific neurologic diseases.

## CONCLUSIONS

This study shows that ultra-fast T2 imaging was feasible with variable refocusing flip angles for SSFSE. Although motion-related signal loss was more prevalent compared with conventional SSFSE, vrfSSFSE came with improved tissue contrast and spatial resolution and SNR. Although the study is limited by the small sample size, our pilot results comparing vrfSSFSE with T2-FSE suggest a potentially broader clinical role for vrfSSFSE, beyond cyst and ventricle evaluation, particularly if sedation-free or a faster MR imaging protocol is considered or when conventional methods are less desirable due to time constraints.

Disclosures: Valentina Taviani—UNRELATED: Employment: GE Healthcare. Shreyas S. Vasanawala—RELATED: Grant: GE Healthcare\*; UNRELATED: Consultancy: Arterys, HeartyVista. \*Money paid to the institution.

## REFERENCES

1. Iskandar BJ, Sansone JM, Medow J, et al. **The use of quick-brain magnetic resonance imaging in the evaluation of shunt-treated hydrocephalus.** *J Neurosurg* 2004;101:147–51 CrossRef Medline
2. Ashley WW Jr, McKinstry RC, Leonard JR, et al. **Use of rapid-sequence magnetic resonance imaging for evaluation of hydrocephalus in children.** *J Neurosurg* 2005;103:124–30 CrossRef Medline
3. Ahn SS, Mantello MT, Jones KM, et al. **Rapid MR imaging of the pediatric brain using the fast spin-echo technique.** *AJNR Am J Neuroradiol* 1992;13:1169–77 Medline
4. Haacke EM, Tkach JA. **Fast MR imaging: techniques and clinical applications.** *AJR Am J Roentgenol* 1990;155:951–64 CrossRef Medline
5. Tekes A, Senglaub SS, Ahn ES, et al. **Ultrafast brain MRI can be used for indications beyond shunted hydrocephalus in pediatric patients.** *AJNR Am J Neuroradiol* 2018;39:1515–18 CrossRef Medline



6. Patel MR, Klufas RA, Alberico RA, et al. **Half-Fourier acquisition single-shot turbo spin-echo (HASTE) MR: comparison with fast spin-echo MR in diseases of the brain.** *AJNR Am J Neuroradiol* 1997;18:1635–40 Medline
7. Sugahara T, Korogi Y, Hirai T, et al. **Comparison of HASTE and segmented-HASTE sequences with a T2-weighted fast spin-echo sequence in the screening evaluation of the brain.** *AJR Am J Roentgenol* 1997;169:1401–10 CrossRef Medline
8. Fellner F, Schmitt R, Trenkler J, et al. **Turbo gradient-spin-echo (GRASE): first clinical experiences with a fast T2-weighted sequence in MRI of the brain.** *Eur J Radiol* 1995;19:171–76 CrossRef Medline
9. Rockwell DT, Melhem ER, Bhatia RG. **GRASE (gradient- and spin-echo) MR of the brain.** *AJNR Am J Neuroradiol* 1997;18:1923–28 Medline
10. Miller JH, Walkiewicz T, Towbin RB, et al. **Improved delineation of ventricular shunt catheters using fast steady-state gradient recalled-echo sequences in a rapid brain MR imaging protocol in nonsedated pediatric patients.** *AJNR Am J Neuroradiol* 2010;31:430–35 CrossRef Medline
11. Rozovsky K, Ventureyra EC, Miller E. **Fast-brain MRI in children is quick, without sedation, and radiation-free, but beware of limitations.** *J Clin Neurosci* 2013;20:400–05 CrossRef Medline
12. Vertinsky AT, Rubesova E, Krasnokutsky MV, et al. **Performance of PROPELLER relative to standard FSE T2-weighted imaging in pediatric brain MRI.** *Pediatr Radiol* 2009;39:1038–47 CrossRef Medline
13. Patel DM, Tubbs RS, Pate G, et al. **Fast-sequence MRI studies for surveillance imaging in pediatric hydrocephalus.** *J Neurosurg Pediatr* 2014;13:440–47 CrossRef Medline
14. Allison J, Yanasak N. **What MRI sequences produce the highest specific absorption rate (SAR), and is there something we should be doing to reduce the SAR during standard examinations?** *AJR Am J Roentgenol* 2015;205:W140 CrossRef Medline
15. Loening AM, Litwiller DV, Saranathan M, et al. **Increased speed and image quality for pelvic single-shot fast spin-echo imaging with variable refocusing flip angles and full-Fourier acquisition.** *Radiology* 2017;282:561–68 CrossRef Medline
16. Loening AM, Saranathan M, Ruangwattanapaisarn N, et al. **Increased speed and image quality in single-shot fast spin echo imaging via variable refocusing flip angles.** *J Magn Reson Imaging* 2015;42:1747–58 CrossRef Medline
17. Busse RF. **Reduced RF power without blurring: correcting for modulation of refocusing flip angle in FSE sequences.** *Magn Reson Med* 2004;51:1031–37 CrossRef Medline
18. Busse RF, Brau AC, Vu A, et al. **Effects of refocusing flip angle modulation and view ordering in 3D fast spin echo.** *Magn Reson Med* 2008;60:640–49 CrossRef Medline
19. Hennig J, Weigel M, Scheffler K. **Multiecho sequences with variable refocusing flip angles: optimization of signal behavior using smooth transitions between pseudo steady states (TRAPS).** *Magn Reson Med* 2003;49:527–35 CrossRef Medline
20. Busse RF, Hariharan H, Vu A, et al. **Fast spin-echo sequences with very long echo trains: design of variable refocusing flip angle schedules and generation of clinical T2 contrast.** *Magn Reson Med* 2006;55:1030–37 CrossRef Medline
21. Brau AC, Beatty PJ, Skare S, et al. **Comparison of reconstruction accuracy and efficiency among autocalibrating data-driven parallel imaging methods.** *Magn Reson Med* 2008;59:382–95 CrossRef Medline
22. Pan J, Quon JL, Johnson E, et al. **Rapid-sequence brain magnetic resonance imaging for Chiari I abnormality.** *J Neurosurg Pediatr* 2018;22:158–64 CrossRef Medline
23. Brenner D, Elliston C, Hall E, et al. **Estimated risks of radiation-induced fatal cancer from pediatric CT.** *AJR Am J Roentgenol* 2001;176:289–96 CrossRef Medline
24. Thompson EM, Baird LC, Selden NR. **Results of a North American survey of rapid-sequence MRI utilization to evaluate cerebral ventricles in children.** *J Neurosurg Pediatr* 2014;13:636–40 CrossRef Medline
25. Koral K, Blackburn T, Bailey AA, et al. **Strengthening the argument for rapid brain MR imaging: estimation of reduction in lifetime attributable risk of developing fatal cancer in children with shunted hydrocephalus by instituting a rapid brain MR imaging protocol in lieu of head CT.** *AJNR Am J Neuroradiol* 2012;33:1851–54 CrossRef Medline
26. Malviya S, Voepel-Lewis T, Prochaska G, et al. **Prolonged recovery and delayed side effects of sedation for diagnostic imaging studies in children.** *Pediatrics* 2000;105:E42 CrossRef Medline
27. Keerthivasan MB, Winegar B, Udayasankar U, et al. **An optimized single-shot sequence for fast T2w imaging of the brain.** In: *Proceedings of the Joint Annual Meeting International Society for Magnetic Resonance in Medicine and the European Society for Magnetic Resonance in Medicine and Biology*, Paris, France. June 16–21, 2018



# Prevalence and Incidence of Microhemorrhages in Adolescent Football Players

 B.R. Shah,  J.M. Holcomb,  E.M. Davenport,  C.M. Lack,  J.M. McDaniel,  D.M. Imphean,  Y. Xi,  D.A. Rosenbaum,  J.E. Urban,  B.C. Wagner,  A.K. Powers,  C.T. Whitlow,  J.D. Stitzel, and  J.A. Maldjian



## ABSTRACT

**BACKGROUND AND PURPOSE:** SWI is an advanced imaging modality that is especially useful in cerebral microhemorrhage detection. Such microhemorrhages have been identified in adult contact sport athletes, and the sequelae of these focal bleeds are thought to contribute to neurodegeneration. The purpose of this study was to utilize SWI to determine whether the prevalence and incidence of microhemorrhages in adolescent football players are significantly greater than those of adolescent noncontact athletes.

**MATERIALS AND METHODS:** Preseason and postseason SWI was performed and evaluated on 78 adolescent football players. SWI was also performed on 27 adolescent athletes who reported no contact sport history. Two separate one-tailed Fisher exact tests were performed to determine whether the prevalence and incidence of microhemorrhages in adolescent football players are greater than those of noncontact athlete controls.

**RESULTS:** Microhemorrhages were observed in 12 football players. No microhemorrhages were observed in any controls. Adolescent football players demonstrated a significantly greater prevalence of microhemorrhages than adolescent noncontact controls ( $P = .02$ ). Although 2 football players developed new microhemorrhages during the season, microhemorrhage incidence during 1 football season was not statistically greater in the football population than in noncontact control athletes ( $P = .55$ ).

**CONCLUSIONS:** Adolescent football players have a greater prevalence of microhemorrhages compared with adolescent athletes who have never engaged in contact sports. While microhemorrhage incidence during 1 season is not significantly greater in adolescent football players compared to adolescent controls, there is a temporal association between playing football and the appearance of new microhemorrhages.

**ABBREVIATION:** SWI = susceptibility weighted imaging

Microhemorrhages result in abnormal blood product and iron accumulation in the brain after vascular injury. Although microhemorrhages are commonly associated with hypertension, *apolipoprotein E ε4* carrier status, and cerebral

amyloid angiopathy,<sup>1</sup> those found in healthy patients younger than 60 years of age are more likely the consequence of trauma. The deposition of such blood products in the brain has been implicated in a host of neurodegenerative disorders<sup>2-5</sup> and has also been identified in athletes who participate in contact sports characterized by repetitive, high-magnitude head impacts.<sup>6-12</sup> Collectively, these findings suggest that some neurodegenerative diseases, including chronic traumatic encephalopathy, may be the sequelae of transient, posttraumatic blood-brain barrier injury from sports-related head trauma.<sup>13</sup>

SWI is an advanced neuroimaging technique that is exquisitely sensitive to magnetic field disruption from the presence of highly paramagnetic and superparamagnetic blood products. Thus, SWI has markedly improved the sensitivity for detecting microhemorrhages. While microhemorrhage prevalences have been reported in adult contact sport cohorts, such rates in adolescent contact sport populations remain largely unexplored.<sup>14</sup> The


Received February 21, 2020; accepted after revision April 20.


From the Department of Radiology (B.R.S., J.M.H., E.M.D., J.M.M., D.M.I., Y.X., B.C.W., J.A.M.), University of Texas Southwestern Medical Center, Dallas, Texas; and Departments of Radiology (C.M.L., C.T.W.), Sports Medicine (D.A.R.), Biomedical Engineering (J.E.U., J.D.S.), and Neurosurgery (A.K.P.), Wake Forest School of Medicine, Winston-Salem, North Carolina.

Bhavya R. Shah and James M. Holcomb are co-first authors.

Support for this research was provided by National Institutes of Health grant R01NS082453 (J.A.M., J.D.S.) and R01NS091602 (C.T.W., J.A.M., J.D.S.).

Please address correspondence to James M. Holcomb, BSA, UT Southwestern, Department of Radiology, 5323 Harry Hines Blvd, Dallas, TX 75390-9178; e-mail: james.holcomb@utsouthwestern.edu

 Indicates open access to non-subscribers at [www.ajnr.org](http://www.ajnr.org)

 Indicates article with supplemental on-line table.

<http://dx.doi.org/10.3174/ajnr.A6618>

purpose of this study was to use SWI to determine whether the prevalence and incidence of microhemorrhages in adolescent football populations are significantly greater than those of adolescent, noncontact control athletes.

## MATERIALS AND METHODS

### Participants

All research procedures were approved by the institutional review board committees of Wake Forest School of Medicine and the University of Texas Southwestern School of Medicine. This study was compliant with the Health Insurance Portability and Accountability Act, and written informed parental consent and assent from the participants was obtained. Between 2012 and 2017, male adolescent football players were recruited via phone, e-mail, and in-person meetings from 6 Junior Pee Wee, 4 Pee Wee, 4 Junior Midget, one 10U, 1 Cadet, 2 Junior Varsity, and 4 Varsity football teams in Winston-Salem, North Carolina. Each football subject was enrolled in the study for the football season immediately following recruitment, with some subjects re-enrolling in the study in subsequent years. Male noncontact sport controls were recruited via phone, e-mail, and in-person meetings with noncontact sports leagues and extracurricular programs also located in Winston-Salem, North Carolina. Because hypertension is known to increase the risk of developing microhemorrhages,<sup>1</sup> football and control participants were excluded from the analysis if they were hypertensive or taking medications known to elevate blood pressure. Medical histories revealed 1 football player using an angiotensin-converting-enzyme inhibitor and 14 football players and 7 control subjects using medications known to elevate blood pressure. To assess microhemorrhage incidence associated with playing football, football players were further excluded from analysis if preseason or postseason imaging was not acquired, imaging was limited by artifacts, or postseason imaging was not performed within 60 days from the conclusion of their season. Control subjects were excluded if medical histories revealed a prior concussion or head injury, imaging was limited by artifacts, or subjects had ever played, as defined by the American Academy of Pediatrics, a “collision” or “contact” sport.<sup>15</sup> All control subjects were athletes who reported a sports history limited to baseball, swimming, tennis, and track.

### MR Imaging Acquisition

MR imaging was performed on a 3T Skyra scanner (Siemens) with a 32-channel head coil. SWI was acquired under 2 protocols. The first SWI protocol parameters included the following: TR/TE, 27/20 ms; flip angle, 15°; FOV, 232 × 256; section thickness, 1.5 mm; and voxel resolution, 0.86 × 0.86 × 1.5 mm. Forty-seven football subjects and 7 controls were scanned under the first protocol. The second SWI protocol parameters included the following: TR/TE, 51/9.75 ms; flip angle, 20°; section thickness, 324 × 416; FOV, 2.0 mm; and voxel resolution, 0.58 × 0.58 × 2.0 mm. Thirty-one football subjects and 20 controls were scanned under the second protocol. T2 images were acquired using the following parameters: TR/TE, 3600/96 ms; flip angle, 160°; FOV, 640 × 640; section thickness, 3.0 mm; and voxel resolution, 0.34 × 0.34 × 3.0 mm. MR imaging data for all football participants were obtained before and after the football season. All MR imaging data for controls were obtained at 1 time point.

### SWI Analysis

All scans were independently reviewed to identify hypointense foci on SWI by 2 board-certified, fellowship-trained neuroradiologists with >10 years of combined experience in practice. Each reviewer was blinded regarding subject cohort stratification. Following independent evaluation, a consensus conference was held to assess interrater agreement. Following consensus, 1 neuroradiologist examined corresponding phase and T2 images for each subject scan to exclude calcifications and cavernous malformations. Hypointensities on phase images were identified as calcifications. “Popcorn-shaped” lesions with a hemosiderin rim were identified as cavernous malformations on T2 imaging.

Prevalence in the football population was calculated as the total number of football players with postseason microhemorrhages divided by the total number of football players. Prevalence in the control population was calculated as the number of control subjects with microhemorrhages divided by the total number of controls.

To determine incidence in the football population, postseason microhemorrhages that were not identified on the corresponding subject’s preseason image were classified as developed microhemorrhages. Incidence in the football population was calculated as the number of football players with developed microhemorrhages, divided by the total number of football players included in the analysis. Microhemorrhage prevalence in the control population was used as a proxy for microhemorrhage incidence in controls.

### Concussion Evaluation

Concussion history before study enrollment was reported by the research subject and each player’s legal guardians. During the season, the Sports Concussion Assessment Tool, 5th edition, was used to assist a certified athletic trainer in screening for concussion at all games and practices.<sup>16</sup> If concussion was suspected, the subject was referred to a sports medicine physician to determine the diagnosis. As summarized by the American Medical Society for Sports Medicine Position Statement on concussion in sport, “Concussion remains a clinical diagnosis made by carefully synthesizing history and physical examination findings as the injury evolves. There is no specific imaging, biologic marker, or neuropsychological test currently able to confirm the diagnosis of sports concussion.”<sup>17</sup>

### Statistical Analysis

The Cohen  $\kappa$  coefficient was calculated to measure interrater agreement. A one-tailed Fisher test of exact probability was performed to determine whether microhemorrhage prevalence in adolescent football players was greater than that observed in the adolescent, noncontact controls. Similarly, a one-tailed Fisher test of exact probability was used to determine whether the incidence of microhemorrhages in adolescent football players was greater than that of adolescent noncontact controls. The  $\alpha$  for all tests was set to .05. To comply with the assumption of independent observations for each test and to avoid selection bias, 1 subject season was selected at random for the 18 football subjects with >1 usable season of data. Random selection was achieved using a random number generator. All statistical analyses and random number

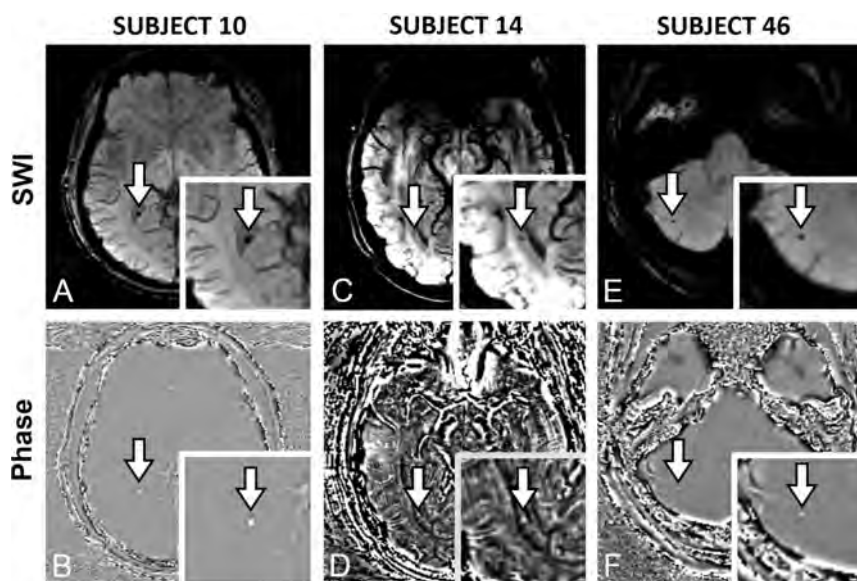


**FIG 1.** SWI and corresponding phase images. A and B, Subject 10. C and D, Subject 14. E and F, Subject 46. Subject 10 is an 18-year-old, male defensive lineman. Subject 14 is a 17-year-old, male defensive end. Subject 46 is an 18-year-old, male quarterback. Microhemorrhages are indicated by a white arrow. A, SWI hypointensity in the choroid plexus of the left lateral ventricle. B, Corresponding hyperintensity in the choroid plexus of the left lateral ventricle on phase imaging, verifying microhemorrhage. C, SWI hypointensity in the periventricular white matter of the left parietal lobe. D, Corresponding hyperintensity in the periventricular white matter of the left parietal lobe on phase imaging, verifying microhemorrhage. E, SWI hypointensity in the cerebellar gray/white matter. F, Corresponding hyperintensity in the cerebellar gray/white matter on phase imaging, verifying microhemorrhage.

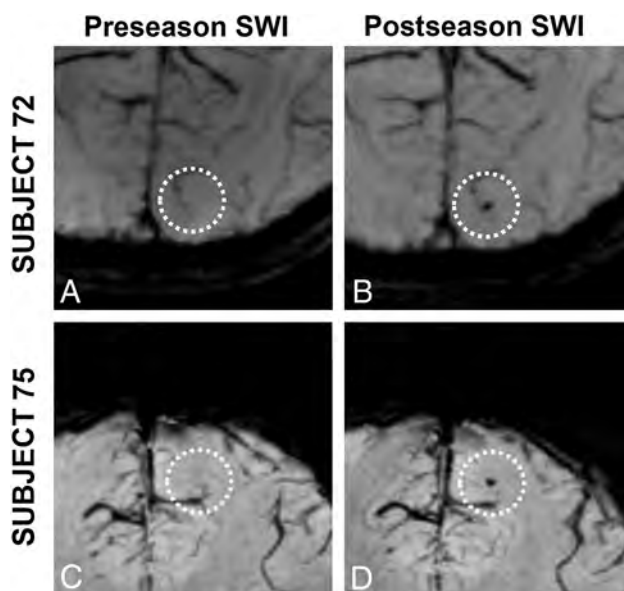


**FIG 2.** Developed microhemorrhages in 2 football players. Dashed circles identify the ROI on each image. A and B, Subject 72. C and D, Subject 75. Subject 72 is a 17-year-old, male quarterback. Subject 75 is a 16-year-old, male cornerback. A, Preseason SWI with no hypointensity in the right occipital lobe white matter. B, Postseason SWI with hypointensity in the right occipital lobe white matter. C, Preseason SWI with no hypointensity in the right frontal lobe white matter. D, Postseason SWI with hypointensity in the right frontal lobe white matter.

generation were performed in R 3.4.3 statistical and computing software (2017; <http://www.r-project.org>).

## RESULTS

### Interrater Agreement

The consensus conference revealed high interrater agreement in the determination of SWI lesion counts with  $\kappa = 1$ .

### Population Demographics

Following exclusion criteria and removal of duplicate subject seasons, 78 (39 pre-high school and 39 high school) male football players (age range, 10–18 years; mean age,  $14.25 \pm 2.63$  years) and 27 adolescent noncontact controls (age range, 8–18 years; mean age  $13.92 \pm 3.09$  years) were used for analysis.

### Adolescent Football Player

#### Summary

Microhemorrhages were not detected in any control subjects. However, 12 football players had evidence of microhemorrhages on postseason imaging. Ten football players had the same microhemorrhages at baseline. Baseline microbleeds were identified in 2 offensive linemen, 2 defensive linemen, 2 defensive ends, 1 quarterback, 1 tight end, 1 fullback, and 1 wide receiver. These positions were self-reported and subject to change throughout a season, especially in pre-high school players.

All pre-existing microhemorrhages were found in the lateral ventricle choroid plexus, white and gray matter of the cerebellum, periventricular white matter of the parietal lobe, and white matter of the brain stem, cerebellar peduncle, and frontal lobe (Fig 1). All football players with preseason microhemorrhages had played football for at least 1 year before study enrollment.

Two football players developed new microhemorrhages during the season. Subject 72, a quarterback, developed a microhemorrhage in the white matter of the occipital lobe, and subject 75, a cornerback, developed a microhemorrhage in the white matter of the frontal lobe (Fig 2). One pre-existing cavernous malformation (subject 33) was identified.

Of 12 football players who reported concussion history before study enrollment, 3 football players had baseline microhemorrhages. Neither of the 2 football players who developed new microhemorrhages reported a history of concussion nor were they diagnosed with a concussion during the football season. Nine football players were diagnosed with concussion during the season they were observed. None of the football players who were concussed during the season developed microhemorrhages or had microhemorrhages at baseline. A summary of data can be found in the On-line Table.

**Contingency table describing relationship between prior concussion diagnosis and microhemorrhage status in adolescent football players**

	Microhemorrhage Found	No Microhemorrhage Found	Total
Prior concussion	3	9	12
No prior concussion	9	57	66
Total	12	66	78

### Microhemorrhage Prevalence

Of 78 football players, 13 microhemorrhages were identified in 12 subjects. Based on these observations, the microhemorrhage prevalence in adolescent football players is 15.38% (95% confidence interval, 8.21%–25.33%). No microhemorrhages were identified in the 27 controls. The microhemorrhage prevalence in the adolescent football population was significantly greater than that in the noncontact control population ( $P$  value = .02).

### Microhemorrhage Incidence

Of 78 football players, 2 subjects developed new microhemorrhages during the season they were observed (subjects 72 and 75). Based on these results, the incidence of microhemorrhage among adolescent football players after one season is 2.56% (95% confidence interval, 0.31%–8.96%). None of the 27 noncontact controls developed microhemorrhages. This study did not demonstrate a greater incidence of microhemorrhage in adolescent football players compared with adolescent controls ( $P$  value = .55).

### Association Between Concussion and Microhemorrhage

Using the Table, a post hoc  $\chi^2$  test of independence was conducted to test the association between prior concussion diagnosis and microhemorrhage status. For analysis, subjects were considered concussed if they had self-reported a prior concussion diagnosis or were diagnosed with a concussion during the study. Postseason imaging was used to assess microhemorrhage status. No statistically significant relationship between prior concussion diagnosis and microhemorrhage status was observed ( $P$  value = .57).

## DISCUSSION

This study demonstrates that there is a significantly greater prevalence of microhemorrhages in adolescent football players than in adolescent noncontact controls, with microhemorrhages preferentially occurring in older football players. Of the 13 total microhemorrhages, 11 were identified in high school football subjects and 2 were identified at the pre-high school level. This disparity could reflect a greater number of high-risk head impacts over a greater number of football seasons, or higher-magnitude head accelerations seen in older, more competitive levels of play.<sup>18,19</sup> Despite a predilection for age, microhemorrhages did not preferentially occur on the basis of player position.

Microhemorrhage prevalence in adolescent contact sports has not been reported in the literature. However, several studies have documented such rates in adult contact sport athletes. The 15.38% microhemorrhage prevalence observed in our adolescent football population is greater than the prevalences of 9.52%, 4.21%, 2.22%, and 8.88%, reported in amateur boxers,

professional fighters, collegiate hockey players, and former professional football players, respectively.<sup>6,8-10</sup> Greater microhemorrhage prevalence in adolescent football players may reflect the unique intersection between sports-specific biomechanics risks and a potentially greater vulnerability to

head injury among younger athletes. Indeed, boxers and professional football players, who demonstrate the highest microhemorrhage rates in the literature, experience similar inertial forces, peak translational head accelerations, and peak rotational head accelerations.<sup>6,8-10,20</sup> The acceleration risk of each head impact may be further magnified in adolescent athletes with underdeveloped neck strength and poor tackling technique.<sup>20-22</sup>

Although the prevalence of microhemorrhages is significantly greater in adolescent football players relative to noncontact controls, this study did not establish a statistically significant difference in incidence between groups. Across studies, microhemorrhages in contact sport athletes are a relatively rare finding with 90.48%–97.78% of contact sport athletes demonstrating no evidence of microhemorrhages on SWI.<sup>6,8-10</sup> Because microhemorrhage prevalence reflects the summation of incidences across broad time intervals, it is feasible that microhemorrhage incidence during 1 football season does not occur with enough frequency to yield statistically significant differences from controls. The abundance of baseline microhemorrhages relative to new microhemorrhages among our adolescent football players supports this notion and may further suggest that head impact intensity was greater in prior, unobserved seasons.

This study also did not establish a statistically significant relationship between concussion and the presence of microhemorrhages. Similarly, low microhemorrhage prevalence has been reported following pediatric concussion,<sup>23</sup> in amateur boxers with no concussion history,<sup>6</sup> and in professional fighters who experienced a high number of concussions and knockouts.<sup>9</sup> Despite these findings, athletes have been known to mask concussion symptoms for a variety of reasons,<sup>24</sup> and common concussion symptoms like headache and dizziness are not easily observable, if not self-reported.<sup>25</sup> As a result, it is possible that some concussions occurred in this study, but were not identified. Nevertheless, our results are consistent with other studies that report blood-brain barrier injury in contact sport athletes who exhibit no concussive symptoms.<sup>6,11,12</sup>

Although the sequelae of blood product–induced neurotoxicity and neurodegeneration are beyond the scope of this work, blood products alter normal choroid plexus function, neuronal electrical activity, and the composition of extracellular and cerebrospinal fluid.<sup>26-28</sup> The presence of hemorrhagic products in the choroid plexus interstitium, paracellular spaces, and ventricles curtails choroid plexus cerebrospinal fluid production and impairs the ability of the choroid plexus to remove toxins and catabolites from the parenchymal extracellular environment.<sup>26-28</sup> After intraparenchymal hemorrhage, lysis of red blood cells starts at 24 hours and lasts several days.<sup>29</sup> Red blood cell lysis releases hemoglobin, which is cytotoxic and results in brain edema, oxidative damage, and free radical injury.<sup>5,30-32</sup>



Hemoglobin is further broken down into heme and iron, which alters cell membrane permeability and electrical conduction and can ultimately result in cell death.<sup>5,30–32</sup>

There are several limitations of this study. Observations did not occur in a controlled environment where all nonfootball activities could be monitored. This limitation is especially true of subjects who had microhemorrhages at baseline. As a result, there is the possibility that microhemorrhages originated as a consequence of other contact sports or other non-sports-related activities. In the football players with baseline microhemorrhages and known sports history, 3 subjects exclusively played football, 1 subject previously played lacrosse and basketball, and another subject previously played lacrosse and soccer. While a relationship may exist between microhemorrhage development and other contact sports, all subjects with microhemorrhages had a history of playing football. Moreover, the 2 football players who developed microhemorrhages during the football season provide evidence of at least a temporal relationship between microhemorrhage development and football participation.

This study is further limited by controversy within the literature on the extent of microhemorrhage resorption. In a study of 13 combat veterans, it was found that 34% of all microhemorrhages disappeared completely from SWI 1 year after the initial scan,<sup>33</sup> while a longitudinal study of 26 civilians demonstrated that all SWI microhemorrhages at baseline were still present 8 years later, albeit with reduced volume.<sup>34</sup> If SWI microhemorrhages become undetectable with time, the prevalence and incidence of microhemorrhages in both football and control populations may be underreported. The imaging modalities also have some limitations. Due to susceptibility artifacts, SWI performs poorly in revealing lesions near bone-air interfaces. Additionally, neither SWI nor T2 imaging can easily distinguish microhemorrhages from small cavernous malformations. Both imaging limitations may have respectively deflated and inflated the number of identified microhemorrhages.

## CONCLUSIONS

This study demonstrates that the prevalence of microhemorrhages in adolescent football players is significantly greater than that observed in adolescent noncontact control athletes. Although microhemorrhage incidence is not significantly greater in adolescent football players compared with adolescent controls, there is a temporal association between playing football and the appearance of new microhemorrhages. Furthermore, this study does not demonstrate a statistically significant relationship between concussion diagnosis and microhemorrhage prevalence in adolescent football players.

Disclosures: Elizabeth M. Davenport—RELATED: Grant: National Institutes of Health, Comments: R01\*; UNRELATED: Grants/Grants Pending: National Institutes of Health, Comments: R01.\* Christopher M. Lack—UNRELATED: Employment: Wake Forest School of Medicine, Comments: employed as a radiologist; Expert Testimony: law firms, Comments: expert witness in neuroradiology; none related to football injuries. Daryl A. Rosenbaum—RELATED: Grant: National Institutes of Health, Comments: ITAKL study grant.\* Jillian E. Urban—RELATED: Grant: National Institutes of Health, Comments: R01NS082453, R01NS091602, R01NS094410\*; UNRELATED: Grants/Grants Pending: R01NS119907, R01NS118243, R01NS119766-01 (as co-investigator) and K25HD010686 pending. The K25 is directly related to youth football and proposes to develop and test head impact intervention in the sport.\* Patents (Planned, Pending or Issued): We have a patent pending for an instrumented mouthpiece form factor. No money

has been paid to us or the institution. Benjamin C. Wagner—RELATED: Grant: National Institutes of Health, Comments: National Institutes of Health grant R01NS082453 and R01NS091602. Christopher T. Whitlow—RELATED: Grant: National Institutes of Health, Comments: R01NS091602.\* Joel D. Stitzel—RELATED: Grant: National Institutes of Health, Comments: R01NS082453, R01NS091602.\* Joseph A. Maldjian—RELATED: Grant: National Institutes of Health, Comments: R01NS082453, R01NS091602.\* \*Money paid to the institution.

## REFERENCES

1. Poels MM, Vernooij MW, Ikram MA, et al. **Prevalence and risk factors of cerebral microbleeds: an update of the Rotterdam scan study.** *Stroke* 2010;41:S103–06 CrossRef Medline
2. Nisenbaum EJ, Novikov DS, Lui YW. **The presence and role of iron in mild traumatic brain injury: an imaging perspective.** *J Neurotrauma* 2014;31:301–07 CrossRef Medline
3. Li K, Reichmann H. **Role of iron in neurodegenerative diseases.** *J Neural Transm (Vienna)* 2016;123:389–99 CrossRef Medline
4. Cordonnier C, van der Flier WM. **Brain microbleeds and Alzheimer's disease: innocent observation or key player?** *Brain* 2011;134:335–44 CrossRef Medline
5. Núñez MT, Urrutia P, Mena N, et al. **Iron toxicity in neurodegeneration.** *Biometals* 2012;25:761–76 CrossRef Medline
6. Hasiloglu Z, Albayram S, Selcuk H, et al. **Cerebral microhemorrhages detected by susceptibility-weighted imaging in amateur boxers.** *AJNR Am J Neuroradiol* 2011;32:99–102 CrossRef Medline
7. Casson IR, Viano DC, Haacke EM, et al. **Is there chronic brain damage in retired NFL players? Neuroradiology, neuropsychology, and neurology examinations of 45 retired players.** *Sports Health* 2014; 6:384–95 CrossRef Medline
8. Jarrett M, Tam R, Hernández-Torres E, et al. **A prospective pilot investigation of brain volume, white matter hyperintensities, and hemorrhagic lesions after mild traumatic brain injury.** *Front Neurol* 2016;7:11 CrossRef Medline
9. Lee J, Wu J, Banks S, et al. **Prevalence of traumatic findings on routine MRI in a large cohort of professional fighters.** *AJNR Am J Neuroradiol* 2017;38:1303–10 CrossRef Medline
10. Kuhn AW, Zuckerman SL, Solomon GS, et al. **Interrelationships among neuroimaging biomarkers, neuropsychological test data, and symptom reporting in a cohort of retired National Football League players.** *Sports Health* 2017;9:30–40 CrossRef Medline
11. Slobounov SM, Walter A, Breiter HC, et al. **The effect of repetitive subconcussive collisions on brain integrity in collegiate football players over a single football season: a multi-modal neuroimaging study.** *Neuroimage Clin* 2017;14:708–18 CrossRef Medline
12. Hähnel S, Stippich C, Weber I, et al. **Prevalence of cerebral microhemorrhages in amateur boxers as detected by 3T MR imaging.** *AJNR Am J Neuroradiol* 2008;29:388–91 CrossRef Medline
13. Tagge CA, Fisher AM, Minaeva OV, et al. **Concussion, microvascular injury, and early tauopathy in young athletes after impact head injury and an impact concussion mouse model.** *Brain* 2018;141:422–58 CrossRef Medline
14. Kulich M, Fisher LM, Voelker C. **Imaging findings in mild traumatic brain injury.** In: Hoffer M, Balaban D, eds. *Neurosensory Disorders in Mild Traumatic Brain Injury*. Academic Press; 2018: 23–47
15. Committee on Sports Medicine and Fitness. **Medical conditions affecting sports participation.** *Pediatrics* 1994;94:757–60
16. Echemendia RJ, Meeuwisse W, McCrory P, et al. **The sport concussion assessment tool 5th edition (SCAT5): background and rationale.** *Br J Sports Med* 2017;51:848–50 CrossRef Medline
17. Harmon KG, Drezner J, Gammons M, et al; American Medical Society for Sports Medicine. **American Medical Society for Sports Medicine Position Statement: concussion in sport.** *Clin J Sport Med* 2013;23:1–18 CrossRef Medline
18. Kelley ME, Urban JE, Miller LE, et al. **Head impact exposure in youth football: comparing age- and weight-based levels of play.** *J Neurotrauma* 2017;34:1939–47 CrossRef Medline

19. Urban JE, Davenport EM, Golman AJ, et al. **Head impact exposure in youth football: high school ages 14 to 18 years and cumulative impact analysis.** *Ann Biomed Eng* 2013;41:2474–87 CrossRef Medline
20. Viano DC, Casson IR, v EJ, et al. **Concussion in professional football: comparison with boxing head impacts, Part 10.** *Neurosurgery* 2005;57:1154–72 CrossRef Medline
21. Broglio SP, Sosnoff JJ, Shin S, et al. **Head impacts during high school football: a biomechanical assessment.** *J Athl Train* 2009;44:342–49 CrossRef Medline
22. Collins CL, Fletcher EN, Fields SK, et al. **Neck strength: a protective factor reducing risk for concussion in high school sports.** *J Prim Prev* 2014;35:309–19 CrossRef Medline
23. Bonow RH, Friedman SD, Perez FA, et al. **Prevalence of abnormal magnetic resonance imaging findings in children with persistent symptoms after pediatric sports-related concussion.** *J Neurotrauma* 2017;34:2706–12 CrossRef Medline
24. Kroshus E, Garnett B, Hawrilenko M, et al. **Concussion under-reporting and pressure from coaches, teammates, fans, and parents.** *Soc Sci Med* 2015;134:66–75 CrossRef Medline
25. Echlin PS, Tator CH, Cusimano MD, et al. **Return to play after an initial or recurrent concussion in a prospective study of physician-observed junior ice hockey concussions: implications for return to play after a concussion.** *Neurosurg Focus* 2010;29:E5 CrossRef Medline
26. Johanson C, Stopa E, Baird A, et al. **Traumatic brain injury and recovery mechanisms: peptide modulation of periventricular neurogenic regions by the choroid plexus-CSF nexus.** *J Neural Transm (Vienna)* 2011;118:115–33 CrossRef Medline
27. Lindvall M, Edvinsson L, Owman C. **Sympathetic nervous control of cerebrospinal fluid production from the choroid plexus.** *Science* 1978;201:176–78 CrossRef Medline
28. Spector R, Johanson CE. **Choroid plexus failure in the Kearns-Sayre syndrome.** *Cerebrospinal Fluid Res* 2010;7:14 CrossRef Medline
29. Wagner KR, Sharp FR, Ardizzone TD, et al. **Heme and iron metabolism: role in cerebral hemorrhage.** *J Cereb Blood Flow Metab* 2003;23:629–52 CrossRef Medline
30. Aronowski J, Zhao X. **Molecular pathophysiology of cerebral hemorrhage: secondary brain injury.** *Stroke* 2011;42:1781–86 CrossRef Medline
31. Huang FP, Xi G, Keep RF, et al. **Brain edema after experimental intracerebral hemorrhage: role of hemoglobin degradation products.** *J Neurosurg* 2002;96:287–93 CrossRef Medline
32. Zheng H, Chen C, Zhang J, et al. **Mechanism and therapy of brain edema after intracerebral hemorrhage.** *Cerebrovasc Dis* 2016;42:155–69 CrossRef Medline
33. Liu W, Soderlund K, Senseney JS, et al. **Imaging cerebral microhemorrhages in military service members with chronic traumatic brain injury.** *Radiology* 2016;278:536–45 CrossRef Medline
34. Daugherty AM, Raz N. **Incident risk and progression of cerebral microbleeds in healthy adults: a multi-occasion longitudinal study.** *Neurobiol Aging* 2017;59:22–29 CrossRef Medline

## Value of Advanced MR Imaging Techniques in Mild Traumatic Brain Injury

This commentary addresses the article, “Prevalence and Incidence of Microhemorrhages in Adolescent Football Players.”<sup>1</sup> The authors performed SWI in 78 adolescent football players before and after the season. The number of examined football players was fairly large. They found a prevalence of microhemorrhages of 15.38% in the group, with an incidence of 2.56% per season. Concussion was evaluated by the Sports Concussion Assessment Tool (SCAT5; <https://bjsm.bmj.com/content/bjsports/early/2017/04/26/bjsports-2017-097506SCAT5.full.pdf>) or by self-reporting history before the study. No statistically significant relationship was found between concussion and the presence of microhemorrhages.

The article by Shah et al<sup>1</sup> is in line with several recent works dealing with MR imaging in mild traumatic brain injury (mTBI; concussion). Providing noninvasive biomarkers in mTBI has implications for any kind of contact sport such as boxing and soccer and perhaps for any situation in which the human brain is accelerated or decelerated such as in traffic collisions, starting and landing fighter jets or rockets by pilots or astronauts, or any kind of minor head trauma (concussion). The results are in good accordance with other studies on SWI in mTBI.<sup>2,3</sup> In brain trauma, shearing forces lead to microhemorrhages, especially at the gray-white matter boundary. However, brain damage may also occur without the consequence of microbleeding if axonal stretching occurs without vessel injury. Besides SWI, other advanced techniques are currently being used as an MR imaging biomarker in mTBI, such as DTI and Tract-Based Spatial Statistics (TBSS; <http://fsl.fmrib.ox.ac.uk/fsl/fslwiki/TBSS>),<sup>4</sup> measurements of cerebral perfusion and metabolism,<sup>5</sup> and MR volumetry.<sup>6,7</sup>

Champagne et al<sup>5</sup> found reductions in metabolic demand despite no significant changes in resting oxygen extraction. Accordingly, hypoperfusion after sports-related mTBI might reflect compromised brain metabolism after injury.<sup>5</sup> In a meta-analysis of 224 references to the terms “white matter,” “mTBI or concussion,” and “TBSS,” Hellewell et al<sup>4</sup> extracted 8 relevant articles on acute ( $n=2$ ), chronic ( $n=4$ ), and subconcussive<sup>8</sup> ( $n=2$ ) injuries. Their most important finding was a dominant, bilateral, increased fractional anisotropy (FA) in the superior longitudinal fasciculus, internal capsule, and arcuate fasciculus. In

subconcussion, defined as “cranial impact that does not result in known or diagnosed concussion on clinical grounds,”<sup>8</sup> the changes in FA were found to be bidirectional. Hellewell et al emphasized the possible future role of DTI in the detection of mTBI.


In our recent study on amateur boxers,<sup>6</sup> we found statistically significant lower volumes in several cerebral substructures compared with nonboxing individuals, such as the nucleus accumbens (14%), caudate nucleus (11%), globus pallidus (9%), and cerebral white matter (9%), respectively, but there was a correlation of neither total brain volume nor any volume of cerebral substructures with intelligence quotient or years of boxing. Our results are in good agreement with the study of Cohen et al,<sup>7</sup> who found brain atrophy in patients with mTBI along with a reduction of whole-brain *N*-acetylaspartate in MR spectroscopy. In a study by Lui et al,<sup>9</sup> classification algorithms using a variety of MR imaging features, such as conventional brain imaging, magnetic field correlation, and multifeature analysis, have been used to define patients with mTBI.

Noninvasive acquisition of biomarkers in mTBI using MR imaging is of growing interest due to the popularity of contact sports such as football, as mentioned in the article by Shah et al,<sup>1</sup> and possibly also for advisory opinions regarding the medical and legal consequences of traffic collisions and interpersonal violence. Advanced MR imaging techniques such as SWI, DTI, MR spectroscopy, perfusion imaging, and MR volumetry in correlation to neuropsychological findings might answer a variety of questions in this field.

### REFERENCES

1. Shah BR, Holcomb JM, Davenport EM, et al. **Prevalence and incidence of microhemorrhages in adolescent football players.** *AJNR Am J Neuroradiol* 2020
2. Hasiloglu Z, Albayram S, Selcuk H, et al. **Cerebral microhemorrhages detected by susceptibility-weighted imaging in amateur boxers.** *AJNR Am J Neuroradiol* 2011;32:99–102 CrossRef Medline
3. Huang YL, Kuo YS, Tseng YC, et al. **Susceptibility-weighted MRI in mild traumatic brain injury.** *Neurology* 2015;84:580–85 CrossRef Medline
4. Hellewell SC, Nguyen VPB, Jayasena RN, et al. **Characteristic patterns of white matter tract injury in sport-related concussion: an image**

- based meta-analysis. *Neuroimage Clin* 2020;26:102253 CrossRef Medline
5. Champagne AA, Coverdale NS, Fernandez-Ruiz J, et al. **Compromised resting cerebral metabolism after sport-related concussion: a calibrated MRI study.** *Brain* 2020 Apr 19. [Epub ahead of print] CrossRef Medline
6. Jesser J, Zidan M, Herweh C, et al. **Brain volume is reduced in amateur boxers as compared to healthy age-matched controls.** *Clin Neuroradiol* 2019;29(Suppl 1):119
7. Cohen BA, Inglese M, Rusinek H, et al. **Proton MR spectroscopy and MRI-volumetry in mild traumatic brain injury.** *AJNR Am J Neuroradiol* 2007;28:907–13 Medline
8. Bailes JE, Petraglia AL, Omalu BI, et al. **Role of subconcussion in repetitive mild traumatic brain injury: a review.** *J Neurosurg* 2013;119:1235–45 CrossRef Medline
9. Lui YW, Xue Y, Kenul D, et al. **Classification algorithms using multiple MRI features in mild traumatic brain injury.** *Neurology* 2014;83:1235–40 CrossRef Medline















 S. Hähnel

Department of Neuroradiology  
University of Heidelberg Medical Center  
Heidelberg, Germany

<http://dx.doi.org/10.3174/ajnr.A6629>



# In Vivo Evaluation of White Matter Abnormalities in Children with Duchenne Muscular Dystrophy Using DTI

 V. Preethish-Kumar,  A. Shah,  M. Kumar,  M. Ingalhalikar,  K. Polavarapu,  M. Afsar,  J. Rajeswaran,  S. Vengalil,  S. Nashi,  P.T. Thomas,  A. Sadasivan,  M. Warriar,  A. Nalini, and  J. Saini



## ABSTRACT

**BACKGROUND AND PURPOSE:** Duchenne muscular dystrophy is an X-linked disorder characterized by progressive muscle weakness and prominent nonmotor manifestations, such as a low intelligence quotient and neuropsychiatric disturbance. We investigated WM integrity in patients with Duchenne muscular dystrophy using DTI.

**MATERIALS AND METHODS:** Fractional anisotropy and mean, axial, and radial diffusivity (DTI measures) were used to assess WM microstructural integrity along with neuropsychological evaluation in patients with Duchenne muscular dystrophy ( $n = 60$ ) and controls ( $n = 40$ ). Exon deletions in the *DMD* gene were confirmed using multiplex ligation-dependent probe amplification. Patients were classified into proximal (*DMD* Dp140+) and distal (*DMD* Dp140-) subgroups based on the location of the exon deletion and expression of short dystrophin Dp140 isoform. WM integrity was examined using whole-brain Tract-Based Spatial Statistics and atlas-based analysis of DTI data. The Pearson correlation was performed to investigate the possible relationship between neuropsychological scores and DTI metrics.

**RESULTS:** The mean ages of Duchenne muscular dystrophy and control participants were  $8.0 \pm 1.2$  years and  $8.2 \pm 1.4$  years, respectively. The mean age at disease onset was  $4.1 \pm 1.8$  years, and mean illness duration was  $40.8 \pm 25.2$  months. Significant differences in neuropsychological scores were observed between the proximal and distal gene-deletion subgroups, with more severe impairment in the distal-deletion subgroup ( $P < .05$ ). Localized fractional anisotropy changes were seen in the corpus callosum, parietal WM, and fornices in the patient subgroup with Dp140+, while widespread changes were noted in the Dp140- subgroup. The Dp140+ subgroup showed increased axial diffusivity in multiple WM regions relative to the Dp140- subgroup. No significant correlation was observed between clinical and neuropsychological scores and diffusion metrics.

**CONCLUSIONS:** Widespread WM differences are evident in patients with Duchenne muscular dystrophy relative to healthy controls. Distal mutations in particular are associated with extensive WM abnormalities and poor neuropsychological profiles.

**ABBREVIATIONS:** AD = axial diffusivity; FA = fractional anisotropy; DMD = Duchenne muscular dystrophy; IQ = intelligence quotient; MD = mean diffusivity; MDFS = Muscular Dystrophy Functional Rating Scale; MLPA = multiplex ligation-dependent probe amplification; RD = radial diffusivity; TBSS = Tract-Based Spatial Statistics

Duchenne muscular dystrophy (DMD), characterized by mutations in the *dystrophin* (*DMD*) gene, results in absent/nonfunctional muscle dystrophin, leading to progressive muscle

weakness.<sup>1</sup> Children with DMD also have nonmotor difficulties such as a lower intelligence quotient (IQ), reading difficulties, and increased prevalence of neurobehavioral disturbances such as anxiety, autism spectrum disorder, and obsessive compulsive disorder.<sup>2-4</sup> Very few studies have attempted to study the relationship between neurobehavioral abnormalities and neuroanatomic changes.<sup>5-7</sup>

The *DMD* gene contains multiple independent tissue-specific promoters, producing several isoforms named according to their length and splicing patterns. The isoform Dp427m is predominantly expressed in the muscles and plays a pivotal role in structural integrity of muscle fibers, the isoform Dp427c is expressed in the cerebral cortex, hippocampus and Dp427p is mainly expressed in the Purkinje cells. The Dp140 isoform is believed to

Received December 9, 2019; accepted after revision March 23, 2020.

From the Departments of Neurology (V.P.-K., K.P., S.V., S.N., A.N.), Neuroimaging and Interventional Radiology (M.K., J.S.), Neuropsychology (M.A., J.R.), Psychiatric Social Work (P.T.T., A.Sadasivan, M.W.), National Institute of Mental Health and Neurosciences, Bangalore, India; and Symbiosis Centre for Medical Image Analysis (A.Shah, M.I.), Symbiosis International University, Mulshi Pune, Maharashtra, India.

Please address correspondence to Jitender Saini, MD, DM, Department of Neuroimaging and Interventional Radiology, 3rd Floor, Neuroscience Faculty Center, National Institute of Mental Health and Neurosciences, Hosur Rd, Bengaluru, KA-560029 India; e-mail: jsaini76@gmail.com



Indicates article with supplemental on-line tables.

<http://dx.doi.org/10.3174/ajnr.A6604>

be expressed in the CNS during development, while Dp71 is expressed in both the CNS and other body tissues.<sup>8,9</sup>

Neuropsychological impairment in DMD is characterized by verbal deficits with relative sparing of nonverbal domains.<sup>10</sup> Patients with DMD with an absence of all isoforms due to distal mutations have the lowest IQ scores, while those with the absence of only the full-length isoform achieve relatively higher scores. Moreover, children with DMD lacking Dp140 isoforms demonstrate impaired verbal memory, attention, and executive function and may develop various neurodevelopmental abnormalities.<sup>3,6,11</sup>

Neuroimaging studies have revealed structural and functional brain abnormalities,<sup>6</sup> with MR spectroscopy<sup>12</sup> and PET<sup>13</sup> showing metabolic derangement. Evidence is also accruing for brain regional volume differences,<sup>14</sup> blood oxygen level-dependent signal abnormalities,<sup>14</sup> and altered WM integrity as measured using DTI.<sup>6</sup> Furthermore, recent imaging studies have highlighted less severe structural abnormalities in patients with retained Dp140 expression compared with those lacking it.<sup>6,7</sup>

This study aimed to comprehensively evaluate brain changes in a larger cohort of children with DMD and further it by probing group-level differences in WM abnormalities in 2 major subtypes based on Dp140 expression, using DTI as the tool. We hypothesize that patients with retained Dp140 (Dp140+) expression will have relatively preserved WM compared with that in patients with loss of the Dp140 (Dp140-) isoform.

## MATERIALS AND METHODS

This prospective study included subjects (total = 100, healthy controls [ $n = 40$ ], and patients with DMD [ $n = 60$ ]) identified at the Neuromuscular Disorders Clinic at National Institute of Mental Health and Neurosciences. The institutional ethics committee of National Institute of Mental Health and Neurosciences (NIMHANS) approved this study. Written informed consent was obtained from the parents or guardian and child.

The diagnosis was based on clinical presentation, including delayed motor milestones, proximal weakness, hypertrophied calves, markedly elevated creatine kinase levels, and the presence of deletions detected using the multiplex ligation-dependent probe amplification (MLPA) test. Right-handed boys 6–10 years of age without any coexistent medical illness, who were ambulant, attending school, and cooperative for MR imaging and neuropsychological assessment were recruited.

Muscle power was assessed using manual muscle testing according to the modified Medical Research Council Scale for Muscle Strength, and disease severity was estimated using the Muscular Dystrophy Functional Rating Scale (MDFRS).

Exclusion criteria were severe mental retardation or suspected dystrophinopathy without obvious deletions. The healthy control children matched for age/sex, education, ethnicity, and social status were recruited from the nearby schools after obtaining approval from the school education officer and necessary consent from the parents. Subjects recruited to the control group underwent a brief neurologic examination by an expert neurologist with 20 years of experience (A.N.), and children with any psychiatric or neurologic comorbidity were excluded.

## MLPA

Blood samples were collected in ethylenediaminetetraacetic acid-coated vacutainers; genomic DNA was extracted using the salting out method and stored at  $-20^{\circ}\text{C}$  until tested.<sup>15</sup> The MLPA reaction was performed to screen all exons of the *DMD* gene using SALSA MLPA, P034, and P035 probe sets (MRC Holland). The procedure was performed according to the manufacturer's instructions. Amplified products were separated using a 3500XL Genetic analyzer (Applied Biosystems), and data were analyzed using the Coffalyser software (<https://coffalyser.updatestar.com/>) with a control sample included in every run.

Genetic results pertaining to the type and location of exon deletion were analyzed, and children were classified into 3 groups: DMD Dp140+, DMD Dp140-, and controls. The expression of the Dp140 isoform was based on the universal mutation *DMD* data base, a French knowledge base derived from functional studies that predicted the effect of several mutations ([http://www.umd.be/DMD/4DACTION/W\\_ISO/L](http://www.umd.be/DMD/4DACTION/W_ISO/L)).

## Neuropsychological Assessment

The battery of neuropsychological tests included the Edinburgh Handedness Inventory,<sup>16</sup> Functional Disability Inventory, Parent Form,<sup>17</sup> Wechsler-Intelligence Scale for Children (3rd ed, WISC-III, 1991), Rey Auditory Verbal Learning Test (WHO/UCLA Version), and Memory for Designs Test.<sup>18</sup> The WISC-III was used to measure verbal IQ, performance IQ, full-scale IQ, verbal comprehension, the Perceptual Organization Index, and the Freedom from Distractibility Index in all children.

## MR Imaging

MR imaging was performed using a 3T clinical scanner (Achieva; Philips Healthcare) and a 32-channel head coil. High-resolution 3D turbo field echo T1-weighted images were acquired (TR/TE = 9.8/4.6 ms, and spatial-resolution =  $1 \times 1 \times 1$  mm). The single-shot spin-echo echo-planar DTI sequence was performed with the following parameters: TR/TE = 5000/65 ms; resolution =  $2.0 \times 2.0 \times 2.0$  mm; noncoplanar diffusion directions = 15; b-values = 0 and 1000  $\text{s/mm}^2$ ; and 2 repetitions, with a total scanning time of 4 minutes 36 seconds.

## DTI Data Processing and Analysis

Diffusion data analysis was performed using FMRIB Software Library tools ([www.fmrib.ox.ac.uk/fsl](http://www.fmrib.ox.ac.uk/fsl)), Version 5.0.11. Raw diffusion tensor images were preprocessed using eddy current correction for distortions. Group comparisons of DTI data were performed using Tract-Based Spatial Statistics (TBSS; <http://fsl.fmrib.ox.ac.uk/fsl/fslwiki/TBSS>). DTI-derived maps (fractional anisotropy [FA], mean diffusivity [MD], axial diffusivity [AD], and radial diffusivity [RD]) were generated using the FMRIB Diffusion Toolbox (<http://fsl.fmrib.ox.ac.uk/fsl/fslwiki/FDT>). Individual skull-stripped FA images were aligned with Montreal Neurological Institute 152 standard space using a nonlinear registration method, followed by the creation of a group mean FA skeleton by thinning mean FA volumes (FA > 0.2 overlaid with the mean FA image). The mean FA skeleton represents the centers of all tracts common to the entire group

**Table 1: Clinical characteristics and MDFS scores**

	Patients with DMD (Range)	Controls (Range)
Age at recruitment (mean) (yr)	8.0 ± 1.2 (6–10)	8.2 ± 1.4 (6–10)
Age at onset (mean) (yr)	4.1 ± 1.8 (1–9)	
Age at presentation (mean) (range) (yr)	7.5 ± 1.4 (4–10)	
Duration (mean) (mo)	40.8 ± 25.2 (6–120)	
MDFS domains (mean)		
Mobility (maximum 36)	24.35 ± 3.272 (15–30)	
Basic ADL (maximum 24)	18.77 ± 2.547 (12–25)	
Arm function (maximum 28)	22.07 ± 1.885 (19–25)	
Impairment (maximum 44)	34.18 ± 3.568 (23–40)	
Total score (maximum 132)	99.37 ± 10.55 (69–117)	

**Note:**—ADL indicates activities of daily living; MDFS, Muscular Dystrophy Functional Rating scale.

of subjects. Each subject's aligned FA data were then projected onto the mean FA skeleton, and the resulting data were fed into voxelwise paired-sample testing. A voxel-by-voxel permutation nonparametric test (5000 permutations) was used to assess group-related differences using threshold-free cluster enhancement, which avoids using an arbitrary threshold for the initial cluster formation. In addition to FA, a similar process of non-linear registration and voxelwise comparison was performed to determine the differences in MD, AD, and RD maps. For all tests, a null distribution was built up over 5000 permutations, and significance was tested at a *P* value corrected for multiple comparisons. To assess the relationship between neuropsychological test scores and each of the DTI measures, we used an FSL General Linear Model (<http://fsl.fmrib.ox.ac.uk/fsl/fslwiki/GLM>). Statistical analysis was performed using the FSL Randomise tool (<http://fsl.fmrib.ox.ac.uk/fsl/fslwiki/Randomise/UserGuide>), with age as a nuisance variable and 5000 permutations; results were considered significant at *P* < .01 (family-wise error-corrected).<sup>19,20</sup>

### Atlas-Based Analysis of Major WM Tracts

Multiple WM ROIs were defined using the JHU-White Matter Atlas (<http://neuro.debian.net/pkgs/fsl-jhu-dti-whitematter-atlas.html>), which is a probabilistic atlas generated by mapping DTI data from healthy subjects to a template image. The mean diffusion metric values of each ROI for individual subjects were extracted.

### Statistics

Continuous variables are expressed as mean ± SD, and categorical variables, as frequencies and percentages. Demographic and neuropsychological data were tested for normality using the Kolmogorov-Smirnov test. Comparisons were performed using an independent-samples *t* test or the Wilcoxon signed rank test based on the normality of the distribution of the data. SPSS, Version 21.0 (IBM) was used for statistical computation. One-way analysis of variance with multiple comparisons using a Bonferroni post hoc test was performed to evaluate the differences in neuropsychological data and WM tract diffusion metrics between age- and sex-matched controls and subjects with DMD (proximal and distal mutations). All mean diffusion metric values of various tracts were tested for potential associations with disease duration, IQ, and Auditory Verbal Learning Test and Memory for Designs Test scores. Scores were adjusted for age

using linear regression, and the resulting standard residuals were used for correlation. The Pearson correlation coefficient was computed, and the significance threshold was *P* < .01. The 95% confidence intervals of the estimated parameters were also computed wherever applicable.

### RESULTS

The mean age of patients with DMD and controls was 8.0 ± 1.2 and 8.2 ± 1.4 years, respectively. The mean age at disease onset was 4.1 ± 1.8 years, and the mean illness duration was 40.8 ± 25.2 months. The mean MDFS scores are shown in Table 1. Children with upstream exon 45 (1–44) and downstream exon 45 (45–79) were subgrouped as proximal DP140+ (*n* = 21) and distal deletions DP140– (*n* = 39), respectively. Fifty-eight patients were on steroid treatment with a mean treatment duration of 9.5 ± 8.6 months (range, 1–37 months). Clinical information is summarized in Table 1. Mean MDFS scores and individual domain scores were compared between the proximal- and distal-deletion subgroups; the distal subgroup had lower MDFS scores. A statistically significant difference in mobility and impairment domains and overall mean MDFS score was observed between subgroups of children with DMD (proximal = 104.13 ± 7.635 and distal = 96.41 ± 11.112, *P* < .05). No significant differences were noted in the dose and duration of steroid treatment between the 2 subgroups. The neuropsychological examination scores and values of the WISC-III scale are summarized in On-line Tables 1 and Table 2, respectively.

### TBSS Results

**Comparison of DTI Metrics between Children with DMD (Proximal and Distal Mutations) and Healthy Controls.** TBSS analysis comparing all patients with DMD and controls demonstrated widespread WM alterations involving both the supra- and infratentorial WM (Fig 1). There was a significant increase in MD and RD values in the WM of patients compared with controls. Focal areas of significant reduction in FA included the corpus callosum, superior longitudinal fasciculus, superior and inferior fronto-occipital fasciculus, corticospinal tract, and uncinate fasciculus in patients compared with controls.

**Comparison of DTI Metrics between DMD Proximal (Dp140+) and Healthy Controls.** No significant differences were observed in any of the diffusivity parameters. FA was significantly higher in healthy controls than in patients in the bilateral fornices, the

**Table 2: Comparison of the intelligent quotient (IQ) values of WISC-III scale between the two patient subgroups (DMD proximal and distal), and healthy controls**

SN	Test	Group (I)	Group (J)	Difference (I-J)	Significance	95% CI, Lower-to-Upper Bounds
1.	Verbal IQ	Control	Proximal	17.258 <sup>a</sup>	.000	8.79–25.73
			Distal	29.699 <sup>a</sup>	.000	22.27–37.12
2.	Performance IQ	Proximal	Distal	12.441 <sup>a</sup>	.002	3.76–21.12
		Control	Proximal	15.350 <sup>a</sup>	.000	6.88–23.82
3.	Full-scale IQ	Control	Distal	24.442 <sup>a</sup>	.000	17.01–31.87
			Proximal	9.092 <sup>a</sup>	.037	0.41–17.77
4.	Verbal Composition	Control	Proximal	18.238 <sup>a</sup>	.000	9.50–26.98
		Proximal	Distal	30.141 <sup>a</sup>	.000	22.48–37.81
5.	Perceptual Organization Index	Control	Proximal	11.903 <sup>a</sup>	.005	2.95–20.86
		Proximal	Distal	17.608 <sup>a</sup>	.000	9.32–25.90
6.	Freedom from Distractibility Index	Control	Proximal	27.612 <sup>a</sup>	.000	20.34–34.88
		Proximal	Distal	10.005 <sup>a</sup>	.015	1.51–18.50
		Control	Proximal	15.352 <sup>a</sup>	.000	7.47–23.23
		Proximal	Distal	23.272 <sup>a</sup>	.000	16.37–30.18
		Control	Proximal	7.920	.056	–0.15–15.99
		Proximal	Distal	8.183	.092	–0.90–17.26
		Control	Distal	23.293 <sup>a</sup>	.000	15.33–31.26
		Proximal	Distal	15.110 <sup>a</sup>	.000	5.80–24.41

**Note:**—SN indicates serial number.

<sup>a</sup> level of significance.

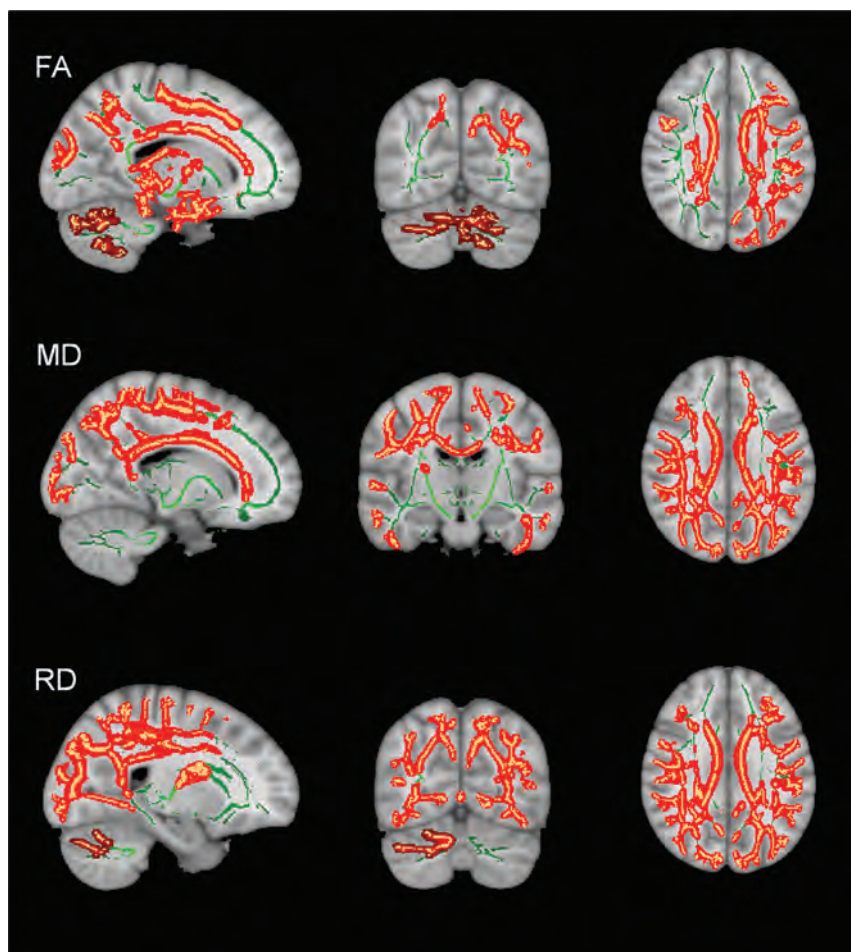


**FIG 1.** DTI TBSS analysis comparing healthy controls with patients with DMD shows areas with significantly ( $P < .01$ , family-wise error corrected) decreased FA and increased MD and RD in patients with DMD. Green represents the WM skeleton, while red and maroon are clusters of significance.

body of the corpus callosum, and parietal WM (Fig 2). Because only FA changes were seen, we used a less stringent threshold of  $P < .05$  to evaluate trends in diffusivity metrics. We noted trends in RD maps using a less stringent threshold of  $P < .05$  family-wise error-corrected, while other diffusivity metrics showed no changes.

**Comparison of DTI Metrics between DMD Distal (Dp140–) and Healthy Controls.** A widespread increase in diffusivity indices was noted in the form of increased MD, AD, and RD involving predominantly cerebellar, occipital, and parietotemporal WM regions with relative sparing of the frontal WM (Fig 3). No significant difference in FA was noted; however, at a reduced threshold ( $0.01 < P < .05$ ), lower FA was seen in the corpus callosum, corticospinal tract, left superior longitudinal fasciculus, inferior longitudinal fasciculus, and fornices.

**Comparison of DTI Metrics between DMD Distal (Dp140–) and Proximal (Dp140+) Subgroups.** Significantly higher AD values were noted in the right occipital-temporal WM, corpus callosum, and cerebellar WM in the DMD distal (Dp140–) than in the DMD proximal (Dp140+) subgroup.



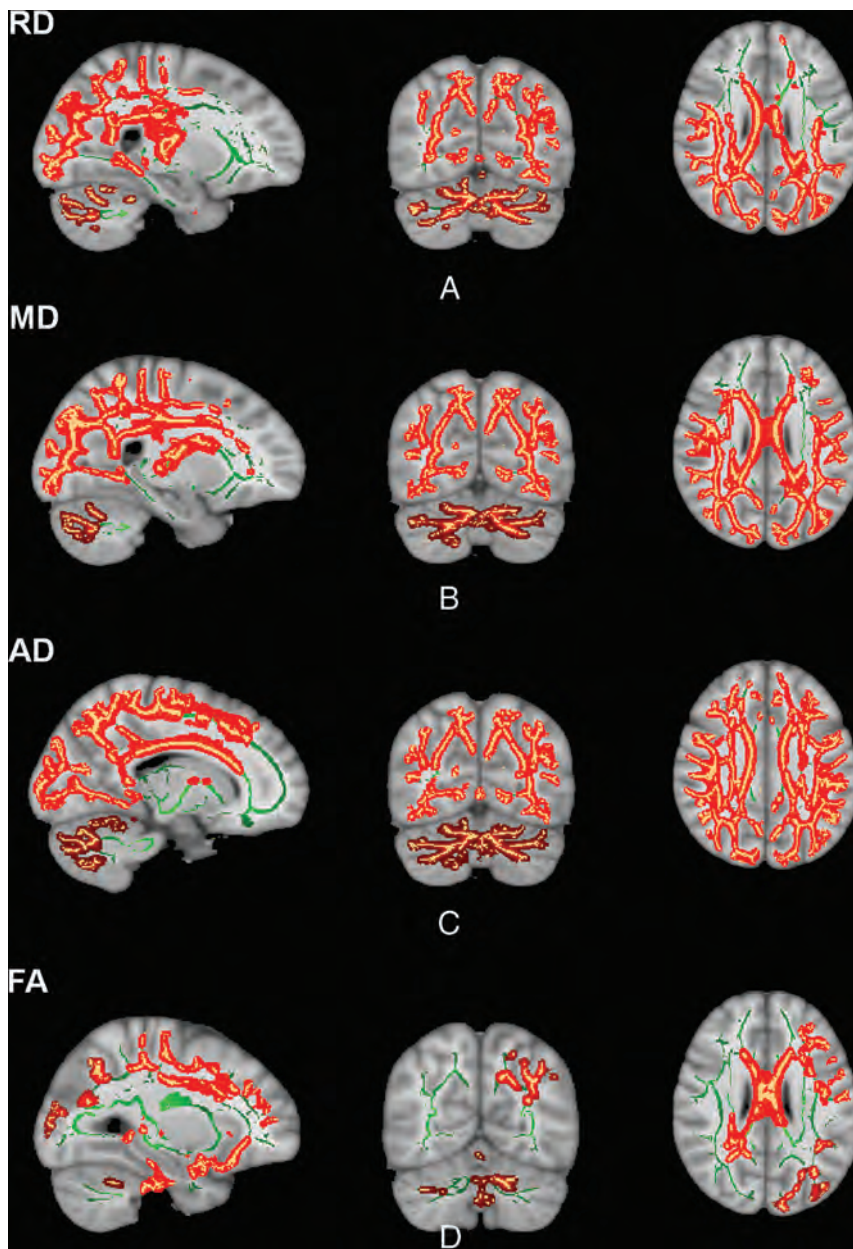


**FIG 2.** Healthy control versus DMD (distal) Dp140- TBSS results. RD (A), MD (B), and AD (C) are significantly increased in patients compared with healthy controls in both the cerebellar WM and cerebral WM with relative sparing of the frontal WM ( $P < .01$  family-wise error-corrected). D, FA did not show any significant differences; however, the trend was noted because many areas showed FA differences at the less conservative statistical threshold of  $P < .05$  (family-wise error-corrected). Green represents the WM skeleton, while red and maroon are clusters of significance.

However, no significant difference was seen in MD, RD, and FA between these 2 subgroups ( $P < .01$ ).

No significant correlations were identified between WM abnormalities and clinical severity, disease duration, or IQ.

#### Atlas-Based WM Analysis

Controls versus Patients with DMD (Dp140+). Significantly reduced FA was observed in multiple tracts in patients with DMD with a proximal mutation, while MD was not found to be significantly different in this group ( $P < .01$ ) (On-line Table 2).

Controls versus Patients with DMD (Dp140-). No significant change in FA was noted in the patients with DMD with distal mutation, while higher MD values were seen in multiple tracts, listed in On-line Table 2 ( $P < .01$ ).

Comparison between DMD (Dp140+) and DMD (Dp140-) Patient Sub-groups. No significant difference in FA or MD was observed between the distal and proximal mutation subgroups ( $P < .01$ ).

#### DISCUSSION

This study revealed lower IQ and neuropsychological abnormalities in patients with DMD, which were more severe in the distal mutation Dp140- subgroup. DTI analysis revealed widespread WM alterations in both supratentorial and infratentorial regions. Comparison of proximal and distal mutation subgroups with healthy controls using TBSS revealed significantly higher MD, RD, and AD values in the Dp140- subgroup, whereas patients in the Dp140+ subgroup demonstrated spatially localized altered FA values with no significant changes in MD. Similar findings were also detected in an atlas-based analysis of tract diffusion metrics.

DMD is a debilitating disorder characterized by progressive muscle weakness and skeletal deformities, followed by an inexorable course to severe respiratory difficulties and overall reduced life span.<sup>1</sup> Although the clinical phenotype exemplified by muscular manifestations is the dominant phenomenon, earlier studies have identified significant non-motor features. Neuropsychological evaluation in these patients has demonstrated impaired language and memory and executive dysfunction, which may possibly be dependent on

the site of mutation.<sup>3,11,21-23</sup> Specifically, the absence of the Dp140 isoform may lead to severe neuropsychological abnormalities.<sup>3,11</sup>

Kim et al<sup>24</sup> have reported that the brains of patients with DMD are devoid of the 427 kDa cortical dystrophin protein. While the functions of dystrophin in the brain have not been categorically described, studies have indicated that the isoform Dp427 is involved in the organization of gamma-aminobutyric acid A receptors and possibly plays a role in signaling. The functions of the shorter isoforms, Dp140 and Dp71, expressed in glial

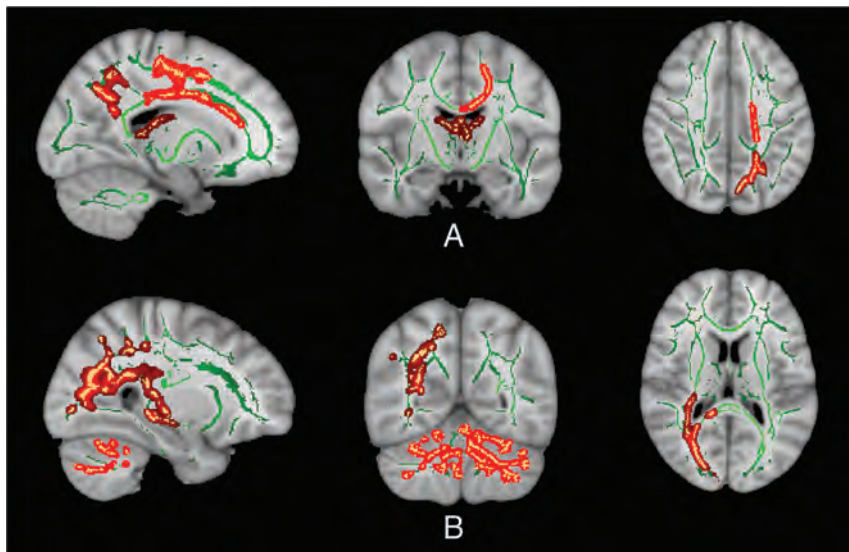


**FIG 3.** (A) Healthy controls versus DMD (proximal) Dp140+: TBSS for FA shows significantly lower FA in the patient group in the areas highlighted in red ( $P < .01$ ). No significant differences in any of the diffusivity metrics are noted. (B) DMD distal (Dp140-) versus DMD proximal (Dp140+): TBSS shows higher AD in patients with a distal mutation involving the cerebellar WM and right occipitoparietal-temporal WM. The rest of the diffusion metrics did not show any significant difference.

cells adjacent to the microvasculature,<sup>25</sup> have not been elucidated. Dp140, given its expression during the early developmental stages of the brain, is purported to modulate axon guidance, transcription factor activity, and neuron differentiation.<sup>9</sup> Postmortem studies in patients with DMD have illustrated pathologic changes such as astrogliosis, neuronal loss, heterotopia, and cortical abnormalities in patients with DMD.<sup>26,27</sup> Functional and quantitative neuroimaging studies have revealed multiple abnormalities in DMD brains. Hippocampal and cerebellar hypometabolism has been documented on PET in DMD.<sup>13</sup> Resting-state fMRI has elucidated reduced local synchronization of spontaneous activity in the neural networks of the motor cortex.<sup>14</sup> Brain MR spectroscopy observations have been varied, with altered choline and phosphorus metabolite concentrations in DMD having been described in a few studies,<sup>12,28-30</sup> while no significant changes were demonstrable in another study.<sup>31</sup> Recently, Doorenweerd et al<sup>6</sup> reported significant brain morphometric changes along with altered WM integrity in patients with DMD. Another study from this group also showed reduced cortical perfusion in DMD, independent of cortical atrophy.<sup>5</sup> However, visual inspection of neuroimaging is usually unremarkable.

DTI measures are surrogate markers of WM integrity, ie, directional WM integrity (FA), tissue breakdown and increased water content (AD), and axonal integrity and myelin sheaths (RD and AD). In our study, we found increased diffusivity along with reduced WM FA in patients with DMD. The Dp140- subgroup showed extensive WM diffusivity alterations with relatively localized FA changes, suggesting that diffusion changes along the direction of the major axis (AD) are commensurate with those of the minor axes (RD).<sup>32</sup> In contrast, the Dp140+ subgroup illustrated a relatively preserved WM structure. Doorenweerd et al<sup>6</sup> reported extensive WM changes in the diffusivity metrics and less

extensive changes in FA, and alterations were more widespread and severe in the distal mutation group. Contrary to these results, another study using ROI-based analysis found only focal abnormality in the splenium of the corpus callosum.<sup>7</sup>

Our study is similar to the study of Doorenweerd et al;<sup>6</sup> however, they had a very small sample size, studied older children with a wide age range, and performed both voxel-based morphometry and DTI analysis. Our study participants were much younger, and the age range was narrower. Another study by Fu et al<sup>7</sup> used only 12 subjects with DMD and performed ROI-based analysis. No subgroup analysis was performed on the basis of the underlying genotype.

Multiple pathophysiologic phenomena like demyelination, WM reorganization, increased membrane permeability with excess free water, intracellular compartment changes, and glial alterations modulate diffusivity.<sup>33</sup> Myelination abnormalities may be a candidate mechanism altering DTI metrics in patients with DMD as shown by Aranmolate et al<sup>34</sup> in the mdx mouse model of DMD. Oligodendrocytes require dystrophin for normal maturation, which, in the case of the mdx murine model, is lacking, potentially explaining the observation of impaired myelination. Another study of the mdx mouse model showed that increased extracellular free water led to increased blood-brain barrier permeability, resulting in increased MD and decreased FA.<sup>35</sup> This mechanism is also supported by studies that have demonstrated increased vascular endothelial growth factor and enhanced *matrix metalloproteinase 2 (MMP-2)* and -9 expression, along with endothelial dysfunction in animal models of DMD.<sup>36-38</sup>

We did not observe any significant voxelwise correlation between any of the neuropsychological examination scores and WM alterations revealed by the DTI metrics. However, we did notice poor neuropsychological scores along with impaired WM integrity in the patients in the Dp140- subgroup. The lack of a correlation between WM changes and the extent of neuropsychological examination abnormalities needs to be resolved. Similarly, a lack of correlation between clinical and radiologic parameters was observed in the DTI study by Doorenweerd et al.<sup>6</sup> However, another study did identify a significant correlation between clinical scores and DTI metrics of the corpus callosum.<sup>7</sup>

In the current study, most patients were receiving steroids at the time of evaluation. Steroids can potentially confound DTI results; a few studies in patients with Cushing disease have shown reduced integrity of the cerebral WM.<sup>39,40</sup> However, no significant difference was noted in the duration or dose of steroids in the patients in the 2 subgroups, which suggests that the observed differences in the DTI metrics were most likely due to the



primary disease and not steroid intake. Steroids partly alleviate intellectual impairment in patients with DMD<sup>41</sup> as well as reverse BBB dysfunction and may increase the levels of shorter isoforms of dystrophin, as demonstrated in animal studies.<sup>42</sup> Longitudinal studies are required to document the time course of the effects of steroidal treatment.

The limitations of the current study include the relatively low directional resolution of DTI. However, considering the pediatric population's proneness to motion, a relatively shorter EPI sequence protocol like ours was considered robust. Accelerating acquisition using a multiband technique holds promise for the future to obtain high-resolution multishell imaging data for structural connectomics analyses and multi-compartment modeling.

## CONCLUSIONS

Children with DMD show widespread structural WM changes, which are more severe and widespread in children with distal mutations. Children with distal mutations have more severe abnormal findings in neuropsychological tests compared with the children with proximal mutations.

## REFERENCES

- Bushby K, Finkel R, Birnkrant DJ, et al; DMD Care Considerations Working Group. **Diagnosis and management of Duchenne muscular dystrophy, Part 1: diagnosis, and pharmacological and psychosocial management.** *Lancet Neurol* 2010;9:77–93 CrossRef Medline
- Pane M, Lombardo ME, Alfieri P, et al. **Attention deficit hyperactivity disorder and cognitive function in Duchenne muscular dystrophy: phenotype-genotype correlation.** *J Pediatr* 2012;161:705–09.e1 CrossRef Medline
- D'Angelo MG, Lorusso ML, Civati F, et al. **Neurocognitive profiles in Duchenne muscular dystrophy and gene mutation site.** *Pediatr Neurol* 2011;45:292–99 CrossRef Medline
- Banihani R, Smile S, Yoon G, et al. **Cognitive and neurobehavioral profile in boys with Duchenne muscular dystrophy.** *J Child Neurol* 2015;30:1472–82 CrossRef Medline
- Doorenweerd N, Dumas EM, Ghariq E, et al. **Decreased cerebral perfusion in Duchenne muscular dystrophy patients.** *Neuromuscul Disord* 2017;27:29–37 CrossRef Medline
- Doorenweerd N, Straathof CS, Dumas EM, et al. **Reduced cerebral gray matter and altered white matter in boys with Duchenne muscular dystrophy: quantitative MRI in DMD brain.** *Ann Neurol* 2014;76:403–11 CrossRef Medline
- Fu Y, Dong Y, Zhang C, et al. **Diffusion tensor imaging study in Duchenne muscular dystrophy.** *Ann Transl Med* 2016;4:109 CrossRef Medline
- Muntoni F, Torelli S, Ferlini A. **Dystrophin and mutations: one gene, several proteins, multiple phenotypes.** *Lancet Neurol* 2003;2:731–40 CrossRef Medline
- Doorenweerd N, Mahfouz A, van Putten M, et al. **Timing and localization of human dystrophin isoform expression provide insights into the cognitive phenotype of Duchenne muscular dystrophy.** *Sci Rep* 2017;7:12575 CrossRef Medline
- Hinton VJ, De Vivo DC, Nereo NE, et al. **Poor verbal working memory across intellectual level in boys with Duchenne dystrophy.** *Neurology* 2000;54:2127–32 CrossRef Medline
- Taylor PJ, Betts GA, Maroulis S, et al. **Dystrophin gene mutation location and the risk of cognitive impairment in Duchenne muscular dystrophy.** *PLoS One* 2010;5:e8803 CrossRef Medline
- Tracey I, Scott RB, Thompson CH, et al. **Brain abnormalities in Duchenne muscular dystrophy: phosphorus-31 magnetic resonance spectroscopy and neuropsychological study.** *Lancet* 1995;345:1260–64 CrossRef Medline
- Lee JS, Pfund Z, Juhász C, et al. **Altered regional brain glucose metabolism in Duchenne muscular dystrophy: a PET study.** *Muscle Nerve* 2002;26:506–12 CrossRef Medline
- Lv SY, Zou QH, Cui JL, et al. **Decreased gray matter concentration and local synchronization of spontaneous activity in the motor cortex in Duchenne muscular dystrophy.** *AJNR Am J Neuroradiol* 2011;32:2196–200 CrossRef Medline
- Miller SA, Dykes DD, Polesky HF. **A simple salting out procedure for extracting DNA from human nucleated cells.** *Nucleic Acids Res* 1988;16:1215 CrossRef Medline
- Oldfield RC. **The assessment and analysis of handedness: the Edinburgh inventory.** *Neuropsychologia* 1971;9:97–113 CrossRef Medline
- Walker LS, Greene JW. **The functional disability inventory: measuring a neglected dimension of child health status.** *J Pediatr Psychol* 1991;16:39–58 CrossRef Medline
- Jones-Gotman M. **Memory for designs: the hippocampal contribution.** *Neuropsychologia* 1986;24:193–203 CrossRef Medline
- Smith SM, Nichols TE. **Threshold-free cluster enhancement: addressing problems of smoothing, threshold dependence and localisation in cluster inference.** *Neuroimage* 2009;44:83–98 CrossRef Medline
- Smith SM, Jenkinson M, Johansen-Berg H, et al. **Tract-based spatial statistics: voxelwise analysis of multi-subject diffusion data.** *Neuroimage* 2006;31:1487–505 CrossRef Medline
- Cotton S, Voudouris NJ, Greenwood KM. **Intelligence and Duchenne muscular dystrophy: full-scale, verbal, and performance intelligence quotients.** *Dev Med Child Neurol* 2001;43:497–501 CrossRef Medline
- Snow WM, Anderson JE, Jakobson LS. **Neuropsychological and neurobehavioral functioning in Duchenne muscular dystrophy: a review.** *Neurosci Biobehav Rev* 2013;37:743–52 CrossRef Medline
- Hinton VJ, Fee RJ, Goldstein EM, et al. **Verbal and memory skills in males with Duchenne muscular dystrophy.** *Dev Med Child Neurol* 2007;49:123–28 CrossRef Medline
- Kim TW, Wu K, Black IB. **Deficiency of brain synaptic dystrophin in human Duchenne muscular dystrophy.** *Ann Neurol* 1995;38:446–49 CrossRef Medline
- Ricotti V, Roberts RG, Muntoni F. **Dystrophin and the brain.** *Dev Med Child Neurol* 2011;53:12 CrossRef Medline
- Dubowitz V, Crome L. **The central nervous system in Duchenne muscular dystrophy.** *Brain J Brain* 1969;92:805–08 CrossRef Medline
- Rosman NP, Kakulas BA. **Mental deficiency associated with muscular dystrophy: a neuropathological study.** *Brain J Neurol* 1966;89:769–88 CrossRef Medline
- Xu S, Shi D, Pratt SJP, et al. **Abnormalities in brain structure and biochemistry associated with mdx mice measured by in vivo MRI and high resolution localized (1)H MRS.** *Neuromuscul Disord* 2015;25:764–72 CrossRef Medline
- Rae C, Scott RB, Thompson CH, et al. **Brain biochemistry in Duchenne muscular dystrophy: a 1H magnetic resonance and neuropsychological study.** *J Neurol Sci* 1998;160:148–57 CrossRef Medline
- Kreis R, Wingeier K, Vermathen P, et al. **Brain metabolite composition in relation to cognitive function and dystrophin mutations in boys with Duchenne muscular dystrophy.** *NMR Biomed* 2011;24:253–62 CrossRef Medline
- Doorenweerd N, Hooijmans M, Schubert SA, et al. **Proton magnetic resonance spectroscopy indicates preserved cerebral biochemical composition in Duchenne muscular dystrophy patients.** *J Neuromuscul Dis* 2017;4:53–58 CrossRef Medline
- Acosta-Cabronero J, Williams GB, Pengas G, et al. **Absolute diffusivities define the landscape of white matter degeneration in Alzheimer's disease.** *Brain* 2010;133:529–39 CrossRef Medline

33. Beaulieu C. **The basis of anisotropic water diffusion in the nervous system: a technical review.** *NMR Biomed* 2002;15:435–55 CrossRef Medline
34. Aranmolate A, Tse N, Colognato H. **Myelination is delayed during postnatal brain development in the mdx mouse model of Duchenne muscular dystrophy.** *BMC Neurosci* 2017;18:63 CrossRef Medline
35. Goodnough CL, Gao Y, Li X, et al. **Lack of dystrophin results in abnormal cerebral diffusion and perfusion in vivo.** *Neuroimage* 2014;102 Pt 2:809–16 CrossRef Medline
36. Nico B, Paola Nicchia G, Frigeri A, et al. **Altered blood-brain barrier development in dystrophic MDX mice.** *Neuroscience* 2004;125:921–35 CrossRef Medline
37. Nico B, Roncali L, Mangieri D, et al. **Blood-brain barrier alterations in MDX mouse: an animal model of the Duchenne muscular dystrophy.** *Curr Neurovasc Res* 2005;2:47–54 CrossRef Medline
38. Nico B, Frigeri A, Nicchia GP, et al. **Severe alterations of endothelial and glial cells in the blood-brain barrier of dystrophic mdx mice.** *Glia* 2003;42:235–51 CrossRef Medline
39. van der Werff SA, Andela CD, Nienke Pannekoek J, et al. **Widespread reductions of white matter integrity in patients with long-term remission of Cushing's disease.** *Neuroimage Clin* 2014;4:659–67 CrossRef Medline
40. Pires P, Santos A, Vives-Gilabert Y, et al. **White matter alterations in the brains of patients with active, remitted, and cured Cushing syndrome: a DTI study.** *AJNR Am J Neuroradiol* 2015;36:1043–48 CrossRef Medline
41. Sato Y, Yamauchi A, Urano M, et al. **Corticosteroid therapy for Duchenne muscular dystrophy: improvement of psychomotor function.** *Pediatr Neurol* 2014;50:31–37 CrossRef Medline
42. Tamma R, Annese T, Capogrosso RF, et al. **Effects of prednisolone on the dystrophin-associated proteins in the blood-brain barrier and skeletal muscle of dystrophic mdx mice.** *Lab Invest* 2013; 93:592–610 CrossRef Medline



# Automatic Machine Learning to Differentiate Pediatric Posterior Fossa Tumors on Routine MR Imaging

H. Zhou, R. Hu, O. Tang, C. Hu, L. Tang, K. Chang, Q. Shen, J. Wu, B. Zou, B. Xiao, J. Boxerman, W. Chen, R.Y. Huang, L. Yang, H.X. Bai, and C. Zhu



## ABSTRACT

**BACKGROUND AND PURPOSE:** Differentiating the types of pediatric posterior fossa tumors on routine imaging may help in preoperative evaluation and guide surgical resection planning. However, qualitative radiologic MR imaging review has limited performance. This study aimed to compare different machine learning approaches to classify pediatric posterior fossa tumors on routine MR imaging.

**MATERIALS AND METHODS:** This retrospective study included preoperative MR imaging of 288 patients with pediatric posterior fossa tumors, including medulloblastoma ( $n=111$ ), ependymoma ( $n=70$ ), and pilocytic astrocytoma ( $n=107$ ). Radiomics features were extracted from T2-weighted images, contrast-enhanced T1-weighted images, and ADC maps. Models generated by standard manual optimization by a machine learning expert were compared with automatic machine learning via the Tree-Based Pipeline Optimization Tool for performance evaluation.

**RESULTS:** For 3-way classification, the radiomics model by automatic machine learning with the Tree-Based Pipeline Optimization Tool achieved a test micro-averaged area under the curve of 0.91 with an accuracy of 0.83, while the most optimized model based on the feature-selection method  $\chi^2$  score and the Generalized Linear Model classifier achieved a test micro-averaged area under the curve of 0.92 with an accuracy of 0.74. Tree-Based Pipeline Optimization Tool models achieved significantly higher accuracy than average qualitative expert MR imaging review (0.83 versus 0.54,  $P<.001$ ). For binary classification, Tree-Based Pipeline Optimization Tool models achieved an area under the curve of 0.94 with an accuracy of 0.85 for medulloblastoma versus nonmedulloblastoma, an area under the curve of 0.84 with an accuracy of 0.80 for ependymoma versus nonependymoma, and an area under the curve of 0.94 with an accuracy of 0.88 for pilocytic astrocytoma versus non-pilocytic astrocytoma.

**CONCLUSIONS:** Automatic machine learning based on routine MR imaging classified pediatric posterior fossa tumors with high accuracy compared with manual expert pipeline optimization and qualitative expert MR imaging review.

**ABBREVIATIONS:** AUC = area under the curve; AutoML = automatic machine learning; CHSQ =  $\chi^2$  score; EP = ependymoma; MB = medulloblastoma; ML = machine learning; PA = pilocytic astrocytoma; TPOT = Tree-Based Pipeline Optimization Tool

**A**mong childhood malignancies, pediatric brain tumors are the second most common and the leading cause of death

Received November 30, 2019; accepted after revision April 30, 2020.

From the School of Computer Science and Engineering (R.H., B.Z., C.Z.), College of Literature and Journalism (C.Z.), Central South University, Changsha, Hunan, China; Departments of Neurology (L.Y.), and Radiology (Q.S., J.W.), Second Xiangya Hospital of Central South University, Changsha, Hunan, China; Department of Diagnostic Imaging (J.B., H.X.B.), Rhode Island Hospital, and Warren Alpert Medical School, Brown University (O.T.), Providence, Rhode Island; Department of Neurology (H.Z., L.T., B.X.), Xiangya Hospital of Central South University, Changsha, Hunan, China; Department of Radiology (R.Y.H.), Brigham and Women's Hospital, Boston, Massachusetts; Department of Radiology (K.C.), Athinoula A. Martinos Center for Biomedical Imaging, Massachusetts General Hospital, Harvard Medical School, Boston, Massachusetts; Department of Neurology (C.H.), Hunan Provincial People's Hospital, Changsha, Hunan, China; Department of Pathology (W.C.), Hunan Children's Hospital, Changsha, Hunan, China; and Mobile Health Ministry of Education-China Mobile Joint Laboratory (C.Z.), China.

This work was supported by National Natural Science Foundation of China grant under award No. 8181101287 to H. Bai; the National Natural Science Foundation of China (No. 61702559); the 111 project under grant No. B18059; the Planned Science and Technology Project of Hunan Province, China (No. 2017WK2074) to Chengzhang Zhu; the National Natural Science Foundation of China (81301988 to

from solid tumors.<sup>1,2</sup> Posterior fossa tumors make up a disproportionate portion of brain tumors in the pediatric population, accounting for 54%–70% of tumors compared with <20% in the adult population.<sup>3</sup> The most common subtypes of posterior fossa tumors among children are medulloblastoma (MB), pilocytic astrocytoma (PA), and ependymoma (EP).<sup>4,5</sup> Discrimination of these 3 malignancies is important due to the differing natural

Li Yang; the Natural Science Foundation of Hunan Province for Young Scientists, China (grant No. 2018JJ3709 to Li Yang) and the National Science and Technology Major Project (No. 2018AAA0102102) to Beijing Zou.

Please address correspondence to Chengzhang Zhu, MD, College of Literature and Journalism, Central South University, No. 932 South Lushan Road, Changsha, Hunan, 410083, China; e-mail: anandawork@126.com

Indicates open access to non-subscribers at [www.ajnr.org](http://www.ajnr.org)

Indicates article with supplemental on-line tables.

Indicates article with supplemental on-line photos.

<http://dx.doi.org/10.3174/ajnr.A6621>

histories and prognoses for each. Accurate preoperative diagnosis could also help in preoperative evaluation and guide surgical planning for patients with different types of tumors.<sup>5,6</sup> MR imaging review is essential for tumor diagnosis and evaluation. However, it is usually far from being a criterion standard, which is diagnosis by histology.

The rapid growth in the field of medical image analysis in the past decade has facilitated the development of radiomics, which converts digital images to mineable data via high-throughput extraction of a large number of quantitative features.<sup>7</sup> The radiomics model has the potential power to improve predictive performance<sup>8</sup> and has been used to improve the differentiation among different brain tumors such as glioblastoma and anaplastic oligodendroglioma,<sup>9</sup> and metastatic brain tumors.<sup>10</sup> However, there have been few studies exploring the classification of pediatric posterior fossa tumors using a radiomics analysis on clinical routine MR imaging.

Machine learning (ML) is a method of data analysis that automates analytic model building. It is a branch of artificial intelligence in which systems are designed to learn from data, identify patterns, and make decisions with minimal human intervention.<sup>11</sup> In recent years, machine learning approaches for radiomics feature selection have developed rapidly. However, few studies have compared these recently developed feature-selection methods and predictive modeling methods.<sup>12</sup> Therefore, selection of the most accurate ML pipeline often requires extensive manual testing by an expert in machine learning.

The Tree-Based Pipeline Optimization Tool (TPOT; <https://pypi.org/project/TPOT/>) is a specific open-source form of automated machine learning (autoML) that automatically chooses the most optimal machine learning pipeline without the need for human intervention.<sup>13,14</sup> TPOT has been benchmarked on many simulated and real-world supervised classification tasks.<sup>14</sup> However, performance of automated TPOT still needs to be proved in different types of data by comparison with manually optimized feature selection and classification.

The primary goal of our study was to investigate the value of autoML (TPOT) to differentiate the main types of pediatric posterior fossa tumors on routine MR imaging and to compare its performance with manual expert optimization and qualitative expert MR imaging review.

## **MATERIALS AND METHODS**

### **Patient Cohort**

All patients included were newly diagnosed with histologically confirmed MB, EP, or PA from 4 large academic hospitals in the Hunan Province in China from January 2013 to December 2018. The study was approved by the institutional review boards of all participating institutions. The inclusion criteria were the following: 1) pathologically confirmed MB, EP, or PA; 2) available preoperative MR imaging examination including a T1-weighted contrast-enhanced sequence, a T2-weighted sequence, and ADC maps; and 3) quality of the images adequate for analysis, without motion or artifacts. All patients included in the analysis did not undergo any treatment before MR imaging. Patients' age and sex were collected and incorporated into the radiomics analysis as clinical variables.

### **MR Imaging Acquisition**

The MR imaging was performed using 3T scanners (Magnetom Trio, Siemens,  $n = 168$  patients; Achieva, Philips Healthcare,  $n = 87$ ) or 1.5T scanners (Avanto, Siemens,  $n = 33$ ). The main MR imaging protocols across hospitals used in our study are listed in On-line Table 1. ADC images were calculated from acquired DWI with b-values of 0- and 1000-s/mm<sup>2</sup>.

### **Image Segmentation**

MR images of all patients were loaded into 3D Slicer software (Version 4.10; <http://www.slicer.org>), which was used as a user-driven manual active contour-segmentation tool to segment tumor volumes. ROIs were manually drawn section by section on the T2WI, T1WI contrast-enhanced sequence, and ADC images by 2 authors (H.Z., with 7 years of clinical experience in neuroradiology, and L.T., with 5 years of clinical experience in neuroradiology). The ROIs defined in our study include both the enhancing and nonenhancing components of tumor as well as peritumoral edema. On-line Figure 1 shows an example of ROI delineation on a T1WI contrast-enhanced sequence, T2WI, and ADC maps. The intra-class correlation coefficient value was used to assess interobserver reproducibility of generated masks.

### **Radiomics Feature Extraction**

Radiomics features were extracted from each patient's MR imaging for the T1WI contrast-enhanced sequence, T2WI, and ADC maps. For each image space, 79 nontexture (morphology and intensity-based) and 94 texture features were extracted according to the guidelines defined by the Image Biomarker Standardization Initiative.<sup>15</sup> Each of the 94 texture features was computed 32 times using all possible combinations of the following extraction parameters, a process known as "texture optimization":<sup>16</sup> 1) isotropic voxels of 1, 2, 3, and 4 mm; 2) a fixed bin number discretization algorithm, with and without equalization; and 3) the number of gray levels of 8, 16, 32, and 64 for a fixed bin number. A total of  $79 + 32 \times 94$  or 3087 radiomics features were thus computed in this study. All the features were normalized using unity-based normalization, and features from the T1WI contrast-enhanced sequence, T2WI, and ADC maps were combined into 1 dataset.

### **Radiomics Model Building and Analysis**

Before radiomics analysis, all included tumor cases were randomly divided into a training set (70% of cases) and testing set (30% of cases). All the radiomics features extracted above with clinical variables (age and sex) were incorporated to train multi-class models for MB, EP, and PA. Different binary models were trained for MBs versus non-MBs, EPs versus non-EPs, and PAs versus non-PAs. An automated optimized pipeline was computed on the dataset by TPOT, which chooses the most optimal machine learning pipeline for an inputted dataset through genetic programming.<sup>17</sup> The following settings were used in the optimization process: number of generations, 5; population size, 5; and 5-fold cross-validation on the training set. In this study, the TPOT pipeline was replicated 10 times to yield 10 different models for comparison. The model with the best performance was finally selected and tested on the testing set.

For the manual expert optimized pipeline, radiomics features were selected for training using 13 different feature-selection methods to reduce the dimensionality of the datasets. Ten machine learning classifiers were trained to yield diagnostic models. Details of the feature-selection methods and classifiers used are shown in On-line Table 2. Each classifier was trained on the training set 13 times using 13 different feature-selection methods and was validated through 5-fold cross-validation. Classifiers were trained on 10, 20, 50, and 100 selected features, and performances on the training set were recorded. The best-performing models on the training set were then tested on the final testing set. When there were multiple combinations with the same cross-validation results on the training set, the combination with the best performance on the testing set was selected. In addition to performance, the stability of classifiers was recorded. The relative SD for classifier stability was calculated. More details and the results of the stability calculations can be found in On-line Table 3. Figure 1 provides the workflow of the machine learning algorithms used in this study.

### Expert Evaluation

The final performance of the model on the test set was compared with 2 expert radiologists' interpretations: Q.S. and J.W. with 7 and 5 years of experience reading brain MR imaging, respectively. The experts were blinded to all clinical data and histopathologic information.

### Statistical Analysis

The following performance metrics were calculated for binary classification: area under receiver operating characteristic curve (AUC), accuracy, sensitivity, and specificity. For multiclass (3-way) classification, micro-averaged AUC, accuracy, sensitivity, and specificity were calculated. The micro-average aggregated the contributions of all classes to compute the average metric, which is more preferable when dealing with multiclass classification.<sup>18</sup> The 95% confidence intervals on accuracy, sensitivity, and specificity were calculated using the adjusted Wald method.<sup>19</sup> The *P* values were calculated using the binomial test. A *P* value < .05 was considered statistically significant.

### Code Availability

The implementation of the radiomics feature extraction was based on the "radiomics-develop" package from the Naqa Lab at McGill University.<sup>16</sup> This code is available for public use on GitHub at <https://github.com/mvallieres/radiomics-develop>. The implementation of the machine learning models was based on the scikit-learn package of Python at <https://github.com/scikit-learn/scikit-learn>. The Auto-ML script used the TPOT package from the Epistasis Lab.<sup>17</sup> This code is publicly available at <https://github.com/subhanik1999/Radiomics-ML>.

## RESULTS

### Patient Characteristics

A total of 288 patients with pediatric posterior fossa tumors (111 MBs, 70 EPs, and 107 PAs) were included in the study cohort. The mean age of all patients was 8.6 years, ranging from 0.25 to 18 years. The mean ages of patients with MB, EP, and PA were

9.0, 9.1, and 7.9 years, respectively (*P* = .291). There were 161 males and 127 females for the whole cohort. The sex ratio for each type of tumor (male/female) was 65:46, 36:34, and 60:47, respectively (*P* = .640).

### Agreement of Segmentation

For each case in the study, the average required time for segmentation was about 10 minutes. The average intraclass correlation coefficient between the 2 segmenters was 0.91 for T2WI, 0.92 for the T1WI contrast-enhanced sequence, and 0.86 for ADC.

### Multiclass Classification for 3 Tumors (MB versus EP versus PA)

For the TPOT pipeline, 10 separate models were generated for differentiation of the 3 tumor types. Overall, all 10 models showed a favorable micro-averaged AUC on the training set (On-line Table 4). Model 8 achieved the best performance with the highest micro-averaged AUC (0.93) among the 10 models. The parameters of all the TPOT models are described in detail in On-line Table 4. The top 20 important radiomics features are listed in On-line Table 5. In the testing cohort, the best model (model 8) achieved a micro-averaged AUC of 0.91 and an accuracy of 0.83 (95% CI, 0.72–0.90). The sensitivity and specificity of the diagnostic model for each type of tumor are shown in Table 1.

For manual expert optimization, micro-averaged AUC scores on the training set from each combination of feature-selection method and classifier are shown in On-line Fig 2. The combination of  $\chi^2$  score (CHSQ) as the feature-selection method and the FSL General Linear Model (GLM; <http://fsl.fmrib.ox.ac.uk/fsl/fslwiki/GLM>) as the classifier achieved the highest micro-averaged AUC of 0.93 on the training set. As the top-performing model, CHSQ + GLM was then tested on the final test set and achieved a test micro-averaged AUC of 0.92 and accuracy of 0.74 (95% CI, 0.62–0.83). The sensitivity and specificity of the diagnostic model for each type of tumor are shown in Table 1. The top 20 important radiomics features used by the CHSQ + GLM model are shown in On-line Table 6.

### Binary Classification

For the TPOT pipeline, 30 separate models were generated for the binary classification of MB versus non-MB, EP versus non-EP, and PA versus non-PA (10 models in each classification).

The performances of all the models on the training set are shown in On-line Table 7. Among all models, model 9 for MB versus non-MB, model 8 for EP versus non-EP, and model 7 for PA versus non-PA achieved the highest AUCs (0.97, 0.84, and 0.96 respectively). The parameters of all the TPOT models are described in detail in On-line Table 7. Then the best models were tested on the test set, and performances were as follows: For all 3 binary classifications, the AUC ranged from 0.84 to 0.94, accuracy ranged from 0.80 to 0.88, sensitivity ranged from 0.52 to 0.95, and specificity ranged from 0.81 to 0.93. The test performances for all 3 models are reported in detail in Table 2.

For manual expert optimization, the AUC scores from each combination of feature-selection method and classifier are shown in On-line Figs 3–5. The combinations of feature-

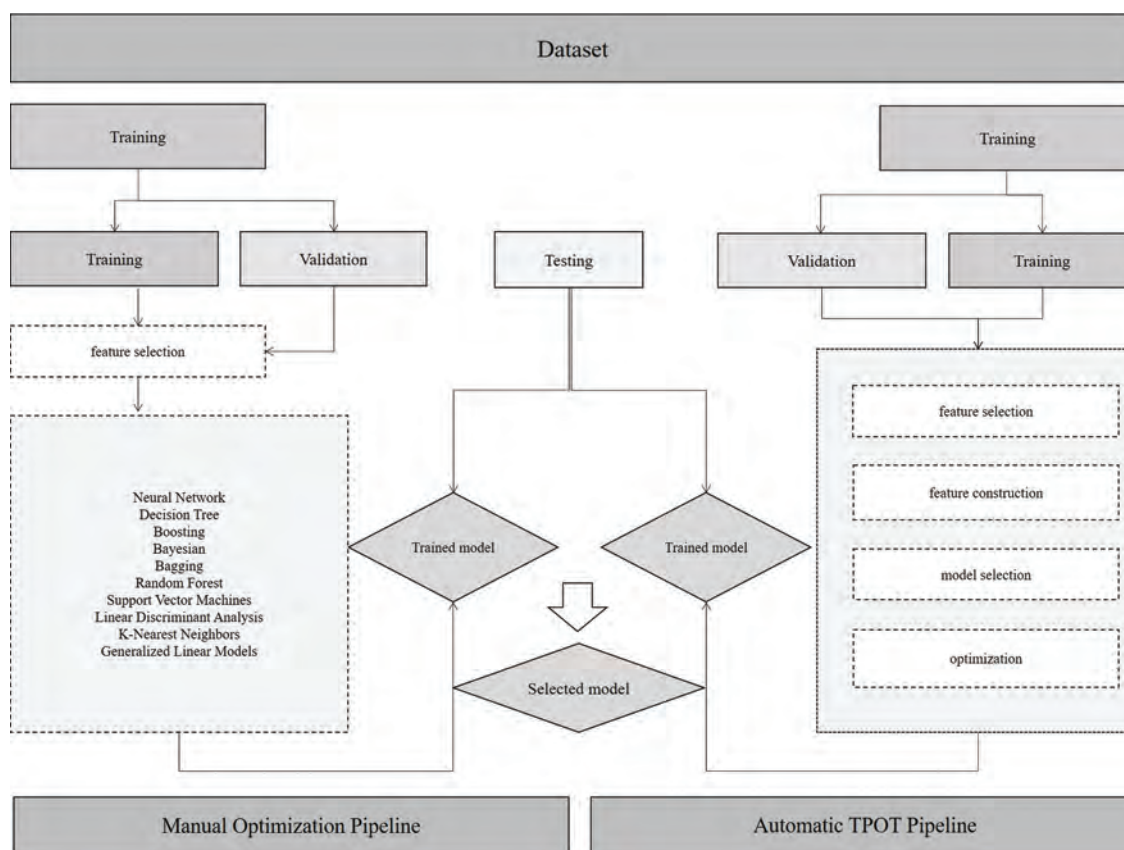


FIG 1. Machine learning workflow.

Table 1: Performance of multiclass classification across all models and experts in test set

Method	Micro-Averaged AUC	Accuracy (95% CI)	Sensitivity (95% CI)	Specificity (95% CI)
Radiomics (by TPOT)	0.91	0.83 (0.72–0.90)	MB: 0.87 (0.67–0.96) EP: 0.67 (0.46–0.83) PA: 0.95 (0.76–1.00)	MB: 0.91 (0.78–0.97) EP: 0.98 (0.88–1.00) PA: 0.86 (0.72–0.94)
Radiomics (by CHSQ and GLM)	0.92	0.74 (0.62–0.83)	MB: 0.96 (0.77–1.00) EP: 0.33 (0.17–0.55) PA: 0.91 (0.71–0.99)	MB: 0.84 (0.70–0.92) EP: 0.93 (0.81–0.98) PA: 0.84 (0.70–0.92)
Expert 1	NA	0.58 (0.46–0.69)	MB: 0.65 (0.45–0.81) EP: 0.57 (0.36–0.75) PA: 0.50 (0.31–0.69)	MB: 0.67 (0.52–0.79) EP: 0.82 (0.68–0.91) PA: 0.86 (0.72–0.94)
Expert 2	NA	0.50 (0.38–0.62)	MB: 0.57 (0.37–0.75) EP: 0.43 (0.25–0.64) PA: 0.50 (0.31–0.69)	MB: 0.66 (0.51–0.77) EP: 0.80 (0.66–0.89) PA: 0.77 (0.63–0.87)

Note:—NA indicates not applicable.

selection method and classifier that achieved the highest AUCs on the training set for the 3 different binary classifications are as follows: Relief + support vector machine (AUC = 0.97) for MB versus non-MB, joint mutual information + neural network (AUC = 0.79) for EP versus non-EP, and CHSQ + GLM (AUC = 0.96) for PA versus non-PA. The models Relief + support vector machine, joint mutual information + neural network, and CHSQ + GLM with the best performance on the training set above were then tested on the final testing set. For all 3 binary classifications and their optimal feature-selection method-classifier combination, the AUC ranged from 0.70 to 0.98, accuracy ranged from 0.71 to

0.91, sensitivity ranged from 0.19 to 0.96, and specificity ranged from 0.88 to 0.95. The test performances for all 3 models are reported in detail in Table 2.

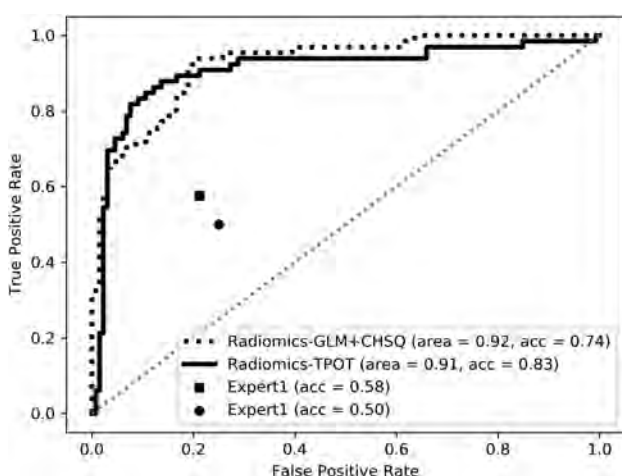
### Expert Evaluation

For multiclass classification, expert 1 had an overall test accuracy of 0.58 (95% CI, 0.46–0.69) with sensitivities of 0.50–0.65 and specificities of 0.67–0.86 across the 3 tumor types. Expert 2 achieved an overall test accuracy of 0.50 (95% CI, 0.38–0.62) along with sensitivities of 0.43–0.57 and specificities of 0.66–0.80 across the 3 tumor types (Table 1). For binary classification, expert 1 achieved a test accuracy of 0.67–0.74 and expert 2 achieved a test accuracy



**Table 2: Performance of binary classification across all models and experts in the test set**

Method	AUC	Accuracy (95% CI)	Sensitivity (95% CI)	Specificity (95% CI)
Radiomics (by TPOT)				
MB vs non-MB	0.94	0.85 (0.74–0.92)	0.91 (0.72–0.99)	0.81 (0.67–0.90)
EP vs non-EP	0.84	0.80 (0.69–0.88)	0.52 (0.32–0.71)	0.93 (0.81–0.98)
PA vs non-PA	0.94	0.88 (0.78–0.94)	0.95 (0.76–1.00)	0.84 (0.70–0.92)
Radiomics (by manual optimized pipeline)				
MB vs non-MB	0.98	0.91 (0.81–0.96)	0.96 (0.78–1.00)	0.88 (0.75–0.95)
EP vs non-EP	0.70	0.71 (0.59–0.81)	0.19 (0.07–0.40)	0.95 (0.83–0.99)
PA vs non-PA	0.93	0.86 (0.75–0.93)	0.77 (0.56–0.90)	0.91 (0.78–0.97)
Expert 1				
MB vs non-MB	NA	0.67 (0.55–0.77)	0.65 (0.45–0.81)	0.67 (0.52–0.79)
EP vs non-EP	NA	0.74 (0.60–0.82)	0.57 (0.36–0.75)	0.82 (0.68–0.91)
PA vs non-PA	NA	0.74 (0.62–0.83)	0.50 (0.31–0.69)	0.86 (0.72–0.94)
Expert 2				
MB vs non-MB	NA	0.64 (0.52–0.75)	0.57 (0.37–0.75)	0.66 (0.51–0.77)
EP vs non-EP	NA	0.68 (0.54–0.79)	0.43 (0.25–0.64)	0.80 (0.66–0.89)
PA vs non-PA	NA	0.68 (0.56–0.78)	0.50 (0.31–0.69)	0.77 (0.63–0.87)

**FIG 2.** The receiver operating characteristic curves of the radiomic models compared with expert MR imaging evaluations in multiclass classification. Acc indicates accuracy.

of 0.64–0.68 across the 3 binary classifications. The sensitivity and specificity of each group are shown in Table 2.

### Comparison of Radiomics Model Performance with Expert Evaluation

For multiclass classification, the TPOT model achieved significantly higher test accuracy compared with average expert MR imaging review (accuracy, 0.83 versus 0.54;  $P < .001$ ). The TPOT model also had higher accuracy than the CHSQ + GLM model by the manual expert optimized pipeline (accuracy, 0.83 versus 0.74), but this difference was not statistically significant ( $P = .160$ ). For binary classification, the TPOT models shared similar performance with the models by manual expert optimized pipeline in the classification of MB versus non-MB (accuracy, 0.85 versus 0.91;  $P = .247$ ), EP versus non-EP (accuracy, 0.80 versus 0.71;  $P = .333$ ), and PA versus non-PA (accuracy, 0.88 versus 0.86;  $P = .385$ ). The TPOT models outperformed average expert MR imaging review in the classification of MB versus non-MB (accuracy, 0.85 versus 0.66;  $P < .001$ ), EP versus non-EP (accuracy, 0.80 versus 0.71;  $P = .177$ ), and PA versus non-PA (accuracy, 0.88 versus 0.71;  $P = .002$ ). The receiver operating characteristic curves of all radiomics models compared with expert

evaluations are shown in Figs 2 and 3). On-line Figure 6 depicts examples of agreement or disagreement between the TPOT model and expert review in multiclass classification of pediatric posterior fossa tumors.

### DISCUSSION

Qualitative MR imaging review is critical for tumor diagnosis and evaluation. However, it often offers limited information regarding tumor type because pediatric posterior fossa tumors share similar appearances across conventional modalities.<sup>20,21</sup> Many studies have suggested that ADC maps may be accurate in the differentiation of these tumors. Parameters such as mean ADC, minimal ADC, and tumor/normal ADC ratio were studied and used as thresholds for discrimination.<sup>22–26</sup> However, studies have shown overlap of ADC values among the different posterior fossa tumor types.<sup>27,28</sup> Several studies have also explored the integration of other advanced MR technologies, including MR spectroscopy and MR perfusion. However, these advanced MR imaging modalities are not used on a routine basis and vary in performance when discriminating the pediatric posterior fossa tumors.<sup>2,21</sup>

In a previous retrospective study of 40 pediatric posterior fossa tumors (17 MBs, 16 PAs, and 7 EPs) by Rodriguez et al,<sup>29</sup> models using support vector machine–based classifiers and ADC histogram features were trained and achieved average correct classifications of 95.8%, 96.9%, and 94.3% on MB, PA, and EP, respectively. The subsequent joint classifier for 3 tumors achieved correct classification of 91.4%. However, a major limitation of this study is the small data size used for analysis. Despite the good performance in the training set, the final models were not tested on a separate dataset. Furthermore, the model performance can vary when using different classifiers during the process. In this study, the authors tested only 1 classifier (support vector machine), which may result in bias and the possibility of missing a model with better performance.

In our study, 288 patients with the most common pediatric posterior fossa tumor subtypes were included, and autoML via TPOT was used to train the diagnostic models based on the T1WI contrast-enhanced sequence, T2WI, and ADC maps. We also compared the models by the automated TPOT pipeline with models by the manual expert optimized pipeline selected by the training

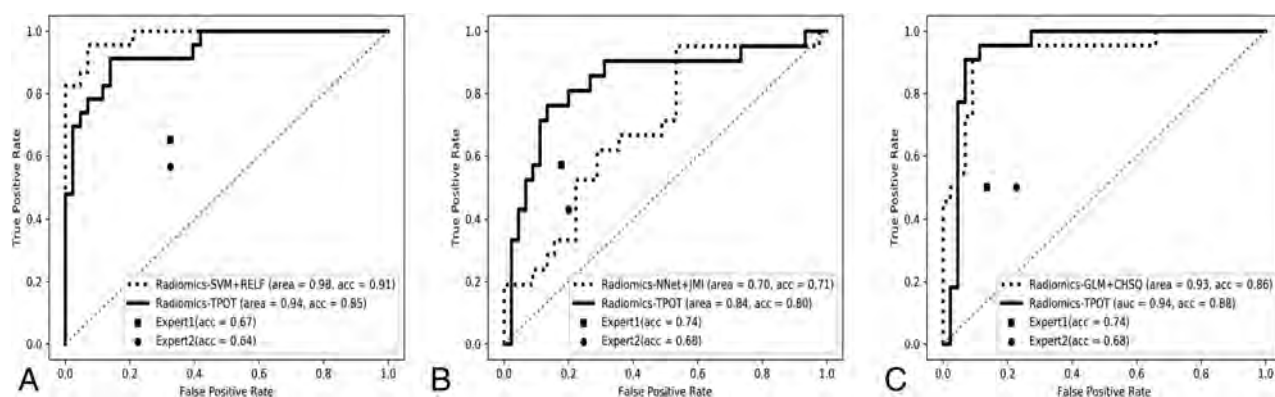


**FIG 3.** The receiver operating characteristic curves of the radiomic models compared with expert MR imaging evaluations in the binary classification for medulloblastoma versus nonmedulloblastoma (A), ependymoma versus nonependymoma (B), and pilocytic astrocytoma versus non-pilocytic astrocytoma (C). RELF indicates Relief; acc, accuracy; SVM, support vector machine; Nnet, neural network; JMI, joint mutual information.

models with different combinations of 13 different feature-selection methods and 10 classifiers. Both pipeline-generation methods were trained and then tested on separate data. Overall, radiomics models based on the TPOT pipeline outperformed MR imaging review by qualitative experts. Although the difference is not statistically significant, the TPOT model achieved better performance than models built by the manual expert optimized pipeline. TPOT has delivered a promising predictive performance in many other studies, including genomics applications<sup>17</sup> and clinical metabolic profiling,<sup>30</sup> and was found to be quite accurate in predicting H3 K27M mutation in gliomas, with accuracy ranging from 0.60 to 0.84 in the testing cohort.<sup>31</sup> In contrast to standard manual ML analysis, TPOT evaluates the complete pipelines of feature selection and classification on the basis of their cross-validated score (mean squared error or balanced accuracy) in addition to model selection and hyperparameter optimization.<sup>14</sup> The automatic TPOT is a valuable tool for construction of an optimal radiomics model without the need for extensive manual testing by experts in ML. Given no prior knowledge about a problem, TPOT frequently outperforms standard manual ML analyses.<sup>17,32</sup>

During model construction, a well-known issue with regard to AutoML is “overfitting,” in which improper tuning during model selection occurs.<sup>14</sup> AutoML is easily affected by the data size; therefore, a small data size could result in overfitting. In our study, 288 samples were included to avoid the issue of high variance. Another issue is data imbalance, which can lead to a biased analysis and results for machine learning. Our study included relatively balanced data from 3 groups (111 versus 70 versus 107) and thus reduced the effect of this issue.

Despite the robustness of these results, the classification scheme in the present study does not obviate tumor diagnosis by histopathology, the criterion standard. Histopathology is needed for a truly confirmatory diagnosis, offers the opportunity to profile nontumor cells in the tumor mass that play an important role in the pathogenesis of these malignancies,<sup>33</sup> and classifies tumors into molecular subgroups that are not appreciated by imaging. In an era of personalized medicine and therapeutic approaches like immunotherapy, these factors are especially important. However, we anticipate that the MR imaging-based classification scheme of this study may improve clinical care for pediatric posterior fossa

tumors in several potential ways. First, an initial imaging-based classification may function as a noninvasive method to plan a surgical approach and resection extent, even before the invasive biopsy required for histopathology has occurred.<sup>29</sup> Second, an earlier indication of a pediatric patient’s potential tumor subtype may expedite the planning of any potential neoadjuvant therapy.<sup>34</sup> Third, the imaging features identified herein may complement, rather than replace, histopathology in the case of diagnosing pediatric fossa tumors with more complex histopathologic features.

There are several possible improvements to our study. First, there can be selection bias for our study because the patients were identified via a search of the pathology data base. Second, future studies can include advanced imaging modalities such as MR spectroscopy and MR perfusion, which may further improve model performance. However, adding these advanced MR images is also a limitation in that these sequences may not be available at every institution. Third, the criterion standard for comparisons was the diagnosis indicated on the final pathology report. Consensus reads by multiple pathologists were not performed due to challenges, including resource constraints and the multi-institutional nature of the study dataset. In addition, we were unable to analyze less frequent pediatric posterior fossa tumors such as atypical teratoid/rhabdoid tumor, hemangioblastoma, and diffuse midline gliomas due to their low sample size in our study cohort and the aforementioned risk of model overfitting. A similar methodology to the present study and a larger multi-institutional cohort may facilitate the future incorporation of these subtypes into our MR imaging-based classification schema. Finally, although there is a good likelihood of achieving greater performance by experts with Certificates of Added Qualification in pediatric neuroradiology, this comparison was unfortunately unable to be facilitated in the present study due to differences in standard practices around the world. As a point of reference, earlier studies have documented human accuracy of pediatric brain tumor classification as approximately between 70% and 80% by pediatric neuroradiologists with Certificates of Added Qualification.<sup>35,36</sup>

## CONCLUSIONS

AutoML of TPOT based on conventional MR imaging can classify pediatric posterior fossa tumors with high accuracy











compared with the manual expert optimized pipeline and expert radiologists.

Disclosures: Ken Chang—*RELATED: Grant:* National Institutes of Health, *Comments:* Research reported in this publication was supported by a training grant from the National Institute of Biomedical Imaging and Bioengineering of the National Institutes of Health under award number 5T32EB1680 and by the National Cancer Institute of the National Institutes of Health under award No. F30CA239407 to K. Chang. Raymond Y. Huang—*UNRELATED: Grants/Grants Pending:* research grant from Agios Pharmaceuticals.\* Li Yang—*RELATED: Grant:* Natural Science Foundation of China/Natural Science Foundation of Hunan Province for Young Scientists, China, *Comments:* This funding came from a government granting agency.\* \*Money paid to the institution.

## REFERENCES

- Curtin SC, Miniño AM, Anderson RN. National Center for Health Statistics. **Declines in cancer death rates among children and adolescents in the United States, 1999–2014.** NCHS data brief, no 257, Sept 2016. <https://www.cdc.gov/nchs/products/databriefs/db257.htm>. Accessed March 21, 2020
- Brandão LA, Poussaint TY. **Posterior fossa tumors.** *Neuroimaging Clin N Am* 2017;27:1–37 CrossRef Medline
- O'Brien D, Caird J, Kennedy M, et al. **Posterior fossa tumours in childhood: evaluation of presenting clinical features.** *Ir Med J* 2001;94:52–53 Medline
- Prasad KS, Ravi D, Pallikonda V, et al. **Clinicopathological study of pediatric posterior fossa tumors.** *J Pediatr Neurosci* 2017;12:245–50 CrossRef Medline
- Bidiwala S, Pittman T. **Neural network classification of pediatric posterior fossa tumors using clinical and imaging data.** *Pediatr Neurosurg* 2004;40:8–15 CrossRef Medline
- Becker LE. **Pathology of pediatric brain tumors.** *Neuroimaging Clin N Am* 1999;9:671–90 Medline
- Rizzo S, Botta F, Raimondi S, et al. **Radiomics: the facts and the challenges of image analysis.** *Eur Radiol Exp* 2018;2:36 CrossRef Medline
- Gillies RJ, Kinahan PE, Hricak H. **Radiomics: images are more than pictures, they are data.** *Radiology* 2016;278:563–77 CrossRef Medline
- Fan Y, Chen C, Zhao F, et al. **Radiomics-based machine learning technology enables better differentiation between glioblastoma and anaplastic oligodendroglioma.** *Front Oncol* 2019;9:1164 CrossRef Medline
- Chen C, Ou X, Wang J, et al. **Radiomics-based machine learning in differentiation between glioblastoma and metastatic brain tumors.** *Front Oncol* 2019;9: 806 CrossRef Medline
- Sidey-Gibbons JA, Sidey-Gibbons CJ. **Machine learning in medicine: a practical introduction.** *BMC Med Res Methodol* 2019;19:64 CrossRef Medline
- Parmar C, Grossmann P, Bussink J, et al. **Machine learning methods for quantitative radiomic biomarkers.** *Sci Rep* 2015;5:13087 CrossRef Medline
- Olson R, Urbanowicz R, Andrews P, et al. **Automating biomedical data science through tree-based pipeline optimization.** In: *Proceedings of the 19th European Conference, EvoApplications 2016*, Porto, Portugal; March 30 to April 1, 2016
- Le TT, Fu W, Moore JH. **Scaling tree-based automated machine learning to biomedical big data with a feature set selector.** *Bioinformatics* 2020;36:250–56 CrossRef Medline
- Zwanenburg A, Vallieres M, Abdalah MA, et al. **The image biomarker standardization initiative: standardized quantitative radiomics for high-throughput image-based phenotyping.** *Radiology* 2020;295:328–38 CrossRef Medline
- Vallieres M, Kay-Rivest E, Perrin LJ, et al. **Radiomics strategies for risk assessment of tumour failure in head-and-neck cancer.** *Sci Rep* 2017;7:10117 CrossRef Medline
- Olson RS, Urbanowicz RJ, Andrews PC, et al. **Automating biomedical data science through tree-based pipeline optimization.** In: *Proceedings of the 19th European Conference, EvoApplications 2016*, Porto, Portugal; March 30 to April 1, 2016
- Van Asch V. **Macro-and micro-averaged evaluation measures [BASIC DRAFT].** <https://pdfs.semanticscholar.org/1d10/6a2730801b6210a67f7622e4d192bb309303.pdf>. Accessed March 21, 2020
- Agresti A, Coull BA. **Approximate is better than “exact” for interval estimation of binomial proportions.** *The American Statistician* 1998;52:119–26 CrossRef
- Poretti A, Meoded A, Huisman TA. **Neuroimaging of pediatric posterior fossa tumors including review of the literature.** *J Magn Reson Imaging* 2012;35:32–47 CrossRef Medline
- Kerleroux B, Cottier JP, Janot K, et al. **Posterior fossa tumors in children: radiological tips & tricks in the age of genomic tumor classification and advance MR technology.** *J Neuroradiol* 2020;47:46–53 CrossRef Medline
- Pierce T, Kranz PG, Roth C, et al. **Use of apparent diffusion coefficient values for diagnosis of pediatric posterior fossa tumors.** *Neuroradiol J* 2014;27:233–44 CrossRef Medline
- Zitouni S, Koc G, Doganay S, et al. **Apparent diffusion coefficient in differentiation of pediatric posterior fossa tumors.** *Jpn J Radiol* 2017;35:448–53 CrossRef Medline
- Rumboldt Z, Camacho DL, Lake D, et al. **Apparent diffusion coefficients for differentiation of cerebellar tumors in children.** *AJNR Am J Neuroradiol* 2006;27:1362–69 Medline
- Gimi B, Cederberg K, Derinkuyu B, et al. **Utility of apparent diffusion coefficient ratios in distinguishing common pediatric cerebellar tumors.** *Acad Radiol* 2012;19:794–800 CrossRef Medline
- Koral K, Alford R, Choudhury N, et al. **Applicability of apparent diffusion coefficient ratios in preoperative diagnosis of common pediatric cerebellar tumors across two institutions.** *Neuroradiology* 2014;56:781–88 CrossRef Medline
- Jaremko JL, Jans LB, Coleman LT, et al. **Value and limitations of diffusion-weighted imaging in grading and diagnosis of pediatric posterior fossa tumors.** *AJNR Am J Neuroradiol* 2010;31:1613–16 CrossRef Medline
- Schneider JF, Confort-Gouny S, Viola A, et al. **Multiparametric differentiation of posterior fossa tumors in children using diffusion-weighted imaging and short echo-time 1H-MR spectroscopy.** *J Magn Reson Imaging* 2007;26:1390–98 CrossRef Medline
- Rodriguez Gutierrez D, Awwad A, Meijer L, et al. **Metrics and textural features of MRI diffusion to improve classification of pediatric posterior fossa tumors.** *AJNR Am J Neuroradiol* 2014;35:1009–15 CrossRef Medline
- Orlenko A, Moore JH, Orzechowski P, et al. **Considerations for automated machine learning in clinical metabolic profiling: altered homocysteine plasma concentration associated with metformin exposure.** *Pac Symp Biocomput* 2018;23: 460–71 Medline
- Su X, Chen N, Sun H, et al. **Automated machine learning based on radiomics features predicts H3 K27M mutation in midline gliomas of the brain.** *Neuro Oncol* 2020;22:393–401 CrossRef Medline
- Olson RS, Cava W, Mustahsan Z, et al. **Data-driven advice for applying machine learning to bioinformatics problems.** *Pac Symp Biocomput* 2018;23: 192–203 Medline
- Quail DF, Joyce JA. **The microenvironmental landscape of brain tumors.** *Cancer Cell* 2017;31:326–41 CrossRef Medline
- Massimino M, Cefalo G, Riva D, et al. **Long-term results of combined preradiation chemotherapy and age-tailored radiotherapy doses for childhood medulloblastoma.** *J Neurooncol* 2012;108:163–71 CrossRef Medline
- Manias KA, Gill SK, MacPherson L, et al. **Diagnostic accuracy and added value of qualitative radiological review of 1H-magnetic resonance spectroscopy in evaluation of childhood brain tumors.** *Neurooncol Pract* 2019;6:428–37 CrossRef Medline
- Manias K, Gill SK, Zarinabad N, et al. **Evaluation of the added value of 1H-magnetic resonance spectroscopy for the diagnosis of pediatric brain lesions in clinical practice.** *Neurooncol Pract* 2018;5:18–27 CrossRef Medline

# Intra-Arterial Chemotherapy for Retinoblastoma in Infants $\leq 10$ kg: 74 Treated Eyes with 222 IAC Sessions

 A. Sweid,  B. Hammoud,  J.H. Weinberg,  P. Texakalidis,  V. Xu,  K. Shivashankar,  M.P. Baldassari,  S. Das,  S. Ramesh,  S. Tjoumakaris,  C.L. Shields,  D. Ancona-Lezama,  L.-A.S. Lim,  L.A. Dalvin, and  P. Jabbour



## ABSTRACT

**BACKGROUND AND PURPOSE:** Intra-arterial chemotherapy for retinoblastoma has dramatically altered the natural history of the disease. The remarkable outcomes associated with a high safety profile have pushed the envelope to offer treatment for patients weighing  $\leq 10$  kg. The purpose was to determine the efficacy and safety of IAC infusions performed in infants weighing  $\leq 10$  kg with intraocular retinoblastoma.

**MATERIALS AND METHODS:** A retrospective chart review was performed for patients diagnosed with retinoblastoma and managed with intra-arterial chemotherapy.

**RESULTS:** The total study cohort included 207 retinoblastoma tumors of 207 eyes in 196 consecutive patients who underwent 658 intra-arterial chemotherapy infusions overall. Of these, patient weights were  $\leq 10$  kg in 69 (35.2%) and  $>10$  kg in 127 (64.8%) patients. Comparison ( $\leq 10$  kg versus  $>10$  kg) revealed that the total number of intra-arterial chemotherapy infusions was 222 versus 436. Periprocedural complications were not significantly different (2 [0.9%] versus 2 [0.5%];  $P = .49$ ). Cumulative radiation exposure per eye was significantly lower in infants weighing  $\leq 10$  kg (5.0 Gy $^2$  versus 7.7 Gy $^2$ ;  $P = .01$ ). Patients weighing  $\leq 10$  kg had a greater frequency of complete tumor regression (82.6% versus 60.9%;  $P = .02$ ). Mean fluoroscopy time was not significantly different (7.5 versus 7.2;  $P = .71$ ). There was a significant difference in the frequency of enucleation (16 [21.6%] versus 52 [39.1%];  $P = .01$ ). Patients weighing  $\leq 10$  kg had greater number of aborted procedures (12 [5.4%] versus 7 [1.6%];  $P = .01$ ). On multivariate analysis, weight  $\leq 10$  kg was not an independent predictor of complications or procedure failure.

**CONCLUSIONS:** Intra-arterial chemotherapy in patients weighing  $\leq 10$  kg is a safe and effective treatment.

**ABBREVIATIONS:** IAC = intra-arterial chemotherapy; ICRB = International Classification of Retinoblastoma; OA = ophthalmic artery; Rb = retinoblastoma

Intra-arterial chemotherapy (IAC) for retinoblastoma (Rb) has dramatically altered the natural history of the disease. Cure rates, globe salvage, and vision preservation have dramatically increased.


<sup>1–10</sup> Yamane et al<sup>11</sup> in 1989 described an IAC delivery technique termed selective ophthalmic artery infusion using a catheter-based approach with an inflated balloon that occludes the supraclinoid internal carotid artery segment distal to the ostium of the ophthalmic artery (OA). Then Abramson et al<sup>12</sup> in 2008 refined the Japanese technique in which the ophthalmic artery was superselectively catheterized. Since then several specialized centers have incorporated ophthalmic artery catheterization into the treatment paradigm with the advantage of delivering a high drug concentration to tumoral tissue while maintaining low systemic concentration, thereby avoiding systemic complications.<sup>12</sup> Moreover, treatment can be delivered in 1 day, and 2–3 sessions can be sufficient for tumor control.<sup>4,13,14</sup> We have previously reported our 5-year experience with IAC.<sup>7,15,16</sup> The remarkable outcomes associated with an acceptable safety profile—despite the risks (retinal toxicity)—and advancement in catheter techniques have pushed the envelope to offer treatment for patients weighing  $\leq 10$  kg. Weight  $<10$  kg or age younger than 3 months have previously been exclusion criteria because of the perceived risk of femoral artery access

Received November 30, 2019; accepted after revision April 14, 2020.

From the Department of Neurosurgery (A.S., J.H.W., V.X., K.S., M.P.B., S.D., S.R., S.T., P.J.), Thomas Jefferson University and Jefferson Hospital for Neuroscience, Philadelphia, Pennsylvania; Department of Pediatric Endocrinology (B.H.), Children Hospital of Philadelphia, Philadelphia, Pennsylvania; Department of Neurosurgery (P.T.), Emory University School of Medicine, Atlanta, Georgia; Ocular Oncology Service (C.L.S., D.A.-L., L.-A.S.L., L.A.D.), Wills Eye Hospital, Thomas Jefferson University, Philadelphia, Pennsylvania; Ocular Oncology Service (D.A.-L.), Instituto de Oftalmología y Ciencias Visuales, Tecnológico de Monterrey, Monterrey, Mexico; and Department of Ophthalmology (L.A.D.), Mayo Clinic, Rochester, Minnesota.

Data sharing statement: The relevant anonymized patient-level data are available on reasonable request from the authors.

Please address correspondence to Pascal Jabbour, MD, Professor of Neurological Surgery, Chief Division of Neurovascular Surgery and Endovascular Neurosurgery, Thomas Jefferson University Hospital, 901 Walnut St, 3rd Floor, Philadelphia, PA 19107; e-mail: pascal.jabbour@jefferson.edu; @PascalJabbourMD

 Indicates article with supplemental on-line table.

<http://dx.doi.org/10.3174/ajnr.A6590>



complications.<sup>8,12</sup> However, a case report and a small series have reported successful IAC delivery for infants weighing  $\leq 10$  kg.<sup>17,18</sup> We herein describe our efficacy and safety outcomes in a large series of IAC infusions performed in infants weighing  $\leq 10$  kg.

## MATERIALS AND METHODS

### Cohort Creation

The study subjects included patients with unilateral or bilateral intraocular Rb undergoing IAC from February 2008 to June 2016. The population was dichotomized according to weight,  $\leq 10$  kg or  $> 10$  kg. The study protocol was reviewed and approved by the institutional review board. Informed consent was waived because of the retrospective design of this study. Ocular exclusion criteria were vitreous hemorrhage, secondary glaucoma, and extension of tumor into the optic nerve, uvea, anterior segment, or extrascleral compartments. Systemic exclusion criteria were history of blood dyscrasia or thrombotic events.

The patient data were retrospectively reviewed for demographic data, including age (months), sex (male, female), race (white, African American, Hispanic, Asian, Arab), hereditary pattern (sporadic, familial), and laterality (unilateral, bilateral). The presenting symptoms and prior treatment details were recorded. Tumor features included the largest basal diameter, thickness, and location and the presence of subretinal seeds and vitreous seeds. The IAC was delivered either as primary therapy in patients who had no previous treatment or as secondary therapy after failure of previous other types of treatment. Treatment-naïve eyes were classified according to the International Classification of Retinoblastoma (ICRB) (Philadelphia) as group A, B, C, D, or E.

### Treatment Protocol

Parents and patients were informed of the risks of ophthalmic artery cannulation, and procedure consents were obtained.

Each patient was examined initially in the office and then under anesthesia with large fundus drawings, photographic documentation, and fluorescein angiographic analysis of all tumors and features in each eye. The decision for IAC was made in consultation with members of the Ocular Oncology Service, the Department of Neurosurgery, and the Department of Pediatric Oncology. Family history and medical history, particularly for thrombotic events, were obtained. This information was used to assess the need for screening tests looking for an increased risk of thrombosis, including factor V Leiden mutation, methylenetetrahydrofolate reductase mutation, and prothrombin 20–21–0 mutation.

At each 4-week follow-up, a detailed ophthalmic examination was performed by the treating ocular oncologist with photographic, fluorescein angiographic, and ultrasonographic documentation. The planned protocol was to deliver 3 sessions of IAC and after that judge whether further sessions would be necessary. Per protocol, adjunctive therapy, including laser photocoagulation, cryotherapy, plaque radiation therapy, or external-beam radiation therapy, was not delivered. If there was documented tumor recurrence or resistance, then these methods were potentially used.

During follow-up, each eye was assessed for regression of the solid tumor, subretinal seeds, vitreous seeds, and subretinal fluid. Tumor recurrence was documented. Other subsequent ocular treatment modalities were recorded.

### Technical Procedure

After a parent or legal guardian consent, the IAC catheterization procedure was performed in the interventional neuroradiology suite under general anesthesia and continuous electro-physiological monitoring as an outpatient procedure. Anticoagulation with intravenous heparin (75 IU/kg) was delivered. All surfaces in the interventional neuroradiology suite in contact with the patient and all catheters were covered with plastic wrap, avoiding the use of cotton fiber material, including linen towels and patient draping material. After careful preparation of the puncture site in the groin, a 4F micropuncture needle was inserted into the femoral artery, and heparin was administered with a target activated clotting time between 200 and 300 seconds. Under fluoroscopic guidance, a Marathon microcatheter (Medtronic) and a Synchro 10 micro-wire (Stryker) were navigated all the way up from the groin to the ostium of the OA. The tip of the microcatheter was allowed to hook the ostium of the OA, without the aid of the microwire. A superselective injection was subsequently performed to confirm the position of the microcatheter and ascertain the lack of reflux into the internal carotid artery. If the Marathon catheter did not track, then a Prowler-10 microcatheter (Codman & Shurtleff) was used. If the latter approach was unsuccessful or if the OA was occluded, catheterization of the OA was alternatively performed through the middle meningeal artery collateral to the OA or by using the balloon-assisted technique. The balloon-assisted technique described by Yamane et al<sup>11</sup> was used when there was a stenosis at the ostium and no good middle meningeal collateral.

Chemotherapeutic medications included melphalan and topotecan. The melphalan dose was 3, 5, or 7.5 mg, increasing with patient age and tumor size, without dosing higher than dose limit, which is 0.5 mg/kg. The topotecan dose was 1 mg. All patients received melphalan, and those with more extensive disease, particularly with vitreous seeding, were given additional topotecan. The microcatheter was subsequently flushed with saline to avoid crystallization of the agent in the OA, and angiograms were obtained to rule out thromboembolic complications. Repeat angiography through the microcatheter was performed immediately after the procedure to ensure the patency of the vessels, and the microcatheter was removed. At the end of the procedure, the heparin was reversed with intravenous protamine, and hemostasis was achieved with manual compression of the femoral artery done only by the senior author. The child was monitored for 6 hours before discharge. Oral aspirin (40 mg) was advised for 2 weeks, and topical ophthalmic application of antibiotic-steroid ointment and cycloplegic eye drops was recommended for 2 weeks. Each session of IAC was planned at a 4-week interval. A blood hemogram was performed at 2 weeks and 4 weeks after the procedure.

### Outcome Variables

The population was divided into  $\leq 10$ -kg and  $> 10$ -kg cohorts. The primary outcomes analyzed were the frequency of periprocedural complications related to the IAC, complete tumor regression, and globe enucleation. Secondary outcomes assessed were the duration of the procedure, fluoroscopy time, mean radiation exposure per eye, cumulative radiation exposure, and procedure termination frequency. Globe preservation was considered as a favorable outcome.

**Table 1: Intra-arterial chemotherapy for retinoblastoma in infants weighing  $\leq 10$  kg (74 treated eyes with 222 IAC sessions)—patient demographics**

Variable	Weight $\leq 10$ kg ( <i>n</i> = 74 Eyes; 35.7% of 69 Patients)	Weight $>10$ kg ( <i>n</i> = 133 Eyes; 64.2% of 127 Patients)	<i>P</i> Value	Total ( <i>n</i> = 207) Eyes (%) of 196 Patients
Age at presentation (months) ( <i>n</i> = 196), mean (median, range)	10 (9, 1–33)	32 (23, 4–387)	.01	24 (15, 1–387)
Age at time of first IAC (months) ( <i>n</i> = 196), mean (median, range)	11 (10, 3–30)	35 (25, 4–387)	.01	24 (15, 1–387)
Weight at first IAC (kg) ( <i>n</i> = 196), mean (median, range)	8.4 (8.9, 3.1–10.4)	16.4 (13.3, 10.3–209)	.01	13.5 (11.5, 3.1–209)
Sex ( <i>n</i> = 196)				
Male	36 (52.2)	68 (53.5)	.85	104 (53.1)
Female	33 (47.8)	59 (46.5)		92 (47.8)
Race ( <i>n</i> = 196)				
White	37 (53.6)	59 (46.5)	.31	96 (49.0)
Asian	12 (17.4)	26 (20.5)		38 (19.4)
African American	11 (16.0)	21 (16.5)		32 (16.3)
Hispanic	9 (13.0)	12 (9.4)		21 (10.7)
Other	0	9 (7.1)		9 (4.6)
Family history ( <i>n</i> = 196)	4 (5.8)	8 (6.2)	.88	12 (6.1)
Genetics ( <i>n</i> = 196)				
Somatic	31 (44.9)	51 (40.2)	.29	82 (41.8)
Germline	20 (28.9)	38 (29.9)		58 (29.6)
13q deletion syndrome	2 (2.9)	0 (0.0)		2 (1.0)
Unavailable	16 (23.2)	38 (29.9)		54 (27.6)
Laterality of disease ( <i>n</i> = 196)				
Unilateral	55 (79.7)	91 (71.7)	.21	146 (74.5)
Bilateral	14 (20.3)	36 (28.3)		50 (25.5)
Involved eye ( <i>n</i> = 196)				
Right eye	31 (41.9)	66 (49.6)	.19	97 (49.5)
Left eye	43 (58.1)	67 (50.4)		110 (56.1)

### Statistical Analysis

Categoric variables were summarized as absolute and relative frequencies and compared with the  $\chi$ -square test, and continuous variables were presented as means and standard deviations and compared with the *t* test. A multivariate logistic regression model was developed to assess whether the weight of  $\leq 10$  kg was a potential predictor of periprocedural complications and procedure failures. For all tests, a *P* value  $< .05$  was considered statistically significant. All analyses were performed with STATA software (version 14.1; StataCorp).

### RESULTS

The total study cohort included 207 Rb tumors of 207 eyes in 196 consecutive patients who underwent 658 intra-arterial chemotherapy infusions overall. Of these, patient weights were  $\leq 10$  kg in 69 (35.2%) and  $>10$  kg in 127 (64.8%) patients. Of the 69 patients weighing  $\leq 10$  kg, 5 patients received IAC treatment for bilateral Rb, and of the 127 patients weighing  $>10$  kg, 6 patients received IAC treatment for bilateral Rb. Thus, a total of 74 eyes of 69 patients weighing  $\leq 10$  kg were compared with 133 eyes of 127 patients weighing  $>10$  kg.

#### Patient Demographics

Comparison ( $\leq 10$  kg versus  $>10$  kg) revealed a significant difference of age at presentation of 10 months (median 9, range 1–33) versus 32 months (median 23, range 4–387) (*P* = .01), age at first IAC treatment of 11 months (median 10, range 3–30) versus 35 months (median 25, range 4–387) (*P* = .01), and weight at first

IAC treatment of 8.4 kg (median 8.9, range 3.1–10.4) versus 16.4 (median 13.3, range 10.3–209) (*P* = .01). There was no difference in the distribution of sex proportions between groups: 36 male patients (52.2%) and 33 female patients (47.8%) versus 68 male patients (53.5%) and 59 female patients (46.5%) (*P* = .85). Also, no significant difference in race distribution was observed: 37 (53.6%) versus 59 (46.5%) whites; 12 (17.4%) versus 26 (20.5%) Asians; 11 (16.0%) versus 21 (16.5%) African Americans; 9 (13.0%) versus 12 (9.4%) Hispanics; and 0 versus 9 (7.1%) others (*P* = .31). There was no difference in family history of Rb among both groups: 4 (5.8%) versus 8 (6.2%) (*P* = .88).

Comparison ( $\leq 10$  kg versus  $>10$  kg) revealed no significant difference in genetic mutations: 31 patients (44.9%) versus 51 patients (40.2%) with somatic mutations; 20 patients (28.9%) versus 38 patients (29.9%) with germline mutations; 2 patients (2.9%) versus 0 patients with 13q deletion syndrome; and 16 patients (23.2%) versus 38 patients (29.9%) with unknown status (*P* = .29). There was no difference in disease laterality: 55 patients (79.7%) versus 91 patients (71.7%) with unilateral involvement; 14 patients (20.3%) versus 36 patients (28.3%) with bilateral involvement (*P* = .21) or right and left eye involvement; 31 (41.9%) versus 66 (49.6%) right eye involvement; and 43 (58.1%) versus 67 (50.4%) left eye involvement (*P* = .19) (Table 1).

#### Tumor Features

Comparison of tumor characteristics ( $\leq 10$  kg versus  $>10$  kg) revealed no difference in greatest basal diameter: 15.0 mm (median 16, range 3–24) versus 16.0 mm (median 16, range 4–24)

( $P = .25$ ). Patients weighing  $\leq 10$  kg had lower tumor thickness: 7.2 mm (median 6.5, range 1–17) versus 8.4 mm (median 8, range 1–22) ( $P = .04$ ) and shorter tumor distance to the foveola 0.7 mm (0, 0–11) versus 2.4 mm (0, 0–15) ( $P = .01$ ) and optic disc 0.8 mm (0, 0–8) versus 2.0 mm (0, 0–18). There was no significant difference in subretinal seeding: 30 eyes (40.5%) versus 51 eyes (38.3) ( $P = .75$ ). Patients weighing  $\leq 10$  kg had a lower frequency of vitreous seeding: 18 eyes (24.3%) versus 70 eyes (52.6%) ( $P = .01$ ). There was no significant difference in anterior chamber seeding: 0 (0.0%) eyes versus 1 eye (0.7%) ( $P = .45$ ). Patients weighing  $\leq 10$  kg presented with less advanced Rb ICRB stage: 12 (16.9%) versus 5 (4.2%) with stage B, 9 (12.7%) versus 6 (5.0%) with stage C, 34 (47.9%) versus 58 (48.3%) with stage D, and 16 (22.5%) versus 51 (42.5%) with stage E ( $P = .01$ ) (On-line Table).

### Treatment Features and Periprocedural Complications

Comparison of treatment details ( $\leq 10$  kg versus  $> 10$  kg) revealed that the total number of IAC infusions was 222 versus 436 (Fig 1A). There was no difference in primary, 38.0 eyes (51.3%) versus 66.0 eyes (49.6%), or secondary IAC treatment, 36.0 eyes (48.6%) versus 67.0 eyes (50.3%) ( $P = .85$ ). There was no significant difference in number of IAC infusions per eye: 3.0 cycles (median 3, range 1–8) versus 3.3 cycles (median 3, range 1–9) ( $P = .26$ ). There was no significant difference in the technique of IAC delivery by using selective OA catheterization: 206.0 (95.4%) versus 397.0 (92.9%) or an alternative approach such as balloon-assisted delivery: 6.0 (2.7%) versus 13.0 (3.0%) or middle meningeal artery 4.0 (1.9%) versus 17.0 (3.9%) ( $P = .65$ ). There was a shorter procedure duration in infants weighing  $\leq 10$  kg: 47.5 minutes (median 42, range 6–156) versus 51.1 (median 48, range 7–200), but this was not statistically significant ( $P = .06$ ). Mean radiation exposure per eye and cumulative radiation exposure per eye ( $\text{Gym}^2$ ) were both significantly lower in infants weighing  $\leq 10$  kg ( $1.7 \pm 2.6$ , 95% CI 1.0–2.3 versus  $2.6 \pm 3.1$ , 95% CI 2.0–3.1;  $P = .02$ ) and ( $5.0 \pm 8.1$ , 95% CI 3.0–7.0 versus  $7.7 \pm 8.4$ , 95% CI 6.2–9.2;  $P = .01$ ), respectively. Mean fluoroscopy time (in minutes) was not significantly different ( $7.5 \pm 4.7$ , 95% CI 6.4–8.6 versus  $7.2 \pm 7.6$ , 95% CI 5.8–8.5;  $P = .71$ ) (Fig 1B). Patients weighing  $\leq 10$  kg had a greater frequency of aborted procedures: 12 (5.4%) versus 7 (1.6%) ( $P = .01$ ).

Of aborted procedures in infants weighing  $\leq 10$  kg, 50% were because of inability to secure femoral artery access, but 70% of aborted cases in patients weighing  $> 10$  kg were because of a thrombosed OA. Infants weighing  $\leq 10$  kg were subgrouped into 3 groups according to weight: group 1,  $\leq 4.5$  kg; group 2, 4.6–6 kg; and group 3,  $> 6$  kg. The incidences of failed femoral access were 0 in the first 2 groups and 2.8% in the third group ( $P = .80$ ) (Table 2 and Fig 1C). Of the 6 failed attempts, 5 had previous successful femoral access. The weight, age, and number of successful previous IAC attempts are presented in Table 3.

Periprocedural complications were not significantly different: 2 (0.9%) (vasospasm; 1 OA vasospasm after 5-cc infusion of the chemotherapy and 1 carotid vasospasm after straightening of a 360 carotid loop) versus 2 (0.5%) (1 incidence of ICA dissection by the microcatheter and 1 anaphylactic shock) ( $P = .49$ ) (Fig 1D).

### Outcomes

Comparison ( $\leq 10$  kg versus  $> 10$  kg) revealed no difference in mean follow-up duration: 31.7 months (median 22.7, range 1.7–157.2) versus 30.0 (median 23.4, range 0.2–112.4) ( $P = .73$ ). Patients weighing  $\leq 10$  kg had a greater frequency of complete tumor regression: 57 (82.6%) versus 81 (60.9%) ( $P = .02$ ). Patients weighing  $\leq 10$  kg had lower frequency of enucleation: 16 (21.6%) versus 52 (39.1%) ( $P = .01$ ) (Table 4 and Fig 1E).

### Multivariate Analysis

By multivariate logistic analysis, weight  $\leq 10$  kg was not an independent predictor of procedural failure (OR: 1.24; 95% CI: 0.30–5.10,  $P = .75$ ), nor an independent predictor of periprocedural complications (OR: 6.4; 95% CI: 0.63–65.6,  $P = .15$ ).

### DISCUSSION

Endovascular intra-arterial drug delivery is a promising field allowing for selective delivery of a high concentration of a therapeutic drug to selected targets. IAC for Rb stands as an inspiring example of the potential of selective drug delivery. IAC is a notable and established therapeutic option for Rb that has altered the natural history of the disease. Impressive cure rates have been reported, reaching 97%, with a dramatic drop in enucleation frequency (Fig 2).<sup>2,19–21</sup> In a previous report of our 5-year experience with IAC, we found globe salvage rates of 100% for group B and C eyes,<sup>7</sup> 94% for group D eyes, and  $\leq 73\%$  for group E eyes with a combination of IAC and intravitreal chemotherapy.<sup>16</sup> Most centers that use IAC for Rb have previously set treatment exclusion criteria for primary IAC of either weight  $\leq 10$  kg or age 3 months or younger, mainly because of the perceived risk of femoral artery complications in this group of patients. However, the importance of early treatment stems from data showing that younger and treatment-naïve patients may achieve better oncologic efficacy when they receive a minimal number of IAC cycles.<sup>6</sup> Gobin et al<sup>22</sup> showed that primary treatment with IAC was associated with an event-free survival rate of 81.7% after 2 years. Such a rate is much higher than 58.4% for eyes that had received intravenous chemotherapy or external-beam radiation in the pre-IAC era. Few reports exist in the literature on neuroendovascular approaches in infants and in particular on IAC treatment. Herein, we share our experience and report the safety and efficacy of IAC as a primary therapy for Rb in infants weighing  $\leq 10$  kg.

On review of our data ( $\leq 10$  kg versus  $> 10$  kg), procedure duration (47.5 minutes versus 51.1 minutes,  $P = .06$ ), fluoroscopy time (7.5 minutes versus 7.2 minutes,  $P = .71$ ), cumulative radiation exposure per eye ( $5.0 \text{ Gym}^2$  versus  $7.7 \text{ Gym}^2$ ;  $P = .01$ ), percentage of aborted procedures (5.4% versus 1.6%,  $P = .01$ ), percentage of periprocedural complications (0.9% versus 0.5%,  $P = .49$ ), percentage of complete tumor regression (82.6% versus 60.9%,  $P = .02$ ), and enucleation frequency (21.6% versus 39.1%,  $P = .01$ ) speak to the safety and efficacy of IAC for infants  $\leq 10$  kg at a high-volume center. Vessel dissection was the only major complication that occurred in 1 patient weighing  $> 10$  kg. Multivariate analysis showed that weight  $\leq 10$  kg was not an independent predictor of complications or procedure termination. As expected, the frequency of failed procedures was significantly higher in infants weighing  $< 10$  kg, mainly

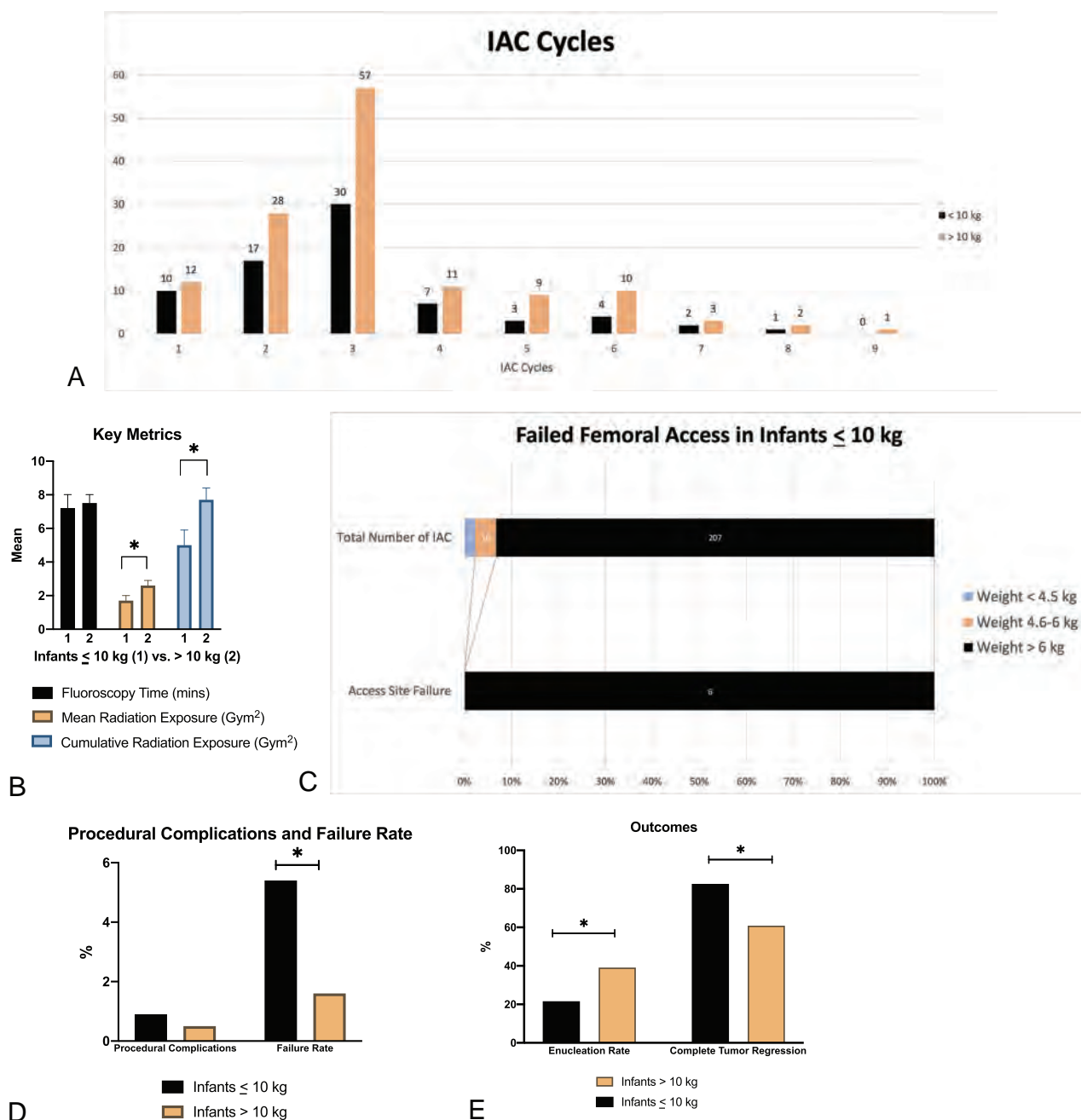


**FIG 1.** A, Bar graph showing the total number of IAC cycles per eye for infants weighing  $\leq 10$  kg and  $> 10$  kg. B, Bar graph showing the mean and standard error of fluoroscopy time (in minutes) and radiation exposure per eye (Gym<sup>2</sup>) of infants weighing  $\leq 10$  kg and  $> 10$  kg. Group 1: infants weighing  $\leq 10$  kg; group 2: infants weighing  $> 10$  kg. C, Bar graph showing the total number of IAC procedures and absolute value of failed femoral access in infants weighing  $\leq 10$  kg. Infants weighing  $< 10$  kg were subgrouped into 3 groups according to weight. D, Bar graph showing the percentage of periprocedural complications and failure rate of infants weighing  $\leq 10$  kg and  $> 10$  kg. E, Bar graph showing the enucleation rate and complete tumor regression of infants weighing  $\leq 10$  kg and  $> 10$  kg. Asterisks indicates significant difference.

because of inability to secure femoral artery access. Enucleation frequency in patients weighing  $< 10$  kg was significantly lower compared with those weighing  $> 10$  kg. Such outcomes highlight the fact that earlier treatment is associated with more favorable outcomes because of earlier stage of the cancer.

We previously reported a case of successful treatment of group D Rb with IAC in a subject weighing  $< 6$  kg. The subject received 2 cycles of IAC with 5 weeks in between and did well without

adverse effects.<sup>18</sup> Kim et al<sup>17</sup> retrospectively analyzed outcomes of IAC for 11 Rb eyes in 6 patients whose average weight was 8.9 kg at the time of the first IAC. They reported excellent overall response to IAC with 100% globe salvage and minimal access site complications. They encountered 1 hospitalized case of severe neutropenia among 6 patients who developed chemotherapy-induced neutropenia. Chen et al<sup>23</sup> retrospectively analyzed 10 patients who started IAC within their first 3 months of life, reporting that



primary IAC was feasible for the treatment of Rb in that age group. Most (12/13) eyes were salvaged, and no signs of ischemia were reported. Interestingly, a recent animal model for Rb reported 100% success rate in rabbits that weighed 3.0–3.2 kg.<sup>24</sup>

IAC is a challenging procedure that requires an experienced neurointerventionalist competent in the cannulation of very small-caliber vessels in infants, an experienced anesthesia team, and well-prepared infrastructure. The procedure is not always straightforward because there are several technical, anatomic, and physiologic

**Table 2: Intra-arterial chemotherapy for retinoblastoma in infants weighing ≤10 kg (74 treated eyes with 222 IAC sessions)—rate of femoral access failure in infants weighing ≤10 kg**

Group <sup>a</sup>	Patients (n)	Attempts (n)	Failed Femoral Access, n (%)
1	3	5	0 (0)
2	4	10	0 (0)
3	67	207	6 (2.8)

<sup>a</sup> Infants were subgrouped into 3 groups according to weight: group 1, ≤4.5 kg; group 2, 4.6–6 kg; and group 3, >6 kg.

**Table 3: Intra-arterial chemotherapy for retinoblastoma in infants weighing ≤10 kg (74 treated eyes with 222 IAC sessions)—weight, age, and number of previous successful attempts for infants of failed femoral access**

Patient No.	Weight (kg)	Age (months)	Previous Successful Attempts (n)
1	9.1	6.0	0
2	10.0	8.0	1
3	6.7	9.0	1
4	7.0	6.0	2
5	10.0	10.0	2
6	9.4	6.0	3

**Table 4: Intra-arterial chemotherapy for retinoblastoma in infants weighing ≤10 kg (74 treated eyes with 222 IAC sessions)—clinical outcomes**

Variable	Weight ≤10 kg (n = 74 Eyes; 35.7% of 69 Patients)	Weight >10 kg (n = 133 Eyes; 64.2% of 127 Patients)	P Value	Total (n = 207) Eyes (%) of 196 Patients
Complete tumor regression	57 (82.6)	81 (60.9)	.02	138 (66.6)
Globe enucleation	16 (21.6)	52 (39.1)	.01	68 (32.8)
Follow-up duration (months) (n = 196), mean (median, range)	31.7 (22.7, 1.7–157.2)	30.0 (23.4, 0.2–112.4)	.73	30.6 (22.8, 0.2–157.2)

challenges. The minute caliber and fragility of access and target vessels is critical; therefore, sonography-guided femoral access is used for all procedures. In our series, we did not encounter any access site complications in either group. However, the small caliber of the femoral artery led to procedure termination in subjects weighing ≤10 kg at a frequency of 2.7% because of an inability to secure femoral access. However, it is paramount to know that femoral access is possible even in very young infants of 3 kg or age of 3 months. A low-profile 4F micropuncture kit may be used to gain access and used instead of a 4F pediatric sheath. In addition, a microcatheter may be used to complete the procedure without the use of a guide catheter. Sick infants in intensive care units receive a femoral line as a standard practice, and along the same line of thought, young infants eligible for IAC should not be denied the possibility based on weight or age alone. Eighty percent of the aborted IAC procedures due to failed arterial access had at least 1 successful attempt before. There was no incidence of procedure abortion in subjects weighing >10 kg because of vascular access. The main reason for procedure termination was OA thrombosis. On multivariate analysis, weight was not an independent predictor of procedure failure.

It is well established from the cardiac literature that larger sheath size relative to the femoral artery diameter is associated with higher rates of femoral artery complications (eg, vasospasm, thrombosis, and arterial disruption).<sup>25–27</sup> The 4F catheter has a diameter of 1.33 mm, which is larger than the size of the femoral artery in subjects weighing <10 kg. Reports of infants who underwent cardiac catheterization describe 8%–14% femoral artery injury leading to leg length discrepancy, with arterial thrombosis in one-third of cases.<sup>28–30</sup> Moreover, late arterial complications can occur because of catheter-induced endothelial

damage. The senior author performs femoral artery compression at the end of the case for 20 minutes and monitors the arterial wave by using a pulse oximeter placed on the ipsilateral big toe. The philosophy is that too much compression may result in vessel damage, vasospasm, or limb ischemia, but poor compression may result in retroperitoneal hematoma, which may be disastrous in this age group. Also, the senior author has modified the IAC technique such that he no longer uses a

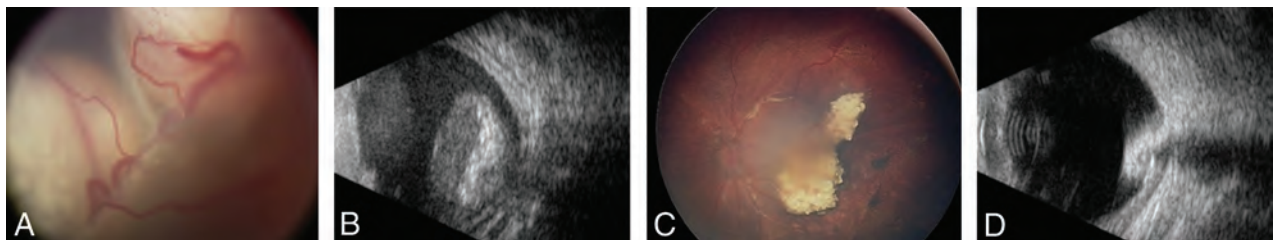


**FIG 2.** Retinoblastoma (A and B) before and (C and D) 9 months after treatment with intra-arterial chemotherapy (IAC). A, An infant presented with left eye leukocoria and unilateral group E retinoblastoma with no view of the optic nerve. B, B-scan ultrasonography demonstrated a calcified intraocular mass with overlying retinal detachment and no optic nerve involvement. C, After 4 IAC infusions using melphalan 5 mg and topotecan 1 mg, the tumor showed complete response with type III regression to a partially calcified mass in the macular region (D) confirmed by B-scan ultrasonography.

guide catheter to avoid vessel dissection and to be able to downsize the groin sheath. Rather, catheterization is performed using a Marathon and a Synchro10 wire all the way from the femoral artery to the OA.

### Limitations

Our study has the natural limitations of selection bias in a non-randomized single-center study. Results have to be interpreted with caution, and conclusions should be validated in a larger population over a longer follow-up period. The strength of our study is a large number of procedures performed by the same group of neurointerventionalists in a single center.

### CONCLUSIONS

IAC for Rb is a therapeutic approach that led to dramatic changes in the natural history of the disease. Cure rates, globe salvage, and vision preservation have significantly improved. The long, encouraging experience along with a high safety profile of IAC pushed the envelope to provide this patient population with such an alternative. Our results speak of the safety and efficacy of IAC in patients weighing  $\leq 10$  kg. Management should be tailored per patient, and variables such as age and weight should not be exclusion criteria to offer IAC.

Disclosures: Stavropoula Tjournakaris—UNRELATED: Consultancy: Medtronic. Pascal Jabbour—UNRELATED: Consultancy: Microvention\*; Grants/grants pending: Medtronic.\* \*Money paid to institution.

### REFERENCES

- Scheffler AC, Kim RS. Recent advancements in the management of retinoblastoma and uveal melanoma. *F1000Res* 2018;7:476 CrossRef
- Kivelä T. *The Epidemiological Challenge of the Most Frequent Eye Cancer: Retinoblastoma, An Issue of Birth and Death*. BMJ Publishing Group Ltd; 2009
- Abramson DH, Shields CL, Munier FL, et al. Treatment of retinoblastoma in 2015: agreement and disagreement. *JAMA Ophthalmol* 2015;133:1341–47 CrossRef Medline
- Shields CL, Bianciotto CG, Jabbour P, et al. Intra-arterial chemotherapy for retinoblastoma: report No. 1, control of retinal tumors, subretinal seeds, and vitreous seeds. *Arch Ophthalmol* 2011;129:1399–1406 CrossRef Medline
- Shields CL, Jorge R, Say EAT, et al. Unilateral retinoblastoma managed with intravenous chemotherapy versus intra-arterial chemotherapy. Outcomes based on the International Classification of Retinoblastoma. *Asia Pac J Ophthalmol (Phila)* 2016;5:97–103
- Shields CL, Kaliki S, Shah SU, et al. Minimal exposure (one or two cycles) of intra-arterial chemotherapy in the management of retinoblastoma. *Ophthalmology* 2012;119:188–92 CrossRef Medline
- Shields CL, Manjandavida FP, Lally SE, et al. Intra-arterial chemotherapy for retinoblastoma in 70 eyes: outcomes based on the International Classification of Retinoblastoma. *Ophthalmology* 2014;121:1453–60 CrossRef
- Shields CL, Mashayekhi A, Au AK, et al. The International Classification of Retinoblastoma predicts chemoreduction success. *Ophthalmology* 2006;113:2276–80 CrossRef
- Gobin P, Marr B, Dunkel I, et al. Intra-arterial chemotherapy (chemosurgery) in the ophthalmic artery for the treatment of retinoblastoma in children: 3 year experience. *J Neurointerv Surg* 2009;1:77–78 CrossRef
- Abramson DH, Daniels AB, Marr BP, et al. Intra-arterial chemotherapy (ophthalmic artery chemosurgery) for group D retinoblastoma. *PLoS One* 2016;11:e0146582 CrossRef Medline
- Yamane T, Kaneko A, Mohri M. The technique of ophthalmic arterial infusion therapy for patients with intraocular retinoblastoma. *Int J Clin Oncol* 2004;9:69–73 CrossRef Medline
- Abramson DH, Dunkel IJ, Brodie SE, et al. A phase I/II study of direct intraarterial (ophthalmic artery) chemotherapy with melphalan for intraocular retinoblastoma: initial results. *Ophthalmology* 2008;115:1398–1404,e1391 CrossRef Medline
- Abramson DH, Marr BP, Francis JH, et al. Simultaneous bilateral ophthalmic artery chemosurgery for bilateral retinoblastoma (tandem therapy). *PLoS One* 2016;11:e0156806 CrossRef Medline
- Shields CL, Bianciotto CG, Jabbour P, et al. Intra-arterial chemotherapy for retinoblastoma: report No. 2, treatment complications. *Arch Ophthalmol* 2011;129:1407–15 CrossRef Medline
- Shields CL, Alset AE, Say EAT, et al. Retinoblastoma control with primary intra-arterial chemotherapy: outcomes before and during the intravitreal chemotherapy era. *J Pediatr Ophthalmol Strabismus* 2016;53:275–84 CrossRef Medline
- Dalvin LA, Kumari M, Essuman VA, et al. Primary intra-arterial chemotherapy for retinoblastoma in the intravitreal chemotherapy era: five years of experience. *Oncol Pathol* 2019;5:139–46 CrossRef
- Kim RS, Dannenbaum MJ, Lin MW, et al. Use of femoral artery ultrasound during intraarterial chemotherapy for children under 10 kg with retinoblastoma. *Retina* 2018;38:1420–26
- Magan T, Khoo CT, Jabbour PM, et al. Intraarterial chemotherapy for retinoblastoma in a 2-month-old infant. *Retin Cases Brief Rep* 2017;11:24–26
- Abramson DH, Fabius AW, Issa R, et al. Advanced unilateral retinoblastoma: the impact of ophthalmic artery chemosurgery on enucleation rate and patient survival at MSKCC. *PLoS One* 2015;10:e0145436 CrossRef Medline
- Abramson DH, Shields CL, Jabbour P, et al. Metastatic deaths in retinoblastoma patients treated with intraarterial chemotherapy (ophthalmic artery chemosurgery) worldwide. *Int J Retin Vitre* 2017;3:40 CrossRef
- Munier FL, Mosimann P, Puccinelli F, et al. First-line intra-arterial versus intravenous chemotherapy in unilateral sporadic group D retinoblastoma: evidence of better visual outcomes, ocular survival and shorter time to success with intra-arterial delivery from retrospective review of 20 years of treatment. *Br J Ophthalmol* 2017;101:1086–93 CrossRef
- Gobin YP, Dunkel IJ, Marr BP, et al. Intra-arterial chemotherapy for the management of retinoblastoma: four-year experience. *Arch Ophthalmol* 2011;129:732–37 CrossRef Medline
- Chen M, Zhao J, Xia J, et al. Intra-arterial chemotherapy as primary therapy for retinoblastoma in infants less than 3 months of age: a series of 10 case-studies. *PLoS One* 2016;11:e0160873 CrossRef Medline
- Daniels AB, Froehler MT, Pierce JM, et al. Pharmacokinetics, tissue localization, toxicity, and treatment efficacy in the first small animal (rabbit) model of intra-arterial chemotherapy for retinoblastoma. *Invest Ophthalmol Vis Sci* 2018;59:446–54 CrossRef Medline
- Franken E Jr, Girod D, Sequeira F, et al. Femoral artery spasm in children: catheter size is the principal cause. *AJR Am J Roentgenol* 1982;138:295–98 CrossRef Medline
- Burrows PE, Benson LN, Williams WG, et al. Iliofemoral arterial complications of balloon angioplasty for systemic obstructions in infants and children. *Circulation* 1990;82:1697–1704 CrossRef Medline
- Burrows PE, Benson LN, Babyn P, et al. Magnetic resonance imaging of the iliofemoral arteries after balloon dilation angioplasty of aortic arch obstructions in children. *Circulation* 1994;90:915–20 CrossRef
- Perry M. Iatrogenic injuries of arteries in infants. *Surg Gynecol Obstet* 1983;157:415–18 Medline
- Fullilove S, Fixsen J. Major limb deformities as complications of vascular access in neonates. *Paediatr Anaesth* 1997;7:247–50 CrossRef Medline
- Macnicol M, Anagnostopoulos J. Arrest of the growth plate after arterial cannulation in infancy. *J Bone Joint Surg Br* 2000;82:172–75 CrossRef Medline

# Changes of Neurotransmitters in Youth with Internet and Smartphone Addiction: A Comparison with Healthy Controls and Changes after Cognitive Behavioral Therapy

H.S. Seo, E.-K. Jeong, S. Choi, Y. Kwon, H.-J. Park, and I. Kim



## ABSTRACT

**BACKGROUND AND PURPOSE:** Neurotransmitter changes in youth addicted to the Internet and smartphone were compared with normal controls and in subjects after cognitive behavioral therapy. In addition, the correlations between neurotransmitters and affective factors were investigated.

**MATERIALS AND METHODS:** Nineteen young people with Internet and smartphone addiction and 19 sex- and age-matched healthy controls (male/female ratio, 9:10; mean age,  $15.47 \pm 3.06$  years) were included. Twelve teenagers with Internet and smartphone addiction (male/female ratio, 8:4; mean age,  $14.99 \pm 1.95$  years) participated in 9 weeks of cognitive behavioral therapy. Meshcher-Garwood point-resolved spectroscopy was used to measure  $\gamma$ -aminobutyric acid and Glx levels in the anterior cingulate cortex. The  $\gamma$ -aminobutyric acid and Glx levels in the addicted group were compared with those in controls and after cognitive behavioral therapy. The  $\gamma$ -aminobutyric acid and Glx levels correlated with clinical scales of Internet and smartphone addiction, impulsiveness, depression, anxiety, insomnia, and sleep quality.

**RESULTS:** Brain parenchymal and gray matter volume-adjusted  $\gamma$ -aminobutyric acid-to-creatine ratios were higher in subjects with Internet and smartphone addiction ( $P = .028$  and  $.016$ ). After therapy, brain parenchymal- and gray matter volume-adjusted  $\gamma$ -aminobutyric acid-to-creatine ratios were decreased ( $P = .034$  and  $.026$ ). The Glx level was not statistically significant in subjects with Internet and smartphone addiction compared with controls and posttherapy status. Brain parenchymal- and gray matter volume-adjusted  $\gamma$ -aminobutyric acid-to-creatine ratios correlated with clinical scales of Internet and smartphone addictions, depression, and anxiety. Glx/Cr was negatively correlated with insomnia and sleep quality scales.

**CONCLUSIONS:** The high  $\gamma$ -aminobutyric acid levels and disrupted balance of  $\gamma$ -aminobutyric acid-to-Glx including glutamate in the anterior cingulate cortex may contribute to understanding the pathophysiology and treatment of Internet and smartphone addiction and associated comorbidities.

**ABBREVIATIONS:** ACC = anterior cingulate cortex; bp- = brain parenchymal volume-adjusted; GABA =  $\gamma$ -aminobutyric acid; gm- = gray matter volume-adjusted; MEGA-PRESS = Meshcher-Garwood point-resolved spectroscopy; wm- = white matter volume-adjusted

Internet addiction is a behavioral addiction characterized by uncontrolled use of the Internet with tolerance, withdrawal symptoms, and compulsiveness. The prevalence of Internet addiction ranges from 1.5% to 8.2%<sup>1</sup> and is much higher in adolescents and young adults in the Far East.<sup>2</sup> Internet gaming addiction was listed as a research criterion for behavioral addiction in the fifth version of the *Diagnostic and Statistical Manual of Mental*

*Disorders*.<sup>3</sup> In recent years, a preoccupation with smartphones and their worldwide spread has resulted in smartphone addiction.

The mesocorticolimbic system is a dopaminergic projection engaged in common neurobiologic pathways of substance addiction.<sup>4</sup> The anterior cingulate cortex (ACC) is part of the mesocorticolimbic system and is associated primarily with salient networks activated by reward-related stimuli.<sup>4,5</sup> The ACC has been postulated to play a critical role with the insula in substance

Received June 28, 2018; accepted after revision May 1, 2020.

From the Department of Radiology (H.S.S.), Korea University Ansan Hospital, Ansan, Korea; Utah Center for Advanced Imaging Research (E.-K.J.), University of Utah, Salt Lake City, Utah; Department of Psychology (S.C., Y.K.), Duksung Women's University, Seoul, Korea; Department of Nuclear Medicine (H.-J.P.), Yonsei University College of Medicine, Seoul, Korea; and Siemens Healthcare (I.K.), Seoul, Korea.

This study was supported by the National Research Foundation of Korea (NRF-2013RIA1A1012361).

Paper previously presented at: Annual Meeting of the Radiological Society of North America, November 26–December 1, 2017; Chicago, Illinois.

Please address correspondence to Hyung Suk Seo, MD, PhD, Department of Radiology, Korea University Ansan Hospital, Jeokgum-ro 123, Gojan-dong, Ansan-si Gyeonggi-do, South Korea 5355; e-mail: seohs@korea.ac.kr

Indicates open access to non-subscribers at www.ajnr.org

<http://dx.doi.org/10.3174/ajnr.A6632>

addiction.<sup>4</sup> PET,<sup>6</sup> SPECT,<sup>7</sup> and electroencephalogram<sup>8</sup> results reportedly show brain regions associated with substance addictions.<sup>9</sup> The ACC has been one of the most frequently implicated regions in Internet addiction.<sup>10-15</sup>

Substance addiction is associated with the neurotransmitter changes in the mesocorticolimbic system. Nicotine and alcohol indirectly enhance dopamine release via modulation of  $\gamma$ -aminobutyric acid (GABA) and glutamatergic neurons.<sup>4,16</sup> MR spectroscopy using an editing pulse to create J-coupling can separate GABA and glutamate signals from other stronger overlying metabolite signals<sup>17,18</sup> and has been used to characterize neurotransmitter changes in dynamic and interactive psychiatric disorders. The use of MR spectroscopy to study the ACC with respect to Internet and smartphone addiction can clarify common neurobiologic mechanisms for behavioral and substance addictions and provide clinical intervention to reduce the prevalence and related functional impairments in young people.

Currently, neurotransmitter changes have not been researched in terms of Internet and smartphone addiction. The purpose of this study was to reveal the associations between neurotransmitter changes and Internet and smartphone addiction and compare them with those in healthy controls and subjects' postcognitive behavioral therapy results. In addition, correlations between neurotransmitter changes and affective changes in youth diagnosed with Internet and smartphone addiction were investigated.

## MATERIALS AND METHODS

### Participants

The institutional review board Korea University Ansan hospital approved this prospective study, and informed consent was obtained from the adolescents and parents. We included young people between the ages of 10 and 24 years who met the following criteria: 1) >50 points on the Internet Addiction Test modified from the Young Diagnostic Questionnaire;<sup>19</sup> 2) >35 points on the Smartphone Addiction Scale-short version for adolescents;<sup>20</sup> and 3) >75 points on the summed Internet Addiction Test and Smartphone Addiction Scale. Subsequently, the Mini-International Neuropsychiatric Interview was administered to exclude subjects who met the diagnostic criteria of psychotic disorders, such as schizophrenia spectrum and other psychotic disorders, bipolar I disorder, or substance use disorder.

We included sex- and age-matched healthy controls who met the following criteria: 1) <30 points on the Internet Addiction Test; 2) <30 points on the Smartphone Addiction Scale; and 3) <60 points on the summed Internet Addiction Test and Smartphone Addiction Scale.

### Psychology Tests

The Young Internet Addiction Test measures the severity of Internet addiction and consists of 20 items scored on a 5-point Likert scale, covering the extent to which Internet use affects daily routines, social life, productivity, sleeping patterns, and feelings.<sup>19</sup> The Smartphone Addiction Scale-short version for adolescents measures the severity of smartphone addiction. It consists of 10 items scored on a 6-point Likert scale.<sup>20</sup>

Affective and cognitive characteristics of people with addiction and controls were evaluated using the Barratt Impulsiveness Scale, Hamilton Depression Rating Scale, Spielberger State-Trait Anxiety Inventory, Pittsburgh Sleep Quality Index, Insomnia Severity Index, and Mini-International Neuropsychiatric Interview. In order to the measurement of intelligence, the Korean version of the Wechsler Adult Intelligence Scale-IV for adolescents and adults older than 16 years of age and the Korean version of the Wechsler Intelligence Scale for Children-IV for children from 6 to 16 years of age were used.

### Cognitive Behavioral Therapy

Cognitive behavioral therapy was modified from the Cognitive-Behavioral Therapy For Internet Gaming Addiction,<sup>21</sup> and the Emotional Identification and Expression Abilities Improvement Program was reinforced. The treatment program consisted of the following 7 areas: recognizing the Internet behavior, modifying the cognitive distortion, finding appropriate alternative activities, promoting self-control, recognizing self-emotions and those of others, expressing emotions, and resolving interpersonal conflicts. The cognitive behavioral therapy consisted of a weekly 75-minute program for 9 weeks. The program was administered to the young subjects with Internet and smartphone addiction who agreed to participate in the therapy. Two or more absences were defined as therapy failure.

### MR Imaging Parameters

MR imaging was performed within an hour after the psychological tests. In addition, 1 or 2 days after finishing the 9-week cognitive behavioral therapy program, MR imaging rescanning was performed within an hour after the psychological retests. MR imaging data were acquired with a 3T MR imaging scanner with a 32-channel phased array head coil (MAGNETOM Skyra; Siemens Healthcare, Erlangen, Germany). Meshcher-Garwood point-resolved spectroscopy (MEGA-PRESS) was programmed by inserting a dual-band radiofrequency pulse into the manufacturer's PRESS sequence. A dual-band radiofrequency waveform was obtained using a public domain pulse design tool, MATPULSE software (<https://cind.ucsf.edu/education/software/matpulse>). GABA measurement was performed using the MEGA-PRESS pulse sequence from a voxel volume of 26.25 mL (voxel dimensions,  $3.5 \times 3.0 \times 2.5$  cm) in the ACC (Fig 1), with the following acquisition parameters: TR, 2000 ms; TE, 68 ms; spectral width, 2000 Hz; number of oversampled data, 2048; number of signal averages, 256. GABA resonance at 3.01 ppm was detected by application of a refocusing pulse at 1.9 ppm during ON spectra and at 7.5 ppm during OFF spectra. Water signal suppression was achieved with the chemical shift selective imaging technique. First- and second-order shimming was performed for the voxels in the ACC, and the water line widths resulted in <16 Hz. Scan time was approximately 9 minutes.

Single-voxel <sup>1</sup>H-MR spectroscopy with TE = 135 ms was obtained at the same voxels in the ACC (Fig 1), with the following parameters: TR, 2000 ms; number of samples, 64. In addition to MR spectroscopy, T1-weighted structural images were obtained using the MPRAGE sequence with the following



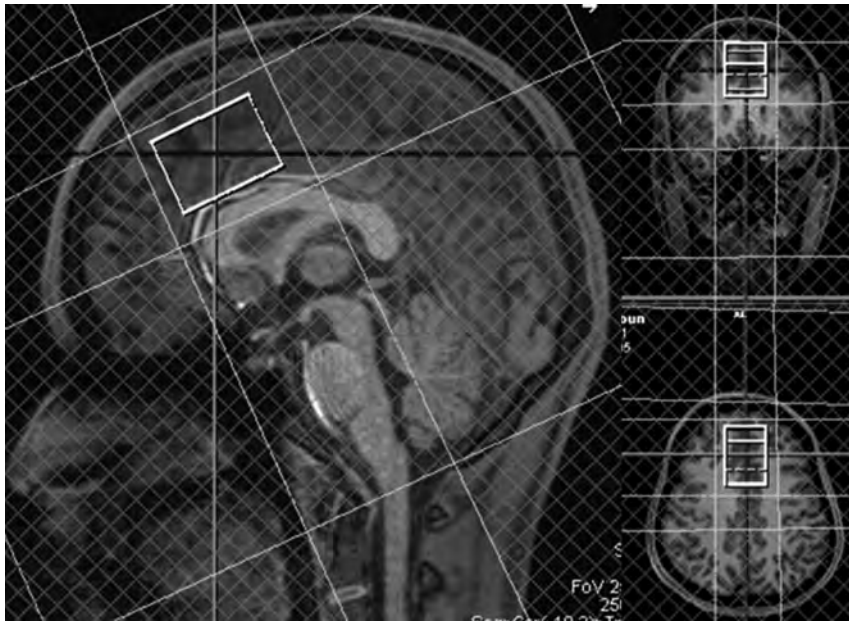


**FIG 1.** GABA, Glx, and creatine measurements in the anterior cingulate cortex. GABA and single-voxel  $^1\text{H}$ -MR spectroscopy with  $\text{TE} = 135$  ms are obtained from a voxel volume of 26.25 mL (voxel dimensions,  $3.5 \times 3.0 \times 2.5$  cm) in the anterior cingulate cortex. The volume fractions of brain parenchyma and gray matter in the MR spectroscopy voxels are obtained from T1 MP-RAGE segmentation using the SPM program. Last, GABA/Cr and Glx/Cr are adjusted by multiplying brain parenchymal and gray matter volume fractions for each individual.

parameters: TR, 2000 ms; TE, 3.55 ms; flip angle,  $8^\circ$ ; section thickness, 1 mm; and acquisition matrix,  $256 \times 256$ .

### MR Spectroscopy Data Processing

The raw GABA MR spectroscopy data were transferred to an off-line computer and processed using home-programmed MR spectroscopy analysis software, which was programmed in Python (<https://www.python.org/>). Raw data were averaged in the time domain and baseline-corrected, and the areas under the GABA and Glx peaks at 3.01 and 3.8 ppm were measured by fitting to double and single Gaussian functions, respectively (Fig 2). The data for  $^1\text{H}$ -MR spectroscopy at  $\text{TE} = 135$  ms were processed using LCModel 6.3 (<http://www.lcmode.com/>), and the creatine peak was measured at 3.0 ppm and used as the internal reference. GABA and Glx relative to creatine were quantified, and the GABA-to-creatine ratio (GABA/Cr) and the Glx-to-creatine ratio (Glx/Cr) were obtained. The GABA-to-Glx ratio (GABA/Glx) was also obtained.

The volume fractions of brain parenchyma and gray matter in the MR spectroscopy voxels were obtained from T1 MP-RAGE segmentation using the Statistical Parametric Mapping program (SPM; <http://www.fil.ion.ucl.ac.uk/spm/software/spm12>) (Fig 1). Last, GABA/Cr and Glx/Cr were adjusted by multiplying brain parenchymal and gray matter volume fractions for each individual.

### Statistical Analyses

All statistical analyses were performed using SPSS Statistics 20 (IBM). Statistical significance was defined as  $P \leq .05$ . GABA and Glx differences between the youth with Internet and smartphone

addictions and controls were evaluated using the Student  $t$  test. Correlations between neurotransmitters and psychological tests were evaluated using the Pearson correlation coefficient. Differences in GABA and Glx levels between pre- and postcognitive behavioral therapy were tested using paired  $t$  tests or paired Wilcoxon signed rank tests based on whether the data met the assumption for a normal distribution.

## RESULTS

The results of demographics and psychological tests are shown in Table 1. The addiction group consisted of 9 males and 10 females diagnosed with Internet and smartphone addictions. The mean age was  $15.47 \pm 3.06$  years and ranged from 11 to 22 years. The control group consisted of 19 young healthy subjects, sex- and age-matched to the addiction group.

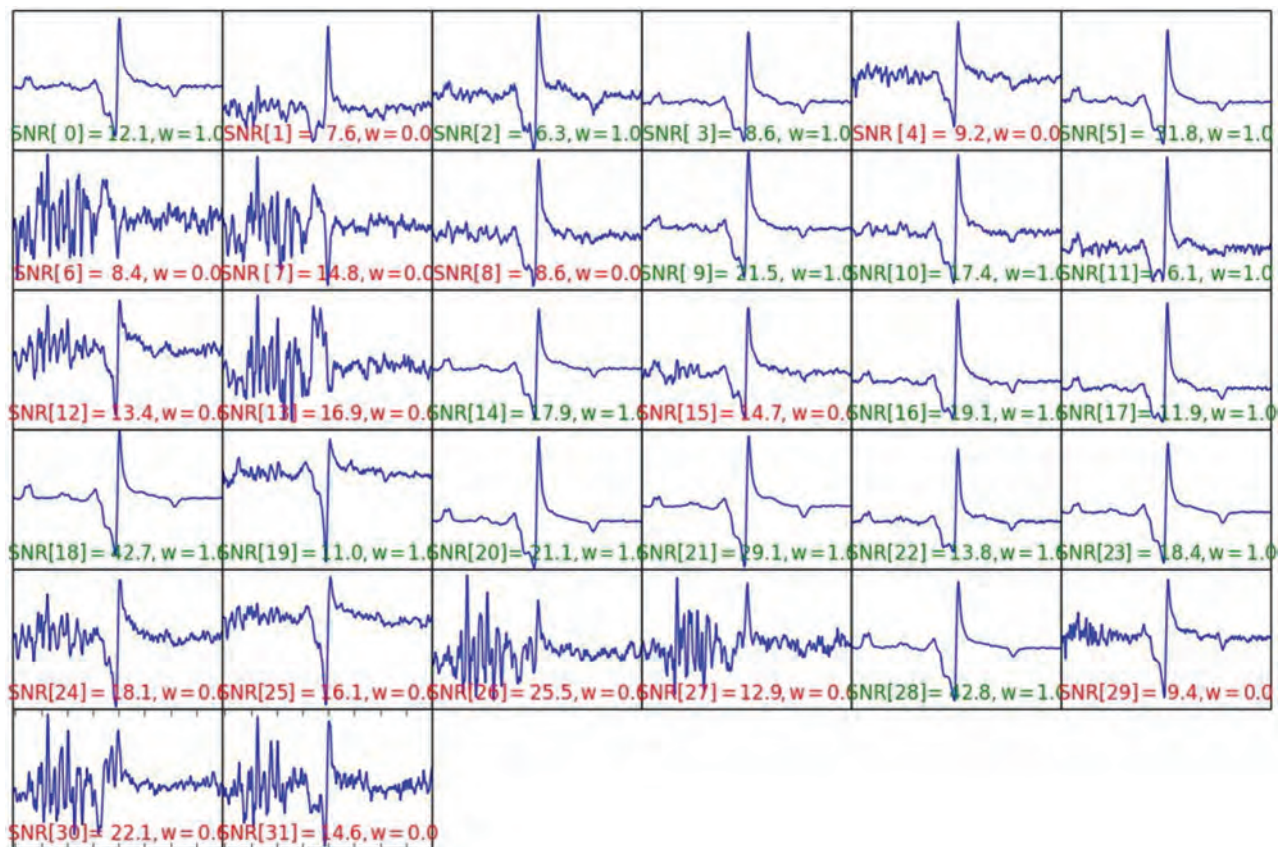
Internet and smartphone addiction scores were significantly higher in the addiction group compared with healthy controls ( $P < .001$ ) as well as depression

( $P = .018$ ), state, trait, and total anxiety scores ( $P < .001$ ,  $P < .001$ , and  $P = .001$ , respectively); the impulsivity score ( $P = .001$ ); insomnia severity ( $P = .006$ ); and poor sleep quality ( $P = .008$ ). A significant difference in the intelligence quotient was not observed between groups ( $P = .467$ ).

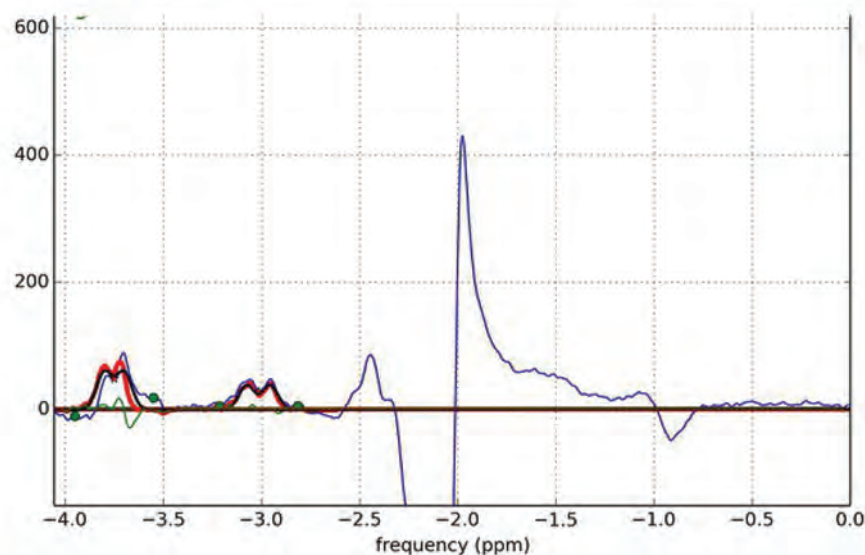
Eight males and 4 females participated in cognitive behavioral therapy. The mean age was  $14.0 \pm 1.95$  years and ranged from 11 to 17 years. Teenagers with Internet and smartphone addiction significantly improved after 9 weeks of cognitive behavioral therapy based on Internet and smartphone addiction scales ( $P = .001$  and  $< .001$ , respectively), though Internet Addiction Test scores and the summed scores of the Internet Addiction Test and Smartphone Addiction Scale still met the criteria of Internet and smartphone addiction. However, psychological and sleep test scores were not significantly changed after therapy.

GABA levels in subjects with Internet and smartphone addictions are summarized in Table 2, and GABA levels after 9 weeks of cognitive behavioral therapy are summarized in Table 3. Brain parenchymal volume-adjusted GABA/Cr (bp-GABA/Cr) was higher in the addiction group compared with the controls ( $P = .028$ ) and significantly decreased after cognitive behavioral therapy ( $P = .034$ ). Gray matter volume-adjusted GABA/Cr (gm-GABA/Cr) was also higher in the addiction group ( $P = .016$ ) and significantly decreased after cognitive behavioral therapy ( $P = .026$ ; Fig 3A).

Glx levels in subjects with Internet and smartphone addiction are summarized in Table 2, and Glx levels after 9 weeks of cognitive behavioral therapy are summarized in Table 3. A significant difference in Glx levels was not observed in the addiction group compared with the control group. Glx/Cr adjusted brain parenchymal (bp-Glx/Cr) and gray matter volumes (gm-Glx/Cr) were



A



B

**FIG 2.** Acquisition and spectral fitting of MEGA-PRESS MR spectroscopy. A, MR imaging data are acquired with a 3T MR imaging scanner with a 32-channel phased array head coil. The signal-to-noise ratio acquired on each channel is visually checked, and raw data with a low signal-to-noise ratio (red characters) are removed from averaging. B, Selected raw data are averaged in the time domain and baseline-corrected, and the areas under the GABA and Glx peaks at 3.01 and 3.8 ppm (red lines) are measured by fitting to double and single Gaussian functions, respectively.

lower in the addiction group but without statistical significance ( $P = .375$  and  $.587$ , respectively; Fig 3B). The Glx level was increased after cognitive and behavioral therapy but without statistical significance ( $P = .096$  and  $.131$ , respectively; Fig 3B).

The results of correlations between neurotransmitters and psychological tests are described in Table 4. The GABA/Cr adjusted with gray-matter volume fraction (gm-GABA/Cr)

positively correlated with the Internet Addiction Test and the Smartphone Addiction Scale as well as the sum of both scales. (Fig 4A) The bp-GABA/Cr correlated with the Internet Addiction Test but was not significantly correlated with Smartphone Addiction Scale.

The gm-GABA/Cr significantly correlated with the depression score ( $P = .046$ ), state anxiety ( $P = .032$ ), and total anxiety ( $P =$

**Table 1: Demographics, psychological tests, and pre- and postcognitive behavioral therapy data**

	Internet Addiction (Mean) (n = 19)	Control (Mean)	P Value	PreTx (Mean) (n = 12)	PostTx (Mean)	P Value
Sex (M/F)	9:10		1.0	8:4		
Age (yr)	15.47 ± 3.06 (range, 11–22)		1.0	14.00 ± 1.95 (11–17)		
IAT	63.32 ± 15.15	27.37 ± 4.83	< .001 <sup>a</sup>	68.42 ± 14.74	52.58 ± 10.24	.001 <sup>a</sup>
SAS	45.53 ± 7.40	17.89 ± 8.12	< .001 <sup>a</sup>	45.83 ± 6.42	30.67 ± 6.85	< .001 <sup>a</sup>
IAT+SAS	108.84 ± 20.19	45.26 ± 11.72	< .001 <sup>a</sup>	114.25 ± 19.43	83.25 ± 15.52	< .001 <sup>a</sup>
HRSD	3.53 ± 5.92	0 ± 0	.018 <sup>a</sup>	2.00 ± 3.69	0.25 ± 0.62	.147
State STAI	46.11 ± 7.75	31.95 ± 9.99	< .001 <sup>a</sup>	46.45 ± 8.55	43.82 ± 10.07	.441
Trait STAI	50.16 ± 7.54	39.05 ± 4.93	< .001 <sup>a</sup>	49.27 ± 7.84	45.36 ± 7.89	.085
Total STAI	95.89 ± 14.56	71 ± 13.58	< .001 <sup>a</sup>	95.06 ± 16.19	89.18 ± 17.55	.253
BIS	57.53 ± 7.63	45.58 ± 11.72	.001 <sup>a</sup>	54.27 ± 6.94	52.45 ± 6.83	.093
ISI	6.89 ± 4.977	3.11 ± 2.558	.006 <sup>a</sup>	5.17 ± 3.74	5.00 ± 4.43	.891
PSQI	5.95 ± 3.24	3.53 ± 1.87	.008 <sup>a</sup>	4.67 ± 2.31	4.83 ± 2.92	.777
IQ	95.18 ± 2.88	98 ± 11.12	.467			

**Note:**—PreTx indicates precognitive behavioral therapy; PostTx, postcognitive behavioral therapy; IAT, Internet Addiction Test; SAS, Smartphone Addiction Scale; HRSD, Hamilton Rating Scale for Depression; STAI, State-Trait Anxiety Inventory; BIS, Barratt Impulsiveness Scale; ISI, Insomnia Severity Index; PSQI, Pittsburgh Sleep Quality Assessment; IQ, intelligence quotient.

<sup>a</sup> P value ≤ .05

**Table 2: Subjects with Internet addiction versus controls**

	bp-GABA/Cr	gm-GABA/Cr	wm-GABA/Cr	bp-GLX/Cr	gm-GLX/Cr	wm-GLX/Cr
IA (mean)	73.85 ± 22.74	49.10 ± 15.27	24.90 ± 8.25	167.74 ± 43.44	106.87 ± 39.90	56.25 ± 13.74
Controls (Mean)	56.03 ± 25.25	36.27 ± 16.02	19.77 ± 9.71	179.55 ± 37.30	117.45 ± 25.86	62.67 ± 13.12
P value	.028 <sup>a</sup>	.016 <sup>a</sup>	.088	.375	.587	.149

**Note:**—wm-GABA/Cr indicates white matter volume-adjusted GABA-to-creatine ratio; wm-GLX/Cr, white matter volume-adjusted glutamine and glutamate-to-creatine ratio; IA, Internet addiction.

<sup>a</sup> P value ≤ .05.

**Table 3: Pre- and postcognitive behavioral therapy data**

	bp-GABA/Cr	gm-GABA/Cr	wm-GABA/Cr	bp-GLX/Cr	gm-GLX/Cr	wm-GLX/Cr
PreTx (mean)	74.20 ± 23.58	46.77 ± 15.95	24.43 ± 8.32 <sup>b</sup>	177.19 ± 47.81	119.07 ± 34.37	58.12 ± 14.81
PostTx (mean)	52.72 ± 14.52	34.60 ± 9.28	18.11 ± 5.67	215.65 ± 48.31	142.46 ± 34.54	73.19 ± 16.40 <sup>b</sup>
P value	.034 <sup>a</sup>	.026 <sup>a</sup>	.071 <sup>b</sup>	.096	.131	.06 <sup>b</sup>

**Note:**—PreTx indicates precognitive behavioral therapy; PostTx, postcognitive behavioral therapy.

<sup>a</sup> P ≤ .05 based on paired t test or Wilcoxon signed rank test.

<sup>b</sup> wm-GABA/Cr in precognitive behavioral therapy was not in a Gaussian distribution, and the nonparametric Wilcoxon signed rank test was applied in statistical analysis.

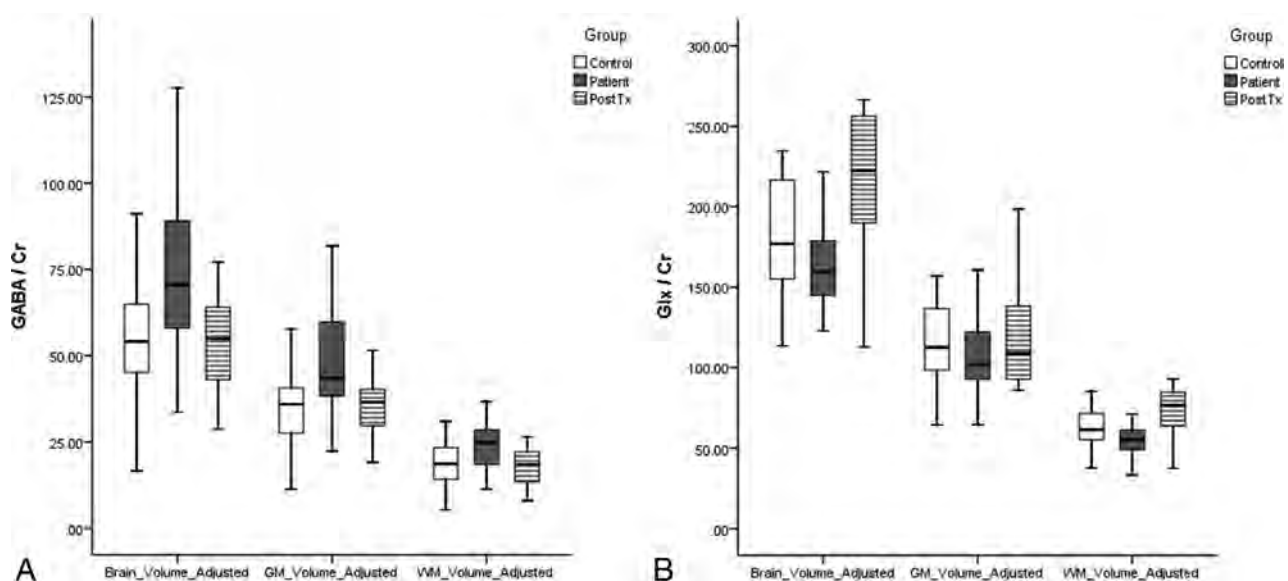


**FIG 3.** The boxplots of GABA/Cr (A) and Glx to Glx/Cr (B) in healthy controls and Internet and smartphone addicted subjects pre- and posttherapy. The horizontal line is the median, and the upper and lower ends of the boxes are the upper and lower quartiles, respectively. The vertical lines represent data ranges. PostTX indicates postcognitive behavioral therapy.



**Table 4: Correlation between neurotransmitter and psychological tests**

		bp-GABA/Cr	gm-GABA/Cr	wm-GABA/Cr	bp-GLX/Cr	gm-GLX/Cr	wm-GLX/Cr
IAT	<i>r</i>	0.345	0.387	0.252	−0.088	−0.029	−0.192
	<i>P</i> value	.034 <sup>a</sup>	.016 <sup>a</sup>	.127	.599	.863	.249
SAS	<i>r</i>	0.300	0.323	0.250	−0.209	−0.172	−0.240
	<i>P</i> value	.067	.048 <sup>a</sup>	.129	.209	.302	.146
IAT+SAS	<i>r</i>	0.336	0.372	0.260	−0.144	−0.093	−0.219
	<i>P</i> value	.039 <sup>a</sup>	.022 <sup>a</sup>	.116	.388	.578	.186
HRSD	<i>r</i>	0.312	0.326	0.298	−0.201	−0.17	−0.201
	<i>P</i> value	.057	.046 <sup>a</sup>	.069	.227	.308	.227
State STAI	<i>r</i>	0.327	0.348	0.274	0.075	0.096	0.028
	<i>P</i> value	.045 <sup>a</sup>	.032 <sup>a</sup>	.095	.655	.566	.867
Trait STAI	<i>r</i>	0.294	0.305	0.263	−0.197	−0.173	−0.212
	<i>P</i> value	.073	.062	.111	.235	.300	.202
Total STAI	<i>r</i>	0.335	0.350	0.291	−0.071	−0.048	−0.097
	<i>P</i> value	.040 <sup>a</sup>	.031 <sup>a</sup>	.077	.674	.770	.564
BIS	<i>r</i>	0.132	0.145	0.109	−0.06	−0.042	−0.079
	<i>P</i> value	.429	.386	.513	.72	.800	.637
ISI	<i>r</i>	0.073	0.037	0.139	−0.386	−0.419	−0.255
	<i>P</i> value	.664	.824	.405	.017 <sup>a</sup>	.009 <sup>a</sup>	.123
PSQI	<i>r</i>	0.235	0.194	0.305	−0.405	−0.439	−0.264
	<i>P</i> value	.155	.242	.063	.012 <sup>a</sup>	.006 <sup>a</sup>	.109

**Note:**—PreTx indicates precognitive behavioral therapy; PostTx, postcognitive behavioral therapy; IAT, Internet Addiction Test; SAS, Smartphone Addiction Scale; HRSD, Hamilton Rating Scale for Depression; STAI, State-Trait Anxiety Inventory; BIS, Barratt Impulsiveness Scale; ISI, Insomnia Severity Index; PSQI, Pittsburgh Sleep Quality Assessment.

<sup>a</sup> *P* value ≤ .05.

.031; Fig 4B). The bp-GABA/Cr significantly correlated with state anxiety ( $P = .045$ ) and total anxiety ( $P = .040$ ).

GLX/Cr did not correlate with Internet and smartphone addictions scores. The bp-GLX/Cr and gm-GLX/Cr significantly correlated with insomnia ( $P = .017$  and  $P = .009$ , respectively) and sleep quality ( $P = .012$  and  $.006$ , respectively; Fig 4C). Impulsivity did not correlate with GABA or Glx levels.

## DISCUSSION

The results of this study showed that GABA levels were higher in the ACC in young subjects with Internet and smartphone addictions and decreased after 9 weeks of cognitive behavioral therapy. The bp-GABA and gm-GABA correlated with depression and anxiety scores as well as Internet and smartphone addiction scores. The bp-GLX and gm-GLX negatively correlated with insomnia severity and sleep quality.

Recently, the high accessibility of smartphones has led to severe functional impairments compared with conventional Internet addiction. Smartphone addiction is a behavioral or technological addiction based on Internet use and shares core symptoms and risk factors with Internet addiction.<sup>22,23</sup> Therefore, smartphone addiction could be considered a category of Internet addiction;<sup>23</sup> thus, Internet and smartphone addictions were not separated in this study.

GABA is the main inhibitory neurotransmitter and is present at approximately one-third of all synapses.<sup>24</sup> The GABA concentration in the human brain is approximately 1 mM.<sup>24</sup> GABA is present in inhibitory local interneurons and is approximately 7-fold more concentrated in gray matter than in white matter.<sup>24,25</sup> Therefore, the gm-GABA level was statistically more significant than wm-GABA in this study (Tables 2–4). Glutamate is the main component in Glx based on MR spectroscopy. Glutamate is the major excitatory neurotransmitter, and GABA is mostly

synthesized from glutamate via decarboxylation.<sup>26</sup> The concentration of glutamate was also approximately 2-fold higher in gray matter.<sup>25</sup> GABA and glutamate are also key opposite modulators of dopamine in mesocorticolimbic pathways, which are closely associated with addiction.<sup>4,27,28</sup>

In previous in vivo MR spectroscopy studies, the decreased GABA level was associated with depression and autism spectrum disorders.<sup>29</sup> Schizophrenia did not show statistical significance in the meta-analysis but tended to exhibit lower GABA levels. In several studies, a low GABA level was reported in subjects with attention deficit/hyperactivity disorder and panic disorder.<sup>30–33</sup> GABA<sub>A</sub> receptor subunit expression has also been shown to exert significant influence on substance and gambling addictions.<sup>28,34</sup> A high signal-to-noise ratio is a technical challenge when using MR spectroscopy to measure GABA levels. However, the occipital or parietal lobes have been evaluated in many GABA MR spectroscopy studies without being implicated in the etiology of psychiatric disorders, though homogeneous magnetic field and increased signal-to-noise ratios were obtained.<sup>29</sup>

The ACC is the dopamine pathway associated with Internet and substance addictions. The ACC also provides a higher signal-to-noise ratio and a homogeneous magnetic field because the ACC is distant from the skull and relatively close to the MR imaging receiver compared with other regions of the mesocorticolimbic system such as the ventral tegmental area, nucleus accumbens, insula, and prefrontal cortex. Therefore, the ACC was thought to satisfy the hypothesis-driven and technical approaches when using MR spectroscopy to study Internet addiction.

In this study, GABA levels were increased in Internet- and smartphone-addicted youth compared with other psychiatric disorders and substance addictions. Two mechanisms can be postulated for the increased GABA levels in Internet and smartphone addiction. One involves the different neurobiology of Internet or



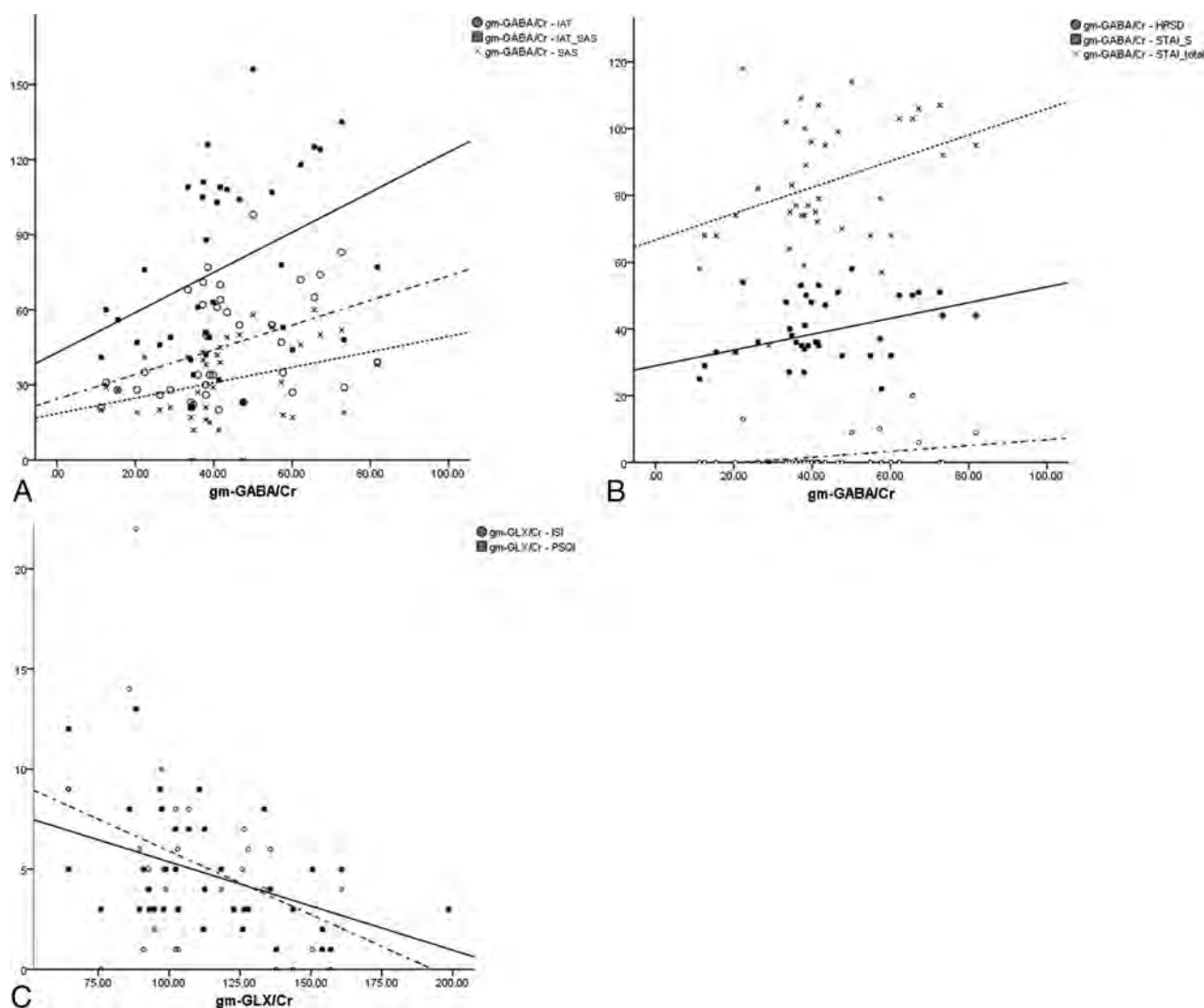


**FIG 4.** The correlations between neurotransmitters and clinical scales of Internet addiction and psychological tests. A, The gm-GABA/Cr is significantly correlated with the Internet Addiction Test (circle and dashed line) and the Smartphone Addiction Scale (x and dotted line) as well as the sum of both scales (square and solid line). B, The gm-GABA/Cr was significantly correlated with the depression scale (circle and dashed line), total anxiety score (x and dotted line), and state anxiety score (square and solid line). C, The gm-GLX/Cr was correlated with insomnia (circle and dashed line) and sleep quality scores (square and solid line). IAT indicates Internet Addiction Test; SAS, Smartphone Addiction Scale; HRSD, Hamilton Rating Scale for Depression; STAI-S, State-Trait Anxiety Inventory to measure state component of anxiety; PSQI, Pittsburgh Sleep Quality Assessment.

behavioral addiction, and the other involves tolerance or an anti-reward mechanism. GABA inhibits synaptic signal transmission in the central nervous system. Activation of GABA<sub>A</sub> and GABA<sub>B</sub> receptors hyperpolarizes neurons and inhibits action potential generation and neurotransmission.<sup>24</sup> The inhibition of GABA at the synapse attenuates the function of involved neural networks. Therefore, the increased GABA levels in subjects with Internet and smartphone addiction may be associated with the down-regulation of ACC functions, including impulsiveness control during the decision-making process under conditions of risk.<sup>18</sup>

The ACC is also important for input integration and regulation of processing in cognitive and emotional neural networks.<sup>35</sup> In many neuroimaging and animal studies, the ACC was shown to be associated with affective disorders (Fig 1).<sup>35-37</sup> ACC functional loss caused by lesions produces symptoms of emotional instability, inattention, and decreased social interaction.<sup>35,37</sup> The

emotional and personal traits caused by neurotransmitter derangement include risk factors for Internet and smartphone addictions and may be shared with the pathophysiology of psychiatric comorbidities in Internet and smartphone addiction, such as depression, attention deficit/hyperactivity disorder, and hostility.<sup>1,2</sup> In a meta-analysis, Internet addiction was strongly associated with comorbid psychopathology, though the causal interaction could not be defined because of the insufficient longitudinal study.<sup>38</sup> In this study, the risk factors and psychiatric comorbidities of Internet and smartphone addiction were possibly associated with decreased ACC function due to increased GABA levels (Table 4 and Fig 4).

Glutamate was shown to enhance the ACC functions in emotion processing and personal traits in previous studies.<sup>13-15</sup> The ACC glutamate concentration was positively correlated with impulsivity.<sup>14</sup> Conversely, reduced ACC glutamate concentration

increased the risk of exposure to noxious stimulation, concerns regarding potential problems, and the fear associated with uncertainty.<sup>13,15</sup> The negative correlations of Glx with insomnia severity and sleep quality in this study may be explained by decreased emotional ACC functions. In this study, the change in GABA levels after cognitive behavioral treatment showed that the GABA change was not the structural change of GABAergic interneurons but a functional change of GABAergic inhibition.<sup>29</sup> The neurotransmitters can be reversed and normalized with improvement regarding Internet and smartphone addiction and comorbidities.

This study had several limitations. First is the reproducibility issue of GABA MR spectroscopy. GABA levels can be affected by age, sex, and circadian rhythm. In a previous study, the GABA level was lower in older subjects on the basis of the age-related gray matter loss; however, the tissue-corrected GABA analysis could correct the age effect.<sup>28,39</sup> Although the neurotransmitters in youth can be changed by the developing brain volume before and after puberty, the change of neurotransmitters in healthy youth has not yet been reported. Males showed higher specific GABA receptor subunits in tissue analysis,<sup>40</sup> and GABA levels were increased at the time of ovulation in females.<sup>41</sup> However, in this study, tissue-corrected GABA analysis and exact sex- and age-matched case and control groups were used to reduce the biologic variability. We tried to improve the technical reproducibility of MR spectroscopy as much as possible with the use of large voxel volume and careful positioning in the ACC, as well as preparing very low first- and second-order shimming values.

Another limitation was the relatively small sample size of the study population, particularly in cognitive behavioral therapy. A future study with a larger sample size could clarify the roles of neurotransmitters in subjects with Internet and smartphone addiction. Last, the MR spectroscopy analysis used did not separate the glutamate peak from the glutamine peak. MEGA-PRESS MR spectroscopy with a 1.9-ppm editing pulse can separate the Glx signal at 3.7 ppm as well as GABA at 2.01 ppm,<sup>42</sup> and the Glx concentration detected on MR spectroscopy was very likely associated with excitatory neurotransmission.<sup>43</sup>

## CONCLUSIONS

A higher GABA level in the ACC was associated with Internet and smartphone addiction. The high GABA level in Internet and smartphone addiction was normalized after cognitive behavioral therapy. In addition, GABA and Glx levels were correlated with clinical scores obtained using standard psychological tests. The abnormal GABA level or disrupted balance between GABA and Glx including glutamate in the ACC may contribute to understanding the biochemical and molecular basis of the Internet and smartphone addiction and the associated comorbidities that could be used to devise appropriate treatments.

Disclosures: Hyung Suk Seo—RELATED: Grant: National Research Foundation of Korea (2013RIA1A1012361).

## REFERENCES

- Weinstein A, Lejoux M. **Internet addiction or excessive internet use.** *Am J Drug Alcohol Abuse* 2010;36:277–83 CrossRef Medline
- Jorgenson AG, Hsiao RC, Yen CF. **Internet addiction and other behavioral addictions.** *Child Adolesc Psychiatr Clin N Am* 2016;25:509–20 CrossRef Medline
- American Psychiatric Association. *Diagnostic and Statistical Manual of Mental Disorders.* American Psychiatric Association; 2013
- Jasinska AJ, Stein EA, Kaiser J, et al. **Factors modulating neural reactivity to drug cues in addiction: a survey of human neuroimaging studies.** *Neurosci Biobehav Rev* 2014;38:1–16 CrossRef Medline
- Hayes DJ, Jupp B, Sawiak SJ, et al. **Brain gamma-aminobutyric acid: a neglected role in impulsivity.** *Eur J Neurosci* 2014;39:1921–32 CrossRef Medline
- Kim SH, Baik SH, Park CS, et al. **Reduced striatal dopamine D2 receptors in people with Internet addiction.** *Neuroreport* 2011;22:407–11 CrossRef Medline
- Hou H, Jia S, Hu S, et al. **Reduced striatal dopamine transporters in people with internet addiction disorder.** *J Biomed Biotechnol* 2012;2012:854524 CrossRef Medline
- Littel M, van den Berg I, Luijten M, et al. **Error processing and response inhibition in excessive computer game players: an event-related potential study.** *Addict Biol* 2012;17:934–47 CrossRef Medline
- Kalivas PW, Volkow ND. **The neural basis of addiction: a pathology of motivation and choice.** *Am J Psychiatry* 2005;162:1403–13 CrossRef Medline
- Lin F, Zhou Y, Du Y, et al. **Abnormal white matter integrity in adolescents with internet addiction disorder: a tract-based spatial statistics study.** *PLoS One* 2012;7:e30253 CrossRef Medline
- Stan AD, Schirda CV, Bertocci MA, et al. **Glutamate and GABA contributions to medial prefrontal cortical activity to emotion: implications for mood disorders.** *Psychiatry Res* 2014;223:253–60 CrossRef Medline
- Graham BM, Milad MR. **The study of fear extinction: implications for anxiety disorders.** *Am J Psychiatry* 2011;168:1255–65 CrossRef Medline
- Gallinat J, Kunz D, Lang UE, et al. **Association between cerebral glutamate and human behaviour: the sensation seeking personality trait.** *Neuroimage* 2007;34:671–78 CrossRef Medline
- Hoerst M, Weber-Fahr W, Tunc-Skarka N, et al. **Correlation of glutamate levels in the anterior cingulate cortex with self-reported impulsivity in patients with borderline personality disorder and healthy controls.** *Arch Gen Psychiatry* 2010;67:946–54 CrossRef Medline
- Kim HJ, Kim JE, Cho G, et al. **Associations between anterior cingulate cortex glutamate and gamma-aminobutyric acid concentrations and the harm avoidance temperament.** *Neurosci Lett* 2009;464:103–07 CrossRef Medline
- Mansvelder HD, Keath JR, McGehee DS. **Synaptic mechanisms underlie nicotine-induced excitability of brain reward areas.** *Neuron* 2002;33:905–19 CrossRef Medline
- Mescher M, Merkle H, Kirsch J, et al. **Simultaneous in vivo spectral editing and water suppression.** *NMR Biomed* 1998;11:266–72 CrossRef Medline
- Fujihara K, Narita K, Suzuki Y, et al. **Relationship of gamma-aminobutyric acid and glutamate+glutamine concentrations in the perigenual anterior cingulate cortex with performance of Cambridge Gambling Task.** *Neuroimage* 2015;109:102–08 CrossRef Medline
- Beard KW, Wolf EM. **Modification in the proposed diagnostic criteria for Internet addiction.** *Cyberpsychol Behav* 2001;4:377–83 CrossRef Medline
- Kwon M, Kim DJ, Cho H, et al. **The smartphone addiction scale: development and validation of a short version for adolescents.** *PLoS One* 2013;8:e83558 CrossRef Medline
- Lee HC, Ahn CI. **Study on the development and effectiveness of cognitive-behavioral therapy for internet addiction.** *Korean Journal of Psychology* 2002;12:463–86
- Choi SW, Kim DJ, Choi JS, et al. **Comparison of risk and protective factors associated with smartphone addiction and Internet addiction.** *J Behav Addict* 2015;4:308–14 CrossRef Medline

23. Lin YH, Chiang CL, Lin PH, et al. **Proposed diagnostic criteria for smartphone addiction.** *PLoS One* 2016;11:e0163010 CrossRef Medline
24. Owens DF, Kriegstein AR. **Is there more to GABA than synaptic inhibition?** *Nat Rev Neurosci* 2002;3:715–27 CrossRef Medline
25. Ganji SK, An Z, Banerjee A, et al. **Measurement of regional variation of GABA in the human brain by optimized point-resolved spectroscopy at 7 T in vivo.** *NMR Biomed* 2014;27:1167–75 CrossRef Medline
26. Danbolt NC. **Glutamate uptake.** *Prog Neurobiol* 2001;65:1–105 CrossRef Medline
27. Gardner EL. **Addiction and brain reward and antireward pathways.** *Adv Psychosom Med* 2011;30:22–60 CrossRef Medline
28. Mick I, Ramos AC, Myers J, et al. **Evidence for GABA-A receptor dysregulation in gambling disorder: correlation with impulsivity.** *Addict Biol* 2017;22:1601–09 CrossRef Medline
29. Schur RR, Draisma LW, Wijnen JP, et al. **Brain GABA levels across psychiatric disorders: a systematic literature review and meta-analysis of (1) H-MRS studies.** *Hum Brain Mapp* 2016;37:3337–52 CrossRef Medline
30. Edden RA, Crocetti D, Zhu H, et al. **Reduced GABA concentration in attention-deficit/hyperactivity disorder.** *Arch Gen Psychiatry* 2012;69:750–53 CrossRef Medline
31. Ende G, Cackowski S, Van Eijk J, et al. **Impulsivity and aggression in female BPD and ADHD patients: association with ACC glutamate and GABA concentrations.** *Neuropsychopharmacology* 2016; 41:410–18 CrossRef Medline
32. Goddard AW, Mason GF, Almai A, et al. **Reductions in occipital cortex GABA levels in panic disorder detected with 1H-magnetic resonance spectroscopy.** *Arch Gen Psychiatry* 2001;58:556–61 CrossRef Medline
33. Long Z, Medlock C, Dziedzic M, et al. **Decreased GABA levels in anterior cingulate cortex/medial prefrontal cortex in panic disorder.** *Prog Neuropsychopharmacol Biol Psychiatry* 2013;44:131–35 CrossRef Medline
34. Stephens DN, King SL, Lambert JJ, et al. **GABAA receptor subtype involvement in addictive behaviour.** *Genes Brain Behav* 2017;16: 149–84 CrossRef Medline
35. Bush G, Luu P, Posner MI. **Cognitive and emotional influences in anterior cingulate cortex.** *Trends Cogn. Sci* 2000;4:215–22 CrossRef Medline
36. Baskin-Sommers AR, Foti D. **Abnormal reward functioning across substance use disorders and major depressive disorder: considering reward as a transdiagnostic mechanism.** *Int J Psychophysiol* 2015;98:227–39 CrossRef Medline
37. Hadland KA, Rushworth MF, Gaffan D, et al. **The effect of cingulate lesions on social behaviour and emotion.** *Neuropsychologia* 2003;41: 919–31 CrossRef Medline
38. Carli V, Durkee T, Wasserman D, et al. **The association between pathological internet use and comorbid psychopathology: a systematic review.** *Psychopathology* 2013;46:1–13 CrossRef Medline
39. Hermans L, Levin O, Maes C, et al. **GABA levels and measures of intracortical and interhemispheric excitability in healthy young and older adults: an MRS-TMS study.** *Neurobiol Aging* 2018;65: 168–77 CrossRef Medline
40. Pandya M, Palpagama TH, Turner C, et al. **Sex- and age-related changes in GABA signaling components in the human cortex.** *Biol Sex Differ* 2019;10:5 CrossRef Medline
41. De Bondt T, De Belder F, Vanhevel F, et al. **Prefrontal GABA concentration changes in women-Influence of menstrual cycle phase, hormonal contraceptive use, and correlation with premenstrual symptoms.** *Brain Res* 2015;1597:129–38 CrossRef Medline
42. Edden RA, Barker PB. **Spatial effects in the detection of gamma-aminobutyric acid: improved sensitivity at high fields using inner volume saturation.** *Magn Reson Med* 2007;58:1276–82 CrossRef Medline
43. Bauer J, Pedersen A, Scherbaum N, et al. **Craving in alcohol-dependent patients after detoxification is related to glutamatergic dysfunction in the nucleus accumbens and the anterior cingulate cortex.** *Neuropsychopharmacology* 2013;38:1401–08 CrossRef Medline

# Brain Cortical Structure and Executive Function in Children May Be Influenced by Parental Choices of Infant Diets

 T. Li,  T.M. Badger,  B.J. Bellando,  S.T. Sorensen,  X. Lou, and  X. Ou



## ABSTRACT

**BACKGROUND AND PURPOSE:** While it is known that breastfeeding promotes healthy brain development in children, the potential effects of formulas substantially differing in composition (ie, milk-based versus soy-based) during infancy on brain development are unclear.

**MATERIALS AND METHODS:** Seventy-one 8-year-old children who were predominantly breastfed, milk formula fed, or soy formula fed during infancy were recruited for an MR imaging examination of the brain and a Behavior Rating Inventory of Executive Function assessment (completed via a questionnaire to the parents). Brain cortical features measured from MR imaging such as cortical thickness and surface area were extracted and compared among groups and correlated with Behavior Rating Inventory of Executive Function test scores.

**RESULTS:** Clusters in the frontal and occipital lobes showed significant differences (cluster-wise  $P \leq .05$ , corrected for multiple comparisons) in cortical thickness or surface area among the 3 diet groups. The effects were more prominent for boys, particularly for comparison of the milk formula fed versus soy formula fed boys. Assessments of executive function and behavior showed significantly lower Behavior Rating Inventory of Executive Function test scores in soy formula fed versus milk formula fed groups, which were mostly attributed to differences in boys. There were no differences between milk formula fed and breastfed groups for either sex. Mean cortical thickness for several of the clusters in the brain showing infant diet-associated effects significantly correlated with Behavior Rating Inventory of Executive Function scores.

**CONCLUSIONS:** Choices of infant diets (ie, breastfed, milk formula fed, soy formula fed) may have long-term and sex-specific effects on the cortical development and executive function and behavior of children's brains.

**ABBREVIATIONS:** BF = breastfed; BRIEF = Behavior Rating Inventory of Executive Function; MF = milk formula fed; SF = soy formula fed

The World Health Organization recommends exclusive breastfeeding for neonates to up to 6 months of age and continued breastfeeding in combination with other foods to age 2 years or


older. The American Association of Pediatrics also reaffirmed its breastfeeding guidelines, which are essentially consistent with the World Health Organization recommendations.<sup>1</sup> With breastfeeding support from all sectors of society, the breastfeeding rate in the United States has been increasing in recent years. The most recent Centers for Disease Control and Prevention Breastfeeding Report Card shows that currently, 83.2% of children born in United States started out breastfeeding, 46.9% of all infants were exclusively breastfed at 3 months, and 57.6% of all infants were at least partially breastfed at 6 months.<sup>2</sup> For those who did not start out breastfeeding or ended sooner than recommended, cow's milk protein-based formula has been the main alternative. Soy protein-based formula currently accounts for a small percentage of the infant formula market in the United States but remains useful for infants allergic to milk formula or for parents wishing to maintain a vegetarian lifestyle. Soy-based formula and milk-based formula sold in the United States meet specific requirements of the US Food and Drug Administration for nutrient content. A major difference in soy formula and all other formulas is that the soy protein


Received December 27, 2019; accepted after revision April 17, 2020.


From the Departments of Radiology (T.L., X.O.) and Pediatrics (T.M.B., B.J.B., S.T.S., X.O.), University of Arkansas for Medical Sciences, Little Rock, Arkansas; Arkansas Children's Nutrition Center (T.L., T.M.B., B.J.B., S.T.S., X.O.), Little Rock, Arkansas; Department of Information Sciences (T.L., X.O.), University of Arkansas at Little Rock, Little Rock, Arkansas; Department of Biostatistics (X.L., X.O.), University of Florida, Gainesville, Florida; and Arkansas Children's Research Institute (X.O.), Little Rock, Arkansas.

This project was supported by US Department of Agriculture–Agricultural Research Service Project 6026-51000-010-055 at the Arkansas Children's Nutrition Center. The Principal Investigator is also supported by National Institutes of Health R01 HD099099.

Please address correspondence to Xiawei Ou, PhD, 1 Children's Way, Slot 105, Little Rock, AR 72202; e-mail: ouxiawei@uams.edu

 Indicates open access to non-subscribers at [www.ajnr.org](http://www.ajnr.org)

 Indicates article with supplemental on-line table.

 Indicates article with supplemental on-line photos.

<http://dx.doi.org/10.3174/ajnr.A6601>



used in soy-based formula contains isoflavones, which can have weak estrogenic activity, and this has led some health professionals to be concerned about sexual development and reproduction in children fed soy formula. Nevertheless, there is no conclusive evidence from the current literature to show adverse effects on human development, reproduction, or endocrine function of dietary soy isoflavones.<sup>3</sup>

Many studies have observed benefits to children's health and development associated with breastfeeding, including promotion of neurodevelopment such as higher intelligence.<sup>4,5</sup> Recent neuroimaging studies have also revealed the effects of breastfeeding or breast milk intake on children's brain development, including increased total brain volume and white matter volume associated with a higher percentage of breast milk intake in boys born preterm;<sup>6</sup> a positive association between the duration of exclusive breastfeeding and cortical thickness in the superior and inferior parietal lobes;<sup>7</sup> better white matter development in frontal and association brain regions associated with exclusive breastfeeding;<sup>8</sup> as well as higher regional gray matter volume in the inferior temporal lobe and superior parietal lobe and higher white matter integrity in the left brain hemisphere (in boys) in breastfed-versus-formula fed children.<sup>9,10</sup> Few studies have evaluated whether there are brain developmental differences associated with soy- versus milk-based formulas, despite findings that estrogen may play an important role in neurodevelopment<sup>11</sup> and soy isoflavone may have important implications in cognitive function.<sup>12</sup> To our knowledge, the only published data on soy formula-brain effects were electroencephalographic and event-related potential evaluations of cortical activity, in which differences in brain electrical activity associated with infant diets were observed during the first year of life.<sup>13,14</sup>

Infant diets may have long-lasting effects on brain anatomy and function and neurobehavioral outcomes, through programming mechanisms that remain to be fully elaborated. In this study, we hypothesized that there are structural differences in the brain cortex of school-age children that are associated with type of diet during infancy, ie, breastmilk, cow's milk formula, or soy formula. We also hypothesized that these brain structure differences are associated with differences in behavior, particularly, parent-reported executive functioning. To test the hypothesis, we recruited healthy 8-year-old children who were predominately breastfed (BF), cow's milk formula fed (MF), or soy formula fed (SF) during the first year of life and evaluated their brain cortical development using MR imaging and their executive function and behavior using the Behavior Rating Inventory of Executive Function (BRIEF) assessment. Specifically, we measured brain cortical thickness and surface area, as well as behavioral regulation and Metacognition Indexes and other BRIEF subscales, and compared those parameters among the 3 diet groups. We also tested whether there are significant correlations between these MR imaging parameters and BRIEF test scores regardless of the infant diet group.

## MATERIALS AND METHODS

### Subjects

Healthy 7.5- to 8.5-year-old children were recruited for this brain power study (Infant Diet Effects on Brain Function and Language Processing; ClinicalTrials.gov Identifier: NCT00735423). All experimental procedures were approved by the institutional review

board of the University of Arkansas for Medical Sciences, and all participants provided assent as well as parental consent. Inclusion criteria for the participants included the following: 90–101 months of age; parental report of full-term gestation at birth (38–42 weeks); parental report of birth weight between the 5th and 95th percentile for age (2.5–4.2 kg); and parental report of predominant use of breast milk, milk-based formula, or soy-based formula during infancy. BF infants were exclusively or partially breastfed for at least 8 months (rounded to the closest number) before completely transitioning to formula or other diets; MF and SF infants were fed for same type of formula (cow's milk-based or soy-based) since the first weeks of life throughout the first year of life. Exclusion criteria for the participants included the following: maternal use of alcohol, tobacco, illicit drugs, or psychotropic medications during pregnancy; illnesses and chronic diseases that may affect children's growth or development; psychological/psychiatric diagnoses; neurologic impairment or injury; history or current use of anticonvulsant, stimulant, or mood-stabilizing medications; and history or current use of remedial special education services. In total, 71 children had valid structural MR imaging data and were included in this study. Among them, 68 children had completed BRIEF assessment by their parents. The demographic information of the study subjects is listed in Table 1.

### MR Imaging Data Acquisition

All children had a brain MR imaging at the radiology department of the Arkansas Children's Hospital on a 1.5T Achieva scanner (Philips Healthcare) with a 60-cm bore size, 33-mT/m gradient amplitude, and 100-mT/m/ms maximum slew rate. The built-in body coil was used as a transmitter, and a standard 8-channel sensitivity encoding head coil was used as a receiver. Structural imaging data of the brain were acquired using a T1-weighted 3D turbo field echo pulse sequence with the following parameters: TR = 7.3 ms; TE = 3.4 ms; flip angle = 8°; acquisition voxel size = 1 × 1 × 1 mm; matrix size = 256 × 232 × 150; two averages; and 7 minutes of scan time. All images were reviewed on the scanner at the time of scanning, and scans with substantial motion artifacts were repeated.

### MR Imaging Processing

All T1-weighted MR images were exported to a Macintosh computer with FreeSurfer software (<http://surfer.nmr.mgh.harvard.edu>) for cortical analysis. Standard preprocessing steps were applied, including motion correction, nonbrain tissue removal, and transformation to the Talairach space. Imaging segmentation (to white matter, gray matter, and CSF) was then performed, followed by intensity normalization, tessellation of cortical gray/white matter boundaries, automated topology correction, and surface deformation. Cortical images were registered to a spherical atlas to match geometry across subjects and parcellated to different brain regions on the basis of anatomy. In addition, a full width half maximum Gaussian blurring kernel of 10 mm was applied to smooth the parameter maps. All processed or intermediate images were visually inspected to ensure quality. Cortical thickness and outer surface area were calculated, respectively, from distances between gray/white and gray/CSF boundaries and the area of all vertices along the surface. The cortical thickness

**Table 1: Demographic information of the 8-year-old children participating in the study**

	BF (n = 22)	MF (n = 25)	SF (n = 24)	P Value
Sex (M/F)	10/12	10/15	11/13	.90
Weight (mean) (kg)	27.8 ± 6.3	27.7 ± 5.1	27.2 ± 4.8	.90
Height (mean) (cm)	127.7 ± 4.7	128.5 ± 4.1	125.9 ± 5.3	.16
Age at MR imaging (mean) (yr)	7.98 ± 0.29	7.93 ± 0.25	7.87 ± 0.25	.33
BRIEF completed (M/F)	10/12	10/13	10/13	.99
Mother's education (no/partial or full/above college)	0/9/5	0/9/6	1/6/7	.54
Father's education (no/partial or full/above college)	2/10/2	2/10/3	3/9/0	.56
Mother's annual income (<\$20,000/\$20,000–\$59,999/>\$59,999)	6/3/3/0	12/3/7/2	11/2/6/3	.52
Father's annual income (<\$20,000/\$20,000–\$59,999/>\$59,999)	14/0/9/5	15/0/8/7	11/0/5/6	.63

**Table 2: Global imaging features for the 3 feeding groups**

Features	BF (Mean)	MF (Mean)	SF (Mean)	F Score	P Value
LH mean cortical thickness (mm)	2.77 ± 0.09	2.76 ± 0.09	2.78 ± 0.09	0.30	.74
RH mean cortical thickness (mm)	2.76 ± 0.08	2.75 ± 0.10	2.78 ± 0.09	0.64	.53
LH surface area (cm <sup>2</sup> )	905 ± 83	893 ± 78	933 ± 104	1.28	.29
RH surface area (cm <sup>2</sup> )	902 ± 80	897 ± 83	937 ± 104	1.43	.25
LH cortical volume (cm <sup>3</sup> )	291 ± 25	289 ± 24	300 ± 31	1.26	.29
RH cortical volume (cm <sup>3</sup> )	290 ± 24	289 ± 26	301 ± 32	1.50	.23
Total intracranial volume (cm <sup>3</sup> )	1490 ± 127	1502 ± 123	1529 ± 149	0.5	.61

**Note:**—LH indicates left hemisphere; RH, right hemisphere.

and surface area parameter maps were then fed to a General Linear Model (GLM) in FreeSurfer for group comparisons.

### BRIEF Assessment

The BRIEF is an 86-item questionnaire for parents that assesses executive function and behavior for their children and adolescents 5–18 years of age.<sup>15</sup> The parents of children who completed MR imaging were requested to complete the BRIEF assessment. Eight clinical subscales were derived from the answers to the questionnaire, including Inhibit, Shift, Emotional Control, Initiate, Working Memory, Plan/Organize, Organization of Materials, and Monitor. These 8 subscales formed 2 indexes regarding the children's executive function and behavior: the Behavioral Regulation Index (BRI) and Metacognition Index, and 1 overall score: Global Executive Composite (GEC). In addition, we also obtained 2 validity scores: Negativity (reflects the extent to which the questionnaire was answered in an unusually negative manner) and Inconsistency (reflects the extent to which the respondent answers similar questions in an inconsistent manner). All BRIEF scores/indexes/subscales were compared among the 3 diet groups, and their correlations with MR imaging-measured cortical thickness and surface area were also calculated.

### Statistical Analysis

All comparisons of demographic parameters were conducted using the  $\chi^2$  test for categorical data and the ANOVA with the distribution assumption test for quantitative data, and  $P \leq .05$  was regarded as significant. Numeric data were presented as mean ± SD. All comparisons of BRIEF scores among different diet groups were conducted using the Mann-Whitney *U* test. All correlation tests between MR imaging parameters and BRIEF scores were conducted using the Spearman correlation test. For imaging parameters, all global features such as mean cortical thickness and

surface area were compared among groups using a 1-way *F* test. Group differences in regional imaging parameters (cortical thickness and surface area) were tested using GLM with the Different Offset, Different Slope (DODS) method in FreeSurfer. Specifically, to test the diet group differences, we used GLMs with DODS to fit in each vertex for cortical thickness or cortical surface area, which was a dependent variable. The feeding type (BF,

MF, or SF) was used as an independent variable, and sex and age were included as covariates because of reported sex differences<sup>16</sup> and continued brain cortical development<sup>17</sup> at this age. Total brain volume was included as a covariate in the surface area analyses but not in the cortical thickness analyses because a previous report showed that normalizing by intracranial volume did not improve the discriminant and predictive performance of cortical thickness measures.<sup>18</sup> All analyses were applied to each hemisphere separately. The  $P \leq .0001$  threshold was used for cluster forming for the vertex-wise analyses. Clusters were obtained after removing the effects of all covariates. To identify clusters with significant differences after appropriate multiple comparison correction, we applied the pre-specified cluster-wise Monte Carlo simulation with 10,000 iterations to every cluster. A corrected cluster-wise  $P \leq .05$  was regarded as significant. In addition, stratified analyses were also applied to the boys' and girls' subgroups, respectively.

## RESULTS

### MR Imaging Findings

There were no significant differences in the demographic characteristics across the 3 feeding groups (Table 1). No significant group effects among BF/MF/SF groups were observed for global imaging features of the brain such as mean cortical thickness, total surface area, total cortical gray matter volume, and intracranial volume. Details are listed in Table 2.

In total, 8 clusters showed significant infant diet-related differences ( $P \leq .05$ , after multiple comparison correction) in the combined or sex-specific regional analyses of cortical thickness and surface area, as summarized in Table 3, and location as illustrated in On-line Fig 1. Specifically, higher cortical thickness ( $P \leq .05$ , corrected) was found in a cluster in the right cuneus (cluster 1) when comparing all MF-versus-all BF children. It appears that the differences in this cluster were primarily driven by differences in

**Table 3: Clusters that showed significant differences ( $P \leq .05$ , corrected) in group comparisons of cortical thickness or surface area<sup>a</sup>**

Cluster No.	Size (mm <sup>2</sup> )	No. of Vertices	Peak Coordinate			Peak Vertex t Value	Cluster-Wise P Value	Relationships
			x	y	z			
1	106	134	9.9	-87.1	17.7	5.05	.007	All: MF>BF
2	132	165	10.7	-87.4	18.5	5.38	.003	Boys: MF>BF
3	128	180	-11.4	-74	12.7	5.34	.004	Boys: MF>BF
4	151	189	11.2	-87.8	18.5	4.76	.001	Boys: MF>SF
5	78	100	3.6	-74.2	14.3	4.88	.02	Boys: MF>SF
6	87	82	-7.8	-87.9	-10.8	4.65	.01	Boys: MF>SF
7	53	117	15.2	-16	64.5	4.38	.046	Girls: SF>MF
8	138	220	-32.9	8.5	55.3	4.77	.01	Boys: MF>SF <sup>a</sup>

<sup>a</sup> For surface area comparison; everything else: for cortical thickness comparison.

the male subgroups because a similar cluster (cluster 2) showed higher cortical thickness ( $P \leq .05$ , corrected) in MF-versus-BF boys, while there were no significant differences between MF and BF girls. In addition, a small cluster in the left pericalcarine cortex (cluster 3) also showed higher cortical thickness ( $P \leq .05$ , corrected) in MF-versus-BF boys. When comparing all MF-versus-all SF children, there were no significant differences between groups in any regions. However, sex-specific analyses showed that 2 clusters (clusters 4 and 5) in the right cuneus and 1 cluster in the left lingual gyrus (cluster 6) showed higher cortical thickness ( $P \leq .05$ , corrected) in MF-versus-SF boys, while 1 cluster in the right precentral gyrus (cluster 7) showed lower cortical thickness ( $P = .046$ ) in MF-versus-SF girls. There were no significant differences in cortical thickness for BF-versus-SF comparisons (combined or sex-specific). Finally, higher surface area ( $P \leq .05$ , corrected) was also observed in a cluster in the left middle frontal gyrus (cluster 8) when comparing MF-versus-SF boys, while no other group differences in surface area were found in the combined or sex-specific analyses.

### BRIEF Assessment Findings

None of the children for any diet groups showed clinically significant symptomatology on the BRIEF assessment (GEC score or Metacognition Index/BRI index of  $>65$ ). The mean Negativity ( $0.1 \pm 0.3$  for BF,  $0.1 \pm 0.5$  for MF,  $0 \pm 0$  for SF) and Inconsistency scores ( $2.3 \pm 1.6$  for BF,  $2.8 \pm 1.4$  for MF,  $2.3 \pm 1.9$  for SF) were low and below the validity threshold, and there were no differences among the 3 diet groups ( $P > .05$  for any comparison). Other BRIEF assessment scores are presented in On-line Fig 2. Specifically, the overall mean GEC scores were not different in BF versus MF or BF versus SF but were significantly higher in MF versus SF ( $46.8 \pm 6.7$  versus  $42.4 \pm 6.4$ ,  $P = .049$ ). The differences were driven by differences in boys (sex-specific analyses showed  $45.3 \pm 3.6$  versus  $38.6 \pm 4.9$ ,  $P = .006$  for boys, and  $48.0 \pm 8.4$  versus  $45.4 \pm 6.0$ ,  $P = .55$  for girls). Likewise, the mean Metacognition Indexes were not different in BF versus MF or BF versus SF but were significantly higher in MF versus SF ( $47.6 \pm 7.0$  versus  $42.7 \pm 7.6$ ,  $P = .016$ ), driven by differences in boys ( $45.5 \pm 5.0$  versus  $38.4 \pm 5.6$ ,  $P = .008$ ) but not girls ( $49.2 \pm 8.1$  versus  $46.0 \pm 7.4$ ,  $P = .21$ ). The mean BRI indexes were not different for the BF/MF, BF/SF, or MF/SF comparisons. However, there was a trend of lower BRI scores in SF boys ( $40.2 \pm 5.9$ ) compared with MF boys

( $45.3 \pm 4.5$ ,  $P = .06$ ) or BF boys ( $47.4 \pm 9.0$ ,  $P = .06$ ). For the 8 specific BRIEF clinical subscales, SF boys had lower scores compared with MF boys in Shift ( $P = .047$ ), Initiate ( $P = .004$ ), Plan/Organize ( $P = .02$ ), and Monitor ( $P = .02$ ), which contributed to lower scores for all SF versus all MF in Initiate ( $P = .01$ ), Plan/Organize ( $P = .03$ ), and Monitor scores ( $P = .007$ ), despite no significant differences between SF and MF girls in any of these 8 measures. None of the BF/SF or BF/MF comparisons showed significant differences in any of these 8 measures. Overall, while all children had BRIEF scores within the normal range, SF boys showed less parent-reported executive functioning or behavior issues.

### Correlations between MR Imaging Measurements and BRIEF Scores

For the clusters that showed significant differences in regional cortical thickness or surface area among different diet groups (see the MR Imaging Findings section above), the correlations between these morphometric features with each of the BRIEF scores/indexes/subscales were also tested. For boys, the overall GEC scores (On-line Fig 3) significantly correlated with cluster cortical thickness in cluster 1 ( $r = 0.51$ ,  $P = .004$ ), cluster 2 ( $r = 0.54$ ,  $P = .002$ ), cluster 4 ( $r = 0.56$ ,  $P = .001$ ), and cluster 6 ( $r = 0.41$ ,  $P = .02$ ). There were no significant correlations between GEC scores and cortical thickness or surface area in other clusters (On-line Table). For girls, there were no significant correlations between GEC scores and any cluster features (cortical thickness or surface area). Similarly, for the BRI and Metacognition indexes and the 8 BRIEF subscales, significant correlations with cortical thickness in clusters 1, 2, 4, and 6 were observed in a number of tests for boys, while no significant correlations were observed for girls (except for correlation between working memory score and cortical thickness in cluster 6,  $r = 0.38$ ,  $P = .02$ ) (On-line Table).

### DISCUSSION

The first year of life is a critical period for normal brain development. Total brain volume doubles in the first year, which includes a 149% increase in gray matter volume and an 11% increase in white matter volume.<sup>19</sup> Influences on the brain development during this time, such as those associated with infant diet, may have profound and prolonged effects on long-term brain development and neurodevelopmental outcomes. In this study, we evaluated brain cortical

thickness and surface area measurements by neuroimaging in 3 groups of 8-year-old children who were predominately BF, MF, or SF during infancy. While there were no group differences on the whole-brain average of these imaging features, we observed significant differences in cortical thickness and surface area associated with infant diets in several clusters in the brain cortex. These findings were mostly attributed to differences in boys but not girls. Likewise, we also observed group differences in assessments of executive function and behavior in these children, with significant findings in boys but not in girls. In particular, SF boys showed lower cortical thickness and smaller cortical surface area in several regions of the brain. Meanwhile, SF boys showed lower parent-reported BRIEF scores compared with MF boys, while MF and BF groups had comparable BRIEF scores for both boys and girls. There were also significant correlations between overall BRIEF scores and mean cortical thickness in several of the cortical clusters that showed significant group differences associated with infant diets, indicating potential structural-functional relationships for these brain regions. In summary, our findings suggested that infant diets may have long-term effects on children's brain structural development and functional outcomes, particularly for boys who were predominately fed milk or soy protein-based formulas. Nevertheless, despite statistically significant regional cortical differences in SF and MF boys in the MR imaging data, the BRIEF data for all children were within the normal range, and formula feeding per se during infancy did not result in clinically significant executive function and behavior abnormalities at 8 years of age.

Brain developmental differences associated with different infant diets such as breastfeeding versus formula feeding have been reported in recent years.<sup>7-10,20</sup> The reported effects apparently were also more prominent in boys versus girls because some of these studies only observed diet-associated brain differences in boys but not in girls. For example, fractional anisotropy, a reflection of white matter microstructural integrity (such as myelination), was significantly higher in several white matter regions in breastfed-versus-formula fed boys, while it was similar in girls.<sup>9</sup> In addition, the percentage of expressed maternal breastmilk in the infant diet positively correlated with total white matter volume in boys but not in girls, though the cohort studied were all born preterm.<sup>6</sup> Benefits to neurodevelopmental outcomes associated with breastfeeding have also been widely reported, and a large-scale randomized controlled trial (randomization to a breastfeeding promotion intervention program targeted at increasing breastfeeding exclusivity and the duration among those already having decided to initiate breastfeeding) did observe a slightly higher treatment effect in verbal intelligence quotient for boys versus girls (8.0- versus 7.0-point increase for the intervention group).<sup>5</sup>

Beyond infant diets, it also appears that in general, the developing brain in boys is more vulnerable to adverse environmental influences and early life experience;<sup>21</sup> this vulnerability may point to a sex-specific difference in brain malleability in response to early life events. One main finding of this study was significant differences in brain cortical development and executive function and behavior between SF and MF boys but not girls. The exact underlying mechanisms for this observation remain to be uncovered. One speculation is that the high concentration of phytoestrogens/isoflavones contained in soy milk may have played a role. SF infants

have circulating phytoestrogen concentrations several magnitudes higher than endogenous estrogens. Although the potency of phytoestrogens is significantly lower than endogenous estrogens, the presence of circulating soy phytoestrogens may account for the effects observed herein. This possibility would be in agreement with reports in lab animals suggesting that phytoestrogens may interfere with the organizational role of estrogen in the developing human brain.<sup>22</sup> While the effects of endocrine disruption on sexually dimorphic brain regions in rodents have been extensively studied, how estrogenic compounds would impact sex-specific changes in human brain development is not as clear. Nevertheless, it is known that male and female brain regions respond differently to estrogens.<sup>23</sup> Therefore, it is possible that the assumed estrogenic effects of soy formula feeding on the infant brain and neurodevelopment were sex-specific. In fact, clinical studies of the effects of soy isoflavones on cognitive function in adults have shown improvement in cognitive functions for women, but results for men have been inconsistent,<sup>24-27</sup> also suggesting that the putative soy isoflavone effects may be sex-specific.

The brain regions showed that infant diet-associated effects on cortical thickness or surface area in these 8-year-old children mostly involved the cuneus and the pericalcarine cortex. These are areas usually regarded as the primary visual cortex, with a main function of basic visual processing. Other brain regions that showed infant diet-related effects included the following: the lingual gyrus, which is also linked to visual processing as well as encoding visual memories; the precentral gyrus, commonly known as the primary motor cortex and controls voluntary movement; and the middle frontal gyrus, which is implicated in a number of brain functions, such as language and cognition. Previous studies reporting associations between infant diets (particularly breastfeeding) and children's brain cortical development (such as cortical thickness or regional gray matter volume) have observed significant effects primarily in the parietal and temporal lobes.<sup>7,10</sup> Our study revealed additional brain regions in the frontal and occipital lobes that were also impacted by infant diets, indicating possibly widespread and profound effects of early nutrition on children's brain development.

Brain regions with diet effects on cortical measurements observed in this study were different from those in a previous study of 8-year-old children focused on regional gray matter volume.<sup>10</sup> It is possible that methodologic differences in these studies contributed to the apparent discrepancy. For example, regional gray matter volume measurements are often normalized to total brain volume, while cortical thickness measurements may be more sensitive without normalization.<sup>18</sup> The sensitivity of cortical thickness to developmental changes may also be impacted in some brain regions by the competing effects of initial development during infancy and normal thinning, which starts in early childhood. The regions observed in this study were primarily involved in visual, motor, and language/cognitive functioning, respectively. While breastfeeding versus formula feeding did not appear to significantly impact children's visual outcome,<sup>28</sup> exclusive breastfeeding or longer breastfeeding duration was favorably associated with physical fitness,<sup>29</sup> language development,<sup>30</sup> and cognition/intelligence in children.<sup>31</sup> In addition, we observed significant correlations between cortical thickness in visual processing areas in the occipital lobe (cuneus and lingual gyrus)



and executive function and behavior evaluated by the BRIEF assessment. While the exact structural/functional relationship of this finding is unclear, the ability to search and process visual information is a prerequisite for many executive function. Furthermore, animal studies<sup>32</sup> and human studies<sup>33</sup> have shown the effects of soy isoflavones on visual memory, which may be a reflection of structural influences, particularly in the visual pathways. Overall, the areas that showed significant differences in cortical thickness or surface area in this study were quite small, and the biologic meaning based on these results remains unclear and will need further investigation.

The main limitation of this study is that the study subjects were recruited at 8 years of age, and the infant diet pattern was self-reported by parents. While parents reported the dominant feeding type (BF, MF, or SF), some of the other important nutritional information is missing, such as the precise nutrient component of the diets, exclusivity of feeding type, and amount of intake per feeding. In addition, while we controlled for age and sex in the data analysis, additional potential confounding factors were not controlled, such as nutrition and lifestyle after infancy and other postnatal factors (limited by the retrospective study design and lack of methods to quantify), possibly impacting children's brain development and neurodevelopmental outcomes as well. Also, family environment and socioeconomic status, which is likely another potential confounder to be considered, was only compared among groups (no significant differences were found) but not included as a covariate in the data analysis due to incomplete data. In this study, we focused on cortical measurements, while other important brain features such as microstructural development and connectivity were not studied. The sample size, if breaking down to each diet group and each sex, was also relatively small; and the parent-reported BRIEF assessment was an indirect measure of executive function. Follow-up MR imaging and neurodevelopmental evaluations on a larger and prospective cohort of children with different infant diets are underway, with key potential covariates carefully measured. This follow-up study will be helpful to confirm the findings in the current report.

## CONCLUSIONS

The composition of the typical choices available for an infant's diet (ie, BF, MF, SF) may have profound and long-term effects on children's brain development, which can be reflected by brain imaging and executive function assessment at 8 years of age. The effects appear to be sex-specific, with boys more likely to show diet-associated effects than girls. The findings support the idea that soy-based formula may alter later life brain anatomy and function but that any changes are modest and do not lead to clinically relevant deficits or abnormal outcomes.

## ACKNOWLEDGMENT

We thank the staff of the Arkansas Children's Nutrition Center Clinical Research Core for their assistance with this study.

Disclosures: Ting Li—UNRELATED: Employment: University of Arkansas at Little Rock. Thomas M. Badger—RELATED: Grant: USDA-ARS. Comments: research grant funded. Xiangyang Lou—RELATED: Grant: National Science Foundation.\* Xiawei Ou—RELATED: Grant: US Department of Agriculture. Comments: The

work presented in this article is funded by a US Department of Agriculture grant\*; UNRELATED: Grants/Grants Pending: US Department of Agriculture. Comments: The authors are supported by a number of National Institutes of Health/US Department of Agriculture grants.\* \*Money paid to the institution.

## REFERENCES

1. Johnston M, Landers S, Noble L, et al. **Breastfeeding and the use of human milk.** *Pediatrics* 2012;129:E827–41 CrossRef Medline
2. Breastfeeding Report Card, United States. 2018. <https://www.cdc.gov/breastfeeding/data/reportcard.htm>.
3. Bhatia J, Greer F, Comm N; American Academy of Pediatrics Committee on Nutrition. **Use of soy protein-based formulas in infant feeding.** *Pediatrics* 2008;122:1062–68 CrossRef Medline
4. Lucas A, Morley R, Cole TJ, et al. **Breast-milk and subsequent intelligence quotient in children born preterm.** *Lancet* 1992;339:261–64 CrossRef Medline
5. Kramer MS, Aboud F, Mironova E, et al; Promotion of Breastfeeding Intervention Trial (PROBIT) Study Group. **Breastfeeding and child cognitive development: new evidence from a large randomized trial.** *Arch Gen Psychiatry* 2008;65:578–84 CrossRef Medline
6. Isaacs EB, Fischl BR, Quinn BT, et al. **Impact of breast milk on intelligence quotient, brain size, and white matter development.** *Pediatr Res* 2010;67:357–62 CrossRef Medline
7. Kafouri S, Kramer M, Leonard G, et al. **Breastfeeding and brain structure in adolescence.** *Int J Epidemiol* 2013;42:150–59 CrossRef Medline
8. Deoni SCL, Dean DC, Piryatinsky I, et al. **Breastfeeding and early white matter development: a cross-sectional study.** *Neuroimage* 2013;82:77–86 CrossRef Medline
9. Ou X, Andres A, Cleves MA, et al. **Sex specific association between infant diet and white matter integrity in eight-year-old children.** *Pediatr Res* 2014;76:535–43 CrossRef Medline
10. Ou X, Andres A, Pivik RT, et al. **Voxel-based morphometry and fMRI revealed differences in brain gray matter in breastfed and milk formula-fed children.** *AJNR Am J Neuroradiol* 2016;37:713–19 CrossRef Medline
11. Crider A, Pillai A. **Estrogen signaling as a therapeutic target in neurodevelopmental disorders.** *J Pharmacol Exp Ther* 2017;360:48–58 CrossRef Medline
12. Lee YB, Lee HJ, Sohn HS. **Soy isoflavones and cognitive function.** *J Nutr Biochem* 2005;16:641–49 CrossRef Medline
13. Jing HK, Gilchrist JM, Badger TM, et al. **A longitudinal study of differences in electroencephalographic activity among breastfed, milk formula-fed, and soy formula-fed infants during the first year of life.** *Early Hum Dev* 2010;86:119–25 CrossRef Medline
14. Pivik RT, Andres A, Badger TM. **Effects of diet on early stage cortical perception and discrimination of syllables differing in voice-onset time: a longitudinal ERP study in 3- and 6-month-old infants.** *Brain Lang* 2012;120:27–41 CrossRef Medline
15. Gioia GA, Isquith PK, Guy SC, et al, eds. *Behavior Rating Inventory of Executive Function (BRIEF).* Psychological Assessment Resources; 2000
16. De Bellis MD, Keshavan MS, Beers SR, et al. **Sex differences in brain maturation during childhood and adolescence.** *Cereb Cortex* 2001;11:552–57 CrossRef Medline
17. Giedd JN, Rapoport JL. **Structural MRI of pediatric brain development: what have we learned and where are we going?** *Neuron* 2010;67:728–34 CrossRef Medline
18. Westman E, Aguilar C, Muehlboeck JS, et al. **Regional magnetic resonance imaging measures for multivariate analysis in Alzheimer's disease and mild cognitive impairment.** *Brain Topogr* 2013;26:9–23 CrossRef Medline
19. Nickmeyer RC, Gouttard S, Kang CY, et al. **A structural MRI study of human brain development from birth to 2 years.** *J Neurosci* 2008;28:12176–82 CrossRef Medline
20. Isaacs EB. **Neuroimaging, a new tool for investigating the effects of early diet on cognitive and brain development.** *Front Hum Neurosci* 2013;7:445 CrossRef Medline

21. Schore AN. **All our sons: the developmental neurobiology and neuroendocrinology of boys at risk.** *Infant Ment Health J* 2017;38:15–52 CrossRef Medline
22. Patisaul HB, Jefferson W. **The pros and cons of phytoestrogens.** *Front Neuroendocrinol* 2010;31:400–19 CrossRef Medline
23. Gillies GE, McArthur S. **Estrogen actions in the brain and the basis for differential action in men and women: a case for sex-specific medicines.** *Pharmacol Rev* 2010;62:155–98 CrossRef Medline
24. Kritz-Silverstein D, Von Muhlen D, Barrett-Connor E, et al. **Isoflavones and cognitive function in older women: the SOy and Postmenopausal Health In Aging (SOPHIA) Study.** *Menopause* 2003;10:196–202 Medline
25. Duffy R, Wiseman H, File SE. **Improved cognitive function in postmenopausal women after 12 weeks of consumption of a soya extract containing isoflavones.** *Pharmacol Biochem Behav* 2003;75:721–29 CrossRef Medline
26. White LR, Petrovitch H, Ross GW, et al. **Brain aging and midlife tofu consumption.** *J Am Coll Nutr* 2000;19:242–55 CrossRef Medline
27. File SE, Jarrett N, Fluck E, et al. **Eating soya improves human memory.** *Psychopharmacology (Berl)* 2001;157:430–36 CrossRef Medline
28. Rudnicka AR, Owen CG, Richards M, et al. **Effect of breastfeeding and sociodemographic factors on visual outcome in childhood and adolescence.** *Am J Clin Nutr* 2008;87:1392–99 CrossRef Medline
29. Tambalis KD, Mourtakos S, Panagiotakos DB, et al. **Exclusive breastfeeding is favorably associated with physical fitness in children.** *Breastfeed Med* 2019;14:390–97 CrossRef Medline
30. Belfort MB, Rifas-Shiman SL, Kleinman KP, et al. **Infant feeding and childhood cognition at ages 3 and 7 years: effects of breastfeeding duration and exclusivity.** *JAMA Pediatr* 2013;167:836–44 CrossRef Medline
31. Horta BL, de Mola CL, Victora CG. **Breastfeeding and intelligence: a systematic review and meta-analysis.** *Acta Paediatr* 2015;104:14–19 CrossRef Medline
32. Lund TD, West TW, Tian LY, et al. **Visual spatial memory is enhanced in female rats (but inhibited in males) by dietary soy phytoestrogens.** *BMC Neurosci* 2001;2:20 CrossRef Medline
33. Gleason CE, Carlsson CM, Barnet JH, et al. **A preliminary study of the safety, feasibility and cognitive efficacy of soy isoflavone supplements in older men and women.** *Age Ageing* 2008;38:86–93 CrossRef Medline

# Spine MRI in Spontaneous Intracranial Hypotension for CSF Leak Detection: Nonsuperiority of Intrathecal Gadolinium to Heavily T2-Weighted Fat-Saturated Sequences

T. Dobrocky, A. Winklehner, P.S. Breiding, L. Grunder, G. Peschi, L. Häni, P.J. Mosimann, M. Branca, J. Kaesmacher, P. Mordasini, A. Raabe, C.T. Ulrich, J. Beck, J. Gralla, and E.I. Piechowiak



## ABSTRACT

**BACKGROUND AND PURPOSE:** Spine MR imaging plays a pivotal role in the diagnostic work-up of spontaneous intracranial hypotension. The aim of this study was to compare the diagnostic accuracy of unenhanced spine MR imaging and intrathecal gadolinium-enhanced spine MR imaging for identification and localization of CSF leaks in patients with spontaneous intracranial hypotension.

**MATERIALS AND METHODS:** A retrospective study of patients with spontaneous intracranial hypotension examined from February 2013 to October 2017 was conducted. Their spine MR imaging was reviewed by 3 blinded readers for the presence of epidural CSF using 3 different sequences (T2WI, 3D T2WI fat-saturated, T1WI gadolinium). In patients with leaks, the presumed level of the leak was reported.

**RESULTS:** In total, 103 patients with spontaneous intracranial hypotension (63/103 [61%] women; mean age, 50 years) were evaluated. Seventy had a confirmed CSF leak (57/70 [81%] proved intraoperatively), and 33 showed no epidural CSF on multimodal imaging. Intrathecal gadolinium-enhanced spine MR imaging was nonsuperior to unenhanced spine MR imaging for the detection of epidural CSF ( $P = .24$  and  $.97$ ). All MR imaging sequences had a low accuracy for leak localization. In all patients, only 1 leakage point was present, albeit multiple suspicious lesions were reported in all sequences (mean, 5.0).

**CONCLUSIONS:** Intrathecal gadolinium-enhanced spine MR imaging does not improve the diagnostic accuracy for the detection of epidural CSF. Thus, it lacks a rationale to be included in the routine spontaneous intracranial hypotension work-up. Heavily T2-weighted images with fat saturation provide high accuracy for the detection of an epidural CSF collection. Low accuracy for leak localization is due to an extensive CSF collection spanning several vertebrae (false localizing sign), lack of temporal resolution, and a multiplicity of suspicious lesions, albeit only a single leakage site is present. Thus, dynamic examination is mandatory before targeted treatment is initiated.

**ABBREVIATIONS:** CDM = conventional dynamic myelography; DCTM = dynamic CT myelography; FS = fat saturation; Gd = gadolinium; GdM = intrathecal gadolinium-enhanced MR imaging; ICC = intraclass correlation coefficient; PMCT = postmyelography CT; SIH = spontaneous intracranial hypotension

Spinal imaging has a central role in the diagnostic work-up of patients with spontaneous intracranial hypotension (SIH). It is widely believed that SIH is commonly triggered by CSF leakage from the intrathecal into the epidural compartment (Fig 1). This is due to an osteodiscogenic microspur (calcified disc protrusion or spondylophyte) penetrating the dura or, less frequently, a

rupture of a spinal nerve root diverticulum (Fig 2).<sup>1</sup> In the setting of a ventral dural tear or leaking around a nerve sheath, imaging may show an abnormal accumulation of CSF and aid in localizing the dural defect.<sup>2</sup> Alternative pathomechanisms without proof of extrathecal CSF collection, like the CSF venous fistula, recently described by Schievink et al,<sup>3</sup> may also be demonstrated on imaging.

Several radiologic examinations may be used in the spinal diagnostic work-up of patients with SIH and include unenhanced MR imaging, intrathecal gadolinium (Gd) enhanced MR imaging (GdM), conventional dynamic myelography (CDM), postmyelography CT (PMCT), dynamic CT myelography (DCTM), digital subtraction myelography, and radionuclide cisternography.<sup>4-7</sup> Some methods are invasive and require intrathecal application of contrast media, and some may be considered complementary. Each examination has its strengths and shortcomings, and different

Received January 15, 2020; accepted after revision April 6.

From the University Institute of Diagnostic and Interventional Neuroradiology (T.D., A.W., P.S.B., L.G., G.P., P.J.M., J.K., P.M., J.G., E.I.P.), Department of Interventional, Pediatric, and Diagnostic Radiology (G.P., J.K.), and Neurosurgery (L.H., A.R., C.T.U., J.B.), University of Bern, Inselspital, Bern, Switzerland; Clinical Trials Unit (M.B.), University of Bern, Bern, Switzerland; and Department of Neurosurgery (J.B.), Medical Center, University of Freiburg, Freiburg, Germany.

Please address correspondence to Eike I. Piechowiak, MD, Institute of Diagnostic and Interventional Neuroradiology, Inselspital, University Hospital of Bern, Freiburgrstr 8, CH-3010, Bern, Switzerland; email: eike.piechowiak@insel.ch

<http://dx.doi.org/10.3174/ajnr.A6592>

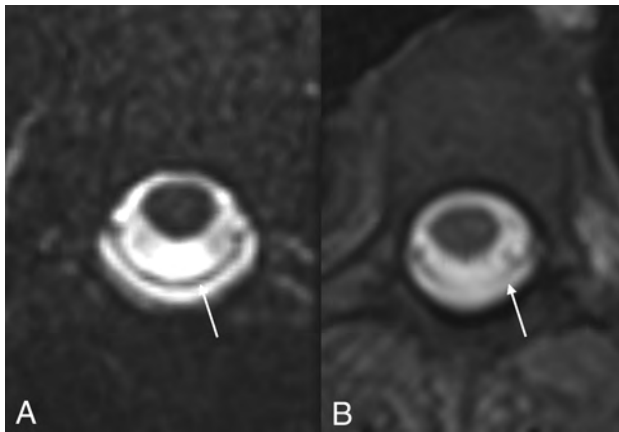


**FIG 1.** Transversal, isotropic, unenhanced, 3D T2WI FS (A) versus a transversal (3 mm), T1-weighted sequence with fat saturation after intrathecal gadolinium (B). The extrathecal fluid and contrast media are visible posterior to the dura mater (arrows).

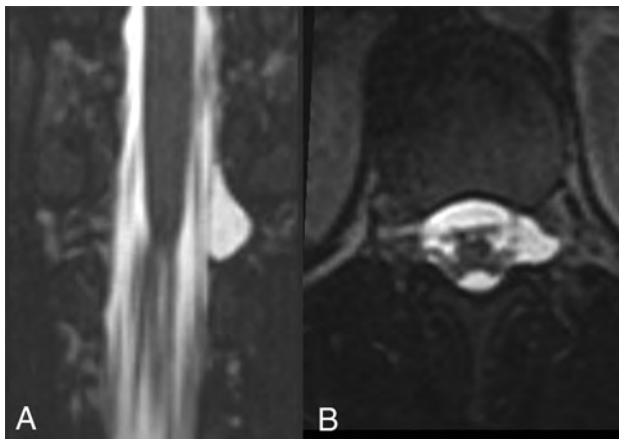


**FIG 2.** Multiplanar reconstruction of 3D T2WI FS sequence showing a large nerve root diverticulum, which demonstrated a leakage on conventional dynamic myelography (not shown).

methods come into play at different stages of the diagnostic process. Spine MR imaging plays a key role as the first-line diagnostic examination because it offers excellent spatial resolution without associated radiation exposure; however, it lacks any temporal resolution. Previous reports have indicated the diagnostic value of spine MR imaging.<sup>8,9</sup> Adjunctive GdM was first described in 1999 by Zeng et al.<sup>10</sup> Since then, several studies have reported its utility in the diagnostic work-up of patients with SIH. Nonetheless, the intrathecal application of Gd has not, so far, been approved by the US Food and Drug Administration and continues to be used off-label.

The goal of our study was to compare the imaging accuracy of 2 different unenhanced spine MR imaging sequences and GdM for visualization of an epidural CSF collection and the accuracy for localizing the precise level of dural dehiscence in the first-line work-up of patients with SIH.

## MATERIALS AND METHODS

This study was granted institutional review board approval, and the need for informed consent was waived due to its retrospective

nature. The registry was approved by the local ethics committee (Kantonale Ethikkommission Bern, Switzerland, number: 2017-00861). Records of all consecutive patients with orthostatic headache and clinical suspicion of SIH evaluated at the University hospital of Bern, Switzerland between February 2013 and October 2017 were retrospectively reviewed. In total, 121 patients with orthostatic headache and clinical suspicion for SIH were investigated according to our routine diagnostic protocol. Patients with postdural puncture headache were not included. Eighteen patients were excluded because of poor-quality MR imaging or absence of MR imaging. The final study population consisted of 103 patients. Patients with a missing spine MR imaging sequence were eligible. In the patients participating in a follow-up study (eg, after microsurgical closure or blood patch), only the preoperative examination was evaluated in our study.

Many patients had been included in previously published studies (study population overlap) investigating different outcome measures, including optic nerve sheath sonography, surgical dural closure, CSF dynamics, DCTM, and brain MR imaging, but none of these studies reported spine MR imaging findings.<sup>1,6,11-14</sup>

## Diagnostic Work-Up

All patients were evaluated according to our standard protocol, as described in previous publications, and are listed below. First, a detailed medical history was obtained, and a physical examination was performed by a neurosurgeon. In most patients, the leading symptom was orthostatic headache; thus, brain MR imaging was performed to rule out any underlying intracranial pathology. The SIH score, based on the 6 most relevant brain imaging findings, which helps predict the likelihood of a CSF leak, was calculated.<sup>14</sup> Further examinations included optic nerve sheath sonography,<sup>12</sup> lumbar infusion testing,<sup>11</sup> unenhanced MR imaging of the spine, GdM, CDM with PMCT, and, in selected patients, DCTM.<sup>6</sup>

## Spine MR Imaging

Unenhanced spine MR imaging was routinely performed in the morning, and GdM, in the afternoon of the same day. Imaging was performed on a 1.5T scanner (Aera; Siemens) using a 20-element head/neck coil and a 32-element table spine coil. The unenhanced spine MR imaging protocol included 3 sagittal T2-weighted spin-echo blocks (TR/TE = 4370/93 ms, number of averages = 3, section thickness = 3 mm, FOV = 150 × 300 mm, FOV phase = 50%, flip angle = 150°, acquisition time = 2 minutes and 20 seconds, matrix size = 192 × 512) and 4 sagittal, isotropic 3D heavily T2-weighted turbo spin-echo sequences with fat saturation (FS) (3D T2WI FS) (TR/TE = 1400/180 ms, number of averages = 2, section thickness = 1 mm, FOV = 300 × 300 mm, FOV phase = 100%, flip angle 150°, acquisition time = 4 minutes and 33 seconds, matrix size = 640 × 640) including the entire neurocranium.

Before GdM, written consent for the intrathecal off-label use of a Gd-based contrast agent was obtained from patients. Lumbar puncture was performed with a 22-ga needle with the patient in a lateral decubitus position, and a mixture of 0.5 mL of Gadovist (gadobutrol, 1.0 mmol/mL, a nonionic macrocyclic agent; Bayer



Shering Pharma) or 0.5 mL of Magnograf (gadopentetate dimeglumine, 0.5 mmol/mL; Berlis) with 9.5 mL of CSF was administered intrathecally.

Three sagittal, isotropic T1-weighted blocks were acquired with the FS technique (T1WI Gd FS) (TR/TE = 9.82/4.77 ms, number of averages = 1, FOV = 288 × 288 mm, FOV phase = 100%, flip angle = 10°, acquisition time = 6 minutes and 9 seconds, matrix size = 288 × 288). Additional high-resolution, axial T1-weighted blocks with FS were acquired if the neuroradiologist was uncertain whether contrast media was truly present in the epidural space on the basis of the sagittal images (TR/TE = 8.62/4.77 ms, number of averages = 1, FOV = 180 × 180 mm, FOV phase = 100%, flip angle = 12°, acquisition time = 3 minutes and 54 seconds, matrix size = 410 × 512). Alternatively, high-resolution T1-weighted spin-echo blocks with FS in a sagittal orientation were acquired.

### **Conventional Dynamic Myelography and Postmyelography CT**

The CDM technique, which has previously been described in detail, is summarized briefly below.<sup>15</sup> For opacification, 20 mL of Iopamiro 300 (iopamidol; Bracco) was injected intrathecally. Patient positioning was adapted depending on the findings of previous imaging: prone when an osteodiscogenic microspur was suspected or lateral decubitus when a spinal nerve root diverticulum was the presumed source of leakage. The patient was tilted into the Trendelenburg position, following the leading edge of the intrathecal contrast. The level at which the contrast exited the intrathecal compartment and started spilling into the epidural space was considered the level of the dural breach (Fig 3). The patient was immediately transferred to the CT imaging suite, and a PMCT was performed (Somatom Definition Edge; Siemens) to identify possible causative pathology at the level of dural dehiscence or a CSF venous fistula. If no epidural contrast was evident in the first PMCT, a late-phase PMCT was performed, usually 4–24 hours after the initial intrathecal injection, to exclude low-flow leaks.

### **Data Analysis**

Blinded evaluation of brain MR imaging was performed by a neuroradiology fellow (G.P.), who reported the SIH score. The spine MR imaging of all subjects was assessed independently by a board-certified neuroradiologist (A.W.) and 2 neuroradiology fellows (P.S.B., L.G.), blinded to clinical presentation and to all other imaging studies performed. All spine sequences (T2WI, 3D T2WI FS, T1WI Gd) were separated, deidentified, and sorted randomly on an established, nonmodifiable layout and reviewed on a PACS station. The readers were instructed to perform their assessment and report the results on a standardized spreadsheet, and a short educational module before beginning the image interpretation was provided. For unenhanced spine MR imaging sequences, the presence of CSF in the epidural compartment was recorded; for GdM, epidural contrast accumulation unrelated to the puncture site in the lumbar spine was evaluated. In patients with leaks, the craniocaudal extent was noted (the number of vertebrae with epidural CSF). The readers also reported the number of suspicious lesions potentially causing CSF leakage (such as spondylophyte, disc protrusion, or spinal nerve root diverticula)



**FIG 3.** A 57-year-old woman with orthostatic headache and tinnitus. A, The sagittal, T2-weighted sequence demonstrates extensive extrathecal CSF and multiple suspicious disc protrusions (black arrowheads). B–D, Conventional dynamic myelography demonstrates a CSF leak at the T10/T11 level with progressive contrast media distribution (arrowheads). Even in retrospect, the MR imaging did not demonstrate any suspicious lesion at the corresponding level (A, white arrowhead). The leak was confirmed intraoperatively and surgically closed. The follow-up spine MR imaging did not show any residual epidural CSF collection (not shown).

and the lesion they considered the most likely to be the cause of the CSF leak.

In addition, information regarding patients' demographic characteristics (age, sex) and type of therapy (conservative, epidural blood patch, microsurgical closure) was extracted from the registry.

### **Standard of Reference**

Multimodal imaging including MR imaging, CDM, PMCT, and microsurgical exploration was considered the criterion standard for the proof of a CSF leak. Two neuroradiologists (T.D. and E.I.P. with 8 and 11 years of experience, respectively) who were not involved in the initial analysis reviewed all available images from all patients for the presence of epidural CSF and the level of dural dehiscence. In cases of disagreement, all imaging modalities were reviewed in a joint session to reach a consensus. In patients undergoing microsurgical closure of the CSF leak, intraoperative reports were reviewed to confirm the presence of epidural CSF and verify the localization of the dural breach.

### **Statistical Analysis**

Statistical analysis was performed using STATA (2017, Release 15; StataCorp). Descriptive analysis was performed using

**Table 1: Spine MR imaging findings for three different sequences in the patient cohort**

	T2WI	3D T2WI FS	T1WI Gd FS
Sequence available in all patients	96/103 (93%)	96/103 (93%)	75/103 (73%)
Sequence available in patients with leaks	65/70 (93%)	64/70 (91%)	45/70 (64%)
Craniocaudal extent of the CSF leak (mean No. of vertebrae)	7.7 ± 6.2	8.5 ± 6.9	7.5 ± 6.7
Interrater agreement for the presence of a CSF leak	0.84	0.91	0.82
Interrater agreement for the location of the CSF leak	0.29	0.67	0.62
Mean number of suspicious lesions potentially causing CSF leakage	4.3 ± 3.0	5.6 ± 3.9	5.1 ± 4.2

**Note:**—T2WI indicates T2-weighted; 3D T2WI FS, three-dimensional, isotropic, T2-weighted turbo SE sequence with fat saturation; T1WI Gd FS, isotropic T1-weighted blocks with fat saturation after intrathecal application of gadolinium.

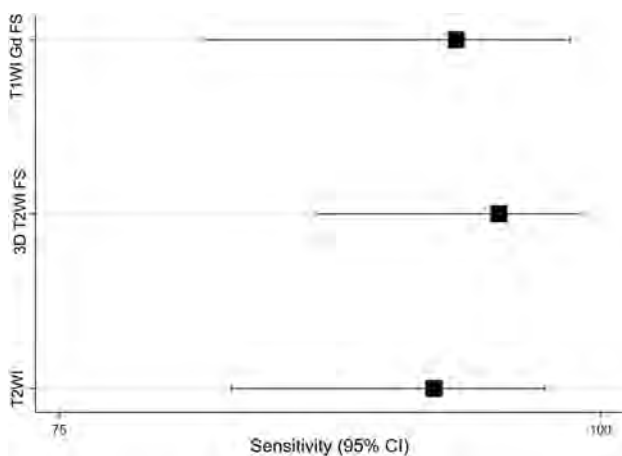


**FIG 4.** Sensitivity and specificity for the 3 different sequences with corresponding confidence intervals. T2WI indicates T2-weighted; 3D T2WI FS, 3D, isotropic, T2-weighted sequence with fat saturation; and T1WI Gd FS, isotropic, T1-weighted sequence with fat saturation after intrathecal application of gadolinium.

frequencies and percentages for categoric variables and mean ( $\pm$  SD) or median (interquartile range) for continuous variables. The results of all 3 readers were aggregated. Continuous measures were averaged among the 3 readers. For dichotomous variables, a qualitative sign was considered positive if 2 or all 3 readers scored it as positive. In cases of categoric variables with  $>2$  categories and about which all 3 readers disagreed, the value given by the first reader was the one taken into consideration. The results are presented for the 3 different MR imaging sequences.

Interrater reliability for categoric data was determined using the Fleiss  $\kappa$ . For continuous data, the intraclass correlation coefficient (ICC) was calculated with the 2-way mixed-effects model estimating absolute agreement. Agreement was defined as almost perfect ( $\kappa$  or ICC  $> 0.80$ ), substantial ( $\kappa$  or ICC = 0.61–0.80), moderate ( $\kappa$  or ICC = 0.41–0.60), fair ( $\kappa$  or ICC = 0.21–0.40), or poor ( $\kappa$  or ICC  $\leq 0.20$ ). If the location was correctly identified, the standard and weighted (with linear weights)  $\kappa$  approach was used.

For each MR imaging sequence, scatterplots were used to graphically depict the agreement among the leak location as reported by the readers and the true location. Sensitivity and specificity were obtained comparing the 3 sequences against the ground truth. To test the diagnostic reliability of different sequences for the diagnosis of a CSF leakage, we determined the

agreement between each sequence and the ground truth using  $\kappa$  statistics and bootstrapping methods.

## RESULTS

A total of 103 subjects (63/103 [61%] women; mean age, 50  $\pm$  14 years; range, 25–90 years) with a clinical suspicion of SIH were included. The final study population consisted of 70 SIH leak-positive patients (70/103; 68%) (48/70 [69%] women; mean age, 46  $\pm$  11 years; range, 25–73 years) and 33 leak-negative patients (33/103;

32%) (18/33 [55%] women; mean age, 57  $\pm$  17 years; range, 25–90 years) who had orthostatic headache without proof of a CSF leak on multimodal imaging (CDM, PMCT, unenhanced MR imaging, or GdM). The mean brain SIH score was 6.4  $\pm$  2.2 in patients with a confirmed spinal CSF leak, and 3.3  $\pm$  2.5 in patients without a CSF leak.

All patients ( $n = 103$ , 100%) underwent CDM and PMCT in addition to spine MR imaging. In SIH patients with a leak ( $n = 70$ ), the underlying pathology was a ventral microspur originating from an intervertebral disc or an endplate osteophyte in 48/70 cases (69%) and a tear in the nerve root sleeve diverticulum in 13/70 cases (19%). The remaining 9 patients with an epidural CSF collection showed improvement after conservative management; the precise level of leakage was established on myelography for 7 of them. In 57/70 (81%) patients with a proved leak on imaging that was refractory to conservative management, microsurgical exploration and dural repair were performed.<sup>16</sup>

## Epidural CSF

Overall, T2WI, 3D T2WI FS, and T1WI Gd FS sequences were available for 96/103 (93%), 96/103 (93%), and 75/103 (73%) patients, respectively (Table 1). The craniocaudal extent of the CSF leak (number of vertebrae with epidural CSF) was 7.7  $\pm$  6.2, 8.5  $\pm$  6.9, and 7.5  $\pm$  6.7 for T2WI, 3D T2WI FS, and T1WI Gd FS, respectively. On the basis of the ground truth (multimodal imaging), the presence of CSF in the epidural space was correctly reported in 60/65 (92%), 61/64 (95%), and 42/45 (93%) for T2WI, 3D T2WI FS, and T1WI Gd FS sequences, respectively. The interrater agreement for the presence of a CSF leak was almost perfect for all sequences: T2WI (0.84), 3D T2WI FS (0.91), and T1WI Gd FS (0.82).

3D T2WI FS demonstrated the highest sensitivity (95%) and specificity (97%) for the detection of epidural CSF (Fig 4 and Table 2). The  $\kappa$  value for T2WI, 3D T2WI FS, and T1WI Gd FS sequences compared with the ground truth was 0.837, 0.908, and 0.833, respectively. The  $\kappa$  statistic comparison between T2WI and 3D T2WI FS ( $P$  value = .24), T2WI and T1WI Gd FS ( $P$  value = .97), and 3D T2WI FS and T1WI Gd FS ( $P$  value = .25) confirmed no relevant differences among the 3 sequences.

## CSF Leak Location

For readers 1, 2, and 3, the location of the leak based on 3D T2WI FS as the most sensitive sequence was identified correctly

in 27/68 (39.7%), 24/68 (35.3%), and 23/68 (33.8%), respectively. The interrater agreement for the location of the leak was fair for T2WI (0.29), substantial for 3D T2WI FS (0.67), and substantial for T1WI Gd (0.62) (Fig 5).

In 1 patient, an inadvertent epidural injection of Gd occurred and the procedure was successfully repeated on the following day. In another patient, an epileptic seizure shortly after image acquisition occurred. No further adverse reaction that could be attributed to the administration of intrathecal contrast agent was reported.

DISCUSSION

According to our results, intrathecal Gd-enhanced MR myelography is nonsuperior to unenhanced MR imaging and provides no significant diagnostic benefit in the standard evaluation of spinal

CSF leaks. Additionally, 3D T2WI FS MR images demonstrate a high diagnostic accuracy necessary for the detection of spinal epidural CSF collections. However, our findings clearly demonstrate that unenhanced spine MR imaging and GdM have a low accuracy, which led to poor interrater agreement on localization of the exact level of the spinal CSF leak. This is due to an extensive CSF collection spanning several vertebral levels (false localizing sign); the lack of temporal resolution, which is inherent to the method; and the multiplicity of suspicious lesions that were reported (mean, 5.0); yet in all patients, only a single leakage site was present.

Our results are in line with those of previous studies and support the role of unenhanced spine MR imaging as a valuable, noninvasive tool in the early phase of the diagnostic work-up.<sup>8,9</sup> We show that isotropic, heavily T2WI with FS is reliable for the detection of a spinal epidural CSF collection, with excellent depiction of anatomy.<sup>17</sup> Because of similar

signal intensities of fluid and fat, standard T2-weighted sequences may mask the epidural CSF collection due to the lack of fat saturation and thus lead to a lower sensitivity (Fig 6). In our experience, multiplanar reconstructions and maximum intensity

Table 2: Sensitivity and specificity of three different MR imaging sequences for detection of epidural CSF<sup>a</sup>

	Sensitivity	Specificity	Youden Index
T2WI	92.3% (83.0%–97.5%)	93.5% (78.6%–99.2%)	0.858
3D T2WI FS	95.3% (86.9%–99.0%)	96.9% (83.8%–99.9%)	0.922
T1WI Gd FS	93.3% (81.7%–98.6%)	90.0% (73.5%–97.9%)	0.833

<sup>a</sup> The numbers in parentheses are confidence intervals.

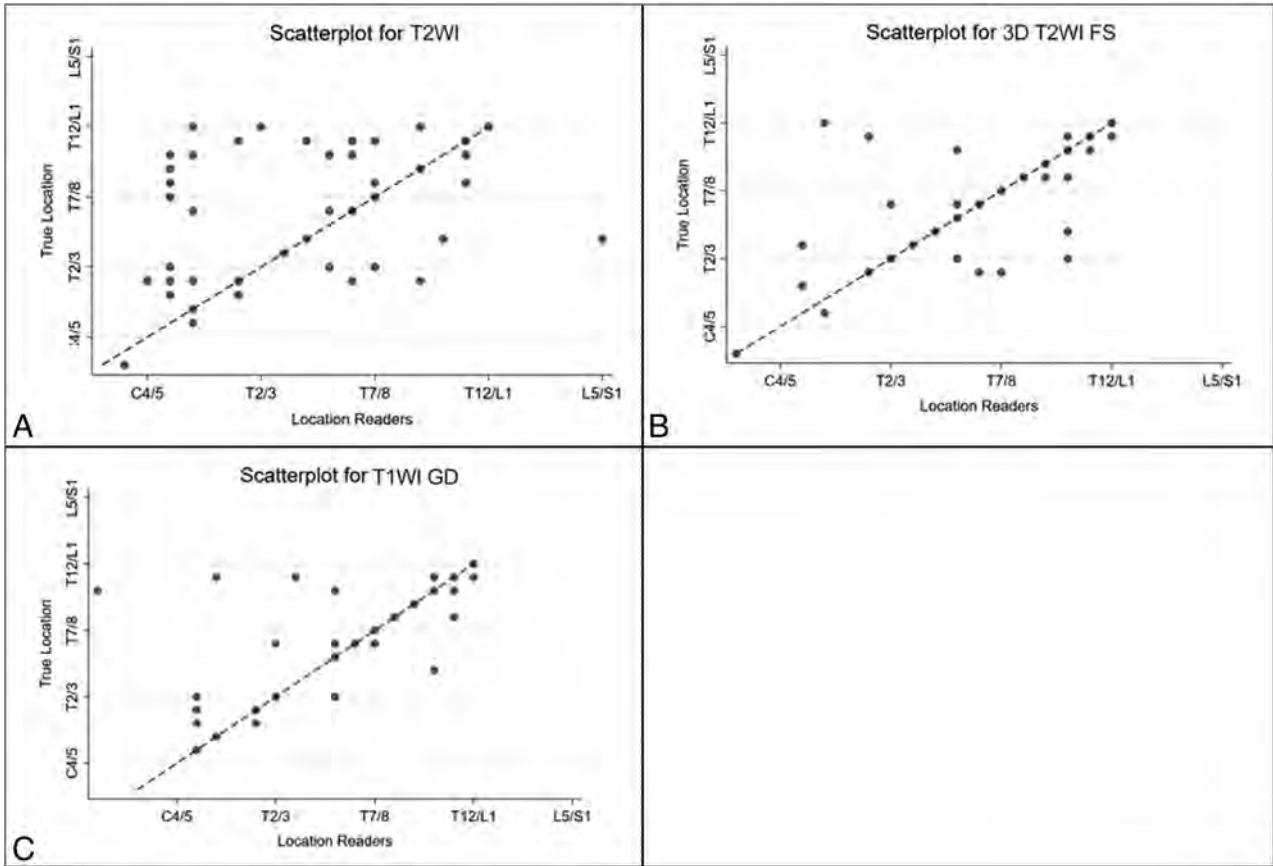


FIG 5. Scatterplots showing the accuracy of each sequence compared with the true location. T2-weighted (A); 3D T2WI FS, 3D T2-weighted sequence with fat saturation (B); and T1WI Gd (C). On the x-axis is the location as reported by the readers. On the y-axis is the true location as found intraoperatively, —57 of 70 (81%); or as determined with multimodal imaging in conservatively managed patients —13 of 70 (19%). Patients in whom the leak has been correctly localized based on the corresponding MR image lie on the reference line.



**FIG 6.** A 38-year-old woman with orthostatic headache and intracranial signs of hypotension (not shown). *A*, Sagittal, T1-weighted, isotropic sequence after intrathecal gadolinium injection, without proof of epidural contrast media distribution. *B*, Unenhanced, sagittal, heavily T2-weighted isotropic sequence with fat saturation shows a CSF collection in the posterior epidural space and the prominent dural membrane (arrow). *C*, Due to lack of fat saturation, the epidural CSF collection could not be discerned on the sagittal T2-weighted sequence.

projections are useful for depicting suspicious spinal nerve root diverticula (Fig 2). In addition, unenhanced spine MR imaging is useful to decide on patient positioning for subsequent dynamic myelography: prone when an osteodiscogenic ventral microspur is suspected or lateral decubitus when a ruptured spinal nerve root diverticulum is the presumed source of leakage.

Intrathecal enhanced GdM is an invasive and time-consuming method requiring a lumbar puncture. Its use was first reported in 2005 by Schumacher et al<sup>18</sup> in a patient with Marfan Syndrome demonstrating multiple leaks. Chazen et al<sup>5</sup> reported a higher rate of CSF leak detection with GdM than with CT myelography and concluded that the method is helpful in the subpopulation of patients with spinal meningeal diverticula. For exact leak localization, in our experience, patients with spinal meningeal diverticula are best evaluated with CDM or DCTM in the lateral decubitus position, which leads to increased contrast concentration along the dependent spinal nerve root diverticulum and may demonstrate contrast leakage or a CSF venous fistula.<sup>6</sup> Akbar et al<sup>19</sup> suggested that GdM is a useful adjunctive method for patients with SIH with negative CT myelography findings and demonstrated a leak in 21% of patients in this subgroup. The increased sensitivity of GdM to slow CSF leaks may be due to repeat myelography rather than a true increase in sensitivity because repeat examinations may reveal intermittent leaks irrespective of the detection method.

Prospective localization of CSF leakage is an endeavor fraught with difficulties. However, it is necessary when microsurgical closure with minimal bone removal or targeted epidural patching is indicated. Epidural CSF accumulation may be misleading because it may not reflect the actual site of the CSF leak (false localizing sign).<sup>20,21</sup> As reported by Albayram et al,<sup>22</sup> in 14 of 17 patients

with CSF leakage, the site of the dural tear was accurately demonstrated using GdM, which was performed 1 hour after intrathecal Gd administration. Ten of their patients demonstrated a single tear site, and 4 had multiple tears. In our experience, contrast leakage into the epidural space often occurs almost instantaneously, spanning several vertebral levels within a few seconds, making localization on nondynamic imaging impossible and potentially simulating multiple tears. Thus, a GdM scan performed 1 hour after intrathecal Gd is unlikely to show the precise site of leakage in patients with high-flow leaks. In addition, none of our patients with a proven CSF leak ( $n = 70$ ) had multiple leakage sites.

Some hold the misconception that leakage occurs at the level harboring a prominent disc protrusion or a large spinal nerve root cyst, thus obviating dynamic imaging (Fig 3). However, as demonstrated in our study, the mean number of suspicious lesions per patient that could potentially cause a CSF leak was 5. Consequently, sensitivity for correct localization of the dural leak is poor, with all spinal MR imaging sequences (Fig 5) emphasizing the need for a method with high temporal resolution when targeted therapy is required.

A few case reports have noted adverse effects of intrathecal Gd administration, such as encephalopathy or neurotoxic manifestations, including a decreased level of consciousness, global aphasia, and visual disturbance in humans—some after applying a high dose.<sup>23–25</sup> In addition, the literature on T1-weighted signal hyperintensities in the globus pallidus and the dentate nucleus in patients receiving serial intravenous administrations of Gd has recently led to a “gado-phobia.”<sup>26–28</sup> Öner et al<sup>29</sup> reported similar signal alterations in patients after intrathecal administration of a linear type of Gd. Although an unremarkable clinical follow-up in 51 patients undergoing intrathecal Gd-enhanced cisternography, for an average period of 4 years, was reported by Bakir et al,<sup>30</sup> the long-term clinical sequelae are not yet certain. Intrathecal Gd remains an off-label use, and the question of whether it provides real added value compared with unenhanced spine MR imaging should be critically reappraised. According to our results, GdM is nonsuperior to unenhanced, heavily T2-weighted spine MR imaging and has been excluded from our standard diagnostic work-up. In fact, it remains a potential field of application in selected cases only (eg, low-flow leaks when all other modalities fail).

The major strength of our study is that leakage and the level of dural dehiscence in a large number of patients have been proved by microsurgical exploration, which is the most precise method. This study has several limitations, the main ones being the retrospective nature of the evaluation, no control group, missing sequences in a small number of patients, and slight differences in MR imaging technique throughout the study because it was not part of a designated study protocol, but a routine MRI.

## CONCLUSIONS

3D T2WI FS is accurate for detection of spinal epidural CSF collection in patients with SIH. GdM is an invasive, off-label method with no added value in the standard diagnostic work-up. All spine MR imaging techniques have a low diagnostic accuracy for the exact localization of the dural breach; thus, a dynamic



imaging method (eg, CDM) is necessary when microsurgical closure or targeted epidural patching is being considered.

Disclosures: Levin Häni—UNRELATED: Grants/Grants Pending: European Association of Neurosurgical Societies Research Grant, Comments: research grant in neuro-oncology. Johannes Kaesmacher—UNRELATED: Grants/Grants Pending: Swiss Academy of Medical Sciences/Bangerter Foundation, Swiss Stroke Society\*; Travel/Accommodations/Meeting Expenses Unrelated to Activities Listed: Stryker, Pfizer.\* Jan Gralla—UNRELATED: Consultancy: Medtronic/Penumbra, Comments: Global Principal Investigator and clinical events committee member in stroke trials\*; Grants/Grants Pending: Swiss National Science Foundation, Comments: stroke studies.\* \*Money paid to the institution.

## REFERENCES

- Beck J, Ulrich CT, Fung C, et al. **Diskogenic microspurs as a major cause of intractable spontaneous intracranial hypotension.** *Neurology* 2016;87:1220–26 CrossRef Medline
- Schievink WI. **Spontaneous spinal cerebrospinal fluid leaks: a review.** *Neurosurg Focus* 2000;9:e8 CrossRef Medline
- Schievink WI, Moser FG, Maya MM. **CSF-venous fistula in spontaneous intracranial hypotension.** *Neurology* 2014;83:472–73 CrossRef Medline
- Kranz PG, Luetmer PH, Diehn FE, et al. **Myelographic techniques for the detection of spinal CSF leaks in spontaneous intracranial hypotension.** *AJR Am J Roentgenol* 2016;206:8–19 CrossRef Medline
- Chazen JL, Talbott JF, Lantos JE, et al. **MR myelography for identification of spinal CSF leak in spontaneous intracranial hypotension.** *AJNR Am J Neuroradiol* 2014;35:2007–12 CrossRef Medline
- Dobrocky T, Mosimann PJ, Zibold F, et al. **Cryptogenic cerebrospinal fluid leaks in spontaneous intracranial hypotension: role of dynamic CT myelography.** *Radiology* 2018;289:766–72 CrossRef Medline
- Morioka T, Aoki T, Tomoda Y, et al. **Cerebrospinal fluid leakage in intracranial hypotension syndrome: usefulness of indirect findings in radionuclide cisternography for detection and treatment monitoring.** *Clin Nucl Med* 2008;33:181–85 CrossRef Medline
- Starling A, Hernandez F, Hoxworth JM, et al. **Sensitivity of MRI of the spine compared with CT myelography in orthostatic headache with CSF leak.** *Neurology* 2013;81:1789–92 CrossRef Medline
- Watanabe A, Horikoshi T, Uchida M, et al. **Diagnostic value of spinal MR imaging in spontaneous intracranial hypotension syndrome.** *AJNR Am J Neuroradiol* 2009;30:147–51 CrossRef Medline
- Zeng Q, Xiong L, Jinkins JR, et al. **Intrathecal gadolinium-enhanced MR myelography and cisternography: a pilot study in human patients.** *AJR Am J Roentgenol* 1999;173:1109–15 CrossRef Medline
- Beck J, Fung C, Ulrich CT, et al. **Cerebrospinal fluid outflow resistance as a diagnostic marker of spontaneous cerebrospinal fluid leakage.** *J Neurosurg Spine* 2017;27:227–34 CrossRef Medline
- Fichtner J, Ulrich CT, Fung C, et al. **Sonography of the optic nerve sheath diameter before and after microsurgical closure of a dural CSF fistula in patients with spontaneous intracranial hypotension: a consecutive cohort study.** *Cephalalgia* 2018;39:306–15 CrossRef Medline
- Fichtner J, Ulrich CT, Fung C, et al. **Management of spontaneous intracranial hypotension: transorbital ultrasound as discriminator.** *J Neurol Neurosurg Psychiatry* 2016;87:650–65 CrossRef Medline
- Dobrocky T, Grunder L, Breiding PS, et al. **Assessing spinal cerebrospinal fluid leaks in spontaneous intracranial hypotension with a scoring system based on brain magnetic resonance imaging findings.** *JAMA Neurol* 2019;76:580–87 CrossRef Medline
- Kranz PG, Amrhein TJ, Gray L. **CSF venous fistulas in spontaneous intracranial hypotension: imaging characteristics on dynamic and CT myelography.** *Am J Roentgenol* 2017;209:1360–66 CrossRef Medline
- Beck J, Raabe A, Schievink WI, et al. **Posterior approach and spinal cord release for 360° repair of dural defects in spontaneous intracranial hypotension.** *Neurosurgery* 2019;84:E345–51 CrossRef Medline
- Tomoda Y, Korogi Y, Aoki T, et al. **Detection of cerebrospinal fluid leakage: initial experience with three-dimensional fast spin-echo magnetic resonance myelography.** *Acta Radiol* 2008;49:197–203 CrossRef Medline
- Schumacher M, Kraemer N, Berlis A. **Intrathecal gadolinium-enhanced MR myelography showing multiple dural leakages in a patient with Marfan syndrome.** *AJR Am J Roentgenol* 2005;185:92–94 CrossRef Medline
- Akbar JJ, Luetmer PH, Schwartz KM, et al. **The role of MR myelography with intrathecal gadolinium in localization of spinal CSF leaks in patients with spontaneous intracranial hypotension.** *AJNR Am J Neuroradiol* 2012;33:535–40 CrossRef Medline
- Hoxworth JM, Patel AC, Bosch EP, et al. **Localization of a rapid CSF leak with digital subtraction myelography.** *AJNR Am J Neuroradiol* 2009;30:516–19 CrossRef Medline
- Schievink WI, Maya MM, Chu RM, et al. **False localizing sign of cervico-thoracic CSF leak in spontaneous intracranial hypotension.** *Neurology* 2015;84:2445–48 CrossRef Medline
- Albayram S, Kilic F, Ozer H, et al. **Gadolinium-enhanced MR cisternography to evaluate dural leaks in intracranial hypotension syndrome.** *AJNR Am J Neuroradiol* 2008;29:116–21 CrossRef Medline
- Reeves C, Galang E, Padalia R, et al. **Intrathecal injection of gadobutrol: a tale of caution.** *J Pain Palliat Care Pharmacother* 2017;31:139–43 CrossRef Medline
- Kapoor R, Liu J, Devasenapathy A, et al. **Gadolinium encephalopathy after intrathecal gadolinium injection.** *Pain Physician* 2010;13:E321–26 Medline
- Tali ET, Ercan N, Krumina G, et al. **Intrathecal gadolinium (gadopentetate dimeglumine) enhanced magnetic resonance myelography and cisternography: results of a multicenter study.** *Invest Radiol* 2002;37:152–59 CrossRef Medline
- Radbruch A, Weberling LD, Kieslich PJ, et al. **Gadolinium retention in the dentate nucleus and globus pallidus is dependent on the class of contrast agent.** *Radiology* 2015;275:783–91 CrossRef Medline
- Stojanov DA, Aracki-Trenkic A, Vojinovic S, et al. **Increasing signal intensity within the dentate nucleus and globus pallidus on unenhanced T1W magnetic resonance images in patients with relapsing-remitting multiple sclerosis: correlation with cumulative dose of a macrocyclic gadolinium-based contrast agent.** *Eur Radiol* 2016;26:807–15 CrossRef Medline
- Kelemen P, Alaoui J, Sieron D, et al. **T1-weighted grey matter signal intensity alterations after multiple administrations of gadobutrol in patients with multiple sclerosis, referenced to white matter.** *Sci Rep* 2018;8:16844 CrossRef Medline
- Öner AY, Barutcu B, Aykol S, et al. **Intrathecal contrast-enhanced magnetic resonance imaging-related brain signal changes: residual gadolinium deposition?** *Invest Radiol* 2017;52:195–97 CrossRef Medline
- Bakir B, Aydin K, Talu G, et al. **Cranial magnetic resonance imaging in spontaneous intracranial hypotension after epidural blood patch.** *Pain Pract* 2008;8:206–10 CrossRef Medline

# Combination of Imaging Features and Clinical Biomarkers Predicts Positive Pathology and Microbiology Findings Suggestive of Spondylodiscitis in Patients Undergoing Image-Guided Percutaneous Biopsy

 S. Kihira,  C. Koo,  K. Mahmoudi,  T. Leong,  X. Mei,  B. Rigney,  A. Aggarwal, and  A.H. Doshi



## ABSTRACT

**BACKGROUND AND PURPOSE:** Pathology and microbiology results for suspected spondylodiscitis on MR imaging are often negative in up to 70% of cases. We aimed to predict whether MR imaging features will add diagnostic value when combined with clinical biomarkers to predict positive findings of spondylodiscitis on pathology and/or microbiology from percutaneous biopsy.

**MATERIALS AND METHODS:** In this retrospective single-center institutional review board–approved study, patients with radiologically suspected spondylodiscitis and having undergone percutaneous biopsies were assessed. Demographic characteristics, laboratory values, and tissue and blood cultures were collected. Pathology and microbiology results were used as end points. Three independent observers provided MR imaging–based scoring for typical MR imaging features for spondylodiscitis. Multivariate logistic regression and receiver operating characteristic analysis were performed to determine an optimal combination of imaging and clinical biomarkers in predicting positive findings on pathology and/or microbiology from percutaneous biopsy suggestive of spondylodiscitis.

**RESULTS:** Our patient cohort consisted of 72 patients, of whom 33.3% (24/72) had spondylodiscitis. The mean age was  $63 \pm 16$  years with a male/female ratio of 41:31. Logistic regression revealed a combination with an area under the curve of 0.72 for pathology and 0.68 for pathology and/or microbiology. Epidural enhancement on MR imaging improved predictive performance to 0.87 for pathology and 0.78 for pathology and/or microbiology.

**CONCLUSIONS:** Our findings demonstrate that epidural enhancement on MR imaging added diagnostic value when combined with clinical biomarkers to help predict which patients undergoing percutaneous biopsy will have positive findings for spondylodiscitis on pathology and/or microbiology.

**ABBREVIATIONS:** AUC = area under the curve; CRP = C-reactive protein; ESR = erythrocyte sedimentation rate; NPV = negative predictive value; PPV = positive predictive value

**D**iagnosis of vertebral spondylodiscitis is often difficult and determined on the basis of a combination of imaging findings, clinical context, inflammatory biomarkers, spondylodiscitis, degenerative changes, and spinal tumors, though it is not a perfect tool; more invasive sampling is frequently still required. The typical findings suggestive of spinal infection include hyperintense T2 disc signal, adjacent vertebral endplate destruction, and epidural/

paraspinal enhancement.<sup>1,2</sup> However, in the absence of these typical features, the diagnosis of spondylodiscitis can be difficult and Modic type 1 degenerative changes and inflammatory disease may often mimic spinal infections. Currently, percutaneous CT or fluoroscopy-guided biopsy is the standard of care for the diagnosis of spondylodiscitis.<sup>3</sup>

In patients with radiologically suspected spinal infection, identification of the organism is useful in directing antibiotic treatment. Per Sehn and Gilula,<sup>4</sup> these organisms “may be identified by blood culture or biopsy and culture of site of suspected infection with reported success rates of 20–59%<sup>5,6</sup> and 46–91%.”<sup>7</sup> The histologic examination is useful for a correct diagnosis when the microbes responsible for spinal infection do not grow in tissue or blood culture medium or in case of anaerobic organisms.<sup>8</sup> In clinical practice today, both microbiology and pathology are typically obtained from the tissue specimen.

Received February 26, 2020; accepted after revision April 23.

From the Department of Radiology, Icahn School of Medicine at Mount Sinai, New York, New York.

Paper previously presented at: Annual Meeting of the American Society of Neuroradiology, May 30–June 4, 2020; Virtual, No. 1140.

Please address correspondence to Amish H. Doshi, MD, Department of Radiology/Neuroradiology, Icahn School of Medicine at Mount Sinai, Mount Sinai Hospital, One Gustave Levy Place, New York, NY 10029; e-mail: amish.doshi@mountsinai.org



Indicates article with supplemental on-line photos.

<http://dx.doi.org/10.3174/ajnr.A6623>



**FIG 1.** Imaging panel in a patient with osteomyelitis with hyperintense T2 disc signal, adjacent vertebral endplate erosions, and paraspinal/epidural enhancement. Thoracic spine MR imaging of a 72-year-old man with radiologically suspected infection at T4–T5. *A*, Disc-centered and bone marrow hypointensity on a T1-weighted image. *B*, Mild hyperintensity of the disc and adjacent bone marrow on T2-weighted image. The *arrow* represents hyperintense T2 disc signal. *C*, Contrast-enhanced T1-weighted image demonstrates epidural (*arrowhead*) and paraspinal enhancement (*asterisk*). The asterisk represents adjacent vertebral endplate erosion. Pathology demonstrated that inflammatory histology and microbiology had no growth. ESR was 123 mm/h, and CRP was 176 mg/L. The patient was febrile on presentation with leukocytosis.

Inflammatory markers such as C-reactive protein (CRP)<sup>9–11</sup> and erythrocyte sedimentation rate (ESR)<sup>12,13</sup> are commonly elevated in patients with spondylodiscitis. The association of spinal infection with biomarkers such as leukocytosis,<sup>10,14</sup> fever status,<sup>15,16</sup> alkaline phosphatase level,<sup>17,18</sup> and hemoglobin count<sup>18,19</sup> have been explored in the past without a clear consensus. Further studies are needed to clarify whether these clinical and laboratory biomarkers are associated with spinal infections.

MR imaging is currently the preferred technique for prediction of spondylodiscitis; however, pathology and microbiology results for radiologically suspected spondylodiscitis are only positive in up to 30% of cases.<sup>20</sup> In this study, we aimed to evaluate whether MR imaging features add diagnostic value when combined with clinical biomarkers to help predict which patients who undergo percutaneous biopsy will have positive findings for spondylodiscitis on pathology and/or microbiology.

## MATERIALS AND METHODS

### Study Population

This is a single-center retrospective study, which was approved by the local institutional review board, with a waiver of informed consent. From July 2014 to August 2019, a total of 187 CT- and fluoroscopy-guided percutaneous bone biopsies were performed at our institution for suspicion of spondylodiscitis based on prior MR imaging findings. Patients were included if they had pathology reports from the biopsy, MR imaging with contrast within 3 weeks of biopsy, and laboratory markers within 2 weeks before biopsy. Patients were excluded if they did not have pathology reports from biopsy ( $n = 17$ ), did not have MR

imaging with contrast within 3 weeks of biopsy ( $n = 24$ ), or did not have laboratory markers within 2 weeks of biopsy ( $n = 50$ ). Furthermore, they were excluded if they had been on broad-spectrum IV antibiotics for >3 days before the biopsy date ( $n = 19$ ). Patients were further excluded if the biopsy yielded nondiagnostic/inadequate tissue specimens ( $n = 5$ ). This process yielded a final cohort of 72 patients.

### Procedure

All biopsies were performed with the patient under CT or fluoroscopic guidance. A 40-section CT scanner (Somatom Definition AS; Siemens) was used. Drill systems varied depending on operator comfort. All biopsies were by a transpedicular approach by 1 of 3 procedural neuroradiologists at our institution.

### Data Collection

Demographic characteristics, comorbidities, fever status, laboratory values, tissue and blood culture results, and antibiotic exposure were collected from our institutional electronic medical record system. Three independent observers, blinded to clinical data and diagnosis, provided MR imaging–based scoring for the presence of hyperintense T2 disc signal, adjacent vertebral endplate erosion, epidural enhancement, and paraspinal enhancement (Fig 1). Each score was obtained in a binary fashion for the presence or absence of these features. Observers were neuroradiologists with 2, 6, and 10 years of attending experience. The presence of inflammatory histology was obtained from the surgical pathology report, and microbiology culture growth was obtained from the microbiology report of the biopsied tissue specimen.

### Statistical Analysis

The SPSS statistical package for Macintosh, Version 25 (IBM) was used for statistical computations. The Spearman rank correlation coefficient was used for categorical/rank variables, and the Pearson correlation coefficient was used for continuous variables. Positive predictive value (PPV), negative predictive value (NPV), sensitivity, and specificity were calculated from cross-tabulation entry. The Cohen  $\kappa$  analysis was used to assess paired interobserver agreement among the 3 independent observers scoring the presence of MR imaging features. Additionally, majority consensus analysis for the 3 observers was performed for each MR imaging feature for each case. Univariate analysis for each clinical and imaging biomarker was used to assess the association with positive pathology and/or microbiology indicating spondylodiscitis. Subsequently, multivariate backward stepwise logistic regression and receiver operating characteristic analysis using clinical and imaging biomarkers were used to find the optimal combination

**Table 1: Demographic characteristics of patient cohort**

Variable	No (%)
Age (mean) (yr)	63 ± 16
Sex (M/F)	41:31
Immunosuppression	33 (46)
Cancer	8 (11)
COPD	6 (8)
Cirrhosis	3 (4)
Diabetes	15 (21)
HIV	4 (6)
Steroid use	12 (17)
IV drug abuse	9 (13)
Postoperative status (within 1 wk)	
Symptoms relevant to discitis	0 (0)
Back pain	72 (100)
Febrile	25 (35)
Radiation	12 (17)
Numbness/weakness	10 (14)
Bowel or bladder incontinence	3 (4)
Time to diagnosis (days) <sup>a</sup>	55 (1–270)
Site of involvement	
Cervical	3 (4)
Thoracic	20 (28)
Lumbar	49 (68)
Biopsy technique	
CT	50 (69)
Fluoroscopy	22 (31)
Either surgical pathology (+)/microbiology (+)	29 (40)
Surgical pathology (+)	24 (33)
Microbiology growth from tissue (+)	12 (17)
Both	7 (10)
Bacterial isolates from tissue culture	12
Staphylococci	5 (42)
Streptococci	3 (25)
Pseudomonas	2 (17)
Klebsiella	1 (8)
Mycobacteria	1 (8)
Blood culture growth (+)	2 (3)
Laboratory leukocyte count (cells/mm <sup>3</sup> ) <sup>a</sup>	8.0 (4.1–17.5)
CRP (mg/L) <sup>a</sup>	46.4 (1–303)
ESR (mm/h) <sup>a</sup>	59.3 (6–156)

**Note:**—COPD indicates chronic obstructive pulmonary disease.

<sup>a</sup> Mean followed by range in parenthesis.

of biomarkers for predicting spondylodiscitis. This analysis was performed for 2 end points: 1) spondylodiscitis as proved on pathology only, and 2) spondylodiscitis as proved on pathology and/or microbiology because clinicians use different criteria to diagnose spondylodiscitis.

## RESULTS

### Clinical Characteristics of the Patient Population

Our cohort consisted of 72 patients, of whom 50 had CT-guided and 22 had fluoroscopy-guided imaging (Table 1). The mean age was 63 ± 16 years with a median of 62 years and a male/female ratio of 41:31. Forty-six percent of our patient cohort was immunosuppressed. All of our patients presented with back pain, and approximately one-third of the patients presented with fever. Additional neurologic symptoms on presentation included radiculopathy, paresthesia, and incontinence. There were 24 patients found to have positive pathology and 12 patients found to have positive microbiology growth in support of spondylodiscitis. A

total of 29 patients had either positive pathology or microbiology results (7 patients had both positive pathology and microbiology, and 5 patients only had positive microbiology with negative pathology results for spondylodiscitis). Of the bacterial isolates from tissue culture, *Staphylococci* and *Streptococci* were most commonly observed.

CRP values for patients with spondylodiscitis averaged 93.4 mg/L with a range of 7–303 mg/L, while they averaged 40.2 mg/L with range of 1–156 mg/L for patients without spondylodiscitis (Table 2). ESR values averaged 65.1 mm/h in patients with spondylodiscitis with a range of 12–150 mm/h, while they averaged 51.0 mm/h and ranged from 6–106 mm/h in patients without spondylodiscitis.

### Clinical Biomarkers and Imaging Features Associating with Spondylodiscitis

Univariate analysis showed that fever status ( $r = 0.26$ ,  $P = .03$ ), CRP ( $r = 0.29$ ,  $P = .02$ ), hyperintense T2 disc signal ( $r = 0.29$ ,  $P = .03$ ), adjacent vertebral endplate erosion ( $r = 0.31$ ,  $P = .02$ ), epidural enhancement ( $r = 0.41$ ,  $P = .001$ ), and paraspinal enhancement ( $r = 0.33$ ,  $P = .01$ ) were associated with positive pathology and/or positive microbiology for spondylodiscitis (Tables 3 and 4). Blood culture growth, leukocytosis, hemoglobin count, platelet count, alkaline phosphatase level,

and ESR did not have statistically significant associations ( $P > .05$ ). In the setting of epidural enhancement, the PPV and NPV ranged from 40.7% to 61.3% and 75.6% to 100% for positive pathology and either positive pathology or positive microbiology, respectively. For paraspinal enhancement, PPV and NPV ranged from 36.9% to 53.8% and 75.8% to 100%, respectively. Hyperintense T2 disc signal and adjacent endplate erosion had similar PPV and NPV ranges with relatively low PPV (ranging from 31.2% to 55.5%) and high NPV (ranging from 79.2% to 100%).

### Combination of Imaging and Clinical Biomarkers Predicting Positive Pathology and/or Microbiology Findings Suggestive of Spondylodiscitis

Logistic regression for an optimal combination of clinical biomarkers showed that a combination of CRP, ESR, and fever status yielded the highest area under the curve (AUC) of 0.72 for positive pathology (On-line Fig 1) and 0.68 for positive pathology and/or microbiology (On-line Fig 2). When clinical biomarkers were combined with imaging features, a combination of CRP,



**Table 2: Inflammatory biomarker characteristics associated with pathology and/or microbiology for spondylodiscitis**

	Pathology		Pathology and/or Microbiology	
	Positive	Negative	Positive	Negative
CRP (mean) (mg/L)	93.4	40.2	86.4	38.3
Median	50	31.5	60.5	22.0
Range	7–303	1–156	2–303	1–156
SD	90.3	38.7	84.9	42.4
ESR (mean) (mm/h)	65.1	51.0	66.8	51.6
Median	59.0	46	61.5	38.5
Range	12–150	6–106	22–156	6–109
SD	36.5	27.5	34.9	33.3

**Table 3: Correlation between individual biomarkers and pathology-proved spondylodiscitis<sup>a</sup>**

	Positive Pathology					
	<i>r</i>	<i>P</i>	PPV	NPV	Sensitivity	Specificity
Epidural enhancement						
Observer 1	0.52	<.001 <sup>c</sup>	61.3	87.8	79.2	75.0
Observer 2	0.36	.002 <sup>c</sup>	42.1	100	100	31.3
Observer 3	0.33	.004 <sup>c</sup>	40.7	100	100	27.1
Majority consensus	0.41	.001 <sup>c</sup>	44.4	100	100	37.5
Paraspinal enhancement						
Observer 1	0.27	.02 <sup>c</sup>	40.7	88.9	91.7	33.3
Observer 2	0.23	.05 <sup>c</sup>	36.9	100	100	14.6
Observer 3	0.24	.04 <sup>c</sup>	43.6	78.8	70.8	54.2
Majority consensus	0.33	.01 <sup>c</sup>	40.7	100	100	27.1
Hyperintense T2 disc signal						
Observer 1	0.37	.02 <sup>c</sup>	55.5	80.1	86.5	45.0
Observer 2	0.19	.03 <sup>c</sup>	33.0	100	100	20.2
Observer 3	0.21	.03 <sup>c</sup>	41.2	79.2	73.1	51.0
Majority consensus	0.29	.03 <sup>c</sup>	51.0	100	100	33.2
Vertebral endplate erosion						
Observer 1	0.333	.01 <sup>c</sup>	46.0	83.4	88.8	30.2
Observer 2	0.22	.05 <sup>c</sup>	35.6	95.5	93.2	25.7
Observer 3	0.30	.0 <sup>c</sup>	39.4	80.6	75.6	56.7
Majority consensus	0.31	.02 <sup>c</sup>	42.1	92.3	92.0	35.6
Blood culture growth	0.06	.63	50	66.7	4.2	97.9
Fever status	0.26	.03 <sup>c</sup>	48.3	76.7	58.3	68.8
Leukocytosis	0.032	.80	40	64.3	16.7	85.7
Hemoglobin count <sup>b</sup>	−0.05	.67	NA	NA	NA	NA
Platelet count <sup>b</sup>	0.20	.11	NA	NA	NA	NA
ALP level <sup>b</sup>	−0.03	.84	NA	NA	NA	NA
ESR <sup>b</sup>	−0.09	.49	NA	NA	NA	NA
CRP <sup>b</sup>	0.29	.02 <sup>c</sup>	NA	NA	NA	NA

**Note:**—NA indicates not applicable; ALP, alkaline phosphatase.

<sup>a</sup> The Spearman correlation was used for rank/categorical variables. PPV, NPV, sensitivity, and specificity numbers are represented in percentages. Continuous variables will not have PPV, NPV, sensitivity, or specificity values without established thresholds.

<sup>b</sup> Continuous variables in which the Pearson correlation was used.

<sup>c</sup> Statistically significant *P* values (<.05).

ESR, fever status, and the presence of epidural enhancement yielded an improved AUC of 0.76–0.87 for positive pathology and 0.73–0.78 for positive pathology and/or microbiology (Table 5). The presence of hyperintense T2 disc signal, adjacent vertebral endplate erosion, and paraspinal enhancement did not improve prediction for positive pathology and/or microbiology findings suggestive of spondylodiscitis in combination with clinical biomarkers.

#### Interobserver Agreement among Multiple Raters and Majority Consensus

Interobserver  $\kappa$  agreement among 3 independent observers for hyperintense T2 disc signal, adjacent vertebral body erosions, epidural enhancement, and paraspinal enhancement was 0.58, 0.55,

0.49, and 0.33, respectively. To overcome fair  $\kappa$  agreement, we used a majority consensus for imaging scores. NPV was 100% for epidural and paraspinal enhancement based on majority consensus for positive pathology and positive pathology and/or microbiology (Tables 3 and 4). When epidural enhancement from majority consensus was combined with ESR, CRP, and fever status, an optimal AUC of 0.80 was obtained for positive pathology (On-line Fig 1) and 0.79 for positive pathology and/or microbiology (On-line Fig 2).

#### DISCUSSION

Diagnosis of spondylodiscitis can be difficult and often delayed or missed due to the insidious onset of symptoms and relative

**Table 4: Correlation between individual biomarkers and spondylodiscitis as proved on pathology and/or microbiology<sup>a</sup>**

	Positive Pathology and/or Microbiology					
	r	P	PPV	NPV	Sensitivity	Specificity
Epidural enhancement						
Observer 1	0.37	.00 <sup>b</sup>	61.3	75.6	65.5	72.1
Observer 2	0.42	.001 <sup>b</sup>	50.9	100	100	34.9
Observer 3	0.39	.001 <sup>b</sup>	49.2	100	100	30.2
Majority consensus	0.47	.001 <sup>b</sup>	53.7	100	100	41.9
Paraspinal enhancement						
Observer 1	0.34	.03 <sup>b</sup>	50.0	88.9	93.1	37.2
Observer 2	0.27	.02 <sup>b</sup>	44.6	100	100	16.3
Observer 3	0.30	.01 <sup>b</sup>	53.8	75.8	72.4	58.1
Majority consensus	0.39	.01 <sup>b</sup>	49.2	100	100	30.2
Hyperintense T2 disc signal						
Observer 1	0.30	.03 <sup>b</sup>	49.2	79.6	82.5	42.6
Observer 2	0.15	.05 <sup>b</sup>	31.2	96.2	95.3	19.6
Observer 3	0.25	.02 <sup>b</sup>	45.5	80.2	74.2	50.4
Majority consensus	0.28	.03 <sup>b</sup>	48.0	95.2	93.5	29.8
Vertebral endplate erosion						
Observer 1	0.29	.02 <sup>b</sup>	48.9	82.4	89.6	33.6
Observer 2	0.17	.03 <sup>b</sup>	37.5	95.8	92.5	27.5
Observer 3	0.33	.01 <sup>b</sup>	38.1	82.5	76.3	59.1
Majority consensus	0.31	.02 <sup>b</sup>	42.6	91.5	91.8	34.7
Blood culture growth	0.03	.79	50	59.4	3.4	97.6
Fever status	0.25	.03 <sup>a</sup>	55.2	69.8	55.2	69.8
Leukocytosis	0.039	.77	40	55.4	13.8	83.8
Hemoglobin count <sup>c</sup>	−0.02	.86	NA	NA	NA	NA
Platelet count <sup>c</sup>	0.17	.18	NA	NA	NA	NA
ALP level <sup>c</sup>	0.05	.73	NA	NA	NA	NA
ESR <sup>c</sup>	−0.07	.62	NA	NA	NA	NA
CRP <sup>c</sup>	0.26	.04 <sup>a</sup>	NA	NA	NA	NA

**Note:**—NA indicates not applicable; ALP, alkaline phosphatase.

<sup>a</sup> The Spearman correlation was used for rank/categorical variables.

<sup>b</sup> Statistically significant *P* values (<.05).

<sup>c</sup> Continuous variables in which the Pearson correlation was used.

**Table 5: Predictive performance of clinical and image-based features<sup>a</sup>**

	Positive Pathology			Positive Pathology and/or Microbiology		
	AUC	Sensitivity	Specificity	AUC	Sensitivity	Specificity
CRP, ESR, and fever	0.72	68.2	67.0	0.68	60.5	64.5
CRP, ESR, fever, and epidural enhancement (observer 1)	0.87	83.1	79.8	0.76	68.4	75.6
CRP, ESR, fever, and epidural enhancement (observer 2)	0.76	75.0	66.5	0.73	59.6	76.2
CRP, ESR, fever, and epidural enhancement (observer 3)	0.79	77.2	70.1	0.78	69.3	75.8
CRP, ESR, fever, and epidural enhancement (majority consensus)	0.80	78.3	75.6	0.79	77.4	74.6

<sup>a</sup> Logistic regression with backward stepwise selection was used to find the optimal combination of clinical and imaging features for 3 independent observers with majority consensus among the observers.

rarity of the disease in the setting of a high prevalence of patients presenting to the hospital with back pain. In our study, we assessed spondylodiscitis with 2 separate end points: as proved on pathology only and as proved on pathology and/or microbiology because clinicians use different criteria for the diagnosis of spondylodiscitis. We demonstrated that epidural enhancement on MR imaging added diagnostic value when combined with clinical biomarkers to help predict which patients undergoing percutaneous biopsy will have positive findings for spondylodiscitis on pathology and/or microbiology.

Clinically, the initial presentation of discitis is often back pain; however, in up to 15% of patients, the initial presentation may be fever or neurologic symptoms without pain.<sup>21–24</sup> Correct diagnosis and treatment are essential to avoid long-term sequelae involving neurologic deficits.<sup>10,15</sup> Fever has been shown in prior studies to be

associated with spondylodiscitis, specifically occurring in up to 60% of patients.<sup>15,21</sup> We observed similar findings in our study, with roughly 58% (14/24) of patients with positive pathology found to be febrile on presentation. Prior studies have shown conflicting associations of discitis with laboratory panels such as leukocytosis,<sup>10,14</sup> anemia,<sup>18,19</sup> and alkaline phosphatase (ALP) levels.<sup>17,18</sup> We did not observe a statistically significant association among these biomarkers in our study.

ESR and CRP are well-studied inflammatory biomarkers and have been shown to have high sensitivity but low specificity for spondylodiscitis in prior studies.<sup>9–13</sup> An and Seldomridge<sup>13</sup> showed elevation of ESR in >80% of cases, with a mean of roughly 60 mm/h. In our study, the mean value was 65 mm/h for positive pathology and 67 mm/h for either positive pathology or microbiology. Most interesting, ESR was not found to have a statistical association with

spondylodiscitis as an independent biomarker; however, it was statistically significant when combined with CRP, fever status, and epidural enhancement through a multiparametric model. CRP was found to be associated with spondylodiscitis independently. In our study, CRP ranged from 1 to 156 mg/L in the negative cohort, while it ranged from 7 to 303 mg/L in the positive cohort. Thus, elevated CRP values above the range of the negative cohort (>156 mg/L) may support the diagnosis of spondylodiscitis if suspected.

The presence of hyperintense T2 disc signal, adjacent vertebral body erosion, epidural enhancement, and paraspinal enhancement are well-recognized MR imaging characteristics of spondylodiscitis.<sup>1,2,25-27</sup> In our study, we had 3 neuroradiologists independently score these characteristics blinded to the diagnosis. However, there was suboptimal interobserver agreement with  $\kappa$  values of 0.58, 0.55, 0.49, and 0.33 for hyperintense T2 disc signal, adjacent vertebral body erosions, and epidural and paraspinal enhancement, respectively. We attempted to overcome this discordance by applying majority consensus in our univariate analysis and prediction model.

Spira et al<sup>25</sup> had previously demonstrated 100% sensitivity and roughly 50% specificity with paraspinal enhancement but 40% sensitivity and 80% specificity with epidural enhancement for microbiology. Our results were similar for paraspinal enhancement with a sensitivity as high as 100% and specificity ranging from 14% to 54%. However, results differed for epidural enhancement with sensitivity ranging from 79% to 100% and specificity ranging from 27% to 75%. Ledermann et al<sup>1</sup> had previously shown high sensitivity for paraspinal/epidural enhancement (97.7% sensitivity), hyperintense T2 disc signal (93.2% sensitivity), and adjacent endplate erosion (84.1% sensitivity) in a cohort of patients with positive pathology and/or microbiology. We also found high sensitivities for these MR imaging features ranging from 70.8% to 100%, 73.1% to 100%, and 75.5% to 93.2% for paraspinal/epidural enhancement, hyperintense T2 disc signal, and adjacent endplate erosion, respectively. These findings also corresponded with high NPVs in all typical MR imaging features of spondylodiscitis and, not surprisingly, indicate that the absence of these typical features can be a helpful tool in excluding pathology- and microbiology-proved spondylodiscitis.

However, the novelty of this study was in demonstrating that MR imaging features, specifically epidural enhancement, when combined with clinical biomarkers, improved predictive performance, increasing the AUC from 0.72 to 0.87. This finding can also be observed in a range of experience levels because our observers ranged from having 2–10 years of attending experience as neuroradiologists. Moreover, this finding is observed in spondylodiscitis proved by either criterion: pathology only or pathology and/or microbiology. Patients suspected of having spondylodiscitis will likely undergo MR imaging, and it is clinically important to recognize that the enhancement pattern should be considered along with clinical biomarkers in the diagnosis of spondylodiscitis.

There are several limitations to our study. First, it was retrospective. A prospective study would facilitate increasing our cohort size by obtaining MR imaging and laboratory markers at the time of tissue biopsy for more patients. There is also an inherent bias of only including patients with high radiologic suspicion of spondylodiscitis requiring biopsy. An ideal study would have

included patients without radiologic suspicion for spondylodiscitis; however, this would imply performing biopsies on patients without suspicion for spinal infection. The limitation of assessing patients who have been on antibiotics for <3 days is arbitrary; however, a recent study showed that antibiotics do not affect tissue yield within 3 weeks before biopsy.<sup>28</sup> Additionally, we acknowledge that the use of pathology and/or microbiology results from percutaneous biopsy for spondylodiscitis may have a large percentage of false-negatives, shown in up to 37% by Nam et al.<sup>29</sup> They previously compared pathology results from open-to-percutaneous needle biopsies and found, within the same cohort, that 70.4% of patients had positive pathology results from open biopsy, whereas only 33.3% of the cohort had positive findings with percutaneous biopsies. We acknowledge that using pathology results from open biopsy may have been an ideal, or perhaps more sensitive, criterion standard; however, open biopsies are no longer routinely performed.

Finally, there was suboptimal interobserver agreement among the 3 observers for MR imaging features. This is likely due to varying experience levels among the observers because the highest AUC for prediction of spondylodiscitis corresponded with scores from the observer with the most experience. We acknowledge that in clinical practice, there is a broad range of experience levels, and we attempted to overcome this limitation by using a majority consensus among the 3 observers.

## CONCLUSIONS

Our findings demonstrated that epidural enhancement on MR imaging added diagnostic value when combined with clinical biomarkers to help predict which patients who undergo percutaneous biopsy will have positive findings for spondylodiscitis on pathology and/or microbiology.

## REFERENCES

1. Ledermann HP, Schweitzer ME, Morrison WB, et al. **MR imaging findings in spinal infections: rules or myths?** *Radiology* 2003;228:506–14 CrossRef Medline
2. Hong SH, Choi JY, Lee JW, et al. **MR imaging assessment of the spine: infection or an imitation?** *Radiographics* 2009;29:599–612 CrossRef Medline
3. Duarte RM, Vaccaro AR. **Spinal infection: State of the art and management algorithm.** *Eur Spine J* 2013;22:2787–99 CrossRef Medline
4. Sehn JK, Gilula LA. **Percutaneous needle biopsy in diagnosis and identification of causative organisms in cases of suspected vertebral osteomyelitis.** *Eur J Radiol* 2012;81:940–46 CrossRef Medline
5. van Thuijl HF, Mazor T, Johnson BE, et al. **Evolution of DNA repair defects during malignant progression of low-grade gliomas after temozolomide treatment.** *Acta Neuropathol* 2015;129:597–607 CrossRef Medline
6. Chew FS, Kline MJ. **Diagnostic yield of CT-guided percutaneous aspiration procedures in suspected spontaneous infectious diskitis.** *Radiology* 2001;218:211–14 CrossRef Medline
7. Rimondi E, Staals EL, Errani C, et al. **Percutaneous CT-guided biopsy of the spine: results of 430 biopsies.** *Eur Spine J* 2008;17:975–81 CrossRef Medline
8. Landi A, Grasso G, Iaiani G, et al. **Spontaneous spinal discitis and spondylodiscitis: clinicotherapeutic remarks.** *J Neurosci Rural Pract* 2017;8:42–46 CrossRef Medline

9. Dufour V, Feydy A, Rillardon L, et al. **Comparative study of postoperative and spontaneous pyogenic spondylodiscitis.** *Semin Arthritis Rheum* 2005;34:766–71 CrossRef Medline
10. Euba G, Narváez JA, Nolla JM, et al. **Long-term clinical and radiological magnetic resonance imaging outcome of abscess-associated spontaneous pyogenic vertebral osteomyelitis under conservative management.** *Semin Arthritis Rheum* 2008;38:28–40 CrossRef Medline
11. Gouliouris T, Aliyu SH, Brown NM. **Spondylodiscitis: update on diagnosis and management.** *J Antimicrob Chemother* 2010;65(Suppl 3):iii11–24 CrossRef Medline
12. Patzakis MJ, Rao S, Wilkins J, et al. **Analysis of 61 cases of vertebral osteomyelitis.** *Clin Orthop Relat Res* 1991;178–83 Medline
13. An HS, Seldomridge JA. **Spinal infections: diagnostic tests and imaging studies.** *Clin Orthop Rel Res* 2006;443:27–33 CrossRef Medline
14. Nolla JM, Ariza J, Gómez-Vaquero C, et al. **Spontaneous pyogenic vertebral osteomyelitis in nondrug users.** *Semin Arthritis Rheum* 2002;31:271–08 CrossRef Medline
15. Mylona E, Samarkos M, Kakalou E, et al. **Pyogenic vertebral osteomyelitis: a systematic review of clinical characteristics.** *Semin Arthritis Rheum* 2009;39:10–17 CrossRef
16. Wirtz DC, Genius I, Wildberger JE, et al. **Diagnostic and therapeutic management of lumbar and thoracic spondylodiscitis: an evaluation of 59 cases.** *Arch Orthop Trauma Surg* 2000;120:245–51 CrossRef Medline
17. Colmenero JD, Jiménez-Mejías ME, Sánchez-Lora FJ, et al. **Pyogenic, tuberculous, and brucellar vertebral osteomyelitis: a descriptive and comparative study of 219 cases.** *Ann Rheum Dis* 1997;56:709–15 CrossRef Medline
18. Beronius M, Bergman B, Andersson R. **Vertebral osteomyelitis in Göteborg, Sweden: a retrospective study of patients during 1990–95.** *Scand J Infect Dis* 2001;33:527–32 CrossRef Medline
19. Nather A, David V, Hee HT, et al. **Pyogenic vertebral osteomyelitis: a review of 14 cases.** *J Orthop Surg (Hong Kong)* 2005;13:240–44 CrossRef Medline
20. Sertic M, Parkes L, Mattiassi S, et al. **The Efficacy of Computed Tomography-Guided Percutaneous Spine Biopsies in Determining a Causative Organism in Cases of Suspected Infection: A Systematic Review.** *Can Assoc Radiol J* 2019;70:96–103 CrossRef Medline
21. Sapico FL, Montgomerie JZ. **Pyogenic vertebral osteomyelitis: report of nine cases and review of the literature.** *Rev Infect Dis* 1979;1:754–76 CrossRef Medline
22. Torda AJ, Gottlieb T, Bradbury R. **Pyogenic vertebral osteomyelitis: analysis of 20 cases and review.** *Clin Infect Dis* 1995;20:320–28 CrossRef Medline
23. Sakkas LI, Davas EM, Kapsalaki E, et al. **Hematogenous spinal infection in Central Greece.** *Spine (Phila Pa 1976)* 2009;34:E513–18 CrossRef Medline
24. Zarrouk V, Feydy A, Sallès F, et al. **Imaging does not predict the clinical outcome of bacterial vertebral osteomyelitis.** *Rheumatology* 2006;46:292–95 CrossRef Medline
25. Spira D, Germann T, Lehner B, et al. **CT-guided biopsy in suspected spondylodiscitis: the association of paravertebral inflammation with microbial pathogen detection.** *PLoS One* 2016;11:e0146399 CrossRef Medline
26. Schellinger D. **Patterns of anterior spinal canal involvement by neoplasms and infections.** *AJNR Am J Neuroradiol* 1996;17:953–59 Medline
27. Longo M, Granata F, Ricciardi GK, et al. **Contrast-enhanced MR imaging with fat suppression in adult-onset septic spondylodiscitis.** *Eur Radiol* 2003;13:626–37 CrossRef Medline
28. Foreman SC, Schwaiger BJ, Gempt J, et al. **MR and CT imaging to optimize CT-guided biopsies in suspected spondylodiscitis.** *World Neurosurg* 2017;99:726–34.e7 CrossRef Medline
29. Nam KH, Song GS, Han IH, et al. **Diagnostic value of biopsy techniques in lumbar spondylodiscitis: percutaneous needle biopsy and open biopsy.** *Korean J Spine* 2011;8:267–71 CrossRef Medline



## Norman Leeds, MD

**D**r Norman Leeds died on March 5, 2020. Dr Leeds was a key figure in the history of the American Society of Neuroradiology (ASNR). As a young neuroradiologist, he was one of the founding members of the ASNR. With his typical modesty, he once told me that he was made a member because someone had to get the coffee. He was one of the forward-thinking society leaders who was instrumental in the founding of the *American Journal of Neuroradiology*. His extensive CV attests to his scientific contributions to neuroradiology.

I want to speak of my personal interactions with Dr Leeds and the effect he had on my life. I could say that Norm was my mentor, but he was much more than that. He was the reason that I became a neuroradiologist, and he inspired me to become an academic neuroradiologist. I worked with Norm as a resident at Montefiore Hospital from 1973 to 1976 and as his colleague as an attending from 1977 to 1983. At that time, the radiology department at Montefiore was an interesting place to train. It was led by brilliant but idiosyncratic and mercurial leaders. Most of my coresidents feared working on the neuroradiology rotation because of a combination of demands of the service and Norm's occasional angry outbursts. He once yelled at a resident, "What do you think I'm talking, tuna fish?" Somehow, we knew what he meant. (There were many such "Normanisms." Syntax was not his strong suit). For whatever reason, I was not afraid of Norm, and I enjoyed working with him, learning how to interpret studies and observing his pivotal role in the clinical care of patients with neurologic disorders.

The 1970s was a time of transition for neuroradiology. At the beginning of the decade, cerebral angiography was the definitive diagnostic imaging technique, relied on by neurosurgeons and neurologists. The interpretation of angiograms was extremely difficult, and those individuals who were experts (including Norm) seemed to have an almost mystical talent. Norm would look at an angiogram with the referring clinician, wave his hands in the general direction of the films, and say "Right parietal parasagitta, I probably a met, see it?" He was almost always correct. Sometimes I wondered if even he knew how he came to the correct answer.

In the mid-1970s, the introduction of CT revolutionized neuroimaging. Lesions were much easier to see and characterize. Some neuroradiologists feared that this would be the end of our specialty. However, CT was new, and most referring clinicians were unsure about interpretation; therefore, they continued to rely on neuroradiologists. Norm's interactions with referring physicians, in particular neurosurgeons, were inspiring to me. He was a crucial part of the team, respected by and respecting of his clinical colleagues. After my fellowship, I returned to Montefiore to work with Norm. Over the next 6 years, we worked together, and I learned an enormous amount about image interpretation. I learned from him that the most important and satisfying aspect of neuroradiology was the interaction with referring physicians. I also came to



know Norm as an individual. Although he still had a temper, I got to see a side of him that was not so apparent to me as a resident. He was incredibly generous, arranging invitations for me to speak at many institutions even when it meant that he would have to shoulder more of the clinical load. He helped develop my research interests and encouraged me to present our findings at national meetings. His love for and devotion to his wife Betty and his children were amazing to witness.

Following my time at Montefiore, I joined the faculty at New York Hospital and Norm went on to become chairman at Beth Israel Hospital in New York and then the chief of neuroradiology at MD Anderson Cancer Center. I took with me the lessons I learned from Norm. When a clinician would come to the neuroradiology reading room and ask to look at a study, the radiology resident would sometimes view this as an interruption. I explained, as Norm had explained to me, that this was the real work and the real source of job satisfaction. I have tried to inspire my residents the way that

Norm inspired me, pointing out how interesting and fulfilling a career in neuroradiology could be. I think of the many neuroradiologists I have trained as Norm's academic grandchildren.

I remained in contact with Norm throughout the remainder of his career. It amazed me that he continued to learn all the new things that MR imaging had to offer.

I will miss him dearly.

**Robert D. Zimmerman, MD, FACR**

<http://dx.doi.org/10.3174/ajnr.A6612>

## James T. Goodrich, MD, PhD

**D**r. James T. Goodrich, MD, PhD was an inspiration to be the best we can be.

Dr. James T. Goodrich, renowned pediatric neurosurgeon, passed away on March 30, 2020, due to complications of COVID-19. An accomplished brain and craniofacial reconstructive surgeon, he is best known for pioneering surgeries to separate craniopagus twins. He was the Director of the Division of Pediatric Neurosurgery at Montefiore Medical Center and Professor of Clinical Neurological Surgery, Pediatrics, Plastic, and Reconstructive Surgery at Albert Einstein College of Medicine, where he spent more than 30 years. He was also Professor Contralto of Neurological Surgery at the University of Palermo in Palermo, Italy.

Dr. Goodrich was born in Portland, Oregon and served in the Marines during the Vietnam War. He completed his undergraduate work at the University of California, Irvine and his graduate and medical studies at Columbia University. Residency training was completed at Presbyterian Hospital in New York City and the New York Neurological Institute. He enjoyed the history of medicine, surfing, and travel.

Dr. Jacqueline Bello, Dr. Goodrich's longtime friend, colleague, and classmate said of him:

Truly a "Man for ALL Seasons", James T. Goodrich was my medical school classmate at Columbia's College of Physicians and Surgeons, fellow trainee at the Neurological Institute of New York, Montefiore colleague for more than 30 years, and close friend. Jim was all about service – serving his country with pride as a Marine, his profession with trailblazing innovation, and his patients with expertise and empathy.

He generously shared the international recognition he received for successful separation of Craniopagus twins, always acknowledging the team effort that was involved. His legacy



The photograph is courtesy of Montefiore Health System.

remains, outshining the many awards he received, both resolute and resilient, as he was . . . an inspiration to be the best we can be, in his memory and honor.

Our thoughts and prayers go out to his wife, his three sisters, and all those who were lucky enough to know him.

**Jacqueline A. Bello  
Adam E. Goldman-Yassen**

<http://dx.doi.org/10.3174/ajnr.A6628>

# Celebrating 35 Years of the AJNR

July 1985 edition

## Intravenous DSA and Duplex Sonography as Screening Examinations for Carotid Disease:

Comparison in 102 Vessels

Michael K. Wolverson<sup>1</sup>  
Elisabeth Heiberg  
Supranee Tantana  
Thomas J. Pilla

Duplex sonography and intravenous digital subtraction angiography (DSA) were compared in 102 carotid bifurcations in 51 patients. Sonograms were adequate in 87 (85%) vessels and angiograms were adequate on at least one view in 86 (84%) vessels. An adequate image was obtained by one or the other method in all but two vessels (98%). Although most vessels were seen well on one view only on DSA, agreement with sonography was exact in 73% of compared vessels and acceptable in 90%. Furthermore, no difference was found in the rate of agreement with sonography for vessels seen well by DSA on two or more views compared with those seen well on one view only. It was concluded that DSA and sonography are comparable screening methods for carotid disease and that a suboptimal study by either can usually be compensated for by performance of the other.

Duplex sonography and intravenous digital subtraction angiography (DSA) are now widely used as screening tests for the evaluation of the extracranial cerebral vessels in patients with suspected cerebrovascular disease. The details of the performance, capabilities, and limitations of each method are well described in the literature as is their acceptable accuracy in the assessment of carotid disease relative to conventional angiography [1-13]. Little information is available, however, directly comparing the two methods for technical adequacy and the extent of agreement in estimates of disease. We compared the DSA and sonographic findings in 102 carotid bifurcations in 51 patients with suspected cerebrovascular disease.

### Subjects and Methods

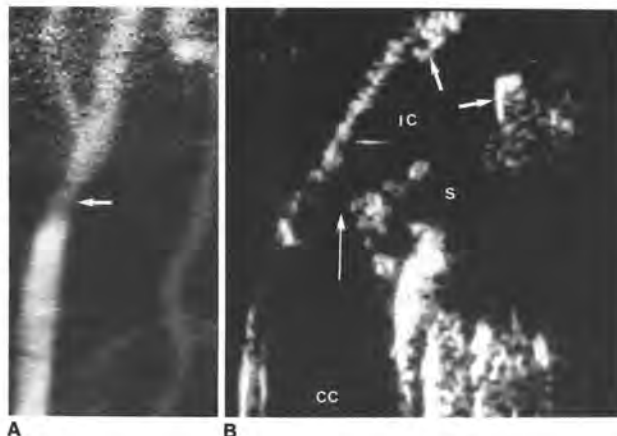
At our hospital intravenous DSA or sonography the carotid bifurcations in patients with suspect common indications for either test are definite disease, asymptomatic neck bruits, or a history of intracranial DSA or conventional angiography is a typical history of cerebral hemispheric or ocular evaluations before carotid endarterectomy. The patients were referred for intravenous DSA. For the performed on all these subjects before or soon after without knowledge of the results of the corresponding DSA was performed using a Technicare DR 160.

Optomarc 100 kV generator, selectable 6 or 9 inch Video-Med 3 TV system. The central processing unit using a 512 × 512 image display matrix and 14 preparation, an 8 in 15 gauge intracatheter was inserted into the common carotid artery over 40 ml Renografin at 12 ml/sec. Exposures commenced 4 sec after image sequence was usually recorded at a frame of 32 mAs. Views obtained routinely were 45°-55° RPO projections of the neck, 55° RPO of the aortic arch.

Received September 14, 1984; accepted after revision November 29, 1985.

<sup>1</sup>Department of Radiology, St. Louis University Hospital, 1325 S. Grand Blvd., St. Louis, MO 63104. Address reprint requests to M. K. Wolverson.

AJNR 6:669-673, July/August 1985  
0195-6108/85/0005-0669  
© American Roentgen Ray Society



## Streptokinase Clot Lysis in Acute Occlusions of the Cranial Circulation: Study in Rabbits

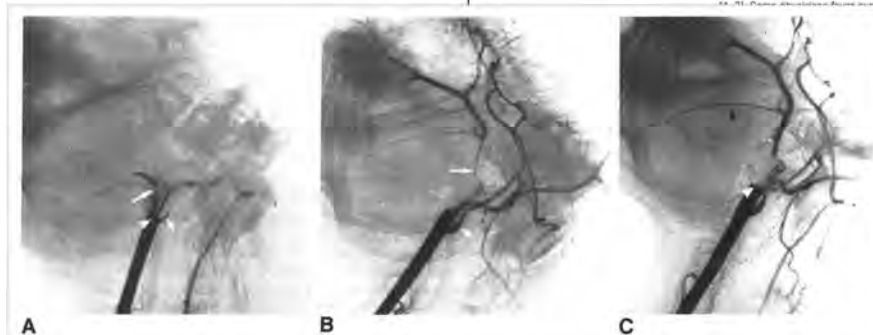
Ricardo S. Centeno<sup>1</sup>  
David B. Hackney<sup>1,2</sup>  
John R. Rothrock<sup>3</sup>

An animal model of acute cerebrovascular thromboembolism was developed to evaluate the feasibility of selective fibrinolytic. In 20 Flemish Giant rabbits, autologous clot was deposited via selective catheterization of the distal end of the common carotid artery. The rates of clot lysis with streptokinase were compared in eight control rabbits and after three different dosage regimens in four rabbits each. Group A received selective infusion of 5000 U/hr; group B received 4000 U/min for 1 hr, 3000 U/min for 2 hr, and 5000 U/hr for 2 hr; and group C was treated similar to group B plus receiving an initial 20,000 U bolus of streptokinase. Lysis was evaluated by serial angiograms obtained hourly for up to 8 hr after the clot was deposited. Five proximal vessels arising from the common carotid artery were chosen for the angiographic grading system. The control group showed beginning lysis after 5-6 hr. Group A appeared to show a slight improvement about 4 hr after clotting. Group B demonstrated an early and greater improvement at 2 hr that appeared to be sustained throughout the experiment. Group C showed no difference compared with the control group. The Dunnett procedure and the Kruskal-Wallis nonparametric analysis of variance were used for comparing the angiograms of the treatment groups with those of the control group at corresponding study times. The results of these animal experiments do not indicate a definite benefit of streptokinase treatment alone over no treatment. Further controlled studies are needed before the value of streptokinase in routine clinical practice can be determined.

Optimal treatment of acute cerebrovascular disease, including transient ischemic attack, reversible ischemic neurologic deficit, and acute stroke, remains a controversial issue. Medical management has been attempted with a variety of agents, most notably anticoagulants, but no clear-cut clinical benefit has been established [1-11].

Optimal management for acute stroke [4, 5]. While surgery where acute surgical intervention can be attempted for most patients with acute stroke, but no controlled studies are available, nor [6, 7]. We tried to determine the efficacy of an animal model that might further serve for

is used in 20 Flemish Giant rabbits (weight range, 10-15 kg) for controls and four each were assigned to three (3 C). A drop of Thrombin was placed on a milliliter of saline for 1 hr in a glass beaker. Then, 0.75 ml of the common carotid artery of each of the 20 rabbits was cannulated. A test injection of a small volume of the clot; the carotid artery was then left in place. The group A rabbits received 5000





# Novel Coronavirus: What Neuroradiologists Should Do



**W**e read with great interest the article “Novel Coronavirus: What Neuroradiologists as Citizens of the World Need to Know,” published by the *American Journal of Neuroradiology* in March 2020.<sup>1</sup> The authors have discussed in detail the epidemiology; virulence of coronavirus causing the current pandemic scenario with the pathogenesis, diagnosis and prognosis of the disease. There is an increasing trend toward a high incidence of infection among health care workers, and certain infection control measures have also been developed for health care workers in radiology departments.<sup>2</sup> Thus, the authors have discussed the role of neuroradiologists in disseminating knowledge and providing guidance to the general public to effectively control the spread. The authors have discussed the contact and airborne precautions that must be followed by neuroradiologists performing lumbar punctures, myelograms, and spine procedures. However, many other distinct procedures performed by interventional neuroradiologists in the emergency setting for active head and neck bleeding, ischemic stroke, and ruptured aneurysms require urgent endovascular attention. Such procedures often need urgent intubation/suctioning, and there is an increased risk of aerosolization of respiratory secretions and human spread of Severe Acute Respiratory Syndrome–coronavirus 2 (SARS-CoV-2) infection. Thus, an interventional laboratory protocol, which has not been discussed previously, must be instituted to limit the spread of the disease and curb human-to-human transmission.

Techniques like preintubation before arrival of the patient in the neurointervention lab, use of powered air-purifying respirator (PAPR) systems by anesthetists, filter systems (eg, high-efficiency particulate air; HEPA) in the anesthesia circuit, and closed circuit bilevel positive airway pressure (BIPAP) machines (when intubation is not done) pose less risk to health care workers because ventilation is managed through a closed circuit. In accordance with considerations for catheterization laboratories published in the *Journal of the American College of Cardiology*,<sup>3</sup> we recommend the use of appropriate personal protective equipment (PPE), including gowns, gloves, goggles (shields), and 3-layered surgical masks for all health care workers who work in a close

environment with patients. Patients with known coronavirus disease 2019 (COVID-19) undergoing endovascular intervention should don appropriate PPE (including N95 masks). A minimal number of health care workers who also have adequate training for doffing and donning of PPE should scrub into procedures. Vendor access inside the catheterization laboratory and use of PPE should be limited when necessary. Because access to rapid testing for COVID-19 is limited, all patients with fever and cough should be evaluated clinically and screened with portable chest radiographs, and elective procedures must be deferred until the source is identified.

After every procedure, interventional laboratories should undergo terminal cleaning using hot water, detergent, and 1% freshly prepared hypochlorite solution, and at least 1 hour of air exchange should be allowed between procedures. Patients with suspected or known COVID-19 should be treated at the end of the day, or a dedicated lab may be of value.

The authors have described very well what neuroradiologists should know during this global pandemic; we suggest practice guidelines for neurointerventional laboratories and what neuroradiologists should actively do to constrain the pandemic.

## REFERENCES

1. Mahajan A, Hirsch JA. **Novel coronavirus: what neuroradiologists as citizens of the world need to know.** *AJNR Am J Neuroradiol* 2020;41:552–54 CrossRef Medline
2. Mossa-Basha M, Meltzer CC, Kim DC, et al. **Radiology department preparedness for COVID-19: Radiology Scientific Expert Panel.** *Radiology* 2020 Mar 16. [Epub ahead of print] CrossRef Medline
3. Welt FG, Shah PB, Aronow HD, et al; American College of Cardiology's (ACC) Interventional Council and the Society of Cardiovascular Angiography and Intervention (SCAI). **Catheterization laboratory considerations during the coronavirus (COVID-19) pandemic: from ACC's Interventional Council and SCAI.** *J Am Coll Cardiol* 2020 Mar 16. [Epub ahead of print] CrossRef Medline

C. Jain  
 V. Bhatia  
 A. Kumar

Department of Radiodiagnosis and Imaging  
 Postgraduate Institute of Medical Education and Research  
 Chandigarh, India

Indicates open access to non-subscribers at [www.ajnr.org](http://www.ajnr.org)  
<http://dx.doi.org/10.3174/ajnr.A6550>

## Neuroradiologists and the Novel Coronavirus



**W**e wish to extend our gratitude to Drs Mahajan and Hirsch for their succinct and informative editorial on the novel coronavirus, COVID-19.<sup>1</sup> The editorial staff at the *American Journal of Neuroradiology*, at large, should also be recognized for broadening the focus of the journal and publishing an accessible, timely, and factual review.

The authors successfully combat uncertainty with science and objective guidance. Their underlying message is critically important. Specifically, all medical professionals—even those in highly subspecialized fields like neuroradiology—must rededicate themselves to the broader goal of promoting public health. The information presented provides a roadmap as we struggle to identify our role in this extraordinary time. While fiscally challenging and counter to the precoronavirus conceptualizations of our profes-

sional responsibility, this may entail promotion of social distancing by placing some of our patient care (for instance, routine outpatient imaging) on hold.

Drs Mahajan and Hirsch are to be commended for educating the neuroradiology community about an issue that impacts us in and outside of the reading room. They have provided a helpful resource, which can enhance our care of patients, friends, family, and ourselves during the challenging days ahead. Thank you.

### REFERENCE

1. Mahajan A, Hirsch JA. **Novel coronavirus: what neuroradiologists as citizens of the world need to know.** *AJNR Am J Neuroradiol* 2020;41:552–54 CrossRef Medline

© M.U. Antonucci

© J.M. Reagan

© M. Yazdani

Department of Radiology and Radiological Science  
Medical University of South Carolina  
Charleston, South Carolina

Ⓚ Indicates open access to non-subscribers at [www.ajnr.org](http://www.ajnr.org)  
<http://dx.doi.org/10.3174/ajnr.A6596>

## Meta-Analysis as a Symptom: The Example of Flow Diverters

**T**he principle of a meta-analysis is to evaluate the effect of a treatment by combining the results of several studies. This method increases the statistical power to test certain hypotheses, especially when several randomized controlled trials are each too small to provide an answer or have provided contradictory conclusions.

Because we have very few randomized trials in interventional neuroradiology, our meta-analyses most often collect data of uncontrolled case series. A meta-analysis then makes sense when the target pathology is rare, with a limited number of cases reported in each publication. However, in this case, a single meta-analysis is sufficient, even if it may need to be updated sometimes.

The excessive use of multiple meta-analyses for the same medical problem is a symptom: the hope that the next one will provide better results than the previous one. Any neuroradiologist can consult PubMed and enter the term, object of his or her research, followed by “AND meta-analysis” and compare the number of responses obtained. Between February 2013 and January 2020, 19 meta-analyses, often redundant, have been published concerning the treatment of cerebral aneurysms by flow diverters. It is at this point that it would become possible to envisage a meta-analysis of meta-analyses!

I know that not all cerebral aneurysms are the same and that it may be necessary to distinguish those of the carotid from those of the vertebrobasilar circulation, to separately examine large and small aneurysms, those of the anterior communicating artery and those of the middle cerebral artery, those treatments for which one antiplatelet has been prescribed rather than another, and so forth. However, all these remarks also apply to coil treatment, and there have been only 2 published meta-analyses on that topic in the 27 years that they have been in clinical use. Why is that?

When a treatment has convinced a discipline of its efficacy and relative safety, meta-analyses are not necessary. There is no meta-analysis concerning usefulness of antibiotic treatment in pulmonary tuberculosis.

This overabundance of meta-analyses expresses the desire to convince physicians and patients of the benefits of this implant. Quantity makes quality. Most meta-analyses (as well as most case series) on flow diversion report a cumulative morbidity/mortality rate of 10% or so, as if this was the normal price to pay for “otherwise untreatable” aneurysms. The argument that flow diversion should fill a therapeutic void is not supported by the number of units used between 2 interventional neuroradiologist centers that treat roughly the same number of aneurysms per year. The regulatory status of implants allows them to be used in indications different from those for which they were initially presented to the health authorities (at least in Europe). Thus, large and giant aneurysms of the carotid siphon, the initial indication for flow diverters, are now only an excuse to extend their use in the treatment of small or even very small aneurysms in multiple other locations, and to “accept” the 10% complication rate without balancing this risk with the one of other management options, including observation. The apparent aim of multiplying meta-analyses may finally be to replace the unquestionable methodologic evaluation, ie, the randomized controlled trial.

The financial crisis to which our insurance systems are subject will probably force health authorities to no longer offer reimbursement for expensive devices if they have not been subjected to rigorous evaluation. While waiting that, we can bet that we will still have the opportunity to read a new meta-analysis about flow diverters in the near future.

● E. Houdart

Service de Neuroradiologie  
Hôpital Lariboisière  
Paris, France

<http://dx.doi.org/10.3174/ajnr.A6594>